

Nitruration gazeuse de l'acier à outil M2 pour amélioration des propriétés mécaniques de surface des molettes de roulage

Yanxue Zhang

▶ **To cite this version:**

Yanxue Zhang. Nitruration gazeuse de l'acier à outil M2 pour amélioration des propriétés mécaniques de surface des molettes de roulage. Autre. HESAM Université, 2022. Français. ⟨NNT : 2022HESAE064⟩. ⟨tel-03986410⟩

HAL Id: tel-03986410

https://pastel.hal.science/tel-03986410v1

Submitted on 13 Feb 2023

HAL is a multi-disciplinary open access archive for the deposit and dissemination of scientific research documents, whether they are published or not. The documents may come from teaching and research institutions in France or abroad, or from public or private research centers.

L'archive ouverte pluridisciplinaire **HAL**, est destinée au dépôt et à la diffusion de documents scientifiques de niveau recherche, publiés ou non, émanant des établissements d'enseignement et de recherche français ou étrangers, des laboratoires publics ou privés.



HAL Authorization

HESAM UNIVERSITÉ

Arts et Métiers Sciences et Technologies

ÉCOLE DOCTORALE SCIENCES DES MÉTIERS DE L'INGÉNIEUR

Laboratoire MSMP-EA7350 – Campus de Aix En Provence

THÈSE DE DOCTORAT

présentée par : **Yanxue ZHANG**

soutenue le : **08 décembre 2022**

pour obtenir le grade de : **Docteur d'HESAM Université**

préparée à : **École Nationale Supérieure d'Arts et Métiers**

Spécialité : Mécanique - Matériaux

Gas nitriding of M2 high-speed steel to improve the surface mechanical properties of rolling die

THÈSE dirigée par :

Laurent BARRALLIER

et co-encadrée par :

Sébastien JÉGOU, David MERCS

Jury

M. Phillipe JACQUET, Enseignant chercheur (HDR), ECAM LYON	Président
M. Mathieu RENOUF, Docteur (HDR), LMGC, Université de Montpellier	Rapporteur
M. Thomas CHRISTIANSEN, Associate Professeur, Technical University of Denmark	Rapporteur
M. David MERCS, Docteur, LISI Automotive	Examinateur
M. Sébastien JÉGOU, Maître de Conférence, MSMP, ENSAM	Examinateur
M. Laurent BARRALLIER, Professeur des Universités, MSMP, ENSAM	Examinateur

THÈSE

CONTENTS

Contents **I**

List of figures **V**

List of Tables **XV**

1 Introduction **1**
1.1 Context . . . 1
1.1.1 Screw-nut unit in EPB system . . . 1
1.1.2 Thread rolling process of EPB screw . . . 2
1.1.3 Problelms of rolling dies and possible solutions . . . 3
1.2 Objectives and outline . . . 5

2 Bibliography **7**
2.1 Steel Surface Engineering . . . 7
2.1.1 Application of tool steels . . . 7
2.1.2 Surface engineering of steels . . . 7
2.1.3 Nitriding and nitrocarburizing . . . 8
2.2 Nitriding . . . 9
2.2.1 Phase diagram . . . 9
2.2.2 Crystal Structures of iron and iron nitrides . . . 11
2.2.3 Microstructure and properties of nitriding layers . . . 12
2.2.4 Nitriding kinetics . . . 13
2.2.5 Nitriding process . . . 19
2.3 The growth of nitriding layer . . . 22
2.3.1 Compound layer formation and growth . . . 22
2.3.2 Diffusion zone . . . 25
2.4 The hardness and residual stress evolutions during nitriding . . . 29
2.4.1 Phase transformation and volume expansion . . . 29
2.4.2 Residual stress . . . 30
2.4.3 Hardness . . . 34
2.5 Materials performance of nitrided steel . . . 38
2.5.1 Fatigue life and Wöhler curves . . . 38
2.5.2 Fatigue resistance . . . 38
2.5.3 Tribological behavior . . . 39

2.6 High-speed steels (HSS) and their heat treatment . . . 40
2.6.1 High-speed steels . . . 40
2.6.2 Carbide and microstructure transformation during steel manufacturing and heat treatments . . . 41
2.7 Nitriding of M2 high-speed steels . . . 51
2.7.1 Microstructure and properties of nitriding layers in M2 steel . . . 51
2.7.2 Precipitation evolution in high-speed steels during nitriding . . . 52
2.7.3 The mechanical behaviors of the nitrided layer of M2 high-speed steels 54
2.7.4 Effect of initial microstructure on nitriding . . . 56
2.7.5 Effect of surface condition on nitriding . . . 57
2.7.6 High-speed steel nitriding in duplex treatment . . . 58
2.8 Rolling contact failure and Dang Van criterion for nitrided steels . . . 59
2.8.1 Mechanism of Rolling contact failure . . . 59
2.8.2 Rolling contact fatigue and Dang Van criterion . . . 61
2.8.3 Nitriding effect on the Dang Van criterion along the paths . . . 62

3 Equipment and methodologies 65
3.1 Chemical analysis by Optical Emission Spectrometry (OES) . . . 65
3.2 Optical microscopy . . . 65
3.3 Scanning electron microscopy . . . 66
3.4 Hardness measurement . . . 66
3.5 Residual stress . . . 66
3.6 Roughness measurement . . . 67
3.7 Thermogravimeter and nitriding process . . . 67

4 Study on rolling dies 69
4.1 Analysis of the rolling die material . . . 69
4.1.1 Chemical composition . . . 69
4.1.2 Microstructure of rolling die E0-1.2 . . . 70
4.1.3 Hardness . . . 72
4.1.4 Residual stress in die . . . 72
4.2 Study on the nitriding conditions of 10 rolling dies . . . 73
4.2.1 Chemical composition . . . 73
4.2.2 Microstructures of the nitriding layers of the rolling dies . . . 75
4.2.3 Hardness . . . 80
4.2.4 N and C concentration profiles . . . 83
4.2.5 Residual stress profile . . . 84
4.3 Failure observation on rolling die . . . 85
4.3.1 Failure mechanism on the thread rolling die . . . 89
4.4 Numerical study on the rolling process . . . 91
4.4.1 Simulation analysis . . . 91
4.5 Conclusions . . . 98

5 Study on gas nitriding of M2 steel 101
5.1 Characterization of samples before nitriding . . . 101
5.1.1 Initial surface conditions of the M2 samples . . . 101
5.1.2 Microstructure of hardened and tempered M2 steel sample . . . 104
5.1.3 Microhardness . . . 105
5.2 The effects of sample surface condition on nitriding . . . 108

5.2.1 Surface condition and the homogeneity of nitriding 108
5.2.2 The effect of surface finishing method on nitriding 110
5.3 Preliminary study on gas nitriding kinetics of M2 steel and the properties of the nitriding layer 113
5.3.1 Mass variation during nitriding treatment 113
5.3.2 Microstructure of nitriding layer 114
5.3.3 The phase transformation and nitrogen concentration in M2 steel (Thermo-Calc) 115
5.3.4 Chemical and mechanical gradient in the nitriding layer 115
5.4 Pseudo Lehrer diagram study 117
5.4.1 Calculation and prediction of the nitriding potential at α/γ' limit in the pseudo-Lehrer diagram for M2 steel 117
5.4.2 Mechanical surface treatment effect on nitriding 118
5.4.3 Experimental study on α/γ' limit in pseudo-Lehrer diagram for M2 steel 122
5.4.4 Mass variation during nitriding 123
5.4.5 Gas nitriding kinetics in M2 steel-Nitriding time effect 124
5.4.6 Nitriding potential effect 131
5.4.7 Nitriding temperature effect 132
5.4.8 Thermo-calc analysis 134
5.5 Nitriding parameters optimization for mechanical behavior of the rolling die 136
5.5.1 Nitriding effect on core hardness 136
5.5.2 Comparison to the nitriding profiles in the rolling die 137
5.6 Conclusions 139

6 Wear resistance of nitrided M2 steel 141
6.1 Experiment set-up 141
6.1.1 Pressure and sliding speed 141
6.1.2 Wear measurement set-up calculation 142
6.1.3 Ball on disk wear systems 143
6.1.4 Wear measurements 144
6.2 Wear study on M2 steel 145
6.2.1 Wear of M2 disk 145
6.2.2 Wear of M2 ball 151
6.2.3 Conclusions of the wear on non-nitrided M2 steel 158
6.3 Effect of nitriding on the wear resistance of M2 steel 160
6.3.1 Wear of nitrided M2 disk 160
6.3.2 Wear on nitrided M2 ball 167
6.4 Conclusions 171

7 Conclusions and perspectives 173
7.1 Conclusions 173
7.2 Perspectives 175

Appendices 177

A Thermo-Calc analysis: phase transformations in M2 steel during nitriding 178

B The contact configurations **194**

C The wear profiles on M2 balls. **196**

Bibliography **207**

LIST OF FIGURES

1.1 Screw-nut unit in EPB system [8]. 2
1.2 Schematic microstructure of rolled and cut threads [10]. 2
1.3 Comparison of rolled and cut threads [10]. 3
1.4 Illustration of thread rolling process with round dies: (a) two rolling dies, (b) three rolling dies [13]. 3
1.5 Typical failures on the rolling die of EPB (photos are from Lisi automotive). 4
1.6 Closer view of the failures on the rolling die thread from LISI Automotive. 4
1.7 The plan of the approach implemented during the thesis. 5

2.1 Classification of surface engineering [27]. 8
2.2 Phase diagram of Fe-C system [31]. 9
2.3 Phase diagram of Fe-N system [38]. 10
2.4 Tentative phase diagram of Fe-N-C system [43]. 10
2.5 Comparison of experimental composition data for ε-Fe_3N phase and several attempts to model the Fe-N-C phase diagram [44]. 11
2.6 The crystal structure of different forms of iron (a) α-Fe, (b) γ-Fe, (c) δ-Fe, (d) ε-Fe [45]. 11
2.7 The crystal structure of different forms of iron nitrides (a) FeN, (b) Fe_2N, (c) Fe_3N, (d) Fe_4N [45]. 12
2.8 Nitrides in the compound layer and their crystallographic structure [49]. . 13
2.9 A structure of compound layer where γ'-Fe_4N and ε-Fe_3N phase coexist (ε-Fe_3N phase: light grey; γ'-Fe_4N phase: dark grey) [51]. 13
2.10 Lehrer diagram (a)Nitriding potential, K_N, (b)Nitrogen activity, a_N [35]. . 15
2.11 Relation between the iron/nitrogen equilibrium diagram and concentration/depth for growth of a bilayer ε-Fe_3N phase and γ'-Fe_4N phase into a substrate α-Fe [56]. 17
2.12 Schematic of plasma nitriding of a gear [58]. 20
2.13 Schematic illustration of gas nitriding [91]. 21
2.14 Schematic illustration of formation of compound layer [92]. 22
2.15 Model of compound layer growth [36]. 23
2.16 Cross section of Fe-Cr-Mo-V alloy nitrided at 550 °C for 5 h with $K_N = 0.1$ $atm^{-1/2}$ [94]. 24
2.17 DC region in Fe-1.81 at%Cr-0.25 at.%Mo alloy nitrided at 580 °C for 72 h with $K_N = 0.1$ $atm^{-1/2}$ [93]. 24

2.18 Fe-1 at.% Mo alloy nitrided at 480 °C for 2 h with $K_N = 0.7$ atm$^{-1/2}$ [95]. 24
2.19 Nitrogen and carbon profiles in Fe-3%Cr-0.35%C after gas nitrided at 550 °C [97]. 25
2.20 Microstructure of (a)Fe and (b) Fe-0.4C nitrided at 460 °C for 65 h, with $K_N = 6.6$ atm$^{-1/2}$ [44]. 25
2.21 Enthalpy (kJ/mol) of formation of the carbides and nitrides [105, 102]. . . 26
2.22 TEM micrograph from a carbon film replica of the nitrided layer at depth=200 μm [104]. 26
2.23 Scheme of the Baker-Nutting crystallographic orientation relationship [104]. 27
2.24 TEM micrograph from a thin foil of semi-coherent CrN precipitates at depth = 200 μm -Zone axis [100] [104]. 27
2.25 Nitrogen concentration profiles on the cross-section of plasma nitrided layer for plain carbon steel with 0.02 wt.% and alloy steels containing 1 wt.% alloying content [110]. 28
2.26 Structure of nitrided case (schematic), concentration distribution of nitrogen [51]. 28
2.27 Quenched and tempered 24CrMo13, salt bath nitrided at 580 °C for 2 h [36]. 29
2.28 Specific volumes of nitrides and carbides for low alloyed steels [113]. 30
2.29 Schematic evolution of volume fraction of carbides and nitrides of low alloyed steel during nitriding [113]. 30
2.30 Schematic evolution of (a) volume expansion and (b) residual stress during nitriding of low alloyed steel [113]. 31
2.31 Schematic relationship between residual stress and microstructure expansion [113]. 31
2.32 Results of nitriding model in case of Fe-C-3%Cr nitrided 10h above, 100 h below [115]. 33
2.33 Precipitation strengthening curve. 35
2.34 Schematic illustration of precipitates impede dislocation motion [148]. . . . 35
2.35 The net effect of increasing the precipitates size on the hardness [152]. . . . 36
2.36 Microstructure and hardness profile of the case of gas nitrided (a) 16MnCr5 and (b) C15, slow cooling conditions [51]. 36
2.37 The hardness distributions on the cross-section of plasma nitrided layer for plain carbon steel with 0.02 wt.% and alloy steels containing 1 wt.% alloying content [110]. 37
2.38 Profiles of hardness and residual stresses in nitrided case of steel 17CrMoV10, 31CrMoV9, and X40CrMoV5, nitrided at 570 °C for 32 h [111]. . . 37
2.39 Woodvine analysis of carburized steel fatigue specimens, predicting subcase/surface origin of failure [111]. 39
2.40 Fatigue failure of the nitrided bar without stress concentration [171]. . . . 39
2.41 Wear resistance of nitrided layers as a function of distance from surface [111]. 40
2.42 The thermal process routine of high-speed steel from the manufacturing to the final heat treatment (The time and temperature information for heat treatment is from ASTM A600 [184].). 42
2.43 Austenite dendrites and eutectic M_2C carbides distributed in the interdendritic region when the cooling rate is (a) 0.6 K/s and (b) 11.5 K/s [211]. . 43
2.44 Carbides in as-cast M2 steel [228]. 43

2.45 (a) schematic diagram of sampling for casting microstructure analysis, (b)area fraction of carbide in the different samples of the M2 steel billets, (c) the grain size at different positions in the sand and continuous casting billets [208]. 44
2.46 SEM micrographs of M_2C in M2 cast ingots after heating at 1150 °C for 1 h: (a) lamellar M_2C, sand mould, (c) rod-like M2C, iron mould. (b) and (d) TEM photography corresponding to (a) and (c) separately [211]. 44
2.47 (a) as-forged to show strain distribution; (b),(c) optical micrographs of points A,B in (a); and (d) strain distribution [232]. 46
2.48 Microstructure of the annealed steel (HVEM) [206]. 46
2.49 Dilatograms of M2 heated from as-quenched state at the rate of 0.05 °C/s [236]. 47
2.50 Continuous heating transformation (CHT) diagram of M2 steel [236]. . . . 48
2.51 Heat treatment sequence of high-speed steels [209]. 48
2.52 Three-dimensional reconstruction of an isothermally hardened sample, distribution of (a) carbon, (b) tungsten, (c) vanadium, and (d) molybdenum atoms [209]. 49
2.53 Three-dimensional reconstruction of a single continuously tempered sample (a) carbon, (b) tungsten, (c) vanadium, (d) molybdenum distribution, and (e) vanadium and molybdenum 6.5 at.% iso-concentration surface [209]. . . 49
2.54 Microstructure of steel after hardening and tempering [206]. 50
2.55 (a)Plate-shaped secondary carbide MC in M2 steel, 5nm. (b)Rod-shaped secondary carbide M_2C in ASP23 steel, 200 nm [177]. 50
2.56 Schematic graph of the nitriding layer of M2 steel. 51
2.57 Residual stress after nitriding, 560 °C for 6h, dissociation degree about 30% [123]. 52
2.58 Schematic nitrogen and carbon profiles in M2 high-speed steel after gas nitriding. 53
2.59 XRD pattern of M2 and CPN (conventional plasma nitriding) treated at various temperature for 4 h with H_2:N_2 = 75%:25% [23]. 54
2.60 (a) Surface roughness, (b)in-depth residual stress distribution, (c) wear lost volume of M2 steel after RF plasma nitriding different plasma gas compositions [119]. 56
2.61 Cross-sectional hardness-depth profiles for M2 steel, A-Nit is a fully annealed sample, T-Nit represent hardened and tempered sample (nitriding at 450 °C for 8 hours with a plasma portion N_2:H_2=25%:75%) [67]. 57
2.62 Schematic cross-sectional view of a surface showing the surface and subsurface layers [24]. 58
2.63 (a) Depth profiles of nitrogen plasma nitriding at 500 °C with 5 vol.% N_2, 5 mbar for different nitriding times [114]. (b) Residual stress depth profiles for polished and sandblasted sample non-nitrided and plasma nitrided at 400 and 500 °C with 5 vol.% N_2 [275]. 59
2.64 Mechanism of rolling contact fatigue (a) when fatigue initiation is at the subsurface, (b) when fatigue initiation is at the surface [314]. 60
2.65 Schematic of the shear stress τ as a function of depth below the free surface, (a) for sliding, (b) for rolling [312]. 60
2.66 Sphere/plane evolution of the maximum shear and its depth [317]. 61
2.67 The stresses on the surface in the direction of the tangential sliding force [317]. 61

2.68 A shakedown map for a general three-dimensional rolling-sliding contact [289, 318]. 62
2.69 Endurance domain and two typical local loading paths Γ_1 and Γ_2 [285]. . . 63
2.70 The Dang Van diagram: a scheme of typical calibration with bending and torsion fatigue test [286]. 63
2.71 Hardness and residual stress effect on Dang Van criterion. 64

3.1 Inductive gauge in the profilometer [328]. 67
3.2 Schematic diagram of the thermobalance. 68

4.1 Small pieces are taken from die E0-1.2. 70
4.2 Microstructure of the die thread under optical microscopy. 70
4.3 Microstructure of the cross-section of the die thread under SEM. 71
4.4 Microstructure of the die thread surface under SEM. 71
4.5 EDS analysis of die E0-1.2. 71
4.6 Hardness map on rolling die E0-1.2. 72
4.7 Hardness profiles from the surface to in-depth on rolling die E0-1.2. 72
4.8 (a) stress tensor profiles and (b) the equivalent stresses from the surface to in-depth on the flat side of rolling die E0-1.2. 73
4.9 Rolling die samples to be characterized (10 pieces from 10 rolling dies). . . 74
4.10 The thread conditions of the 10 rolling die samples. 74
4.11 Chemical analysis on the die surface. 76
4.12 Microstructure of rolling die G2-0.33 under an optical microscope. 76
4.13 Microstructure of die E2-0.16 under an optical microscope. 77
4.14 Microstructure of rolling die (a) E3-1 and (b) E1-0.13 under optical microscope. 77
4.15 Locally non-homogeneity of nitriding treatment on E3-1. 78
4.16 Microstructure of rolling die (a) E4-0.82 and (b) E5-0.51 under an optical microscope. 78
4.17 Microstructure of rolling die (a) E2-0.16 and (b) G2-0.33 under SEM. . . . 79
4.18 Microstructure of die G1-0.15 under SEM (a) lower magnification with the carbide segregation marked with blue dot lines, (b) higher magnification, non-smooth surface. 79
4.19 Microstructure of dies under SEM (a) E1-0.13 thread surface has no compound layer or cracks, (b) E2-0.16 thread surface presents compound layer and cracks. 80
4.20 Microstructure of E3-1 under SEM. 80
4.21 Hardness profiles of two types rolling dies at the thread surface. 81
4.22 Hardness of the base material of two types rolling dies. 81
4.23 Hardness profile of G rolling dies. 82
4.24 Hardness profiles of rolling die E1-0.13 and E3-1 from the thread surface and the flat surfaces to in-depths. 83
4.25 Hardness profiles of rolling die G1-0.15 and G2-0.33 from the thread surface and the flat surfaces to in-depths. 83
4.26 N concentration profiles of the rolling dies 84
4.27 C profiles of the rolling dies. 84
4.28 residual stress profile of the rolling dies. 85
4.29 Failures rolling die E0-1.2. 85
4.30 The similar failures on the tread of die E0-1.2. 86

4.31 Some failure types in the failure on the tread of die E0-1.2: (a) scales, (b) plastic deformation, (c) cracks along the carbides bands, (d) some marks looks like beach mark and brittle failure at the carbide segregation. 87
4.32 Cracks propagation in the failure on the tread of die E0-1.2 (a) top view of the thread crest, (b) side view along the crack. 87
4.33 Sample preparation by cutting the thread in the middle of the failure along the red line. 88
4.34 Cross-section of the failure. 88
4.35 Cracks in the circles 1, 2 and 3 in Figure 4.34. 88
4.36 Cracks in circles 4, 5 and 6 in Figure 4.34. 89
4.37 The damage on the crest surface next to the right border of the failure. . . 90
4.38 Some failures on the flank surface of the tread of die E0-1.2 (a) surface wear and (b) cracks. 90
4.39 Cross-section of the thread. 91
4.40 Sketch of thread rolling process with two round dies [13]. 92
4.41 3D diagram of the FEM. 92
4.42 3D diagram of the modeling focusing on the thread forming. 92
4.43 Tresca-Hydrostatic stresses for all elements from step 0 to step 26. 93
4.44 The 106 points in the fatigue zone after doubling the fatigue strength. . . . 94
4.45 The localization of the 106 elements where fatigue could occur, (a) global localization on the whole rolling die, (b) the specific localization on the teeth. 94
4.46 The hydrostatic and Tresca stress profile along the path starting from the crest of the thread to in-depth. 95
4.47 Dang Van criterion along path 1 as given by Figure 4.46. 95
4.48 Distance from Tresca-Hydrostatic stress curve to Dang Van Line along path 1 in Figure 4.46. 95
4.49 The hydrostatic and Tresca stress profile along different paths. 96
4.50 Dang Van criterion along path 4 starting from the valley to in-depth. . . . 96
4.51 Nitriding profile of M2 steel sample nitrided at 540°C for 5 hours under nitriding potential 3.7 $atm^{-1/2}$, (a) hardness profile, (b) residual stress profile. 96
4.52 Dang Van criterion of path 1 in rolling process modified with a nitriding profile. 97
4.53 Distance from the modified stress curve to the modified Dang Van line as a function of depth along path 1. 97
4.54 Distance from the stress curve to the Dang Van line as a function of depth along (a) path 2, (b) path 3. 98
4.55 The nitriding conditions and the lifetime of the observed dies. 99

5.1 M2 steel samples (a) ground surface, (b) sandblasted surface, (c) polished surface, (d) annealed sample with the milled surface. 102
5.2 Surface analysis of M2 steel samples (a) sandblasted surface, (b) ground surface. 102
5.3 Surface roughness profiles (using the same scale) of M2 steel samples (a) ground surface, (b) sandblasted surface, (c) polished surface, (d) annealed sample with the milled surface. 103
5.4 Surface roughness analysis of (a) ground surface, (b) sandblasted surface, (c) polished surface, (d) annealed sample with the milled surface. 103
5.5 Carbide bands in the hardened and tempered M2 steel sample (cross-section view). 104

5.6 Micrographs of (a) the cross-section (the carbide bands are observed parallel) and (b) the surface (no carbide band is observed because they are perpendicular to the surface). 105
5.7 Hardness near the surface (a) the hardness at each measurement, (b) the mean value at the same depth from the surface. 106
5.8 Carbon concentration as a function of depth in M2 sample. 106
5.9 Indents at (a) carbide band 1, (b) carbide band 2, (c) matrix. 106
5.10 Hardness mapping before and after etching 106
5.11 Hardness measurement with Knoop indenter. 107
5.12 Knoop indentations on the sample with the highest hardness. 107
5.13 Hardness of AISI M2 steel and corresponding hardening and temperature (considering 1 h× 2 tempering) [329]. 108
5.14 Surface of ground M2 samples after nitriding. 108
5.15 Microstructure and hardness of nitrided M2 steel sample with a ground surface. 109
5.16 Hardness profiles at different locations of ground M2 sample after nitriding. 109
5.17 Nitrided Surface of M2 samples with (a) initially ground surface, (b) 1200 grade polished surface. 110
5.18 Microstructure of the compound layer of nitrided M2 steel with surface polished 1200 grade under the optical microscope. 110
5.19 Microstructure of the compound layer of nitrided M2 steel with surface polished 1200 grade under SEM. 110
5.20 EDS analysis of the contaminated zone on the ground surface of M2 sample. 111
5.21 Nitrided Surface of M2 samples with one side 1200 grade polished and another side a sandblasted, (b) ground and (c) mirror polished. 111
5.22 Microstructure of the nitrided sample with the 4 different surface conditions under the optical microscope. 112
5.23 Mass variation during nitriding of M2 sample with different surface conditions 112
5.24 Hardness profile from the surface to in-depth of M2 sample after nitriding with different surface conditions 113
5.25 Initial residual stresses in the ferritic matrix under the surface. 113
5.26 Mass variation during nitriding at different temperatures or with different nitriding potential of M2 steel sample. 114
5.27 Microstructure of nitriding layer of M2 steel samples nitrided at 540 °C for 5 h with a nitriding potential (a) $K_N = 3.7\ atm^{-1/2}$, (b) $K_N = 0.5\ atm^{-1/2}$. 114
5.28 Phase transformation diagram of M2 steel (with carbon concentration 0.8%) as a function of N concentration at 500 °C 115
5.29 Surface to in-depth profile of M2 steel after gas nitriding with $K_N = 0.5\ atm^{-1/2}$ at different temperature (a) N/C profile, (b) residual stress, (c) hardness profile. 116
5.30 The in-depth profile of M2 steel after gas nitriding at 540 °C with different nitriding potential (a) N/C profile, (b) residual stress, (c) hardness profile. 117
5.31 The definitions of the surfaces of the sample. 119
5.32 Microstructure of the cross-section of the M2 sample after nitriding at 500 °C with $K_N = 1\ atm^{-1/2}$ for 5 hours (a) from the main front surface, (b) from the small side surface. 119
5.33 Microstructure of the nitriding layer in M2 steel sample nitrided at 500 °C with $K_N = 1\ atm^{-1/2}$ for 5 hours. 119

5.34 Surface microstructure of the M2 sample after nitriding at 500 °C with K_N = 1.2 $atm^{-1/2}$ for 5 hours. 120
5.35 Surface microstructure and EDS analysis of the M2 sample after nitriding at 500 °C with K_N = 1.2 $atm^{-1/2}$ for 5 hours. 120
5.36 Optical micrograph of the M2 sample surface after nitriding at 500 °C with K_N = 1.2 $atm^{-1/2}$ for 5 hours. The red arrow marks the polishing direction. 121
5.37 The surface roughness on the M2 sample before nitriding (μm). 121
5.38 The roughness profiles on the M2 sample surface in the direction transversal to the polishing path. 122
5.39 Nitriding parameters studied and the definition of the α/γ' limit for M2 steel (CL: compound layer). 124
5.40 Comparison of the α/γ' limit in the Lehrer diagram for pure iron and M2 steel. 124
5.41 Mass variation during nitriding with different parameters as a function of time. 125
5.42 Mass variation during nitriding as a function of different nitriding parameters. 125
5.43 Microstructure of the nitriding layer in M2 steel sample nitrided at 500 °C with K_N = 1 $atm^{-1/2}$ for 10 hours. 126
5.44 Grain boundary cementite in nitrided M2 steel. 126
5.45 Layer depth as function of the square root of nitriding time (T=500 °C, K_N = 1 $atm^{-1/2}$). 127
5.46 N and C concentration profile as function of nitriding depth (T=500 °C, K_N = 1 $atm^{-1/2}$). 128
5.47 Hardness profile as function of nitriding depth (T=500 °C, K_N = 1 $atm^{-1/2}$). 129
5.48 Residual stress profile of the M2 sample nitrided for 5 and 15 hours (T=500 °C, K_N = 1 $atm^{-1/2}$). 129
5.49 The schematic diagram of the evolution of N/C concentration and residual stress as a function of time at the surface and in-depth. 131
5.50 Nitriding profiles of M2 steel (520 °C, 0.5 $atm^{-1/2}$, 5-50 h) 132
5.51 Nitriding profiles of M2 steel (500 °C, 0.8 $atm^{-1/2}$, 5-50 h) 133
5.52 Chemical and mechanical gradient in the M2 sample nitrided at 500 °C for 15 hours with nitriding potential 0.5, 0.8 and 1 $atm^{-1/2}$. 134
5.53 Hardness profile in the M2 sample nitrided with different nitriding parameters. 135
5.54 Chemical and residual stress profile in the M2 sample nitrided at for 5 hours with nitriding potential 1 $atm^{-1/2}$, (a) N/C profile, (b) residual stress. . . . 135
5.55 Phase composition as function of depth of the M2 sample after nitriding at 500 °C with K_N = 0.8 $atm^{-1/2}$ for 15 hours. 136
5.56 The core hardness of M2 samples nitrided at two temperatures as a function of nitriding time 137
5.57 Hollomon Jaffe T-t relations in tempering steels 137
5.58 The relation between the tool lifetime and nitriding profile. 138
5.59 The best nitriding profile among the rolling die specimen the close profiles in M2 samples 138

6.1 Sliding speed (in mm/s) and normal stress (in MPa) distribution (from the FEM result). 142
6.2 Sliding speed (in mm/s) and normal stress (in MPa) values on different locations of the threads. 142

6.3 Hertz theory of ball/disk contact. 143
6.4 Roughness measurement on the spindle and rolling die thread (2D profiles are measured with Surfascan 3D). 144
6.5 (a) the measurement set-up for the wear measurement, (b) the pin/disk contact, (c) the lubricant system. 144
6.6 The moment equilibrium of force 145
6.7 The M2 disk used to study the wear parameters. 145
6.8 The friction coefficient as a function of the number of cycles. 146
6.9 The mean friction coefficient of the sapphire ball/M2 disk measurements (the measurements details see in Table 6.1). 147
6.10 The wear analysis on the M2 disks (the measurements details see in Table 6.1.) 148
6.11 The wear on the M2 disk after the measurement SM04 (23.4 N, 1 Hz, 10 h). 149
6.12 The wear on the M2 disk after the measurement SM05 (79 N, 1 Hz, 10 h). 149
6.13 The wear on the rolling die thread crest. 150
6.14 The sapphire balls after the wear measurement (a) SM05, (b) SM06. 150
6.15 The wear on M2 disk after the measurement SM06 (23.4 N, 1 Hz, 2h). . . . 150
6.16 The powder produced on M2 disk after measurement SM06 (23.4 N, 1 Hz, 10h). 151
6.17 The microstructure of M2 steel ball used during wear measurements, (a) in the cross-section, (b) on the surface. 152
6.18 The friction coefficient of the M2 ball/EPB disk wear measurements. . . . 153
6.19 The wear depth measurements on the EPB disks. 154
6.20 The M2 balls after wear measurements. 155
6.21 The wear on the M2 balls under SEM. 156
6.22 The adhesion wear on M2 balls after wearing under 79 N on EPB disk for 4 hours. 156
6.23 EDS analysis on the transferred film (the adhesion wear), corresponding to the zone in the red square in Figure 6.22. 157
6.24 Formation and removal of a transfer particle [175, 348]. 157
6.25 The measurement on the wear track of M2 ball ME01 (23.4 N, 14h), (a) on the sliding direction, (b) transversal direction. 157
6.26 The wear track profile on the sliding direction of M2 ball ME01 (23.4 N, 14h). 158
6.27 The wear measurement of M2 ball ME01 (23.4 N, 14 h) on the direction perpendicular to the sliding. 158
6.28 The wear profile on the sliding direction of M2 ball ME03 (42 N, 4 h). . . . 159
6.29 The wear profile on the sliding direction of M2 ball ME02 (79 N, 4 h). . . . 159
6.30 3D view of the wear on M2 ball ME03 (42 N, 4h). 160
6.31 Linear profiles on the wear on M2 ball ME03 (42 N, 4h). 160
6.32 The nitriding profiles of the M2 disk (the profiles are measured on other equivalent nitrided M2 steel samples) used for wear measurements (a) hardness, (b) residual stress. 161
6.33 The friction coefficient as a function of wear cycle on the nitrided M2 disk. 162
6.34 The damage on the sapphire balls after wear measurements. 163
6.35 The M2 sample disk used to study the nitriding effect. 163
6.36 The wear track profiles on the non-nitrided and nitrided M2 disks. 164
6.37 The microphotograph of the nitrided M2 disks after wear measurements. . 165
6.38 The surface wear on the flank of the rolling die thread. 166

6.39 The EDS spectrum of the particle found on the M2 disk after the wear measurement. 166
6.40 The microstructure of nitriding layer of M2 ball (a) under an optical microscope, (b) under SEM. The nitriding parameter is 500 °C-5 h-0.8 $atm^{-1/2}$. 167
6.41 The in-depth hardness profile of nitrided M2 balls and M2 sample. 168
6.42 The wear profiles on the EPB disks. 168
6.43 The observation of the wear on the M2 balls under SEM (a) with secondary electron, (b) with back-scattered electron. 169
6.44 The friction coefficient as a function of wear cycle (nitrided M2 balls on the EPB disk). 169
6.45 The wear profiles on the M2 ball nitrided with 500 °C-15 h-0.8 $atm^{-1/2}$. . . 170
6.46 The 3D view of the wear on the M2 ball nitrided with 500 °C-15 h-0.8 $atm^{-1/2}$.171
6.47 The 3D view of the wear on the M2 ball nitrided with 520 °C-5 h-0.5 $atm^{-1/2}$.171

A.1 Phase transformation diagram of M2 steel (with carbon concentration 0.8%) as a function of N concentration at 500 °C 178
A.2 Carbides transformation diagram of M2 steel (with carbon concentration 0.8%) as a function of N concentration at 500 °C 179
A.3 Nitrides transformation diagram of M2 steel (with carbon concentration 0.8%) as a function of N concentration at 500 °C 179
A.4 Phase transformation diagram of M2 steel (with carbon concentration 0.8%) as a function of N concentration at 520 °C 180
A.5 Phase transformation diagram of M2 steel (with carbon concentration 0.8%) as a function of N concentration at 540 °C 180
A.6 Phase transformation diagram of M2 steel (with carbon concentration 0.9%) as a function of N concentration at 500 °C 181
A.7 Phase transformation diagram of M2 steel (with carbon concentration 0.9%) as a function of N concentration at 520 °C 181
A.8 Phase transformation diagram of M2 steel (with carbon concentration 0.9%) as a function of N concentration at 540 °C 182
A.9 Phase composition in the nitriding layer of M2 steel as a function of depth (nitriding: 500 °C-10 h-1 $atm^{-1/2}$) 182
A.10 Chemical composition in each phase in the nitriding layer of M2 steel as a function of depth (nitriding: 500 °C-10 h-1 $atm^{-1/2}$) 183
A.11 Phase composition in the nitriding layer of M2 steel as a function of depth (nitriding: 500 °C-15 h-0.5 $atm^{-1/2}$) 184
A.12 Chemical composition in each phase in the nitriding layer of M2 steel as a function of depth (nitriding: 500 °C-15 h-0.5 $atm^{-1/2}$) 185
A.13 Phase composition in the nitriding layer of M2 steel as a function of depth (nitriding: 500 °C-15 h-0.8 $atm^{-1/2}$) 186
A.14 Chemical composition in each phase in the nitriding layer of M2 steel as a function of depth (nitriding: 500 °C-15 h-0.8 $atm^{-1/2}$) 187
A.15 Phase composition in the nitriding layer of M2 steel as a function of depth (nitriding: 500 °C-15 h-1 $atm^{-1/2}$) 188
A.16 Chemical composition in each phase in the nitriding layer of M2 steel as a function of depth (nitriding: 500 °C-15 h-1 $atm^{-1/2}$) 189
A.17 Phase composition in the nitriding layer of M2 steel as a function of depth (nitriding: 520 °C-5 h-0.8 $atm^{-1/2}$) 190

A.18 Chemical composition in each phase in the nitriding layer of M2 steel as a function of depth (nitriding: 520 °C-5 h-0.8 $atm^{-1/2}$) 191
A.19 Phase composition in the nitriding layer of M2 steel as a function of depth (nitriding: 520 °C-5 h-1 $atm^{-1/2}$) 192
A.20 Chemical composition in each phase in the nitriding layer of M2 steel as a function of depth (nitriding: 520 °C-5 h-1 $atm^{-1/2}$) 193

B.1 3 types of contact for measuring wear rate. 194
B.2 Dimensions of the pin and disk for wear rate measurement. 195

C.1 The wear profiles on the M2 ball nitrided with 500 °C-5 h-0.8 $atm^{-1/2}$ (3D plot). 196
C.2 The wear profiles on the M2 ball nitrided with 500 °C-15 h-0.8 $atm^{-1/2}$ (3D plot). 197
C.3 The wear profiles on the M2 ball nitrided with 520 °C-5 h-0.5 $atm^{-1/2}$ (3D plot). 197
C.4 The wear profiles on the M2 ball nitrided with 520 °C-15 h-0.5 $atm^{-1/2}$ (3D plot). 198
C.5 The wear profiles on the sliding direction of M2 ball ME01 (23.4 N, 14 h). 199
C.6 The wear profiles on the sliding direction of M2 ball ME03 (42 N, 4 h). . . 200
C.7 The wear profiles on the sliding direction of M2 ball ME02 (79 N, 4 h). . . 201
C.8 The wear profiles on the M2 ball nitrided with 500 °C-5 h-0.8 $atm^{-1/2}$. . . 202
C.9 The wear profiles on the M2 ball nitrided with 500 °C-15 h-0.8 $atm^{-1/2}$. . . 203
C.10 The wear profiles on the M2 ball nitrided with 520 °C-5 h-0.5 $atm^{-1/2}$. . . 204
C.11 The wear profiles on the M2 ball nitrided with 520 °C-15 h-0.5 $atm^{-1/2}$. . . 205

LIST OF TABLES

2.1 Crystal structure and composition ranges of Fe-N-C phases [36]. 12
2.2 Lattice parameters (a, b, c), specific volume, and volume misfit ($\frac{\Delta v}{v}$) between the precipitates and the pure ferrite matrix, for various alloying element nitrides and carbides. As the initial carbides owe complex composition, the information of single element carbides crystal structure is given. The specific volume and volume expansion are calculated with the data from the database [133] if not marked. The volume expansion is calculated with the method in [134]. 33
2.3 Chemical composition of M2 high-speed steel (wt.%) 41
2.4 Chemical composition of primary carbides of M2 high-speed steel (A sample made by powder metallurgical process and hot rolled into 20 mm diameter bar, subsequently austenitized 3 min in a salt bath at 1220 °C, step quenched into molten salt at 550 °C, for 10 min followed by air cooling through the Ms temperature (about 200 °C) to room temperature, 3 times of 1-hour tempering with intermediate air cooling) [203]. 50
2.5 Chemical composition of secondary carbides in M2 high-speed steel (The iron content in all precipitates has been set to zero because of the difficulty of accurately measuring the iron content. In reality, all precipitates contain a small amount of iron, typically 5% of the metal content, and consequently a somewhat lower carbon content) [177]. 50

4.1 Chemical composition of rolling die E0-1.2 (wt.%). 69
4.2 Details given of rolling die samples. 74
4.3 Chemical composition of rolling dies on the surface and in the core (wt.%). The standard deviation for each element on the equivalent measured areas is close and given with one value. 75
4.4 Results from microstructure and hardness analysis on the rolling dies. . . 82

5.1 Chemical composition of M2 steel samples (wt.%). 101
5.2 3D roughness of the four measured surfaces. 102
5.3 Parameters studied and the corresponding compound layer (CL) conditions. 123

6.1 Wear measurements of Sapphire ball/M2 steel disk. 147
6.2 The two EDS spectrums analyzed in the powder produced on the M2 disk during the wear measurement SM06. 151

6.3 M2 ball/EPB disk (23MnB6 steel) wear measurements. 152
6.4 Wear measurements on nitrided M2 steel disks. 163
6.5 Wear measurements on nitrided M2 steel balls. 168

CHAPTER 1
INTRODUCTION

1.1 Context

This Ph.D. thesis is dedicated to the requirement of LISI Automotive for improving the working performance of the thread rolling die used for forming EPB (electric parking brake) screws with a spindle that has a hardness higher than 400 HV10 after quenching and tempering. Innovating since 1777, LISI Automotive is an international enterprise specializing in the design and production of quick-fastening automotive assembly solutions and safety-critical components.

1.1.1 Screw-nut unit in EPB system

Brake-by-wire systems are installed in different vehicles nowadays [1]. The benefits of this system include weight reduction, increased cabin space, complete access to vehicle dynamics control, and environment-friendly design [2]. An EPB system is a kind of electromechanical brake-by-wire system which generates a parking force by using an electric motor torque instead of manual pressure. Therefore, it can be used to replace the conventional lever parking system [3]. EPB system responds quickly and over a large force range using the electrical system. Compared to the traditional parking brake, EPB has several additional functions, such as dynamic braking, anti-lock braking, key-out application, hill hold, and drive-away release [4, 5]. By simply pushing a button, a user can easily apply or release the parking brake, making it possible to apply a full braking load on highly inclined surfaces quickly.

EPB system maintains the desired braking force steadily even after the power is off. To reach this requirement, a screw-nut system is introduced to provide a self-locking function. In the screw-nut unit, the screw is strictly connected to the rotor, the angular displacement of the screw can be transformed to the nut, which can therefore generate a clamping or pulling force [6, 7, 5, 2].

Figure 1.1 shows a screw-nut system. During the braking process, the screw rotates under the torque provided by the motor. At the same time, the nut moves forward or backward in the axial direction. The nut can then push or release the braking disk to control the movability of the vehicle. However, the mechanical contact between the screw and nut must be strictly controlled. Stable mechanical properties for the two parts, especially on the threads, such as high toughness, good wear resistance, and high fatigue

strength, are thus required.

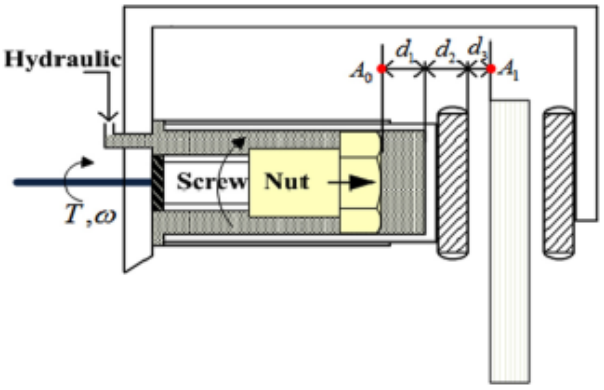


Figure 1.1 – Screw-nut unit in EPB system [8].

1.1.2 Thread rolling process of EPB screw

Threads on the fasteners in automobiles can be made in several ways, for example, grinding, machining, and cold rolling. Grinding and machining produce threads by removing material and shaping the rest. Unlike machining, thread rolling is a cold forging forming method where a matched pair of rolling dies having the reverse form of threads are used. The blank material is displaced by simultaneous radial penetration of the dies to form the threads with no chips produced, no material is wasted [8]. The first advantage of threads rolling is the process efficiency (productivity and economy) since 100% of the raw material is used. The second advantage is that the work hardening generated during the rolling process strengthens the threads (the rolling process is after heat treatment), as shown in Figure 1.2. In addition, the rolling process can provide a smoother finishing surface on the thread, leaving no cutting marks. This improves assembly quality between the screw and the nut, and reduces the wear rate between the mating parts, offering them a better working performance [9].

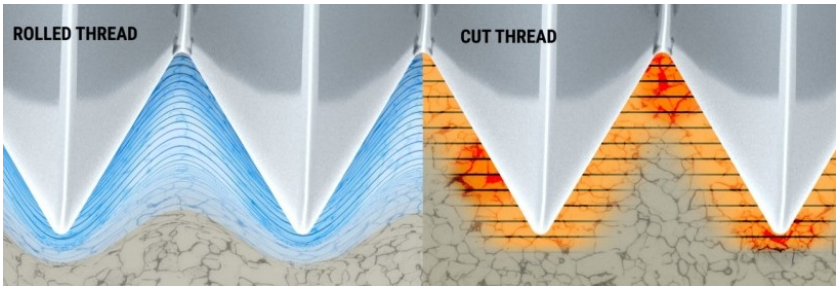


Figure 1.2 – Schematic microstructure of rolled and cut threads [10].

Figure 1.3 compares the threads obtained from rolling and cutting processes. To reach the same thread profile, a smaller blank diameter is required when using rolling process. In other words, the same blank can be transferred to a threaded fastener with a larger diameter by rolling process, leading to less material cost [11]. Consequently, thread rolling has virtually eliminated thread cutting as a competitive technique for fasteners produced in quantity [12].

There exist rolling processes with two or three rolling dies (Figure 4.40). This work concerns the rolling process with two rolling dies. The workpiece is placed on a support,

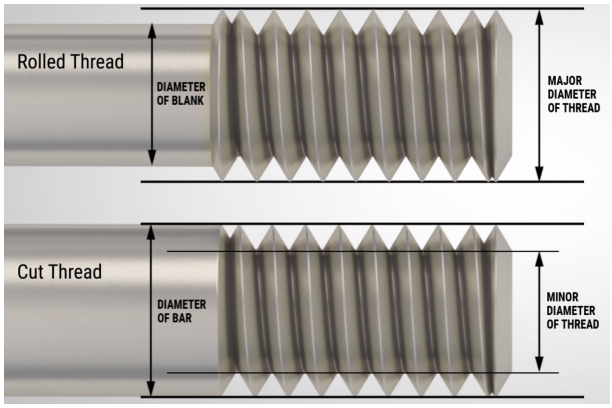


Figure 1.3 – Comparison of rolled and cut threads [10].

and at least one rolling die has a feed movement to perform the forming process. Simultaneously, the dies rotate synchronously in contact with the workpiece, then the profile will be formed. Infeed thread rolling is based on one parameter: the workpiece lead is equal to the rolling die lead. In other words, no axial displacement occurs to rolling dies or the workpieces. This results in a synchronic rotational movement of part and dies. The thread diameter, length, and process speed define the required rolling force.

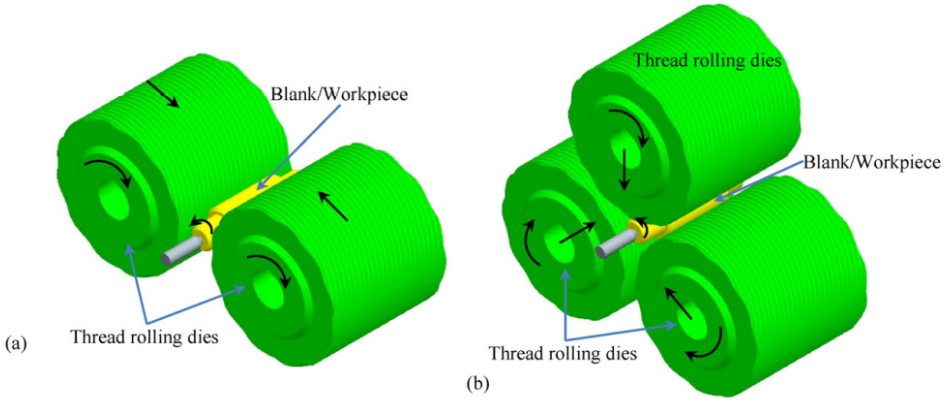


Figure 1.4 – Illustration of thread rolling process with round dies: (a) two rolling dies, (b) three rolling dies [13].

1.1.3 Problelms of rolling dies and possible solutions

In the automobile industry, fasteners and bolts demand increasingly higher durability and reliability, which has led to the use of higher-strength materials such as high-strength steel, stainless steel, and pre-heat treated steel [14]. Especially, as a safety mechanical component, the screw in the EPB system requires higher assurance. Consequently, higher-level hardness of rolling dies is demanded.

Manufacturers face the problem of a short lifetime and premature failures of their thread rolling dies. The frequent replacement of rolling dies reduces productivity by losing the service time of the rolling machine, and the associated cost of the rolling dies will directly affect the cost of the EPB screw [15].

High-speed steel materials have been widely used for extrusion, blanking, molding, and punching thanks to their mechanical properties, including high hardness, high wear

resistance, excellent toughness and high-temperature properties [16, 17, 18]. To increase the lifetime of the rolling dies, along with finding a suitable combination of hardness and toughness by adjusting the heat treatment parameters, surface properties such as wear resistance, tribological behavior, and fatigue are other factors with great importance to work with [16, 19].

According to the industrial experience, the failure can be especially found at the thread start (the beginning or end of the thread on the edge of the die) of the thread rolling dies, as shown in Figure 1.5 (a). Figure 1.5 (b) shows the failure on the thread in the body of the rolling die. These failures are in series. Once the first failure occurs, it will be copied to another location on the rolling die by the cyclic rolling of the workpiece. A clearer view of the failures on the die is shown in Figure 1.6, the failures located on the crests of the threads with a length of more than 1 mm.

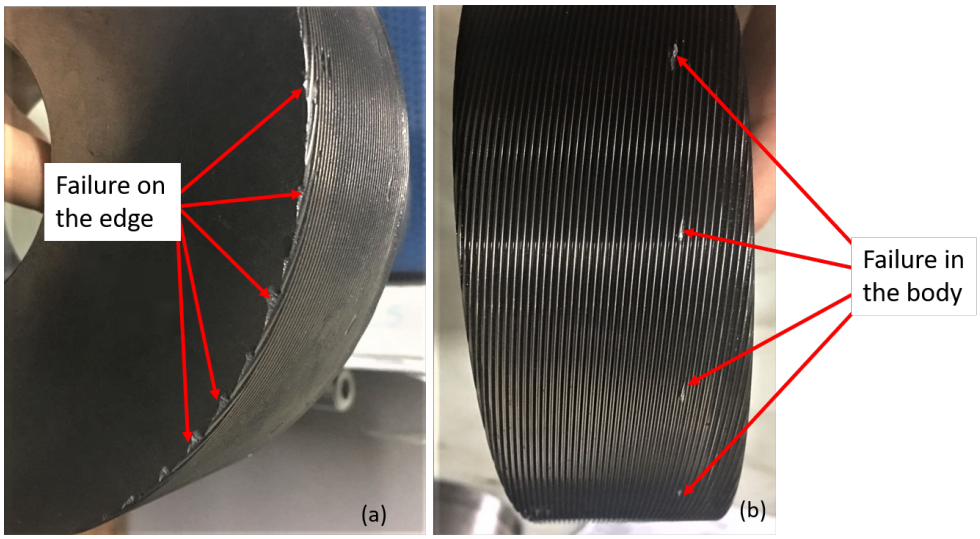


Figure 1.5 – Typical failures on the rolling die of EPB (photos are from Lisi automotive).

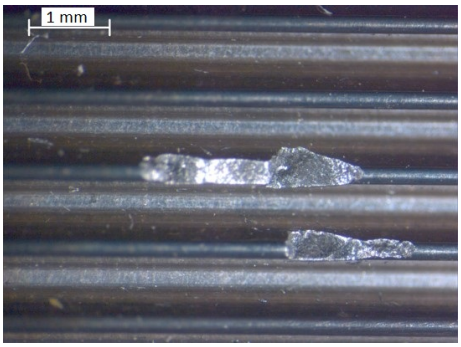


Figure 1.6 – Closer view of the failures on the rolling die thread from LISI Automotive.

In surface engineering, nitriding (nitrocarburization, if a carbon-delivering medium is also added) is one of the most used industrial processes to increase the resistance of steels against plastic deformation and fatigue [20, 21]. Plasma nitriding has been widely applied to tool steels to modify surface properties. But the special geometry of threads can lead to a different bombardment rate of plasma on the surface. Thus defects or a non-homogeneous nitriding layer will be formed. In this case, plasma nitriding could be replaced by gas nitriding.

1.2 Objectives and outline

On the one hand, the objectives of this work are to study the evolution of the mechanical failures on the rolling die by characterizing the actual failed rolling dies, and to analyze the load applied to the system with a FEM (Finite Element Modelling) of the rolling process. On the other hand, this work aims to investigate the gas nitriding kinetics on the die material concerning surface strengthening and optimize nitriding parameters. Eventually, the results of this work will help to define optimized gas nitriding parameters and transfer them to the industrial scale for effectively improving the production efficiency of the thread rolling process.

The first part of the thesis is the literature review, where the knowledge concerning nitriding, M2 steel, and the relation between the microstructure and mechanical properties can be found. The following chapter illustrates the methodology and devices in the experimental study. The results of this work will be given and discussed in the following chapters, as shown in Figure 1.7. The characterization of the actual rolling dies and

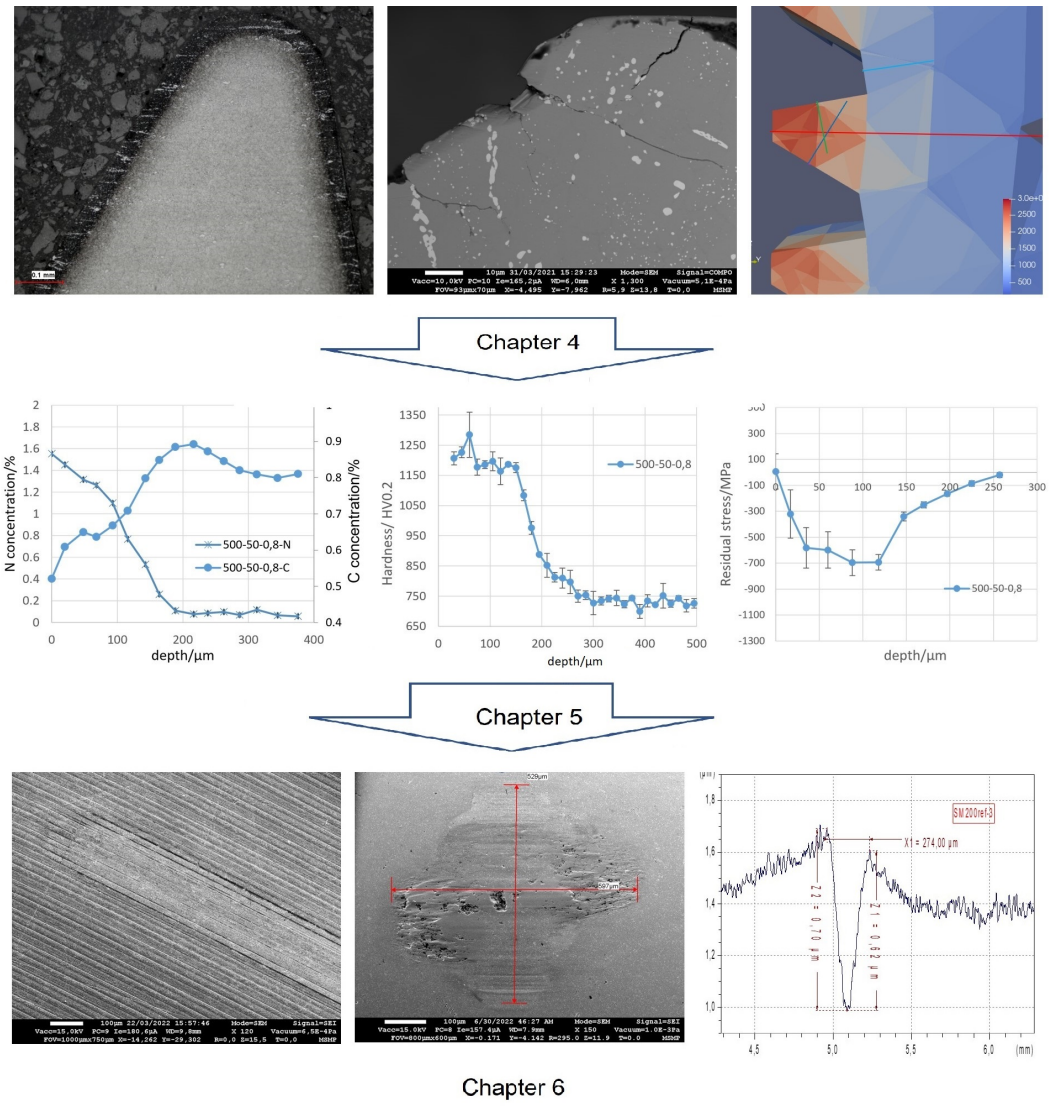


Figure 1.7 – The plan of the approach implemented during the thesis.

the simulation analysis of the rolling process will be firstly introduced to recognize the

current situation and the complication encountered. In the next chapter, the kinetics of gas nitriding in M2 steel and the consequent mechanical properties of the material will be detailed. Finally, the impact of nitriding on the wear resistance of the studied steel will be demonstrated.

CHAPTER 2
BIBLIOGRAPHY

2.1 Steel Surface Engineering

2.1.1 Application of tool steels

Steels have many practical applications in various aspects of life. For instance, in the metal-mechanical industries, low carbon steel, with favorable properties such as good toughness, flexibility and ductility for producing goods, is often used to manufacture mechanical components which are used in daily life, such as screws, automobile body panels, tin plates, wire products, etc... However, sometimes wear and battering on the steel surface occurs, surface treatment is then needed to improve its properties [22]. Tool steels are often used for cold forging or machining in which other materials, generally softer than the cutting tools, are cut or deformed. The forming tools are usually subjected to non-lubricated or lubricated working conditions, where their useful life is limited by surface damage during sliding contact, compromising the final quality of the products [23]. Most of engineering component failures in practice are surface-initiated through mechanisms such as fatigue cracking, stress corrosion cracking, fretting wear, excessive abrasive or adhesive wear, corrosion, erosion, etc. [24].

These mechanisms of surface degradation generally involve mechanical interaction of material components considered with loads imposed by the environment, and corrosion which is mainly due to chemical interaction [23, 25]. To achieve the intrinsic surface properties, surface engineering was born and developed up to recent a significant number of surface engineering process variants to tailor the possible combination of structural or functional properties in use [26].

2.1.2 Surface engineering of steels

Surface engineering aims to modify the microstructure of the surface and near-surface region to improve the function and serviceability, offering different properties from the bulk of the material [27]. Surface engineering practices generally involve either microstructural modification, compositional changes, or both. Figure 2.1 depicts a brief classification of surface engineering practices used in metallurgical industries. Suitable heat treatment is often applied to modify microstructure [28]. An extensive range of processes includes transformation hardening and surface texturing, carburizing, nitriding, anodizing, electroplating, weld hard facing, thermal spraying, and physical vapor deposition (PVD),

covering most of materials [27].

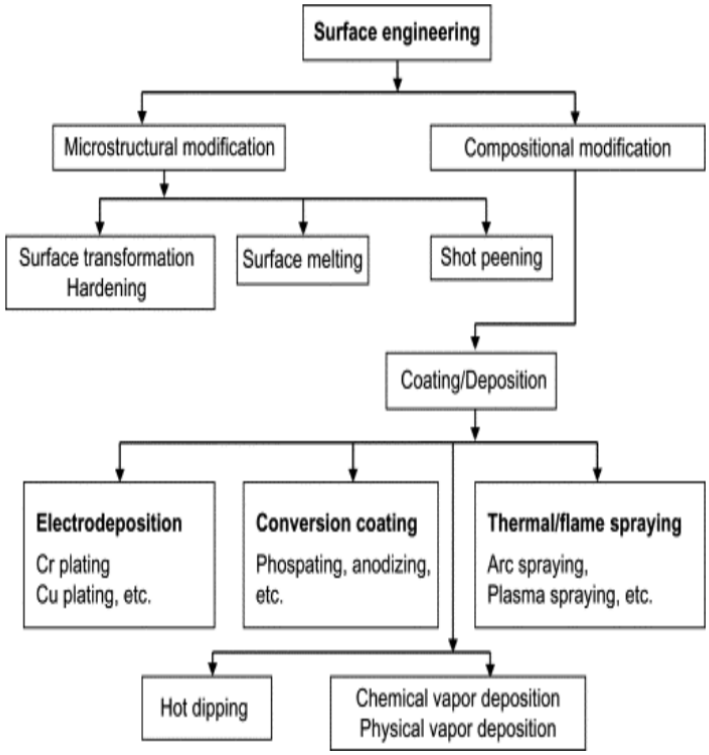


Figure 2.1 – Classification of surface engineering [27].

However, from the beginning, the thermochemical processes dominate surface engineering, which are accomplished by thermally activated chemical reactions on the material's surface. During these processes, one or more components are supplied by an appropriate environment, such as a gas, a plasma, a salt bath, etc. Dissolution happens to the externally supplied components onto the material surface, followed by thermally activated interdiffusion. The chemical composition near the surface is changed, leading to a desired microstructure modification. Phase transformations are possibly but not necessarily accompanied [26].

Both carburizing and nitriding are commonly applied thermochemical treatments for case hardening [26]. The application dictates whether nitriding or carburizing should be the process. In this study, the thread rolling die is a precision component, of which the deformation during the treatment can be a significant consideration. Nitriding is the appropriate choice because the subsequent quenching of carburizing increases the possibility of distortion of the component.

2.1.3 Nitriding and nitrocarburizing

Nitriding and nitrocarburizing of steels are carried out at a relatively low temperature, at least 30 degrees lower than steel tempering temperature, to not lose the toughness of the bulk material [29]. And they are essentially applied to ferritic steels. Moreover, since the nitriding process is carried out at a low temperature below Ac1 (Figure 2.2) where no phase transformation occurs, deformation caused by phase transformation will be limited [30]. Nitriding and nitrocarburizing are considered the most versatile surface engineering

treatments available and are widely applied today. They can be carried out in many ways according to the specification of the parts.

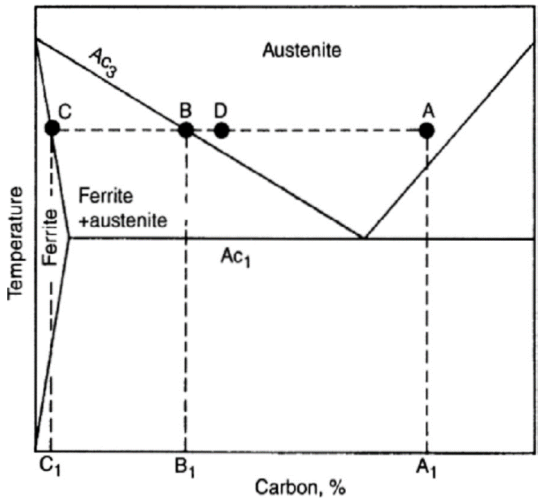


Figure 2.2 – Phase diagram of Fe-C system [31].

Along with carburizing and boriding, nitriding involves the dissolution of interstitials into the host materials and brings a hard and well-wear-resistant surface layer onto the steel surface [32, 33, 34].

2.2 Nitriding

2.2.1 Phase diagram

2.2.1.1 Fe-N phase diagram

Nitriding is a phase transformation-dominated process. Although it becomes easier to predict and analyze the relation between the phase and chemical composition in different steels, the Fe-N binary phase diagram helps strongly to understand the phase revolution in the ferritic matrix as N concentration varies. Figure 2.3 is the experimental iron-nitrogen binary phase diagram at 'normal' 1 atm pressure, which shows the phase stability regions as a function of temperature and nitrogen concentration. The eutectoid temperature is around 590 °C. Nitriding is generally carried out below 590 °C to avoid any allotropic transformation and possible distortion of parts during cooling. The nitrogen solubility in α-Fe is 0.1 wt.%. When the nitrogen content reaches 5.75 wt.%, the γ'-Fe_4N is first developed. After a narrow region, the ε-Fe_3N phase is formed [35, 36, 37].

2.2.1.2 Fe-C-N phase diagram

Pure Fe shows a low hardness and is insufficient for most real applications. With the addition of carbon, the material becomes more capable of forming complex components with a more interesting microstructure. However, the presence of carbon induces some differences in phase transformations and stabilities of the Fe-N system. Fe-N-C diagram then needs to be understood.

Naumann and Langenscheid [39] firstly published a phase stability diagram for iron powder nitrocarburized in flowing NH_3-H_2-CO gas mixture and part of the ternary Fe-N-C phase diagram. However, there is not enough experimental data to support the accuracy

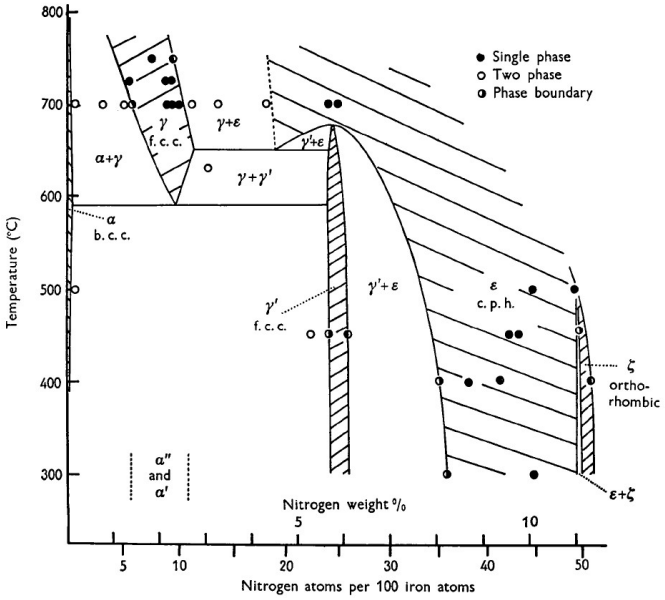


Figure 2.3 – Phase diagram of Fe-N system [38].

of this phase diagram. Figure 2.4 shows a tentative phase diagram of the Fe-N-C system calculated using Thermo-calc at 570 °C. Figure 2.5 shows the comparison of experimental composition data and several calculations of the boundary of ε-Fe_3N phase [40, 41, 42].

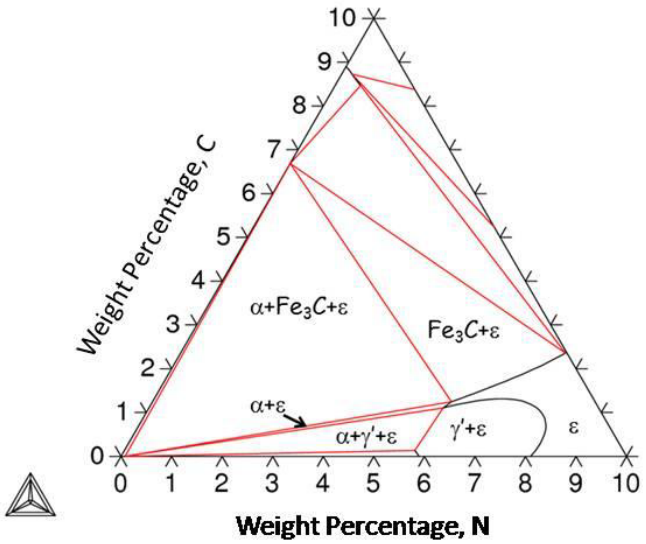


Figure 2.4 – Tentative phase diagram of Fe-N-C system [43].

From these phase diagrams, γ'-Fe_4N phase is first formed when the carbon content is relatively low, and it coexists with the ε-Fe_3N phase when carbon concentration is above the limit (0.4 wt.% in Figure 2.5). While the C content is higher than about 1.5 wt.% (Figure 2.5), the ε-Fe_3N phase is formed first, and a single ε-Fe_3N phase can be developed by controlling the nitrogen and carbon content. On the other hand, cementite ϑ-Fe_3C exists when carbon has a higher content. To conclude, controlling the steel's carbon content can help modify the phase composition of the iron nitrides.

Decarburization is found during nitriding due to low carbon activity in the gas atmosphere. Sometimes carbon is introduced during nitriding (this method is also called

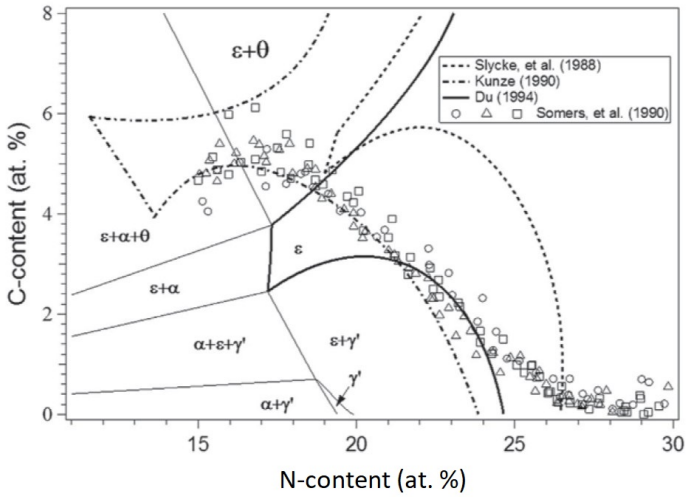


Figure 2.5 – Comparison of experimental composition data for ε-Fe_3N phase and several attempts to model the Fe-N-C phase diagram [44].

nitrocarburizing) for low-carbon steel or simply for overcoming decarburizing [29].

2.2.2 Crystal Structures of iron and iron nitrides

Figure 2.6 shows the different iron crystal structures. They exist at different temperature ranges and can transform into others when the temperature changes. In the early 1950s, iron nitrides like Fe_3N, Fe_4N, etc., started to be studied systematically [38]. And they are getting more attention in recent years due to their extraordinary properties such as anti-abrasion, anti-corrosion and anti-oxidant.

Crystal structures of FeN, Fe_2N, $Fe_{(2-3)}N$, and Fe_4N are shown in Figure 2.7 [45]. In ε-Fe_3N phase (Figure 2.7 (c)), the iron atoms arrangement is close-packed hexagonal. In ideal ε-Fe_3N phase, there are two nitrogen atoms closest to every iron atom, and nitrogen atoms occupy one-third of the octahedral interstices of the layered iron atoms. With more octahedral interstices occupied, the ratio of Fe:N will decrease from 3 to 2 [46, 38, 47, 45].

The γ'-Fe_4N phase (Figure 2.7 (d)) has a face-centered cubic close packing of iron atoms. The nitrogen atoms keep the same distance from each other and occupy one-fourth of the number of octahedral interstices in a completely ordered manner [48].

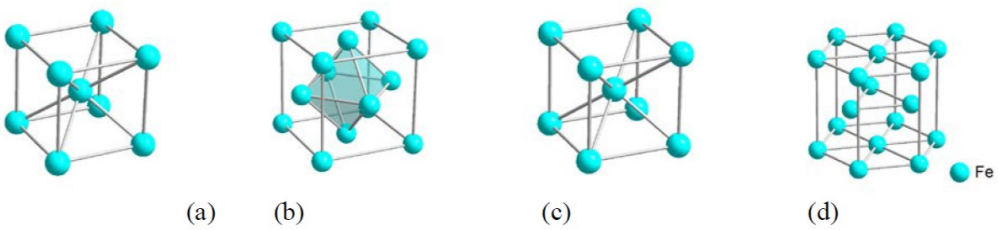


Figure 2.6 – The crystal structure of different forms of iron (a) α-Fe, (b) γ-Fe, (c) δ-Fe, (d) ε-Fe [45].

Table 2.1 summarizes the phases often formed during nitriding of Fe-C alloys [36]. The formation of ε-Fe_2N_{1-z} and γ'-Fe_4N_{1-x} phases produces a certain layer called compound layer at the surface, which significantly modifies the surface properties, more detail will be given in the following sections.

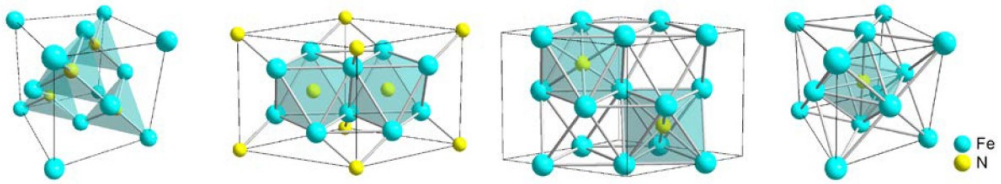


Figure 2.7 – The crystal structure of different forms of iron nitrides (a) FeN, (b) Fe_2N, (c) Fe_3N, (d) Fe_4N [45].

Table 2.1 – Crystal structure and composition ranges of Fe-N-C phases [36].

phase	**crystal structure**	**nitrogen content** at.%	**Carbon content** at.%
α-Fe[N,C]	Body-centered cubic Fe,N and C disordered in octahedral interstices	<0.4	<0.1
γ-Fe[N,C]	Face-centered cubic Fe N and C disordered in octahedral interstices	<10.3	<9.1
α"-$Fe_{16}N$	Body-centered tetragonal Fe sublattice N ordered in octahedral interstices	∼ 12.5(vacancies)	···
γ'-Fe_4N_{1-x}	Face-centered cubic Fe sublattice N ordered in octahedral interstices	19.4-20	<0.7
ε-$Fe_3(N,C)_{1+y}$	Hexagonal close-packed Fe sublattice N and C more or less ordered in octahedral interstices	15-33	<8
Θ-Fe_3C	Orthorhombic Fe sublattice C in bicapped trigonal prisms	∼ 0	25

2.2.3 Microstructure and properties of nitriding layers

The nitriding layer mainly consists of a compound layer and a diffusion zone (see Figure 2.8), below that is the core material.

During nitriding, the nitrogen first fills up the interstitial spaces of α-Fe. In steels containing carbon and alloy element M (M = Cr, V, Mo...), the alloy nitridesMN_n are often formed due to the high chemical affinity between these alloy elements M (M = Cr, Mo, V...) and nitrogen. The carbon may lead to the formation of cementite Fe_3C. When the nitrogen solubility limit is reached in α-Fe, the diffused nitrogen expands the iron lattice and forms complex compounds with iron atoms. The layer is called the compound layer, also known as the white layer, due to its color under optical microscopy [29]. The compound layer consists mainly of iron nitrides, with a thickness that can reach tens of micrometers. It comprises sublayers of ε-Fe_3N phase and γ'-Fe_4N phase. On top of the compound layer, the porous layer may be formed due to the inherent metastability of iron nitrides at 0.1 MPa concerning Fe and N_2, [50]. It can also contain oxides and sulfides, depending on the process.

The well-defined ε-Fe_3N phase and γ'-Fe_4N phase sublayer structure can be replaced by a mixture of both in the steel because of the existing carbon. Figure 2.9 shows a structure of the compound layer where γ'-Fe_4N and ε-Fe_3N phase coexist, pores are also very clear near the surface [51]. The thickness of the compound layer depends on the alloying elements, nitriding time, and temperature. The compound layer can reach a very high hardness and greatly improve the wear and corrosion resistance [52].

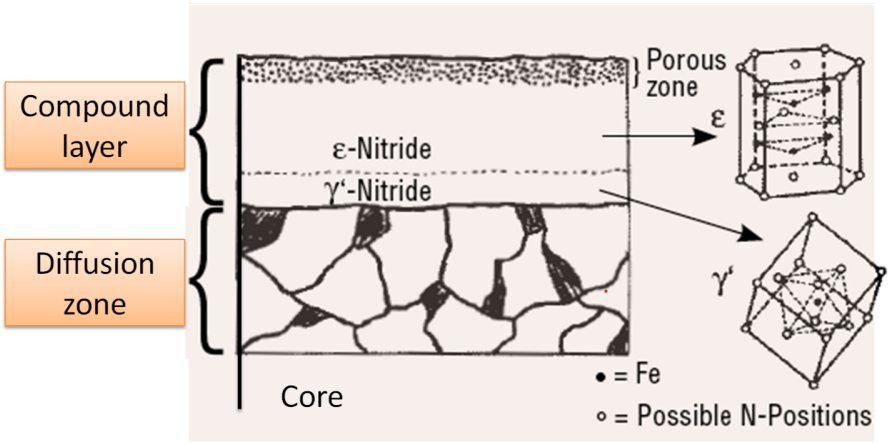


Figure 2.8 – Nitrides in the compound layer and their crystallographic structure [49].

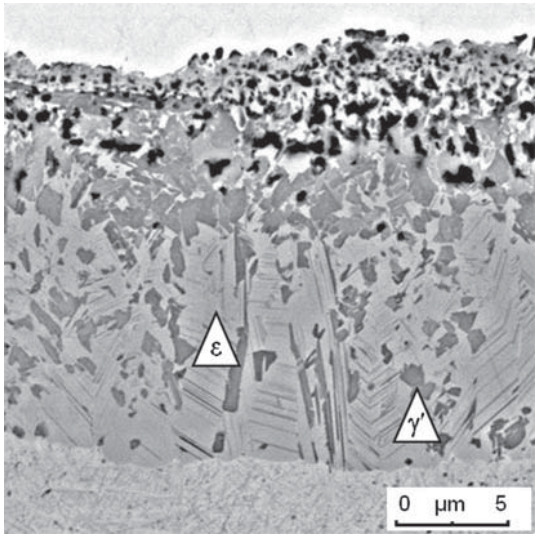


Figure 2.9 – A structure of compound layer where γ'-Fe_4N and ε-Fe_3N phase coexist (ε-Fe_3N phase: light grey; γ'-Fe_4N phase: dark grey) [51].

In the diffusion zone, the nitrogen dissolves interstitially in the ferrite lattice and alloy nitrides are formed in steels. The expanded lattice and dispersed nitrides precipitate immobilize the dislocations. The steel surface is therefore hardened [53]. The hardened diffusion zone is relatively more responsible for the considerable enhancement of fatigue endurance due to the high compressive residual stress level and high hardness [54]. The thickness of the diffusion zone can be several hundred microns, and it can be explained as the mixture of the original microstructure with some solid solution and precipitated nitrides [55].

2.2.4 Nitriding kinetics

2.2.4.1 Interactions at solid/gas interface in gas nitriding

As a thermo-chemical treatment, diffusion of nitrogen and precipitation are always the core in any nitriding case. Generally, nitriding can be explained by three phenomena [54, 56]:

— NH_3 transfer from the nitriding atmosphere to the surface of solid,

— chemical reaction at the surface including NH_3 ammonia dissociation (depends on the partial pressure) and nitrogen adsorption and desorption (depends on the total gas flow rate),

— adsorbed nitrogen diffuses, and the nitrides layer grows.

These processes can occur at the same time. The NH_3 decomposes at a temperature below 590 °C which is defined by both the half-life time of ammonia at such temperature following its decomposition and no allotropic transformation in the steel. As shown in Figure 2.13, the adsorption and diffusion of nitrogen in steel occurs via the dissociation of ammonia at the surface:

$$NH_3 \rightarrow N_{ad} + \frac{3}{2}H_2 \tag{2.1}$$

Here N_{ad} represents nitrogen adsorbed by the material's surface. The nitrogen diffuses into the steel:

$$N_{ad} \rightarrow [N] \tag{2.2}$$

Here [N] indicates the nitrogen atoms diffused into the material. The formation of nitrogen gas:

$$N_{ad} + N_{ad} \rightarrow N_2 \tag{2.3}$$

The interaction between the atmosphere and steel surface is a combination of the dissociation rate of ammonia, adsorption of nitrogen and desorption of nitrogen at the steel surface [35, 36].

2.2.4.2 The interaction of the atmosphere and the steel surface in plasma nitriding

Plasma nitriding is the most popular industrial high-speed steel surface modification method due to the lower temperature and shorter process time required [57, 58, 59]. During plasma nitriding, nitrogen ions are formed and activated to impinge onto the surface of the steel. The interaction between ions and surface results in sample heating and sputtering, benefiting the nitrogen diffusion and impinging species to the steel surface [60].

4 steps of reactions could be summarized [29]:

— The energized electrons produce the ionized and neutral nitrogen atoms : $e^- \rightarrow N_2 = N^+ + N + 2e^-$.

— Iron and other contaminants are removed from the steel surface by the sputtering action: the impact of the nitrogen ions bombarding. This reaction helps nitrogen to diffuse into the steel.

— The formation of iron nitrides: Sputtered Fe + N = FeN, and at the same time, intensive surface cleaning of the workpiece occurs due to the sputtering on the surface.

— Continual plasma bombardment causes the instability of FeN at the steel surface, which then breaks down into the ε-phase, followed by the γ'-phase and an iron/nitrogen compound zone.

2.2.4.3 Nitriding potential and Lehrer diagram

The nitriding medium is generally a mixture of nitrogen and hydrogen. Thus it can have an extensive range of chemical potentials for nitriding as the composition varies, called nitriding potential or potential of nitrogen. On the other hand, the dissociation rate of ammonia is another critical parameter in understanding and controlling the nitriding process [35, 36].

For local equilibrium between N in the gas and N in the steel surface:

$$NH_3 \rightarrow [N] + \frac{3}{2}H_2 \tag{2.4}$$

Nitrogen activity can be deducted:

$$a_N = K\frac{P_{NH_3}P_0^{\frac{1}{2}}}{P_{H_2}^{\frac{3}{2}}} \tag{2.5}$$

The nitriding potential defines the nitridability of the atmosphere thermodynamically. For an atmosphere containing NH_3 and H_2 in gaseous nitriding, the nitriding potential can be deducted according to the reactions on the interaction surface (section 2.2.4.1):

$$k_N = \frac{P_{NH_3}}{P_{H_2}^{\frac{3}{2}}} \tag{2.6}$$

A nitriding potential diagram was determined by E. Lehrer experimentally for the first time in 1930, so the diagram is also called the 'Lehrer diagram.' Lehrer diagram depicts the phases stability in the case of pure iron nitriding, that is to say, the gas-solid phase diagram Fe-N is related to the nitriding potential k_N, the NH_3 content in the mixture and the temperature as shown in Figure 2.10 (a) [61]. Nitrogen activity and nitriding potential can be easily converted to each other mathematically. Figure 2.10 (b) depicts the stability of Fe-N phases as a function of nitrogen activity, a_N, nitrogen pressure and temperature. In both figures, there are four single-phase areas, and at the lines, two phases exist.

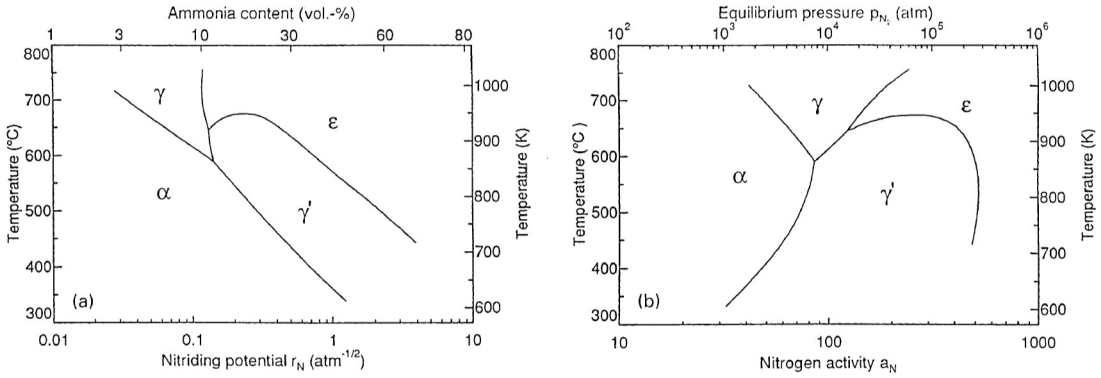


Figure 2.10 – Lehrer diagram (a)Nitriding potential, K_N, (b)Nitrogen activity, a_N [35].

To control the nitriding process, the critic is to define the composition and phase distribution at the surface of the steel, which can be realized by measuring and controlling the nitriding potential. For this reason, the Lehrer diagram is widely used. However, in Figure 2.10, the Lehrer diagram only shows phase stability for nitriding of pure iron concerning nitriding potential and temperature. The Lehrer diagrams for alloy steels have not been determined, essentially because the catalytic decomposition of ammonia would vary according to the chemical composition and surface microstructure of the considered steel grade. Misusing Figure 2.10 will lead to incorrect phase prediction [54].

To control the nitriding process and guarantee the nitriding quality, the nitriding potential of the nitriding atmosphere must be controlled and maintained at a certain value.

This can be reached by keeping the composition of gas mixture in the furnace at a certain ratio. In this case, it is impossible to have a stationary gas atmosphere due to the decomposition of ammonia, only the nitrogen rate at the exhaust of the furnace can be used to assume an estimation of the nitriding potential at the surface of the steel in the furnace. The flow rate and gas composition are set up to get the desired nitriding potential depending on the surface microstructure and the decomposition of ammonia (including the natural decomposition and the effect of the furnace walls and nitrided part) at the nitriding temperature [35, 36]. If the gas composition at the outlet is identical to that at the furnace entrance, one can say that the nitriding atmosphere has a fixed nitriding potential. To apply this approach, several conditions are required [36]:

— Equilibrium $NH_3 \rightarrow [N] + \frac{3}{2}H_2$ (combine (1) and (2)) is established instantaneously.

— All other potential gas components in the furnace act as inert gases.

— The developing iron-nitrogen phases in the nitrided zone of the solid have not yet reached the thermodynamic equilibrium.

However, the realistic case can hardly reach all the requirements. The deviation from the equilibrium may occur primarily in the initial stage [54].

2.2.4.4 Nitrogen diffusion kinetics

The nitriding process includes several steps. The diffusion of nitrogen atoms in the solid is the step much slower compared to others, so it is considered the controlling process. For a given set of nitriding parameters, α-Fe(N,C), ε-Fe_3N and γ'-Fe_4N phases are formed at the beginning of the treatment. But in the case of very low nitriding potential, the ε-Fe_3N and γ'-Fe_4N can not be formed [29]. Surface contamination also plays a role in the enrichment of nitrogen on the surface, and it can lead to the compound layer appearing after a certain time the diffusion zone grows [62].

The kinetics of nitriding layer growth can be described by the shift of the interfaces between the three phases α, ε-Fe_3N and γ'-Fe_4N because of the fluxes of nitrogen arriving at and leaving the interfaces are different [56]. The diffusion of nitrogen into iron or iron-based alloy steels is considered a development of interstitial solid solutions [34]. The diffusion flux of nitrogen is related to the corresponding concentration gradient by Fick's first law:

$$J = -D\frac{\partial c_N}{\partial x} \tag{2.7}$$

where c_N is the nitrogen concentration, in mol/m^3, x is the depth from the surface, and D represents the intrinsic diffusion coefficient of nitrogen in a certain phase. It's a function of temperature and is also affected by chemical bonding, type of solid solution, chemical composition, and crystal defects.

Fick's second law can be used to define the change of concentration with time and depth:

$$\frac{\partial c_N}{\partial t} = \frac{\partial}{\partial x}(D\frac{\partial c_N}{\partial t}) \tag{2.8}$$

Adopting these models to nitride layer growth, monolayer γ'-Fe_4N and bilayer ε-Fe_3N and γ'-Fe_4N have been derived in nitriding process for the pure iron [63] shown in Figure 2.11. According to the Fe-N phase diagram, at a certain nitriding temperature, the concentration of the current phase at a certain depth can be defined, so as the thickness of different layers.

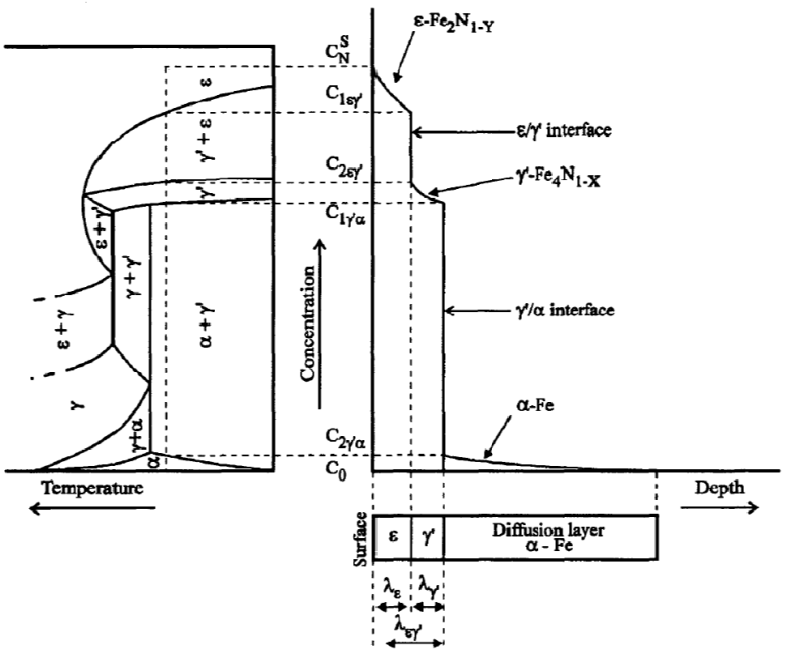


Figure 2.11 – Relation between the iron/nitrogen equilibrium diagram and concentration/depth for growth of a bilayer ε-Fe_3N phase and γ'-Fe_4N phase into a substrate α-Fe [56].

The diffusion of nitrogen in bcc ferrite is interstitial diffusion in a semi-infinite matrix. The diffusion coefficient of nitrogen can be assumed as independent of concentration, reflecting the small solubility range of nitrogen in ferrite, which is smaller by orders of magnitude than that of nitrogen or carbon in austenite [34].

Nitrogen diffusivity defines not only the nitrogen diffusion in the substrate but also the growth of nitrides. Silva and Mclellan have discovered that the diffusivity of C and N in ferrite at high temperature does not respect the classical diffusion formula [64]:

$$\ln D = \ln D_0 - \frac{Q}{kT} \tag{2.9}$$

instead, for carbon and nitrogen, the relation between the diffusivities lnD and temperature is given:

$$\ln D_C = -2.087 - \frac{1.19 \times 10^4}{T} + \frac{3.7 \times 10^5}{T^2} \tag{2.10}$$

and

$$\ln D_N = -4.485 - \frac{0.9979 \times 10^4}{T} + \frac{1.4 \times 10^5}{T^2} \tag{2.11}$$

carbon has a greater diffusivity in α-Fe than nitrogen, and the difference at higher temperatures is higher [64].

At 843 K, the nitrogen diffusion coefficient in α-Fe, ε-Fe_3N, γ'-Fe_4N are about 9.93 $\times 10^{-12}$ $m^2 \cdot s^{-1}$ (when a compound layer presents), and $\times 10^{-14}$ $m^2 \cdot s^{-1}$, $\times 10^{-14}$ $m^2 \cdot s^{-1}$ [63]. Others summarized the diffusion coefficient of nitrogen in ε-Fe_3N and γ'-Fe_4N-phase as described below [65]:

$$\ln[D_N^{\varepsilon}/(m^2 s^{-1})] = -15.6 - 118 kJ \cdot mol^{-1}/(RT), \tag{2.12}$$

and

$$\ln[D_N^{\gamma'}/(m^2 s^{-1})] = -20.5 - 116 kJ \cdot mol^{-1}/(RT). \tag{2.13}$$

The diffusion coefficient calculation is effect by the nitrogen concentration at the interface, so different values can be obtained when nitriding potential (the boundary condition of the maximum nitrogen concentration) changes [63].

2.2.4.5 Precipitation kinetics

Precipitation of second phase particles in a homogeneous supersaturated matrix can occur once the solubility product for the components in the parent matrix is exceeded [34]. For instance, for 2[Cr] + 2[N] $\Longleftrightarrow$ 2CrN, the equilibrium solubility product is K_{CrN} = [Cr][N] = $6.75 \cdot 10^3 \cdot \exp[-126847.9(\pm > 27209)/RT]$ [66]. Isothermal precipitation kinetics in this situation can be described by JMAK (Johnson-Mehl-Avrami-Kolmogorov) equation [34]:

$$f = 1 - \exp\left[-(kt)^n\right] \tag{2.14}$$

with

$$k = k_0 \exp\left[-\frac{Q}{RT}\right] \tag{2.15}$$

f represents the degree of transformation (0∼1), n is the growth exponent, k_0 is a rate constant, Q is the effective activation energy, T is absolute temperature, R is the gas constant. This equation describes the development of precipitation transition with time under a certain temperature.

The precipitation kinetic for an inhomogeneous matrix is more complex. This includes the cases where one of the components necessary for the precipitation of the second phase particles is supplied from outside the system by diffusion. The diffusion component is nitrogen during nitriding, and the precipitates are alloying element nitrides, MN_n . A competition between the kinetics of nitrogen diffusion and nitride precipitation can occur. Consequently, a zone of nitride precipitation develops, starting from the surface and growing to a more significant depth. There is a transition zone from the zone with maximum precipitates to the unaffected matrix core. Here, the degree of precipitation gradually reduces to zero with increasing depth. However, no generally valid treatment has been provided for this type of precipitation kinetic. A simple relationship can be given between the thickness of the nitrided region, ξ, and the nitriding time, t, only for the strong M-N interaction at constant temperature [34].

$$\xi^2 = \left[\frac{2c_N^s D_N}{nc_M}\right]t \tag{2.16}$$

here, c_N^s represents the concentration of dissolved nitrogen at the surface of the diffusion zone, D_N is diffusion coefficient of nitrogen in the ferrite matrix, c_M .

Nitriding is a process where diffusion is coupled with nitride precipitation. The principles for pure diffusion are no longer suitable for calculating the nitriding depth. The diffusion of carbon in steels during nitriding is a mixed process of phase transformation and co-diffusion with the interaction with nitrogen diffusion.

By fitting the experimental nitriding depth (precipitation hardened) and nitriding time at a different temperature, the relation between the nitrogen diffusion coefficient and nitriding temperature for M2 high-speed steel is presented in [67],

$$D = 1.9 \times 10^{-9} \exp(-62828/RT) \tag{2.17}$$

R is the universal gas constant, R = 8.314 J/mol · K, T is the Kelvin temperature. The nitrogen diffusion coefficient at 500 °C is then $D_N = 1.08 \times 10^{-13}$ m^2/s.

When the nitrogen concentration increases to a value, which allows the formation of iron nitrides, the compound layer can be formed at the surface. The time before that is called the incubation time of the compound layer, and this nitrogen concentration is decided by the content of the nitride-forming alloy elements.

2.2.5 Nitriding process

To improve the surface hardness and tribological properties, the addition of nitrogen to iron was studied in the early 1900s [68]. In 1923 in Germany, nitriding was developed by Adolph Fry of Krupp Steel Works in Essen [69] and then applied as a technological application in surface engineering. The nitriding process up to now has already many approaches [50, 70]. According to the medium which provides the nitrogen, there are plasma nitriding, gaseous nitriding, and salt bath nitriding.

2.2.5.1 Plasma nitriding

Plasma nitriding, also known as ion-nitriding, was developed by Wehnheldt and Berghause in 1932 and became commercially viable in the 1970s [58]. The reactor wall acts as the anode and the sample holder acts as the cathode [71]. Plasma nitriding is a glow discharge process in a mixture of nitrogen and hydrogen gases, introducing nascent nitrogen to the steel surface. In plasma nitriding, an ionized gas is used as a medium for heating and nitriding [53]. The sputtering mechanism of plasma nitriding allows both bulk diffusion and grain boundary diffusion compared to only grain boundary diffusion in the conventional gas nitriding [72]. It is possible to obtain a single phase in the compound layer (ε or γ' iron nitride phase) instead of a mixed-phase in gas nitriding. A compound layer with a single γ' phase has comparatively higher toughness with minimum residual stress [72]. Compared to conventional nitriding processes, plasma nitriding is better at reducing cycle time, reducing distortion, eliminating white layer, controlling the growth of nitrided layer, and able to be performed at a relatively lower temperature (450-550 °C) [58, 59].

In plasma nitriding, an electrical voltage is generated between the furnace (as the anode) and the treated part (as the cathode), as shown in Figure 2.12. The vessel is first evacuated. Then, the mixture of gases nitrogen and hydrogen is introduced. Subsequently, a vacuum is created. When the pressure is stabilized in the range of 13.3-133.3 Pa (containing a mix of diluted gases, mainly nitrogen and hydrogen), the electrical discharge is switched to generate a glow discharge. The nitrogen plasma is then formed by high-voltage electrical energy in a vacuum. With high kinetic energy, the nitrogen ion strikes the surface of the treated part, emits heat, leads to sputtering of the treated part, and atomizes its surface. When the atomized ions combine with nitrogen ions in the plasma, the iron nitride is formed and then deposited in an even iron nitride layer on the surface of the treated part. Some iron nitrides are broken down on the surface, and the nitrogen diffuses into the treated material and results in nitriding [58, 32]. Cold-wall furnaces use exclusively the plasma energy absorbed by the part for heating, whereas hot-wall furnaces have a regular active heating system [32].

In the case of high-speed steel nitriding in vacuum arc discharge plasma, the microstructure of the nitriding layer is mainly influenced by the composition of the nitrogen-containing atmosphere. A common gas mixture for plasma nitriding is 25% N_2 + 75% H_2. If the nitrogen application rate were increased to 50%, the nitriding layer would grow faster. But a further increase of nitrogen results in a thickening of the compound layer [73].

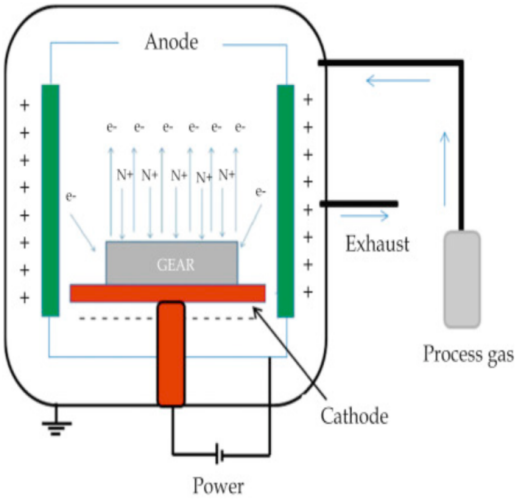


Figure 2.12 – Schematic of plasma nitriding of a gear [58].

The time and temperature (350-580 °C) mainly affect the thickness and microhardness of the nitriding layer [74]. It also depends on the plasma variables [75] and the geometry of the part [76, 77, 78]. All the modes of vacuum plasma processing are interdependent and should be optimized in a complex manner for the specific working condition of the tool.

The wear of the tool used for discontinuous turning is optimized while the gas mixture contains 60% N_2 + 40% Ar or 30% N_2 + 70% Ar, which suppresses the formation of ε compound layer on the surface [74]. An optimal model in terms of wear resistance of electrolytic-plasma nitriding of M2 high-speed steel (flat sample) is found under two conditions: a voltage at a heated temperature of saturation 260-320 V when the current density is 3-4 A·cm^{-2}, or a voltage of 110-180 V with aging when the current density is around 2 A·cm^{-2}, the nitriding for 5-7 minutes [79].

2.2.5.2 The effect of component geometry during plasma nitriding

The component's geometry can strongly affect the plasma nitriding behavior, and the nitriding layer often obtains a non-homogeneous microstructure profile [76, 77, 78, 80, 81, 82].

The forming or cutting tools often possess a shape with a sharp point as the working point. The specific geometry leads the local temperature to be higher than other parts as the bombardment rate increases. The nitrogen concentration at the cutting edge of a drill or the summit of a fillet was always higher than that in a flat coupon or other parts of the component due to the high current density at the sharp edge caused by elevated temperature [78, 80, 82]. The different heights between each sample treated in the same plasma nitriding surface can affect the uniformity of their nitriding layer as the edges also contribute to the formation of eroded rings [81]. When there is insufficient distance between the treated parts, the glow discharge of close specimens can be overlapped in cavities, leading to the cascading of current densities and severe overheating of the components [77, 83].

Because of these problems, plasma nitriding has been developed into many different methods, conventional DC plasma nitriding, pulsed DC glow discharge plasma nitriding, active screen plasma nitriding, radiofrequency (RF) plasma nitriding, and other plasma

nitridings [84].

2.2.5.3 Salt bath nitriding

Salt bath nitriding is a nitriding process using a liquid bath that contains cyanide and cyanate. Since the molten salt contains carbon and nitrogen, which generally diffuse into the surface of steel parts, salt bath nitriding is a nitrocarburizing process. At nitriding temperature, 550-570 °C, the cyanate, for example, decomposes, and nascent nitrogen is released.

$$4\mathrm{NaCNO} \rightarrow \mathrm{Na_2CO_3} + 2\mathrm{NaCN} + 2\mathrm{N}$$

The nascent released nitrogen is very active and diffuses into a component forming a diffusion layer and iron nitride compounds on the surface. Usually, with liquid nitriding, a thick compound layer of predominantly ε-$\mathrm{Fe_{2-3}N}$ is formed, which provides good hardness, corrosion, and scuffing resistance. The advantage of salt nitriding is that it achieves higher diffusion and homogeneous depth in the same period compared to other methods [85, 86, 87]. Salt bath nitriding has shorter times due to the direct contact with the hot liquid, which means that the heating of the parts is much faster [32, 88].

However, this process causes poisonous waste, which can not be used for other materials except steel [89, 90]. The Toyota Motor Company started the production of automobile parts in 1963 and installed the world's most extensive automated salt bath nitriding lines in the engine components plant. However, the requirements on environmental protection made the company replace the treatment of engine parts in cyanide baths with soft nitriding in a gas medium [86].

2.2.5.4 Gaseous nitriding

Gas nitriding is generally carried out at a temperature range of 500 to 570 °C in an atmosphere with a nitrogenous gas, usually $\mathrm{NH_3}$, $\mathrm{H_2}$ and sometimes with $\mathrm{N_2}$ [36, 29]. Compared to gas nitrogen, $\mathrm{N_2}$, which has an extremely low chemical potential, the potential of nitrogen is relatively higher. The ammonia decomposes catalytically at the steel surface into elemental nitrogen, which after adsorption diffuses into the surface of the treated material, as shown in Figure 2.13 [53]. After decomposition, the hydrogen and the rest nitrogen are then exiled [91].

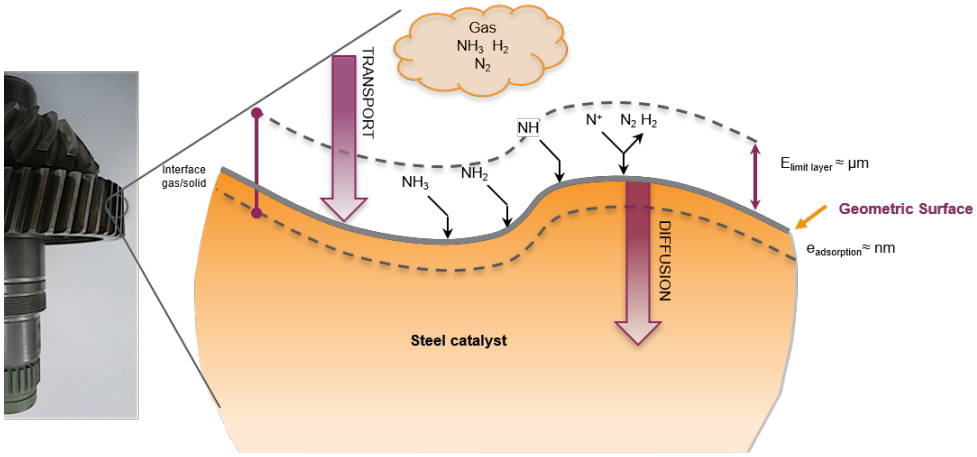


Figure 2.13 – Schematic illustration of gas nitriding [91].

In gas nitriding, the nitriding depth (where the alloy nitrides precipitate starts to be formed) is positively related to nitriding time, temperature, and nitrogen concentration at the surface. The parameters affecting each step can be concluded:

— nitriding potential defines thermodynamically the nitridability of the atmosphere [35, 36], and consequently the reachable maximum nitrogen concentration at the surface and creates a nitrogen gradient in the material,

— nitriding temperature is a crucial factor affecting the diffusion kinetics and, therefore, critical to this thermodynamic process,

— nitriding time is not a factor affecting the nitriding kinetics but a key parameter for the final nitriding profile.

Apart from the nitriding parameters, it also strongly depends on the alloy type in the substrate, the initial microstructure, and the initial surface condition.

2.3 The growth of nitriding layer

2.3.1 Compound layer formation and growth

2.3.1.1 Formation of compound layer

From the phase diagrams, the γ'-Fe_4N phase is the first phase transformed during nitriding when the carbon content is very low in steel or pure iron. And this can only occur when nitrogen concentration on the surface surpasses the value compatible with the α/γ' equilibrium (nitrogen solubility in ferrite) [63]. The time before that is the incubation time for iron nitride formation. As the steel contains nitride-forming alloy elements, alloy nitrides are formed immediately. When the compound layer grows, the alloy nitrides already exist, slowing nitrogen diffusion in the matrix. The ε-Fe_3N phase nucleares on top of γ'-Fe_4N for pure iron, and then these two layers grow under the influence of nitrogen with time. Eventually, a compound layer composed of sublayers of γ'-Fe_4N phase and ε-Fe_3N phase is formed, which is closer to the surface, as shown in Figure 2.14 (a). Before the nitride layer is not closed, the nitrogen prefers to diffuse from the neighbor α phase rather than diffuse through the nitrides due to the lower diffusion rate. But after the nitride layer is closed, nitrogen has to diffuse through the compound layer [63, 65].

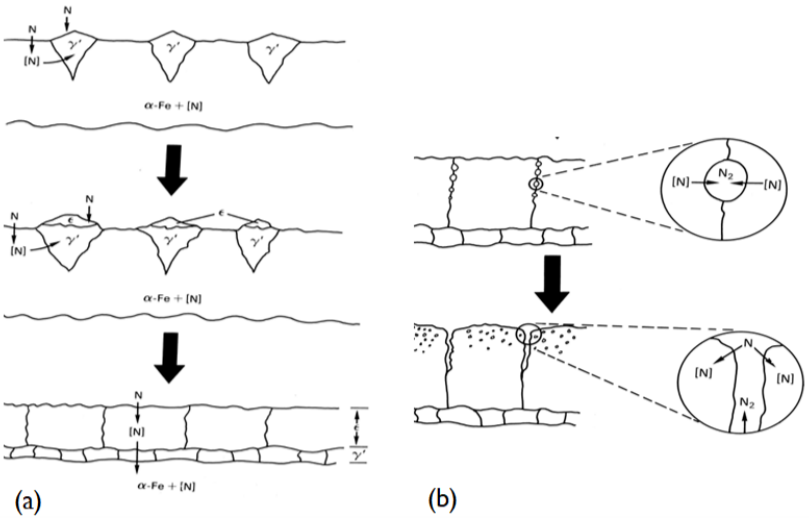


Figure 2.14 – Schematic illustration of formation of compound layer [92].

During the nitriding process, beneath the very surface, iron nitrides (especially ε-Fe_3N) are not in thermodynamic equilibrium at 1 atm and tend to decompose into N_2 and Fe. The nitrogen desorbs from the surface, especially through grain boundaries (the energetically favorable nucleation sites) near the surface where nitrogen concentration is higher, as shown in Figure 2.14 (b) [92]. Porosity is formed mainly in the ε-Fe_3N phase.

2.3.1.2 Kinetics of compound layer growth

The growth of the nitrided layer can be described by the shifts of the ε/γ'interface and the γ'/α interface resulting from mass accumulating over infinitesimal distances, along with the diffusive fluxes arriving at and departing from the interfaces [36]. Figure 2.15 shows a popular model for describing the growth of the compound layer. At a given time, ε/γ' and γ'/α interfaces are located at ξ and ζ, after a time Δt the positions of the interfaces are respectively $\xi + \Delta\xi$ and $\zeta + \Delta\zeta$, like this one can tell that the ε-Fe_3N and γ' sublayers have grown $\Delta\xi$ and $\Delta\zeta$, respectively.

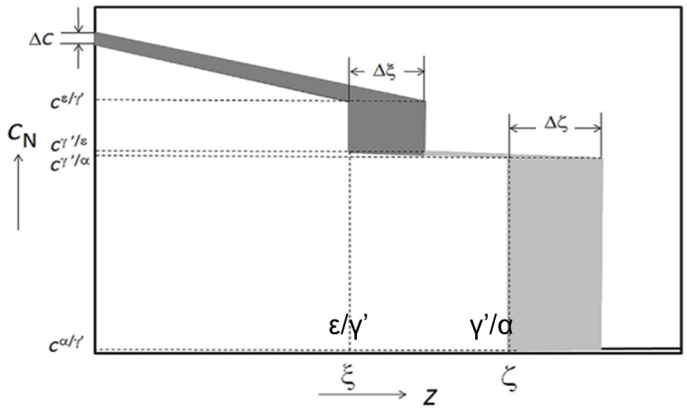


Figure 2.15 – Model of compound layer growth [36].

Information below can be read from Figure 2.15:

— composition-depth profiles in ε-Fe_3N and γ',

— vertical dashed lines mark possible positions of ε/γ' and γ'/α interfaces,

— nitrogen content at the surface increases with time.

Composition at interfaces obeys local equilibrium on phase diagram within experimental accuracy (Figure 2.11).

2.3.1.3 Nitride-forming alloying element effect

However, the growth of the compound layer of alloyed metallic material is also strongly impacted by the existence of alloy elements and carbon in the form of carbides. Alloying elements with a strong nitrogen affinity are likely to form stable compounds with nitrogen. For instance, Ti, V, Cr, and Mo are the alloying elements commonly present in steel and can form nitrides easily, so they have a strong affinity with nitrogen, in other words, the nitrides of these alloying elements will have a strongly negative Gibbs energy of formation from the elements [93, 94]. Alloying elements such as Ni, Co, or Cu can only form nitrides at chemical potentials of nitrogen even higher than those required for the development of iron nitrides (at the surface), they have weak interaction with nitrogen [93].

In pure Fe-based alloys, strong affinity elements M can cause the iron nitrides γ' to grow through the diffusion zone along the grain boundaries(GB) and at the interface of discontinuous coarsened (DC) microstructure and continuous precipitates, shown in Figure 2.16. Nitrides of strong affinity alloy elements precipitate immediately when they contact nitrogen, and they stay in the compound layer during the growth of the iron-nitride compound layer. Therefore iron-nitrides develop along the grain boundaries of the matrix. Moreover, the segregation of alloy elements M at the grain boundary causes nitrogen supersaturation. After M is depleted, iron nitride develops with the prevailing supersaturated nitrogen adjacent to grain boundaries. Continuous precipitation(CP) may coarsen via a discontinuous coarsening reaction, resulting in a discontinuous coarsened(DC) microstructure (Figure 2.17), where lattice strain is relieved by increasing dislocation, ferrite can contain much less excess nitrogen. The released nitrogen reacts with iron [93, 94, 36].

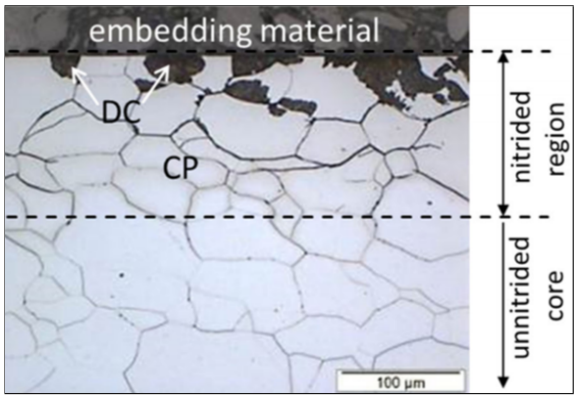


Figure 2.16 – Cross section of Fe-Cr-Mo-V alloy nitrided at 550 °C for 5 h with $K_N = 0.1$ $atm^{-1/2}$ [94].

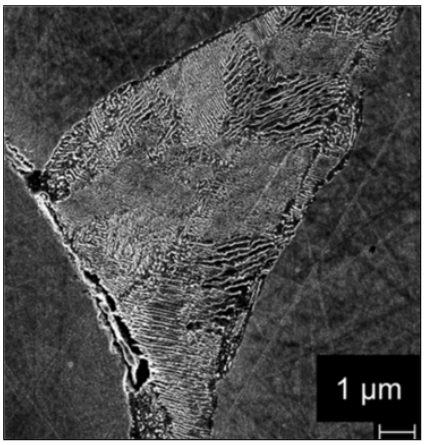


Figure 2.17 – DC region in Fe-1.81 at%Cr-0.25 at.%Mo alloy nitrided at 580 °C for 72 h with $K_N = 0.1$ $atm^{-1/2}$ [93].

The alloy elements with weak interaction with nitrogen can not form nitrides as fast as the strong affinity elements. Precipitation of γ' iron nitrides occurs either after some alloy nitrides MN_n (MN_n indicates all types of alloy nitride, M represents alloy element, such as Mo, Cr, etc..) are precipitated, develop a possible M free γ' or allow M dissolved in it. Alloying elements having weak Me-N interaction, such as Si and Mo, simultaneously have low solubility in iron nitride. The competition between MN_n and γ' make both the two ways of forming γ' difficult and allow nitrogen diffuse deeper, which leads to high nitrogen supersaturation in ferrite, finally developing a platelike morphology γ' across the whole depth range of supersaturated nitrogen, shown in Figure 2.18 [95, 36, 96].

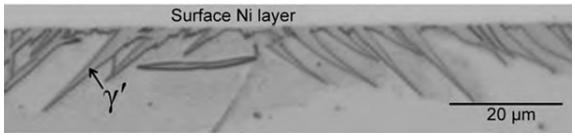


Figure 2.18 – Fe-1 at.% Mo alloy nitrided at 480 °C for 2 h with $K_N = 0.7$ $atm^{-1/2}$ [95].

2.3.1.4 Carbon effect

Due to the higher thermodynamic stability of nitrides, carbides in steel tend to transform into (carbo) nitrides during nitriding. The released carbon atoms can either leave the

steel or diffuse deeper into the steel with interaction with the diffusing nitrogen. Figure 2.19 shows an example of carbon accumulation ahead of nitriding front and depletion close to the surface, the accumulation contributes to the growth of primary carbides [92, 97].

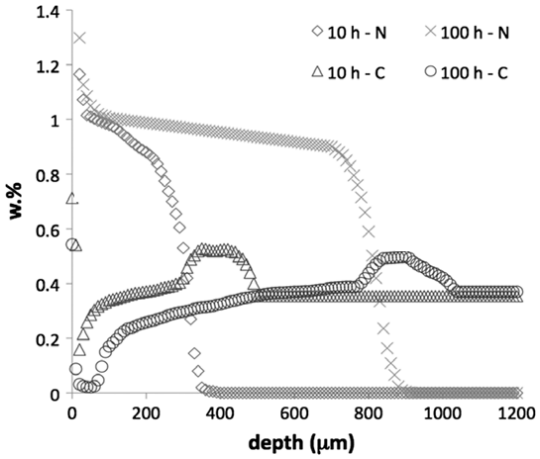


Figure 2.19 – Nitrogen and carbon profiles in Fe-3%Cr-0.35%C after gas nitrided at 550 °C [97].

Figure 2.20 shows the effect of carbon co-diffusion on the microstructure of the compound layer. In the compound layer, carbon diffusion can cause a more ragged interface between ε and γ'-layers due to the opposite fluxes of N atoms (inwardly) and C atoms (outwardly). Moreover, carbon diffusion outwardly can result in the porosity along grain boundaries in the ε-layer because that carbon promotes N_2 formation or, in other words, carbon facilitates the nucleation of pores [44].

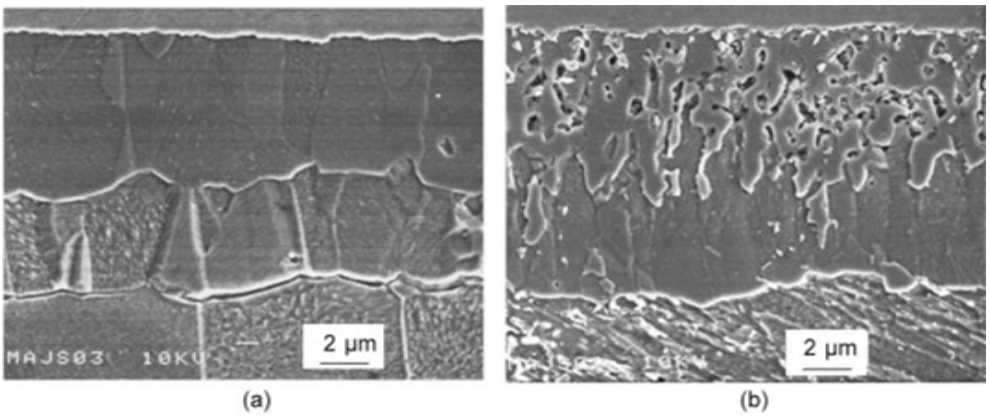


Figure 2.20 – Microstructure of (a)Fe and (b) Fe-0.4C nitrided at 460 °C for 65 h, with $K_N = 6.6$ $atm^{-1/2}$ [44].

2.3.2 Diffusion zone

2.3.2.1 Kinetics of diffusion zone growth

For pure iron or carbon steels, the concentration of nitrogen c_N at depth x and time t at temperature T can be described by solving Fick's laws with specific boundary conditions [35, 36]. The kinetics of the precipitation (nucleation and growth) process of MN_n alloy nitrides strongly impact nitriding kinetics for the steels with nitrides forming alloying elements. Only for M-N strong interaction, the kinetics of precipitation can be applied [35, 36, 98] with the assumptions below:

— The activity of nitrogen in ferrite exhibits henrian behavior: thermodynamic factor is unity, the diffusion coefficient is independent of concentration, it is a function of temperature.

— Local equilibrium at the surface, so that the dissolved nitrogen concentration at the surface equals the lattice solubility of nitrogen

— Amount of nitrogen building up the concentration profile is negligible compared to those forming nitrides.

— Nitrides MN_n formation occurs only and completely at the interface between the diffusion zone and compound layer.

— Diffusion of M is neglected and not determining nitriding rate.

However, in reality, the co-diffusion of carbon is effective and not negligible in complex alloys. Alloy element M atoms are supposed not diffuse (the diffusion coefficient of Cr in α-Fe is 3.72 $\times 10^{-20}$ $m^2 s^{-1}$ at 885 K [99]) but can play a role in nitriding rate due to precipitation of alloying elements nitrides. Therefore the nitriding kinetics in the diffusion zone is a competition between diffusion kinetics and precipitation kinetics.

2.3.2.2 Precipitation of nitrides

Nitrides can be formed directly with the alloy elements in the solid solution thanks to their high chemical affinity with N. These nitrides will be semi-coherent to the matrix with a size of tens of nanometers [100]. Otherwise, nitrides can also be formed with the carbides' alloy elements [101]. This is because the thermal stability of nitrides is relatively higher than the carbides, in other words, the enthalpy heat of forming nitrides is lower than forming corresponding carbides, as shown in Figure 2.21 [102, 103]. These nitrides keep the original site of the carbide and are incoherent with the matrix. Figure 2.22 shows the two types of nitrides. Due to the strong chemical affinity between the alloy element and nitrogen, nitrides such as CrN, VN, have the same FCC crystal structure for both precipitates [104].

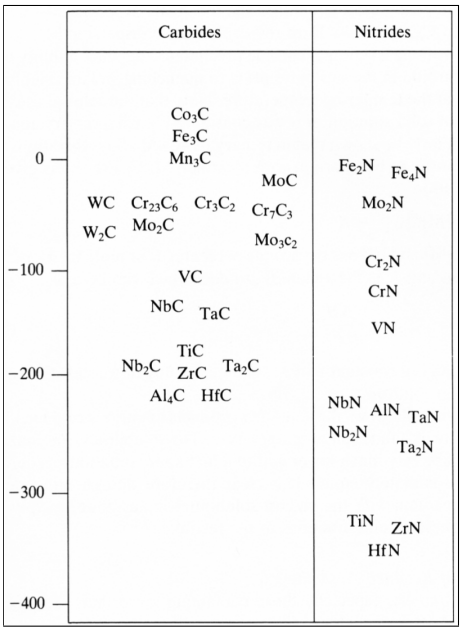


Figure 2.21 – Enthalpy (kJ/mol) of formation of the carbides and nitrides [105, 102].

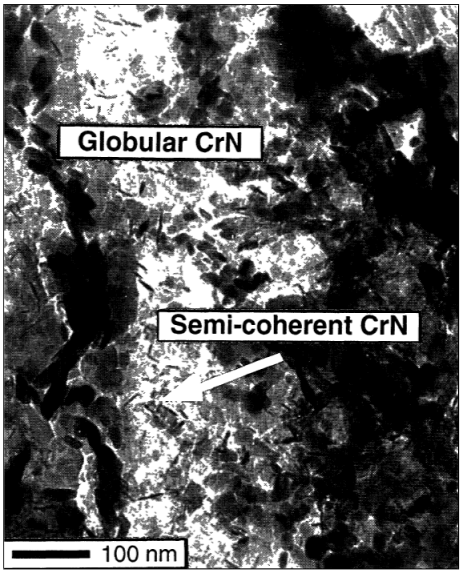


Figure 2.22 – TEM micrograph from a carbon film replica of the nitrided layer at depth=200 μm [104].

The orientation relationship between the semi-coherent nitrides and ferrite is called Baker-Nutting orientation and is written as follows:

$$(001)\alpha//(001)\mathrm{CrN}, [100]\alpha//[110]\mathrm{CrN}$$

Figure 2.23 shows the relationship scheme with an example of CrN. This relation leads to three different spatial orientations for CrN precipitates on 100 plane faces of ferrite structure. For example, in Figure 2.24, the matrix is oriented along a [100] zone axis, two different populations of precipitates are observed as lines oriented at 90 °from each other. $\{110\}_{\alpha\text{–Fe}}$ planes have a misorientation of ± 45 °with respect to the CrN precipitates. Thus, CrN precipitates are parallel to the $\{100\}_{\alpha\text{–Fe}}$ set of planes [104].

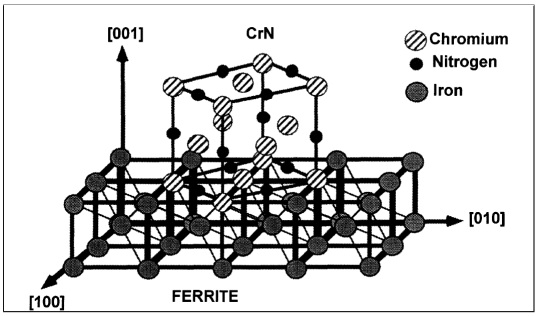


Figure 2.23 – Scheme of the Baker-Nutting crystallographic orientation relationship [104].

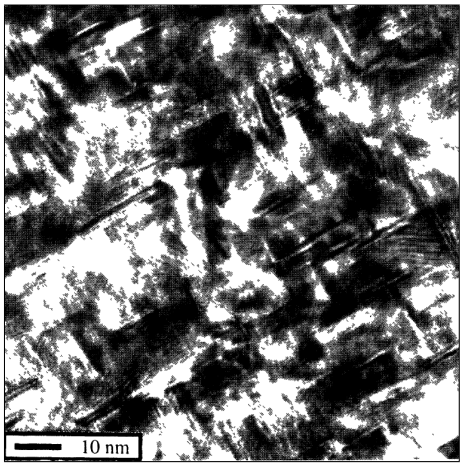


Figure 2.24 – TEM micrograph from a thin foil of semi-coherent CrN precipitates at depth = 200 μm -Zone axis [100] [104].

If the MN_n particle forms within a grain of the ferrite matrix, it is constrained by the surrounding matrix and the strains arise due to the volumetric misfitting of the nitride precipitates and the ferrite matrix, and the crystallographic constraints as exposed at the precipitate/matrix interface. The strain energy, which arises during precipitation, may slow the nitride-precipitation process considerably [93].

2.3.2.3 Nitride-forming alloying element effect

When no nitride-forming alloying elements exist, the diffusion zone is a nitrogen solution in ferrite at nitriding temperature. The solubility of nitrogen in ferrite decreases with temperature, so during cooling, the iron-based nitrides γ'-Fe_4N_{1-x} and α"-$Fe_{16}N_2$ develop from a supersaturated solution. With cementite, ε-Fe_3N phase can be reached by the transformation from the current phases [92].

When there is strong nitride forming alloying elements like Cr, V and Ti, nitrides MN_n develop preferentially. Their nitrides are platelike on the nanoscale and dispersed in the matrix with a NaCl lattice (CrN, TiN, VN). The nitrogen dissolved in ferrite is only considered mobile, so the growth of the diffusion zone is only related to the diffusion of nitrogen in the ferrite matrix. Hence a higher concentration of nitride forming element slows the growth of the diffusion zone and reduces the compound layer thickness [92]. It allows to arrange the reactivities of various M with N in binary ferritic alloys in roughly this order: Ti>V>Cr>Si>Mo [106, 107, 108, 109]. Alloying with different elements leads

to different nitrogen concentrations in the nitriding layer, as some examples are given in Figure 2.25 [110].

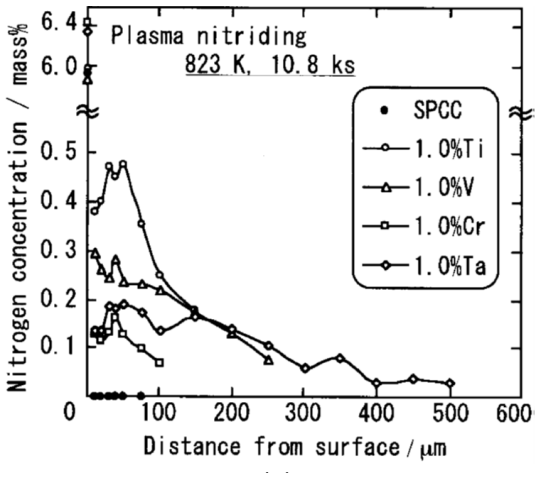


Figure 2.25 – Nitrogen concentration profiles on the cross-section of plasma nitrided layer for plain carbon steel with 0.02 wt.% and alloy steels containing 1 wt.% alloying content [110].

Figure 2.26 shows nitrogen concentration distribution in each nitrided layer in pure iron and binary iron alloy with nitride forming elements M. In Figure 2.26 (a) α refer to the diffusion zone, which mainly consists of α-Fe and interstitial diffused nitrogen, $c^{\alpha}_{N,max}$ refers to the maximum of nitrogen solubility within the ferrite. In Figure 2.26 (b), N_y exists besides interstitial nitrogen, which corresponds to nitrogen in the formed nitride precipitates, which is the primary reason causing the high nitrogen concentration in the diffusion zone. A precipitation front (also called diffusion front) is observed where the nitrogen concentration drops at a rate related to the affinity of alloy elements with nitrogen [111].

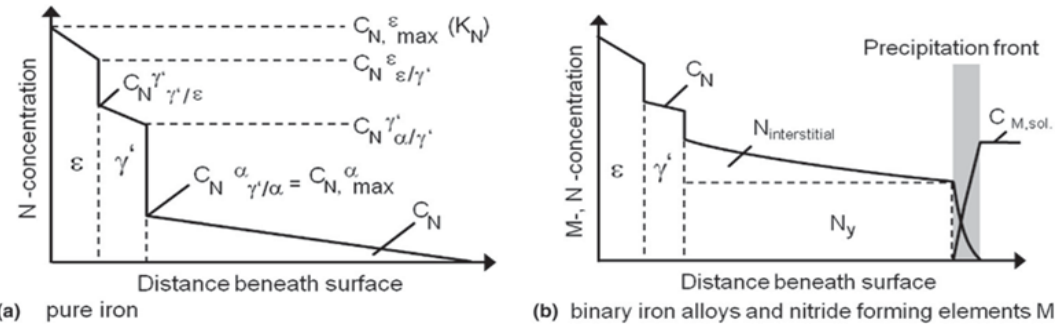


Figure 2.26 – Structure of nitrided case (schematic), concentration distribution of nitrogen [51].

2.3.2.4 Carbon effect

In the diffusion zone, the released carbon from carbide transformation can diffuse towards the compound layer depending on the chemical potential of carbon with the gas atmosphere at the gas-solid interface, and to the nitriding diffusion front due to the high chemical potential of carbon (absolute value) in the presence of nitrogen. Cementite is formed as carbon reacting with iron and precipitation along the grain boundaries parallel to the surface under the influence of compressive residual stress, shown in Figure 2.27 [36].

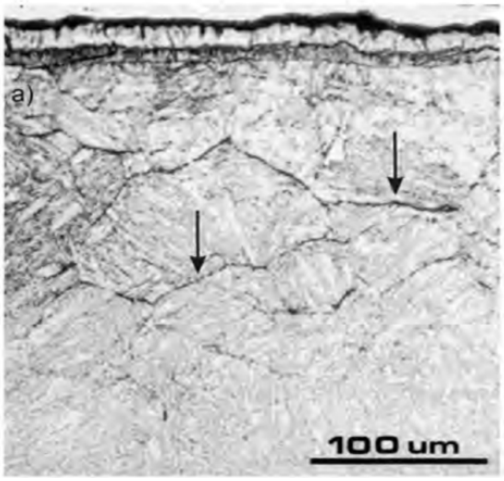


Figure 2.27 – Quenched and tempered 24CrMo13, salt bath nitrided at 580 °C for 2 h [36].

As carbon diffuses faster than nitrogen at nitriding temperature, thanks to its higher thermodynamic activity, carbon accumulates at the diffusion front (it does not diffuse deeper because the chemical potential decrease without the presence of nitrogen), as shown in Figure 2.26. The accumulated carbon reacts with alloy elements in the solid solution, and the initial carbides grow. As the nitrogen concentration increase, the carbides transform into incoherent nitrides. Co-diffusion of carbon decreases the kinetics of nitriding due to the accompanied phase transformations [64, 97].

For steels with nitride forming elements, local chemical conditions induced in the matrix by the increased nitrogen concentration during nitriding treatment allow the dissolution of former carbides and the nucleation of MN_n platelets precipitates from the substitutional solid solution during nitriding treatment [104]. The MN_n semi-coherent precipitates transform quickly into globular incoherent precipitates since the alloying element concentration is very high in the carbides zones [112]. The MN_n nitride precipitation rate is limited by the tempering carbide dissolution rate [104].

2.4 The hardness and residual stress evolutions during nitriding

Nitriding is a good approach for increasing hardness and compressive residual stress generation. Hardness is related to nitride formation with a smaller size than the primary carbide ones. Stress generation is directly linked to volume changes due to phase transformations [113].

2.4.1 Phase transformation and volume expansion

During nitriding, phase transformation can be classified as [97, 114, 115, 116]:

— Precipitation of MN_n nitrides: at the beginning of the treatment, fine semi-coherent nitrides precipitate from solid solution owing to its high nitrogen affinity.

— Initial carbides M_xC_y transformed into incoherent nitrides causing lower volume change due to a less important specific volume difference than the change of precipitation from solid solution.

— Diffusion of carbon at the diffusion front: alloy elements form carbides first and then transform to nitrides, causing the quantity of semi-coherent nitrides decreases and the number of incoherent nitrides from the transformation of carbides increases.

— Surface decarburization causes carbides volume fraction to decrease.

According to Figure 2.28, the precipitation of MN_n from the solid solution causes the most evident volume expansion due to the biggest difference between MN_n and α-Fe. All other transformations result from carbon redistribution and weaken positive volume change. So, volume expansion is always influenced by the redistribution of carbon apart from nitride formation and excess nitrogen.

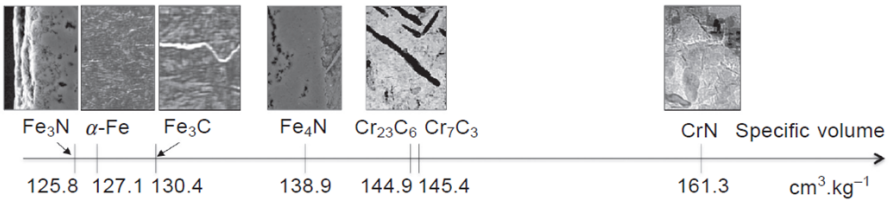


Figure 2.28 – Specific volumes of nitrides and carbides for low alloyed steels [113].

These transformations lead directly to a change of volume fractions of different nitrides and carbides in the material (Figure 2.29) according to the different specific volumes of carbides and nitrides (Figure 2.28) [113, 97, 117, 115, 116]. Figure 2.29 and Figure 2.30 (a) show the evolution of volume fraction and volume change as a function of depth as the nitriding time increases. When the phase composition evolves as shown in Figure 2.29 marked with the blue lines, due to the difference of the precipitates, the volume expansion evolves as shown in Figure 2.30 (a) at depth Z_2. As the CrN concentration increases, the precipitates volume expands more significantly.

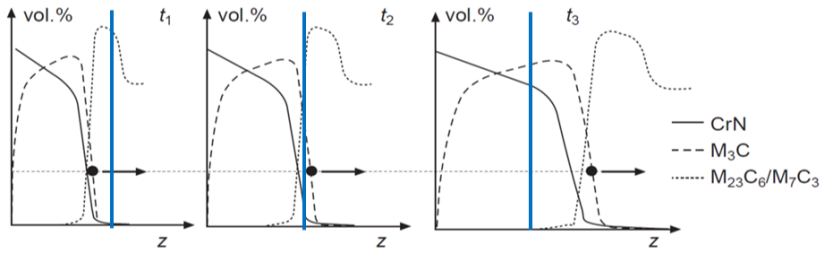


Figure 2.29 – Schematic evolution of volume fraction of carbides and nitrides of low alloyed steel during nitriding [113].

2.4.2 Residual stress

Residual stress can be detrimental when it reduces the tolerance of the material to an externally applied force. On the other hand, it can be exploited to design materials or components resistant to damage, toughened glass being a good example [118].

According to XRD diffractograms, compressive residual stresses are often generated after nitriding, indicated by the shift and broadening of the 110 peak of α-Fe [119, 120, 121, 76, 122, 123, 124]. The residual stress measured in this way is the average phase-specific stress in ferrite, which can be different from the overall average macro stress in the sample [125].

2.4.2.1 Residual stress generated during nitriding

Residual stress remains in a component that is stationary and at equilibrium with its surroundings [126]. Formation of the precipitates in the diffused case results in volume

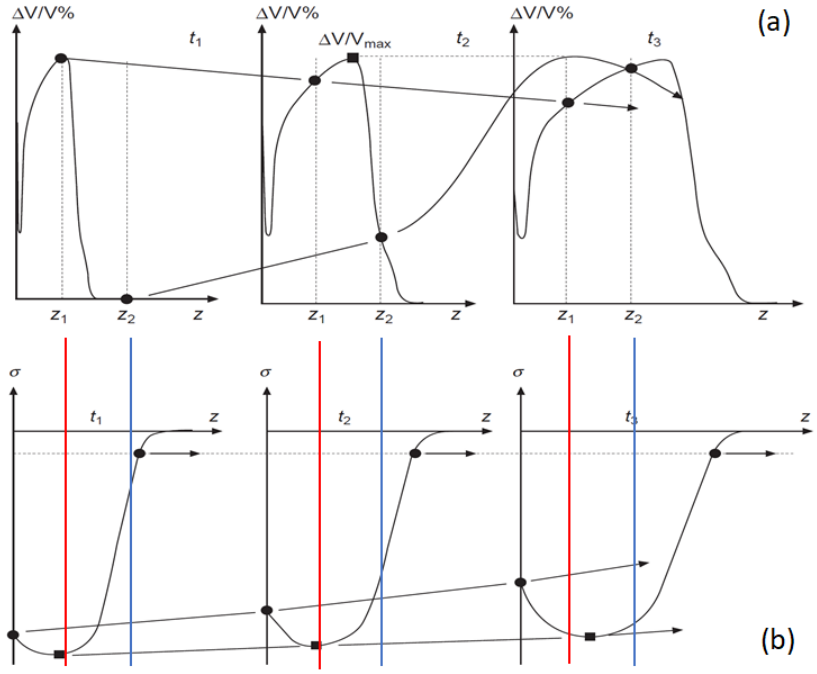


Figure 2.30 – Schematic evolution of (a) volume expansion and (b) residual stress during nitriding of low alloyed steel [113].

expansion and, consequently, the generation of eigenstrains whose incompatibility induces a compressive residual stress field. Meanwhile, in an attempt to maintain its original dimensions according to mechanical equilibrium, the core material holds the nitrided case in compression [127].

Figure 2.31 schematically shows the volume expansion among different layers, where the black square represents carbon, and the white square represents nitrogen [113].

According to data shown in Figure 2.28, compared to the solid solution containing alloy elements, the volume accompanying nitride precipitates is more considerable. Compared to the initial carbides, the nitride precipitates are normally bigger.

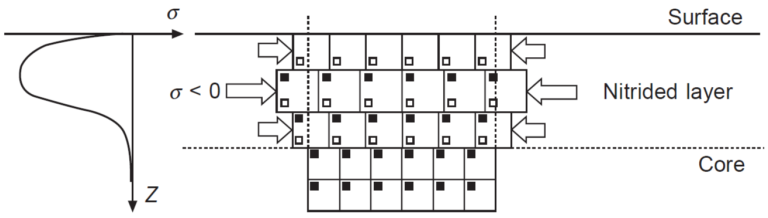


Figure 2.31 – Schematic relationship between residual stress and microstructure expansion [113].

Residual stresses result from interactions among time, temperature, deformation, and microstructure [128]. The diffusion-based thermo-chemical reactions at nitriding temperature lead to significant differences in the structure and morphology of nitrided layers, reflected in the stress-strain state of the layers [129].

In the compound layer, the volume expansion resulting from the iron nitride formation generates macroscopic residual stresses due to different thermal expansion coefficients between ferrite and ε- and γ'-nitrides. The formation of pores and the precipitation of secondary γ'-nitride during cooling offer a further expansion [130].

In the diffusion layer of unalloyed steels, interstitial nitrogen causes lattice expansions. During slow cooling, precipitation of α"- and γ'-nitrides are formed [111]. The residual stress is further developed with the different thermal expansion coefficients between the nitrides and the ferritic matrix. In the diffusion layer of alloyed steel with nitride-forming elements, gradients of the volume expansions caused by nitride precipitations play the main role in forming residual stresses.

2.4.2.2 Residual stress and phase transformation

The maximal compressive residual stresses do not always appear in the near-surface area (Figure 2.38) [131, 132, 111]. The evolution of residual stress during nitriding can be explained by the volume change at different depths and time as shown in Figure 2.30. Positive volume expansion cause compressive residual stress, and vice versa.

Firstly, the interstitial nitrogen causes lattice expansion during nitriding. Then, the formation of new phases causes a gradient of a volumetric misfit by possessing different lattice parameters and specific volumes.

Some explained the relation between phase transformation and residual stresses evolution [113, 97, 117, 115, 116]. According to the different specific volume of carbides and nitrides, corresponding volume changes defines the residual stress level. The maximum value is reached when the phase composition gives the maximum volume [97, 117, 116].

When the MN_n (M represents nitride forming alloying elements) particle forms within a grain of the ferrite matrix, it is constrained by the surrounding matrix, and the strains arise due to the volumetric misfitting of the nitride precipitates and the ferrite matrix and the crystallographic constraints as exposed at the precipitate/matrix interface, see in Table 2.2. The strain energy arises during precipitation, and may slow the nitride-precipitation process considerably.

The nitrides transformed from initial carbides keep the original site of the carbide and are incoherent with the matrix. This step causes minor volume change due to a less significant specific volume difference. For example, the volume expansion from VC to VN is less important than that from precipitation of VN in α-Fe solid solution [133].

The carbon at the diffusion front reacts with alloying elements, and carbides grow. The subsequent phase transformation forms incoherent nitrides, leading the fraction of semi-coherent nitrides to decrease and a less critical volume expansion [97]. The volumetric expansion varies depending on the fraction of nitrogen that reacts with alloying elements initially in the ferritic solid solution or the initial carbides [117, 97, 113]. The nitrides precipitation from the solid solution offers the most significant volume expansion, the maximum residual stress decreases while the transformation of carbides takes place more significantly [97] at a deeper depth.

2.4.2.3 Residual stress redistribution

The residual stress profile at each depth changes differently as a time function. In Figure 2.30 (b), at depth z_1, the compressive residual stress decrease as the volume expansion decrease, but at depth z_2, volume expansion increase and compressive residual stress increase. This can be explained by the different stages of nitriding. After a certain time, z_2 would experience the similar change as z_1 has experienced. The phenomenon that the compressive residual stress decreases after reaching the maximum value is called residual stress redistribution [139, 140, 141].

Table 2.2 – Lattice parameters (a, b, c), specific volume, and volume misfit ($\frac{\Delta v}{v}$) between the precipitates and the pure ferrite matrix, for various alloying element nitrides and carbides. As the initial carbides owe complex composition, the information of single element carbides crystal structure is given. The specific volume and volume expansion are calculated with the data from the database [133] if not marked. The volume expansion is calculated with the method in [134].

Phases	**Crystal lattice**	**Lattice parameters, Å**	**M atom number unit cell,**	**Specific volume,** cm^3kg^{-1}	$\frac{\Delta v}{v}$, **%**
α-Fe	Cubic	a = 2.8664	2	126.6	-
Fe_4N	Cubic	a = 3.791	4	137.9	16
Fe_3N	Hexagonal	a = 2.695, c = 4.362	6	138.5	18
Fe_3C	Orthorhombic	a = 5.09, b=6.74, c = 4.5	4	130	10
VN	Cubic	a = 4.139	4	174	51
Mo_2N	Cubic	a = 4.163	4	-	53
CrN	Cubic	a = 4.14	4	164.1	51
Cr_2N	Hexagonal	a = 4.795, c = 4.463	6	-	26 [135]
δ_3-MoN	Hexagonal	a = 5.63, c = 5.736	8	109.6	67 [136]
$CrMoN_2$	Hexagonal	a = 2.85, c = 15.63	6	-	56 [137]
WN	Hexagonal	a = 2.89, c = 2.83	2	-	- [138]
W_2N	Cubic	a = 4.126	4	-	- [138]
VC	Cubic	a = 4.165 at $VC_{0.87}$ a = 4.131 at $VC_{0.73}$	4	177	- [138]
W_2C	Hexagonal	a = 2.992, c=4.722	1	58	- [138]
Mo_2C	Hexagonal	a = 2.898, c=2.809	1	105.7	- [138]

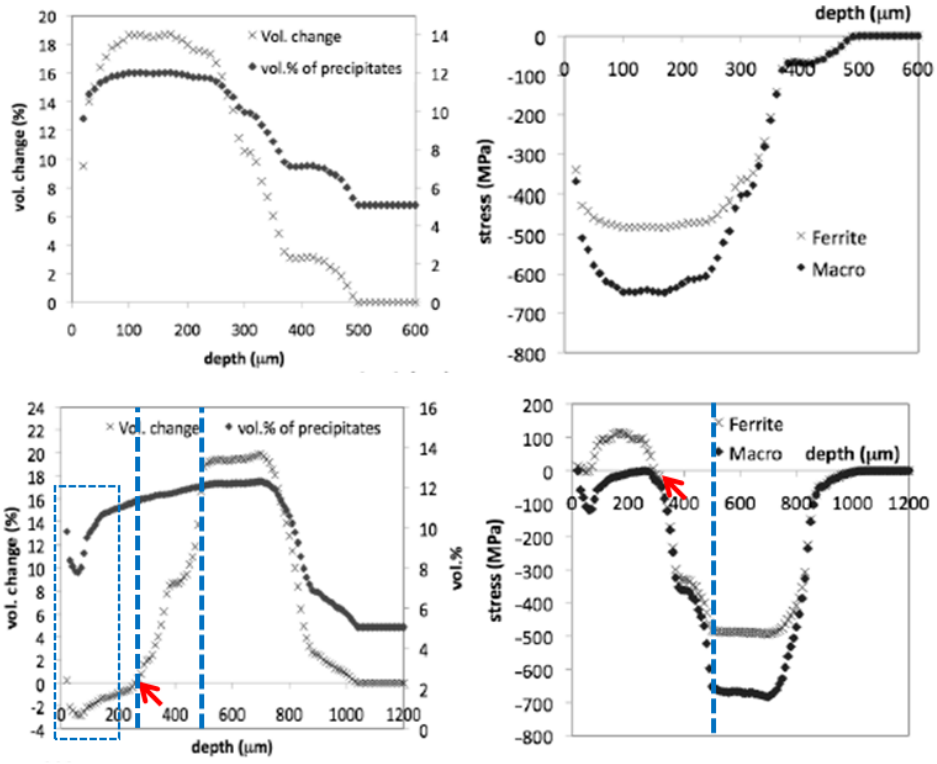


Figure 2.32 – Results of nitriding model in case of Fe-C-3%Cr nitrided 10h above, 100 h below [115].

A nitriding concerns a series of phase transformations, and most early transformations

result in positive volume exchange, generating compressive residual stress. But some phase transformation in the later stage leads to a decrease in precipitates volume fraction compared to the previous steps. This causes the unloading of the elastic strain induced by the former phase transformations [113]. According to the loading-displacement behavior of elastic-plastic steel, the same displacement or minor is required during unloading. This explains why compressive residual stress decrease after reaching the maximum and can even become tensile stress.

Figure 2.32 shows the volume expansion and residual stress profile after nitriding for 10 and 100 hours, respectively. Compared to nitriding for 10 h, the volume change and residual stress curve deeper after about 500 micrometers of the sample nitrided for 100 h show the same shape and a comparable value. Otherwise, residual stress redistribution, and more profound as closer to the surface, negative volume change directly results in a tensile residual stress [115, 97].

When no compound layer is formed, the cementite near the surface reacts with the hydrogen in the atmosphere and leads to decarburization [142, 143]. The residual stress of the ferrite matrix beneath the compound layer with only γ' iron-nitride becomes more compressive, this is a straightforward consequence of a less extent of decarburization of the ferrite matrix. γ' iron nitride has only very low solubility for carbon [144], the carbon tends to leave the surface. The ε-phase has a broad solubility range for both carbon and nitrogen, which allows the C to stay and transform into nitrides underneath the compound layer. For this reason, the C diffused to the outer surface is distinctly reduced and the thickness of the decarburized region is smaller [144].

Precipitate coarsening plays the most important role in stress redistribution in the case of Fe-M alloys (not the main effect in steels). The coherent, sub-microscopical MN_n precipitates are replaced by incoherent, relatively large MN_n lamellae. Redistribution of the (initial) compressive stress occurs and is most pronounced near the surface [115, 145, 117, 105].

2.4.3 Hardness

The major material performance improvement from the diffusion zone is contributed by dispersed alloying element nitrides. Material hardening during nitriding respects precipitation hardening. Precipitation hardening depends on the size, volume fraction, shape, nature, and distance of the precipitate particles [146, 147]. The shape of the precipitation particles is spherical due to the lowest intersurface energy, and the segregation is plate-like, thanks to the minimum elastic distortions of the crystal lattice of the matrix in ferritic Fe-based materials [93].

The MN_n nitrides precipitated from the solid solution are finer than the initial carbides [113]. According to the principle of age hardening Figure 2.33, precipitates growth leads to pronounced initial hardening and cyclic saturation by impeding dislocation motion. However, overaging induces the precipitates to coarsen, which is negative for hardness increasing. After the precipitates grow over a certain size, the interaction between the precipitates and matrix becomes incoherent and more distanced [148, 149, 150]. The small coherent precipitates prevent the dislocation from moving by submitting the shear stress [151]. The contribution to the strengthening includes the coherency/size effects, the modulus effects, the interfacial energy/chemical effects and the ordering/anti-phase boundary effects. This strengthening can be generally given by [152]:

$$\tau_{\mathrm{cut}} = \mathrm{A}\varepsilon^{\frac{3}{2}}\mathrm{G}(\frac{\mathrm{rf}}{\mathrm{b}})^{\frac{1}{2}}, \tag{2.18}$$

where A is the constant, ε is a dimensionless mismatch parameter, f is the volume fraction of precipitates, r is the precipitate radius, and b is the magnitude of the Burgers vector.

The larger incoherent particles drive the dislocation bow around [153] (see in Figure 2.34). The governing equation is defined as:

$$\tau = \frac{Gb}{L - 2r}, \tag{2.19}$$

where τ is the material strength, G is the shear modulus, b is the magnitude of the Burgers vector, L is the distance between pinning points, and r is the second phase particle radius.

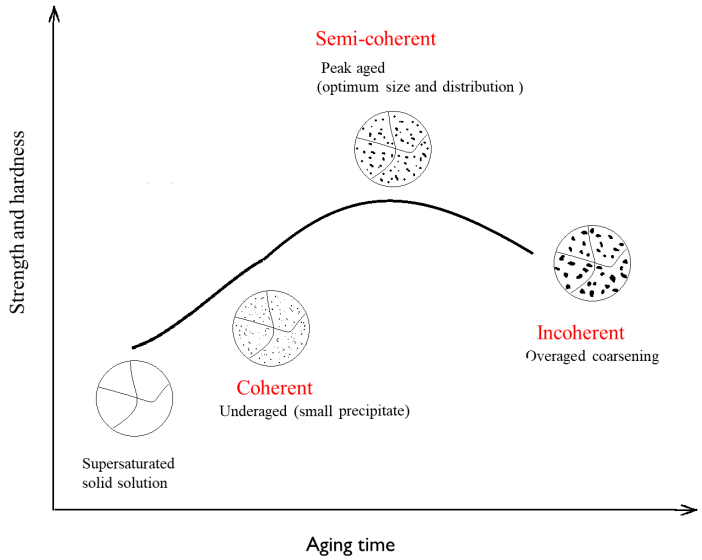


Figure 2.33 – Precipitation strengthening curve.

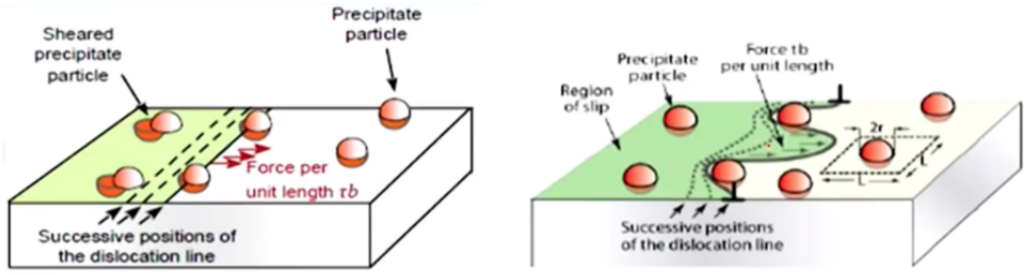


Figure 2.34 – Schematic illustration of precipitates impede dislocation motion [148].

The net effect of increasing the particle size in these systems is illustrated in Figure 2.35. The effect of the dislocation shearing precipitates mechanism on the hardness as the precipitate size increases, while the effect of dislocation bowing around the precipitates evolves oppositely. Therefore, a maximum strengthening can be attained at the critical particle size, and the magnitude of this maximum depends on the magnitude of the fractional coherency strain and the volume fraction of particles [152].

Figure 2.36 shows that alloyed steel has higher hardness at the diffusion layer thanks to the nitrides formed from the alloying element (the chromium nitrides formed from Cr in the steel) [51]. Alloy elements with different affinities with N lead to different hardness profiles in the nitriding layer (Figure 2.37) coherent to Nitrogen concentrations (Figure 2.25). At

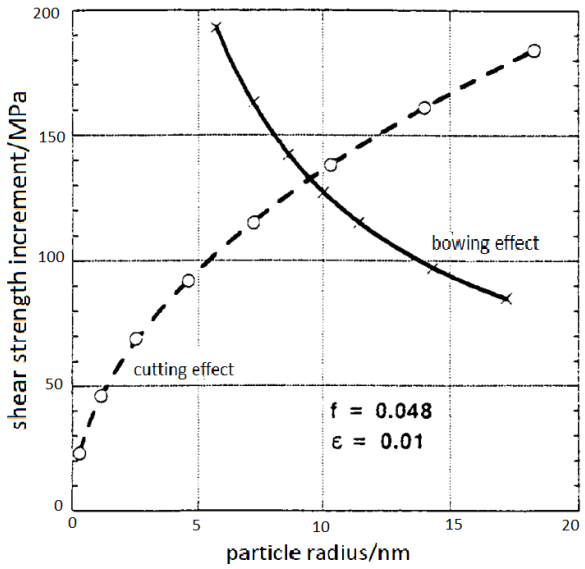


Figure 2.35 – The net effect of increasing the precipitates size on the hardness [152].

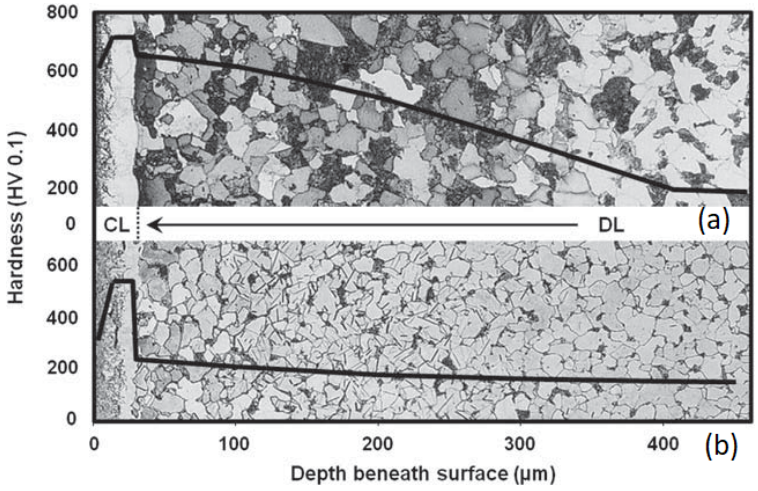


Figure 2.36 – Microstructure and hardness profile of the case of gas nitrided (a) 16MnCr5 and (b) C15, slow cooling conditions [51].

the same time, the alloy elements' concentration also affects the nitrided layer's depth and hardness. After the same nitriding treatment, the hardness at the same nitriding depth is higher for the alloy with a higher concentration of alloy elements, while the depth of the nitrided layer decreases as increasing the alloying content [110].

However, the combined effects with C are more complex. For instance, Cr dissolves in Fe can be less with higher C content. The impact of nitride formers (Mo, Cr, V...) on the precipitation hardening significantly decreases above a concentration range of 1 wt.%, etc. Figure 2.38 shows the hardness profile of different materials after nitriding with the same condition, all these materials offer a higher hardness as closer to the surface, and they increase with rising content on nitride-forming elements dissolved within the ferrite. The differences between the steels result from the different grades of chromium being bonded as carbide [154, 155].

Hardness increase from nitriding is also strongly influenced by the chemical composition of the materials, carbon and nitride formers Al, Cr, V, etc. effect in different ways [154, 155].

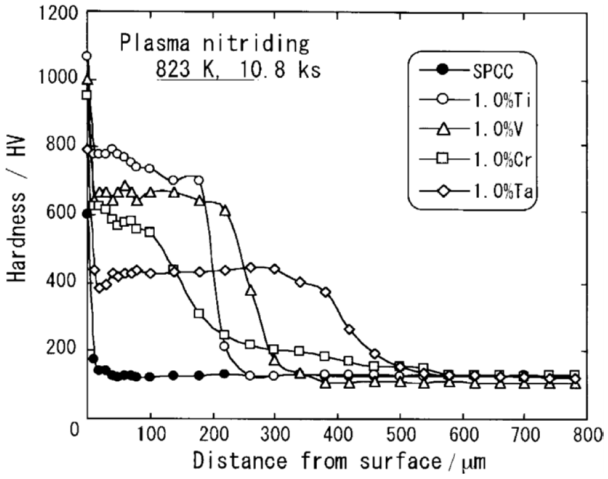


Figure 2.37 – The hardness distributions on the cross-section of plasma nitrided layer for plain carbon steel with 0.02 wt.% and alloy steels containing 1 wt.% alloying content [110].

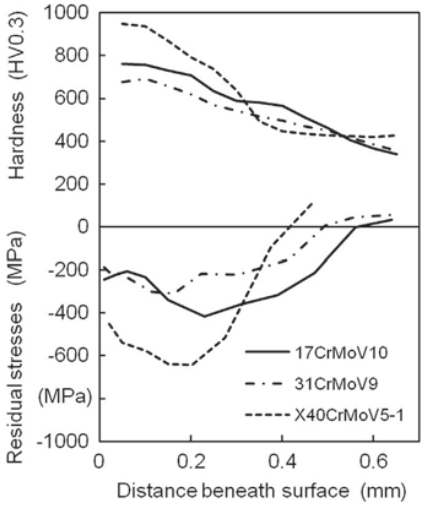


Figure 2.38 – Profiles of hardness and residual stresses in nitrided case of steel 17CrMoV10, 31CrMoV9, and X40CrMoV5, nitrided at 570 °C for 32 h [111].

— Nitride forming alloy elements: chromium and vanadium on the precipitation hardening effect is in a comparable range. At equal concentrations, aluminum causes a considerably stronger hardness increase.

— With the growing chromium content, MN_n precipitates increase, and the maximal nitrogen content in the diffusion layer increases, so the hardness increases.

— The increase in hardness decreases when carbon fraction increases in the steel because the nitride formers exist as carbides. This changes the concentration of nitride formers dissolved within ferrite.

The existence of alloying elements (Cr, V, Mo, W) enhances the dissolution of nitrogen in iron and increases the efficiency of the solid-solution hardening by nitrogen [156, 157]. In the binary system, the size of coherent nitrides in a Fe-based binary system is 1-5 nm, and 5-10 nm for the incoherent particles [158]. The hardness is found to rise to a maximum level due to the formation of coherent alloy nitride precipitates (Mott-Nabarro model) [157].

The major contribution to the hardness improvement is brought by the globular inco-

herent nitrides, less by the semi-coherent nitrides due to a relatively low volume fraction [112]. In general, the precipitation of nitrides from carbides leads to a decrease in the average size of precipitates so that the hardening effect increases.

It is found that the globular incoherent nitrides show an increase in the size of the precipitates as a function of the depth [112]. This is explained by a decrease in the number of germination sites on the tempered carbides due to the decrease of the nitrogen flux as a function of depth. On the other hand, the size distribution of semi-coherent nitrides seems not to vary as a function of depth because they have very fast germination kinetics but slow coalescence kinetics because of the very high stability of the MN_n [104, 112].

The effective nitriding depth is defined as the depth where hardness equals the core hardness plus 100 HV 0.2. The effective nitriding depth is also a characteristic diffusion depth of nitrogen. Considering the nitrided sample as a semi-infinite plate of normal axis z, the characteristic diffusion depth Z_{eff} can be approximately described as a function [159, 160, 161], given by:

$$Z_{eff} = (2D_N^{\alpha\text{–}Fe}t)^{1/2}, \tag{2.20}$$

where t is the nitriding time, $D_N^{\alpha\text{–}Fe}$ is the effective diffusion coefficient of nitrogen in the ferritic matrix (which take into account the kinetics of precipitation).

2.5 Materials performance of nitrided steel

2.5.1 Fatigue life and Wöhler curves

Fatigue is a kind of failure that often takes place on the structure under cyclic loading, where the fluctuating stresses are lower than the stress required to cause failure in a single loading cycle. Fatigue failure has been estimated to contribute to about 90% of all mechanical service failures [162]. High-cycle fatigue involves an elastically applied stress with a cycle number above 10^5. A lifetime lower than that is the low-cycle fatigue, and higher than 10^7 is the very high-cycle fatigue [163].

According to the American Society for Testing and Materials, fatigue life is defined as the number of stress cycles of a specified stress level. Fatigue life is affected by cyclic stresses, residual stresses, material properties, internal defects, grain size, temperature, design geometry, surface quality, oxidation, corrosion, etc.. S-N curve is a method most commonly used to characterize the relationship between the stress level and the number of loading cycles, which is also known as the Wöhler curve [164, 165].

2.5.2 Fatigue resistance

Hardness and residual stress distribution critically affect fatigue resistance and are characteristic features of nitriding. Technical products are generally stressed by repetitive loads in the region of the elastic strength. Thus, the material can fail because of fatigue. Materials with high strength and low ductility behavior should resist crack initiation and have good fatigue strength properties. The fatigue strength of quenched and tempered material increases linearly with their hardness. The surface condition, such as surface roughness and scratches, affect the fatigue strength remarkably as fatigue failures start predominantly from cracks at the surface [132]. The better fatigue resistance compared to quenched and tempered microstructures was realized early in 1930 [166, 167]. It was subsequently explained by the simultaneous effect of compressive residual stresses in the case and the high hardness of the nitrided microstructure [168, 169, 170].

Normally, when a material is under a load (a bending or a torsion), the maximal stress (tension or compression) very often exists at the surface and lower stress (sometimes zero) in the core. The stress in the material is locally heterogeneous. Materials with high strength at the surface and a strength gradient toward the core are often used to optimize the behavior of components. This profile can be established by surface hardening, carburizing and nitriding are most often used [132]. For many years, nitriding has been used to enhance the fatigue behavior of components, especially parts subjected to complex cyclic mechanical, chemical and tribological loads. It is proved that the fatigue strength is defined by the core strength and the nitriding case [132].

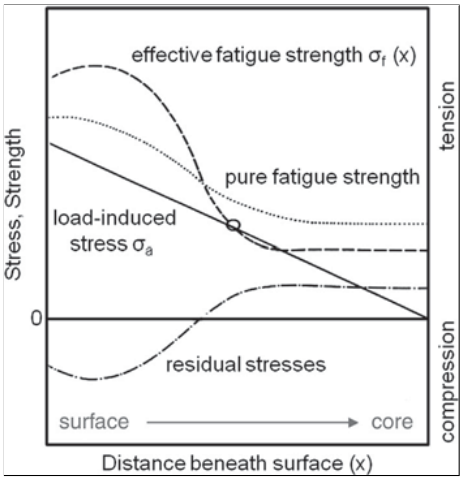


Figure 2.39 – Woodvine analysis of carburized steel fatigue specimens, predicting subcase/surface origin of failure [111].

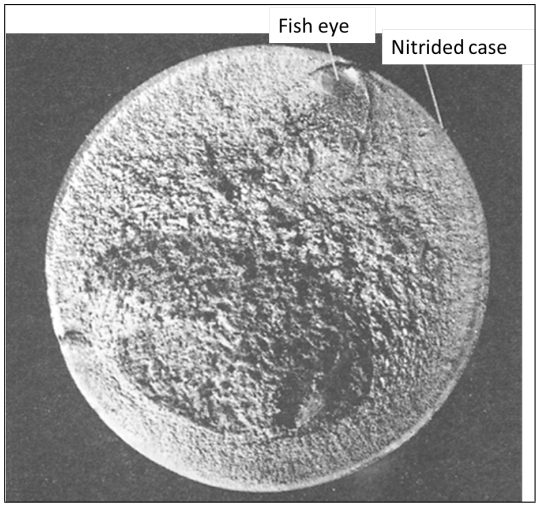


Figure 2.40 – Fatigue failure of the nitrided bar without stress concentration [171].

Local fatigue strength, according to Woodvine, is used for evaluating the influencing variables on the fatigue behavior of surface hardened components, shown in Figure 2.39. This approach is feasible because the residual stresses are not decreased by plastic flow due to the microstructures with high hardness. For example, compressive residual stress in a tension mode enlarges the allowed stress field and significantly increases the fatigue limits of the component [132]. In the case of flat load-induced stress distribution, the fatigue failure in the high cycle region arises by local crack initiation due to inhomogeneities in the microstructure, particularly nonmetallic inclusions within the core near the strengthened case. In Figure 2.40, for a straight shaft with a hardened layer, failure occurs at depth h beneath the surface. As the load changes, the position of fatigue failure may change accordingly [111, 132, 171].

2.5.3 Tribological behavior

Abrasive wear is the most rapid form of wear. A justified hardness and metallurgical phase can considerably enhance the abrasive wear resistance of steels. The morphology of the carbide inclusions is critical to abrasive wear resistance [172]. Large lamellar inclusion contributes more to the abrasion resistance when the grits are big, while the small spherical inclusions prevent the abrasion when the grits are comparable [172, 173]. The high content of carbon and alloy elements provides M2 steel with high amounts of inclusions of hard carbides (chromium and molybdenum carbides) that provide additional abrasive wear resistance. The basic method of abrasive wear control is to raise the hardness of the worn surface.

Adhesive wear is a serious form of wear that may cause high wear rates and unstable friction coefficients. The adhesion between two metals can be explained by electron transfer between contacting surfaces. Free electrons on the metal surface can transfer to another body when the distance between two surfaces is smaller than 1 nm and establish bonding [174]. The formation of transfer film is a characteristic feature of adhesive wear and distinguishes it from other wear mechanisms. Adhesion can be reduced by increasing the surface roughness or hardness of the contacting bodies [175].

Nitriding can provide a hard diffusion zone and generate a compound layer with low friction tribological properties. The improvement of tribological properties can be expected from several points [119, 111].

— The high surface hardness can better resist plastic deformation, increasing adhesion and abrasion resistance.

— Microstructure. Adhesive wear arises due to the formation of atomic bonds between the friction partners and a following shearing outside the initial contact area. Compared to metals with fcc and bcc crystal structures, the ε nitride phase exhibits minor adhesive behavior with a hexagonal structure. Plus high hardness, ε-nitrides have strongly limited plastic deformability.

— The high compressive residual stress in the nitrided layer tends to close the formed microcracks or impede their formation during wear. Contact fatigue occurs in rolling contacts, frequently accompanied by slip and sliding contacts, and is a major cause of failure in rolling-elements bearings, teeth, wheel-rail contacts, etc.

Figure 2.41 shows nitriding layers' hardness and wear resistance distribution. Porosity leads to reduced hardness and lowers the wear resistance near the surface. The wear resistance reaches the highest level at the compound layer due to the high hardness, the special structure of ε-nitrides, and the high-level compressive residual stress [111, 176].

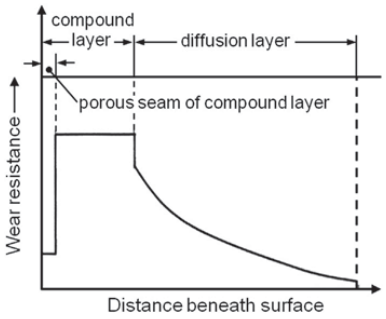


Figure 2.41 – Wear resistance of nitrided layers as a function of distance from surface [111].

2.6 High-speed steels (HSS) and their heat treatment

2.6.1 High-speed steels

High-speed steels are often known as HSS or HS. As a subset of tool steels, they are commonly used as cutting tool material, such as drill bits, taps, saws, also dies. HSS can withstand higher temperatures than carbon steel and other tool steels without losing hardness. This allows the requirement of fast cutting. High-speed steels are used for cutting and cold forming operations, which require hot hardness, wear resistance, and sufficient toughness. These properties are brought about by alloying with high amounts of

strong carbide-forming elements such as tungsten, molybdenum, vanadium and chromium [177].

High-speed steels are often used for cold forging or machining in which other materials, generally softer than the cutting tools, are cut or deformed [178, 179, 180, 181, 182, 183]. High-speed tool steels are so named as their ability of high-speed cutting speed [184]. The high hardness, hot hardness, and softening resistance of high-speed steels can be attributed to a large number of excess alloy carbides, the microstructure, and fine grain size achieved from the special processing during the steel fabrication, and heat treatments [185, 186, 187, 188, 189, 190, 183, 191, 192, 179, 193].

High-speed steels are generally classified into molybdenum (M type) and tungsten (T type) based steels depending on the major alloying element. High-speed steels are iron-based steel containing carbon (0.7-1.6%) [180, 183] and a significant quantity of carbide forming elements, such as chromium, vanadium, molybdenum, tungsten, etc., which can increase the hardenability and the matrix hardness by developing martensite [194] and carbides. Cobalt is a weak carbide forming element, it is added in some of them to reach super high hardness, and high hot hardness [195, 196, 180, 183, 179].

The addition of tungsten benefits the hardness and hot hardness of the material [197]. Molybdenum forms the same carbide with iron as tungsten and can be substituted for tungsten. Molybdenum decreases the hardening temperature, leading to a slight decrease in hot hardness but a better toughness [198, 199, 200, 201]. The chromium concentration in high-speed tool steels is between 3% to 5%, which is responsible for the hardenability as chromium carbides can dissolve entirely in austenite at 950-1000 °C [202, 183]. The addition of vanadium can increase the cutting efficiency of the tools. With properly carbon balanced, the toughness can be little affected [181, 203, 179].

Adequate load-carrying capacity requires the high hardness of both the core material and the surface layer. Controlled substrate heat treatment should offer the core material high toughness. High-speed steels usually have a close hardness (minimum hardness: 61-66 HRC) [184] and a similar heat treatment path (Figure 2.42).

M2 steel is one of the most popularly used high-speed steel. It has high toughness and good cutting ability but low hot hardness and wear resistance. It is based in the tungsten-molybdenum series, and the chemical composition is shown in Table 2.3.

Table 2.3 – Chemical composition of M2 high-speed steel (wt.%)

C	W	Mo	V	Cr	Si	Standard
0.80-0.88	5.9-6.7	4.7-5.2	1.7-2.1	3.8-4.5	-0.45	ISO 4957 [204]
0.78-0.88	5.5-6.75	4.5-5.5	1.75-2.2	3.75-4.5	0.2-0.45	ASTM A600 (regular C) [184]
0.95-1.05	5.5-6.75	4.5-5.5	1.75-2.2	3.75-4.5	0.2-0.45	ASTM A600 (high C) [184]

2.6.2 Carbide and microstructure transformation during steel manufacturing and heat treatments

The evolution of carbides depends on each step of production, from casting to surface treatment [205, 177, 206]. Conventionally, high-speed steel ingots are produced by mold casting and hot working like forging or rolling. Hot-working can break the coarse carbides network and refine the structure [207, 208]. In recent years, the production of M2 steel has been realized by adopting continuous casting in some advanced steel mills [207, 207, 209, 210, 211, 208]. The main features of the as-cast structure are the distribution, morphology,

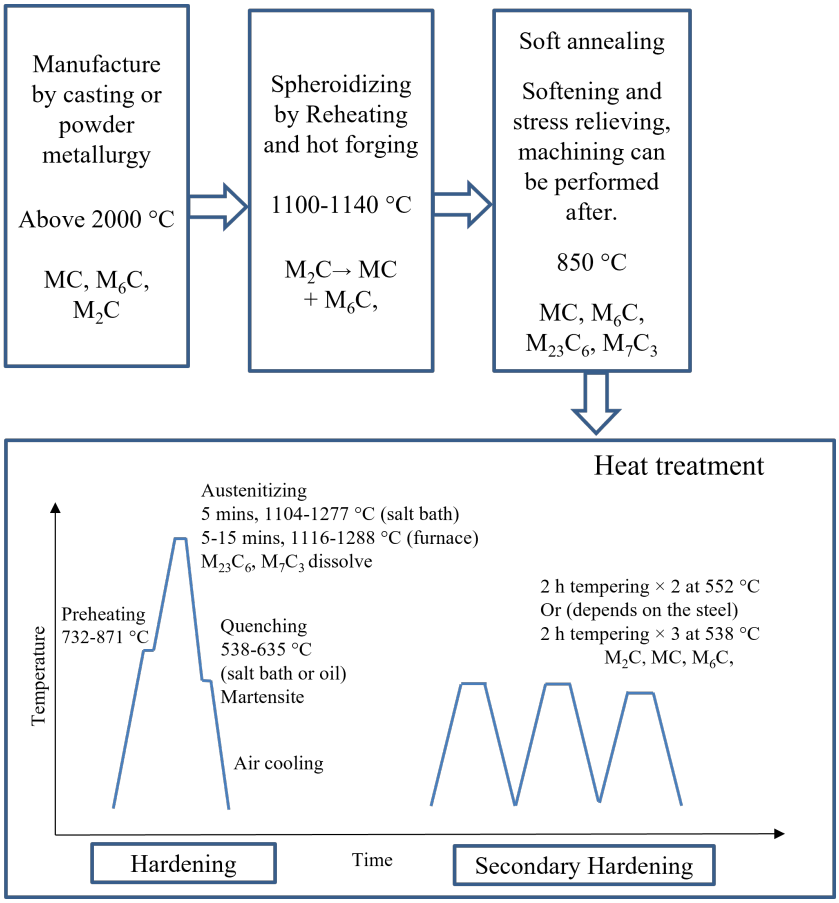


Figure 2.42 – The thermal process routine of high-speed steel from the manufacturing to the final heat treatment (The time and temperature information for heat treatment is from ASTM A600 [184].).

and size of the carbides and dendrites, which have a crucial influence on the mechanical properties of final products [208].

The size and the segregation of these primary carbides lead the material to a low toughness and ductility [180, 212]. Powder metallurgy technology has been widely studied and applied to high speed tool steels [213, 214, 215, 216, 217, 218, 219, 220]. By avoiding the large amount of coarse eutectic Mo, W and V rich carbides [212, 221], powder metallurgy offers better uniformity in microstructure, grain size and hardness to the material, smaller average carbide size [222, 223, 224], better grindability [225], improved toughness and wear resistance [226] higher fatigue strength comparing to casting [227].

2.6.2.1 Solidification

The solidification of M2 steel starts at about 1400 °C with the formation of low-alloyed bcc δ-Fe. The remaining melt is enriched with the alloying elements C, W, Mo, V, Cr, and Co. Therefore, around 1330-1300 °C, the peritectic reaction starts, and the already formed δ-Fe reacts with the melt transforms into γ-Fe. This further leads to the formation of coarse M_2C particles at the center of dendrites, as shown in Figure 2.44, resulting from a peritectic decomposition of δ-ferrite. Subsequent enrichment of solute atoms around the growing austenite dendrites leads to the formation of coarse interdendritic eutectic carbides of MC, M_2C and M_6C. The eutectic temperature is about 1250 °C, further cooling below the solidus results in general precipitation of small carbides of M_2C and MC. Inter-

dendrite M_2C eutectic carbides are predominant carbides in as-cast M2 steel, see Figure 2.43. Here occurs the reaction: liquid → austenite + eutectic carbides. The eutectic and small carbides have different morphologies and chemistry [228, 229, 230].

The cooling rate during solidification is the key factor that differentiates continuous casting from mold casting. Figure 2.43 shows the morphology of eutectic M_2C carbides when solidifying with different cooling rates, which, as can be seen, change from plate-like to rod-like. Because the fast cooling rate does not allow alloy elements diffuse with as a large amount as the slow cooling rate, rod-like carbides have a much lower concentration of alloy elements [211, 231].

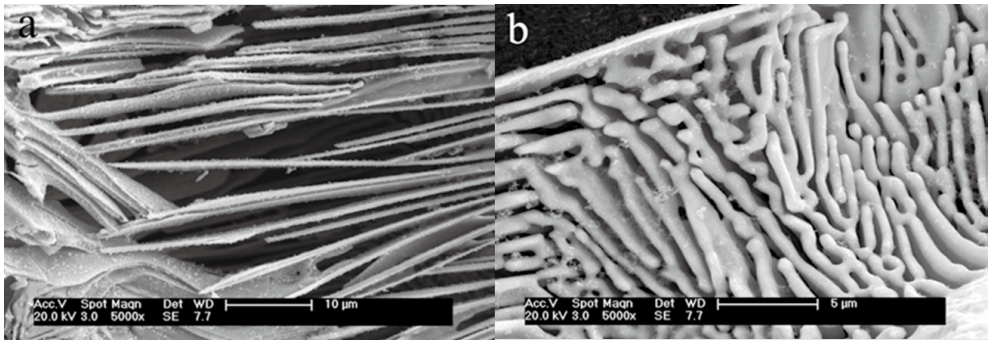


Figure 2.43 – Austenite dendrites and eutectic M_2C carbides distributed in the interdendritic region when the cooling rate is (a) 0.6 K/s and (b) 11.5 K/s [211].

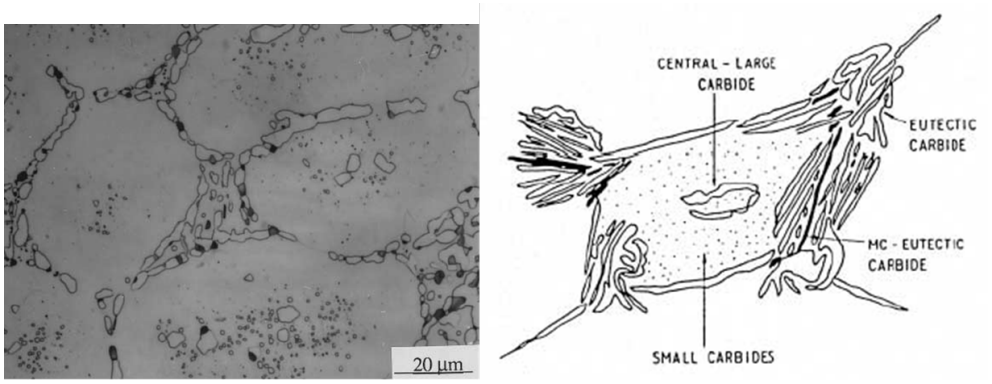


Figure 2.44 – Carbides in as-cast M2 steel [228].

The continuous casting process can effectively refine the grain size and improve eutectic carbides' uniformity. However, central segregation often occurs during continuous casting. This is attributed to the cooling rate gradient from the surface to the core. Figure 2.45 shows the carbide fraction and grain size distribution concerning the location in the billet, the higher cooling rate (near to the surface) can effectively reduce the average content of carbides, and the grain size of the samples increased by more than 2 times from the edge to center. The continuous casting process can effectively refine the grain size, but it does not have a distinct effect on the grain distribution uniformity. Hence, it requires considering where the tool material is taken from the casting billets [208].

2.6.2.2 Carbides refinement and spheroidization

Reheating can refine and spheroidize the carbides. Hot deformation can help to break down the big carbide network and accelerate the refinement. M_2C is metastable, at high

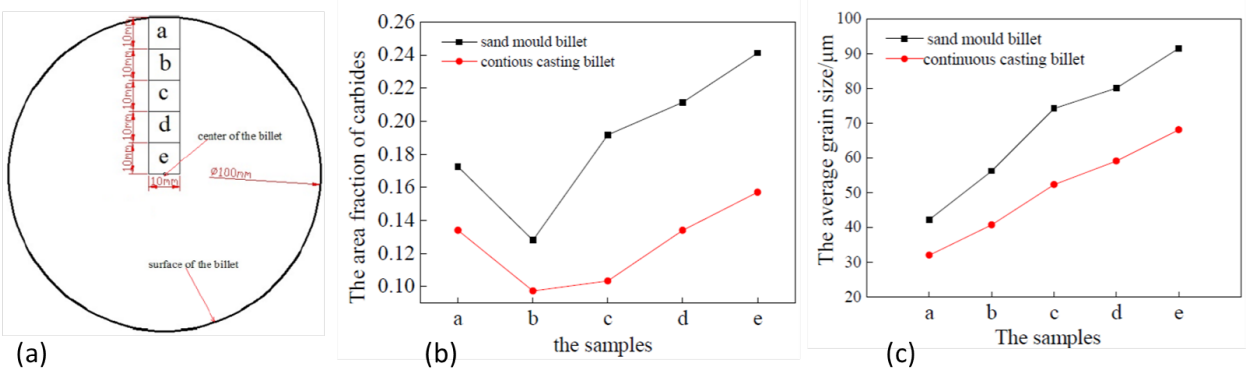


Figure 2.45 – (a) schematic diagram of sampling for casting microstructure analysis, (b)area fraction of carbide in the different samples of the M2 steel billets, (c) the grain size at different positions in the sand and continuous casting billets [208].

temperature, it decomposes into M_6C and MC: M_2C + austenite → M_6C + MC. Generally, reheating at 1150 °C for 1 hour, M_2C formed by continuous casting can completely decompose, as shown in Figure 2.46 (c). Rod-like M_2C carbides formed from fast cooling are easier to decompose than plate-like ones formed from conventional casting. In Figure 2.46 (b) and (d), the arrows show new phases after the decomposition of M_2C, it can be noticed that M_6C are much bigger than other MC carbides, so the refinement and spheroidization are more effective on M_6C carbides [211, 230, 232, 233].

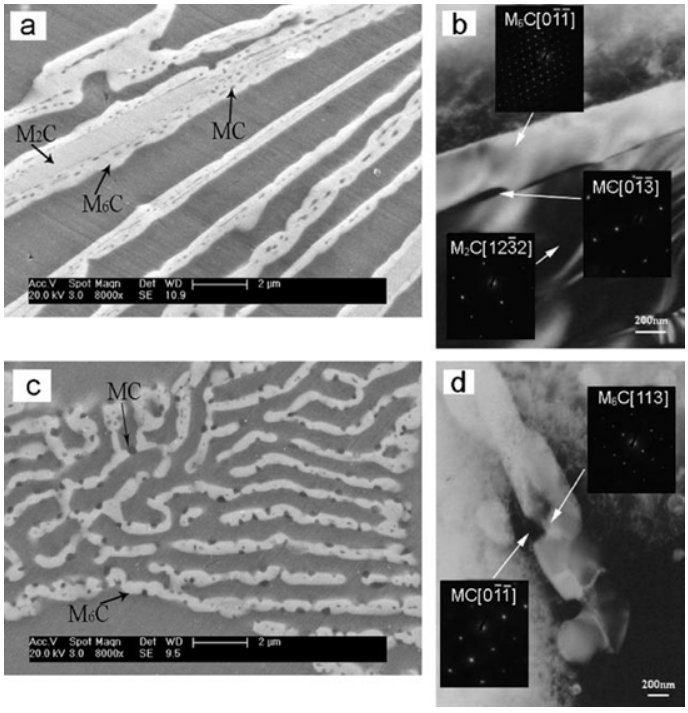


Figure 2.46 – SEM micrographs of M_2C in M2 cast ingots after heating at 1150 °C for 1 h: (a) lamellar M_2C, sand mould, (c) rod-like M2C, iron mould. (b) and (d) TEM photography corresponding to (a) and (c) separately [211].

Generally, high-temperature deformation of steel increases the rate of spheroidization and coarsening of carbides. The theories proposed to explain spheroidization are all based on enhanced diffusivity due to the following [232]:

— formation of short-circuiting diffusion paths during deformation, such as dislocations and/or subgrain boundaries;

— generation of excess vacancies and formation of solute/vacancy complexes;

— geometric role played by substructures formed in one or both phases, which leads to enhanced diffusion rate and subsequent spheroidization.

However, hot forging accelerates the spheroidization rate of M_6C, of which the mechanism is dominated by mechanical fragmentation of plates depending on the reduction rate, and diffusion plays almost no role in this process. And according to the experiment result from M.R. Ghomashchi, hot forging has little apparent effect on carbide coarsening. MC carbides remain almost unchanged during hot forging, and center carbide spheroidization happens along with a dissolution of small carbides [232].

Small substructure-free grains form during hot forging and grow during the subsequent annealing. Figure 2.47 shows the microstructure in M2 material after hot forging. It's important to notice that the residual stress distribution occurs in the material, and carbides redistribute at the position where strain exists. Plastic deformation breaks the original grain boundaries, and the carbides exist at the grain boundaries in the segregation way, as shown in Figure 2.47(c). Inner residual stress can easily cause defects in the material. To relieve the residual stress in the material and soften the material for the subsequent machining process, annealing is necessary after hot forging [230, 232, 233].

The mechanism of spheroidization of M_6C plates is slightly accelerated during annealing after deformation, while the coarsening process is almost the same as the heat-treated specimens. This might be attributed to the damaging of carbide plates during forging [232].

Hot forging generally is applied at 1100-1140 °C and finished at above 900 °C. Annealing temperatures are above 850 °C. During annealing, the iron matrix reduces its alloying content, with annealing carbides forming. After soft annealing, high-speed steels contain a ferritic matrix with primary and annealing carbides as shown in Figure 2.48, the big ones in the center are the primary carbides formed during solidification and spheroidized during hot forging, with a diameter about 2 μm, as well as the small carbides in the matrix which are secondary carbides formed during annealing with diameter between 50 μm to 300 μm. Many dislocations can also be noticed in the ferrite matrix, which is caused by hot plastic deformation during forging. At annealed state the carbides in M2 steel includes $M_{23}C_6$, MC, M_6C, M_7C_3, and $M_{23}C_6$, M_6C, M_7C_3 can easily dissolve into austenite during austenitization, also the annealing secondary carbides are very small, so $M_{23}C_6$ and M_7C_3 can often completely dissolved after austenitization [234].

2.6.2.3 Hardening

High-speed steel tools are shaped in the annealed condition and subsequently heat-treated by hardening from about 1200-1220 °C and tempering at 550-560 °C, usually, one-hour for 3 times usually [177]. During austenitization, some primary carbides dissolve, and the austenite becomes rich in carbon and carbide-forming alloying elements. The hardening temperature and holding time are critical. They must be carefully chosen to keep a sufficient amount of primary carbides to ensure good wear resistance and to guarantee the content of carbide-forming alloy elements in the solution for the precipitation of secondary hardening carbides during tempering. High-speed steels generally have good hardenability thanks to the high content of alloying elements. They are normally hardened by step-quenching into a molten salt bath at 500 °C and air cooling to room temperature

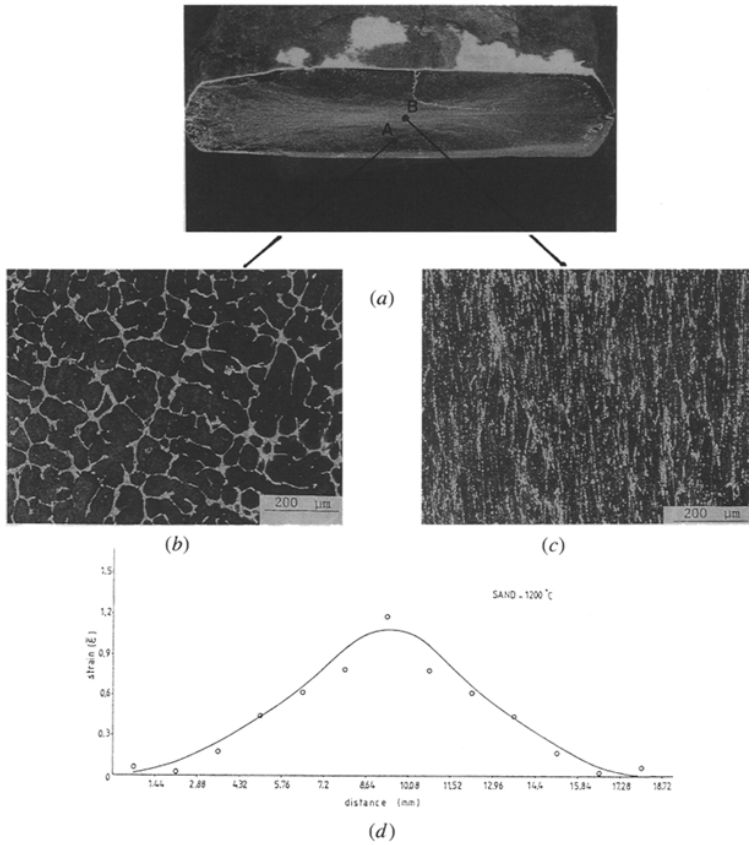


Figure 2.47 – (a) as-forged to show strain distribution; (b),(c) optical micrographs of points A,B in (a); and (d) strain distribution [232].

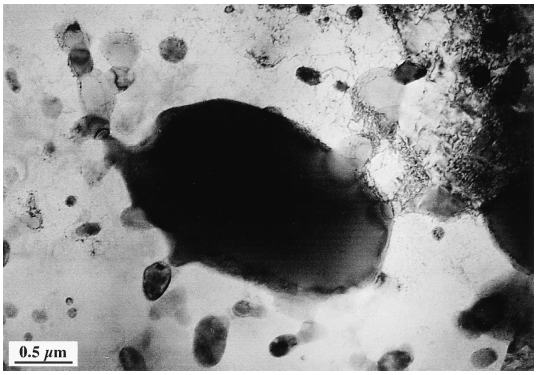


Figure 2.48 – Microstructure of the annealed steel (HVEM) [206].

as shown in Figure 2.42. Generally, In the as-quenched state, the microstructure of M2 steel consists of partially twinned martensite, retained austenite (in the amount of up to 30% vol.), and carbides undissolved during austenitizing, mainly M_6C, and occasionally MC [235, 236, 177, 203]. A small volume fraction of 'proeutectoid' carbides is possible to be present because of precipitation at temperatures in the range 1000-900 °C during the hardening operation [203].

2.6.2.4 Secondary hardening

Martensite is a hard, metastable, carbon-supersaturated phase with a body-centered tetragonal (BCT) crystal structure. It is a product of diffusionless transformation when

austenite is fast-cooled, the carbon atoms don't have time to diffuse out of the crystal in large enough quantities for cementite formation. Fresh martensite is very brittle if the carbon content is greater than approximately 0.2 to 0.3% and cannot be used for most applications. This brittleness can be significantly reduced (with some loss of hardness) by heating to tempering temperature. The tempered martensite is a binary phase composed of a continuous stable ferrite matrix and extremely small and uniformly dispersed cementite particles embedded [237].

High-speed steels have a large amount of retained alloyed austenite at quenched state. Multiple tempering is given during the last critical heat treatment step to transform the retained austenite and produce the secondary carbides. The heating and cooling processes are necessary to repeat several times because a significant part of retained austenite is transformed only during cooling after tempering and during consecutive heatings for temperings [238]. Due to the high carbon amount in M2 steel, the martensite finish temperature Mf is lower than room temperature. When the steel is cooled after first heating to the tempering temperature (560 °C), carbon diffuses from retained austenite to martensite (also called conditioning of austenite), and the martensite start and finish temperature Ms and Mf of such regions rise. Retained austenite then transforms to martensite during cooling. As not enough carbon diffusion occurred in the first heating, multiple tempering cycles must be given to bring the retained carbide-forming acceptable level. By reducing the austenitization time, continuous heat treatment is studied [239, 209, 210]. Less primary carbides dissolve, less austenite is retained, also fewer carbide-forming alloy elements diffuse into the solution. These lead the martensite to start temperature Ms increases, so tempering temperature needs to increase [209, 210].

For M2 high-speed steel, four transformation steps regarding secondary hardening are involved during tempering. These steps are in sequence but can also overlap [238, 240, 236].

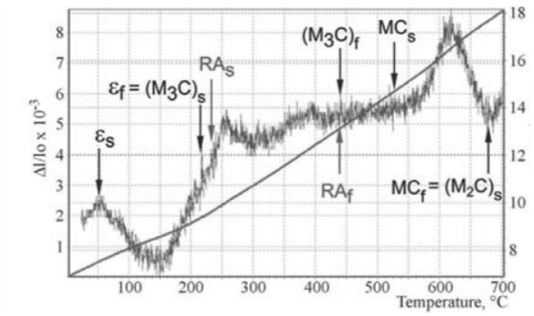


Figure 2.49 – Dilatograms of M2 heated from as-quenched state at the rate of 0.05 °C/s [236].

— 100-200 °C. Metastable ε carbide ($Fe_{2.4}C$) with a hexagonal crystal structure precipitates from the supersaturated martensite.

— 200-320 °C, the transformation of the retained austenite, a non-homogeneous mixture consisting of supersaturated ferrite and cementite, i.e., lower bainite, forms.

— 200-420 °C, Cementite is formed. This results in further decarburization of the matrix and dissolution of metastable ε carbides allowing for the steel matrix recovery.

— Above 400 °C, diffusion of alloying elements (V, Mo and W) occurs. Then, cementite gradually dissolves to make the nucleation of MC and M_2C carbides coherent with the alloy matrix possible. This leads to secondary hardening.

After this heat treatment, the steels consist of about 6.15 vol.% of micron size hard carbides of type MC and M_6C (primary carbides), dispersed in a matrix of temped martensite.

The matrix contains a fine and dense dispersion of nanometer-size precipitates (secondary carbides), which contribute to the high hot hardness of the steels.

The heating rate during tempering is also important as it can change the transformation temperature and time, affecting the final phase composition in the material. Continuous heating transformation (Figure 2.50) describes the revolution of the transformation as a function of the heating rate [236].

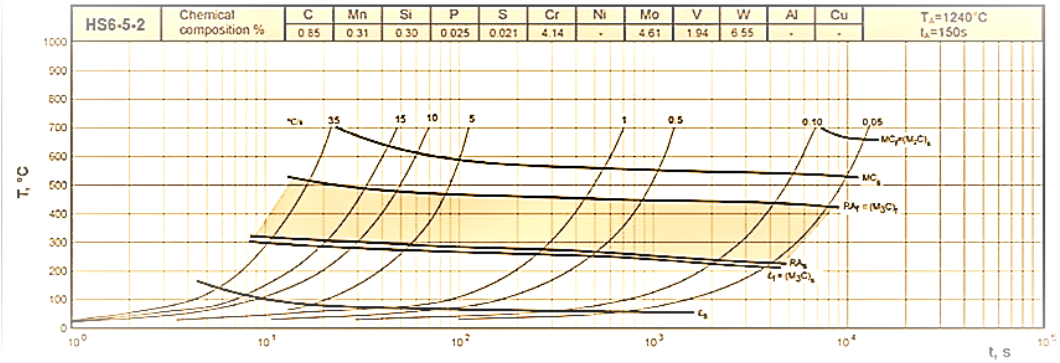


Figure 2.50 – Continuous heating transformation (CHT) diagram of M2 steel [236].

In recent years, continuous heat treatments have been studied. By reducing the austenitization time, fewer primary carbides dissolve, less austenite is retained, also fewer carbide-forming alloy elements diffuse in the solution. Therefore, martensite start temperature Ms increases, so tempering temperature needs to increase as shown in Figure 2.51 [209, 210]. All these time-reducing processes lead to the change in the final chemical composition of carbides. In the matrix, a higher alloy element content is found in the matrix of the isothermally treated sample.

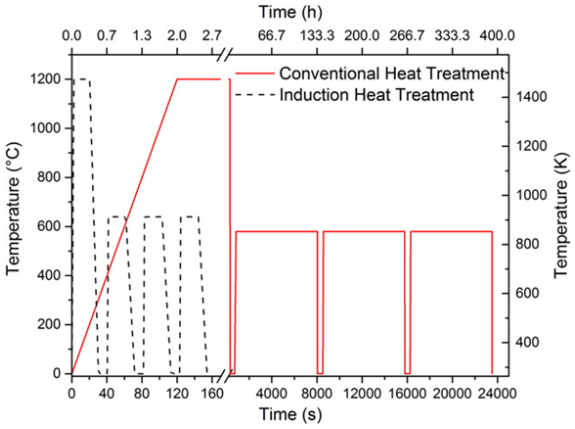


Figure 2.51 – Heat treatment sequence of high-speed steels [209].

However, in both cases, the carbide-forming elements are homogeneously distributed in the matrix, which indicates that homogenous austenite is obtained. Inhomogeneous austenite could result, for example, in differences in martensitic block size or increased stabilization of retained austenite in regions enriched in alloying elements [239, 209, 210]. Nevertheless, a non-homogeneous distribution of carbon is present, and carbon is segregated to lattice defects and lath boundaries due to auto-tempering during quenching. After tempering, however, the segregation appears to all carbide-forming elements as well, as shown in Figure 2.53, at the original position of carbon segregation, and the smaller

carbides and larger plate-shaped precipitates at lath or twin boundaries do not differ in chemical composition [209].

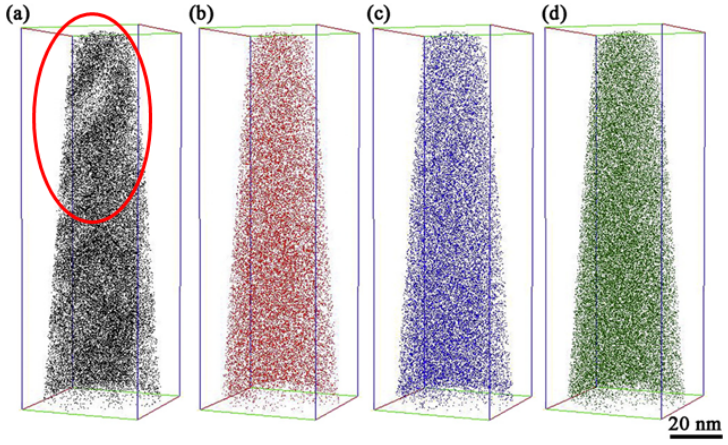


Figure 2.52 – Three-dimensional reconstruction of an isothermally hardened sample, distribution of (a) carbon, (b) tungsten, (c) vanadium, and (d) molybdenum atoms [209].

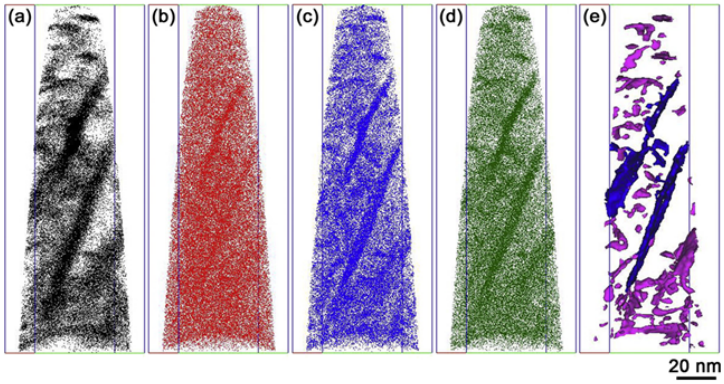


Figure 2.53 – Three-dimensional reconstruction of a single continuously tempered sample (a) carbon, (b) tungsten, (c) vanadium, (d) molybdenum distribution, and (e) vanadium and molybdenum 6.5 at.% iso-concentration surface [209].

2.6.2.5 Final microstructure and carbides composition in M2 steel after heat treatment

The microstructures of primary and secondary carbides in high-speed steel after tempering are shown in Figure 2.54 and Figure 2.55.

As discussed above, the heating rate, temperature and holding time in each process affect the final chemical composition of the carbides. Following the general industrial production route, the composition of primary and secondary carbides in M2 steel would be similar. Table 2.4 shows the chemical composition of primary carbides [203]. The approximate chemical composition of secondary carbides from another commercially used fully hardened and tempered M2 sample are given in table 2.5 [177].

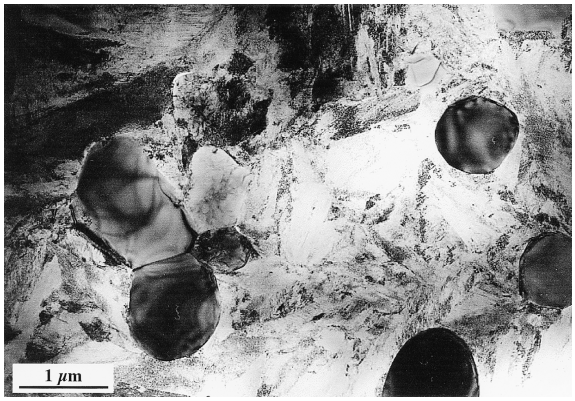


Figure 2.54 – Microstructure of steel after hardening and tempering [206].

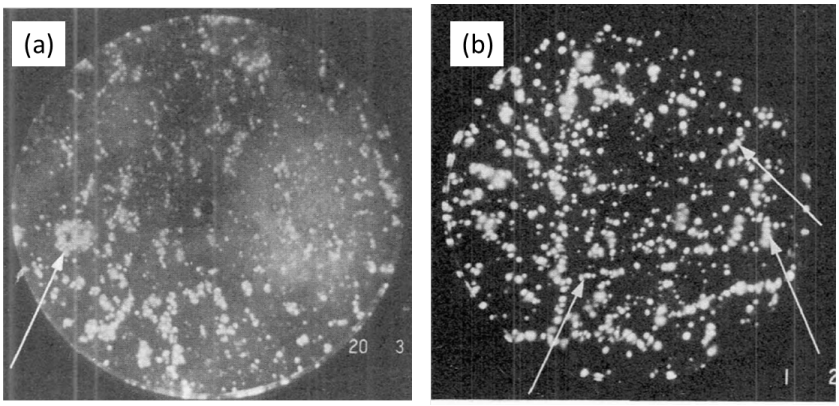


Figure 2.55 – (a)Plate-shaped secondary carbide MC in M2 steel, 5nm. (b)Rod-shaped secondary carbide M_2C in ASP23 steel, 200 nm [177].

Table 2.4 – Chemical composition of primary carbides of M2 high-speed steel (A sample made by powder metallurgical process and hot rolled into 20 mm diameter bar, subsequently austenitized 3 min in a salt bath at 1220 °C, step quenched into molten salt at 550 °C, for 10 min followed by air cooling through the Ms temperature (about 200 °C) to room temperature, 3 times of 1-hour tempering with intermediate air cooling) [203].

Carbide	**Volume fraction**	**Mo/at%**	**V/at%**	**Cr/at%**	**W/at%**	**Si/at%**	**Fe/at%**
MC	1.4	11.9±1.3	67.7±4.5	6.4±1.1	6.6±1.0	-	7.4±1.6
M_6C	6.1	20.8±1.3	5.4±0.5	5.1±0.6	16.0±1.0	5.0±5.0	47.7±1.0

Table 2.5 – Chemical composition of secondary carbides in M2 high-speed steel (The iron content in all precipitates has been set to zero because of the difficulty of accurately measuring the iron content. In reality, all precipitates contain a small amount of iron, typically 5% of the metal content, and consequently a somewhat lower carbon content) [177].

Precipitate type	**Approximate precipitate formula**
MC	$(W_{.05}Mo_{.42}V_{.36}Cr_{.22})C_{1.1}$
M_2C	$(W_{.08}Mo_{.45}V_{.16}Cr_{.31})C_{1.1}$

2.7 Nitriding of M2 high-speed steels

2.7.1 Microstructure and properties of nitriding layers in M2 steel

Like other steels, the nitrided layer of M2 steel mainly consists of a compound layer and a diffusion zone (Figure 2.56) [82, 23, 119]. The compound layer is avoidable by controlling the nitriding parameters. When the solubility limit is reached, the diffused nitrogen expands the iron lattice and forms complex compounds with iron nitrides. The expanded lattice and dispersed nitride precipitates immobilize dislocations. The steel surface is therefore hardened [53]. The compound layer consists mainly of iron nitrides, with a thickness that can reach tens of micrometers according to the process parameters. The well-defined ε-Fe_3N phase and γ'-Fe_4N iron nitrides phase sublayer structure in the compound layer can be replaced by a mixture of both in steel because of the existing carbon [52, 92]. In M2 high-speed steel, the compound layer often consists of ε-Fe_3N iron nitrides because of the high concentration of carbon according to the Fe-C-N phase diagram. However, the γ'-Fe_4N is still found in some nitriding layers of M2 steels with special nitriding methods [82, 123, 241]. On top of the compound layer, the porosity may be formed due to the inherent metastability of iron nitrides and the recombination of N atoms into N_2 when the saturation is reached [242, 243, 52]. The compound layer can reach a very high hardness (it can be 1300 HV for M2 steel with a core hardness of about 600 HV at quenched and tempered state), and the oil retaining porous structure improves wear resistance [52, 244]. However, its brittleness and particular structure are still avoided in many applications, such as drills, forging tools [245, 246, 247, 25].

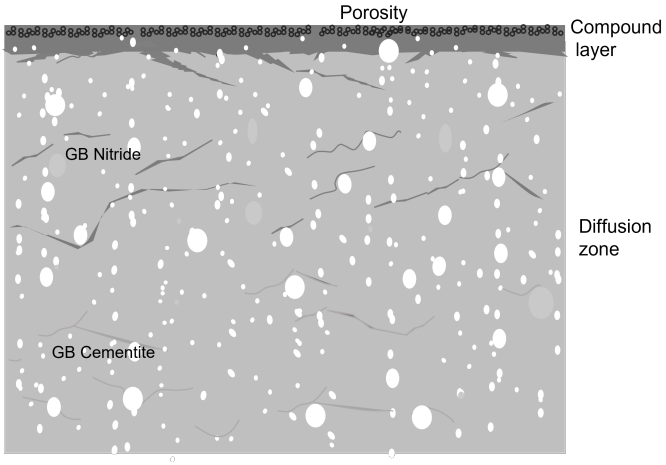


Figure 2.56 – Schematic graph of the nitriding layer of M2 steel.

Beneath the compound layer, it is the diffusion zone where alloy nitrides, grain boundary iron nitrides, and cementite can be formed (Figure 2.56). The high-speed steel nitriding layer may have better surface properties when the compound layer is not presented [74]. Except for the embrittlement of the ε-Fe_3N phase and porosity, the tensile residual stress is another reason to facilitate the early tool failure [80, 119, 248, 249, 250, 251, 252].

However, it does not give a complete denial of the compound layer. It was found that the compound layer effectively reduced adhesive wear by reducing material pickup and welding on the specimens [253]. Some treatments (eg. gas nitriding at 540 °C with 50% H_2 + 50% NH_3 [254], low-pressure nitriding [123]) obtained a compound layer on M2 steel consisting only of γ'-Fe_4N phase which offers a great improvement of work performance. Nitriding under an ammonia partial pressure of 2×10^3 Pa [123] forms a nitriding layer

where both the hardness and compressive residual stress reach the maximum value at the surface rather than the others in which both the hardness and the compressive residual decreases near the surface (Figure 2.57 (a)).

Figure 2.57 (b) shows the residual stress profile after annealing at different temperatures after nitriding, the temperature under 500 °C does not cause much residual stress redistribution. This is important to ensure that the hardness and residual stress stay relatively stable and reliable during working at a relatively high temperature depending on the application [123].

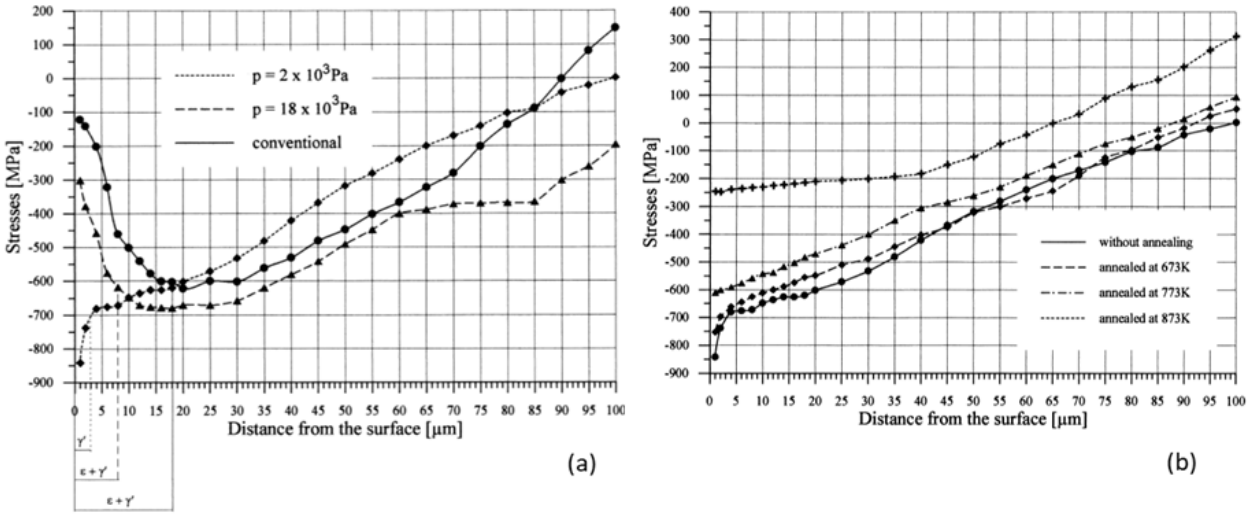


Figure 2.57 – Residual stress after nitriding, 560 °C for 6h, dissociation degree about 30% [123].

2.7.2 Precipitation evolution in high-speed steels during nitriding

In high-speed steels, Cr, Mo, and V form nitrides MN_n [111, 154]. The nitrogen dissolved in ferrite is only considered mobile, so the growth of the diffusion zone is only related to the diffusion of nitrogen in the ferrite matrix. Hence a higher concentration of nitride-forming element cause the slower growth of the diffusion zone and thinner compound layer [92]. The Cr and V elements are strong affinities with nitrogen, while Mo has a weak affinity [95, 96], so their nitrides forms before (instantaneously) and after iron nitrides start to form in binary alloys. Meanwhile, it is not yet found the relative information about W.

The tungsten nitrides are found in high-speed steels during plasma nitriding [255, 256], and also determined as the reason for hardening [254]. The existence of different alloy elements in the material leads the nitrided layers to different nitrogen concentrations, so as the depth of the nitrided layer and its hardness gradient [110].

Same as other steels, the carbon co-diffusion is found in high-speed steel during nitriding [250, 248, 64, 114, 78, 257]. As nitrides are thermodynamically more stable than carbides, some carbides transform into nitrides, and the released carbon co-diffuse with nitrogen, as introduced previously [257, 258]. The released carbon diffuses towards the outer surface because of the activity imposed at the surface by the outer atmosphere (presence of H_2 for instance), and the developed compound layer has higher carbon solubility (ε-Fe_3N iron nitride, with interstitial atoms in octahedral holes, can dissolve large amounts of carbon [259, 260]). Decarburization occurs depending on the process, and a carbon depletion is usually observed close to the surface [261, 262, 263]. It is also found that the formation of the compound layer can decrease the decarburization because the carbon diffusion

coefficient in the ε-Fe_3N or γ'-Fe_4N nitride layer is about 1/60 of that in α matrix [264]. The released carbon atoms also diffuse into a greater depth, interacting with the diffusing nitrogen [92, 97]. Carbon accumulation occurs ahead of the nitriding front (Figure 2.58) (thanks to the higher thermodynamic activity), which contributes to the growth of initial carbides [248]. In the diffusion zone, cementite is formed as carbon reacting with iron and precipitation along the grain boundaries nearly parallel to the surface under the influence of compressive residual stress [258, 36].

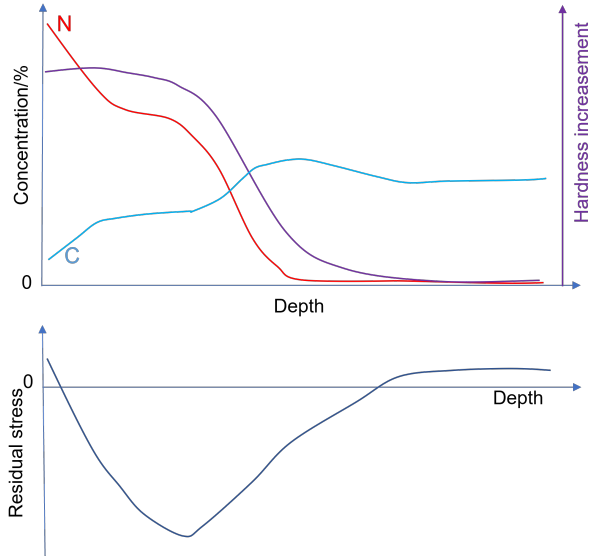


Figure 2.58 – Schematic nitrogen and carbon profiles in M2 high-speed steel after gas nitriding.

Due to the complexity of the carbides in the steel and the many possibilities of the precipitates, the phase transformation for each stage has not yet been systematically studied. Some phases are defined by different researchers.

— Carbide MC and M_6C increase after nitriding (Figure 2.59) [119, 23].

— $(FeWMo)_6C$ type carbides decrease due to the decarburization close to the surface [265, 78].

— Fe_4N, $VWC_{1.88}$ phases are formed at the surface of high-speed steel after plasma nitriding at low temperature, which is responsible for the hardness increase [82].

— ε-$(Fe, M)_{2+x}(N, C)$ phase is often found in the compound layer, and it is attributed to the transformation from the α'-Fe(C,N) [121].

— $(Fe, M)_{2+x}C$ and $(Fe,M)_7C_3$ are formed during plasma immersion ion implantation [121].

— The nitrides composition at the surface after nitriding for different times has been studied, β-Cr_2N, γ'-Fe_4N, γ'-Mo_2N, $Mo_{16}N_7$, δ-W_2N, ε-Fe_3N, Fe_5N_2 have been found. Some other nitrides like AlN, Mo_5N_6, W_3N_4 were mentioned to be detected [266].

— Due to the continuous phase transformation, the phase composition varies at each depth of the nitriding layer. For example, the concentration of Mo_2N nitrided was found to decrease from 5.5-5.6% at a depth of about 2 μm to 1% at a depth of about 7% in a nitriding layer of M2 steel [74].

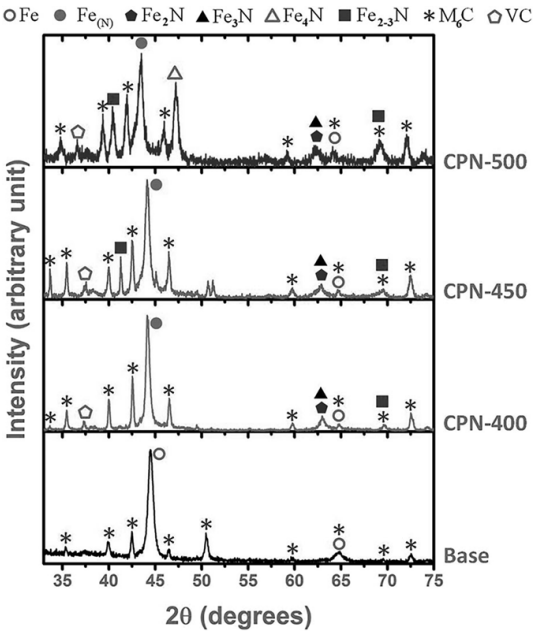


Figure 2.59 – XRD pattern of M2 and CPN (conventional plasma nitriding) treated at various temperature for 4 h with H_2:N_2 = 75%:25% [23].

2.7.2.1 Hardness

The surface hardness can increase by about 500 HV for quenched-tempered M2 steel. The effect nitriding depth is defined as the depth where the hardness is 100 HV higher than that in the core. By fitting the experimental nitriding depth (precipitation hardened) and nitriding time at different temperatures, the relation between the nitrogen diffusion coefficient and nitriding temperature for M2 high-speed steel is presented in [67],

$$D = 1.9 \times 10^{-9} \exp(-62828/RT) \tag{2.21}$$

R is the universal gas constant, R = 8.314 J/mol · K, T is the Kelvin temperature. The nitrogen diffusion coefficient at 500°C is then $D_N = 1.08 \times 10^{-13}$ m^2/s.

2.7.3 The mechanical behaviors of the nitrided layer of M2 high-speed steels

2.7.3.1 Residual stress

Some have reported that the first nitriding stage contributes the most to the growth of compressive stresses where the nitrogen is distributed in the solid solution. They can reach up to -750 MPa when only the saturated α-solid solution is formed [267, 268]. It is also reported that the maximum residual stress can reach -963 MPa on an as-ground tool [80] and even -1600 MPa under the surface of an sand-blasted M2 steel [114] (see in 2.7.5). The appearance of any nitride precipitation leads to a decrease in compressive stresses, when the phase ε-Fe_3N starts to grow, the decrease is noticeable [269].

2.7.3.2 Wear resistance

High-speed steels are often subjected to high pressure, low roughness, good lubrication, high hardness and residual stress and no ε-Fe_3N compound layer are expected to achieve a good wear resistance [270, 119, 271, 272, 273, 274, 182, 270]. Therefore, the maximum hardness in high-speed steel can be achieved at the surface when nitriding with a nitriding

potential below the limit for the compound layer formation. The maximum residual stress appears typically at the end of the plateau of the hardness peak [117, 97]. The nitriding must not be performed over time or under a high nitriding potential or temperature [123, 23, 119, 182, 275, 248]. The residual stress redistribution and the possible varied surface must be limited.

The tribological behavior includes abrasion, adhesion, tribo-oxidation and contact fatigue. It highly depends on the hardness, which resists plastic deformation. High compressive residual stresses should contribute to delaying crack initiation and propagation. Particularly, the ε-Fe_3N phase with an HCP structure has a high resistance to adhesion. However, it is a brittle material and can not withstand and support high contact loads without cracking. Surface crack generated in the ε-Fe_3N phase can easily propagate into the diffusion zone, leading to faster wear [119].

The wear resistance of high-speed steel decreases when the nitriding layer (compound layer free) depth is higher than 50 µm (or 38 µm [84]) due to the embrittlement, which might be related the edge effect during plasma nitriding [80, 276].

Some found that the friction coefficient of the nitrided sample decreased (from 0.90 to 0.65), and the wear resistance increased 25% (A nitriding layer with a thickness of 20 to 40 µm with an increased microhardness of 9-12.2 GPa was obtained on M2 steel from electrolytic plasma nitriding.) [277]. Others found that the roughness of the M2 steel surface increases after nitriding, and the increment is more significant when nitrogen fraction is higher in the atmosphere [119], which is linked to the nitrides concentration at the surface and the nitriding depth [67]. The roughness increases the wear rate even though the wear resistance is still better than the non-nitrided sample (Figure 2.60). It is found that plasma nitriding at 450-500 °C benefits the wear resistance of the high-speed steel, while 550 °C plasma nitriding produces a brittle layer [253].

2.7.3.3 Fatigue strength

Nitriding has been widely used to increase the fatigue properties of steel. The increased hardness in the surface layer and compressive residual stress could slow down the crack propagation in the in-depth direction [278, 279]. The fatigue life of the tools made of M2 steel increases with nitriding depth [23, 82]. However, it is also found that the accumulation of compressive residual stresses may result in premature fractures of the diffusion interlayer while subjected to a high contact pressure [251]. The compressive residual stress close to the surface decreases after the maximum residual stress is obtained [117, 97]. It is also found that the compound-free nitrided layer has more excellent fatigue properties [247]. Nevertheless, nitriding can sometimes decrease fatigue limit due to the increased roughness [280].

The type of loading is an important factor regarding the fatigue life of a component. Indeed, in the case of uniaxial loading, the ratio of the low-cycle fatigue strength between nitrided and un-nitrided cross-sections is linked to the residual stress [281]. High-cycles fatigue behavior of a material can be described with the uniaxial fatigue criterion based on the Goodman-Gerber diagram in terms of only the hardening but not the residual stress effect [282]. As for the multi-axial loading, the nitriding contributes the most when the maximum residual stress and hardness occur at the depth where the maximum shear stress locates according to the Dang Van criterion [283, 284, 285, 286, 287] (see in 2.8.3). In the case of sliding contact, the fatigue cracks usually initiate at the surface due to the high surface tension stress [288]. The maximum hardness and residual stress are expected to have the highest value at the surface to strengthen the surface [288, 289, 290].

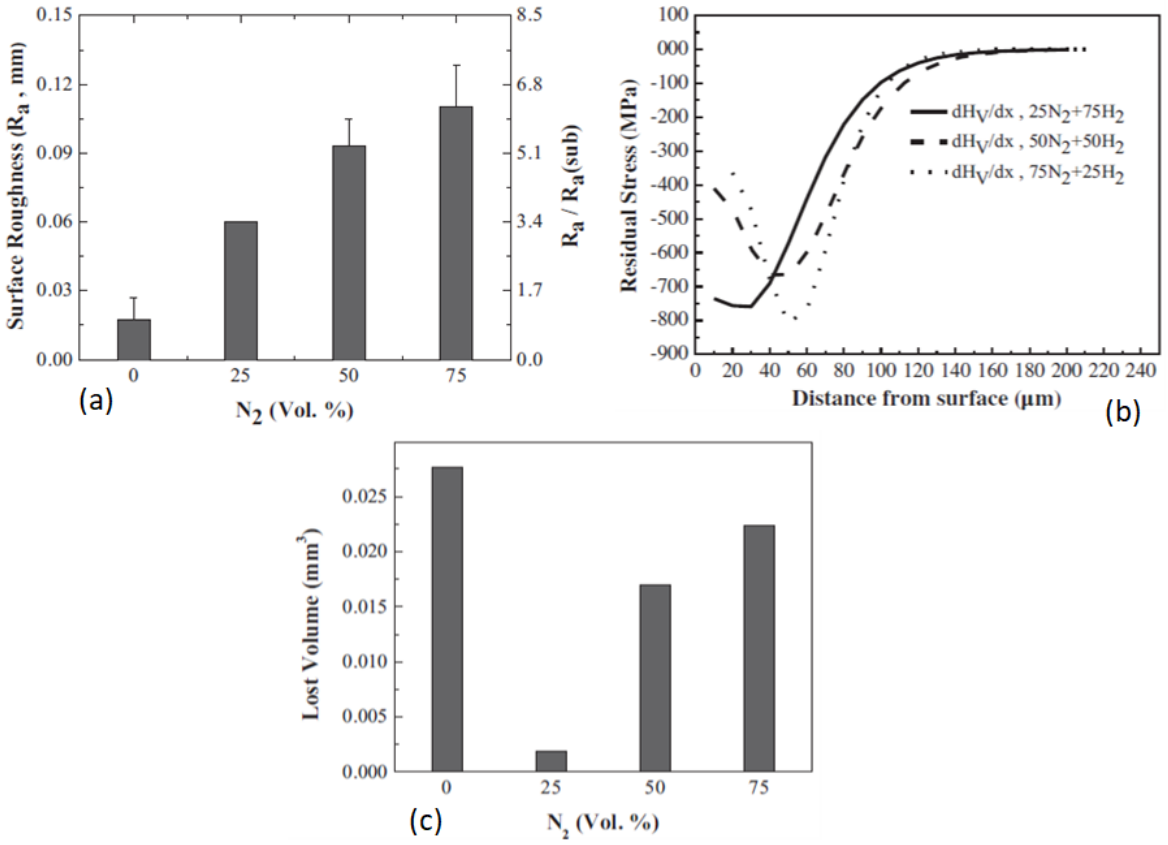


Figure 2.60 – (a) Surface roughness, (b)in-depth residual stress distribution, (c) wear lost volume of M2 steel after RF plasma nitriding different plasma gas compositions [119].

2.7.3.4 Corrosion resistance

The formation of alloy nitrides depletes the alloy element in the solid solution during nitriding, and the depletion can subsequently decrease the corrosion resistance of the steel [291, 292]. However, the nitrogen saturation in the solid solution can improve the corrosion resistance [293, 294]. It is also found that the compound layer can act as a barrier against corrosion attacks [295], and the corrosion resistance increases as the compound layer thickness increase [293]. The corrosion often occurs in the diffusion zone [296]. The corrosion in the diffusion zone is studied by removing the compound layer after nitriding [297]. It is found that plasma nitriding with a low flow rate (25% N_2 - 75% H_2) can improve the corrosion resistance of M2 steel. However, a higher flow rate causes a decrease in corrosion resistance, and the general corrosion evolves into rapid pitting due to the high volume fraction of nitrocarbides because the corrosion attacks start from the interface of nitrocarbides and the matrix [297].

2.7.4 Effect of initial microstructure on nitriding

The heat treatment affects the microstructure of the steel and alters nitrogen diffusivity during nitriding [67, 298, 299, 300]. The different carbide composition is obtained at each stage of thermal treatment of the steel (see 2.6.2) and will participate in the phase transformations during nitriding. Therefore, nitriding steels with different initial states can obtain different nitriding profiles [123, 300, 299]. However, very few papers have studied the effects of the initial microstructure on the nitriding profile induced by the heat

treatment.

It is found that the increase in hardness of the ferritic matrix is more significant than in the martensitic matrix, even though the overall hardness is much lower due to the different microstructure of the core material [299]. Similarly, the difference in maximum hardness after nitriding also occurs when the steel substrate is tempered under different temperatures or times after quenching, longer time, and higher temperature offers the nitriding layer a lower hardness with the same nitriding condition, as shown in Figure 2.61. Meanwhile, only a diffusion zone is formed in the hardened and tempered sample, while the annealed sample shows a compound layer composing ε-$Fe_{2-3}N$ and γ'-Fe_4N phases [67]. The explanations are given as [67]:

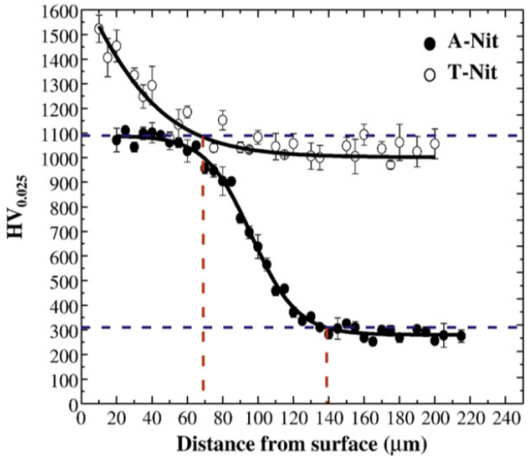


Figure 2.61 – Cross-sectional hardness-depth profiles for M2 steel, A-Nit is a fully annealed sample, T-Nit represent hardened and tempered sample (nitriding at 450 °C for 8 hours with a plasma portion N_2:H_2=25%:75%) [67].

— Compressive residual stresses existing in the hardened and tempered sample parallel to the surface result in the nitrogen a preference to diffuse transversely. Therefore, the nitriding layer grows slower.

— Remaining carbon in the martensitic matrix reduces interstitial sites where nitrogen atoms can stay.

— Alloying elements in the bct-α-lattice (body-centered tetragonal) in tempered martensite, trapping nitrogen atoms and forming fine nitride precipitates.

However, the different composition of carbides at these two initial has not been considered (for example, the $M_{23}C_6$ and M_7C_3 at annealed state, the M_2C at tempered state), as well as their nature and morphology, which can act an important role in the kinetics of carbides transformation during nitriding.

2.7.5 Effect of surface condition on nitriding

It is important to understand the mechanical conditions on the surface before nitriding because the manufacturing method affects the topology and the microstructure of the surface layer directly. A cross-section of machined steel consists of a topographic boundary, an oxide layer, a plastically deformed layer, and a metallurgically deformed layer over the bulk material (Figure 2.62) [24]. These might affect the nitriding process. For example, the plastic deformation of the lattice results from the surface finishing methods before

nitriding could induce a local change in the space between the grains which can affect the diffusion kinetics of nitrogen, or the residual stress caused by lattice deformation could change the favorable diffusion direction of the nitrogen. As for the surface itself, the developed surface has an expanded area to contact with nitrogen, benefiting the nitrogen enrichment at the gas-solid interface. For example, a thin and sharp tip on the surface is surrounded by nitrogen. And the nitrogen uptake level can be higher than other parts of the material on the surface. Therefore, the ε phase is more likely to be formed. This assumption is considered based on the experiment results of nitriding on M2 film [25].

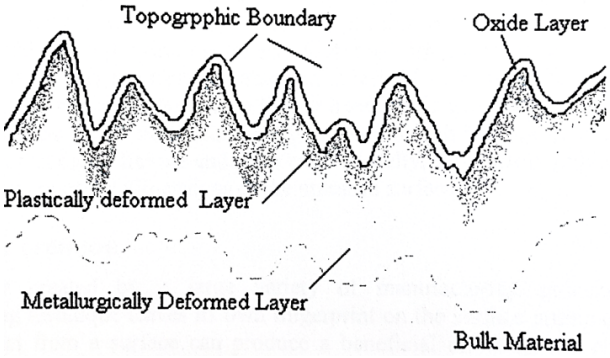


Figure 2.62 – Schematic cross-sectional view of a surface showing the surface and subsurface layers [24].

The final mechanical surface finishing methods, such as grinding, sandblasting, and polishing is often applied to treat the tool surface, and they enormously vary the residual stress level at or close to the surface. Grinding can generate maximum residual stress of -620 MPa at the surface. Sandblasting can generate compressive residual stress with a maximum value of -1350 MPa in the sub-surface, and the high level can continue until 50 μm under the surface. Polishing is the most moderate method, and the maximum residual stress after polishing can reach -150 MPa [275]. Nitriding profiles of the same material with different surface mechanical conditions are shown in Figure 2.63.

Smaller nitrided layer depths were found in the ground and sandblasted samples compared to polished ones due to the high compressive residual stresses, plastic deformation, and consequences for the submicron structure at the surface layer of the material [275, 114]. High compressive residual stresses induced by mechanical loading like sandblasting result in the lattice contraction in the direction perpendicular to loading and parallel to the surface [301, 302, 303]. This lattice directional distortion facilitates nitrogen diffusion parallel to the surface and obstructs a diffusion towards in-depth [304, 305, 114]. It is also claimed that the plastic deformation from sandblasting can lead to an extended amount of nitride precipitates and a higher compressive residual stress level in the deeper layer [114].

2.7.6 High-speed steel nitriding in duplex treatment

Plasma nitriding is often used on high-speed steels prior to a PVD coating (TiN or other hard nitride or carbide coatings) to create a duplex surface layer to achieve good wear resistance [306, 80, 250, 251, 252]. The presence of a compound layer with an elevation of hardness and brittleness leads the duplex layer lower wear resistance than a solely coated layer due to the reduction of the bond strength between the coating and the nitrided substrate [182, 74]. But the diffusion zone is believed to increase the load-bearing capacity of the substrate and improve the coating adhesion strongly [307, 308, 309, 276]. The duplex

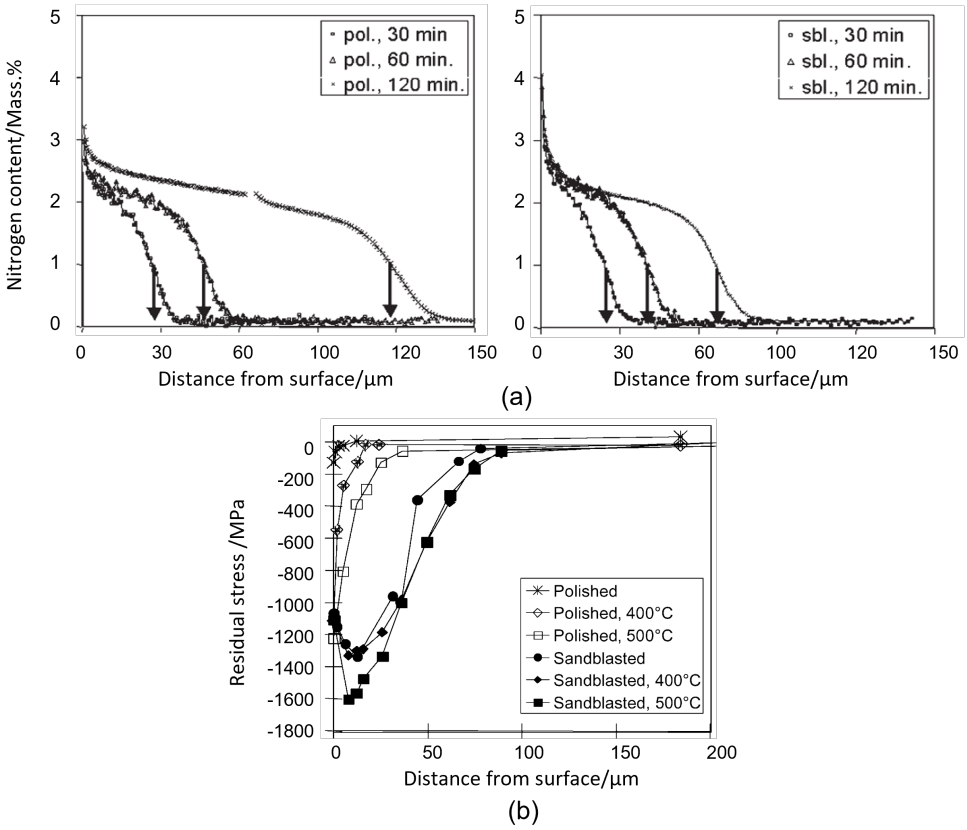


Figure 2.63 – (a) Depth profiles of nitrogen plasma nitriding at 500 °C with 5 vol.% N_2, 5 mbar for different nitriding times [114]. (b) Residual stress depth profiles for polished and sandblasted sample non-nitrided and plasma nitrided at 400 and 500 °C with 5 vol.% N_2 [275].

treatment using bright plasma nitriding (no compound layer) and TiN coating dramatically improves the wear resistance [80]. However, the thickness of the nitriding case depth needs to be carefully controlled (50 µm) because the accumulation of the cementite at the grain boundaries causes excessive embrittlement [80, 310, 311].

Presence and elevation of high nitrogen phase Hardness and brittleness of nitrided surface significantly reduce the bond strength between the coating and the nitrided substrate and limit the effect of using a combined vacuum-plasma treat.

2.8 Rolling contact failure and Dang Van criterion for nitrided steels

2.8.1 Mechanism of Rolling contact failure

Three essential factors for the initiation of micro-cracks can be summarized [290, 312, 313] as below:

— the high levels of contact pressure,

— the surface traction (friction),

— the inclusions (carbides) located at a critical position in the subsurface.

In the rolling contact fatigue failure mechanism, cracks usually initiate below the raceway surface at depths close to the location of the maximum shear stress before propagating upwards, as shown in Figure 2.64 (a). Nevertheless, the cracks may also initiate at the

surface where the tangential shear stresses are large [290], as shown in Figure 2.64 (b). When foreign particles are present in the lubricant, the indentation might be formed the same as the wear in the die shown in Figure 4.38 (a).

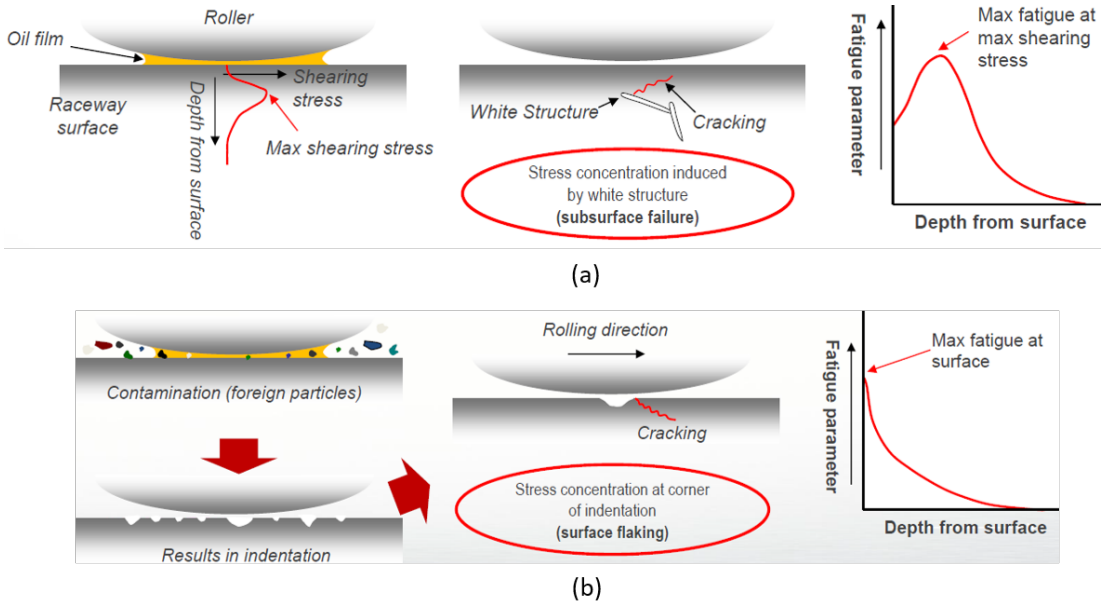


Figure 2.64 – Mechanism of rolling contact fatigue (a) when fatigue initiation is at the subsurface, (b) when fatigue initiation is at the surface [314].

Rolling contact is always accompanied by surface sliding, which severely impacts the fatigue life of the component [288]. As shown in Figure 2.65, sliding and rolling contact leads to the maximum shear stresses located at different depths. In sliding, the maximum shear stress is at the surface when the surface is ideal smooth, below but very close to the surface when the surface is in a certain roughness [290, 312]. A higher sliding/rolling ratio and higher friction coefficient increase the sliding effect [270].

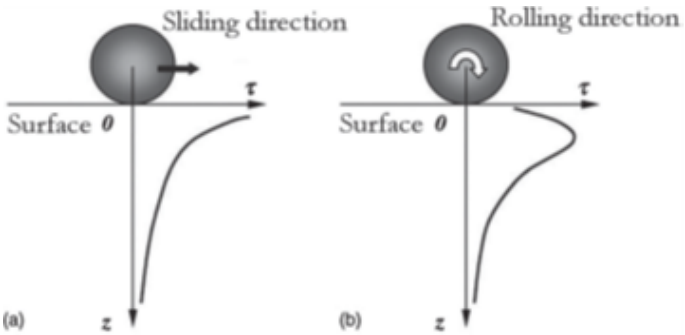


Figure 2.65 – Schematic of the shear stress τ as a function of depth below the free surface, (a) for sliding, (b) for rolling [312].

Hertz theory [315, 316] is often applied to analyze the rolling contact issues. The ratio of the maximum shear stress depth Z and the contact zone radius a is shown in Figure 2.66. The friction coefficient affects the surface stress distribution, as shown in Figure 2.67. μ is the friction coefficient. The stress on the contact ellipse loses its symmetry under the effect of friction, and the effect becomes more significant when the friction coefficient increases.

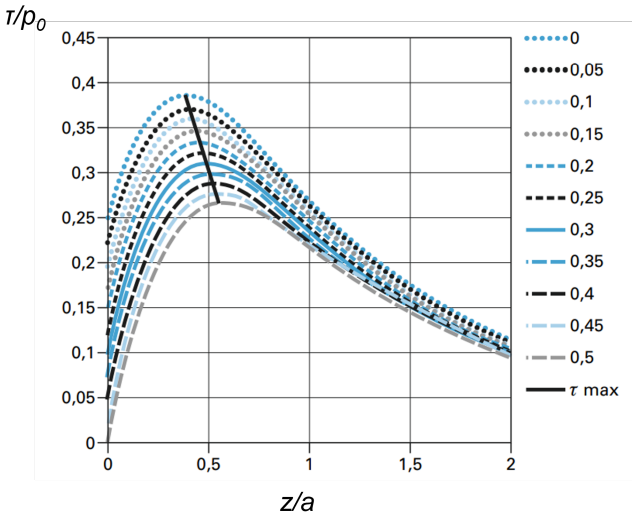


Figure 2.66 – Sphere/plane evolution of the maximum shear and its depth [317].

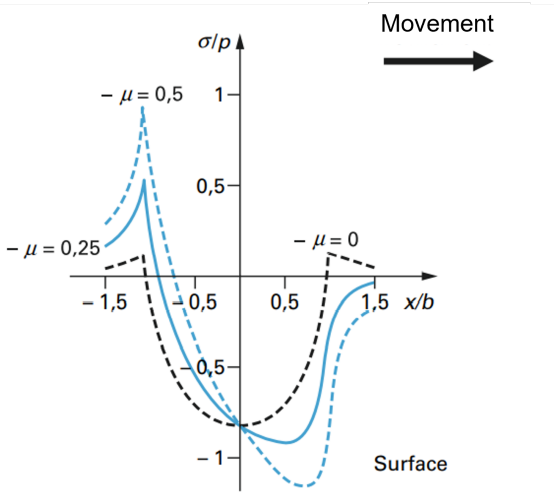


Figure 2.67 – The stresses on the surface in the direction of the tangential sliding force [317].

2.8.2 Rolling contact fatigue and Dang Van criterion

Rolling contact fatigue failure (RCF) is a damaging phenomenon in the bearing systems, rail-wheel systems, and thread rolling processes. It is a damage induced by the stress field. Rolling contact fatigue is perhaps one of the most complicated problems considering out-of-phase multiaxial fatigue because all six components in the stress tensor may change [286]. This kind of failure is often analyzed with the shakedown map, which includes four stages concerning the asymptotic responses under cyclic loadings (Figure 2.68) : elastic behavior, elastic shakedown, plastic shakedown, and ratcheting [289, 318, 319, 320]. According to the von Mises yield criterion, the shakedown map shows the tangential traction and load factor's effect on the elastic and shakedown limits. However, the shakedown limit only considers perfectly plastic materials or kinematic hardening laws. It is for these reasons that an extension of shakedown maps is proposed by introducing a surface fatigue index [321, 322, 323]. The Dang Van fatigue criterion is better suited for analyzing the subsurface fatigue under multiaxial loading [285].

The Dang Van criterion is based on the application of the elastic shakedown principles

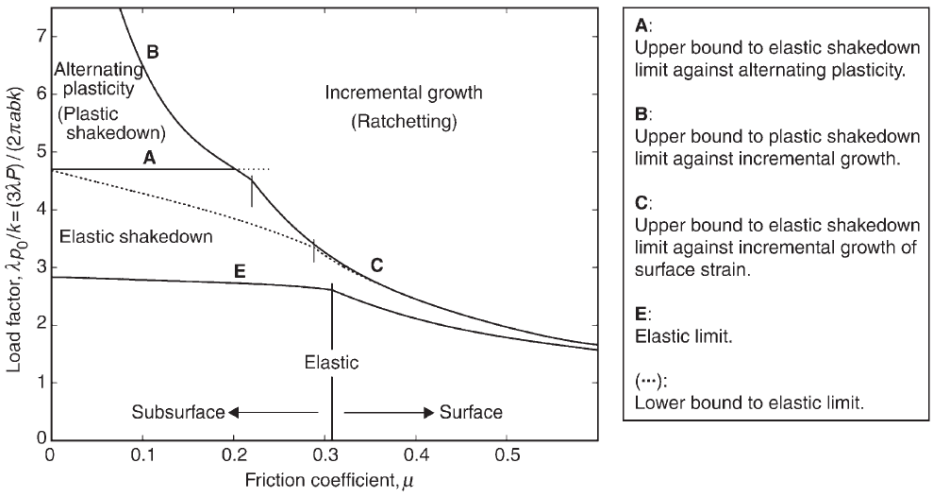


Figure 2.68 – A shakedown map for a general three-dimensional rolling-sliding contact [289, 318].

at the mesoscopic scale [286]. The microscopic variables in the stabilized state are used in the Dang Van criterion. The main theory is that the usual characterization of the fatigue cycle is replaced by the local loading path at each cycle. Thus, the damaging loads can be defined [285]. As cracks usually occur in intragranular slip bands, the local shear stress acting on the planes is an important parameter. Similarly, hydrostatic stress is also an important parameter for opening cracks. The Dang Van criterion can then be expressed by:

$$\tau_w = \tau(t) + \alpha_{DV} \cdot p_H(t), \tag{2.22}$$

here, α_{DV} is a constant that need to be determined, τ_w is the fatigue limit of the material in reversed torsion, $p_H(t)$ is the instantaneous hydrostatic component of the stress tensor, given by:

$$p_H(t) = \frac{1}{3} tr\sigma, \tag{2.23}$$

$\tau(t)$ is the instantaneous value of the Tresca shear stress, expressed with equation:

$$\tau(t) = \frac{1}{2} \max(|\sigma_1 - \sigma_2|, |\sigma_1 - \sigma_3|, |\sigma_3 - \sigma_2|), \tag{2.24}$$

where sigma$_1$, σ_2 and σ_3 are the three principal stresses.

In the Dang Van criterion, the endurance domain is delimited by two intersecting straight lines D and D' symmetric about the P_H axis. For example, in Figure 2.69, two paths Γ_1 and Γ_2 have been plotted, and damage occurs at Γ_2 but not Γ_1 even though both paths show the same shear stress amplitude and the mean hydrostatic stress. It's worth to mention that the Dang Van criterion is limited to elastic shakedown [318, 288].

The constant α_{DV} in the Dang Van criterion is usually calibrated with two fatigue tests, pure torsion and pure bending (tension-compression) [287], as shown in Figure 2.70. With two known loading modes (stress ratio $R = \sigma_{min}/\sigma_{max}$ and the maximum stresses), two points on the Dang Van line can be defined, so and the Dang Van line.

2.8.3 Nitriding effect on the Dang Van criterion along the paths

The Dang Van criterion in equation (2.22) was developed as:

$$\tau_w \cdot \beta_{DV} = \tau + \alpha_{DV} \cdot p_H. \tag{2.25}$$

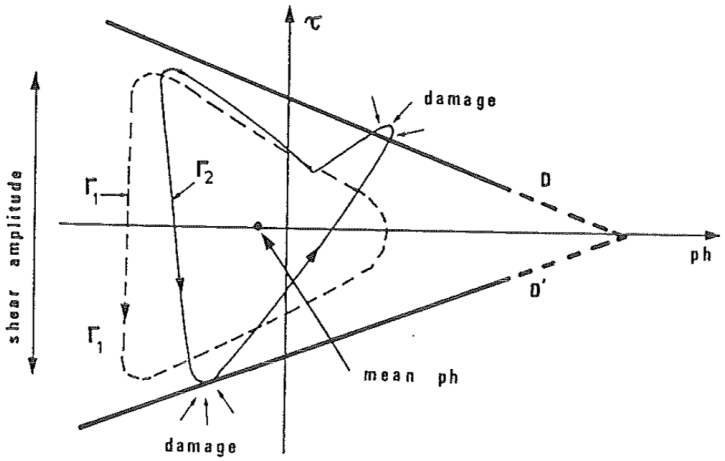


Figure 2.69 – Endurance domain and two typical local loading paths Γ_1 and Γ_2 [285].

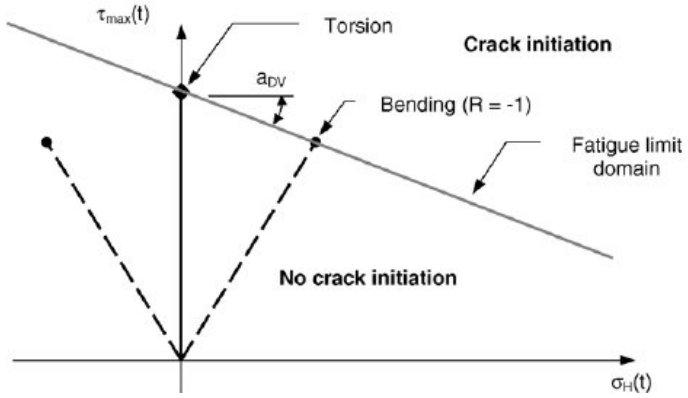


Figure 2.70 – The Dang Van diagram: a scheme of typical calibration with bending and torsion fatigue test [286].

The fatigue limit is finally obtained when $\tau_w = 1$ while the coefficients α_{DV} and β_{DV} need to be calculated with a given life cycle and probability of fatigue failure [324]. An increase in hardness can strongly affect the coefficient β_{DV} [325]. According to the Deperrois model:

$$\beta_{DV} = \beta_0 (\frac{HV}{HV_0})^n, \tag{2.26}$$

where, β_0 is the fatigue limit coefficient in the core material, HV_0 is core hardness. The coefficient n was taken as 1/2 as it allows better calibration of the calculation of the limit in fatigue [284]. Dang Van criterion equation (2.25) can be therefore written as:

$$\tau_w \cdot \beta_0 \cdot (\frac{HV}{HV_0})^n = \tau + \alpha_{DV} p_H. \tag{2.27}$$

The residual stress in the material ($\sigma_{H,res}$) can be superimposed on the applied stresses. Therefore the hydrostatic stress $p_H(t) = \frac{1}{3} tr\sigma$ can be replaced by $p'_H = \frac{1}{3} tr(\sigma + \sigma_{H,res})$. Then the Dang Van criterion will become [286]:

$$\tau_w \cdot \beta_{DV} = \tau + \frac{1}{3} \alpha_{DV} \cdot tr(\sigma + \sigma_{H,res}). \tag{2.28}$$

After nitriding, the material gains a gradient in hardness and residual stress from the surface to in-depth. The hardness gradient causes the gradient of the fatigue limit coefficient, while the residual stress gradient leads to a different change in the total loading (the residual stress will be added to the external load). If both gradients are considered at the same time, the Dang Van criterion of the steel after nitriding at each depth (Z) could be written as:

$$\tau_w \cdot \beta_0 \cdot (\frac{HV(Z)}{HV_0})^n = \tau + \frac{1}{3}\alpha_{DV} \cdot tr(\sigma_Z + \sigma_{H,res}(Z)). \tag{2.29}$$

Figure 2.71 shows how hardness and compressive residual stress affect the Dang Van criterion.

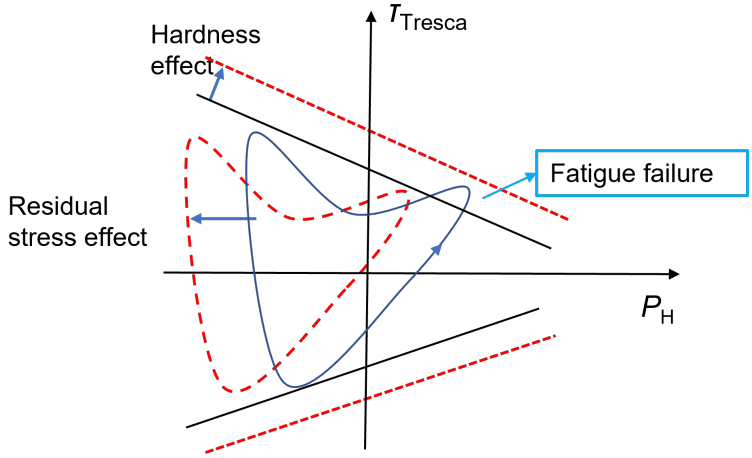


Figure 2.71 – Hardness and residual stress effect on Dang Van criterion.

The grey heart-shaped curve stands for the loading path in the material, and the black straight lines are the original Dang Van lines. When the loading path is out of the Dang Van line, fatigue may occur. An increase in hardness can move the Dang Van line toward higher equivalent stress, as shown by the red dash straight lines in Figure 2.71. Compressive residual stress can move the loading path to the left, as shown by the red dash heart-shaped curve.

CHAPTER 3
EQUIPMENT AND METHODOLOGIES

In this chapter, the equipment and sample preparation methods will be summarized.

3.1 Chemical analysis by Optical Emission Spectrometry (OES)

The measurements of chemical compositions are performed using a spark spectrometer, SPECTROMAXx LMM05 from Ametek. The in-depth concentration analyses are carried out by successive measurements at different depths reached by grinding with a SiC disk of 120 grade to remove about 20 µm in thickness of the material after each series of measurements.

The result gives the mean value of the concentration for each element of all the removed material. If the samples have a homogeneous chemical composition or nitriding layer on the whole surface, the chemical composition is obtained from the compilation of four measurements on the same face. The variability of the results is indicated by an error bar and corresponds to one standard deviation. If the sample has a bigger surface like the rolling die, more tests could be performed to have a better deviation. If the samples are processed heterogeneously, the indicated concentration is obtained only from one serie of measurements, and no error bar is shown.

Method M-Fe-grand N (created at MSMP laboratory) will be used to measure the N and C profiles from the sample surface to in-depths. The calibration of this method allows the analysis of N concentrations of up to 2.05 wt.%. The nitrogen concentration in the compound layer is higher than 5.7 wt.% for pure iron and cannot be measured with the calibration method used. For both carbon and nitrogen measurements, the detection limits are 0.0016 wt.% and 0.0024 wt.%, respectively. The equivalent background concentrations are 0.00483 wt.% and 0.0728 wt.%, respectively.

3.2 Optical microscopy

The observation is carried out with an optical microscope Olympus BX41M equipped with a PixelLink PL-A662 camera with a 13 Mpx resolution. The acquisition is performed with the help of the software Images&Mesures from Buehler.

The samples are cut transversely using a Struers Discotom 6 device, and cross-sections parallel to the surface of 13 mm × 5 mm are obtained. Samples are hot mounted by using a CitoPress-1 from Struers. Grinding is carried out gradually using 120, 500, 2000 grade

SiC disk and mirror-polished with 3 and finally 1 micrometer diamond suspension from Struers. The etching is carried out with 2% nitric acid (HNO_3) in ethanol (C_2H_5OH) for about 8-15 seconds.

3.3 Scanning electron microscopy

The samples that are observed under the scanning electron microscope (SEM), are mounted with a conductive Struers Polyfast resin and polished. In some particular studies, the samples are mounted with Epoxy resin and cured at room temperature. Some samples are not mounted to avoid the destruction of the white layer during the hot mounting process. The samples are then diamond polished to a disk size of 1 μm (0.05 μm for EBSD analysis), cleaned under C_2H_5OH in an ultrasonic tank for a few minutes to remove the polishing residues, then rinsed with C_2H_5OH and dried with a hair-dryer. The samples are then placed in a JEOL 7001F microscope, equipped with an Oxford Instrumentations X-Max energy dispersive spectrometer. The energy dispersive X-ray Spectroscopy (EDS) results are normally obtained with an accelerating voltage of 12 kV, but they can vary slightly depending on the elements analyzed. Back-scattered electrons (BSE) and secondary electrons (SE) are used to study the microstructure using a chemical or topographical contrast, respectively.

3.4 Hardness measurement

The measurement is carried out with a hardness test device Q10A+ from Qness. The machine is equipped with an Vickers indenter as well as objectives with magnifications of ×10, ×20, ×40, and ×65. Both Vickers and Knoop indenters are used, with loads 2-5 N and 0.5-1 N, respectively, and a loading time of 10 seconds. All the measurements are automatically performed with the help of the programming function of the software QpixControl2.

The same procedure as used previously for sample preparation (see section 3.2) is applied. Hardness measurements are all performed on a mirror-polished surface. Three tests or more are performed at equivalent positions on each sample. The results are given as a mean hardness with one standard deviation. The distance between two neighboring measurements is 3 times greater than the diagonal of indentation. While programming a hardness profile measurement from the surface to in-depth, the first test point is often at 30 μm from the surface according to the load and corresponding size of indents.

The effective nitriding depth of the nitrided sample is defined as the depth where the hardness is 100 HV 0.2 higher than that of the base material.

3.5 Residual stress

The stress analyses are performed on a Siemens D500 diffractometer, equipped with a linear detector from Elphyse, a chromium anode $\lambda_{K_\alpha} = 0.2291$ nm and a vanadium filter. The $\sin^2(\psi)$ method is used on the family of {211} planes of the ferrite, which is assumed to be polycrystalline and isotropic. The analysis is performed on 13 angles, including an oscillation of +/− 3° and an acquisition time varying between 40 and 300 s depending on the diffraction peak intensity. The radiocrystallographic constants of the ferritic phase are $\frac{1}{2}S_2 = 5.81\times10^{-6}$ MPa^{-1}, $S_1 = -1.27\times10^{-6}$ MPa^{-1}. They are determined

by the macroscopic elasticity constants and Kröner-Eshelby type model: Young module E = 210000 MPa, Poisson ratio $\nu = 0.29$, anisotropy factor ARX = 1.39 [326]. The in-depth profile below the surface is obtained by successive electrochemical polishing (Struers polisher, with electrolyte A2) using a depth increment of 20 µm and measured with an electronic micrometer.

3.6 Roughness measurement

To perform roughness measurement, the samples are firstly put in acetone (C_3H_6O) and cleaned in an ultrasonic device for 3-4 minutes. A sampling area of 4 mm × 4 mm is chosen. Defects visible by human eyes on the sample are avoided.

The roughness in 2D or 3D is measured with a Surfascan 3D device from SOMICRONIC with the help of the software Surfascan. The 3D surface texture measurement consists of the measurement of parallel profiles linked together in the orthogonal direction and linked to a tangential reference line. Therefore, the measurement is made by an instrument that allows the displacement of a surface texture probe in both orthogonal horizontal X and Y directions, as well as the measurement of the vertical amplitudes on the Z-axis with the probe [327]. A stylus consists of a diamond probe with a radius of 2 µm, and a cone shape with an angle of 60 degrees is used in the measurement. Figure 3.1 shows the working principle of the inductive gauge in the profilometer. Before the measurement, calibration is performed with a standard alumina ball with a radius of 25.009 mm. The load applied during the measurement is 20 N, and the scan speed of the stylus is 0.8 mm/s.

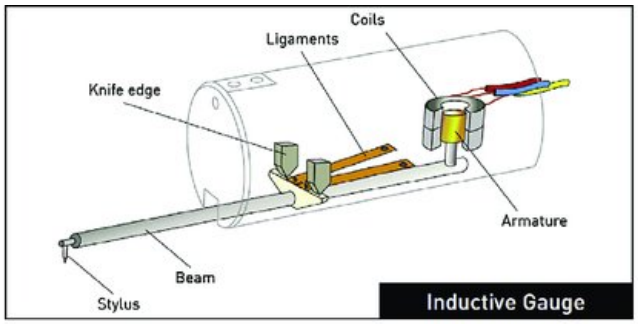


Figure 3.1 – Inductive gauge in the profilometer [328].

3.7 Thermogravimeter and nitriding process

The samples for nitriding are cleaned with the product and water progressively to remove lubricant, then rinsed in ethanol with an ultrasonic device, and dried with a hair drier. For the M2 samples with a ground surface, gradually polishing of 200, 500, and 1200 grade SiC disks is applied additionally.

The nitriding treatment is performed in a thermogravimetric analyzer Setsys Evolution ATG-ATD/DSC from SETARAM Instrumentations, unless otherwise specified. The schematic graph of the equipment is shown in Figure 3.2. The thermogravimeter serves as a nitriding furnace. It is composed of a beam from which the sample is suspended by hanging with platinum hooks in a furnace. The thermogravimeter allows following the sample mass increase during the reaction with the reactive atmosphere composed of NH_3, H_2 and N_2, and therefore to check the good progress and kinetics of the nitriding. The walls of the thermobalance furnace are made of alumina.

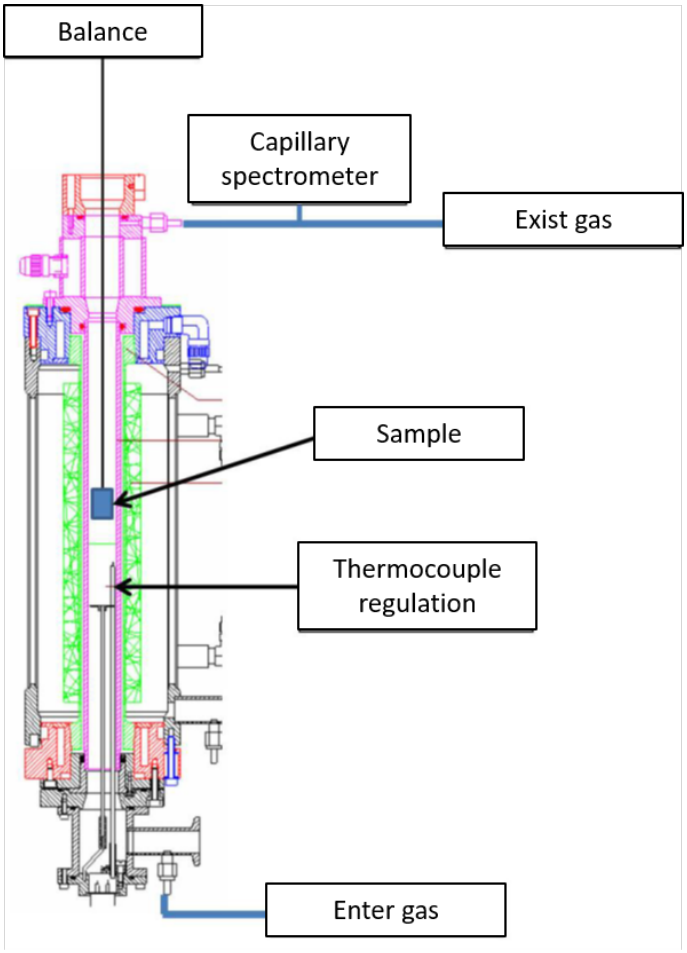


Figure 3.2 – Schematic diagram of the thermobalance.

The equipment allows analyzing a total variation in the mass of 400 mg, for a measurement accuracy of 30 ng. A thermocouple located at 20 mm from the sample allows for analyzing a temperature up to 1650 °C. Any treatment carried out in thermobalance is preceded by two times vacuum down to 0.18 Pa, each followed by a flow of Helium and gas Nitrogen at 200 mL/min. This process is to prevent the possible degradation of the sample by oxidation under air before treatment and the reaction of oxygen with hydrogen from the nitriding atmosphere.

The nitriding treatment is carried out for a period of 5, 10, or 15 hours at a temperature of 500, 520, or 540°C and a nitriding potential from 0.5 to 3.7 $atm^{-1/2}$. The atmosphere used is a mixture of ammonia, hydrogen, and nitrogen. All these gases are fed to the thermobalance at a total flow rate of 200 mL/min. This flow rate allows considering the natural decomposition kinetics of ammonia in the furnace as negligible compared to the kinetics of the catalytic decomposition at the iron surface and renewal of the atmosphere due to the saturation of ammonia on the surface. The nitriding potential can therefore be considered constant during the whole treatment. In such conditions, the composition of the atmosphere at the furnace outlet and the inlet are identical.

In the nitriding temperature programming, all temperature variations are realized with a rate of 10 °C/min. During each experiment, a helium flow from the head of the thermobalance is constantly introduced to protect the measuring elements from a possible corrosive atmosphere.

CHAPTER 4
STUDY ON ROLLING DIES

In this chapter, the investigation of the rolling dies provided by LISI Automotive and their surface conditions will be first carried out. The die failures will be observed afterward, accompanied by the mechanism analysis and the comparison of the FEM (Finite Element Modeling) results.

4.1 Analysis of the rolling die material

4.1.1 Chemical composition

The rolling die 18T0274A and 18T0274B are a pair of dies used to form threads on EPB screws with a profile of s9 × 1.25 (s represents spindle, 9 mm is the diameter of the screw, 1.25 mm is the pitch size). The diameter of the dies is 177.85 mm. After 1.2 working cycles (the lifetime of the rolling dies is given in a normalized value in this work regarding the confidential issues), the screw threads start to show a decline in quality and ask for the die replacement. 18T0274B will be named die E0-1.2 for simplification and comparison in this work. The number 1.2 represents the number pieces produced by this die before the die fails. The die is cut into small pieces to perform the examinations (see Figure 4.1). According to the standards, the chemical composition of M2 steel is shown in Table 2.3. Table 4.1 gives the chemical composition of the rolling die material in the core and at the surface layer (on the flat side because the measurement needs a larger area, so it can not represent the thread condition). The die is made of M2 high-speed tool steel, and the main alloying elements W, Mo, and V concentrations are around 6, 5 and 2 wt.%, respectively. The value is the mean concentration of the removed material from the measurement, the measuring depth is about 20 µm. However, the nitrogen concentration at the surface is not higher than that in the core, indicating that this die is not (effectively) nitrided.

Table 4.1 – Chemical composition of rolling die E0-1.2 (wt.%).

Test area	**C**	**W**	**Mo**	**V**	**Cr**	**Mn**	**N**
core	0.89±0.005	6.23±0.036	4.63±0.021	1.72±0.005	3.94±0.010	0.20±0.000	0.03±0.003
surface	0.91±0.004	6.35±0.034	4.62±0.020	1.71±0.015	3.94±0.008	0.20±0.000	0.03±0.001

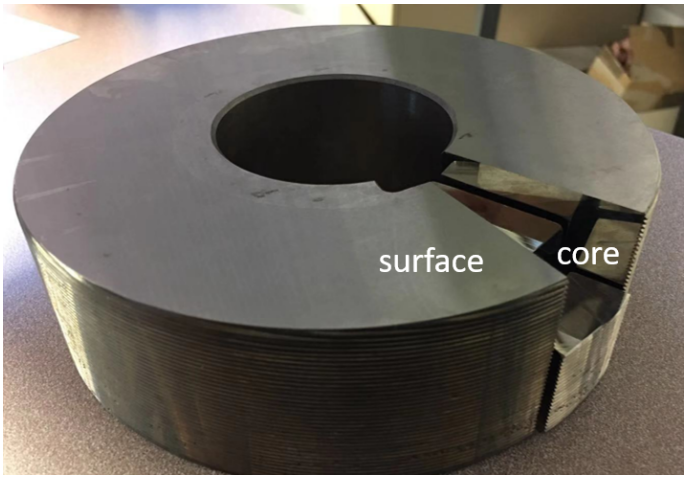


Figure 4.1 – Small pieces are taken from die E0-1.2.

4.1.2 Microstructure of rolling die E0-1.2

Figure 4.2 shows the thread microstructure from the cross-section view presenting the crest surface. Here, the carbide bands are observed while no nitriding layer is detected. In Figure 4.3, the orientation of carbide bands is shown by the yellow arrow. They are parallel to the die axis and perpendicular to the rolling direction. These carbide bands are formed due to casting and forging processes.

In Figure 4.4, the micrography under SEM shows the surface of a thread crest and the carbide bands transverse to the rolling thread. In addition, some surface wear is observed (the failure analysis will be presented in the later section 4.3). In Figure 4.5, three phases are analyzed with the EDS technic, the dark grey phases (spectrum 1 and 2) are vanadium carbides (MC type) and the white phases (spectrum 3 and 4) are assumed tungsten-molybdenum carbides (M_6C and M_2C types) while spectrum 5 and 6 present iron-based matrix.

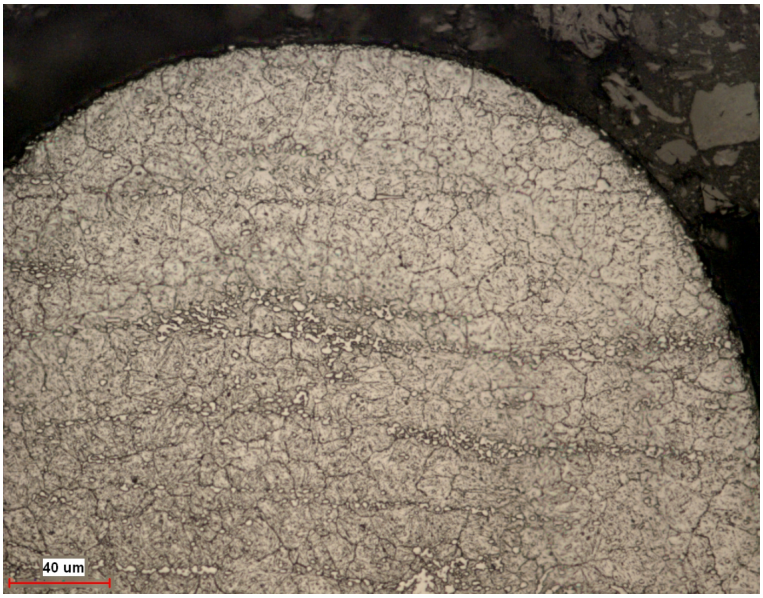


Figure 4.2 – Microstructure of the die thread under optical microscopy.

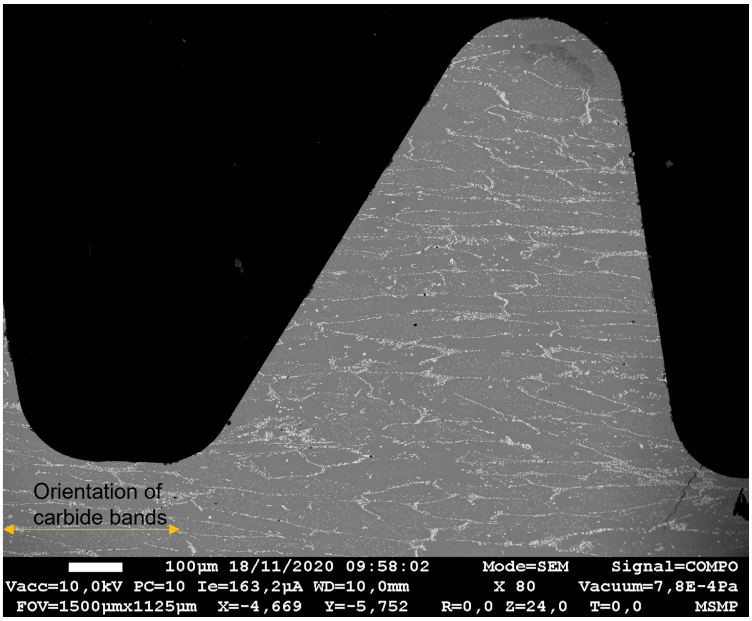


Figure 4.3 – Microstructure of the cross-section of the die thread under SEM.

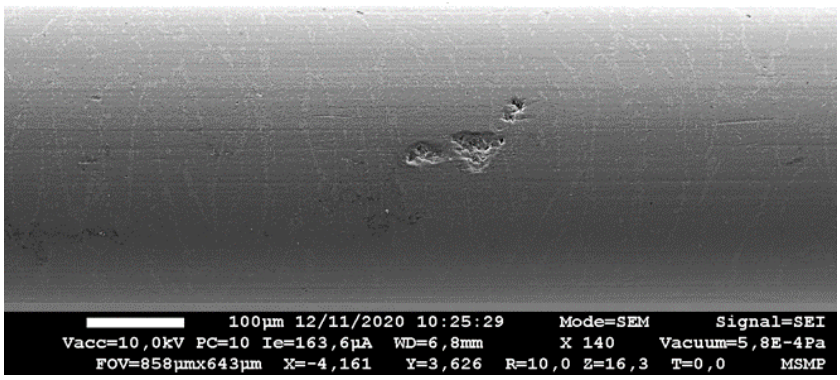
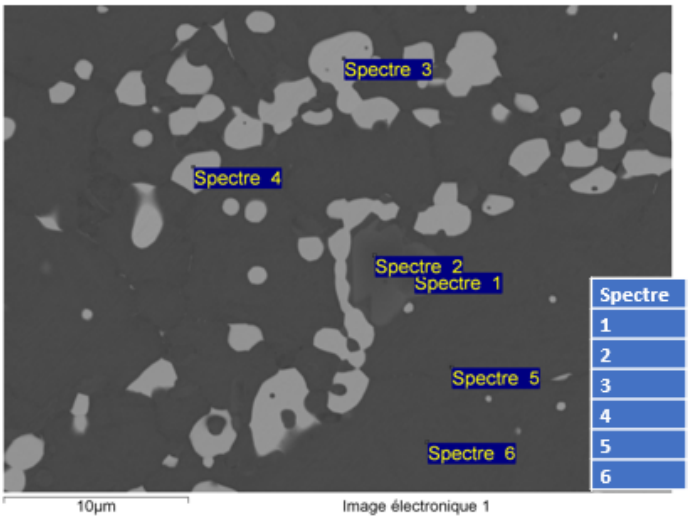


Figure 4.4 – Microstructure of the die thread surface under SEM.



The intensity of the spectra for the elements indicate mass.% (normalized)

Spectre	C	V	Cr	Fe	Mo	W
1	13.9	44.8	8.5	1.6	12.9	17.6
2	14.1	43.2	8.7	1.8	13.5	18.3
3	5.8	2.4	6.6	32.6	20.6	32.1
4	5.6	2.4	6.5	33.0	20.5	31.9
5	2.8	0.8	6.0	85.2	2.4	2.8
6	2.8	0.9	6.3	84.7	2.5	2.8

Figure 4.5 – EDS analysis of die E0-1.2.

4.1.3 Hardness

Figure 4.6 shows the hardness mapping at and below the thread teeth on the die. The colors represent the different levels of hardness. The blue color for the range of 880-920 HV dominates the map. The mean value of the hardness on the map is 902±54 HV0.2. This is more than 100 HV higher than the standard hardness of industrial using M2 steel, which is 750-800 HV (according to steelmaker ERASTEEL [329]). In-depth hardness profiles at different locations of the threads are given in Figure 4.7. No significant hardness gradient close to the surface is observed. It can then be assumed that no surface modification is (effectively) performed in terms of case hardening.

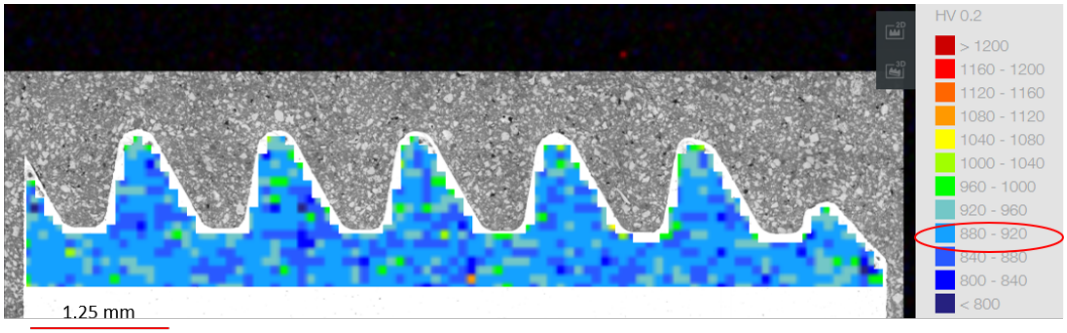


Figure 4.6 – Hardness map on rolling die E0-1.2.

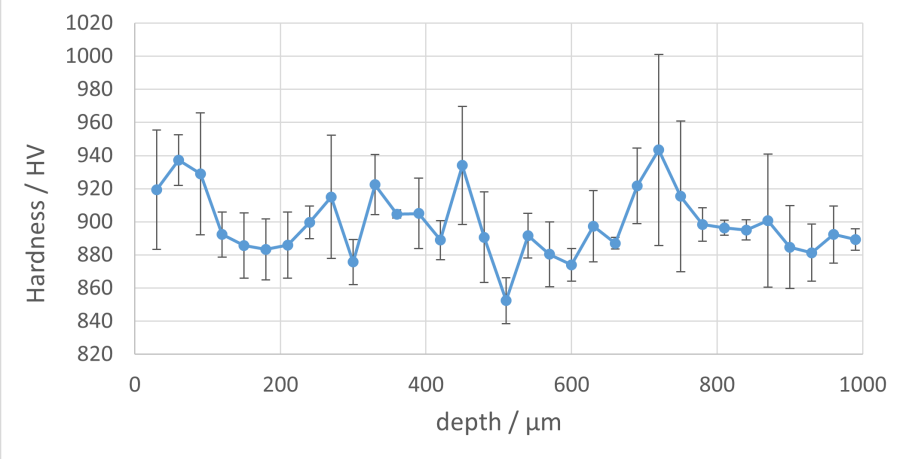


Figure 4.7 – Hardness profiles from the surface to in-depth on rolling die E0-1.2.

4.1.4 Residual stress in die

The residual stress tensors in the material are measured on the flat side from the surface to in-depth with X-ray diffraction, see Figure 4.8 (a). S12, S13, and S23 stand for the shear stresses and S11, S22 represent the two principal stresses in the plane of the specimen surface. The Principle stresses reach the highest value (compressive residual stress is negative) at the surface and decrease dramatically in-depth. Figure 4.8 (b) shows the profiles of three equivalent stresses. The residual stresses stabilize after 20 µm, and the maximum residual stress is found at the surface. The residual stress in the die is assumed to be introduced by the mechanical surface treatment - the grinding, which is directional (the grinding direction) and characterized by the shear stresses.

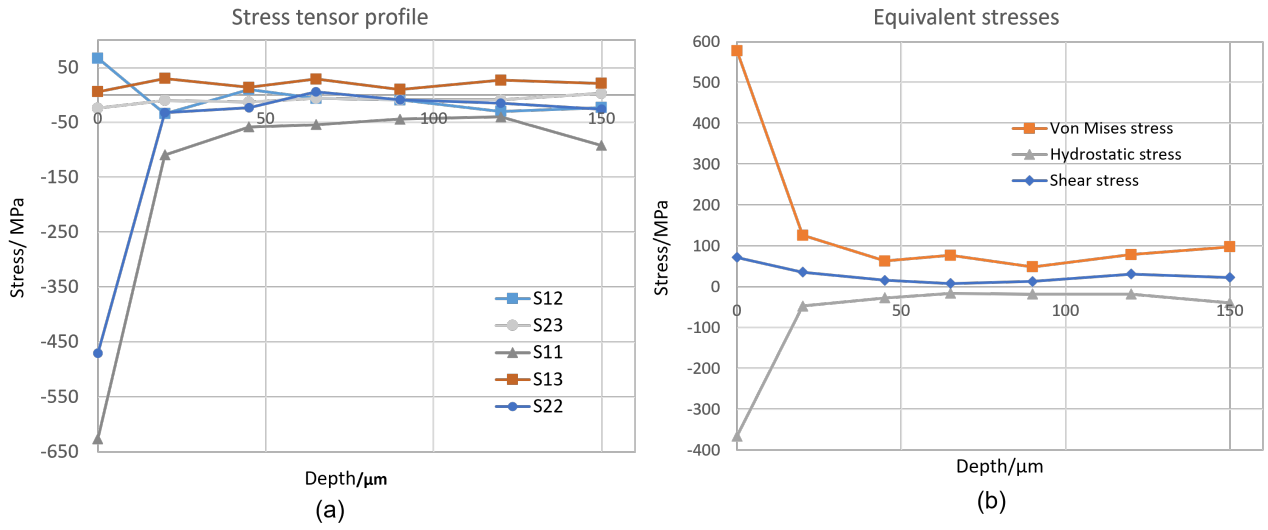


Figure 4.8 – (a) stress tensor profiles and (b) the equivalent stresses from the surface to in-depth on the flat side of rolling die E0-1.2.

4.2 Study on the nitriding conditions of 10 rolling dies

Ten pieces of rolling die samples are provided by LISI Automotive (Figure 4.9). The thread conditions are shown in Figure 4.10, some failures can be observed. Five (1-5) among them are E type and manufactured by casting, which are the essential objects to be studied in this work. The other five (6-10) dies are manufactured with powder metallurgy and are type G. The E type dies are treated with plasma nitriding, whereas the G dies were treated with salt-bath nitriding followed by sandblasting. E and G types of dies are used to manufacturing different threads with different profiles.

Table 4.4 gives information about the lifetime of the 10 dies on the production line. The indexes indicate these dies' names in this work: G and E stand for the two types of dies, respectively. The following number stands for the number of the die in G or E type. The number after the dash represents the number of parts they have produced before failure. For instance, G2-0.33 refers to die number 2 in G dies group, which produced 0.33 EPB screws before being replaced for quality issues of the screws. The references are the name of these dies in the plant. In the life cycle column, some dies that might fail for an accidental reason are marked 'A'.

However, the die samples from type E and G are not used to produce the same thread profile, and the hardnesses of the screws that they work on are different. Comparisons of the lifetime and nitriding conditions can thus not be performed between two types but only among each series, as the same properties in the core material are considered for the same type of dies.

4.2.1 Chemical composition

Table 4.3 presents the chemical composition on the surface of the 10 rolling dies and some of the core material (assuming the core material should be identical from the same type). The chemical composition of the core material of the G dies shows that they are not made of M2 steel. A relatively low W concentration but higher Mo and Co content compared to the M2 steel standard are disclosed. Mo and Co can increase the material's hardness, hardenability, and corrosion resistance. Compared to the core material, surface



Figure 4.9 – Rolling die samples to be characterized (10 pieces from 10 rolling dies).

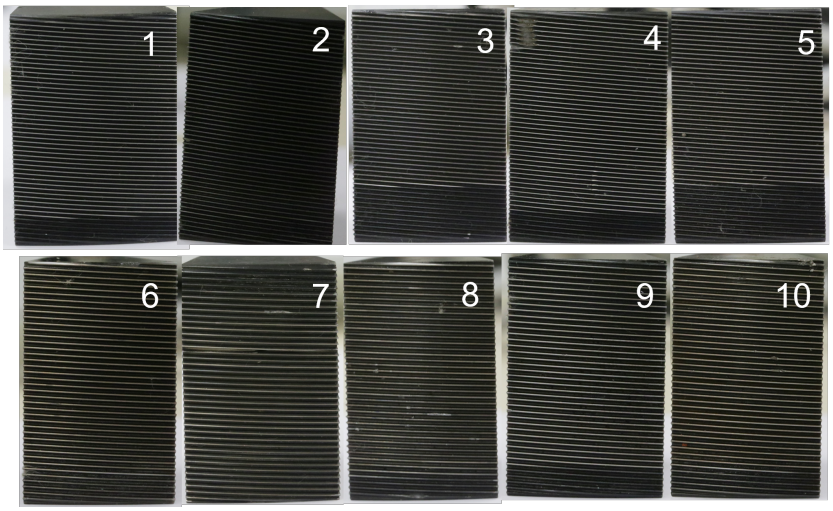


Figure 4.10 – The thread conditions of the 10 rolling die samples.

Table 4.2 – Details given of rolling die samples.

Information given	Index	Reference	Life cycles/P
Type G, powder metallurgy	G1-0.15	W30374800	37460
	G2-0.33	W31191800 NS02	82630
	G3-0.12	W31191800 NS03	A 3568
	G4-0.15	W30715200	37147
	G5-0.4	W31191800 NS04	101078
Type E, M2 steel, casting	E1-0.13	18T0627	A 33664
	E2-0.16	18T0534	39524
	E3-1	18T0614	250800
	E4-0.82	19T0505	204565
	E5-0.51	18T0544	127599

modifications are revealed. All the dies show a higher nitrogen concentration at the surface than in the core. However, the deviations are high for the dies from both types. For the

G dies, the carbon concentration at the surface is higher than that in the core except for G1-0.15. If only dies G2-0.33 to G5-0.4 are considered, no decarburization occurs on the surface of the G dies. On the contrary, all the E dies show less carbon concentration at the surface than in the core.

Table 4.3 – Chemical composition of rolling dies on the surface and in the core (wt.%). The standard deviation for each element on the equivalent measured areas is close and given with one value.

Test area	**V**	**Cr**	**Mo**	**W**	**Mn**	**Co**	**C**	**Si**	**Fe**	**N**
G1-0.15 surface	1.225	3.438	9.123	1.566	0.252	7.909	0.850	0.940	73.545	0.196
G2-0.33 surface	1.028	3.755	8.278	1.433	0.286	7.848	1.049	1.057	71.392	2.247
G3-0.12 surface	0.971	3.505	7.493	1.840	0.243	6.798	1.161	1.583	68.279	2.744
G4-0.15 surface	1.114	3.800	8.254	1.243	0.273	7.725	1.025	1.367	71.496	1.844
G5-0.4 surface	0.900	4.272	5.210	3.588	0.357	5.809	1.200	2.113	65.244	2.181
E1-0.13 surface	1.781	3.774	4.612	5.989	0.313	0.746	0.644	0.410	79.376	1.024
E2-0.16 surface	1.800	3.818	4.488	6.075	0.257	0.573	0.607	0.449	79.611	1.016
E3-1 surface	1.643	4.123	4.383	5.406	0.245	0.399	0.506	0.360	78.848	3.023
E4-0.82 surface	1.766	3.811	4.601	6.115	0.292	0.951	0.471	0.331	78.634	1.572
E5-0.51 surface	1.780	3.784	4.630	5.939	0.283	0.499	0.539	0.325	79.846	1.073
G1-0.15 core	1.248	3.418	9.145	1.572	0.249	7.859	0.982	0.953	73.601	0.003
G2-0.33 core	1.266	3.417	9.165	1.579	0.248	7.891	0.998	0.950	73.516	0.004
E1-0.13 core	1.813	3.757	4.631	6.047	0.302	0.752	0.830	0.450	79.960	0.022
E2-0.16 core	1.849	3.780	4.573	6.082	0.249	0.576	0.841	0.475	80.163	0.022
SD E surface	±0.013	±0.009	±0.032	±0.044	±0.002	±0.007	±0.012	±0.011	±0.024	±0.015
SD G surface	±0.012	±0.006	±0.101	±0.105	±0.002	±0.140	±0.180	±0.239	±0.461	±0.047
SD G core	±1.26	±0.004	±0.031	±0.009	±0.000	±0.001	±0.013	±0.011	±0.071	±0.002
SD E core	±0.011	±0.022	±0.040	±0.010	±0.001	±0.002	±0.014	±0.008	±0.026	±0.004

Since the thread is too small to be measured under optical emission spectroscopy (OES), the chemical composition tests are performed on the side surface of the die in the dark color zone, as indicated in Figure 4.11. As assumed, the dark color zone is plasma nitrided. In the nitriding furnace, the components are piled one on the other, so other nitrided components might cover the surface. The covered part will not be effectively nitrided due to the spark arc effect of plasma and presents a similar chemical composition (mostly C, N concentration) as the core, and the color will be different from the nitrided part. In the following sections 4.2.2.1 and 4.2.3, more results will be given for comparing the side surface and the threaded surface.

4.2.2 Microstructures of the nitriding layers of the rolling dies

4.2.2.1 Optical microscopy

Figure 4.12 shows the microstructure of G2-0.33. As it is manufactured with powder metallurgy, no significant carbide segregation is observed. G1-0.15 has the same microstructure and surface layer as G2-0.33, so it will not be presented. From these micrographs after nitral etching, it can be found that the surface of the die is modified. There exists a modified layer with a thickness of less than 10 μm. The treatment is relatively homogeneous according to the micrographs of the valley and the summit.

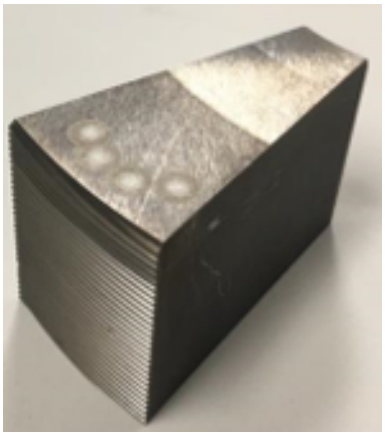


Figure 4.11 – Chemical analysis on the die surface.

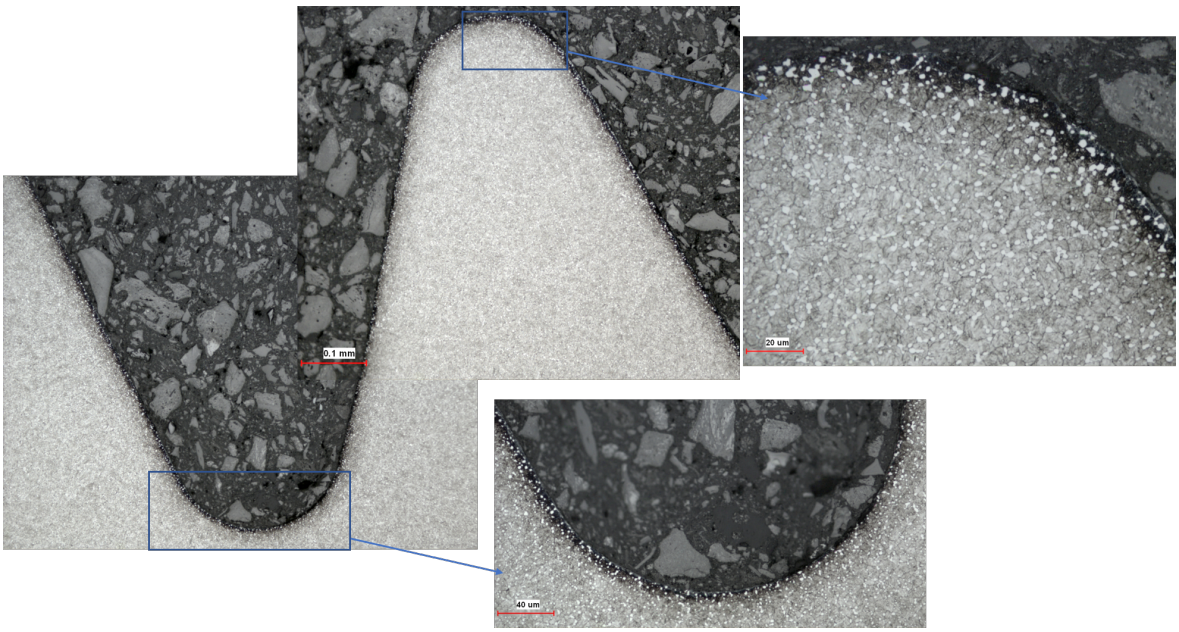


Figure 4.12 – Microstructure of rolling die G2-0.33 under an optical microscope.

Figure 4.13 shows that die E2-0.16 has a thicker modified surface layer (about 80 µm) compared to G2-0.33 with an additional compound layer of a thickness of nearly 3 µm. The white color carbide bands are observed. The cracks near the compound layers are observed on the flank, which might be generated during sample preparation due to the brittleness of the compound layer.

E3-1 has almost the same microstructure as E2-0.16. On the crest of the thread, a compound layer is observed. Figure 4.14 shows the 'thread start' (the threads on the die edge), the left side in Figure 4.14 (a) is the flat surface of die E3-1, and the nitriding layer is not formed in the same way as it is on the thread. This may be due to the surface coverage surface in the plasma nitriding furnace. The valley of the thread also shows a thinner nitriding layer due to its small size and complex geometry. On the contrary, in Figure 4.14 (b), the flat surface of die E1-0.13 shows a more considerable nitriding layer than the thread surface. Indeed, each die can be re-machined several times to reduce material cost by reducing the radius after the quality of the thread is no longer sufficient. Therefore, multiple times of nitriding are possibly performed on the flat surface of the die (nitriding is applied after each re-machining of the threads). In contrast, the threads are

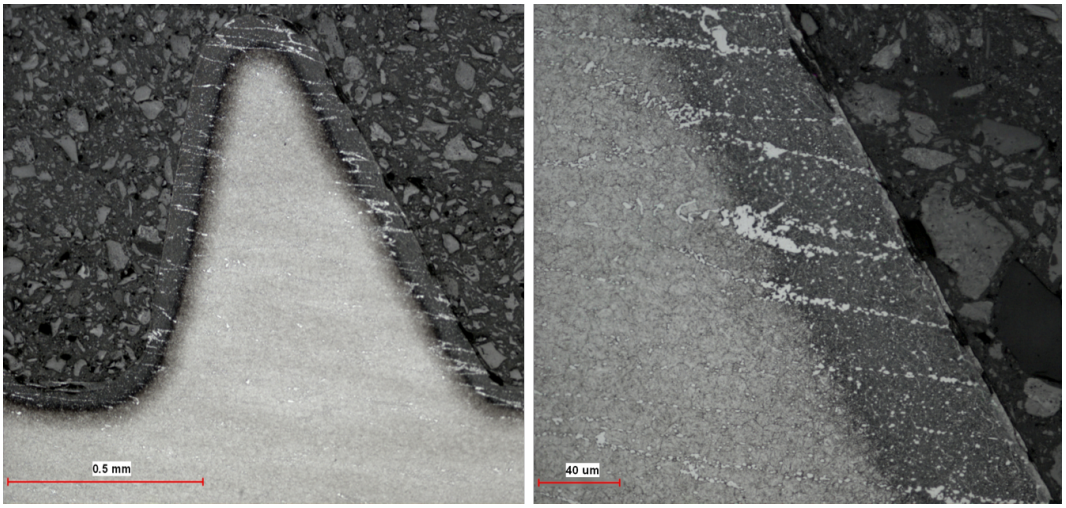


Figure 4.13 – Microstructure of die E2-0.16 under an optical microscope.

nitrided only once, as the previous nitrided layer is all removed.

Another type of non-homogeneity of nitriding is exposed, as shown in Figure 4.15. A variation of the nitriding layer thickness is detected on a small zone on the thread. This might be owing to the impurities or the micriostructure on the die surface before the nitriding treatment.

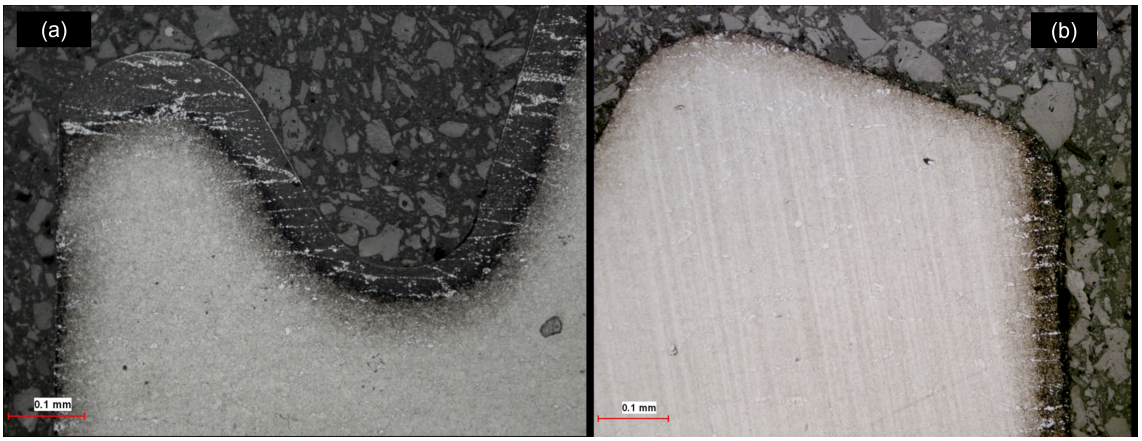


Figure 4.14 – Microstructure of rolling die (a) E3-1 and (b) E1-0.13 under optical microscope.

Among the 5 E dies, E2-0.16 and E3-1 possess compound layers, the compound layer can be discontinuous. No compound layer is observed on the other dies (Figure 4.16). E1-0.13 shows a very thin nitriding layer on the thread surface. E4-0.82 seems to have been treated with a relatively thicker nitriding layer, but no evident compound layer is observed. The micrograph of E5-0.51 presents the last thread, and the nitriding layer is again not homogeneous.

According to the optical observations, the surface treatment of the E dies is often not homogeneous on the different parts of the thread and is inconsistent between the flat surface and the thread surface. The nitriding layers are found different between each die, some dies show a compound layer and thick nitriding layer, and some of them show a very thin nitriding layer.

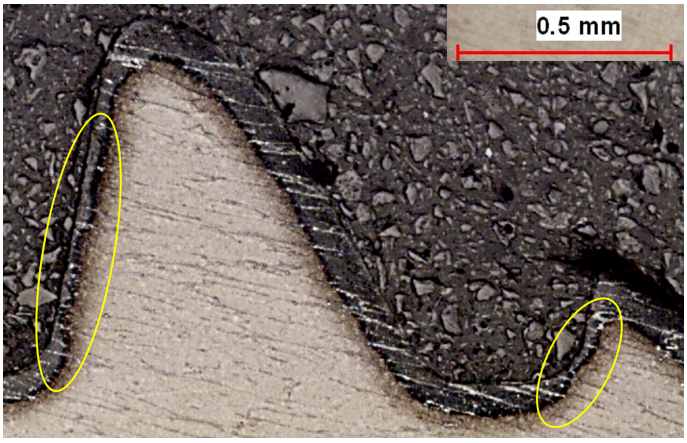


Figure 4.15 – Locally non-homogeneity of nitriding treatment on E3-1.

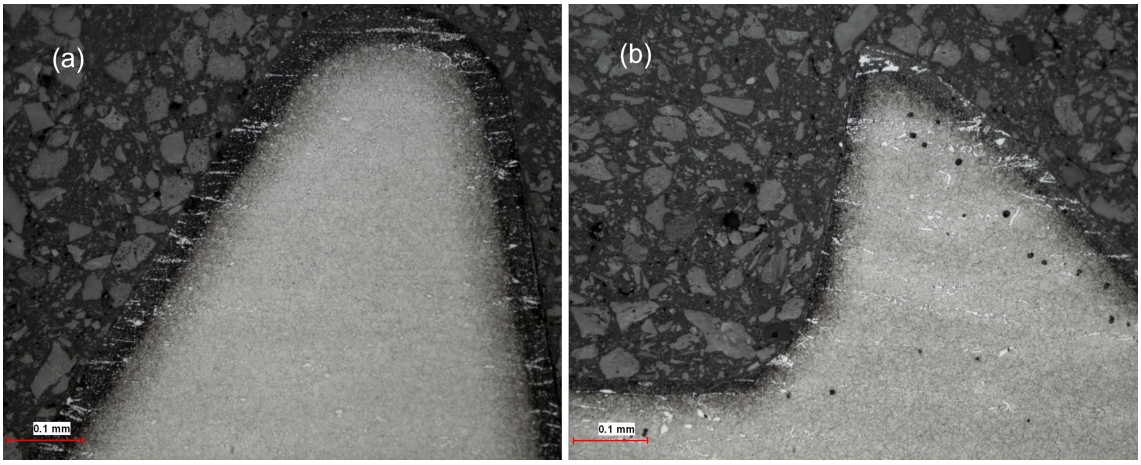


Figure 4.16 – Microstructure of rolling die (a) E4-0.82 and (b) E5-0.51 under an optical microscope.

4.2.2.2 SEM microscopy

Figure 4.17 shows the microstructure of rolling die G2-0.33 and E2-0.16. Besides the difference in the nitriding layer, the microstructures of the core materials are also different. As mentioned above, G dies is made with powder metallurgy, and the carbides are almost homogeneously distributed. In Figure 4.18 (a), slight carbide segregations are observed in G dies, as marked with blue dot lines. However, this carbide segregation does not cause big carbide bands. In contrast, in the E type dies, carbide segregation is remarkable, which consequently leads to non-homogeneity or discontinuity in the microstructure of the material. From Figure 4.17, the grain size and carbide size in G dies are smaller than those in E dies. According to the standard ASTM E112, the grain sizes were estimated [330]. Heyn lineal intercept procedure is applied with the help of etching techniques with 2% nital on G1-0.15 and E1-0.13 as representative of G and E dies. The average grain diameter of the G die steel is 7.9-9.4 µm, while that of E dies is 11.2-13.3 µm.

In Figure 4.18 (b), it can be noticed that the surface of the thread is not smooth. According to the manufacturer, this could be due to the sandblasting process after nitriding.

The microstructures on the flank of rolling die E1-0.13 and E2-0.16 are shown in Figure 4.19. E1-0.13 is plasma nitrided without a compound layer and no sandblasting after nitriding. Its surface is smoother compared to that of die G1-0.15. In Figure 4.19 (b), a compound layer can be observed at the surface of the thread of die E2-0.16 with a

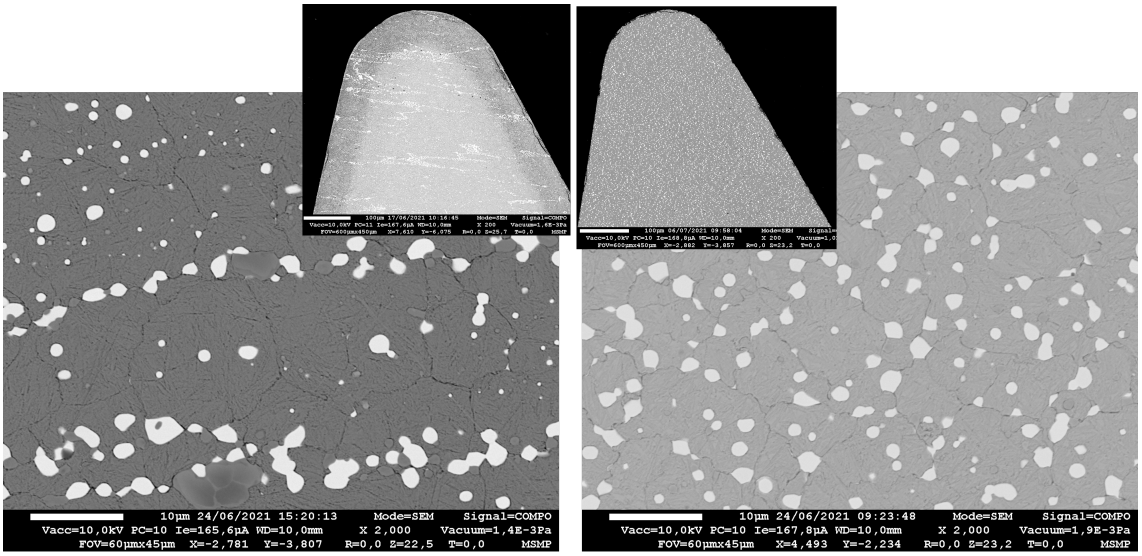


Figure 4.17 – Microstructure of rolling die (a) E2-0.16 and (b) G2-0.33 under SEM.

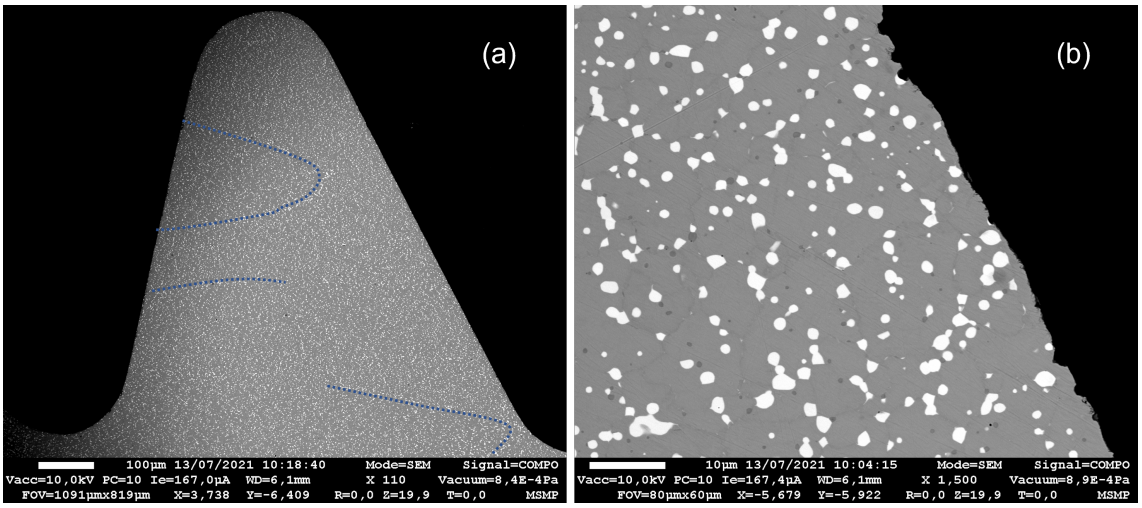


Figure 4.18 – Microstructure of die G1-0.15 under SEM (a) lower magnification with the carbide segregation marked with blue dot lines, (b) higher magnification, non-smooth surface.

thickness of about 3 µm, including a porous layer on the top. Below the compound layer, the precipitates at the grain boundary are formed due to the phase transformation during nitriding. Long cracks parallel to the surface are found in the compound layer and at the interface between the compound layer and diffusion zone. The grain boundary nitrides or cementite precipitates are also found almost parallel to the surface.

Since the compound layer is very brittle, cracks are easy to be generated in it during loading or sample preparation. The hot mounting process is considered, during which a high mechanical load is applied. To study the effect of mounting, an unmounted sample with a compound layer is prepared with manually polishing and then observed under SEM. In Figure 4.20, the materials are removed during polishing from the left side of the tread surface. Hence, it can be deduced that the occurrence of the cracks is not an effect of the mounting process but the polishing process.

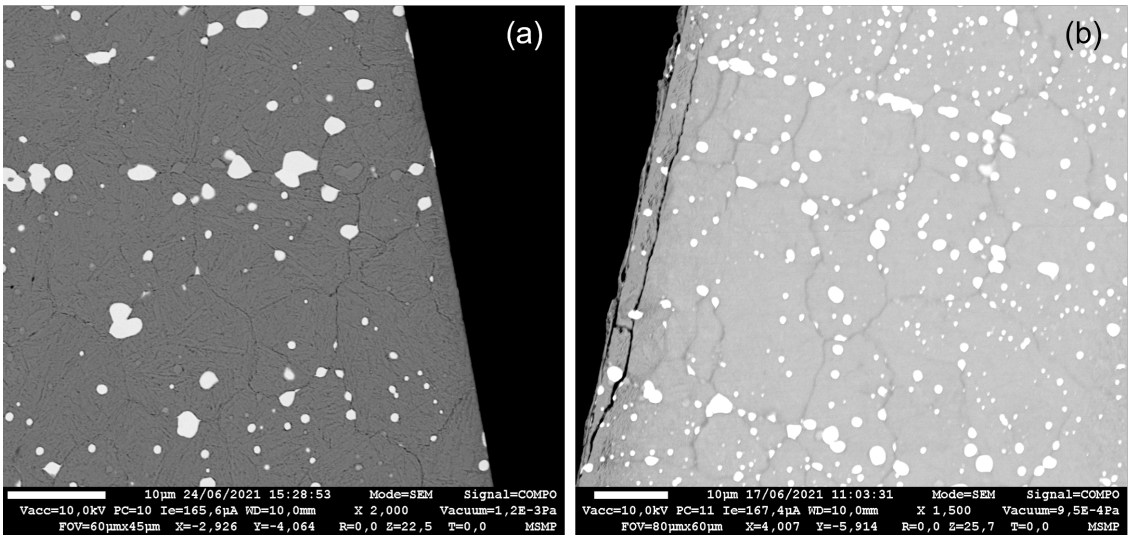


Figure 4.19 – Microstructure of dies under SEM (a) E1-0.13 thread surface has no compound layer or cracks, (b) E2-0.16 thread surface presents compound layer and cracks.

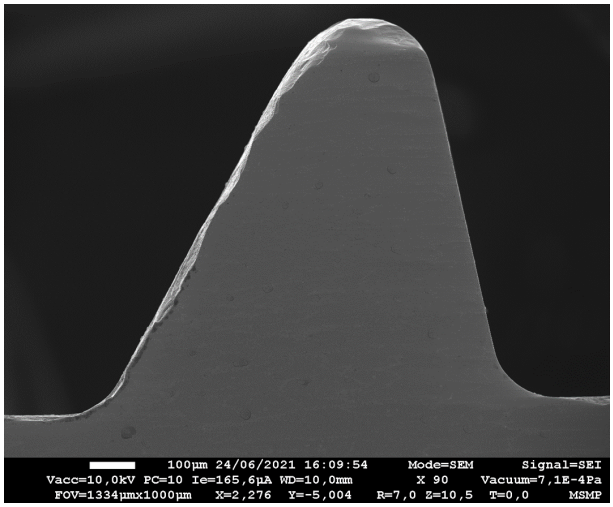


Figure 4.20 – Microstructure of E3-1 under SEM.

4.2.3 Hardness

The hardness is measured on the thread from the surface of the flank to the depth (see Figure 4.21). Three measurements are performed at equivalent locations for each die. Since the dies are larger in the axial direction than the workpieces, there is always a load-free zone during the rolling process. The difference between the loaded and the unloaded part can be distinguished by the colors. In Figure 4.10, the dark-colored part is a load-free area (the initial color of the die before being used). The hardness measurements are performed on the unloaded threads. Meanwhile, the hardness of the core is measured by 10 randomly selected measuring points in the base material, and the results are shown in Figure 4.22.

Die G1-0.15 and G2-0.33 have a very high core hardness of about 990 HV 0.2. The surface hardness increases by about 100 HV 0.2, which is not significant compared to the other rolling dies.

The hardness profile from the surface to 5 mm in-depth of die G1-0.15 is shown in Figure 4.23. A slight hardness gradient is observed through the core, marked by the red

line. This is due to the different cooling rates during heat treatment.

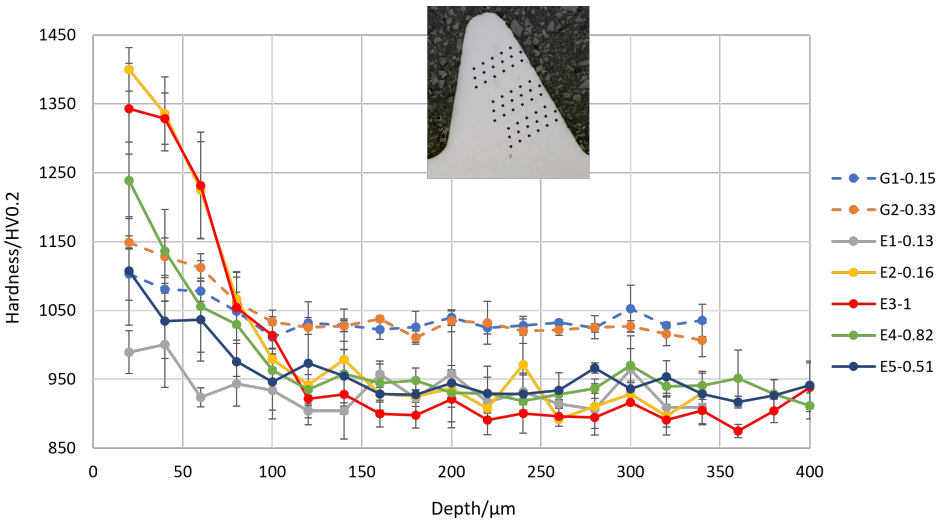


Figure 4.21 – Hardness profiles of two types rolling dies at the thread surface.

E dies have a relatively lower core hardness (900 HV 0.2), which is still much higher than the expected hardness of M2 steel used in industry (750 HV 0.2). The deviation in surface hardness is considerable for all 5 dies. E2-0.16 and E3-1 show the highest surface hardness and effective nitriding depth. This gives good agreement with their microstructure (Figure 4.13 and 4.14 (a)) in which die E2-0.16 and E3-1 have thicker nitriding layers with a compound layer. The core hardness of E3-1 is lower than that of E2-0.16. E1-0.13 shows a less important increase in surface hardness. This is also consistent with the microstructure of the thin nitriding layer on the thread (Figure 4.14 (b)).

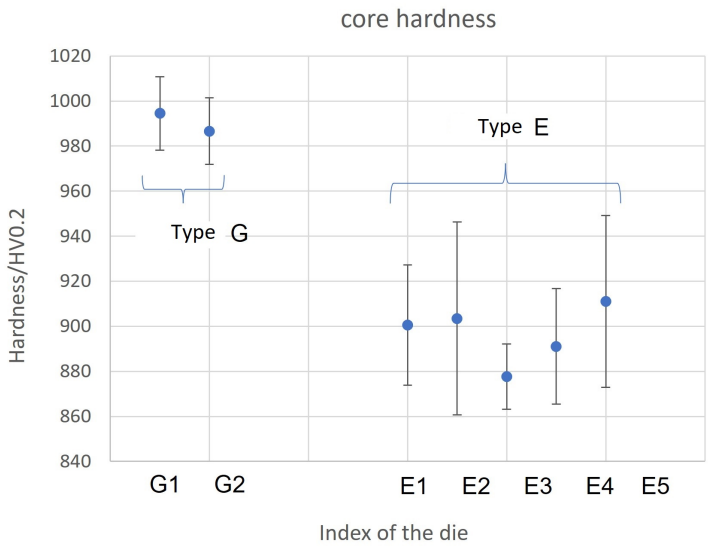


Figure 4.22 – Hardness of the base material of two types rolling dies.

The maximum hardness and effective nitriding depth vary from part to part, as shown in Table 4.4. Hardness profiles are also measured on the flat side because micrographs show that nitriding on the flat side surface and on the thread surface is not performed

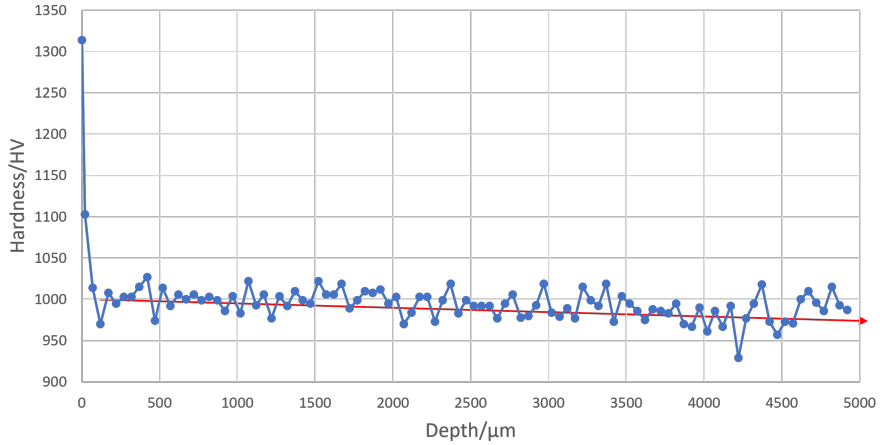


Figure 4.23 – Hardness profile of G rolling dies.

equally (see in Figure 4.14). The hardness profiles of the threads and flat surfaces of the E1-0.13 and E3-1 dies are shown in Figure 4.24. As assumed, the flat side surface could be nitrided multiple times and have a greater nitriding depth and higher hardness. In Figure 4.24, the hardness profiles of E1-0.13 are in agreement with its microstructures in Figure 4.14. A thinner nitriding layer is formed on the thread surface due to the surface coverage or geometry effect.

Table 4.4 – Results from microstructure and hardness analysis on the rolling dies.

Information	**Index**	**Reference**	**Life cycles** /P	**Nitriding**	**Core hardness** /HV	**Surface hardness** /HV	**Effective nitriding depth**/μm
Type G, powder metallurgy, not M2 steel, salt bath nitriding	G1-0.15	W30374800	0.15	NO CL	994	1103	32
	G2-0.33	W31191800 NS02	0.33	NO CL	986	1149	71
	G3-0.12	W31191800 NS03	A 0.12				
	G4-0.15	W30715200	0.15				
	G5-0.4	W31191800 NS04	0.4				
Type E, M2 steel, casting, plasma nitriding	E1-0.13	18T0627	A 0.13	NO CL	900.5	989	40
	E2-0.16	18T0534	0.16	With CL	903.5	1400	96
	E3-1	18T0614	1	With CL	877.7	1343	103
	E4-0.82	19T0505	0.82	NO CL	891	1239	90
	E5-0.51	18T0544	0.51	NO CL	911	1107	65

According to the die references (in Table 4.4), the die G2-0.33 could be made from die G1-0.15 with one time of re-machining (removing the thread and reducing the die diameter) after failure. The hardness on the flat side and threaded surfaces of G1-0.15 has similar profiles (Figure 4.25) because nitriding is performed on this die homogeneously in the salt bath. However, the nitriding layer on the flat surface of G2-0.33 is more remarkable than that on the thread surface because of the repetition of nitriding. No coverage and geometry will cause non-homogeneity problems during salt-bath nitriding.

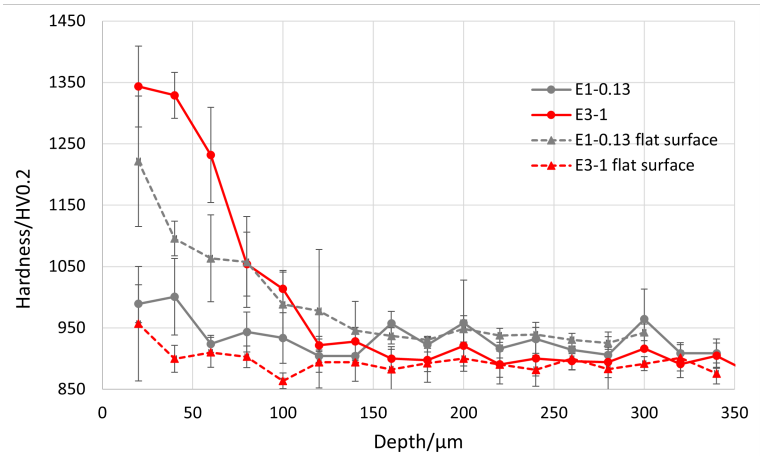


Figure 4.24 – Hardness profiles of rolling die E1-0.13 and E3-1 from the thread surface and the flat surfaces to in-depths.

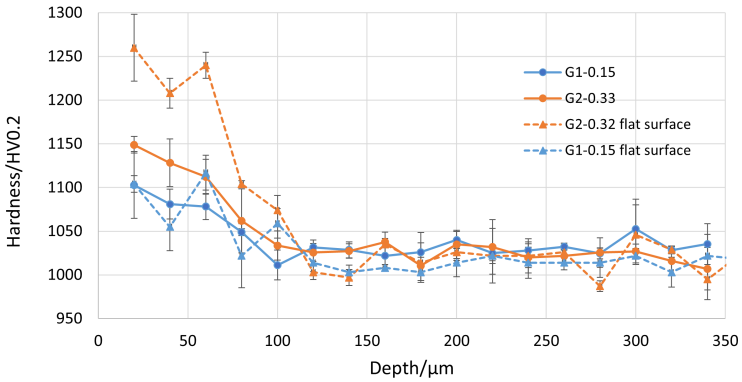


Figure 4.25 – Hardness profiles of rolling die G1-0.15 and G2-0.33 from the thread surface and the flat surfaces to in-depths.

4.2.4 N and C concentration profiles

Due to the small size of the threads, chemical analysis can only be performed on the flat surface of the rolling die, as shown in Figure 4.11. Figure 4.26 and Figure 4.27 show the N and C profiles from the flat surface to depth in E and G type dies, respectively. G2-0.33 has a higher concentration of N near the surface than G1-0.15, which is in agreement with their hardness profiles from the flat surface to depth, as shown in Figure 4.25. Similarly, for E1-0.13 and E3-1, the N concentration profiles do not show the same trend as the hardness on the thread surface profile in Figure 4.21, but are compatible with the hardness profile on the flat surface in Figure 4.24. The microstructure also confirms this difference in Figure 4.14.

Since two factors are responsible for the uncertainty of nitriding on the flat surface of E rolling dies, it is easier to study G dies first. The N profiles of G1-0.15 and G2-0.33 are consistent with the hardness profiles on their flat surface. Multiple times of nitriding provides the flat surface with a higher nitrogen concentration and diffusion depth, resulting in a more remarkable nitriding depth and surface hardness. However, the characterization of the flat surface for chemical composition analysis cannot be used to study the nitriding condition of the threads.

Figure 4.27 shows the corresponding carbon profiles of the dies whose nitrogen profiles are shown in Figure 4.26. G1-0.15 and G2-0.33 have relatively higher C concentrations

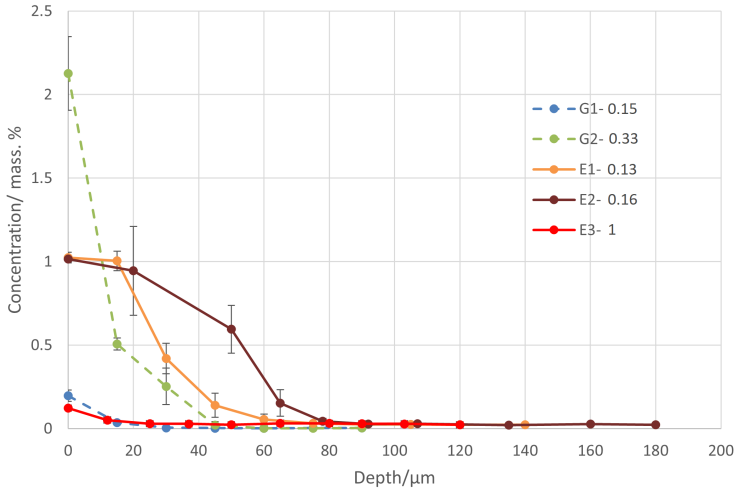


Figure 4.26 – N concentration profiles of the rolling dies

than E1-0.13 and E2-0.16 due to the different chemical compositions of the core material. The C curves of G2-0.33 and E2-0.16 evolve in the same way as those of G1-0.15 and E1-0.13, but move to a greater depth because of the repetition of nitriding. Near the surface, less carbon is found for all samples due to phase transformation and co-diffusion of carbon during nitriding. It is also possible to have decarburization near the surface during plasma nitriding, whereas decarburization does not occur in salt bath nitriding because the salt bath can provide a carbon source. Thus, as shown in Table 4.3, the carbon concentration is normally somewhat higher at the surface than in the core.

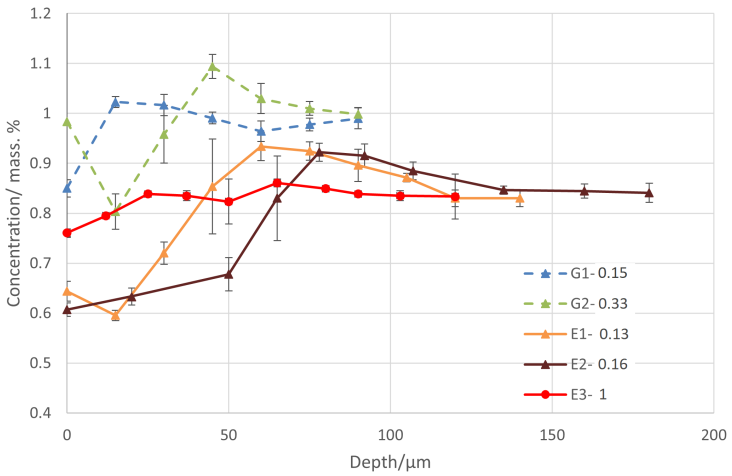


Figure 4.27 – C profiles of the rolling dies.

4.2.5 Residual stress profile

Residual stress measurement also requires a relatively large area, it can only be measured on the flat surfaces of the die. The residual stress profiles are measured only on die G1-0.15 and E2-0.16, the profiles are shown in Figure 4.28. The depth of compressive residual stress of G1-0.15 is less than 30 µm, while that of E2-0.16 is about 80 µm. The maximum compressive residual stress is lower in E2-0.16. The high compressive residual

stress at the surface of G1-0.15 is mainly generated by sand-blasting but not by nitriding because the nitrogen concentration is very low.

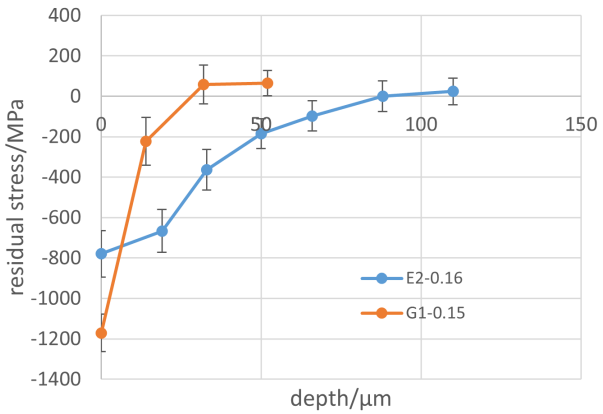


Figure 4.28 – residual stress profile of the rolling dies.

4.3 Failure observation on rolling die

Some failures occur at the end of the lifetime of the rolling dies. Figure 4.29 shows some failures on the threads of die E0-1.2.

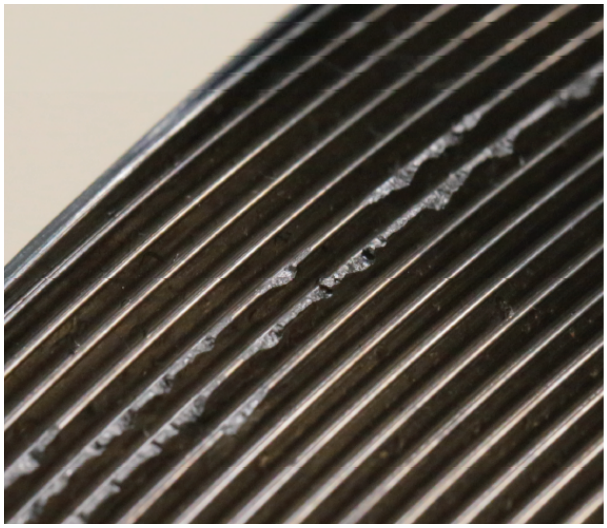


Figure 4.29 – Failures rolling die E0-1.2.

Most of the failures have a similar shape and size. Two of them are presented in Figure 4.30. Different types of failure are found within these failures, as shown in figure 4.31, including:

— scales,

— plastic strain of matrix,

— cracks,

— groups of spheres.

Where the spheres are observed, there are marks resembling beach marks. However, they could be caused by the continuous rolling contact after the top material is removed rather than by fatigue.

Figure 4.32 shows the cracks of the failure, which propagate parallel to the surfaces. In Figure 4.32 (b), it is assumed that if the die continues to operate, cracks 1 and 2 can meet and result in material removal.

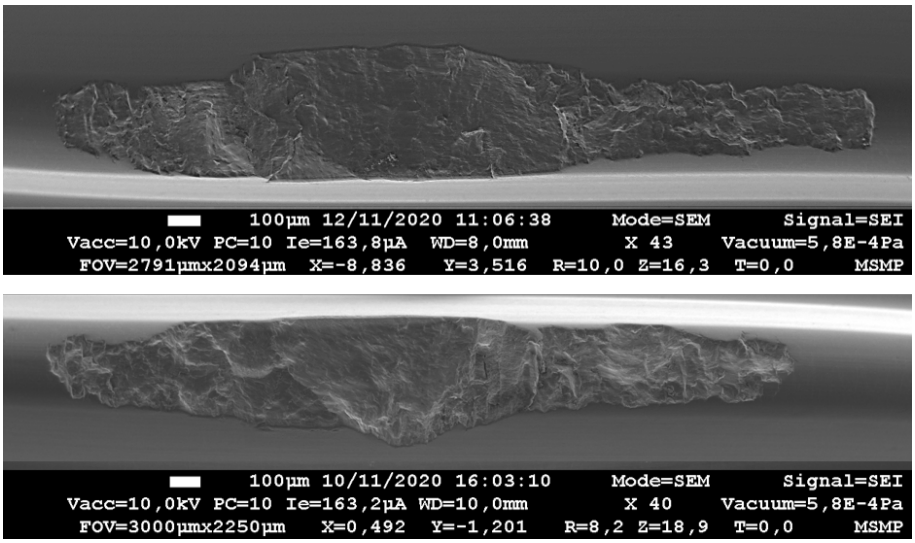


Figure 4.30 – The similar failures on the tread of die E0-1.2.

The failure in Figure 4.30 is cut along the thread, as shown in Figure 4.33. The cross-section is then polished. The red circle indicates the location of the failure. On this cross-section, the depth of the failure is about 100 µm (see Figure 4.34). The parts within the yellow circles are analyzed, and micro-cracks can be noticed as shown in Figures 4.35 and 4.36.

Circle 1 shows the left edge of this failure. A crack below the surface opens onto the failure from the lower left. Below it, another internal crack exists that is not yet open on the fracture surface from the view of this observed cross-section (in the yellow circle in Figure 4.35). These two cracks have a similar angle to the surface of the thread. In other words, the angles between the cracks and the surface are similar. Circle 2 is also shown in Figure 4.35, the cracks go through the carbide bands close to the surface, which could be the reason why the cracks change the propagation direction. In circle 1, a micro-crack occurs in the local fracture valley, similar to the cracks in circle 3. These cracks could be caused by the stress concentration that occurs at the corner of the fracture valleys. They are initiated from the fracture surface and propagate to depth. The direction of crack propagation is related to the local geometry and carbide inclusions.

On the right side of the fracture, most of the cracks in circles 4, 5, and 6 in Figure 4.36 occur due to the stress concentration induced by the geometry discontinuity. Meanwhile, the discontinuity in the microstructure (linked to carbides) also contributes to crack initiation. However, the cracks propagate mainly to the right rather than downward to the left, in contrast to those on the left side of the fracture. This is related to the overall geometry of the fracture and the direction of rolling (or the direction of the EPB screw passage over the fracture). In circle 5, the cracks propagate along the carbide band. In circle 4, the carbides change the propagation direction and split the crack into several, propagating in different directions. Finally, a crack is observed open at the crest surface close to the right edge of the fracture in circle 6 and about to meet the crack below. If

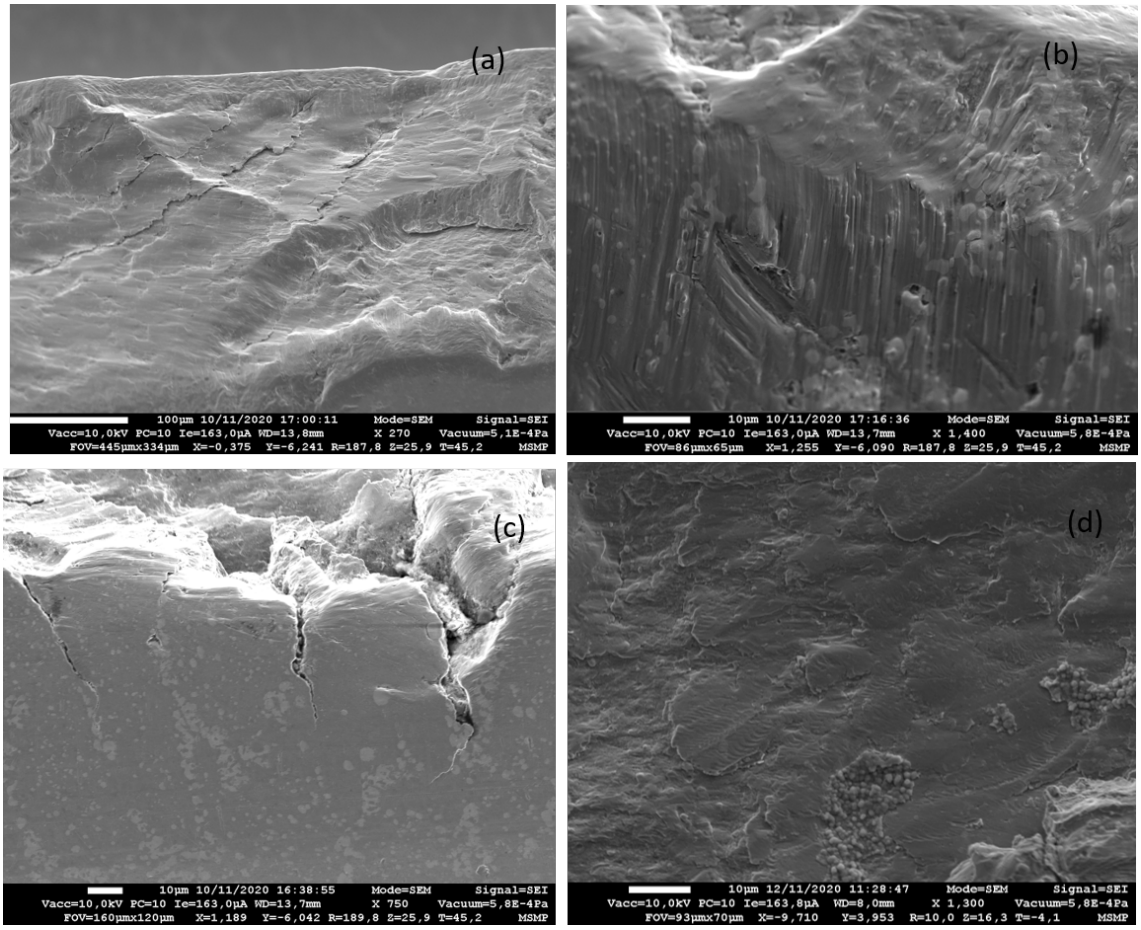


Figure 4.31 – Some failure types in the failure on the tread of die E0-1.2: (a) scales, (b) plastic deformation, (c) cracks along the carbides bands, (d) some marks looks like beach mark and brittle failure at the carbide segregation.

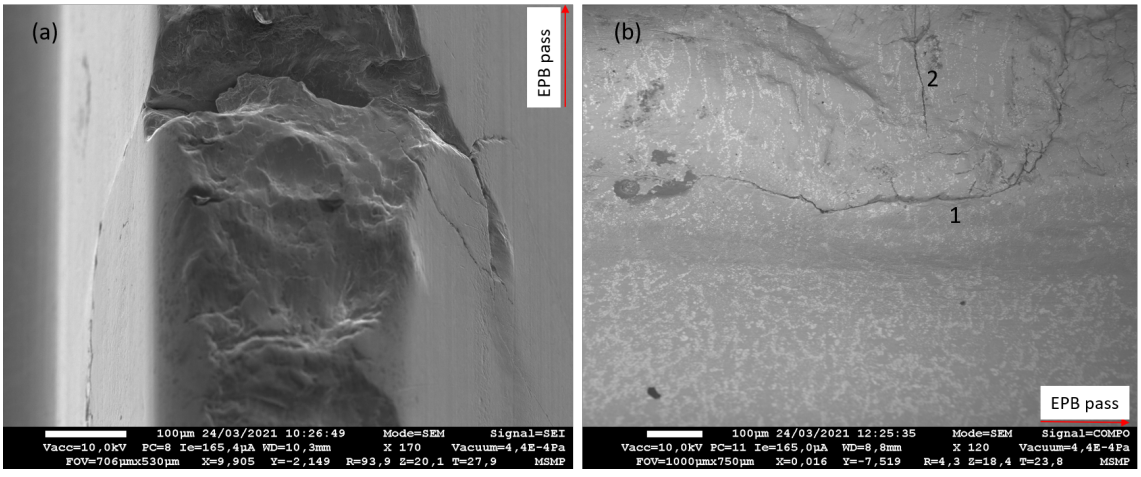


Figure 4.32 – Cracks propagation in the failure on the tread of die E0-1.2 (a) top view of the thread crest, (b) side view along the crack.

the die continues to operate, the two cracks will meet, and the material will eventually be removed. This illustrates how the fracture is enlarged during cyclic loading.

On the thread crest surface, surface degradation is observed near the right-hand edge of the failure (see Figure 4.37). In the blue rectangle, a few cracks initiate in the carbide

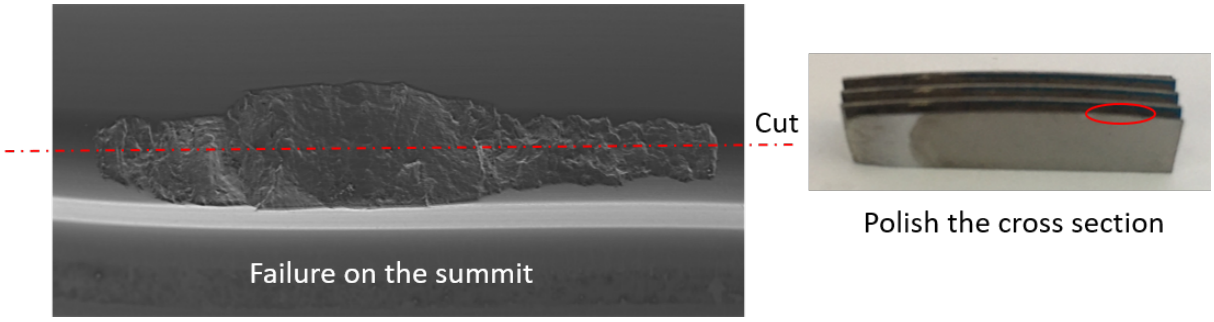


Figure 4.33 – Sample preparation by cutting the thread in the middle of the failure along the red line.

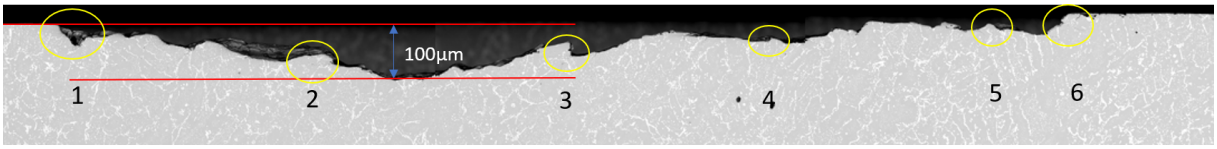


Figure 4.34 – Cross-section of the failure.

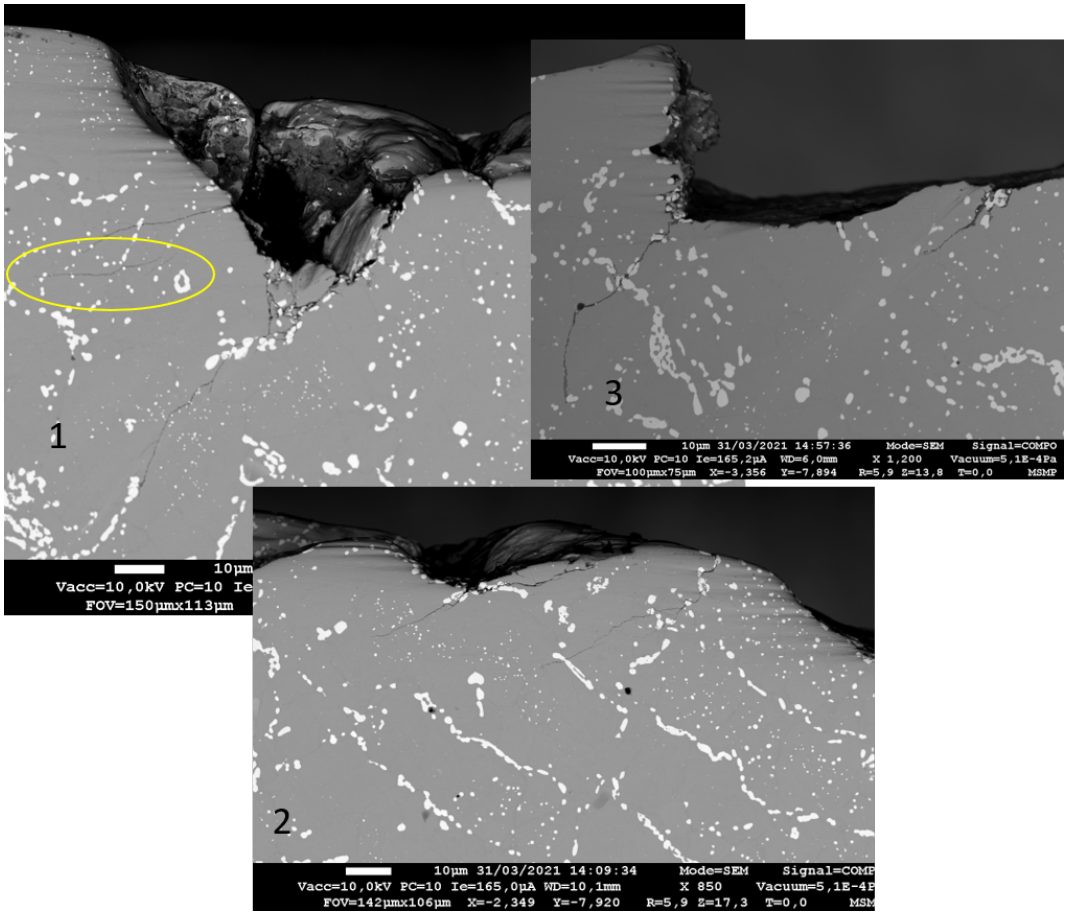


Figure 4.35 – Cracks in the circles 1, 2 and 3 in Figure 4.34.

bands, which could be the same crack as in circle 6 in Figure 4.36. In the red square, surface wear is observed and assumed to be the cause of stress concentration on the surface, leading to new cracks.

Surface wear and micro-cracks are also observed on the flanks of the thread (see Figure

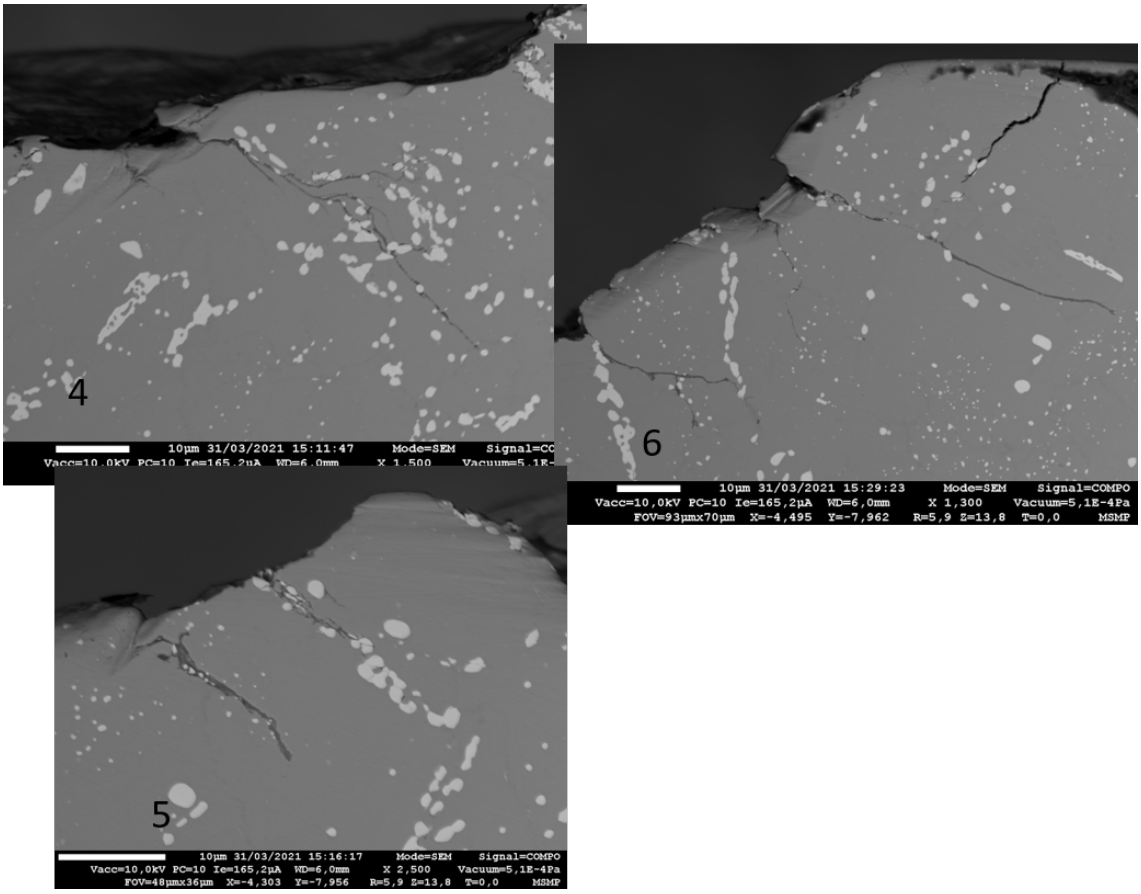


Figure 4.36 – Cracks in circles 4, 5 and 6 in Figure 4.34.

4.38). Surface wear is evident, which could be influenced by foreign particles. In Figure 4.38 (b), micro-cracks are observed along the carbide bands. These wear and cracks can not be observed under low magnification, and they might not yet lead to defects on the parts produced, but they can lead to further damage on the die and initiate the final failure.

Some regions without obvious failures are examined in cross-section, as shown in Figure 4.39. Some cracks are found at the subsurface even though no failure is visible at the surface. In Figure 4.39 (a), the two cracks are already joined to each other (despite the low visibility). The crack on the right could be initiated in the carbides (white tungsten carbide and dark vanadium carbide). This crack eventually opened at the surface with an angle of 18-20 degrees, as shown in Figure 4.39 (c). Figure 4.39 (b) shows the same angle between the cracks and the surface. In addition, the crack on the right has already resulted in the removal of a small piece of material. This is the pitting initiation mechanism [313]. The distance between these cracks and the surface is about 3 µm. Most of the cracks have a similar angle to the surface (18-20°).

4.3.1 Failure mechanism on the thread rolling die

The failure mechanism includes rolling contact fatigue and the sliding effect. The crack should initiate at depths close to where the maximum shear stresses locate in the rolling contact fatigue failure mechanism before propagating upwards. Nevertheless, the cracks may also initiate at the surface where the tangential shear stresses are large due to the high roughness or friction coefficient. The sliding/rolling ratio and friction coefficient are

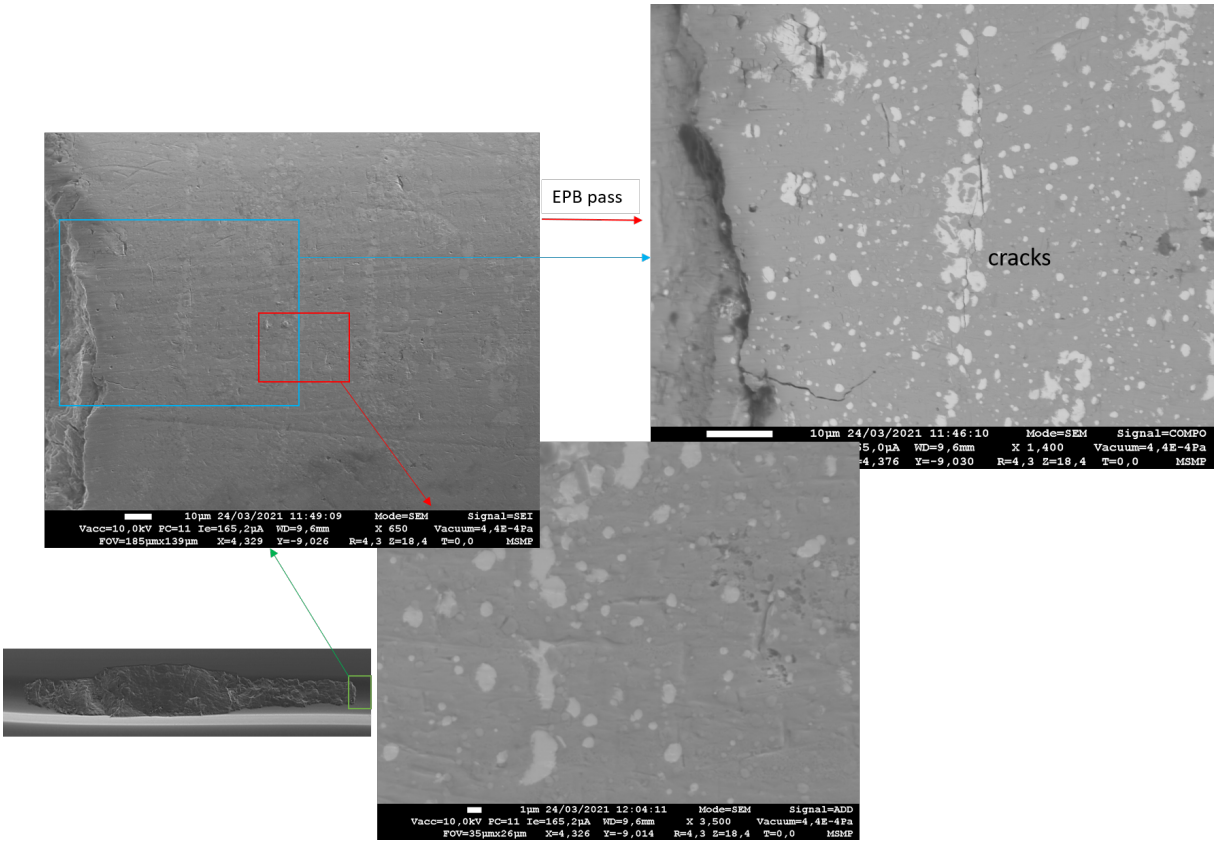


Figure 4.37 – The damage on the crest surface next to the right border of the failure.

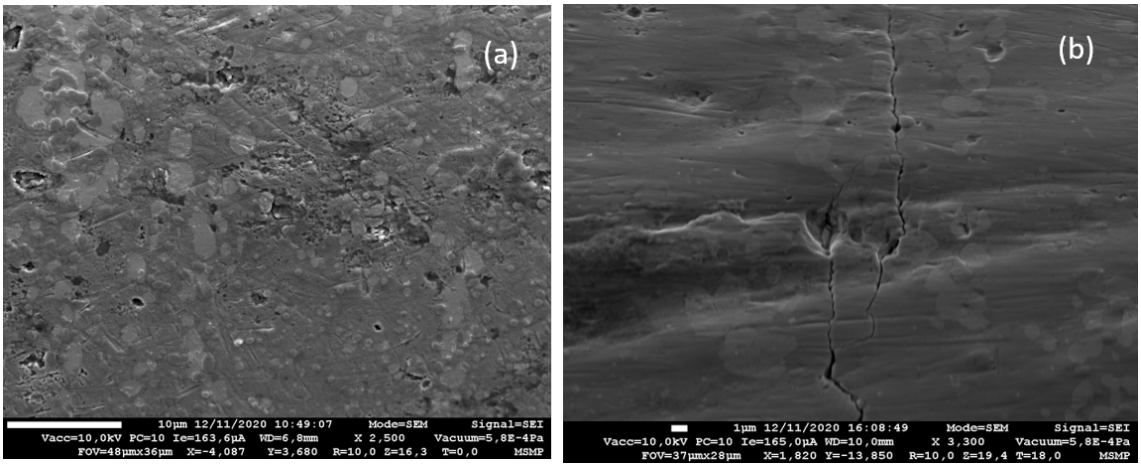


Figure 4.38 – Some failures on the flank surface of the tread of die E0-1.2 (a) surface wear and (b) cracks.

the main factors controlling the sliding effect. From the die observation, most microcracks occur at several micrometers under the surface. It is then considered that the sliding significantly affects the rolling die failure. However, it is more complicated to define the maximum shear stress depth for a special geometry like the rolling thread.

On the other hand, the foreign particles that remain in the lubricant between the contact parts during the rolling process can be a critical reason for causing the degradation on the rolling die's surface, and lead to a final failure initiated from the surface.

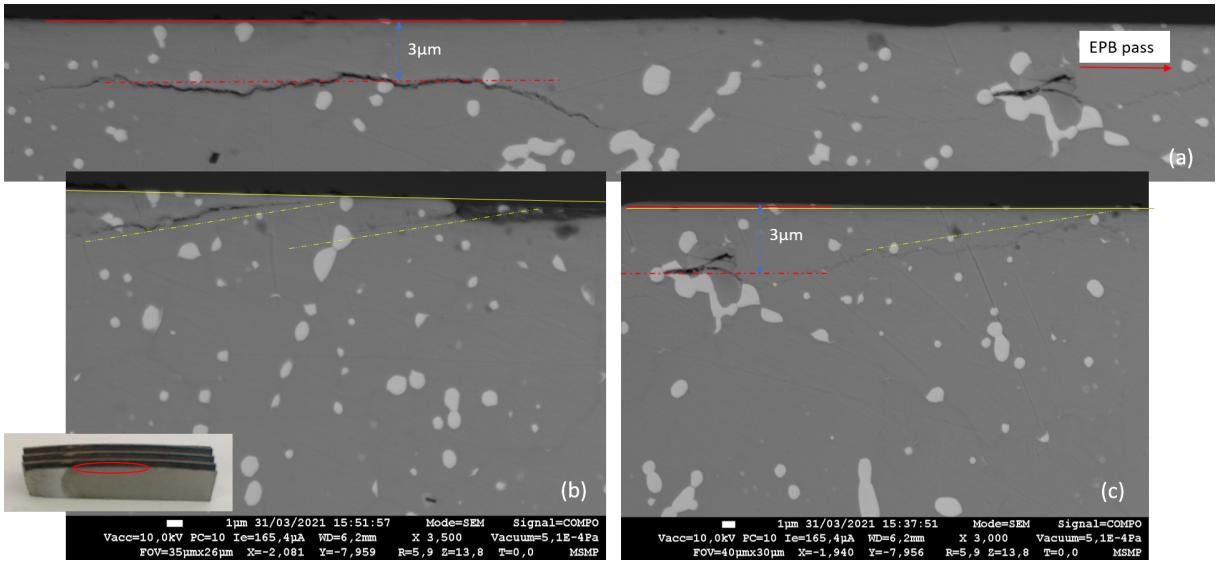


Figure 4.39 – Cross-section of the thread.

4.4 Numerical study on the rolling process

The numerical method (Finite Elements modeling) is applied to simulate the rolling process and to predict the potential location of the fatigue failure on the rolling dies. The FEM is performed with the software Forge NxT 3.1 by Transvalor. The results are provided by LISI Automotive. Forge 3.0 and ParaView are used for post-processing. Figure 4.41 shows the three main components in this modeling, and Figure 4.42 shows the thread forming during the process.

4.4.1 Simulation analysis

In the in-feed thread rolling process, the workpiece lead is equal to the rolling die lead. No axial displacement (nor relatively) takes place to the rolling dies or the workpieces. This results in a synchronic rotational movement of part and dies. The thread diameter, the spindle length, and the processing speed define the necessary rolling force. The diameter of the dies is 184.7 mm. The die thread dimension and geometry are defined by the screw thread profile. The workpiece is placed on a supporting blade in the thread rolling process (Figure 4.40). One rolling die moves towards another to realize the forming process. The two dies rotate synchronously in the same direction with an angular velocity of 30 tr/min once they start to contact the workpiece. The feed speed of the rolling die is 0.65 mm/s, and the total penetration is 1.04 mm.

In this modeling, the rolling die triangularly meshes into 2034739 elements. The process contains 31 steps. The material of the rolling die is considered a rigid body elastic with a Young Modulus of 205000 MPa. The friction coefficient between the die thread surface and the workpiece is 0.2 (an experienced value for the thread rolling process). While the EPB workpiece is considered plastically deformable with a Young modulus of 205000 MPa and Yield strength of 480 MPa. The feeding speed if the dies are -0.019 and 0.019, and the speed of revolution is 1 rpm. No axial displacement and the spindle is placed on support before rolling.

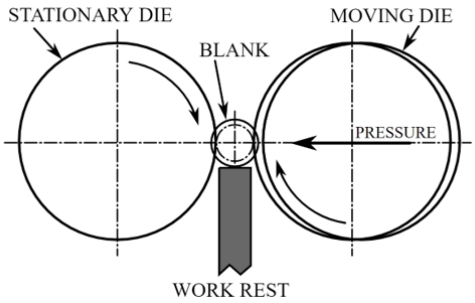


Figure 4.40 – Sketch of thread rolling process with two round dies [13].

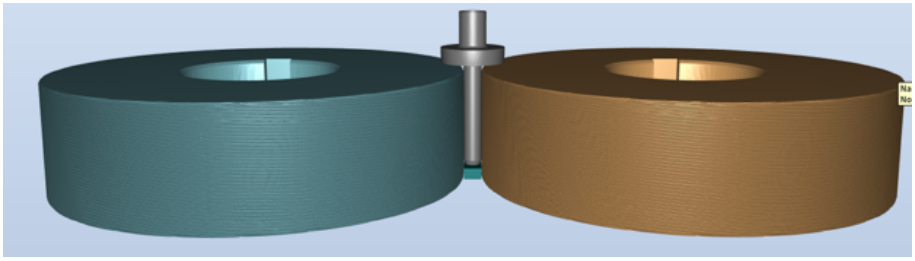


Figure 4.41 – 3D diagram of the FEM.

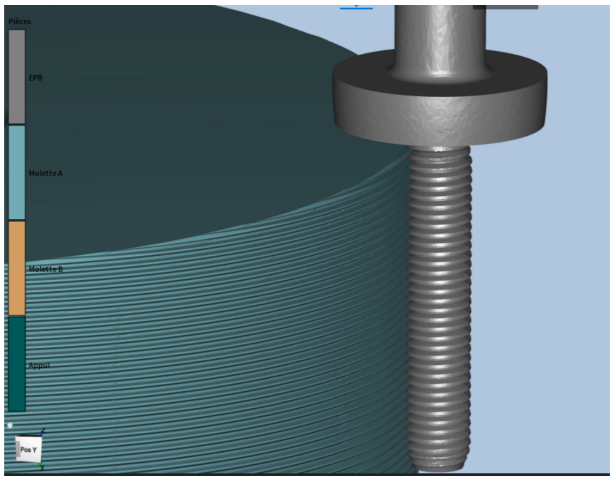


Figure 4.42 – 3D diagram of the modeling focusing on the thread forming.

4.4.1.1 The Dang Van criterion applied on the whole rolling die

The FEM results were exported using Forge 3.0 as .unv type files for each step. The Hydrostatic and Tresca stress for each element are calculated with a python script. After step 26, the spindle is visibly bent in the axial direction, and the data will no longer be reliable for analysis. Figure 4.43 shows the diagram of Tresca-Hydrostatic stresses for all elements from steps 0 to 26. The darker color represents the stress at the beginning of the process while the lighter color corresponds to the later steps in the process. Thus, it is found the stresses increase during the process.

To define the Dang Van line, two points are found from the literature for quenched and tempered M2 high-speed tool steel for a lifetime over 10^6 cycles with a failure probability of 50%. M2 steel has a fatigue strength of 800 MPa in a tension-compression loading mode with mean stress of 0, and stress ratio R=-1. According to the Dang Van criterion, one point on the Dang Van line A: (260,390) [331] is defined (Figure 4.43). According to

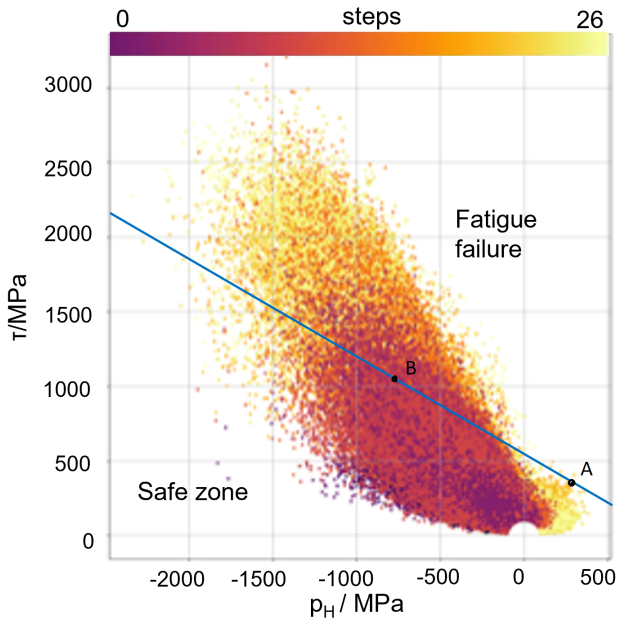


Figure 4.43 – Tresca-Hydrostatic stresses for all elements from step 0 to step 26.

another study [332], fatigue occurs after 4.3 $\times 10^6$ cycles under the tension-compression loading of -2316 to 386 MPa. Thus the second point B: (-772,1158) on the Dang Van line is defined.

Some other Wöhler curves in the literature of M2 steel under rotating bending modes show the fatigue strength between 1000 and 1100 MPa depending on the surface topology and case hardening condition [333, 334]. However, the stress gradient in the material under a rotating bending load allows the material to present a higher fatigue strength than under the axial loading mode [335]. Some works have studied the relation between rotary bending fatigue strength and axial fatigue strength. The ratio of the latter to the former varies from 0.59 to 0.9 depending on the model [336, 337, 338]. Due to the issue of uncertainty, in this work, these fatigue strength values will not be considered.

The blue line in Figure 4.43 presents the Dang Van line, which indicates the endurance domain corresponding to a lifetime over 10^6 cycles with a 50 % probability of failure. Above the line, the fatigue failure occurs, and below the line, it's the safety zone for fatigue. A great number of points are located in the danger zone. Therefore, some treatment is needed to strengthen the material. Expecting that nitriding induces a doubling of the fatigue limit for quenched and tempered steel [339, 278], the Dang Van line is simply modified by increasing the fatigue strength to 1600 MPa. 106 points on the Tresca-Hydrostatic stress diagram are left in the fatigue zone (see Figure 4.44). These elements are found on the die, as shown in Figure 4.45 (a). All the fatigue takes place after step 17, and the possibility of fatigue is higher later. Figure 4.45 (b) shows that fatigue occurs to the elements located on the crests of the threads.

4.4.1.2 Dang Van criterion along the paths

The stresses rise during the process and reach the maximum at step 26 (the last step taken into account). Dang Van criterion is applied along some paths at step 26. Figure 4.46 shows the hydrostatic and Tresca stress profile along the path that starts from the crest of the thread to in-depth. The stresses are very high close to the surface and decrease

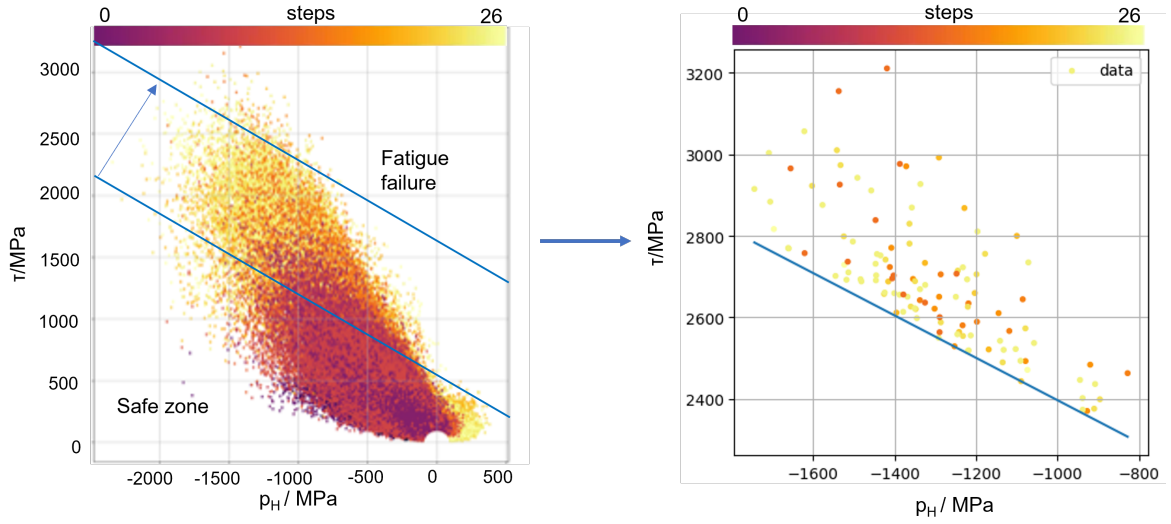


Figure 4.44 – The 106 points in the fatigue zone after doubling the fatigue strength.

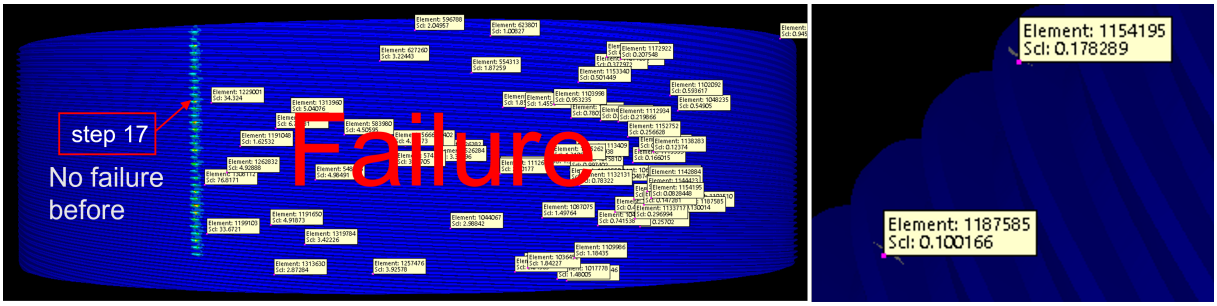


Figure 4.45 – The localization of the 106 elements where fatigue could occur, (a) global localization on the whole rolling die, (b) the specific localization on the teeth.

in-depth. Figure 4.47 shows that most points along this path are in the fatigue zone. The distances from the stress curve to the Dang Van line are plotted as a function of depth, as shown in Figure 4.48. When the stress curve is above the Dang Van line, the distance to the Dang Van line is positive. Therefore, fatigue failure can occur from the surface to less than 1 mm depth.

The same analysis is also performed along other paths, as shown in Figure 4.49. Path 4 runs from the valley surface to depth and has a relatively lower stress range. The Dang Van criterion is illustrated in Figure 4.50. All points are below the Dang Van line, all elements are in the safe zone, and fatigue would not occur. Paths 2 and 3 have similar profiles to path 1, with very high-level stresses near the surface. Further results will be presented in the section 4.4.1.3.

4.4.1.3 Nitriding effect on the Dang Van criterion along the paths

A new Dang Van criterion will be developed if the hardness and residual stress effects are calculated for each depth in the material after nitriding. Path 1 in section 4.4.1.2 as an example. The hardness and residual stress gradient in M2 steel after gas nitriding (at 540 °C for 5 hours under a nitriding potential of 3.7 $atm^{-1/2}$) given in Figure 4.51 will be considered and the method in 2.8.3 is applied in the calculation.

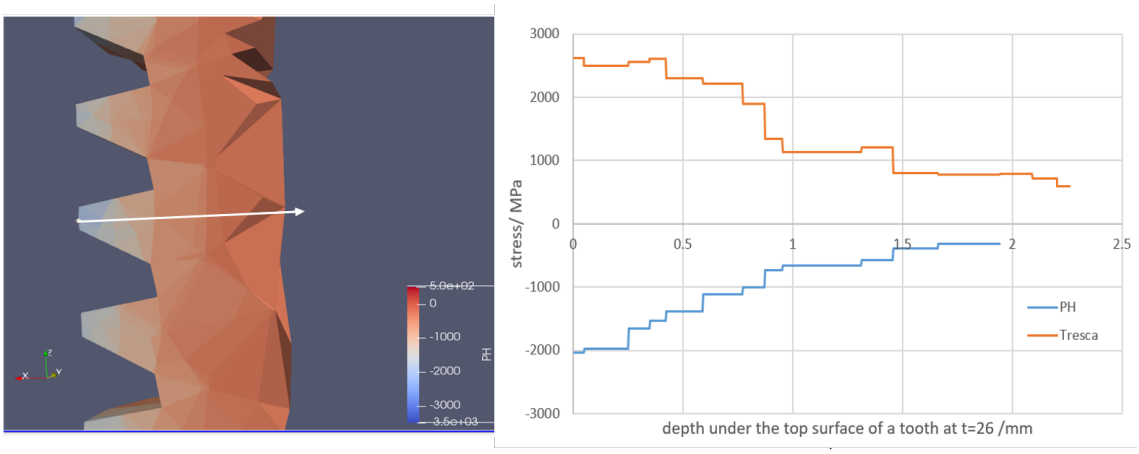


Figure 4.46 – The hydrostatic and Tresca stress profile along the path starting from the crest of the thread to in-depth.

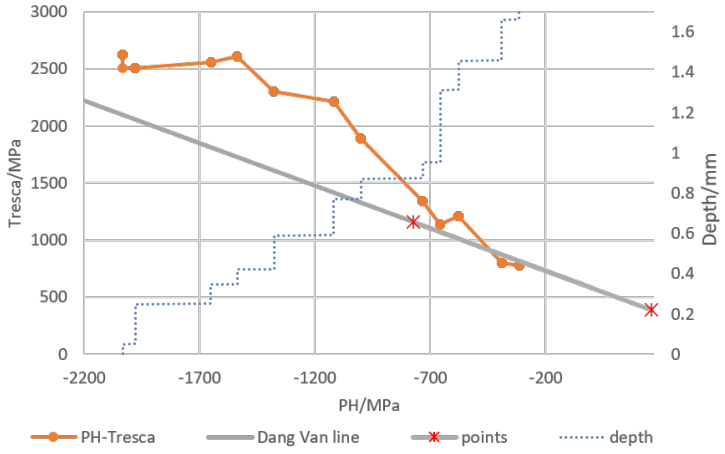


Figure 4.47 – Dang Van criterion along path 1 as given by Figure 4.46.

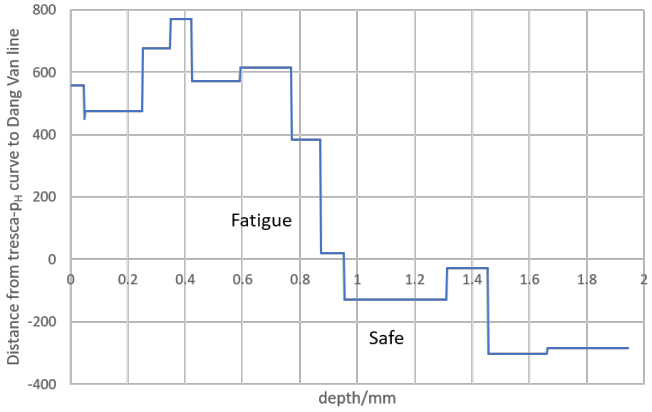


Figure 4.48 – Distance from Tresca-Hydrostatic stress curve to Dang Van Line along path 1 in Figure 4.46.

The new Dang Van criterion is illustrated in Figure 4.52. The gray dashed line represents the original Dang Van line, as shown in Figure 4.47. A series of Dang Van lines reveal the effect of nitriding hardness gradient. However, the mesh size of the modeling

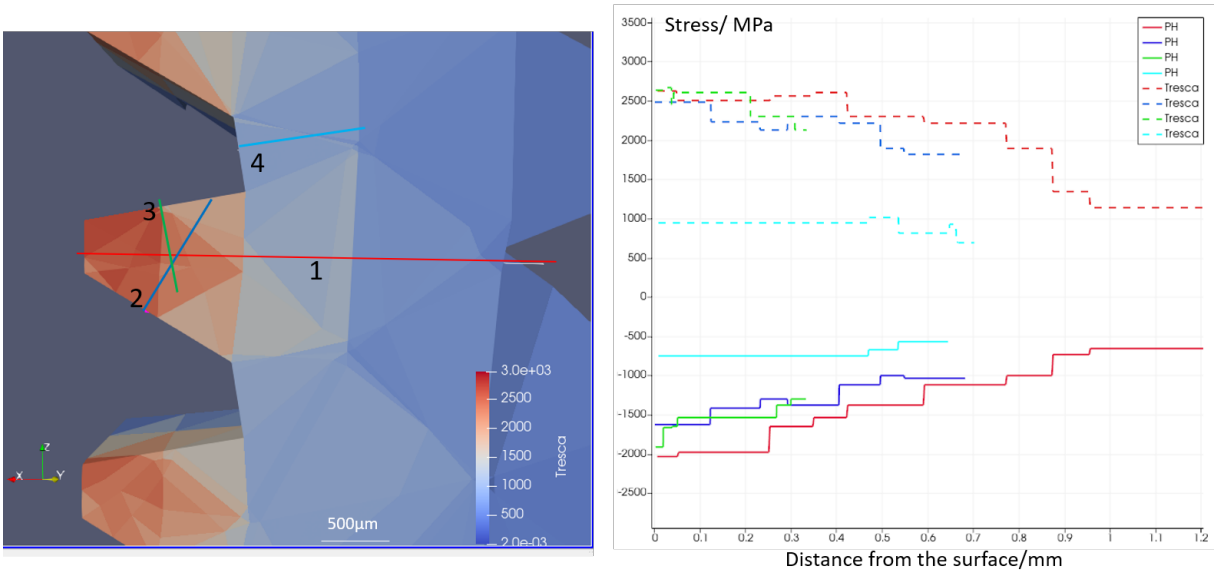


Figure 4.49 – The hydrostatic and Tresca stress profile along different paths.

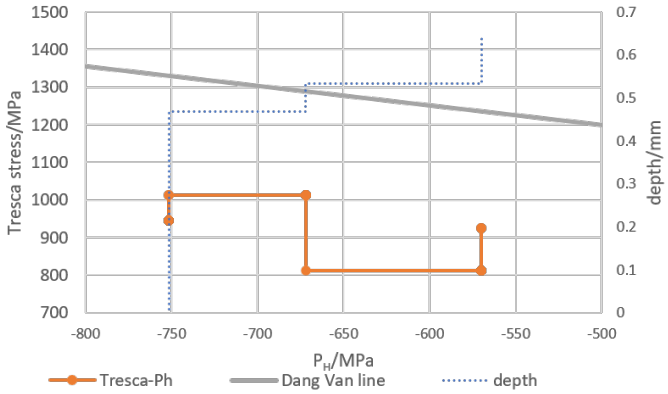


Figure 4.50 – Dang Van criterion along path 4 starting from the valley to in-depth.

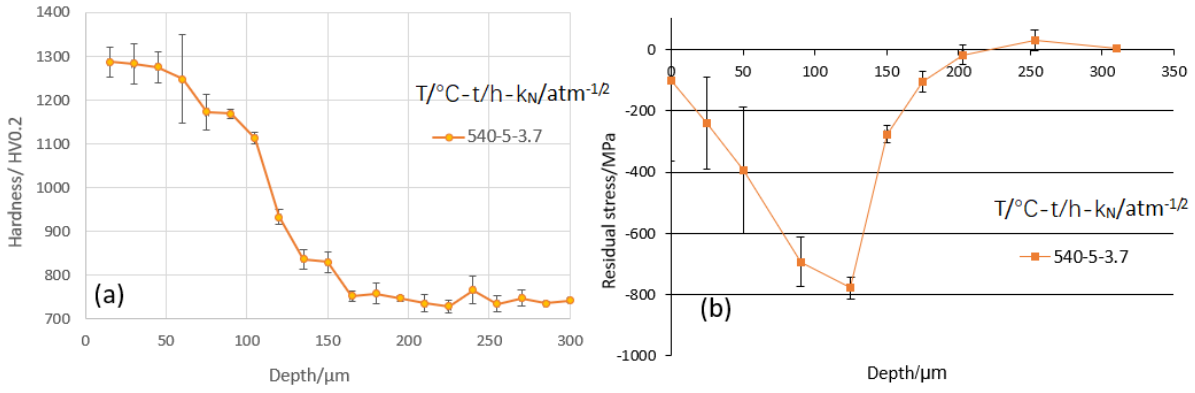


Figure 4.51 – Nitriding profile of M2 steel sample nitrided at 540°C for 5 hours under nitriding potential 3.7 $atm^{-1/2}$, (a) hardness profile, (b) residual stress profile.

does not allow the nitriding gradient to be presented continuously. Meanwhile, the residual stress modifies the stress curve. The new distances from the stress curve to the new Dang Van lines as a function of depth are presented in Figure 4.53. The positive values

become negative near the surface. Similar results for path 2 and path 3 from the surface of the flank at 30 and 10 degrees to depth, respectively, are shown in Figure 4.54. This confirms that nitriding could be effective in improving near-surface rolling contact fatigue.

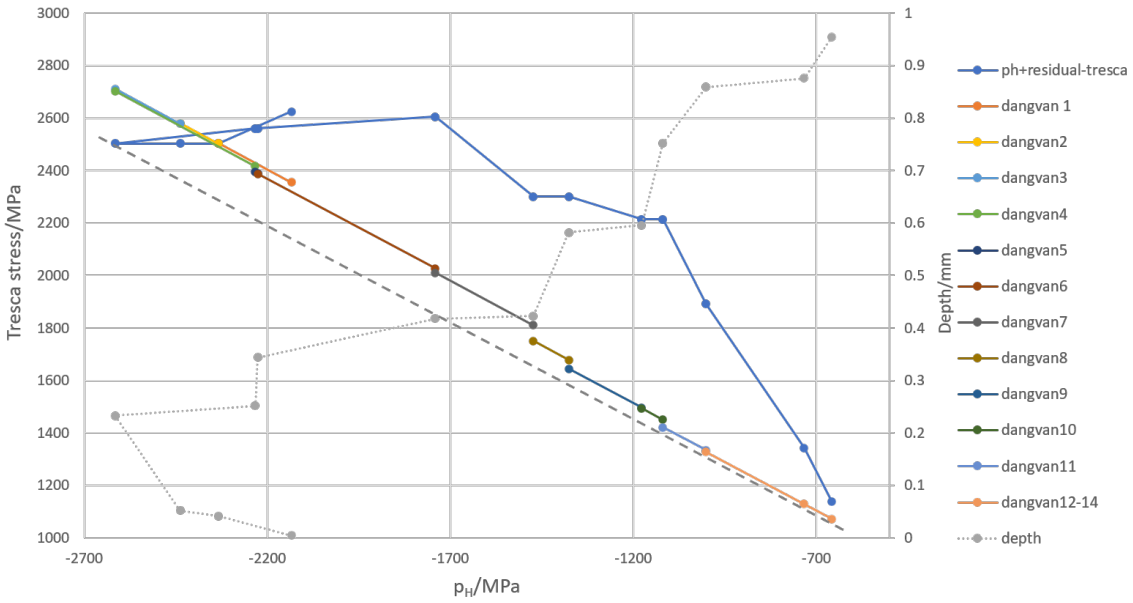


Figure 4.52 – Dang Van criterion of path 1 in rolling process modified with a nitriding profile.

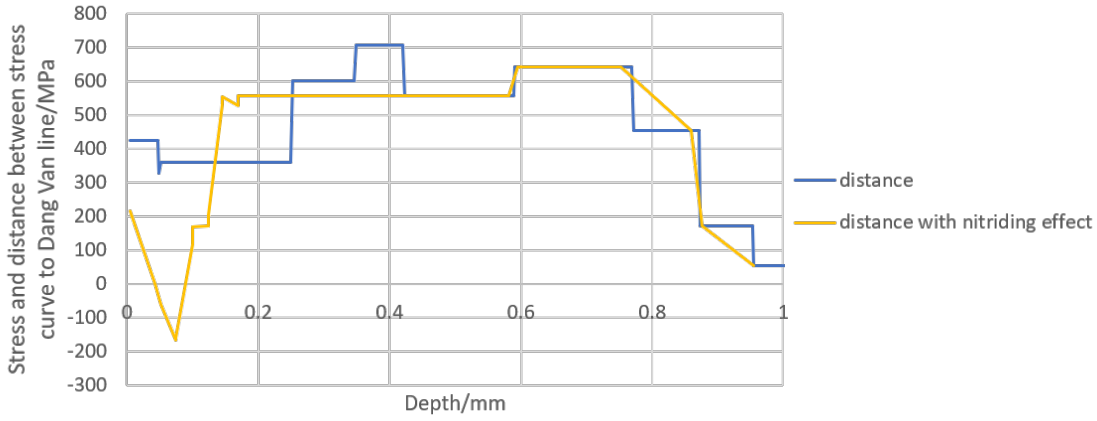


Figure 4.53 – Distance from the modified stress curve to the modified Dang Van line as a function of depth along path 1.

Rolling contact fatigue is a very complex phenomenon, and many factors are involved, such as the contact stresses, lubrication, surface topography and surface traction [340, 341, 342]. On the other hand, contact fatigue crack initiation is a local phenomenon. Dang Van criterion should be only applied locally, and the parameters of the criterion are usually only for the volume material [343]. The lubrication and surface topographic conditions in the real rolling process may vary from those in the FEM. Numerical results must then be considered with precaution. The fatigue criterion can also be applied on the surface if all the surface information is provided. High surface traction (friction effect for a surface with a certain roughness) and rolling contact loading can induce the crack to initiate below but close to the surface [290].

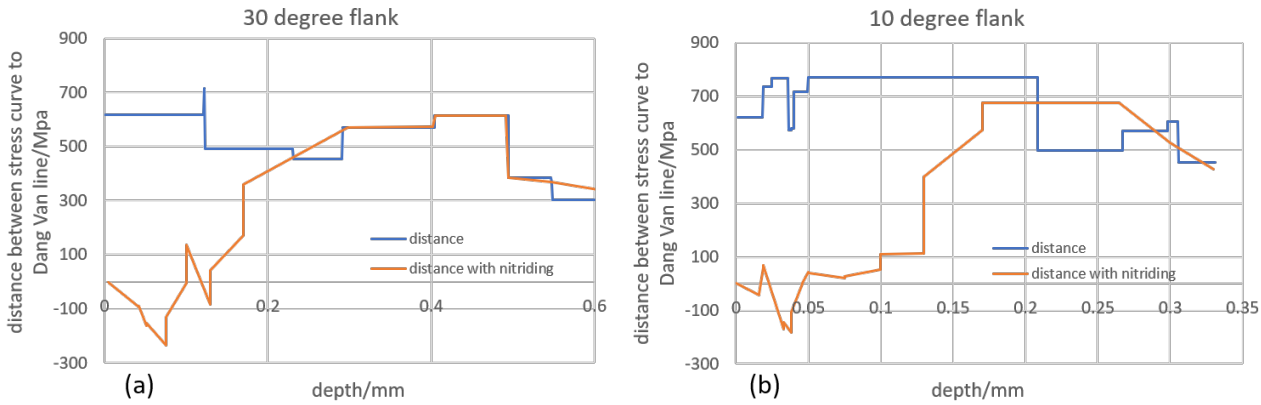


Figure 4.54 – Distance from the stress curve to the Dang Van line as a function of depth along (a) path 2, (b) path 3.

4.5 Conclusions

The study of this chapter is concentrated on the actual rolling dies and their failures. E rolling dies are made in M2 high-speed steel but have a very high core hardness of about 900 HV. The significant carbide segregation formed during casting is found along the axis of the die. However, G dies have a different chemical composition than M2 steel by containing less W, but more Mo and Co. Powder metallurgy manufacturing method offers the dies more homogeneous carbide distribution and finer grain size.

The nitriding conditions of these dies are characterized. Salt bath nitriding provides G dies with homogeneous case hardening layers. Controlled surface hardening and a finer microstructure result in more stable performance. In contrast, surface nitriding profiles on E dies are variable. Figure 4.55 shows all the information provided by the manufacturers and the experimental results. The relation between life and nitriding depth and maximum hardness is plotted for G and E dies. For E dies, two groups with and without compound layers are distinguished. The service life increases as the maximum surface hardness increases. At the same time, it is also proportional to the effective nitriding depth. However, the service life of E2-0.16 cannot be taken into account because it is much lower than that of the other matrices and could have failed accidentally. The two dies with compound layers have relatively high surface hardness and nitriding depth. However, they show a big difference in their lifetime. One produces the most pieces, while the other one shows the opposite performance. Despite the number of the specimen, it is possible to have a good performance of rolling dies nitrided with a controlled compound layer.

Residual stress is also an important factor in mechanical behavior. However, nitriding on the flat side surface is incompatible with that on the threads. The results cannot be used to analyze the performance of the working area (the threads) of the rolling dies.

The fracture starts below the surface but close to it and eventually opens on the surface with an angle of about 18-20 degrees. The crack is often carbide related, on the one hand, the micro-crack often initiates from the carbide inclusion; on the other hand, the carbide can change the direction of crack propagation. The initiation of microcracks often requires high contact pressure, high shear stress and inclusions (carbides) located at a critical position in the subsurface. In the current study, rolling contact (high pressure) with sliding effect (related to surface friction) and carbide segregation are the main factors causing microcracks.

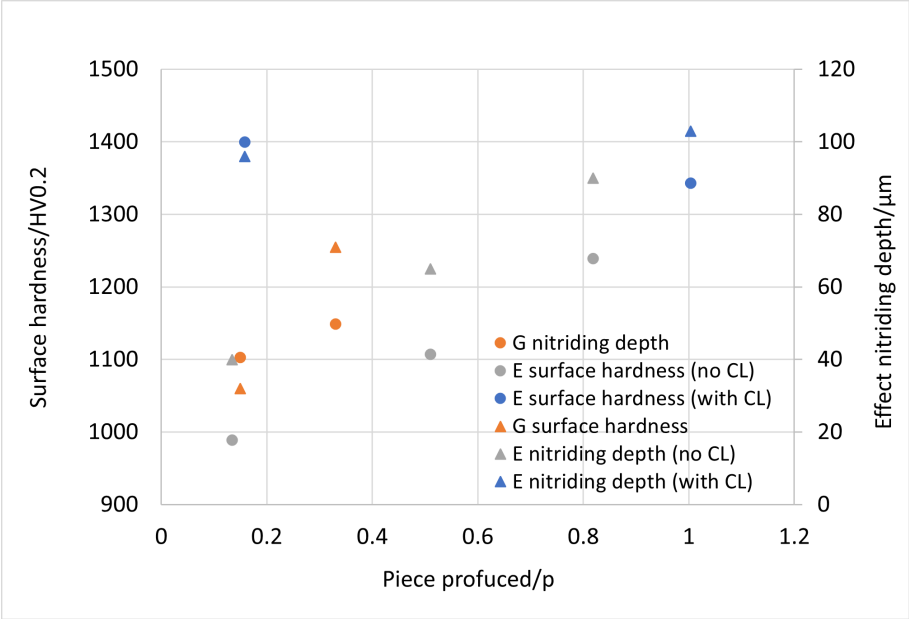


Figure 4.55 – The nitriding conditions and the lifetime of the observed dies.

The Dang Van criterion is applied to analyze the FEM results. Failure is more likely to occur in the later processing steps (after step 17) and the thread crest stars. Analysis along the loading paths demonstrates that nitriding works best near the surface to prevent fatigue failure initiation. However, rolling contact fatigue is very complex, and the simulation simplified many conditions.

CHAPTER 5

STUDY ON GAS NITRIDING OF M2 STEEL

In this chapter, the gas nitriding kinetics in M2 steel is studied. Firstly, the preliminary study with a high nitriding potential of 3.7 $atm^{-1/2}$ at 540 °C for 5 hours is carried out for approaching a visible nitriding layer in a short time. The effects of the surface mechanical conditions and the importance of sample preparation on nitriding are then introduced. The kinetics of nitriding will be investigated on a broad scale. Furthermore, the kinetics study focuses on a small scale to find the nitriding potentials that define the α/γ' limit at two nitriding temperatures. The phase transformation analysis during nitriding is conducted with the help of Thermo-Calc. Longer nitriding will then be carried out with the selected nitriding potentials and temperatures to discover the effect of nitriding time and temperature on the core hardness. Eventually, gas nitriding parameters are optimized to obtain good mechanical properties by comparing them to the nitriding profile of the best performant rolling die.

5.1 Characterization of samples before nitriding

AISI M2 steel samples of 17 × 13 × 5 mm^3 are provided by LISI Automotive with four different types of surface finishing (G: grinding, S: sandblasting, P: polishing, A: annealing), as shown in Figure 5.1. The chemical composition is measured with OES, as shown in Table 5.1. (Details about the heat treatments are not given concerning the confidential issues.)

Table 5.1 – Chemical composition of M2 steel samples (wt.%).

Elements	**C**	**W**	**Mo**	**V**	**Cr**	**Si**	**Co**	**Mn**	**N**
Concentration	0.884	6.352	4.513	1.729	3.807	0.306	0.372	0.271	0.025
SD	0.007	0.017	0.010	0.002	0.012	0.003	0.001	0.001	0.000

5.1.1 Initial surface conditions of the M2 samples

Under optical microscopy, the ground surface shows directional tracks, while the sandblasted presents an irregular texture with the indentation from the impact (Figure 5.2).

Figure 5.3 shows the surface roughness of the four samples. The displacement of the stylus probe on the Z axes is greater on the sandblasted and milled surfaces, and smaller

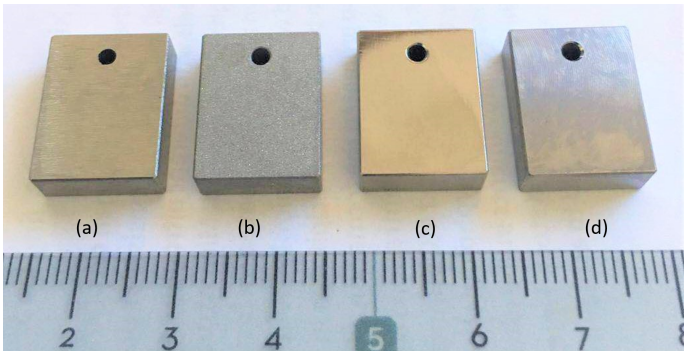


Figure 5.1 – M2 steel samples (a) ground surface, (b) sandblasted surface, (c) polished surface, (d) annealed sample with the milled surface.

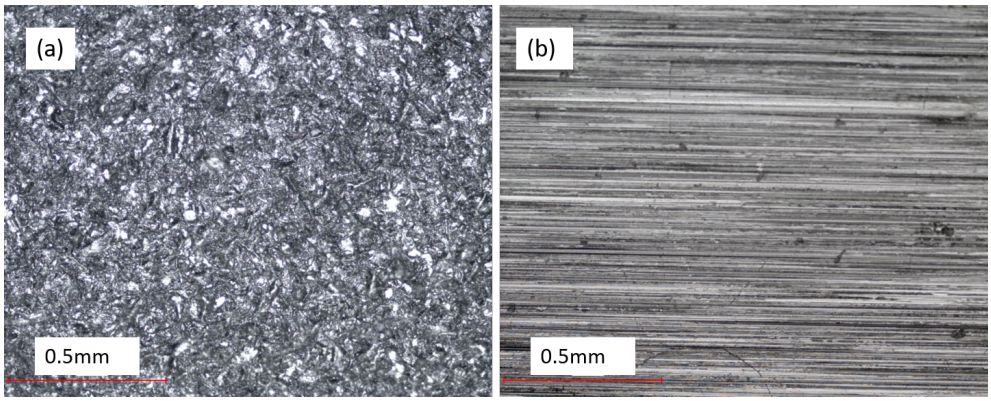


Figure 5.2 – Surface analysis of M2 steel samples (a) sandblasted surface, (b) ground surface.

on the polished surface. A profile at X = 2 mm is extracted from all four samples to analyze the roughness in two dimensions, shown in Figure 5.4. The depth of the grooves is the greatest of the sandblasted surface and the smallest of the polished surface.

Table 5.2 presents the 3D roughness parameters [24] of the four samples from the entire measured area, including the amplitude parameters (S_z: the maximum height of the topographic surface, S_q: the root-mean-square deviation of the surface, S_{sk}: the skewness of topography height distribution, S_{ku}: the kurtosis of topography height distribution), the spatial parameters (S_{ds}: the density of summits of the surface, S_{al}: the fastest decay auto-correlation length, S_{tr}: the texture aspect ratio of the surface), and the hybrid parameters (S_{sc}: the arithmetic mean summit curvature of the surface, S_{dr}: the developed interfacial area ratio, S_{dq}: the root-mean-square slope of the assessed topographic surface). They describe the topology from different aspects.

Table 5.2 – 3D roughness of the four measured surfaces.

Surface	$S_z/\mu m$	S_{ds}/mm^2	$S_q/\mu m$	$S_{sc}/\mu m^{-1}$	S_{sk}	S_{ku}	S_{dq}	S_{dr}	S_{al}	S_{tr}
Ground	12.63	2615.13	1.15	0.025	0.82	5.64	0.12	0.73	277.96	0.10
Sandblasted	30.79	1453.02	3.39	0.076	0.41	3.75	0.45	8.64	44.34	0.52
Polished	6.65	3090.36	0.72	0.010	0.47	4.10	0.04	0.10	454.90	0.16
Milled	13.54	1898.17	2.04	0.023	0.52	2.39	0.12	0.58	47.05	0.08

As for the amplitude parameters, the sandblasted surface has the largest S_z and S_q, it has a larger amplitude and the surface deviation in a larger range. In the contrary, the

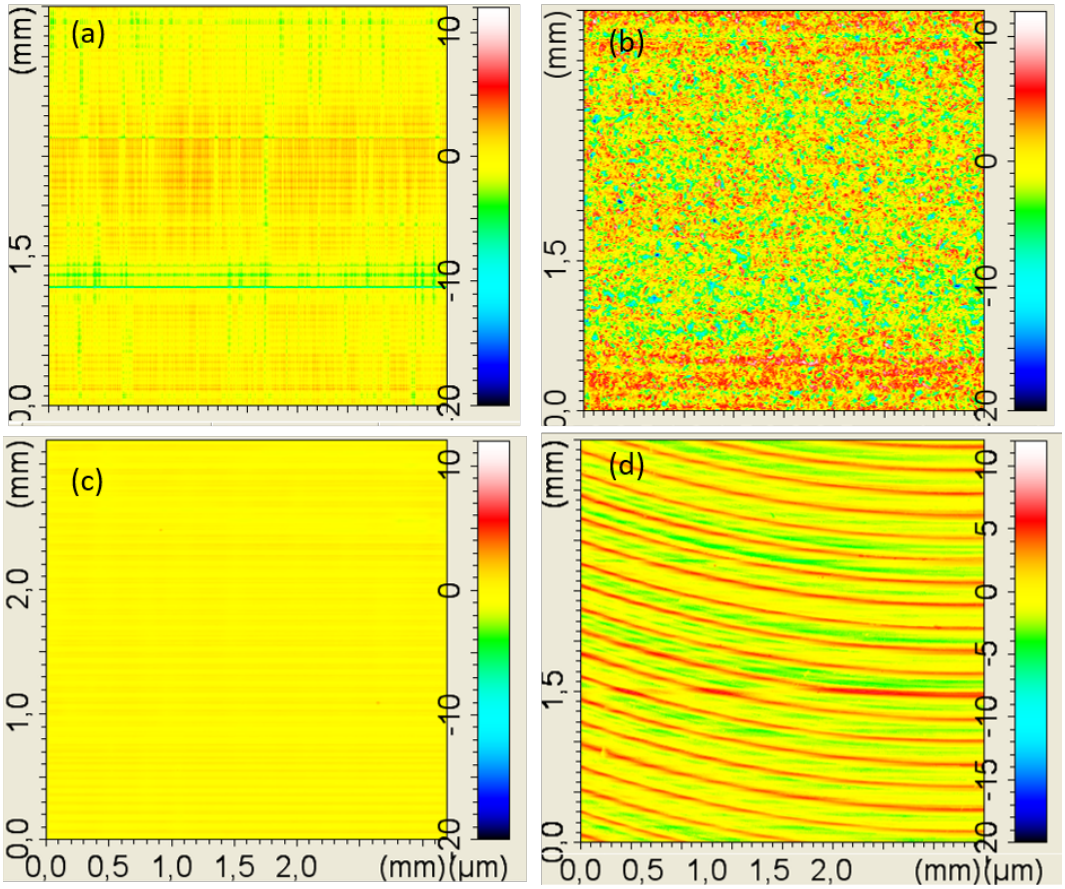


Figure 5.3 – Surface roughness profiles (using the same scale) of M2 steel samples (a) ground surface, (b) sandblasted surface, (c) polished surface, (d) annealed sample with the milled surface.

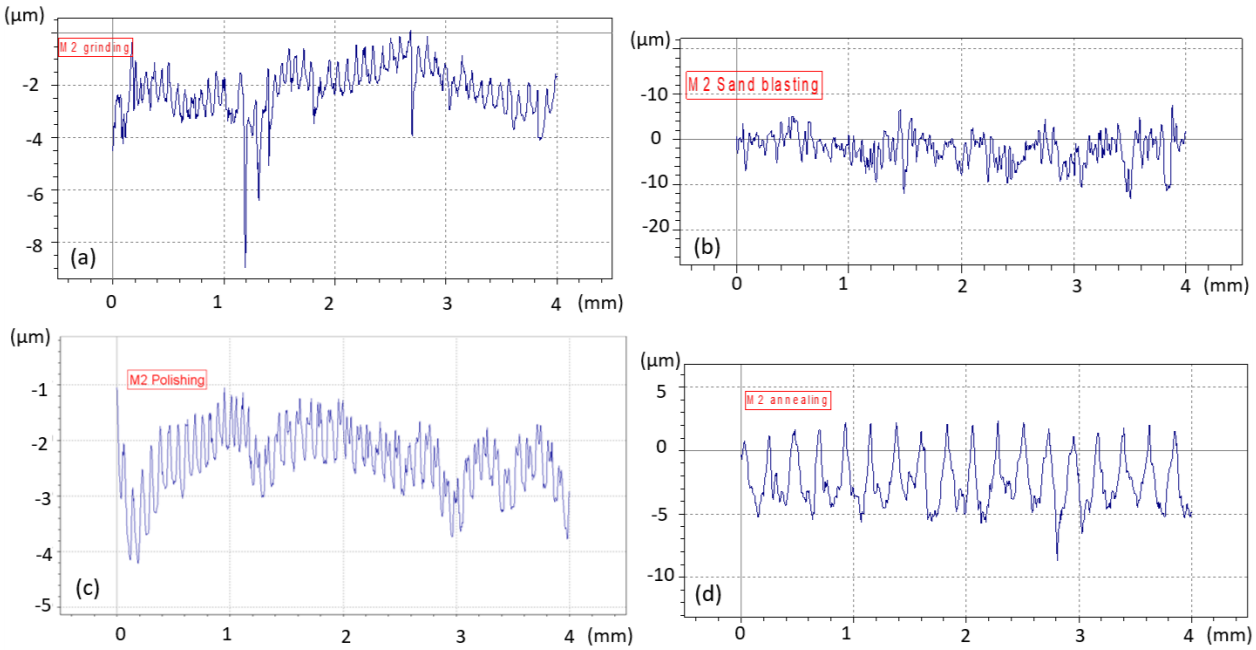


Figure 5.4 – Surface roughness analysis of (a) ground surface, (b) sandblasted surface, (c) polished surface, (d) annealed sample with the milled surface.

polished surface has the lowest S_z and S_q. S_{sk} values for all surfaces are positive, which

means the surfaces are not symmetric, and the heights are more likely to be above the root-mean-square surface. The ground surface has the greatest S_{sk} and S_{ku}, indicating that the height above the root-mean-square surface is larger and the height distribution is in a narrower range.

The polished surface has the largest summit density and decay auto-correlation length according to the spatial parameters. This indicates that the polished surface decays from the summit the most gently, which agrees with the smallest value of S_{dr}. On the contrary, the sandblasted surface and the machined surface on the annealed sample have the smallest summit densities, and the decay auto-correlation length, which means the shorter wavelength relatively dominates the surfaces. However, only the sandblasted surface has a texture aspect ratio greater than 0.5, all other surfaces show that lower than 0.3, which means apart from this sample, the surface texture of other samples is all directional. Even for the polished surface, it might be the result of the direction or polishing process, it can also be related to the process before polishing, for example, grinding.

Obviously, the hybrid parameter of sample S (sandblasted surface) presents the largest values for all the hybrid parameters, and that of sample P (polished surface) was the smallest. S sample has the largest developed surface, leading to the largest contact area with nitrogen during nitriding. The hybrid parameters of the machined surface and the ground surface are close.

5.1.2 Microstructure of hardened and tempered M2 steel sample

The microstructure of the M2 samples is observed on the cross-section. After polishing and etching, carbide bands are visible to the naked eye. Figure 5.5 shows that the carbide bands are regularly distributed. The average width of carbide bands is 5-15 μm, and the average space between two carbide bands is 20-30 μm. Different carbide bands contain different densities of carbide particles. Some carbide bands are discontinuous (Figure 5.6 (a)), while most of them lay through the whole cross-section (Figure 5.5 (a)).

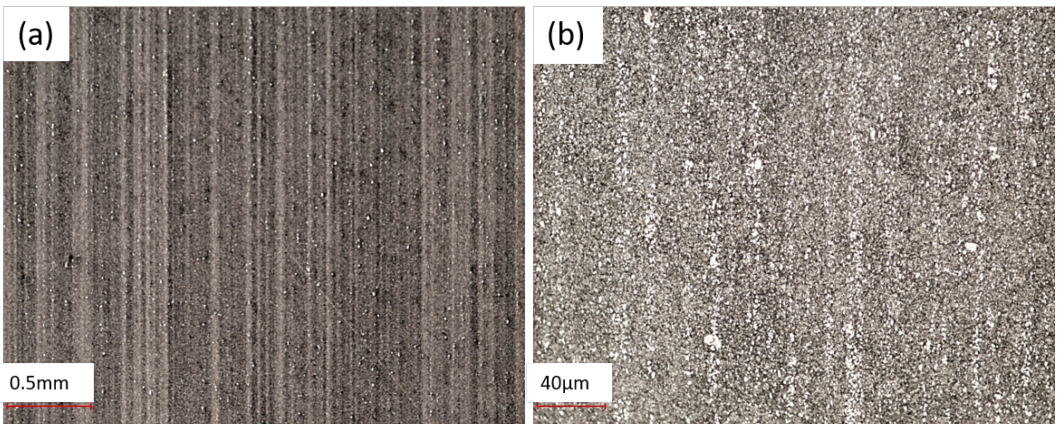


Figure 5.5 – Carbide bands in the hardened and tempered M2 steel sample (cross-section view).

However, carbide bands are not observed from the surface (Figure 5.6 (b)). The direction of carbide bands mainly depends on the casting and hot forging processes (see 2.6.2). The size of these carbides is about several micrometers.

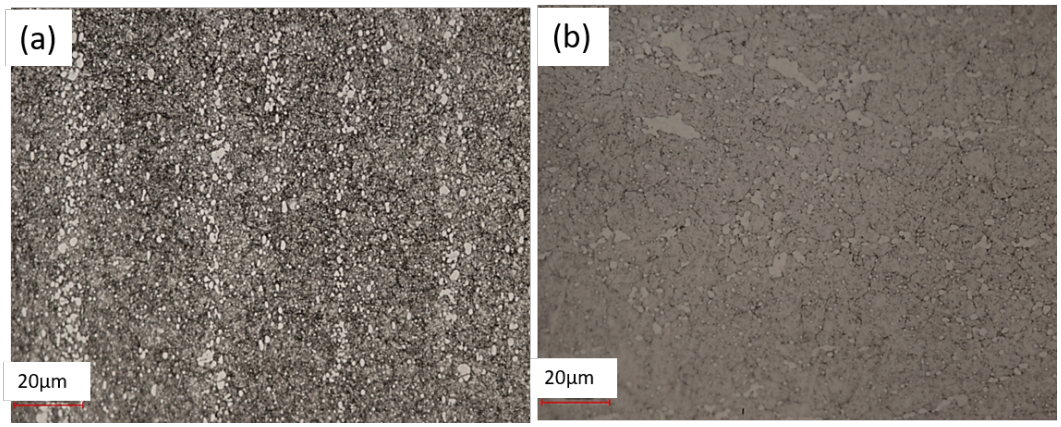


Figure 5.6 – Micrographs of (a) the cross-section (the carbide bands are observed parallel) and (b) the surface (no carbide band is observed because they are perpendicular to the surface).

5.1.3 Microhardness

The hardness value from random tests covering the cross-section of the whole sample is 735 ± 31 HV0.2, while the tests on the layer parallel to the surface show a hardness of 754 ± 21 HV0.2. The microhardness is measured close to the surface on the cross-section to a depth of 600 µm, as shown in Figure 5.7. No significant decrease in hardness is observed close to the surface. Accompanied by the carbon concentration profile from the surface to in-depth (Figure 5.8), it can be confirmed that no decarburization has occurred near the surface.

Three tests are performed parallel to the carbide bands (Figure 5.9). Blue line 1 shows the hardness of the carbide band, red line 2 shows the hardness measured on the border of a carbide band which contains fewer carbides, and green 3 shows the hardness of the matrix. In figure 5.10, the three series of measurements from right to left correspond to blue 1, red 2 and green 3. After etching, the white carbide bands are more noticeable, and the hardness test indentations are observed. The results show that the hardness on the carbide bands is higher than that of the matrix. The larger the carbide density, the higher the hardness is. The hardness of test point a is the highest, it locates on the carbide band that contains a great carbide density. The point is also shown in Figure 5.9 (a). The black dots in Figure 5.9 are linked to the presence of carbides. The test point b locates in the matrix that contains few carbides (Figure 5.9 (b)). The hardness at point b is more than 100 HV0.2 lower than at point a.

The hardness of the annealed M2 sample is 295 ± 9 HV0.2 on the cross-section and 301 ± 8 HV0.2 on the surface.

Knoop indenter is used in the case when the thin carbide bands can not cover the whole indentation (see in Figure 5.9). Two loads are used to study the effect of the indentation location and carbide bands. The average hardness is 806 ± 47 HK 0.05 and 811 ± 34 HK 0.1 by using different loads of 0.5 and 1 N, respectively (Figure 5.11). The highest hardness reaches 1041 HK 0.05 (Figure 5.12), and the indentation locates at a dense and large carbide band with a width of about 10 µm.

Generally, the microstructure and the phase composition reflect the heat treatment of the material. From the surface view, the carbides exist between the grain boundaries. They are originally formed during the casting process. Primary intergranular carbides first precipitate to control the austenite grain size during austenitization. The number of carbides and the size are more significant in the annealed sample due to the isothermal

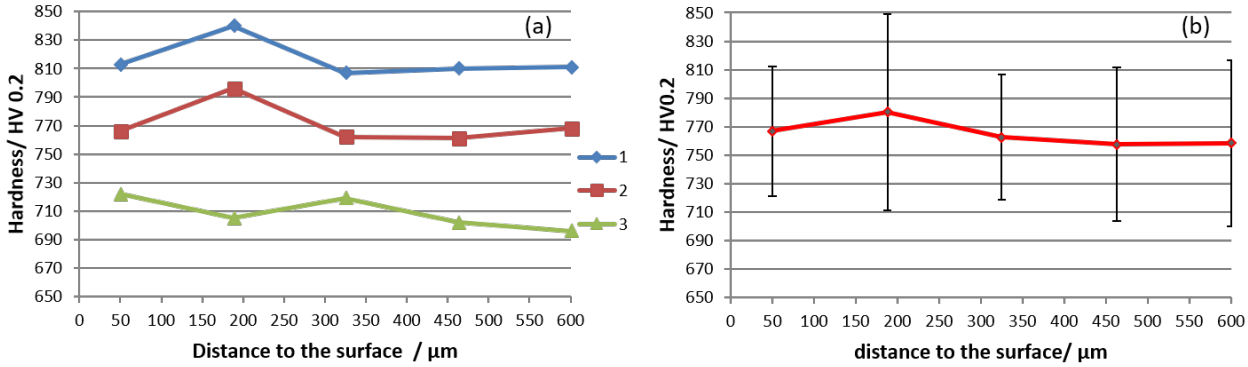


Figure 5.7 – Hardness near the surface (a) the hardness at each measurement, (b) the mean value at the same depth from the surface.

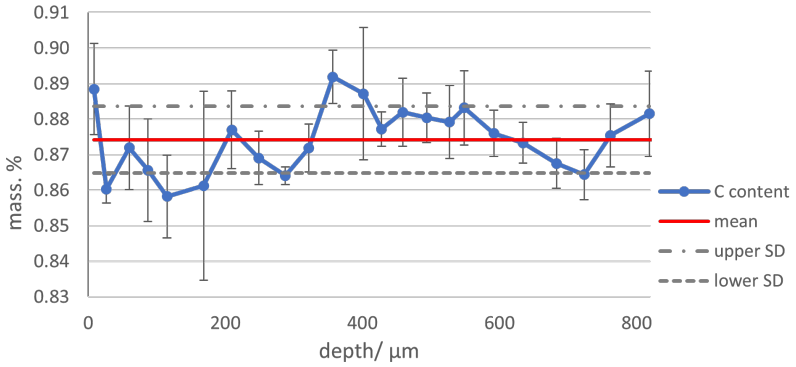


Figure 5.8 – Carbon concentration as a function of depth in M2 sample.

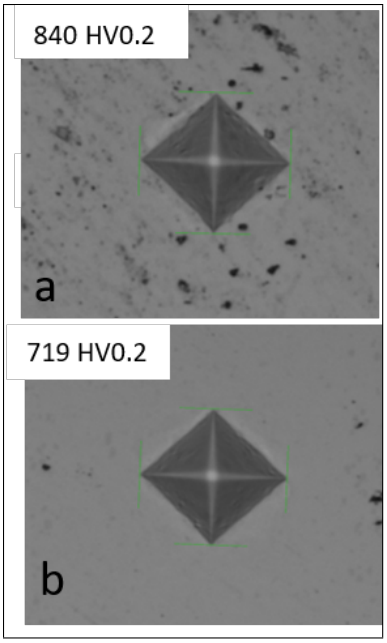


Figure 5.9 – Indents at (a) carbide band 1, (b) carbide band 2, (c) matrix.

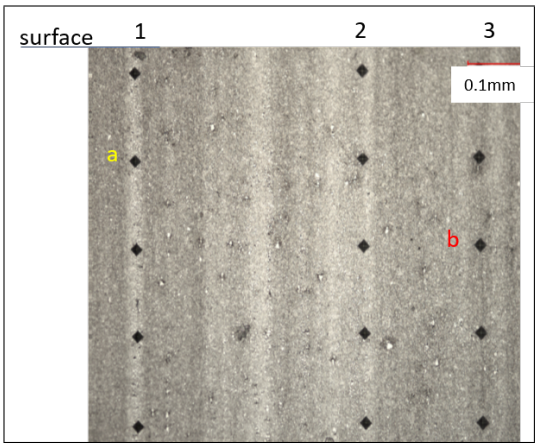


Figure 5.10 – Hardness mapping before and after etching

transformation for a longer time at annealing temperature (about 870 °C), and the slow cooling gives enough time for carbides to grow. As for the hardened and tempered samples,

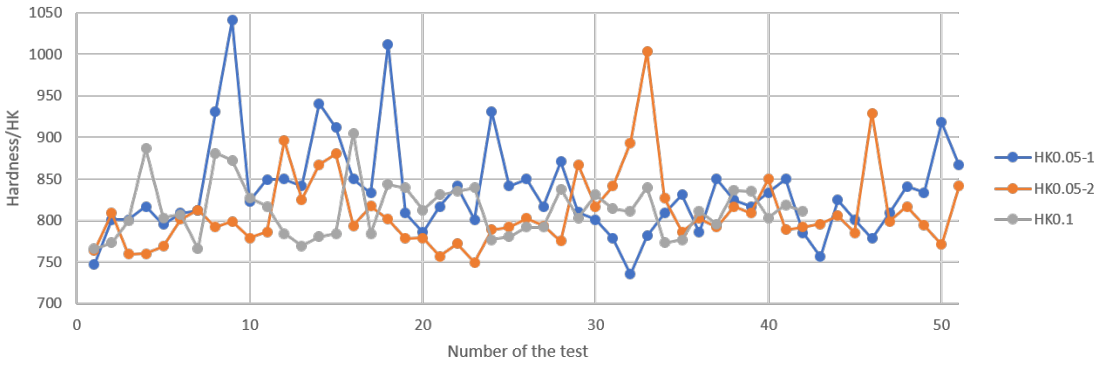


Figure 5.11 – Hardness measurement with Knoop indenter.

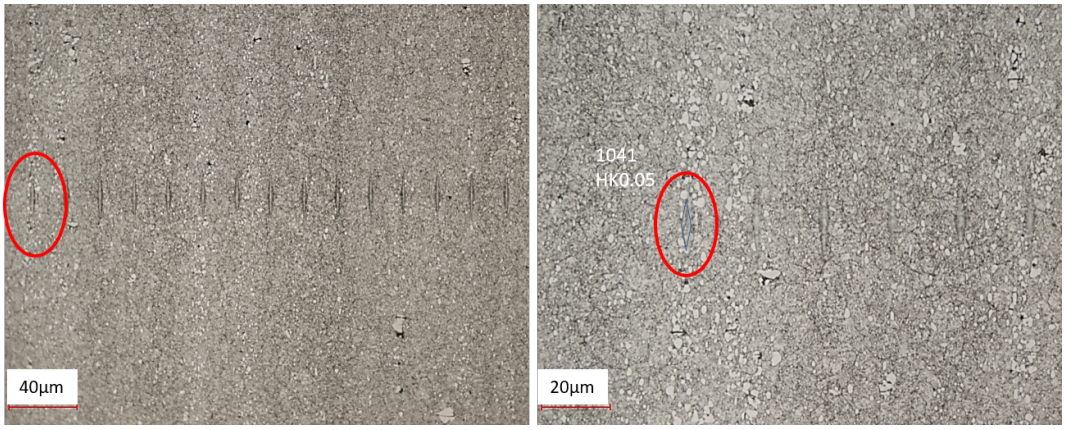


Figure 5.12 – Knoop indentations on the sample with the highest hardness.

during austenitization, some carbides dissolved, and alloy elements were transformed into the retained austenite phase. The secondary carbides are formed during tempering and can not be observed with optical microscopy.

Furthermore, the microstructure defines microhardness. The annealed sample has a lower hardness mainly because the main phase is generally α ferrite. After secondary hardening, the tempered martensite contains extremely small and uniformly dispersed cementite particles embedded within a continuous ferrite matrix. It keeps the high hardness of martensite but also has substantially enhanced ductility and toughness. Carbide is another important factor contributing to the hardness regarding precipitation hardening. The hardness on the carbide band is higher than that on the matrix. The quantity and size of carbides are essential.

The hardness of the M2 samples is about 60-62 HRC after conversion. It is in agreement with the industrial standard for cold forging tools from the data of steel supplier ERASTEEL, as shown in Figure 5.13. As for M2 steel used for cold forging, the common temperature for austenitization is 1050-1150 °C, and the tempering temperature is 560 °C.

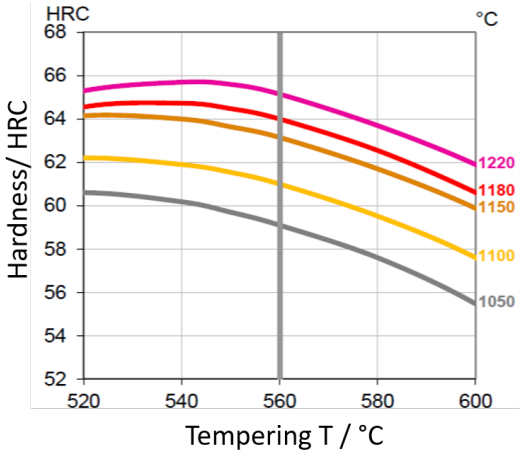


Figure 5.13 – Hardness of AISI M2 steel and corresponding hardening and temperature (considering 1 h× 2 tempering) [329].

5.2 The effects of sample surface condition on nitriding

5.2.1 Surface condition and the homogeneity of nitriding

Nitriding with a high nitriding potential of 3.7 $atm^{-1/2}$ at 540 °C is applied on M2 samples with a ground surface for 5 hours. However, the surface is not homogeneously treated, as shown in Figure 5.14 (a).

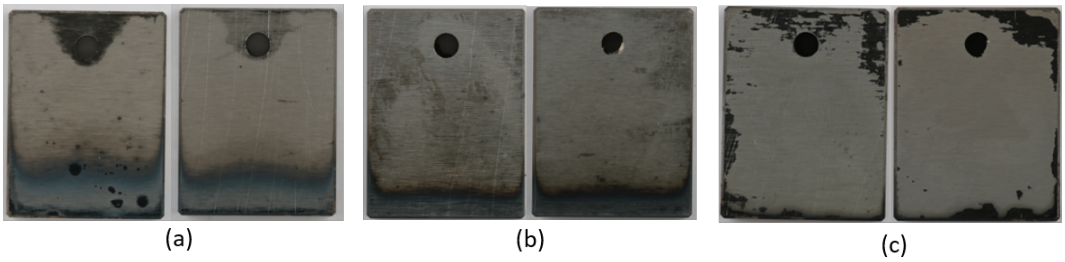


Figure 5.14 – Surface of ground M2 samples after nitriding.

The cleaning process is improved by increasing the cleaning time and using cotton and a brush instead of using hands and rubber gloves only. However, the surface is still not homogeneously treated (Figure 5.14 (b) and (c)). The samples are then analyzed as shown in Figure 5.15, and the hardness profiles are investigated along the border. The hardness profiles are shown in Figure 5.16, the hardness profiles correspond to the measurements marked with the same colors on the sample. From top to bottom, the nitriding depth becomes greater, and the surface hardness is higher. For example, hardness profile 1 (shown by the dark green curve) is measured close to the top border in Figure 5.15, the low surface hardness and nitriding depth are in agreement with the microstructure where a thin nitriding layer is observed (Figure 5.15). In contrast, profile 11 (red curve) represents the hardness profile on the bottom (the red position in Figure 5.15), corresponding to the microstructure with a thicker nitriding layer. This confirms that the adsorption of nitrogen atoms at the steel surface during nitriding is not homogeneously realized. The hardness increment depends on the amount and the size of the nitrides precipitates.

To obtain a homogeneous nitriding surface, one side of the surface was ground with a sequence of 220, 500, and 1200 grade SiC disks accompanied by the same cleaning process.

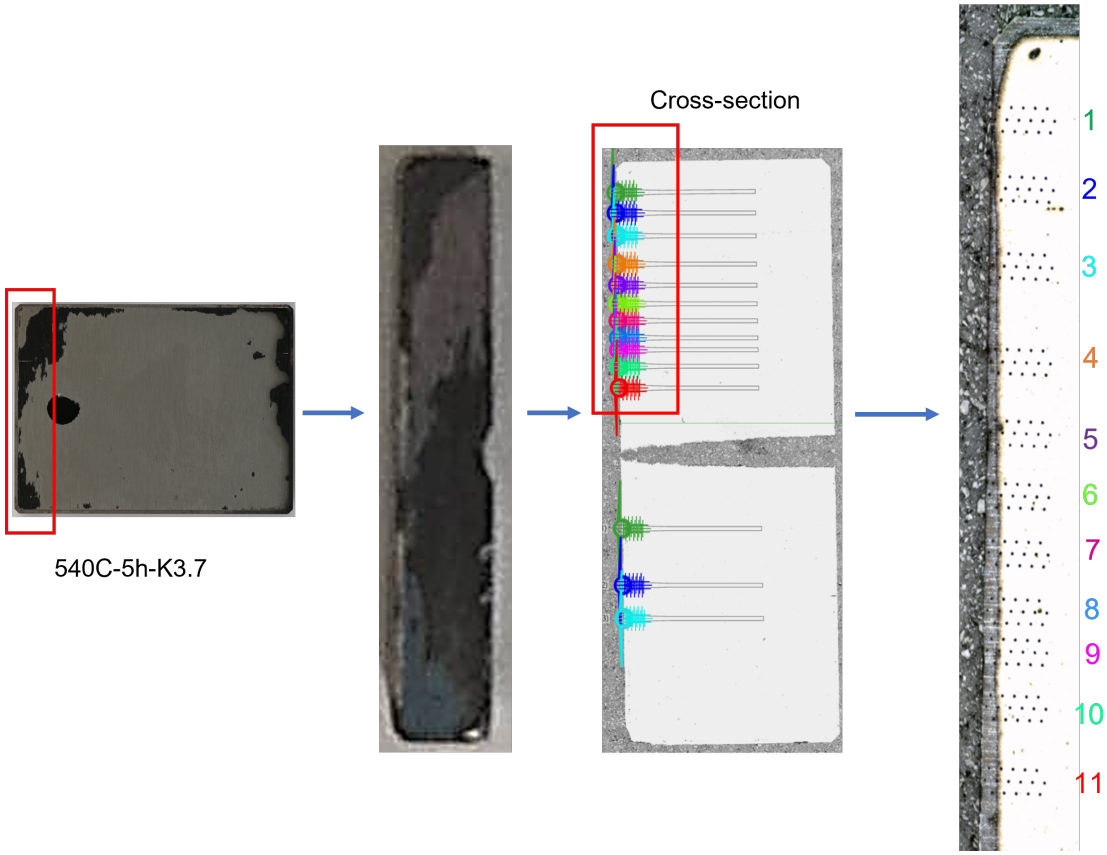


Figure 5.15 – Microstructure and hardness of nitrided M2 steel sample with a ground surface.

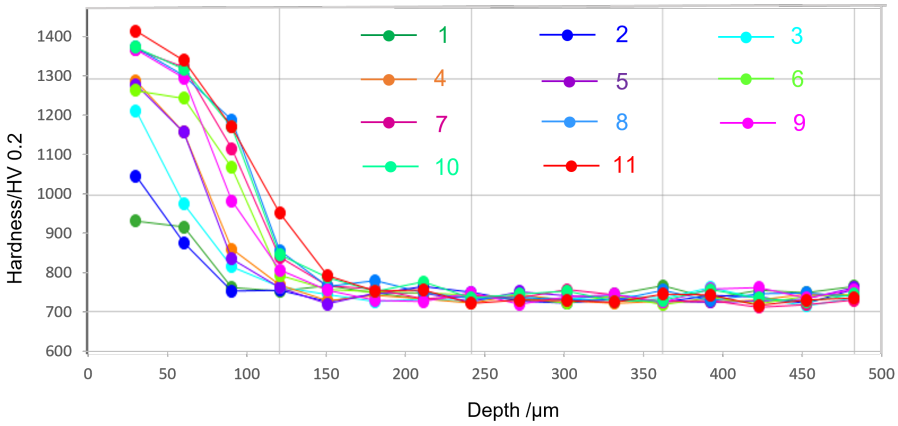


Figure 5.16 – Hardness profiles at different locations of ground M2 sample after nitriding.

Both sides of the treated surface are shown in Figure 5.17. The initially ground surface (a) is not homogeneously nitrided. In contrast, surface (b) is polished before nitriding and is homogeneously treated, covered with a homogeneous compound layer. Gas nitriding of M2 steel is then confirmed sensitive to the surface preparation and the mechanical finishing method [91].

Figure 5.18 shows the microstructure of the compound layer of the M2 sample under an optical microscope (from the 1200 grade polished surface). The pore zone and the cracks are observed within the compound layer, and the nitrides precipitates are observed at the grain boundary below the compound layer quasi parallel to the surface. The microstructure of the compound layer was observed using SEM in Figure 5.19. The sample is observed

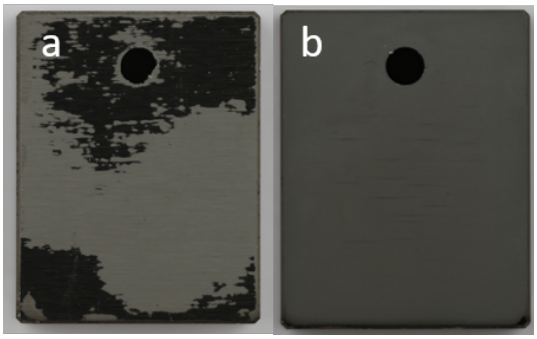


Figure 5.17 – Nitrided Surface of M2 samples with (a) initially ground surface, (b) 1200 grade polished surface.

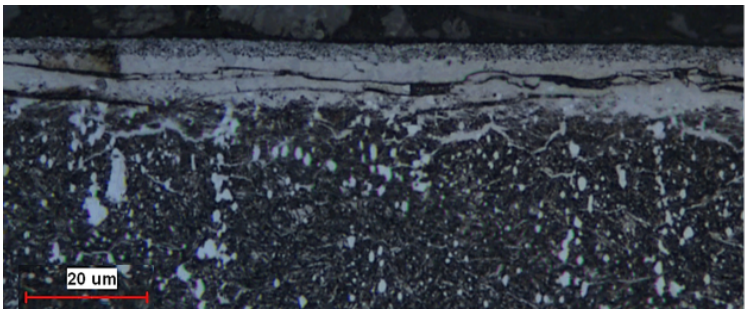


Figure 5.18 – Microstructure of the compound layer of nitrided M2 steel with surface polished 1200 grade under the optical microscope.

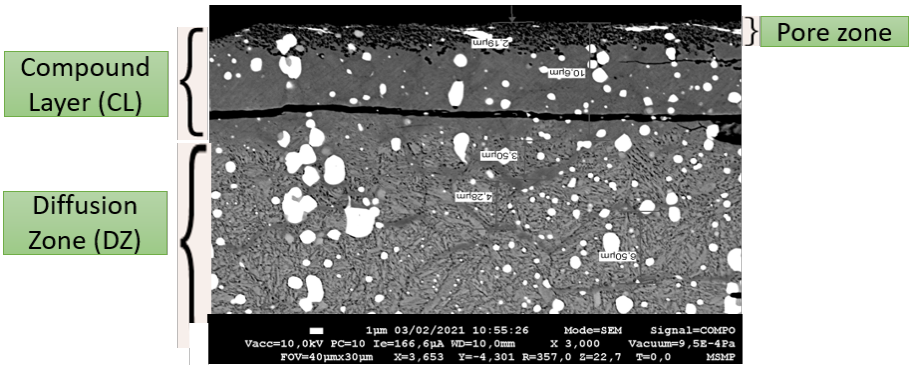


Figure 5.19 – Microstructure of the compound layer of nitrided M2 steel with surface polished 1200 grade under SEM.

under SEM before nitriding to determine the reason for the non-homogeneity of nitriding treatment for the ground surface. Certain area is covered with external elements as shown in Figure 5.20. From the EDS analysis with a voltage of 5 kV, some elements included in the contamination mark are determined. O, Si, C and a relatively lower content of Fe are found in this zone. It is considered from the organic lubricant that is hard to be removed from the ground surface due to the special topology [62].

5.2.2 The effect of surface finishing method on nitriding

More surface conditions are studied to check if the nitriding could be homogeneously performed. As the samples are one side treated differently and another side ground when they are received, the ground surface will all be polished until 1200 grade before nitriding.

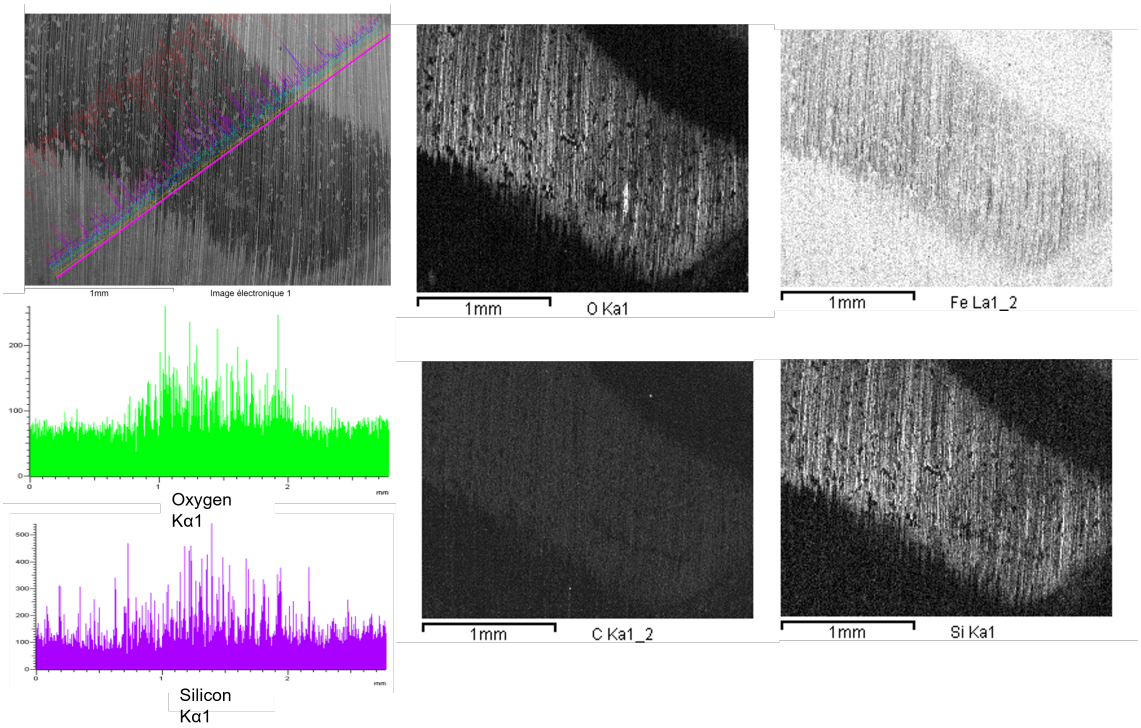


Figure 5.20 – EDS analysis of the contaminated zone on the ground surface of M2 sample.

In Figure 5.21, except for the ground surface, all other surface has an appearance of homogeneous treatment, including sandblasted surface. The microstructures of the nitriding layers with the 4 different surface conditions are shown in Figure 5.22. All samples are characterized by a compound layer. The mirror-polished surface and 1200-grade polished surface are smooth after nitriding, and the ground surface keeps a relatively rough surface after nitriding. The sandblasted surface still shows the sandblasted dents after nitriding. Cracks are generated from the compound layers during the sample preparation because of their high brittleness.

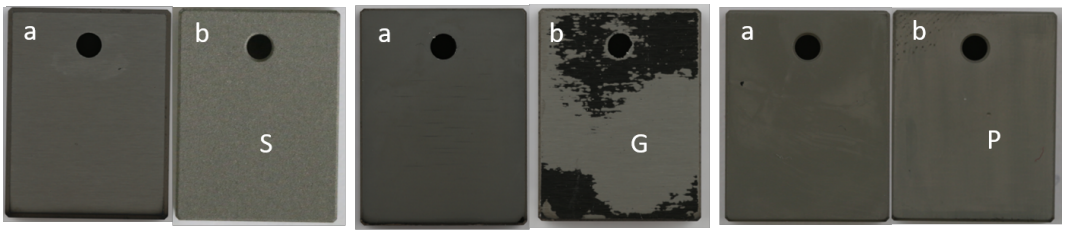


Figure 5.21 – Nitrided Surface of M2 samples with one side 1200 grade polished and another side a sandblasted, (b) ground and (c) mirror polished.

Figure 5.23 shows the mass gain during nitriding of the four samples. Each sample has one surface mechanically finished differently while other surfaces are considered undthe er same condition as other sample surfaces. The mirror-polished and 1200-grade polished samples obtain the highest mass gain, while the sandblasted surface the least, resulting in the different thicknesses of the nitriding layer (Figure 5.22). Figure 5.24 shows the hardness profiles of the nitriding layers from the 3 surfaces with different conditions. The nitriding

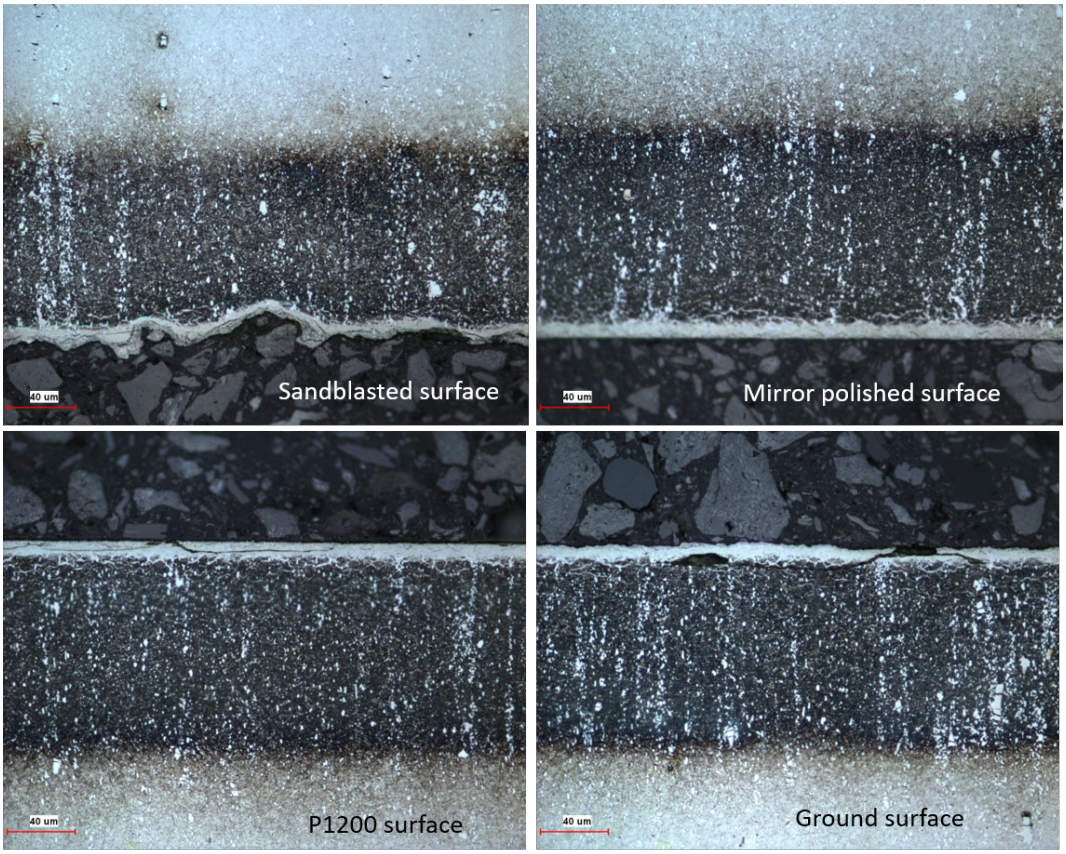


Figure 5.22 – Microstructure of the nitrided sample with the 4 different surface conditions under the optical microscope.

depth of sandblasted sample is lower, and the thickest nitriding layer is found in the polished sample. Despite the sandblasted surface allowing a homogeneous treatment, the high compressive residual stresses (Figure 5.25) generated by sandblasting are estimated to decrease the nitrogen adsorption and diffusion leading to a less profound nitriding depth [275].

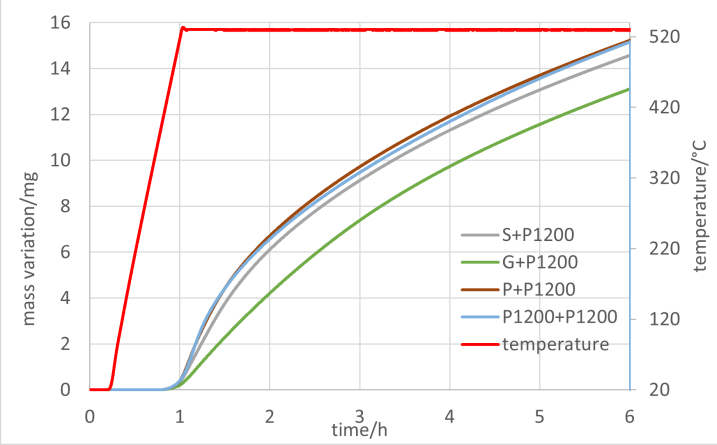


Figure 5.23 – Mass variation during nitriding of M2 sample with different surface conditions

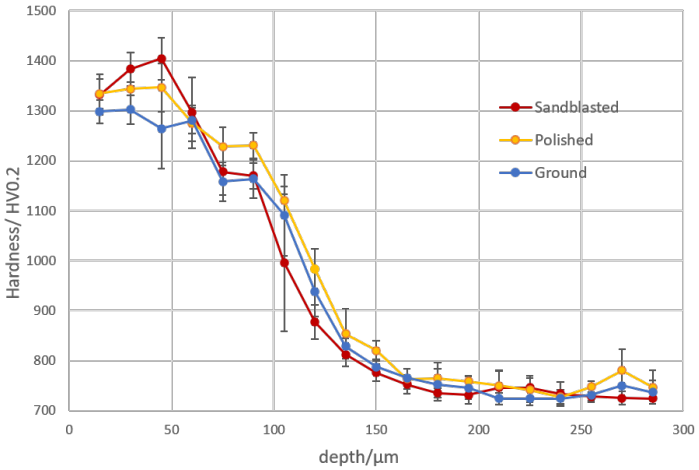


Figure 5.24 – Hardness profile from the surface to in-depth of M2 sample after nitriding with different surface conditions

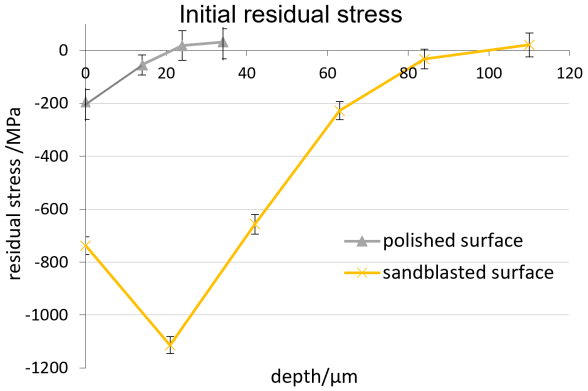


Figure 5.25 – Initial residual stresses in the ferritic matrix under the surface.

5.3 Preliminary study on gas nitriding kinetics of M2 steel and the properties of the nitriding layer

In this section, nitridings at 500 and 540 °C for 5 hours are carried out to investigate the effect of gas nitriding parameters on the kinetics. Because the tempering temperature of industrial M2 steel for cold forging is about 560 °C, temperatures higher than 540 °C will not be studied concerning the tempering (softening) effect on the core material. From this section, all the M2 samples with the ground surface will be cleaned and also polished to 1200 grade before nitriding to avoid any effect of surface preparation and contamination (see in section 5.2.1).

5.3.1 Mass variation during nitriding treatment

Figure 5.26 shows the mass increment during nitriding. The mass gain increases with a high nitriding potential or nitriding temperature. As nitriding is a diffusion-controlled process, the temperature is a key factor. A higher temperature increases the kinetics of nitrogen diffusion and nitride precipitation. Higher temperatures can promote the equilibrium of the decomposition reaction of ammonia and accelerate nitrogen adsorption at the gas-solid interface.

A higher nitriding potential indicates a higher ammonia partial pressure. It increases the nitrogen gradient from the surface to the inner material and accelerates the nitrogen to diffuse to the low concentration. In conclusion, higher temperature makes the thermochemical reaction and diffusion faster, and higher ammonia partial pressure provides more nitrogen and a higher concentration gradient.

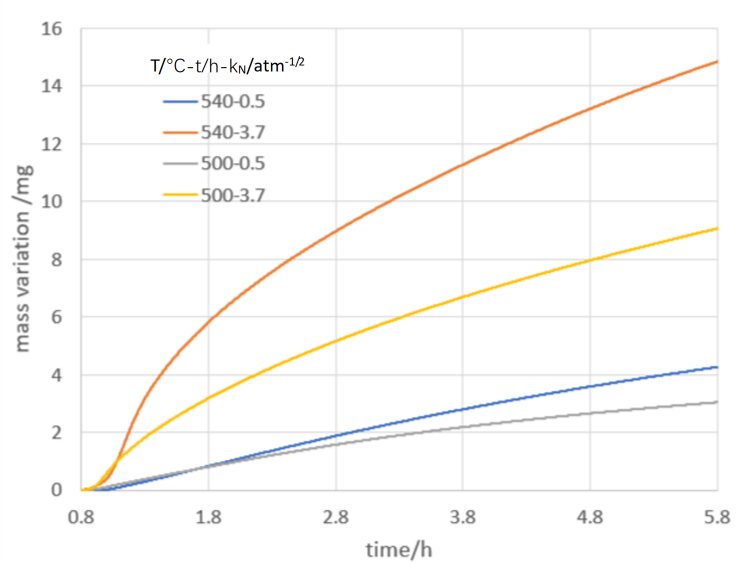


Figure 5.26 – Mass variation during nitriding at different temperatures or with different nitriding potential of M2 steel sample.

5.3.2 Microstructure of nitriding layer

The samples nitrided with nitriding potential $K_N = 3.7$ atm$^{-1/2}$ show a compound layer at both 500 and 540 °C, while no compound layer is observed with $K_N = 0.5$ atm$^{-1/2}$ (Figure 5.27). The nitriding layer of the sample nitrided with $K_N = 3.7$ atm$^{-1/2}$ (160 µm) is much thicker than that of the sample nitrided with $K_N = 0.5$ atm$^{-1/2}$ (80 µm). The hardness profile defines the effective nitriding depth, which will be detailed and explained in section 5.3.4.

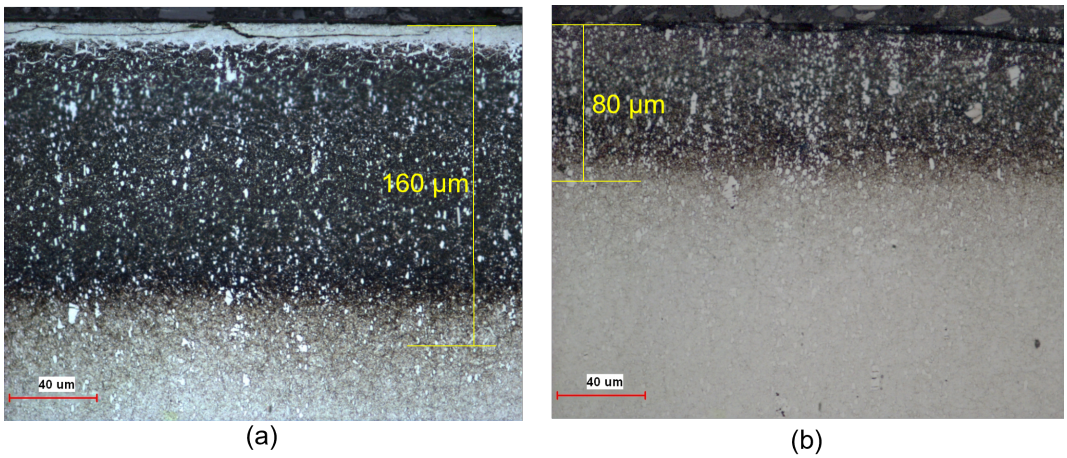


Figure 5.27 – Microstructure of nitriding layer of M2 steel samples nitrided at 540 °C for 5 h with a nitriding potential (a) $K_N = 3.7$ atm$^{-1/2}$, (b) $K_N = 0.5$ atm$^{-1/2}$.

5.3.3 The phase transformation and nitrogen concentration in M2 steel (Thermo-Calc)

Thermo-calc is used for the phase transformation analysis during nitriding. Figure 5.28 presents the phase transformation diagram of M2 steel (with carbon concentration of 0.8%) as a function of N concentration at 500 °C. As the N concentration rises, the MN-type nitrides first precipitate, as shown by the solid red line. Carbides (M_2C, MC, and M_6C types) decrease and the released carbon diffuses inward and accumulates at the nitrogen diffusion front. With the increased carbon concentration, the cementite phase starts to form.

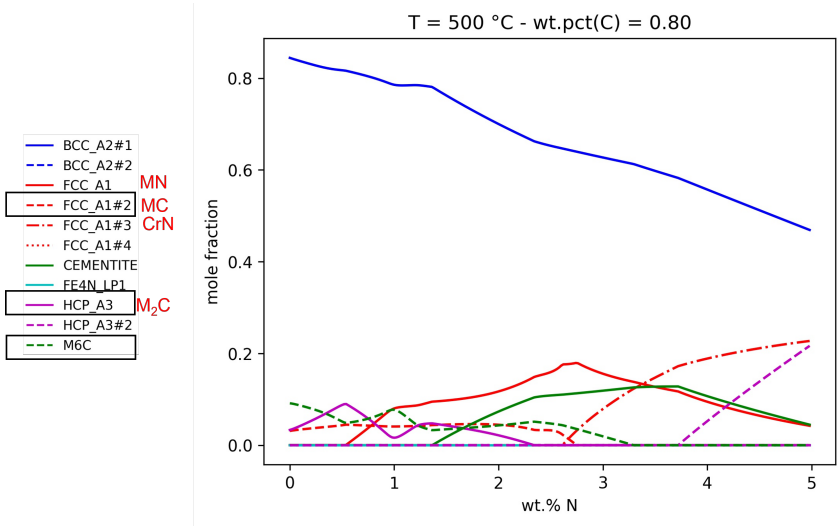


Figure 5.28 – Phase transformation diagram of M2 steel (with carbon concentration 0.8%) as a function of N concentration at 500 °C

5.3.4 Chemical and mechanical gradient in the nitriding layer

5.3.4.1 Temperature effect

Figure 5.29 shows the chemical and mechanical property profiles of the M2 samples after nitriding with $K_N = 0.5$ atm$^{-1/2}$ at temperature 500 and 540 °C. Both the nitrogen concentration and hardness reach the maximum at the surface and gradually decrease to the same level as the core. Hardening is related to the precipitation of alloying element nitrides MN (M=Cr, V, Mo...), which are finely dispersed into the ferritic matrix, and thus to the content and diffusion of nitrogen through the treated surface [97]. Lower temperature (500 °C) nitriding leads to a lower nitriding depth (Figure 5.29 (c)), corresponds to less nitrogen enrichment (see Figure 5.29 (a)).

In Figure 5.29 (a), the carbon concentration of the sample nitrided at 540 °C is lower near the surface because carbides participate in the phase transformation, and carbon has been diffused (details will be given in 5.4.5). The hardness in the core material of the sample nitrided at 540 °C is declined. Nitriding is equivalent to a tempering effect for the core material, as 540 °C is close to the tempering temperature of 560 °C. This is the reason that 540 °C will not be further studied in the future.

Residual stress generation is linked to phase transformation and the corresponding volume change. The nitrogen atoms diffuse faster with increased nitriding temperature, and the maximum residual stress occurs deeper below the surface. In Figure 5.29 (b), the

residual stress shows the highest value at the surface of the sample nitrided at 500 °C, while at about 50 µm in-depth of the sample nitrided at 540 °C. The residual stress at the surface decreases as temperature increases. This stress unloading is because of the volume decrease induced by certain decarburization and the precipitates coarsening.

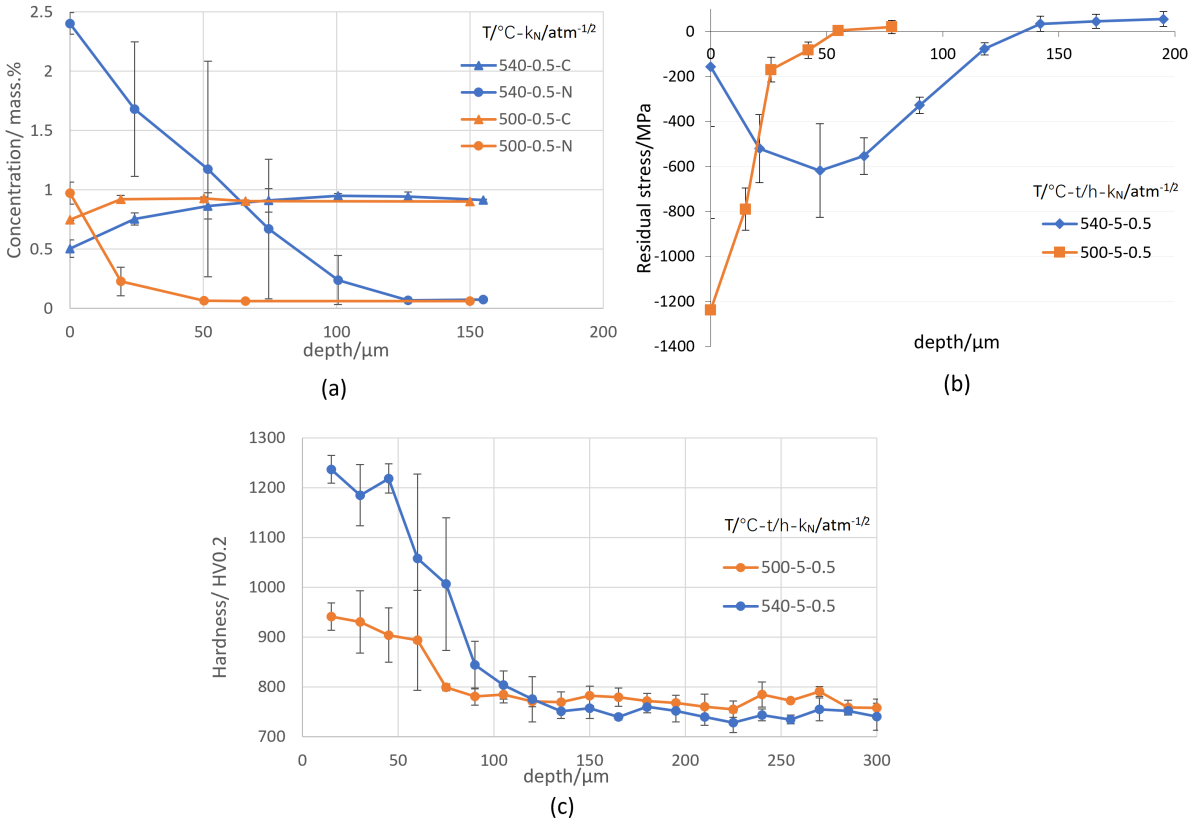


Figure 5.29 – Surface to in-depth profile of M2 steel after gas nitriding with $K_N = 0.5$ atm$^{-1/2}$ at different temperature (a) N/C profile, (b) residual stress, (c) hardness profile.

5.3.4.2 Nitriding potential effect

Nitriding potential directly affects the concentration of nitrogen in the atmosphere at the solid-gas interface (the boundary conditions for diffusion). Higher nitriding potential means more elevated ammonia partial pressure, increasing the nitrogen fraction at the surface and the nitrogen gradient.

Figure 5.30 shows the N/C profile, the hardness and residual stress profiles. Effective nitriding depth is greater when nitriding potential is 3.7 atm$^{-1/2}$, so is the depth of the maximum residual stress. They result from nitride precipitation. The nitrogen concentration is higher in the sample nitrided with K_N=3.7 atm$^{-1/2}$. The residual stress and carbon concentration are lower near the surface (see in 5.4.5). The nitrogen concentration of the sample nitrided with 3.7 atm$^{-1/2}$ exceeds the scale of the calibration of the OES device (2.05 wt.%) because of the presence of compound layer (N concentration in a compound layer is higher than 5.7 wt.%).

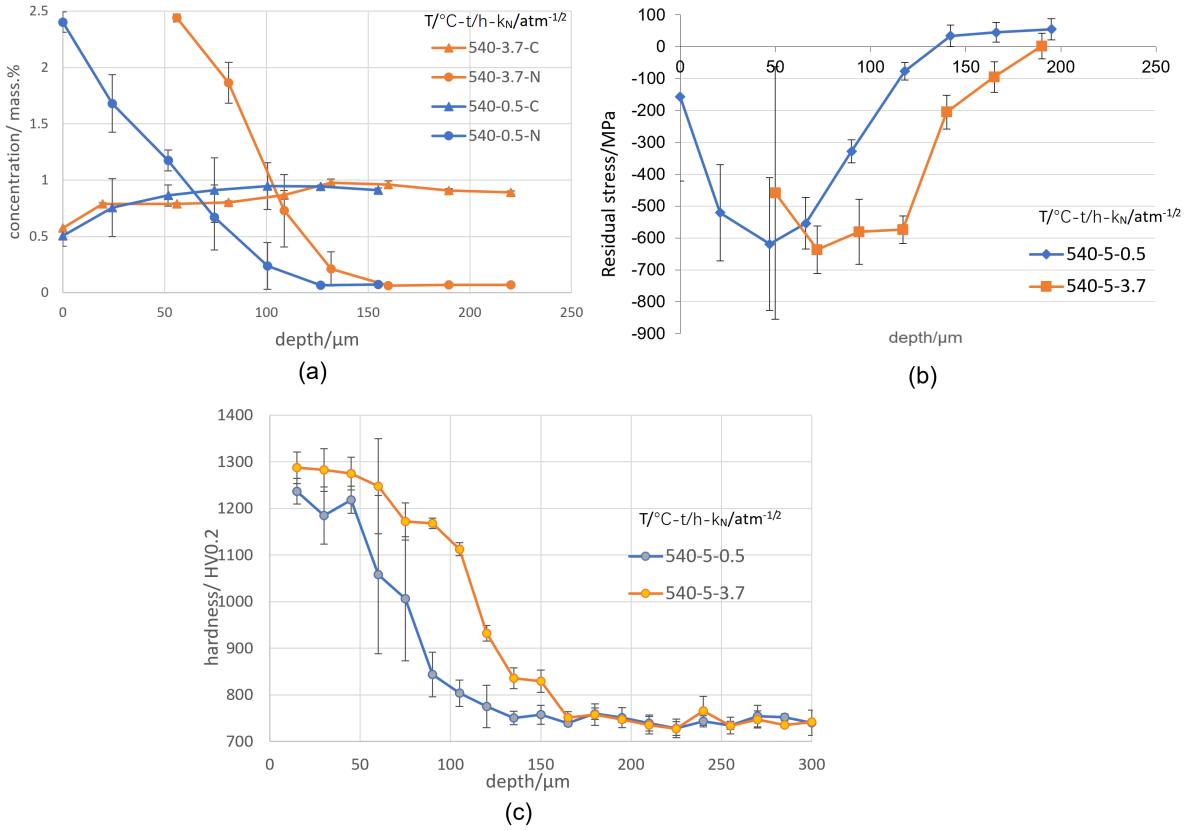


Figure 5.30 – The in-depth profile of M2 steel after gas nitriding at 540 °C with different nitriding potential (a) N/C profile, (b) residual stress, (c) hardness profile.

5.4 Pseudo Lehrer diagram study

Due to the special microstructure and the brittleness of the compound layer, it is easy for cracks or peels to be formed under high pressure. It is essential to limit the compound layer to avoid the severe problem of crack initiation from the compound layer. Finding the limit nitriding parameters for the compound layer formation is one of the objectives of the study on the nitriding kinetics of M2 steel.

5.4.1 Calculation and prediction of the nitriding potential at α/γ' limit in the pseudo-Lehrer diagram for M2 steel

In low alloyed steels, the diffusion layer is defined by the precipitation of fine alloying-element nitrides MN (M = Cr, V, Mo...) from the reaction of nitrogen with alloying elements either in the solid solution of the ferritic matrix or within the initial carbides from tempered martensite before nitriding [159, 142, 344]. The γ'-Fe_4N and ε-$Fe_{(2-3)}N$ phases can only form when nitrogen concentration in the material reaches a value that allows all alloying elements to react with saturated nitrogen in the ferritic matrix. Knowing the chemical composition of the steel, this nitrogen concentration is possible to calculate.

The high affinities of the elements Cr, and V with nitrogen allow them to react with nitrogen instantaneously, while the low affinity of Mo delays its nitride form before the nucleation of iron nitride in the binary alloy [95, 93, 94, 96]. 33CrMoV12-9 grade material is a widely studied nitriding steel grade at the MSMP laboratory. The nitride-forming alloying elements are considered mainly Cr and V with an average mass fraction of 3, and

0.2 wt.% according to the standard. 0.1 wt.% N is needed to fill all the interstitial spaces in the iron matrix. Assuming all nitrides are MN type with atom ratio M:N = 1:1, when all alloys participate in the nitride precipitation, the nitrogen concentration reaches 0.86 wt.%. Thus, the enrichment of nitrogen in the material reaches 0.96 wt.% [159]. A recent study at MSMP laboratory of gaseous nitriding kinetics of 33CrMoV12-9 steel found the limit nitriding potential for the limit of compound layer formation in the 33CrMoV12-9 steel is 0.33 $atm^{-1/2}$ at 550 °C [159]. The same value of nitrogen concentration can be calculated for M2 steel as the weight percentages of Cr, and V are 4 and 2 wt.%, respectively. 1.72 wt.% nitrogen is obtained to allow the alloy nitrides to precipitate completely (the 0.1 wt.% N in the matrix is considered). An assumption is made in this calculation, W is not considered due to a lack of information on its infinity with nitrogen and the high stability of W carbides [345, 102].

Nitrogen activity is another way to express nitriding potential, they are proportional. With the assumption that the decomposition rate of ammonia at the surface of the steels is the same for 33CrMoV12-9 steel and M2 steel, the same ratio between the maximum nitrogen concentration at the material surface and the nitriding potential of the gas atmosphere is then can be deducted for M2 steel. The nitriding potential for the compound layer limit for M2 steel then can be estimated close to 0.59 $atm^{-1/2}$ at 550 °C. However, the temperature in this work will not exceed 540 °C. According to the Lehrer diagram for pure iron, the nitriding potential on α/γ' limit could increase at a lower temperature. With this assumption, the nitriding potential starts to be investigated from 1 $atm^{-1/2}$ at 500 °C and 520 °C .

5.4.2 Mechanical surface treatment effect on nitriding

The compound layer is not observed under the optical microscopy at the front surface (Figure 5.31) after nitriding at 500 °C with K_N = 1 $atm^{-1/2}$ for 5 hours. However, a compound layer appears on the side surfaces (Figure 5.32). On the front surface, a thin compound layer of about 0.5 µm is only found under SEM at a small zone, as shown in Figure 5.33. This is because the surfaces are applied to different mechanical processes before nitriding, the front surfaces are milled and then ground before being received, and the side surfaces are machined. The plastic deformation and residual stress induced by machining accelerate the adsorption kinetics of nitrogen at the surface compared to the ground surface [346, 114, 275]. However, the condition of the front surface is closer to the reality of the rolling die (finishing with grinding before nitriding), and will be taken into account only. The compound layer is not found on the front surface under the optical microscopy until the nitriding potential is increased to 1.2 $atm^{-1/2}$ for 5 hours nitridings at 500 °C. Figure 5.34 shows the surface and the corresponding microstructure of the M2 sample. A new phase is visibly and discontinuously formed on the surface. Under SEM, small precipitates are observed on the surface, and they prefer to precipitate along the tracks left from polishing (1200 grade). From Figure 5.34 (a) to (d), the density of the precipitates decreases to nearly 0. EDS analysis demonstrates that the new phase contains more nitrogen (see in Figure 5.35).

A compound layer is formed after nitriding at 500 °C with K_N = 1.2 $atm^{-1/2}$ for 5 hours. This discontinuity is related to the mechanical condition before nitriding. If the nitriding time increase, a continuous compound layer will be formed. This phenomenon is also observed for the nitriding potential 1 $atm^{-1/2}$.

Under optical microscopy, the cross-section along the blue line of the sample shows a white layer (the compound layer) with a thickness of about 0.5 µm at the surface. The

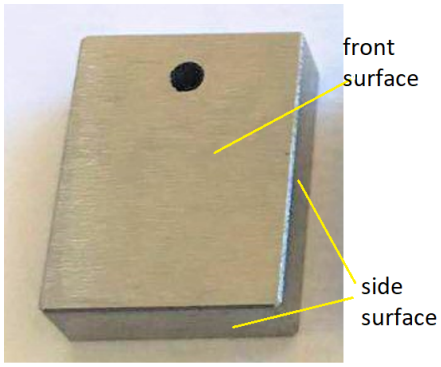


Figure 5.31 – The definitions of the surfaces of the sample.

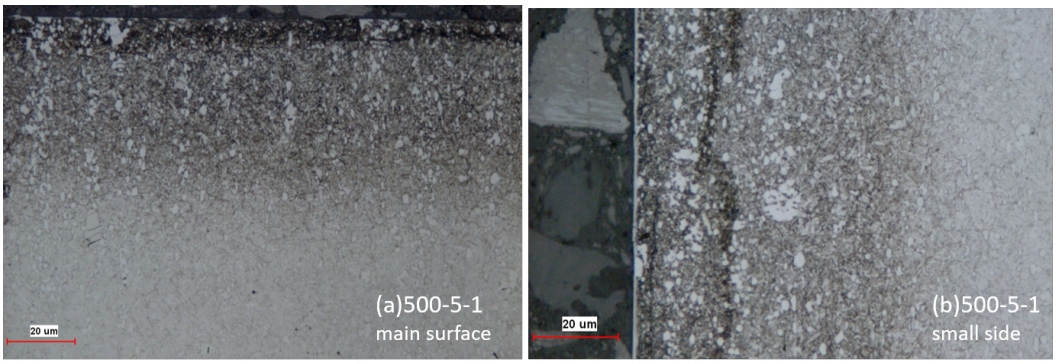


Figure 5.32 – Microstructure of the cross-section of the M2 sample after nitriding at 500 °C with $K_N = 1$ atm$^{-1/2}$ for 5 hours (a) from the main front surface, (b) from the small side surface.

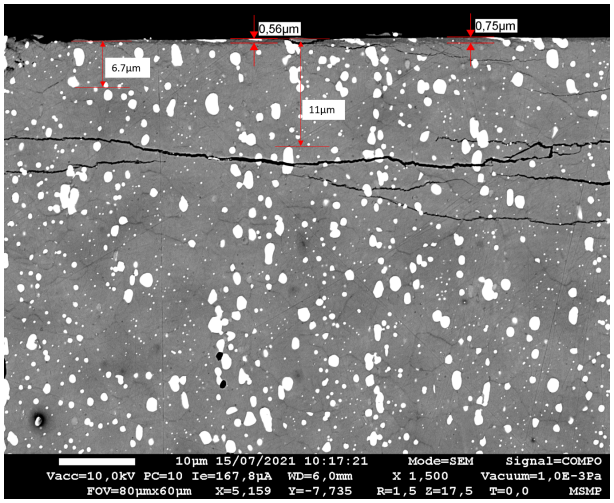


Figure 5.33 – Microstructure of the nitriding layer in M2 steel sample nitrided at 500 °C with $K_N = 1$ atm$^{-1/2}$ for 5 hours.

same phenomenon is observed on the front surface on the opposite side. On both front surfaces, the border where the polishing starts (the SiC disk rotates under the material from this border) has more precipitates. Figure 5.36 shows the surface topological non-homogeneity caused by polishing. The red arrow shows the polishing direction. The micrographs in Figure 5.36 (b) and (c) show deeper tracks at position A than B. Under optical microscopy, the precipitates in Figure 5.34 are present as black dots.

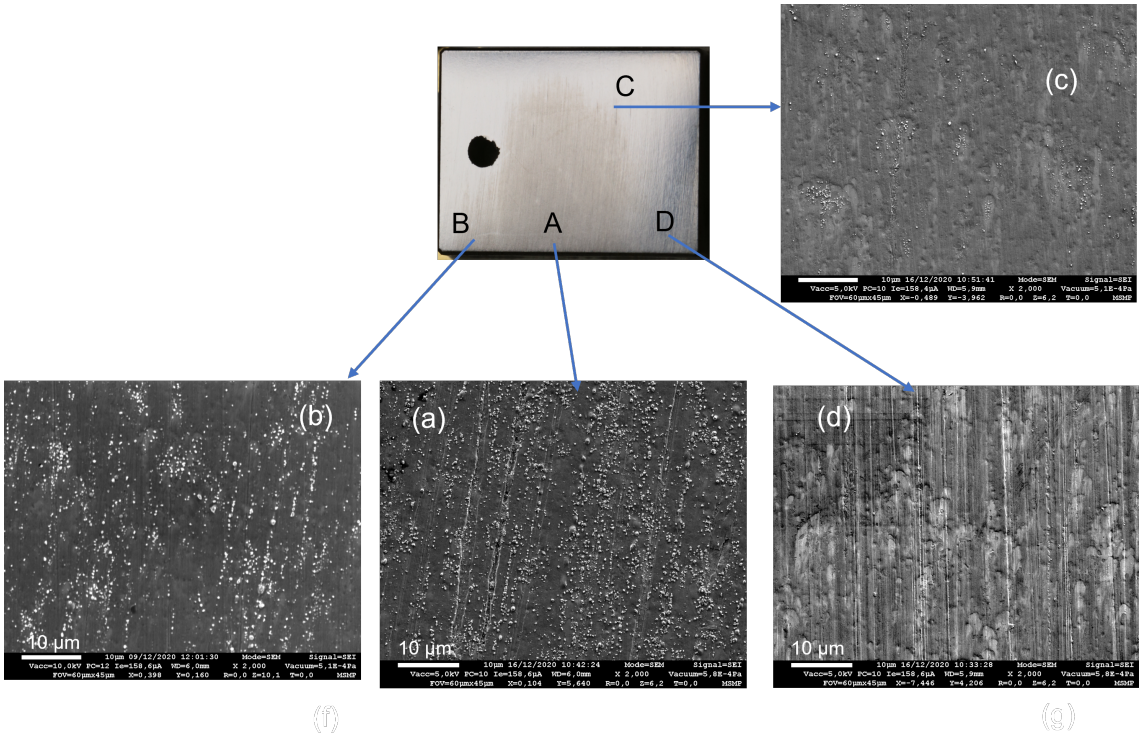


Figure 5.34 – Surface microstructure of the M2 sample after nitriding at 500 °C with $K_N = 1.2$ $atm^{-1/2}$ for 5 hours.

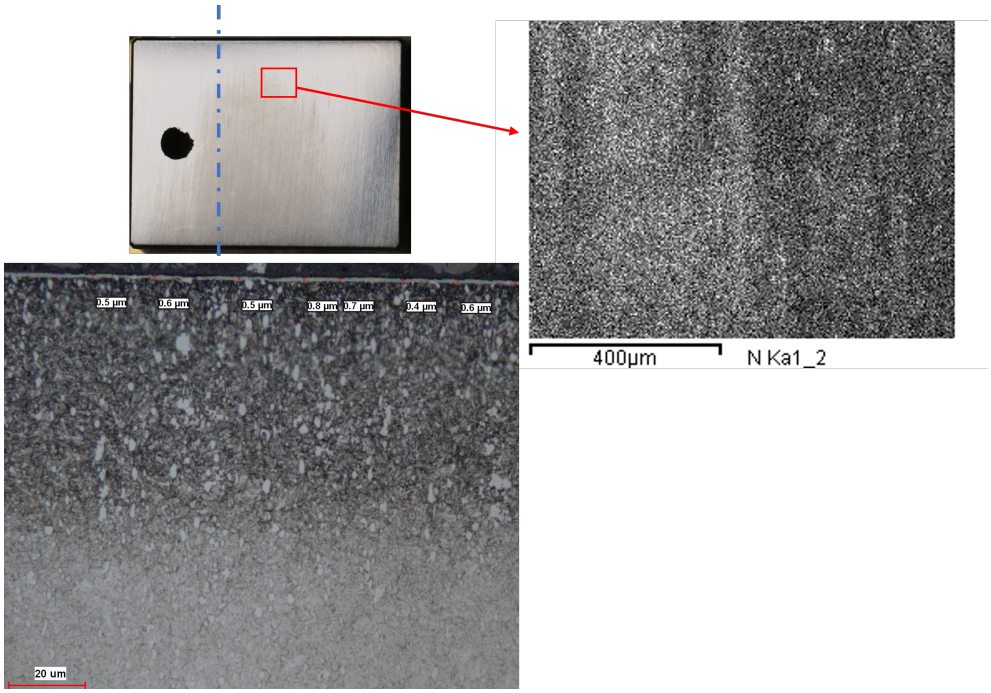


Figure 5.35 – Surface microstructure and EDS analysis of the M2 sample after nitriding at 500 °C with $K_N = 1.2$ $atm^{-1/2}$ for 5 hours.

The surface roughness of the M2 sample before nitriding is measured along and transverse to the polishing direction. The roughness values Ra are marked on the corresponding location, as shown in Figure 5.37. The roughness in the transversal direction is generally higher than that along the polishing path. A coherent relation is found between the rough-

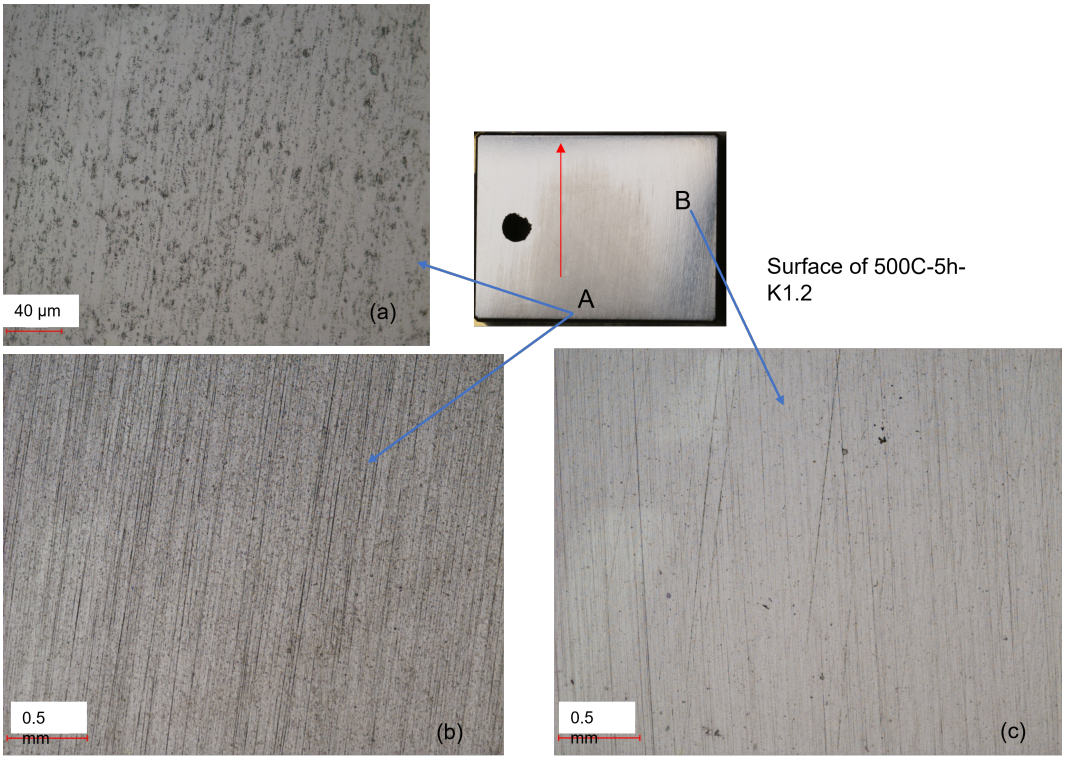


Figure 5.36 – Optical micrograph of the M2 sample surface after nitriding at 500 °C with K_N = 1.2 $atm^{-1/2}$ for 5 hours. The red arrow marks the polishing direction.

ness of the transversal direction and the density of the precipitates on the surface. For example, the area covered with compound layer color (or new precipitates) shows a roughness above 0.33 µm, and the maximum roughness of 0.55 µm corresponds to the highest density of the precipitates (Figure 5.34 (a)).

Figure 5.38 shows the roughness profiles of all the measurements transversal to the polishing direction. The depth of the track caused by polishing or the previous grinding is also found to be coherent with the roughness and precipitate density. The compound layer is formed when the track depth exceeds 0.6 µm. However, it must also be related to the number of deep tracks.

These non-uniformities are assumed to be related to the nonuniform pressure on the sample during manually polishing, and the surface condition affects the kinetics of nitriding for short-time nitriding. However, it is not certain whether the roughness itself or the different residual stress and plastic deformation induced by the non-uniform roughness affect the precipitation.

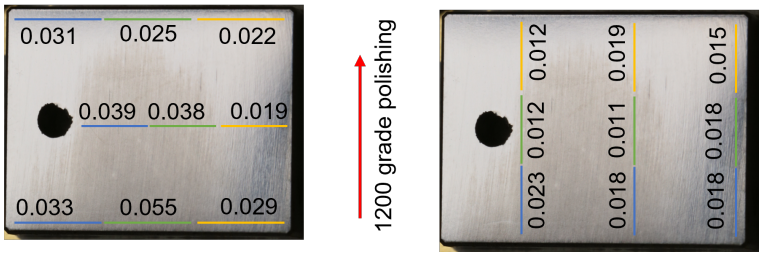


Figure 5.37 – The surface roughness on the M2 sample before nitriding (µm).

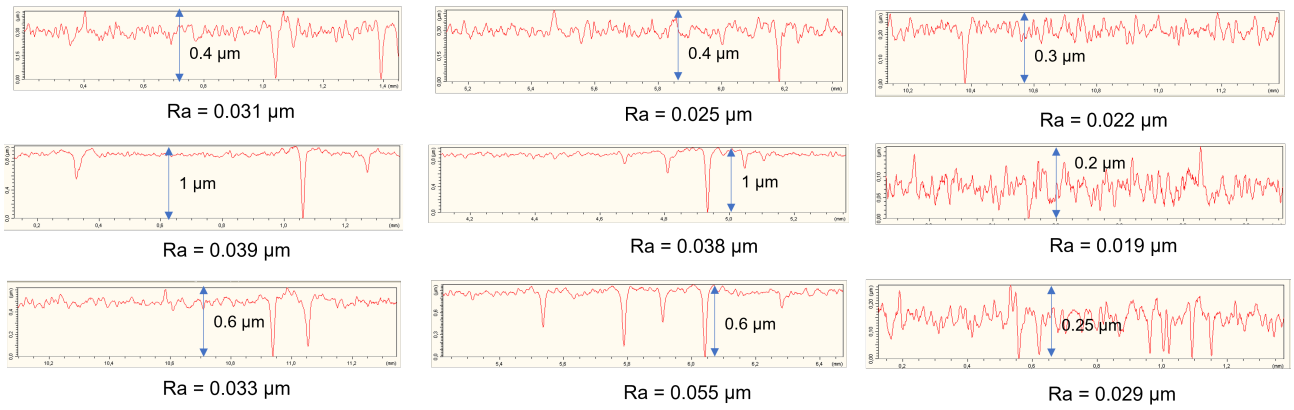


Figure 5.38 – The roughness profiles on the M2 sample surface in the direction transversal to the polishing path.

5.4.3 Experimental study on α/γ' limit in pseudo-Lehrer diagram for M2 steel

As given from the experimental results in section 5.4, a discontinuous compound layer is formed on the main front surface after the nitriding at 500 °C with $K_N = 1.2$ atm$^{-1/2}$ for 5 hours, and a full compound layer on the small side surface after nitriding at 500 °C with $K_N = 1$ atm$^{-1/2}$ for 5 hours. The nitriding potential corresponds to the α/γ' limit at 500 °C in the pseudo-Lehrer diagram for M2 steel should be lower. In nitriding, the first new phase γ' can only occur when nitrogen concentration on the surface surpasses the value compatible with the α/γ' equilibrium. Before that, it is the incubation time for iron nitride formation. To make sure if a complete compound layer could form at these parameters, longer time nitridings are performed. After both 10 and 15 hours nitriding with $K_N = 1$ atm$^{-1/2}$, compound layer is observed, the incubation time of compound layer formation at 500 °C with $K_N = 1$ atm$^{-1/2}$ for the main surface of the M2 sample is between 5 hours and 10 hours.

After a series of nitriding treatments, as shown in table 5.3, the α/γ' limits in the pseudo-Lehrer diagram for M2 steel at 500 and 520 °C are found. The compound layer normally consists of γ' and ε phases. Assuming the pseudo-Lehrer diagram for M2 steel might have a similar curve tendency as that for iron, the purpose is to define two points on the curve of the α/γ' limit. Figure 5.39 shows all the nitriding potentials applied. The nitriding time is between 5 and 15 hours. Longer nitriding treatments are performed when no compound layer is formed after 5 hours of treatment to avoid the error considering the incubation time.

In Figure 5.39, the orange dots stand for the nitriding where a compound layer presents, and the blue dots represent the nitriding in which no compound layer is formed. Figure 5.39 (b) shows the closest points which allows to define a approximate limit of α/γ'. They are nitriding potentials between 0.8 and 0.9 atm$^{-1/2}$ at 500 °C, and between 0.5 and 0.6 atm$^{-1/2}$ at 520 °C. A few treatments are carried out at 540 °C only for 5 hours, it is then not certain if the compound layer will form when the nitriding is longer. The nitriding potentials for compound layer limits are compatible with the value found in the calculation, which is 0.59 atm$^{-1/2}$ at 550 °C (see in 5.4.1).

Compared to the α/γ' limit in the Lehrer diagram for pure iron, the limit shifts to the higher N concentration in M2 steel due to the existence of alloying elements, as shown by the red line in Figure 5.40.

Table 5.3 – Parameters studied and the corresponding compound layer (CL) conditions.

Nitriding time t/h	**Temperature /°C**	**Nitriding potential** $/\mathrm{atm}^{-1/2}$	**Thickness of CL /μm**
5	500	0.5	no
5	500	0.8	no
5	500	0.9	0.5
5	500	1	0.7
5	500	1.2	1
5	500	3.7	5
5	520	0.7	0.3
5	520	0.8	0.7
5	520	0.9	1
5	520	1	1.5
5	540	3.7	11
5	540	0.5	no
10	500	1	1.7
15	500	0.8	1
15	500	0.5	no
15	500	1	1.5
15	520	0.5	no
15	520	0.6	no

5.4.4 Mass variation during nitriding

During nitriding, nitrogen atoms diffuse into the material, and the mass of the sample increases due to the enrichment of nitrogen (the mass gain). The nitrided samples have the same dimensions and surface area. Figure 5.41 (a) shows the mass variation during nitriding at 500 °C with different nitriding potential. As nitriding potential increases, the mass gain increases. However, the mass gain increases from $K_N = 0.5$ $\mathrm{atm}^{-1/2}$ to $K_N = 0.8$ $\mathrm{atm}^{-1/2}$ less significantly than that from $K_N = 0.8$ $\mathrm{atm}^{-1/2}$ to $K_N = 1$ $\mathrm{atm}^{-1/2}$. This is because that there is no compound layer formed for both $K_N = 0.8$ $\mathrm{atm}^{-1/2}$ and $K_N = 0.5$ $\mathrm{atm}^{-1/2}$, the increased nitrogen is only for the growth of diffusion zone, while a compound layer is formed when $K_N = 1$ $\mathrm{atm}^{-1/2}$. In the compound layer, the nitrogen concentration (5.7% in γ' phase and more than 6% in ε phase) is higher than in the diffusion zone. Even a little compound layer growth could require as much nitrogen as a large extension of the diffusion zone.

In Figure 5.41 (b), the temperature effect on mass gain during nitriding is presented. Higher temperature accelerates ammonia decomposition and nitrogen diffusion, so the mass gain is more remarkable. In addition, the two nitridings with 1 $\mathrm{atm}^{-1/2}$ generate a compound layer that allows more significant nitrogen adsorption. Figure 5.41 (b) also shows the double effect of nitriding potential and temperature. When the nitriding potential decrease from 1 $\mathrm{atm}^{-1/2}$ to 0.8 $\mathrm{atm}^{-1/2}$, the impact on mass variation is less important than that when decrease the temperature from 520 °C to 500 °C.

The total mass gain can be plotted in another form as a function of different nitriding parameters, as shown in Figure 5.42. Mass gain increases as temperature and nitriding potential increase. The relation between the mass variation and the square root of nitriding time (in second) is linear (Figure 5.42 (c)), and the slope ratio is 0.849. With the decarburization near the surface, the mass variation might not represent the mass gain from nitrogen only, but also the lost carbon (mass gain concerns the total mass change, including the carbon and nitrogen in the steel).

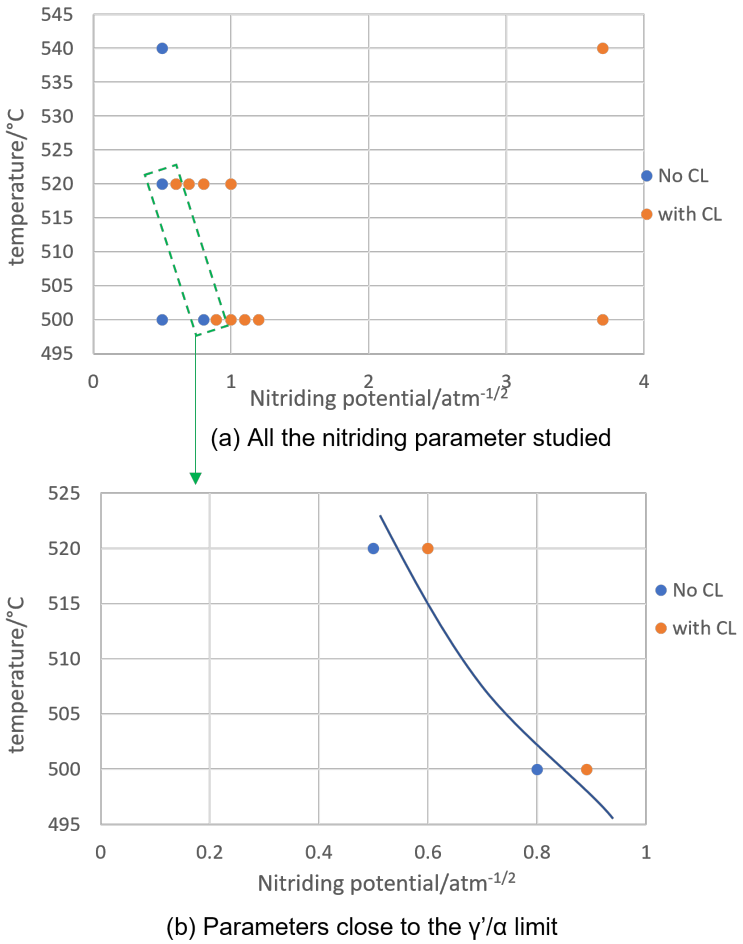


Figure 5.39 – Nitriding parameters studied and the definition of the α/γ' limit for M2 steel (CL: compound layer).

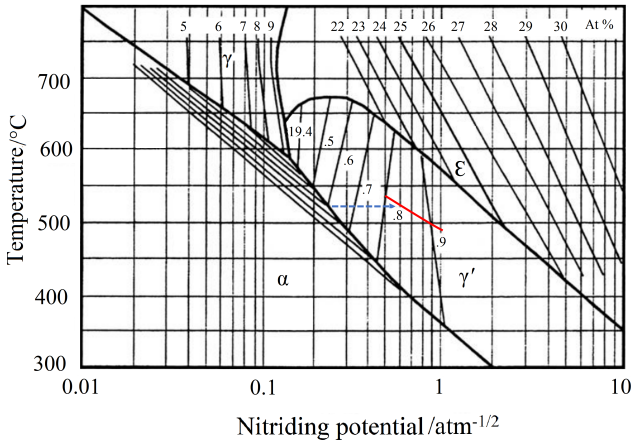


Figure 5.40 – Comparison of the α/γ' limit in the Lehrer diagram for pure iron and M2 steel.

5.4.5 Gas nitriding kinetics in M2 steel-Nitriding time effect

5.4.5.1 Microstructure of nitriding layer

Figure 5.43 shows the microstructure of the nitriding layer in M2 steel sample nitrided at 500 °C with $K_N = 1$ atm$^{-1/2}$ for 10 hours. A compound layer of about 1.5 μm is

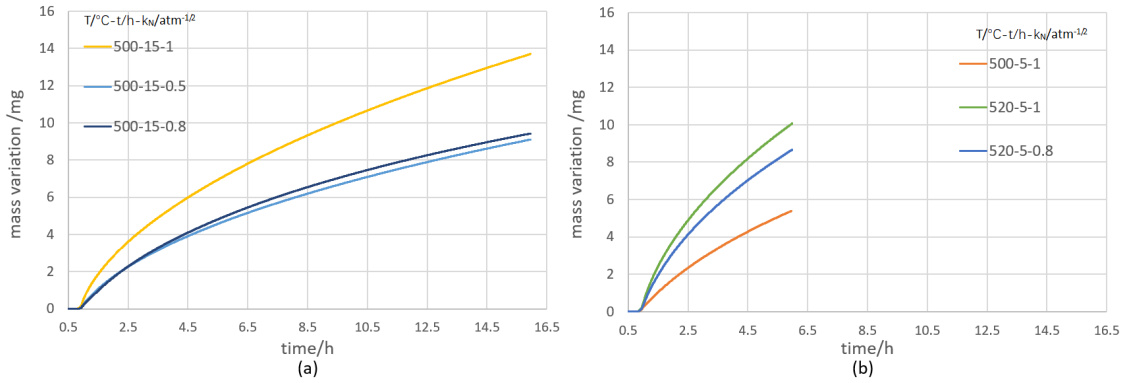


Figure 5.41 – Mass variation during nitriding with different parameters as a function of time.

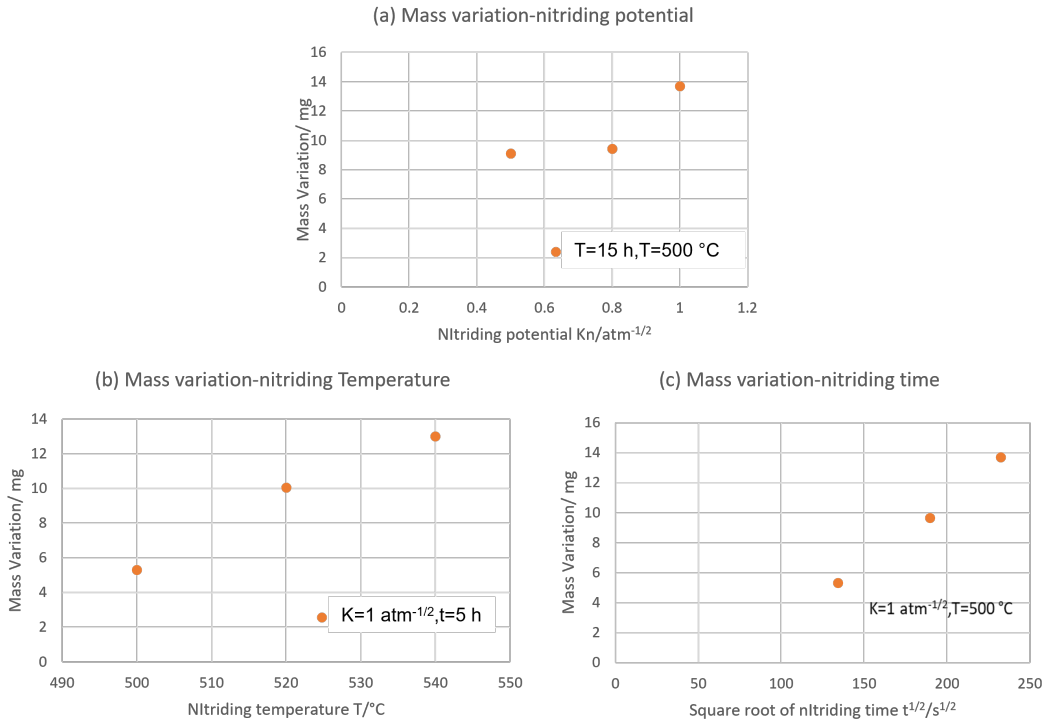


Figure 5.42 – Mass variation during nitriding as a function of different nitriding parameters.

formed. The nitride precipitates and cementite at the grain boundaries are observed at grain boundaries nearly parallel to the nitrided surface. The grain boundaries close to the compound layer could compose of iron nitrides depending on the nitriding conditions. In Figure 5.43, the darker phase at the grain boundaries closer to the surface is iron nitrides (same phase as in the compound layer), while the grey color phase at the grain boundaries in deeper depth is cementite. Between them, the mixture of these two phases co-exists at the grain boundaries [159]. Under back-scattered electron mode, the cementite presents a grey color due to the high concentration of carbon, and iron nitrides are darker grey, the same as the compound layer. Hence, by working with the contrast, the two phases can be distinguished [159]. Due to the low volume fraction of precipitates, X-ray analysis cannot be performed to identify the nature of iron nitrides at grain boundaries. However, the higher carbon concentration can be found at the grain boundary with EDS analysis (Figure 5.44). The presence of γ' nitrides at grain boundaries at the interface between the

compound layer and the diffusion zone was confirmed by Jegou et al.[97, 159].

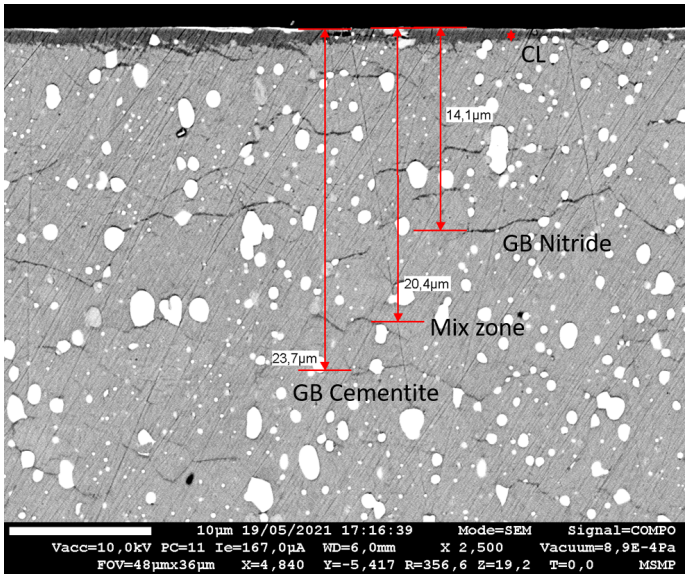


Figure 5.43 – Microstructure of the nitriding layer in M2 steel sample nitrided at 500 °C with $K_N = 1$ atm$^{-1/2}$ for 10 hours.

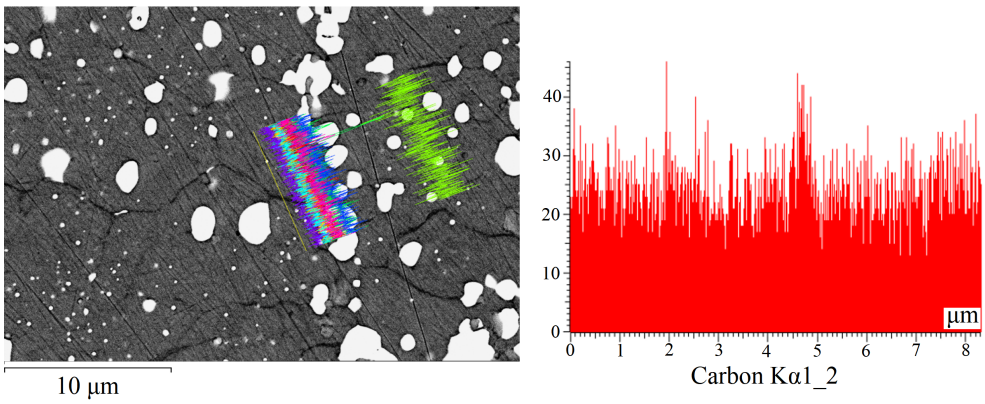


Figure 5.44 – Grain boundary cementite in nitrided M2 steel.

During the nitriding treatment, when the carbides turn into nitrides at a certain depth. The released carbon will diffuse both to the depth under the driving force of nitrogen flow and to the surface. Cementite forms at the grain boundaries as the carbon diffuses to the surface (there are no free alloying elements left in the solid solution). When the nitrogen concentration reaches a higher value that allows iron nitrides to form (close to the compound layer), the cementite at the grain boundaries transforms into iron nitrides [159].

The evolution of carbides involved in nitrogen diffusion can be summarized as four mechanisms [36, 97],

— transformation of initial carbides into nitrides that release carbon in ferrite and are free to diffuse,

— carbon diffusion at grain boundary to precipitate as cementite,

— carbon diffusion at the surface due to carbon activity imposed by the gas atmosphere (hydrogen),

— carbon diffusion at the nitrogen diffusion front due to the lower chemical potential when no nitrogen is present.

Other samples are observed under SEM back-scattered electron mode with the same method. The depths of the deepest grain boundary nitrides (GB nitride) and grain boundary cementite (GB cementite) closest to the surface are measured. According to the diffusion and precipitation kinetics, the layer depths as a function of the square root of nitriding time are plotted. In Figure 5.45, the four colors correspond to compound layer depth, grain boundary nitride depth, grain boundary cementite depth (closest to the surface), and the effective nitriding depth. These curves fit linear functions with different ratios, and the compound layer shows the lowest ratio. Cementite starts to form at the nitrogen diffusion front after the nitrogen concentration exceeds the solubility in iron and all the alloying elements in the solid solution precipitate as nitrides. The hardness depth corresponds to the diffusion depth of nitrogen, and the slope of the corresponding curve is 0.8853, which is close to that of the mass gain to the square root of the time function in 5.4.4.

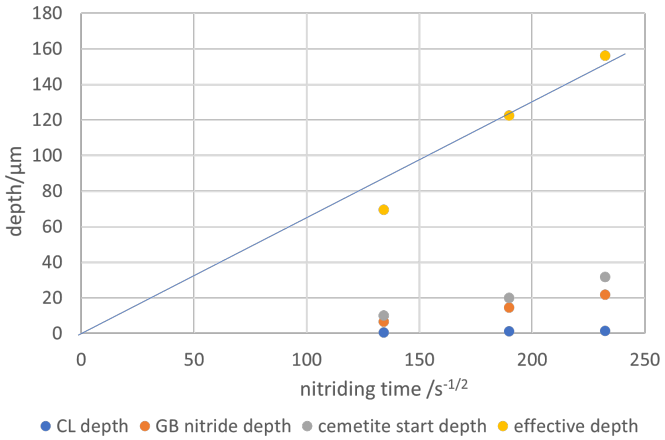


Figure 5.45 – Layer depth as function of the square root of nitriding time (T=500 °C, K_N = 1 $atm^{-1/2}$).

5.4.5.2 N/C profile

Figure 5.46 shows the chemical profile of nitrogen and carbon from the surface to in-depth of the three samples nitrided for 5, 10 and 15 hour, respectively (500 °C, K_N = 1 $atm^{-1/2}$). At the surface, with the presence of the compound layer, the nitrogen concentration should be equal to the N concentration in iron nitride. However, the scale of the characterization method for nitrogen is 2.05 wt.%, it is impossible to give a precise value for a higher concentration. The maximum nitrogen concentration in the diffusion zone presents at the interface of the compound layer and the diffusion zone. As the nitriding time increases, nitrogen diffuses to a greater depth. The carbon released from carbides accumulates at the nitrogen diffusion front, which is demonstrated by the plateau in the carbon concentration curve. The plateau span is about 100 µm. Together with Figure 5.45, high nitrogen concentrations are found at the depth where GB nitrides and the onset of GB cementite are measured. Longer nitriding achieves lower carbon concentration at the surface. The carbon curve for the sample nitrided for 15 hours shows a lower carbon concentration at the surface than that in the other samples nitrided for shorter times.

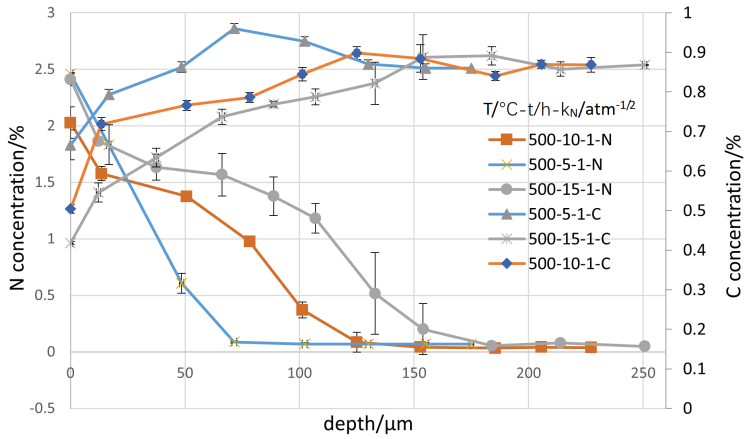


Figure 5.46 – N and C concentration profile as function of nitriding depth (T=500 °C, K_N = 1 $atm^{-1/2}$).

5.4.5.3 Hardness profile

Figure 5.47 shows the hardness profile of these three samples, of which the N/C profiles have been analyzed. The effective nitriding depth increases as the nitriding time increases, but no strong difference in the maximum hardnesses is observed at the surface. The increment in hardness involves the precipitation of alloying element nitrides in the nitriding layer, especially in the diffusion zone. It is limited by the alloying element concentration in the steel. Nitrogen diffuses deeper in a longer nitriding time, consequently, the hardening depth is greater. Nevertheless, the maximum hardness increment keeps stable despite the different nitriding parameters once the compound layer is formed, which is limited by the alloy element concentration.

The effective nitriding depth is linear to the square root of nitriding time (Figure 5.45). According to the relation in 2.4.3, the diffusivity is assumed independent from the concentration as a function of the depth. Linest fitting is applied (Figure 5.45), and the effective nitrogen diffusion coefficient in α iron at 500 °C is found, and that is $D_N^{\alpha-Fe} = 1.02 \times 10^{-13} m^2/s$. This value is very close to the diffusion coefficient calculated using the equation $D = 1.9 \times 10^{-9} \exp(-62828/RT)$ from the literature [67] ($1.08 \times 10^{-13} m^2/s$).

This calculation is correct at $K_N = 1\ atm^{-1/2}$ or when a compound layer forms. With a lower nitriding potential that does not allow a compound layer to form, the boundary condition changes (the nitrogen concentration at the interface of the solid/gas is lower than that of the diffusion zone/compound layer), this method must be applied with precautions. Under a less important concentration gradient, diffusion is slower. However, it does not change the diffusivity of nitrogen.

5.4.5.4 Residual stress profile

During nitriding, the development of compressive residual stress is dominated by phase transformation. The sample is heated and cooled with a rate of 10 °C/min, the effect of thermal expansion is assumed to be negligible.

Figure 5.48 shows the in-depth residual stress profiles measured with X-ray diffraction. Compressive residual stress profiles are characterized, which involve positive volumetric eigenstrains along with the precipitation of alloying elements nitrides within the ferritic matrix. MN nitrides (M=Cr, V...) are characterized by a higher specific volume than

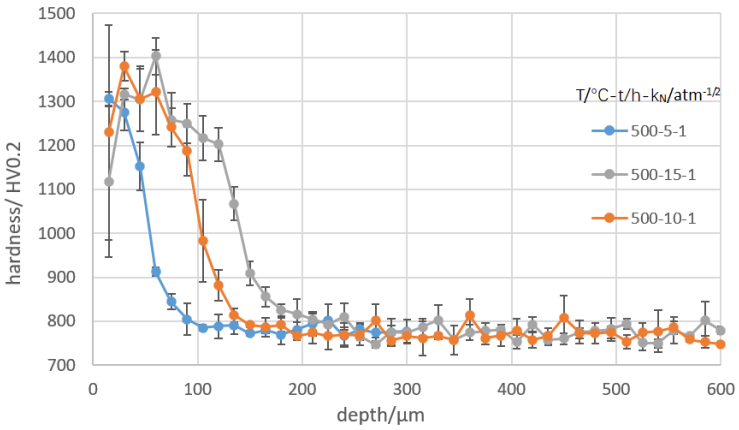


Figure 5.47 – Hardness profile as function of nitriding depth (T=500 °C, K_N = 1 $atm^{-1/2}$).

the ferritic matrix (10.7 and 7.1 cm^3mol^{-1} respectively) [159, 97, 113]. The volumetric expansion varies depending on the fraction ratio of nitrogen that reacts with alloying elements initially in the ferritic solid solution and carbides.

In Figure 5.48, the maximum compressive residual stress is less important and occurs at a greater depth when nitriding for 15 hours compared to 5 hours. The compressive residual stress near the surface decreases and can even become in tension. During the earlier period of nitriding, the nitride precipitation from the solid solution and the carbides transformation induce volume expansion, and the elastic strain leads to compressive residual stress. Compared with Figure 5.46, the maximum residual stress locates at the end of the carbon plateau (the end at lower depth). This means that the maximum residual stress occurs after the carbon accumulation and starts to reduce to a value lower than that in the core. At the depth where the residual stresses reach the maximum value (if not the surface), all the alloying elements transform into alloying element nitrides. The transformation of initial carbides into nitrides decreases the kinetics of nitriding and is counteracted by the precipitation of cementite.

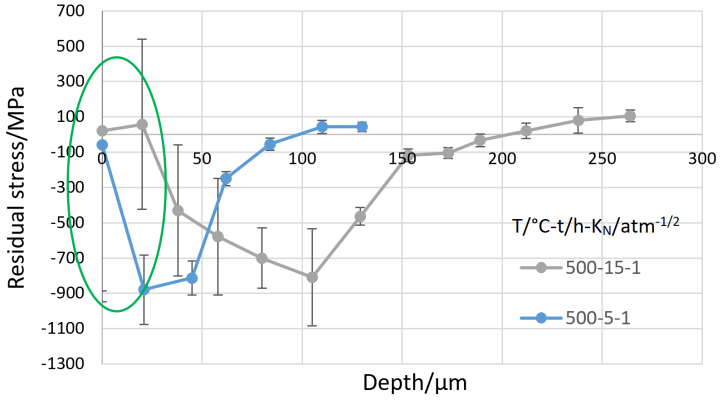


Figure 5.48 – Residual stress profile of the M2 sample nitrided for 5 and 15 hours (T=500 °C, K_N = 1 $atm^{-1/2}$).

During nitriding, the evolution of nitrides and carbides can be summarized in 4 steps [64, 159, 97] as shown below, which can take place at the same time in different depths.

— Precipitation of MN type nitrides: at the beginning of the treatment, fine semi-coherent MN nitrides precipitate from solid solution due to its high nitrogen affinity.

This realizes the first phase transformation and generates the first compressive residual stress.

— Initial carbides transformed into incoherent nitrides due to their relatively high thermal stability. In other words, the enthalpy heat of forming nitrides is lower than forming corresponding carbides. These nitrides keep the original site of the carbide and are incoherent with the matrix. This step results in less volume change due to a lower specific volume difference.

— The released carbon from transformation accumulates at the diffusion front and reacts with alloying elements to form carbides first and then transform to incoherent nitrides, decreasing the quantity of semi-coherent nitrides and less volume expansion.

— The transformation from cementite to iron nitrides leads to decarburization close to the surface, which decreases the elastic loading induced by the former phase transformations during nitriding.

These steps lead to different volume changes. Figure 5.49 illustrates the difference between the N/C and residual stress evolutions at the surface and in-depth of the steel. At the surface, the initial carbides participate in the phase transformation, and carbon diffuses to in-depth, but no carbon accumulation could occur. That's the most important reason that the carbon concentration at the surface is lower than in-depth. But the compressive residual stress increases until the maximum because the nitrides increase along with the nitrogen concentration. It starts to decrease because of the continued carbon loss due to decarburization while nitrogen reaches its limit. At a depth, the carbon arrives before nitrogen, more alloy elements form carbides first before transforming to nitrides, leading to a decrease in the fraction of the nitrides that directly precipitate from the solid solution (fewer alloying elements join the first type of phase transformation). The maximum volume expansion is then less significant. When the maximum compressive residual stress occurs in the deeper material, the value is generally less important than those close to the surface. The carbon concentration is higher than that at the surface, which provides a gradient for carbon to diffuse to the surface and form cementite. At the surface, decarburization involves a decrease in the volume fraction of cementite during nitriding. This results in unloading at the surface and, thus, a reduction of compressive residual stresses. The reduction is more significant near the surface of the sample nitrided for 15 hours, which is in agreement with the lower carbon concentration near the surface (Figure 5.46).

Another reason responsible for the decrease of residual stress is the precipitate coarsening. After the maximum residual stress is reached, similar to the aging time effect on the precipitates sizes, continuing nitriding leads that the coherent, semi-coherent nitrides being replaced by incoherent and relatively larger nitrides, leading to the redistribution of residual stress [117]. This means these steps occurred in different proportions in the two samples.

The standard deviation of residual stress value near the surface is very considerable. This is because of a lower accuracy in determining the position of the maximum of the spectrum peak since the peak is broadened due to the high concentration of precipitates in the lattice. Another reason responsible is that the detector is kept at a fix position during the analysis, which sometimes can not cover the broadened peak completely.

5.4.5.5 Nitriding time effect when no compound layer formed

The nitriding potentials for limiting the compound layer formation have been found at 500 and 520 °C, which are 0.8 and 0.5 $atm^{-1/2}$, respectively. Longer nitridings with these

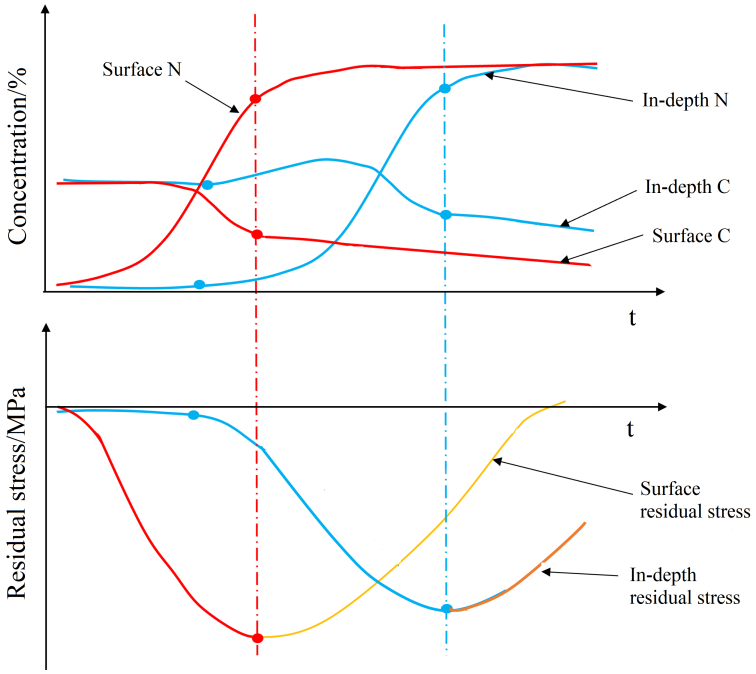


Figure 5.49 – The schematic diagram of the evolution of N/C concentration and residual stress as a function of time at the surface and in-depth.

parameters have been carried out. After 50 hours of nitriding, there is still no compound layer formed. Their N/C, hardness, and residual stress profiles are given in Figure 5.50 and 5.51. The relation of the three profiles respects the same rules as nitriding with the compound layer. As marked with the red stars in Figure 5.50, the residual stress reaches the maximum value at the depth where nitrogen concentration and hardness profile evolve into the end of the plateau. It is also where the carbon accumulation plateau ends.

The maximum residual stress decreases when it occurs in greater depth, and the maximum at 520 °C is -832 MPa after 5 hours of nitriding (Figure 5.50), -969 MPa at 500 °C after nitriding for 15 hours (Figure 5.51). Both maximum residual stresses are at about 60 µm in-depth. This shows that a temperature difference of 20 °C is critical to the nitriding kinetics and that the maximum residual stress can reach a higher value at a lower temperature. Higher temperature affects also more significantly the core hardness. Longer nitriding results in deeper nitriding depth, more complex phase transformations occur at each depth, and more stress redistribution close to the surface.

5.4.6 Nitriding potential effect

Nitriding potential affects nitriding as the temperature does. The evolutions of the residual stress and hardness are attributed to the evolution of the chemical and phase composition in the material in all circumstances.

Figure 5.52 shows the N/C, the residual stress, and hardness profiles in the M2 samples after nitriding at 500 °C for 15 hours with nitriding potential of 0.5, 0.8 and 1 $atm^{-1/2}$. No compound layer is observed from the samples nitrided with the nitriding potentials of 0.5 and 0.8 $atm^{-1/2}$, while 1 $atm^{-1/2}$ results in a thin compound layer. Once a compound layer is formed, the nitrogen concentration and surface hardness reach a stable maximum value limited by the iron nitride phase. The surface hardness will no longer increase as the nitriding potential increases. The compressive residual stress decreases in the compound

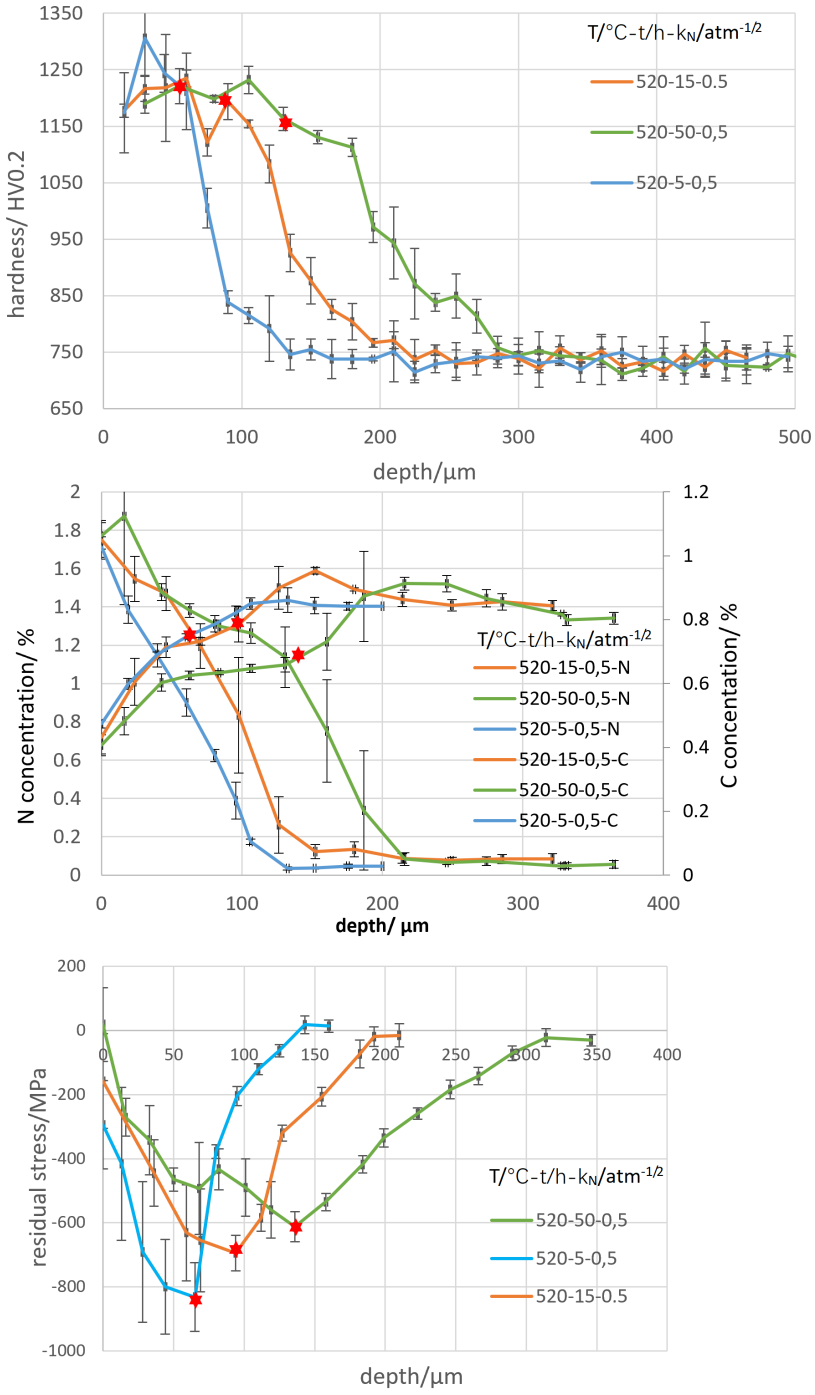


Figure 5.50 – Nitriding profiles of M2 steel (520 °C, 0.5 atm$^{-1/2}$, 5-50 h)

layer due to the phase composition and porosity.

5.4.7 Nitriding temperature effect

As explained in 5.3.4.1, regarding the two nitridings without a compound layer, an increased temperature changes the thermodynamic equilibrium of ammonia decomposition and accelerates the diffusion kinetics. Figure 5.53 presents some hardness profiles after nitriding at 500 and 520 °C for 5 and 15 hours. The yellow and orange curves study the temperature effect with the same nitriding potential. Because the compound layers

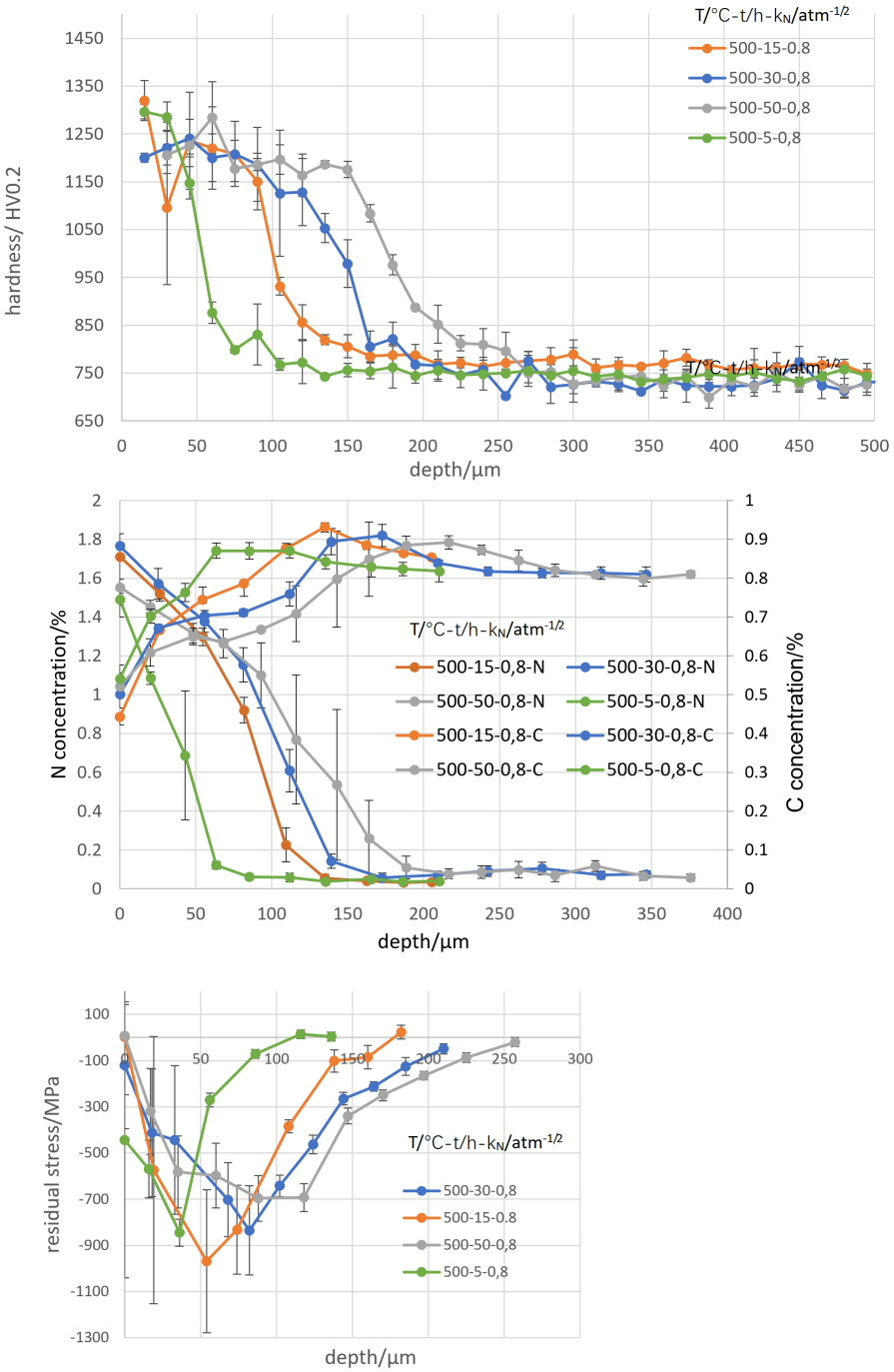


Figure 5.51 – Nitriding profiles of M2 steel (500 °C, 0.8 $atm^{-1/2}$, 5-50 h)

are formed in both temperatures, the surfaces reach the same maximum hardness. The nitriding depth at 520 °C with 1 $atm^{-1/2}$ is greater (120 µm) than that at 500 °C (70 µm). The corresponding N/C and residual stress profiles are given in Figure 5.54, same as hardness, their evolutions when increase temperature present the same trends as increasing the nitriding potential or time.

The blue and brown curves show the nitriding at different temperatures and nitriding potentials. The nitriding at 500 °C (the blue curve) with a nitriding potential 0.3 $atm^{-1/2}$ higher shows an less important nitriding depth than nitriding at 520 °C with 0.5 $atm^{-1/2}$. Both nitriding kinetics and the boundary condition need to be considered to reach a

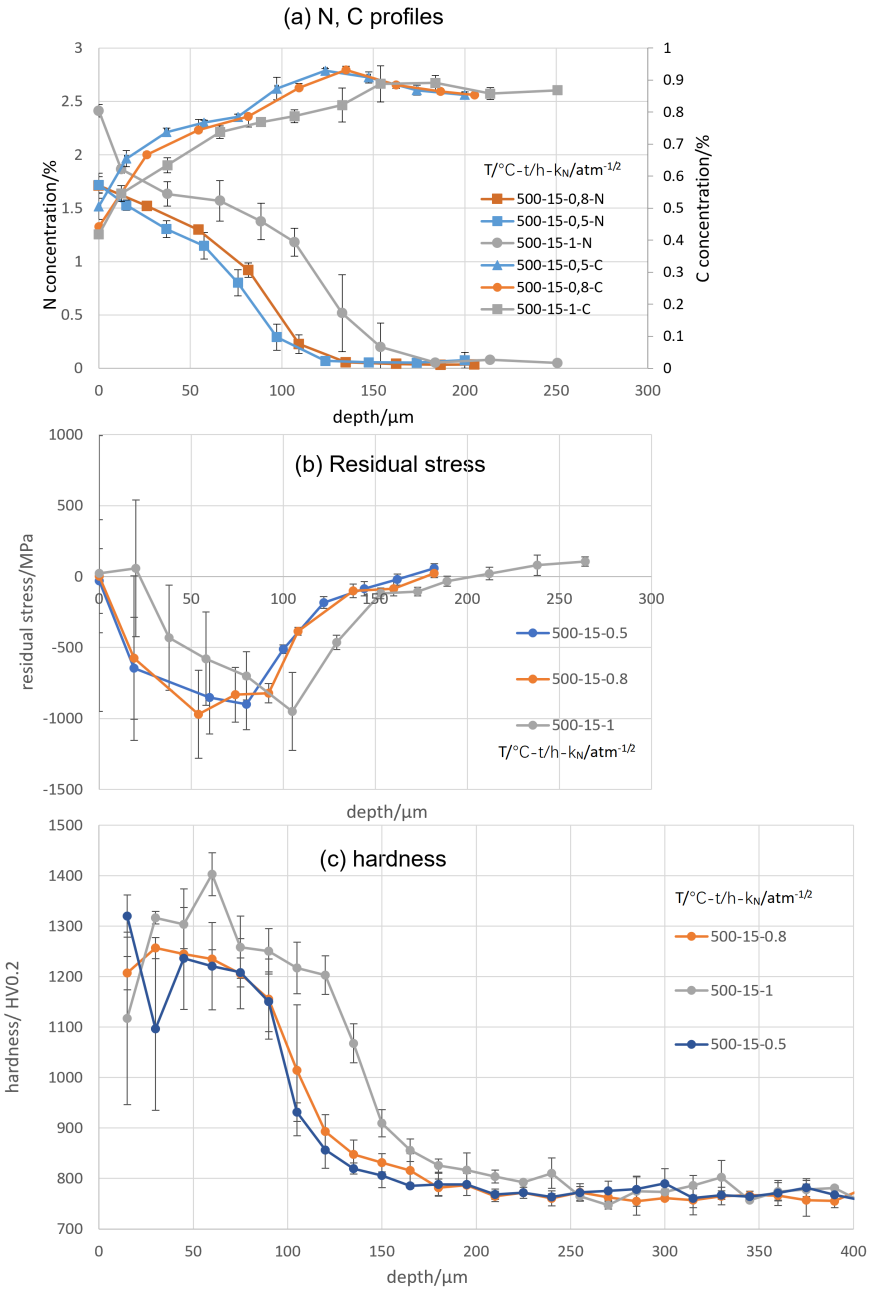


Figure 5.52 – Chemical and mechanical gradient in the M2 sample nitrided at 500 °C for 15 hours with nitriding potential 0.5, 0.8 and 1 $atm^{-1/2}$.

reasonable profile at a reasonable condition.

5.4.8 Thermo-calc analysis

The phase transformation is analyzed with the chemical composition in the nitriding layer as a function of depth measured with OES (optical emission spectroscopy). Figure 5.55 shows the analysis of the nitriding profiles (N/C profile residual stress profile) of the M2 sample (nitrided at 500 °C with $K_N = 0.8$ $atm^{-1/2}$ for 15 hours) as a function of depth and the corresponding phase composition (from Thermo-Calc). The profile can be divided into 4 zones. Zone 1 represents the core material where the nitrogen starts to increase and nitriding begins. Zone 2 is the nitrogen diffusion front. Here the M_6C-

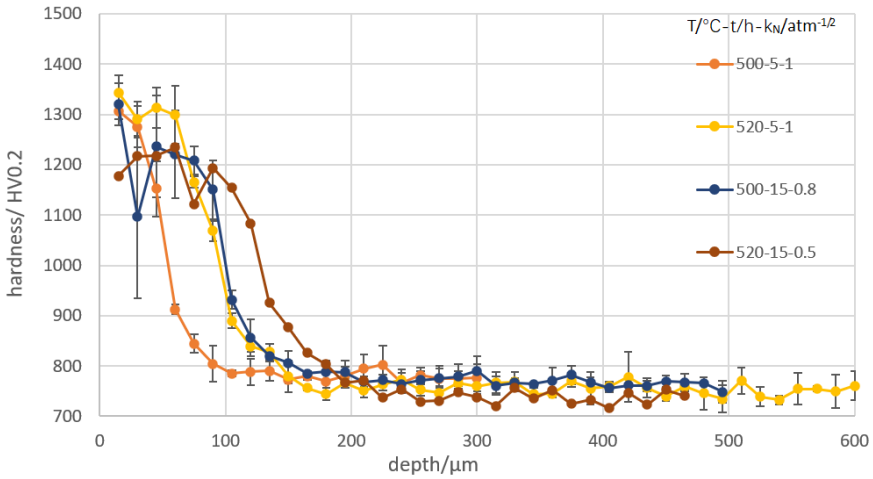


Figure 5.53 – Hardness profile in the M2 sample nitrided with different nitriding parameters.

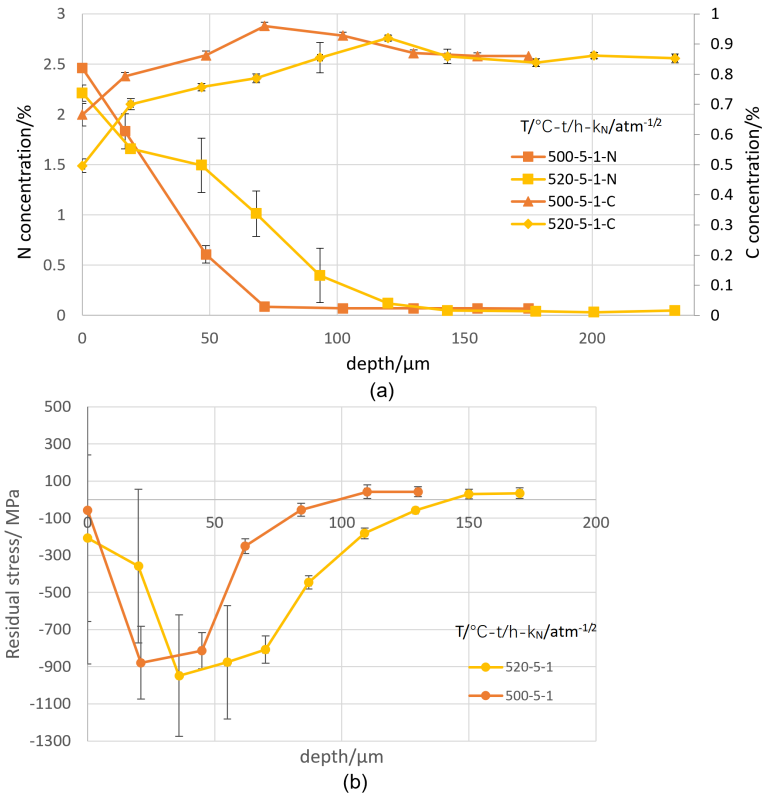


Figure 5.54 – Chemical and residual stress profile in the M2 sample nitrided at for 5 hours with nitriding potential 1 $atm^{-1/2}$, (a) N/C profile, (b) residual stress.

type carbides decompose, the released carbon accumulates, then the M_2C-type carbides increase, resulting in an increase in compressive residual stress. In zone 3, the nitrogen concentration continues to increase, and the nitride precipitation increases, leading to the maximum residual stress. Along with the decomposition of M_2C-type carbides, the cementite phase starts to form. In zone 4, M_2C carbides continue to decompose, M_6C carbide and cementite fractions increase. The nitrides (FCC-A1) fraction, along with nitrogen concentration, reaches the maximum value. These phase transformations, accompanied by decarburization, decrease the compressive residual stress considerably.

More thermo-calc calculations will be given in Appendix A.

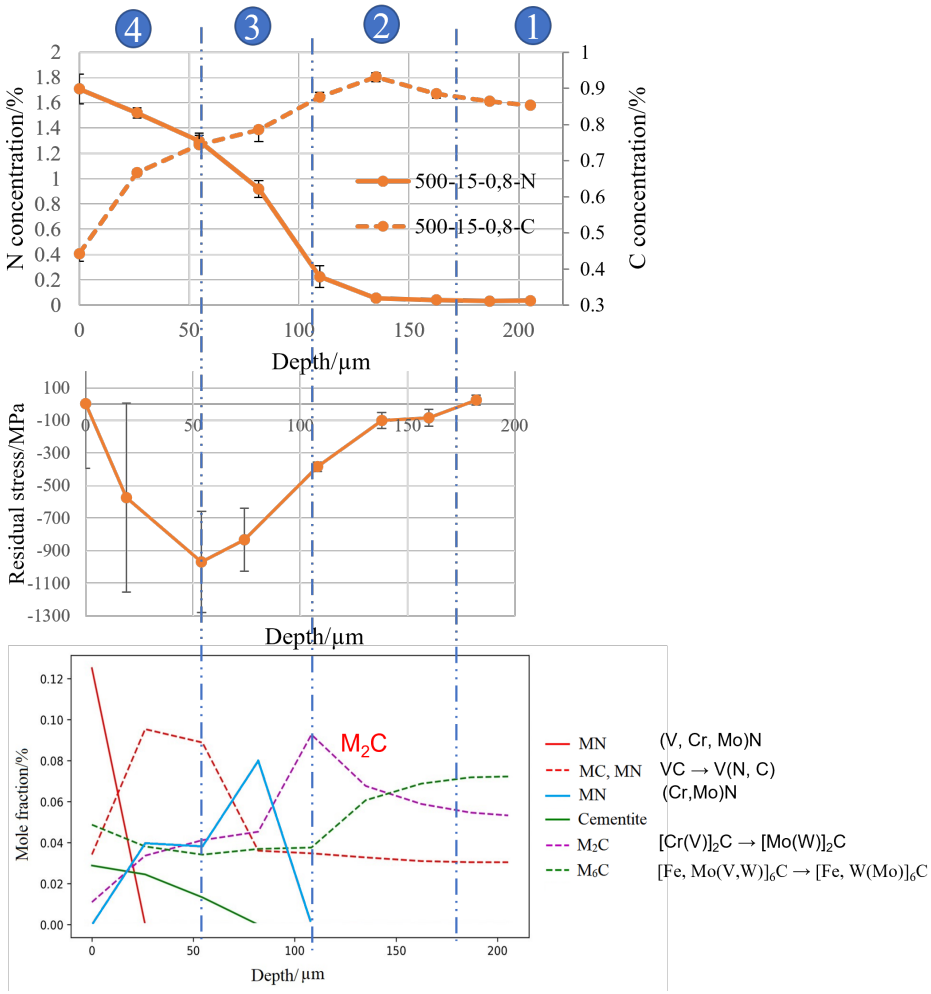


Figure 5.55 – Phase composition as function of depth of the M2 sample after nitriding at 500 °C with $K_N = 0.8$ atm$^{-1/2}$ for 15 hours.

5.5 Nitriding parameters optimization for mechanical behavior of the rolling die

5.5.1 Nitriding effect on core hardness

From the nitriding hardness profiles in section 5.3 and 5.4, nitriding is found also affect the core hardness, which can be critical to cause the decrease in the working performance of the thread rolling die. The nitriding potentials at 500 and 520 °C are found to reach a high surface hardness and fast nitriding kinetics. Besides the surface modification, the nitriding temperature and nitriding time are also defined considering the impact on the core hardness. Figure 5.56 shows the core hardness as a function of nitriding time at these two temperatures. Both temperature and time affect the core hardness negatively. Hollomon Jaffe graph [347] proposed a combined relation of temperature and time and the effect on the steel hardness during tempering. It is applied to study the effect of nitriding time and temperature on the core hardness, as shown in Figure 5.57. P is a factor considering both the temperature and time, given as:

$$P = T(c + \log(t)). \tag{5.1}$$

with a parameter function of the carbon concentration of the steel c, given by:

$$c = 21.3 - 5.8 \times (\text{wt.\%C}). \tag{5.2}$$

The nitriding time needs to be controlled to avoid the loss of core hardness.

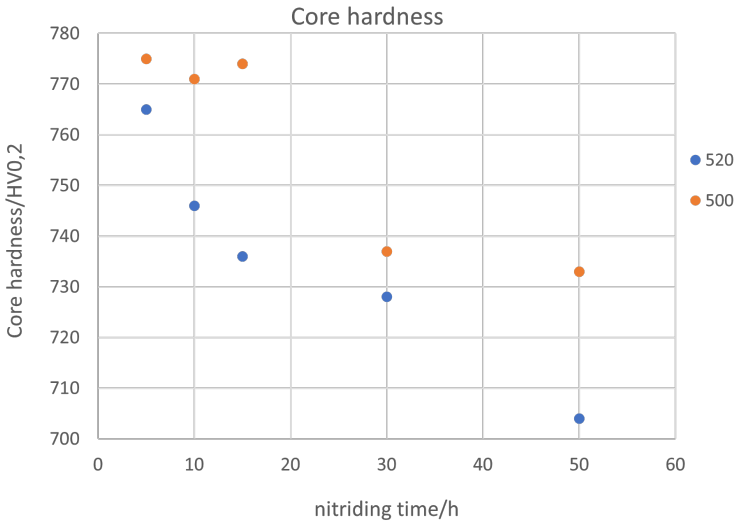


Figure 5.56 – The core hardness of M2 samples nitrided at two temperatures as a function of nitriding time

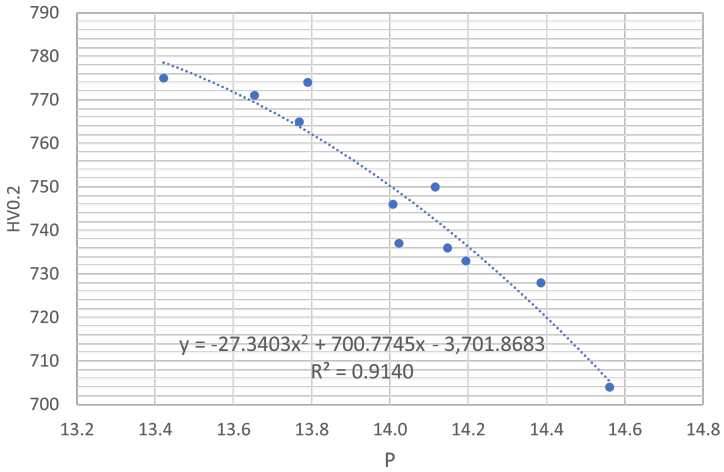


Figure 5.57 – Hollomon Jaffe T-t relations in tempering steels

5.5.2 Comparison to the nitriding profiles in the rolling die

As the nitriding is studied to improve the working performance of the thread rolling dies, the comparison of the nitriding profile on the sample and the rolling die is carried out. A good nitriding for the rolling die should consider the hardness, the residual stress, the compound layer, and the depth of the hardened layer. The residual stresses can not be used to compare due to the incompatibilities of that on the rolling die flat surface and the threads (in chapter 4). The hardness profile is the only concern. The lifetime of the rolling

die is positively related to the nitriding depth and surface hardness, as shown in Figure 5.58. The hardness profile between the nitrided sample and the real die that produced the most screw pieces (among the specimen) are compared as shown in Figure 5.59. The nitriding depth is defined as the depth where the hardness is 100 HV higher than that in the core. Despite the difference of the core hardness, the nitriding depth is close to the nitriding at 500 °C with $K_N = 0.8$ atm$^{-1/2}$ for 15 hours.

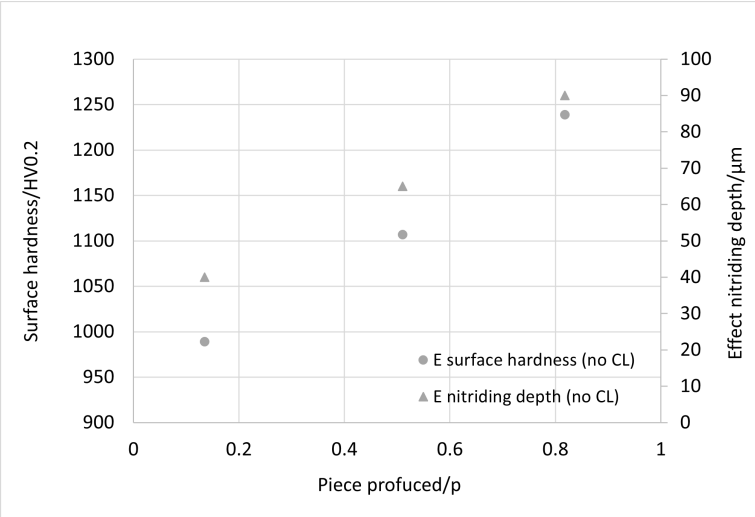


Figure 5.58 – The relation between the tool lifetime and nitriding profile.

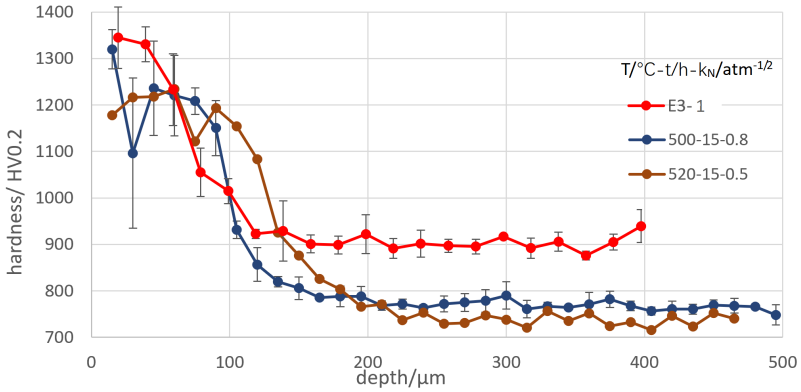


Figure 5.59 – The best nitriding profile among the rolling die specimen the close profiles in M2 samples

A short nitriding time is also desired considering the economic and energetic reasons if the nitriding profiles are also appropriate. The 5 hours nitridings at the same temperature and same nitriding potential have close surface hardness, but smaller nitriding depth. They also satisfy the high compressive residual stress and no compound layer conditions. Especially, the shorter time nitridings have less impact on core hardness and the redistribution of residual stresses. It is then possible that 5 hours of nitriding can replace 15 hours.

Based on the nitriding potential and temperature that has been selected, the parameters for further wear measurements are 500 °C-0.8 atm$^{-1/2}$-15 h, 500 °C-0.8 atm$^{-1/2}$-5 h,

520 °C-0.5 $atm^{-1/2}$-15 h, 520 °C-0.5 $atm^{-1/2}$-5 h.

5.6 Conclusions

This chapter presents the study on gas nitriding of M2 steel samples. The M2 steel is cast, and the carbide segregation is present in the microstructure. The samples with a hardness of about 750 HV are industrial quenched and tempered. The sample surfaces are finished with polishing, grinding, and sandblasting industrially, and this contributes to the nitriding kinetics variation. The sandblasted surface gains the least nitrogen due to the high level of compressive residual stress before nitriding. On the other side, the ground surface is the most difficult to be homogenously nitrided due to the contamination, which is hard to remove from the particular topology. The laboratory-level grinding (1200 grade polishing) is used for nitriding kinetic study.

A high nitriding temperature and/or nitriding potential can promote nitriding kinetics, consequently, increase nitriding depth and evolve the compressive residual stress to a deeper depth. A longer nitriding gives a similar effect to nitriding. However, increasing any of these parameters leads to a non-negligible residual stress redistribution. In contrast, the maximum hardness of the nitriding layer stays consistent when the compound layer is formed because the maximum nitrogen concentration reaches the limit, and coarsening kinetics of nitrides is slow.

The pseudo-Lehrer diagram for M2 steel is studied, and the α/γ' limit is found at 500 and 520 °C. The relations of the N/C profile, hardness profile and residual stress profile are explained in terms of phase transformations. The hardness profile is basically in agreement with the N profile. The residual stress profile involves more carbide transformation and carbon redistribution along with nitrogen enrichment and nitride precipitation. When carbides start to decompose, carbon accumulates at a certain depth, more carbides are formed. The extra volume expansion leads to the maximum compressive residual stress. The decrease in compressive residual stress can be summarized by:

— decarburization due to the reaction between carbon and the atmosphere,

— coarsening, depending on the N concentration nitriding time t,

— phase transformations lead to negative volume expansion, but more experiments are needed to identify the nature of the initial carbides and newly formed precipitates (TEM).

Longer nitriding is performed, and it is found that increasing nitriding time or temperature decreases the core hardness. The potential hardness profiles in the nitrided M2 samples are compared with that in the best performant rolling die, and the most similar profile is from nitriding 500 °C-0.8 $atm^{-1/2}$-15 h. Based on the study in this chapter, a few nitriding parameters are selected for further study in the next chapter for wear resistance.

CHAPTER 6

WEAR RESISTANCE OF NITRIDED M2 STEEL

This chapter aims to study the wear behavior of M2 high-speed steel and the improvement of nitriding are studied in several different groups. The wear measurement set-up is briefly introduced, where the calculation relied on the FEM analysis. Then the results of the tests of friction coefficient and the wear rate measurements are given and analyzed.

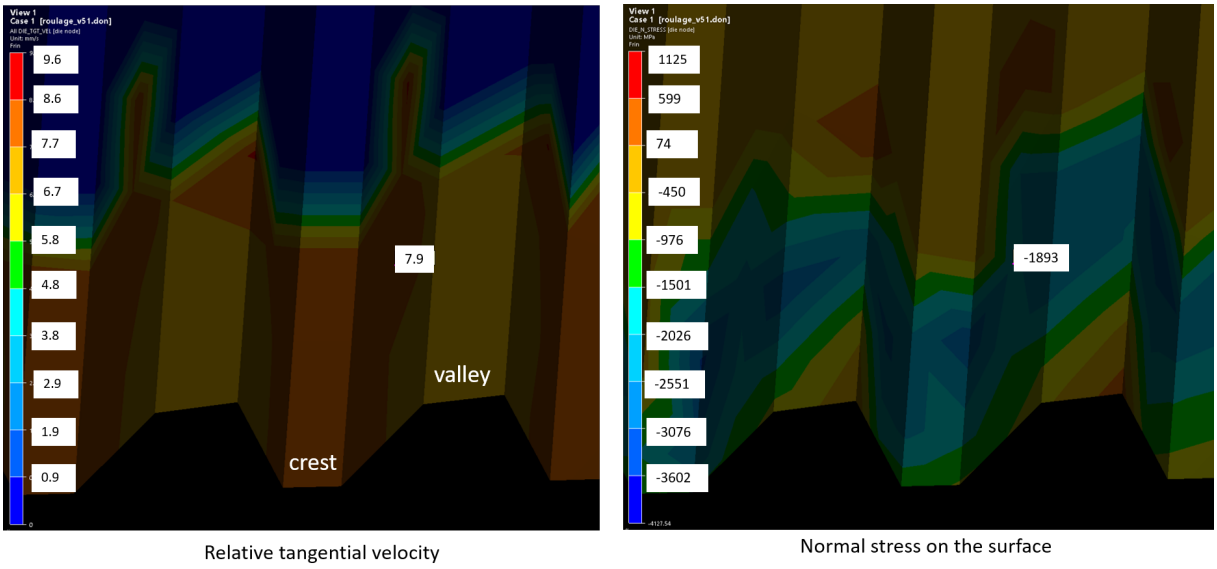
6.1 Experiment set-up

6.1.1 Pressure and sliding speed

High friction coefficients are necessary for the rolling process for forming a thread to enable a good reproduction of the measured profile geometry (for instance, 0.30 is an appropriate value) [270]. Low friction coefficients (lower than 0.15) lead to higher deviations and thus do not produce the measured geometry profile well. Static friction is the major influence during the rolling process [270]. Friction is not only a factor in fatigue initiation but also a primary parameter for wear. As gas nitriding is studied to improve the rolling die's lifetime, the wear resistance needs to be defined by measuring the wear rate of the M2 samples nitrided with the selected nitriding parameters. To make the wear rate measurement method as representative of the real rolling process as possible, the pressure and sliding speed results are exported from the FEM, as shown in Figure 6.1.

The sliding speed (relative tangential velocity) and the pressure (normal stress on the surface) distribute differently. The sliding velocity is higher along the edge around the contact center, but the normal stress shows the highest value at the contact center. This is due to the special geometry of the rolling sphere, the diameter, and different tangential velocities. Some data is given in Figure 6.2: the normal stress values cover a big range from -2923 MPa to 269 MPa, while the sliding speeds vary from 7.5 to 8.9 mm/s. To be noticed, the highest pressure doesn't appear at the same location as the highest sliding speed does.

The pressure of 3000 MPa and sliding speed of 10 mm/s are chosen to calculate the possibilities of contact geometries for the wear measurement as they present the most severe case.



Relative tangential velocity

Normal stress on the surface

Figure 6.1 – Sliding speed (in mm/s) and normal stress (in MPa) distribution (from the FEM result).

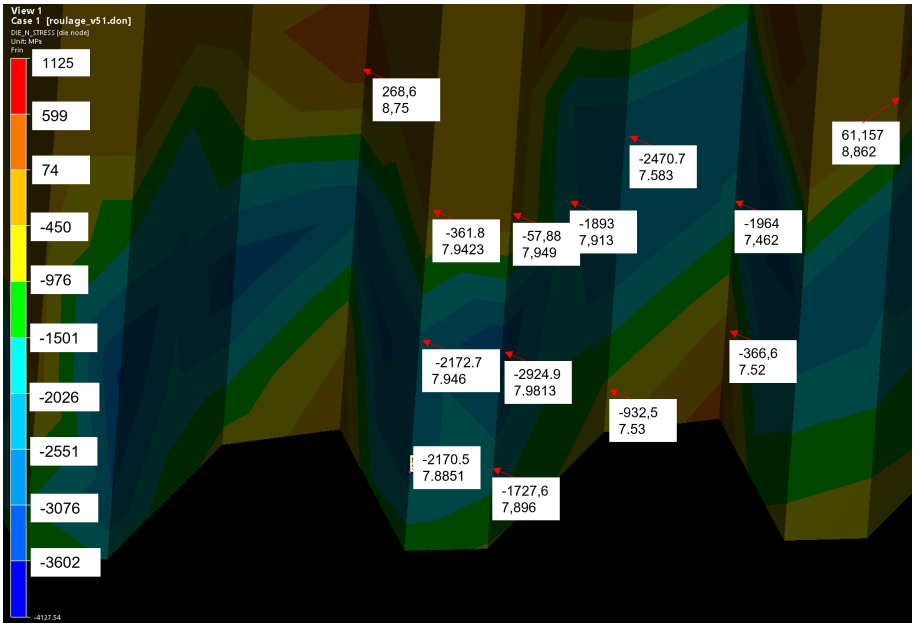


Figure 6.2 – Sliding speed (in mm/s) and normal stress (in MPa) values on different locations of the threads.

6.1.2 Wear measurement set-up calculation

The set-up with a sphere surface on the pin will be used for the wear rate measurement to reach the high-pressure value of 3000 MPa (see in Appendix B).

Hertz theory is used to calculate the required load for reaching the maximum pressure (Figure 6.3), the contact area, and the depth of the maximum shear stress [317]. The two contact parts are assumed to be elastic in this theory. R is the effective radius of the contact system, which can be calculated by:

$$\frac{1}{\mathrm{R}} = \frac{1}{\mathrm{R}_1} + \frac{1}{\mathrm{R}_2}. \tag{6.1}$$

In the case of the ball on a flat surface, R equals the ball radius. a is the radius of the contact zone, expressed by:

$$a = \frac{\pi p_0 R}{2E^*}. \tag{6.2}$$

The effective elastic modulus is a function of Youngs modulus (E_1, E_2) and Poisson's ratios (ν_1, ν_2) of the two contact parts, written as:

$$\frac{1}{E^*} = \frac{1-\nu_1^2}{E_1} + \frac{1-\nu_2^2}{E_2}, \tag{6.3}$$

and p_0 is the maximum contact pressure, given by:

$$p_0 = \frac{3F_N}{2\pi a^2}. \tag{6.4}$$

F_N can then be calculated.

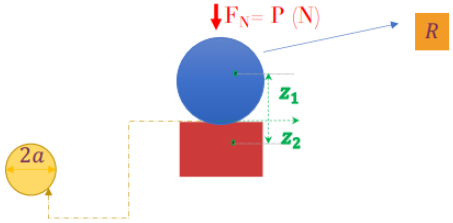


Figure 6.3 – Hertz theory of ball/disk contact.

The Poisson ratio of the M2 steel disk is 0.3, From Figure 2.66, the ratio of the maximum shear stress depth Z and the contact zone radius a is 0.48. Then

$$Z = 0.48a. \tag{6.5}$$

It is linked to the pressure and the equivalent Youngs modulus.

6.1.3 Ball on disk wear systems

The friction coefficients in the actual rolling process are measured to create a more representative measurement setup. Some disks and pins are fabricated with the same roughness on the die thread and the blank spindle. The roughness is measured with 2D characterization. Three measurements are performed for each result at equivalent locations, and the Ra values are treated. In Figure 6.4, the roughnesses on the axial and rolling direction on the spindle are different induced by the grinding process before threading, they are 0.566 ± 0.088 µm and 0.672 ± 0.063 µm. On the rolling die threads, it is only possible to measure the roughness Ra along the thread because of the low height of the thread, and the roughness is 0.375 ± 0.015 µm.

M2 pins and M2 disks are manufactured by LISI Automotive with the same roughness Ra as the EPB screw and the M2 rolling die, respectively. The disks are also fabricated in the lab MSMP of 23MnB6 steel from the EPB part, and the surface is polished to 1200 grade with roughness of 0.016 ± 0.004 µm. The same M2 steel samples used for nitriding kinetic study (17 × 13 × 5 mm^3) are used as disks, their roughness is the same as the EPB disks. Meanwhile, M2 balls with a diameter of 4.762 mm ± 2 µm with a polished surface of the roughness of 0.01 µm are provided by Metal Ball. Considering the high-level hardness of M2 steel, sapphire balls are also used to perform the wear measurement.

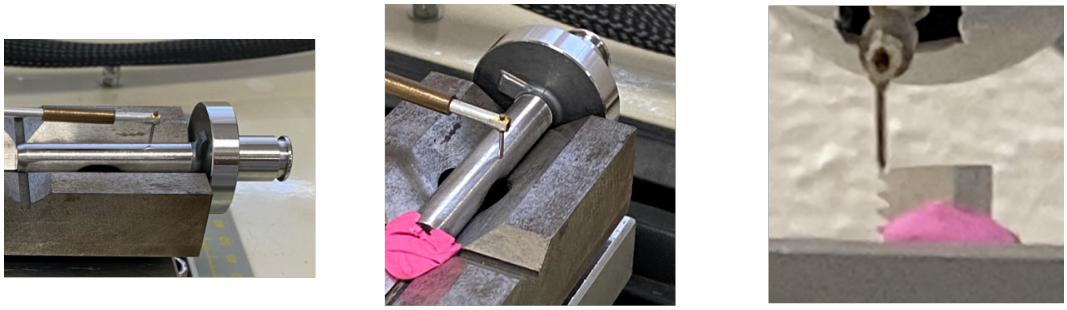


Figure 6.4 – Roughness measurement on the spindle and rolling die thread (2D profiles are measured with Surfascan 3D).

The experiments are carried out in the following directories: Sapphire ball/M2 disk, Sapphire ball/Nitrided M2 sample, M2 ball/EPB disk, and Nitrided M2 ball/EPB disk. The elastic modulus used: 205 GPa for steels, 430 GPa for sapphire, and the Poisson's ratios: 0.3 for steels and 0.28 for a sapphire.

6.1.4 Wear measurements

The wear measurement is set up with a tribometer, as shown in Figure 6.5. The lubricant is the same oil (new) for the actual rolling process in LISI Automotive.

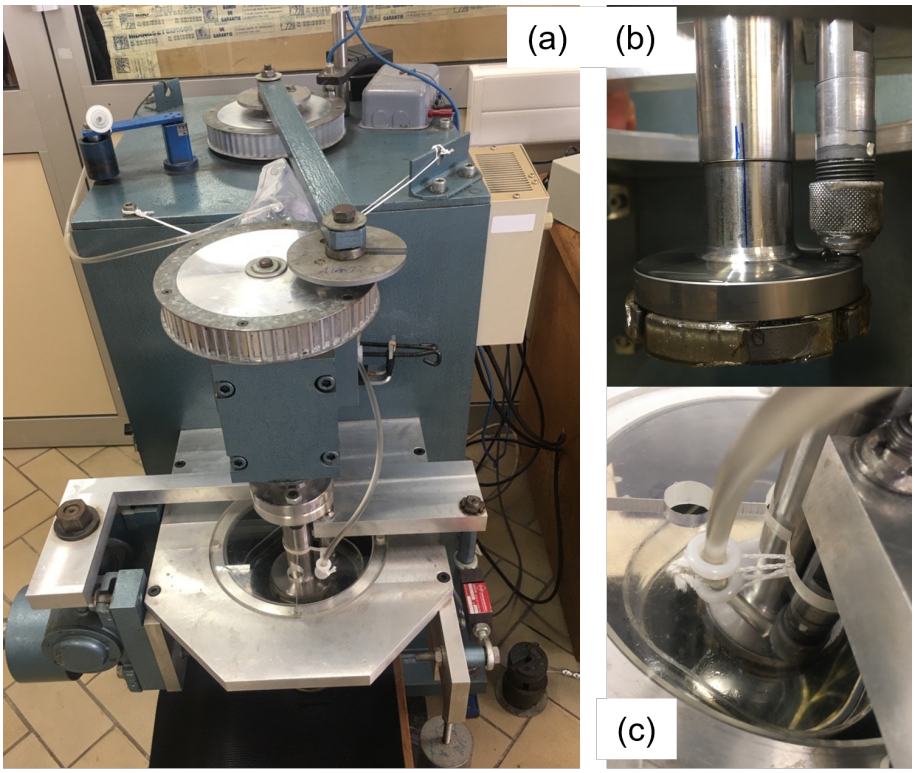


Figure 6.5 – (a) the measurement set-up for the wear measurement, (b) the pin/disk contact, (c) the lubricant system.

Both continuous and alternative rotations are available. The radius of the contact

position (rotation of the ball on the disk) is 30 mm, and the circumference is 188 mm. The continuous rotation frequency can be 0-10 Hz, and the sliding speed can reach 0-2 m/s, while the frequency under the alternative mode is 0-1 Hz. Alternative rotation is adopted. The maximal normal load is 300 N, the maximal tangential load is 250 N, and the minimum tangential load is 0.25 N. In alternative movement, the maximum speed is in the middle of the track, and the speed at the two ends is 0. A track of 10 mm long has been defined for the measurements. As the sliding speed of 10 mm/s is required, the frequency of 0.5 Hz was first introduced. One cycle is counted as two times contacts. To reach the maximum contact pressure $P_0 = 3000$ MPa, the load $F_N = 66.9$ N for the steel ball/steel disk system, and $F_N = 36.7$N for sapphire ball/steel disk system. The corresponding charges (Figure 6.6) are 42 and 23.4 N, respectively. Considering the contact area increases while the wear forms, which will lead to a decrease in the maximum pressure, the increased load to reach the mean pressure $p_{mean} = 3000$ MPa is also calculated. They are 79 N for Sapphire ball/M2 steel disk and 147 N for steel ball/steel disk.

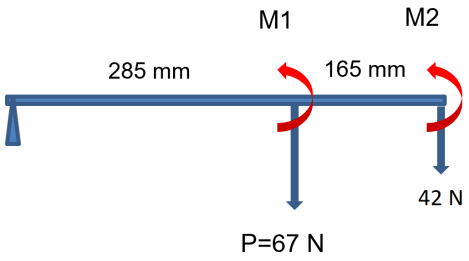


Figure 6.6 – The moment equilibrium of force

6.2 Wear study on M2 steel

6.2.1 Wear of M2 disk

In this section, the wear behavior of the M2 steel disk is studied by using sapphire balls. Due to the high hardness of the M2 steel disk, especially after nitriding, their counterparts (the balls) need a higher hardness. Sapphire balls are made of monocrystal Alumina. Its high hardness (more than 2000 HV) makes it possible to perform the wear measurement on the M2 disk before significantly damaging itself. 6 experiments are carried out on the same M2 disk (Figure 6.7) to study the effect of the wear parameters on the friction coefficient and the final wear profiles.

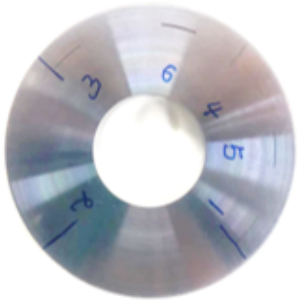


Figure 6.7 – The M2 disk used to study the wear parameters.

6.2.1.1 The friction coefficient

Figure 6.8 illustrates the friction coefficients of the 6 measurements. The friction coefficient is calculated with the equation f = T/N, N is the normal load which is constant, and T is the mean tangential load which is measured 21 times per cycle. The moving average for every 50 points and linear fitting curves are presented. The friction coefficient decreases during each measurement, disregarding the ratio is not considerable. This may be due to the increment of the contact area during wear, which might give rise to a change in the lubrication pattern. On the contrary, the dispersion of the friction coefficient values for all the measurements is large. This might be owed to the different sliding speeds on the worn track of the alternative movement.

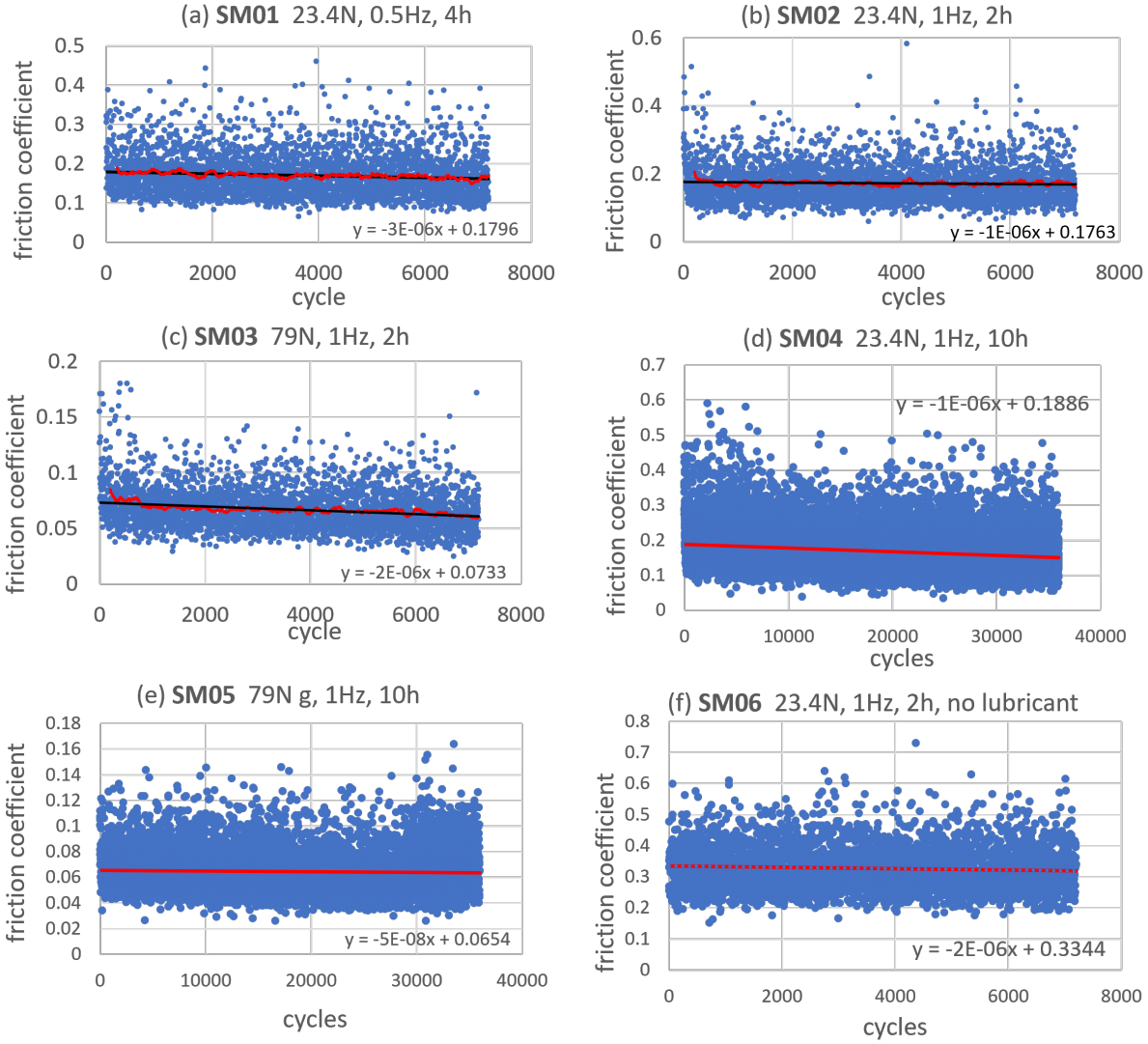


Figure 6.8 – The friction coefficient as a function of the number of cycles.

The mean friction coefficients are plotted in Figure 6.9. SM01 is performed with the calculated parameters, 0.5 Hz has been chosen to fulfill the sliding speed of 10 mm/s, and the load of 23.4 N to reach $P_0 = 3000$ MPa. The friction coefficient value is in the range of 0.15-0.3, fitting the thread rolling process (see in 6.1.1). SM01 and SM02 study the effect of the frequency (see Figure 6.8 (a) and (b)), and both the mean values and the deviations are close.

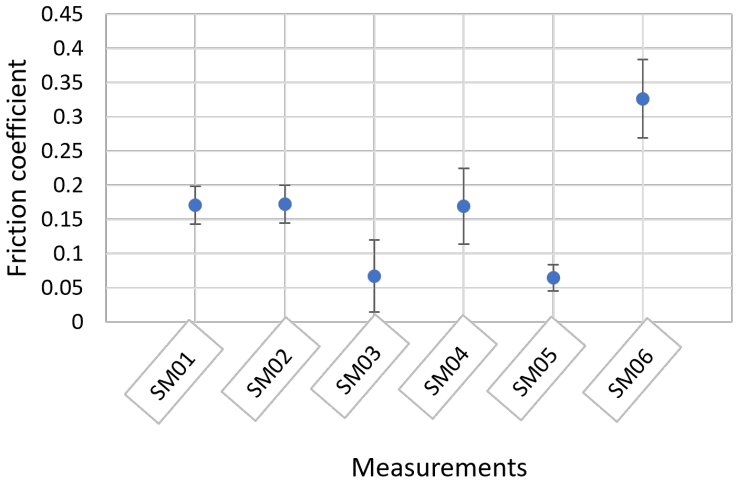


Figure 6.9 – The mean friction coefficient of the sapphire ball/M2 disk measurements (the measurements details see in Table 6.1).

The friction coefficient brings about the asymmetry of the surface normal stress (σ_{xx}) distribution (Figure 2.67) [317]. When the friction coefficient decreases from about 0.17 to 0.065, the stress asymmetry decreases despite the increased pressure. Here the friction coefficient can not represent that in the real rolling process. Because the sapphire balls and their surface are not in the same condition as the steel parts. The absolute value should not be considered, but the relative comparison results related to the M2 disk.

6.2.1.2 Wear track measurements on the M2 disks

Table 6.1 shows the measurements performed, the frequency, the load, the number of cycles, and the lubricant are varied to study their effect. The tribometer is calibrated with charges of 0, 7.2, and 23.4 N while the load of 23.4 is applied, and 79 N is added while the load is 79 N.

Table 6.1 – Wear measurements of Sapphire ball/M2 steel disk.

Measurement	**Load/N /N**	P_0 **/MPa**	**Frequency /Hz**	**Cycles**	**Time /h**	**Lubricant**	**Friction coefficient**
SM01	23.4	3000	0,5	7200	4	oil	0.17±0.05
SM02	23.4	3000	1	7200	2	oil	0.172±0.055
SM03	79	4500	1	7200	2	oil	0.067±0.019
SM04	23.4	3000	1	36000	10	oil	0.169±0.058
SM05	79	4500	1	36000	10	oil	0.064±0.017
SM06	23.4	3000	1	7200	2	nothing	0.327±0.071

Figure 6.10 presents the wear on the M2 disk after the measurements. The wear depths for both measurements are about 0.43 μm, and the widths are about 117 μm. The M2 disk surface is machined with periodical peaks and grooves. Increasing the frequency to 1 Hz does not affect the friction behavior during the wear of the sapphire ball/M2 disk, or the final wear on the disk.

SM02 and SM03 study the effect of the load. An increased load of 79 N results in a decreased friction coefficient of 0.067 ± 0.018. This might be related to the lubrication condition. The radius of the contact area a is 76 and 116 μm according to equation

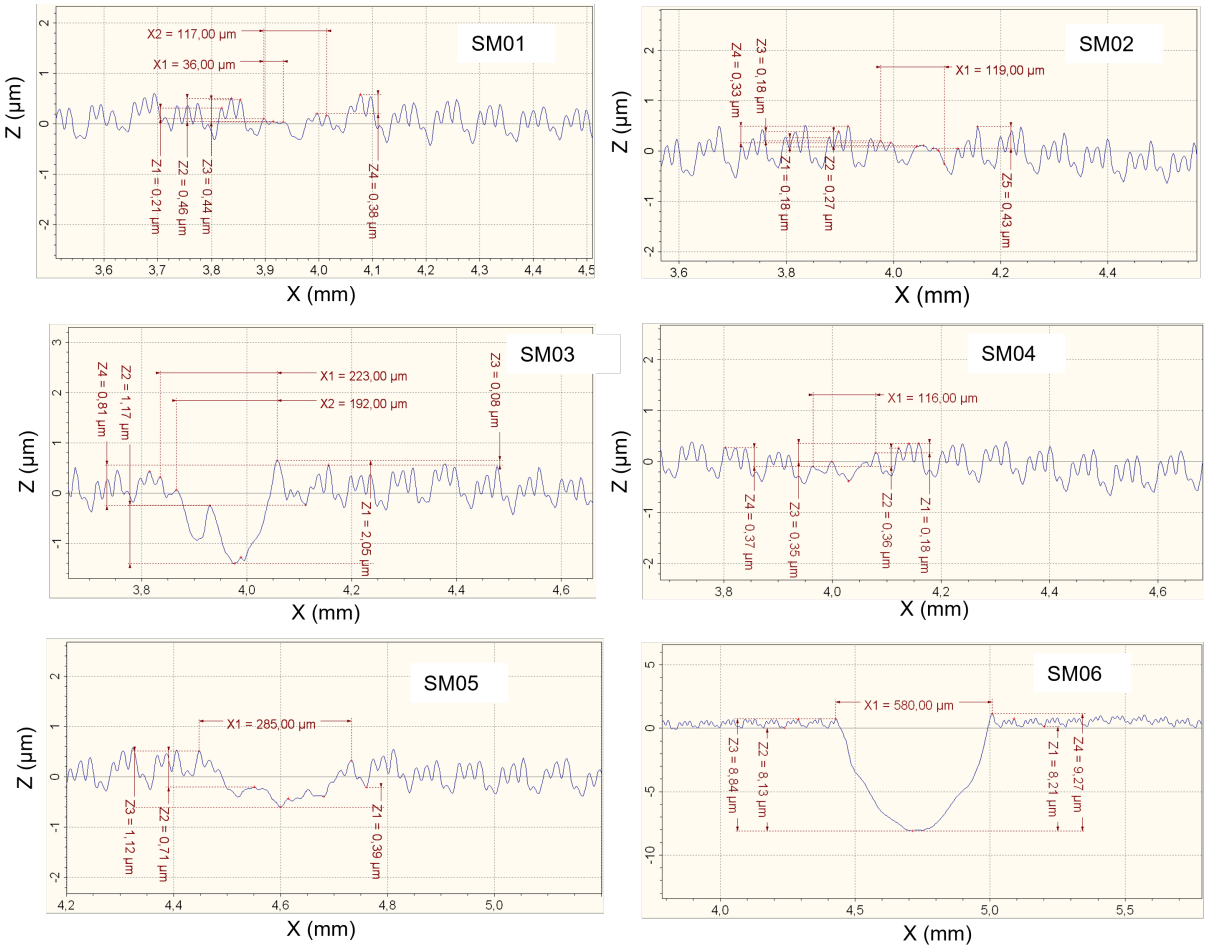


Figure 6.10 – The wear analysis on the M2 disks (the measurements details see in Table 6.1.)

6.2 under the two loads 23.4 and 79 N, respectively. The characterization of the wear dimensions is disturbed by the initial grooves (from machining). In Figure 6.10, one complete cycle of the peak and groove resulting from the machining process is about 80 µm. The contact zones of measurement SM01, SM02, and SM04 focus mainly on one period of machined peaks. The contact area under a higher load (SM03 and SM05) is larger to cover more initial periodical grooves formed from machining. The space between the ball and disk under higher load is greater due to the presence of more large periodical valleys, allowing more lubricant between the contacted surfaces during the wear process. The increased lubricant allows the formation of an oil film and significantly reduces the friction coefficient. In Figure 6.10, the wear depth on the SM03 disk is about 120 µm, which is more significant than that on the SM02 disk due to the high-level loading. The width reaches up to 200 µm.

SM04 and SM05 study the effect of the number of cycles by comparing them to SM02 and SM03. The measurements are prolonged to 10 h with loads of 23.4 and 79 N. In Figure 6.9, the average friction coefficient keeps the same range for both loads after changing the wear cycles. The wear track depth and width on the M2 disk SM04 are nearly the same as those on the disk worn with the same load but shorter time SM02. However, The SM05 disk shows a greater wear width but less important depth than the SM03 disk. This might be because the initial contact point of these two measurements is different in terms of the valley and peak of the initial grooves from machining. If the contact center locates on the peak, the wear tends to evolute a larger width, while if the contact center is at the valley,

the wear tends to evolute a greater depth.

6.2.1.3 Observation of the wear tracks

Figure 6.11 and Figure 6.12 present the micrographs in the wear track of the M2 disks after the measurement SM04 and SM05, respectively. With the same magnification, it's easy to see the wear width on SM05 disk is more significant than that on SM04 disk due to the higher load level. Meanwhile, more cracks can be observed on SM05 disk. In figure 6.12 (b), some micro-cracks are initiated in the carbides. This mechanism is close to what has been observed on the rolling die thread crest (Figure 6.13 or see in 4.3).

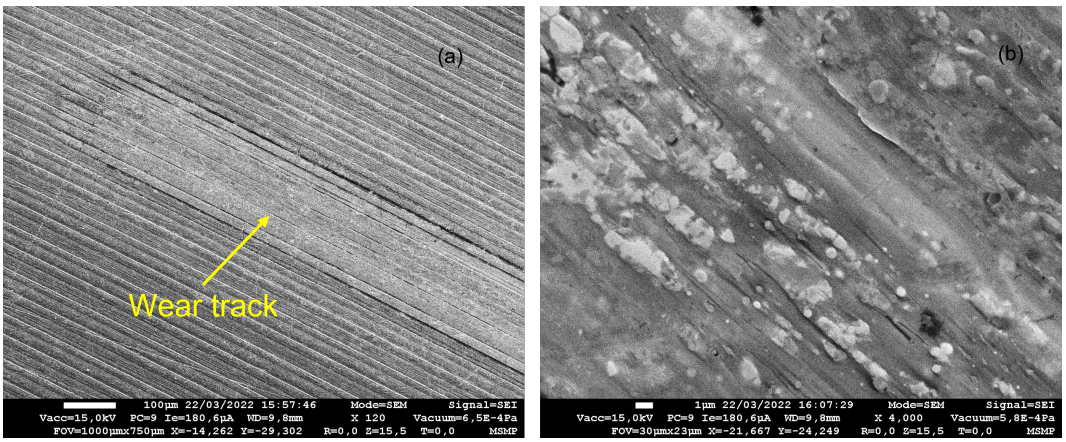
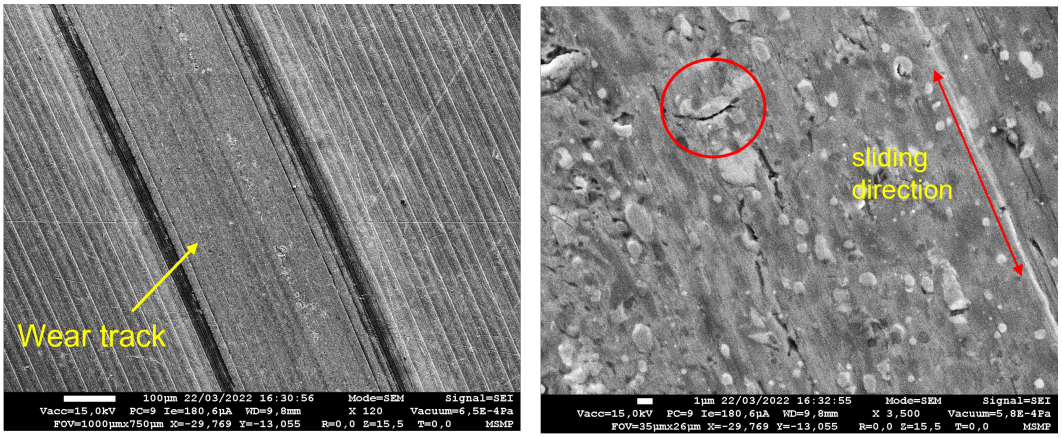


Figure 6.11 – The wear on the M2 disk after the measurement SM04 (23.4 N, 1 Hz, 10 h).



(a) (b)

Figure 6.12 – The wear on the M2 disk after the measurement SM05 (79 N, 1 Hz, 10 h).

SM06 studies the wear behavior when the lubricant is absent. The friction coefficient increases up to 0.33. This proves from another aspect the necessity and importance of lubrication control during the rolling thread process. Figure 6.14 shows the sapphire balls after the friction tests. The sapphire balls, after all the friction tests with lubricant from SM01 to SM05, present no wear (Figure 6.14 (a)). On the contrary, the non-lubricant measurement SM06 leads to significant wear on the sapphire ball (Figure 6.14 (b)) dispite the less considerable load and wear time.

Figure 6.15 presents a micrograph in the wear track of M2 disk SM06 after the wear without lubricant. Figure 6.15 (a) shows the end of the wear track. Figure 6.15 (b) shows

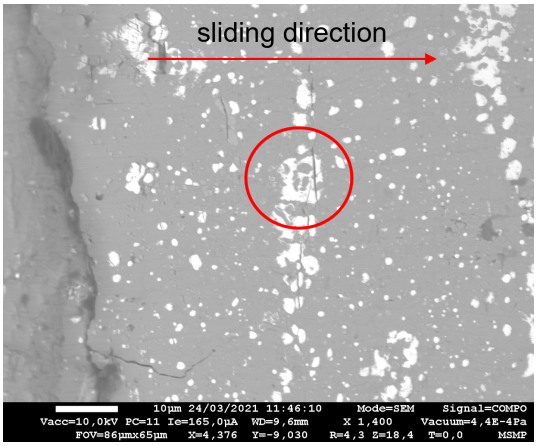


Figure 6.13 – The wear on the rolling die thread crest.

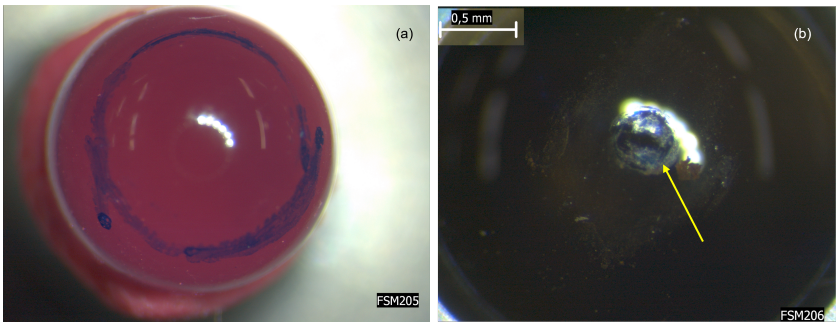


Figure 6.14 – The sapphire balls after the wear measurement (a) SM05, (b) SM06.

some particles in the track, it seems some material particles or small precipitates have been displaced. The dark part in Figure 6.15 (a) is presented in Figure 6.15 (c). The material at the end of the track forms the scales due to the accumulated worn powder and the cyclic load.

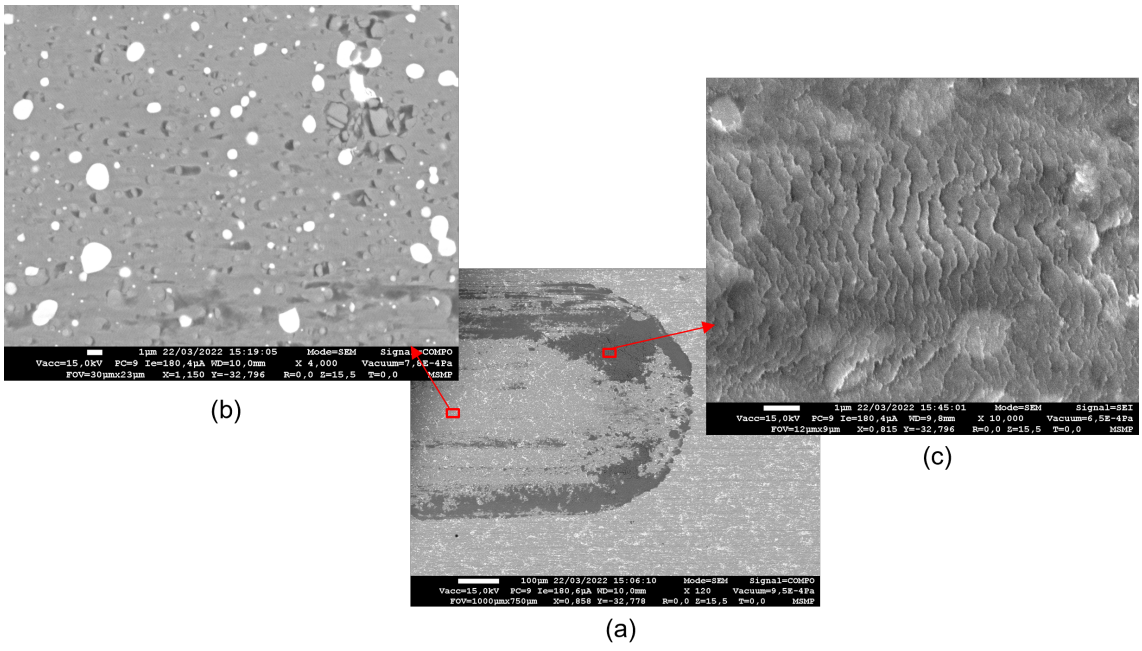


Figure 6.15 – The wear on M2 disk after the measurement SM06 (23.4 N, 1 Hz, 2h).

Some powder is produced during measurement SM06 due to the abrasive wear, as shown in Figure 6.16. With the energy dispersive X-ray spectroscopy (EDS) under SEM, two kinds of chemical composition are analyzed (see in Figure 6.16 (b)), and the normalized results are shown in table 6.2. In the bright zone, a high amount of Al is detected. It is a particle from the sapphire ball (Al_2O_3).

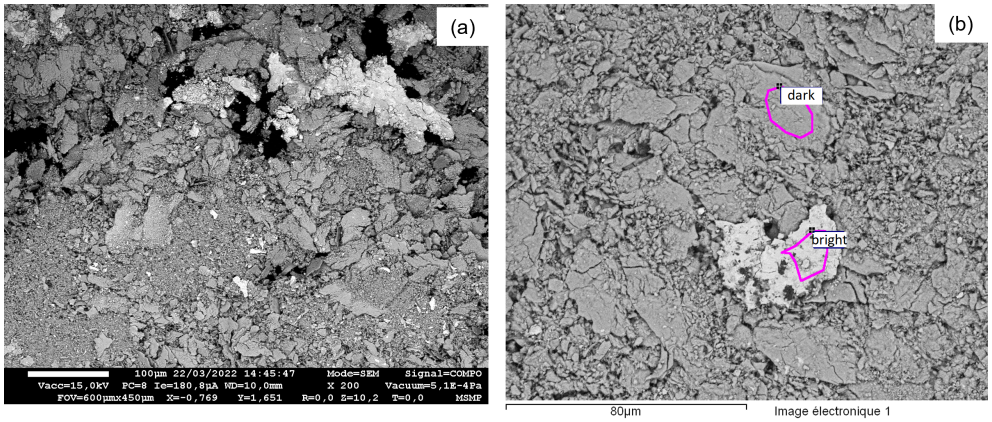


Figure 6.16 – The powder produced on M2 disk after measurement SM06 (23.4 N, 1 Hz, 10h).

Table 6.2 – The two EDS spectrums analyzed in the powder produced on the M2 disk during the wear measurement SM06.

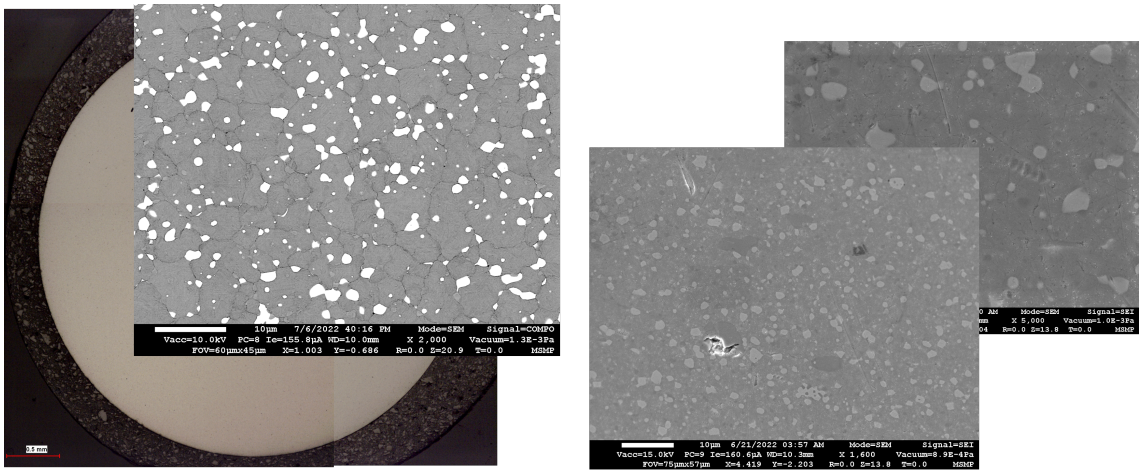
Spectre	O	Al	V	Cr	Fe	Mo	W	Total
bright	18.1	3.7	1.4	3.5	63.7	4.3	5.4	100
dark	36.6	0.3	1.2	2.7	50.8	3.6	4.8	100

6.2.2 Wear of M2 ball

6.2.2.1 Initial condition of the M2 ball

In the thread rolling process, the die thread made in M2 steel penetrates into a flat spindle made of 23MnB6 steel. The tribological behavior between these two materials must be studied. Due to the low hardness, 23MnB6 steel can only be the disk in the wear measurements. Therefore, M2 balls are introduced. The microstructure of the M2 ball at the cross-section is shown in Figure 6.17 (a). No significant carbide segregation is observed due to the powder metallurgy manufacturing method. The carbides and grain sizes are smaller than those in the actual thread rolling dies and the M2 steel samples used for studying the nitriding. However, initial defects are observed from the surface (Figure 6.17 (b)).

The hardness of the ball is 823 ± 7.4 HV0.2 (measured at the cross-section, which is higher than the hardness of the M2 samples (750 HV) and lower than that of the rolling dies (900 HV for casted die, 990 HV for powder metallurgy dies). The higher hardness of the M2 balls should be linked to the manufacturing method (powder metallurgy) and the heat treatment processes.



(a) (b)

Figure 6.17 – The microstructure of M2 steel ball used during wear measurements, (a) in the cross-section, (b) on the surface.

6.2.2.2 M2 ball/ EPB disk wear measurements

This section will study the wear behavior between the M2 ball and the disk made from the EPB part (23MnB6 steel). The measurements were performed under different loads and for different cycles, as shown in Table 6.3 to study their effect on the wear behavior. For the steel ball to steel disk system, a load of 42 N is applied to reach the maximum pressure of 3000 MPa. Meanwhile, the lower and higher loads (23.4 and 79 N) are kept for comparison. The time for the measurements varies from 2 hours to 14 hours for the same load. The measurements for 4 hours are carried out with all different loads.

Table 6.3 – M2 ball/EPB disk (23MnB6 steel) wear measurements.

Measurement	Load/N	Frequency/Hz	Cycles	Time/h	disk	p_0/MPa
ME00	23.4	1	7200	2	EPB disk	2430
ME01	23.4	1	50000	14	EPB disk	2430
ME02	79	1	14400	4	EPB disk	3650
ME03	42	1	14400	4	EPB disk	3000

6.2.2.3 Friction coefficient

Figure 6.18 depicts the friction coefficient between the M2 ball and EPB disk during the wear measurement under different loads. Same as in the sapphire ball/M2 disk system, the friction coefficient decreases slightly as the wear continues in each measurement due to the development of the contact geometry (see figure 6.19) and lubrication condition, as explained in 6.2.1.2. The mean friction coefficient decreases as the load increases. When the load is 23.4 N, the corresponding maximum pressure is 2430 MPa, and the mean friction coefficient is 0.116 ± 0.054. Under the high load of 79 N, the maximum pressure reaches 3650 MPa, the friction coefficient decreases to 0.049 ± 0.017.

The maximum pressure is 3000 MPa under 42.8 N, but the friction coefficient in the M2 ball/EPB disk system is 0.099 ± 0.042, which is lower than the range proposed in the literature [270] adapted for the thread-forming process (0.15-0.3). But this result can not be used to deny the actual rolling process because the roughness of both the M2 ball

(mirror polished Ra = 0.01 μm) and the EPB disk (polished to 1200 grade, Ra = 0.016 ± 0.004 μm in the sliding direction, Ra = 0.323 ± 0.011 μm) is lower than the roughness on the blank spindle and the die thread.

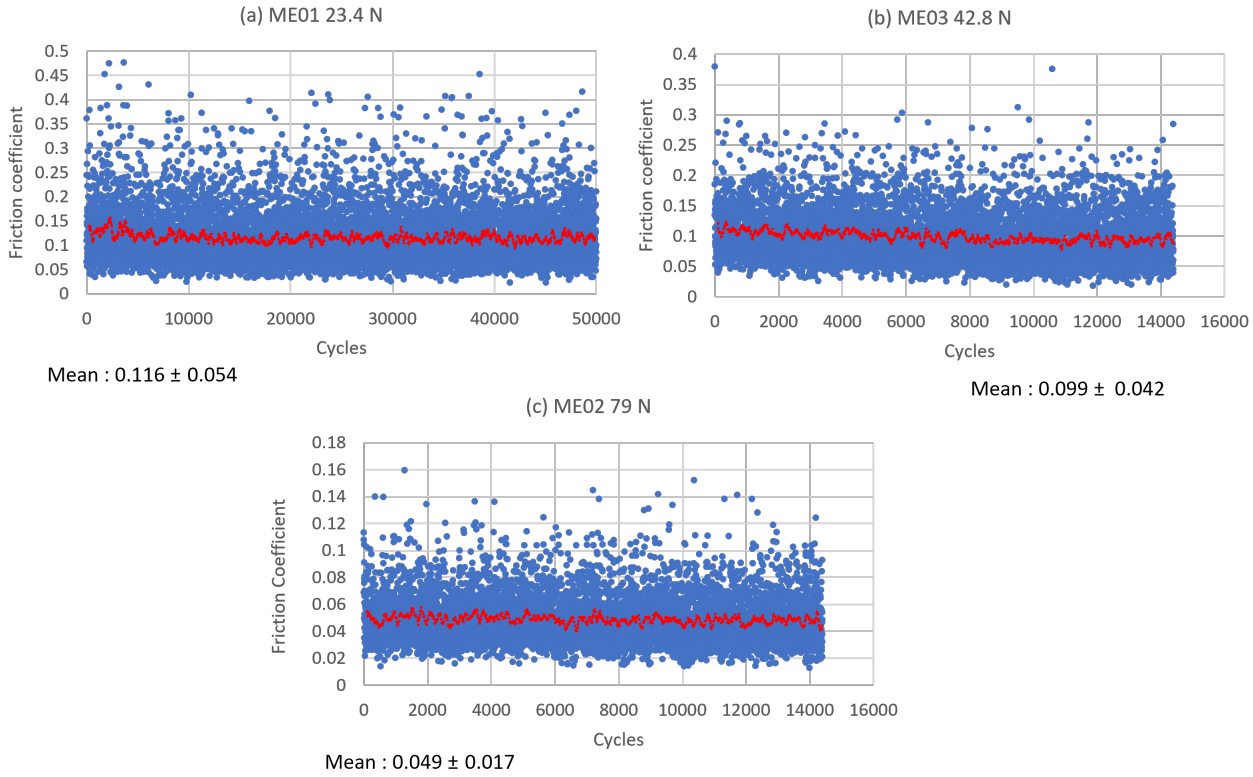


Figure 6.18 – The friction coefficient of the M2 ball/EPB disk wear measurements.

6.2.2.4 Wear track measurements on the EPB disks

The wear tracks on the EPB disks are measured as shown in Figure 6.19. When the number of cycles increases under a low load, the wear volume increases. Figure 6.19 (b) shows both the width and the depth after wear for 14 hours are larger than those after 2 hours in Figure 6.19 (a). The piling-ups are observed due to the locally plastic deformation of the EPB disk under the load of the M2 balls. The height of the piling-up peaks in these two situations (ME00, ME01) is about the same. When the load increases, the plastic deformation becomes more remarkable. The height of the piling-up peaks at 23.4, 42, and 79 N are 0.81, 3.39, and 8 μm, respectively. Similarly, the wear width increases gradually. However, the wear depth develops irregularly due to the occurrence of the transfer film on the ball (the adhesion wear, see 6.2.2.5).

6.2.2.5 Observation of the wear on the M2 balls

Figure 6.20 shows the M2 balls after the wear measurements. Four lights can be controlled during the observation (the bright strips in Figure 6.20), the worn part is located in the light reflection circles. The wear area on ball ME00 is the least, the width seems the same as the wear on the ME01 ball. But the longer time wear area is greater. The wear on the ME03 ball shows two bright parts, of which the analysis will be present later. The wear on ME02 is in the darker area, which seems larger than on other balls.

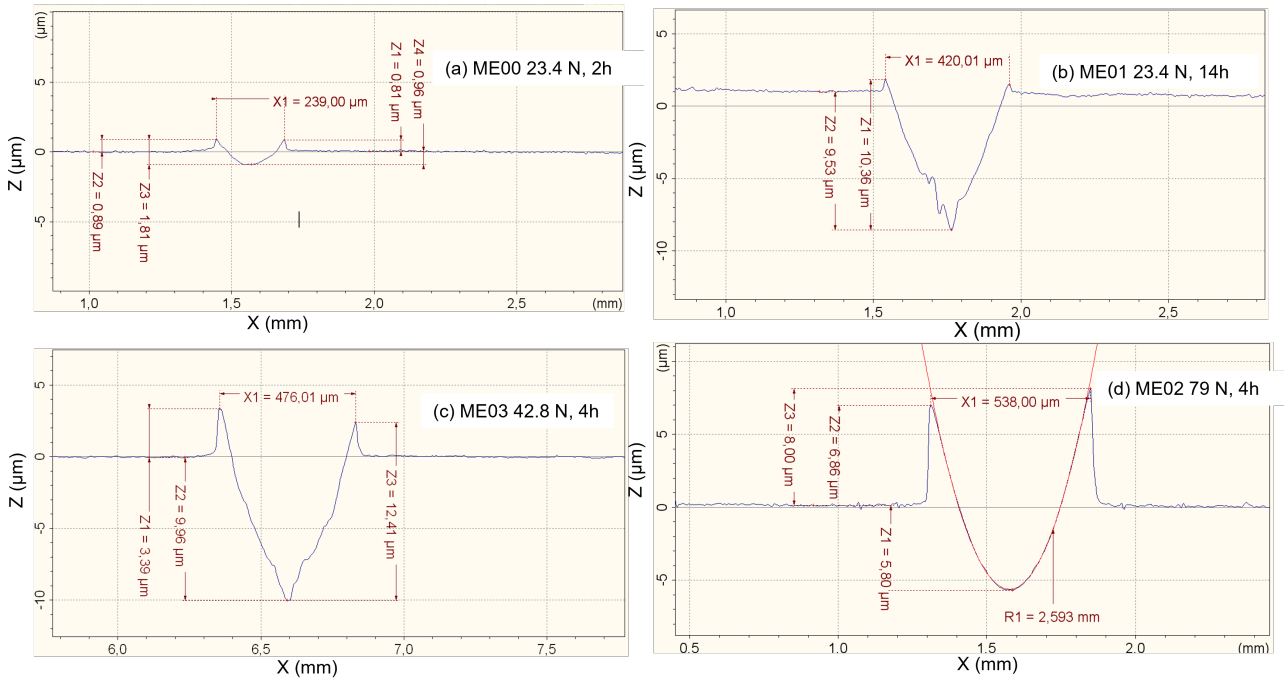


Figure 6.19 – The wear depth measurements on the EPB disks.

The wear on the M2 balls is observed under SEM, as shown in Figure 6.21. Except for the different wear areas, it is found that no significant adhesion wear on the ball worn under 23.4 N, but on those worn under higher loads.

The transfer film has a different chemical composition, as shown in a different color with back-scattered electrons in SEM (Figure 6.22 (a)). Figure 6.22 (b) shows the wear under secondary electron mode, the topology of the transfer film is better presented. The zone in the red square is analyzed with EDS, and the result is shown in Figure 6.23. Spectrum 1 shows the transferred material containing Mn element, which only exists in the EPB disk (23MnB6 steel). Spectrum 2 shows the base material, all the elements exist in M2 steel. Spectrum 3 shows the black dots in the observed zone. They are considered contamination because the Zn element is found, which exists in the lubricant.

In Figure 6.21, the size of the transfer film on the ball worn under 42 N is larger than that under 79 N. This could be explained by Figure 6.24. The formation of transfer film is a characteristic feature of adhesive wear. The material is transferred from one surface to another before being released as a wear particle. The M2 ball rubs against the EPB disk, and 23MnB6 steel leaves and forms a transfer film and covers the wear track (as shown in Figure 6.21). Eventually, the big transfer particle will be removed under the increased stress at their interface with the body material [175, 348].

It is worth to mention that the transfer film could be highly work-hardened and capable of wearing the disk itself. The formation of a transfer film or transfer particles can have a dramatic effect on the wear rate, and it distinguishes adhesive wear from other wear mechanisms [175].

6.2.2.6 Measurements of the wear track on the M2 balls

Due to the small diameter of the balls. It is impossible to perform a 3D measurement with Surfscan 3D devices in the current condition. 2D measurements are carried out in the sliding direction on the wear track, as shown in Figure 6.25 (a). The distance between

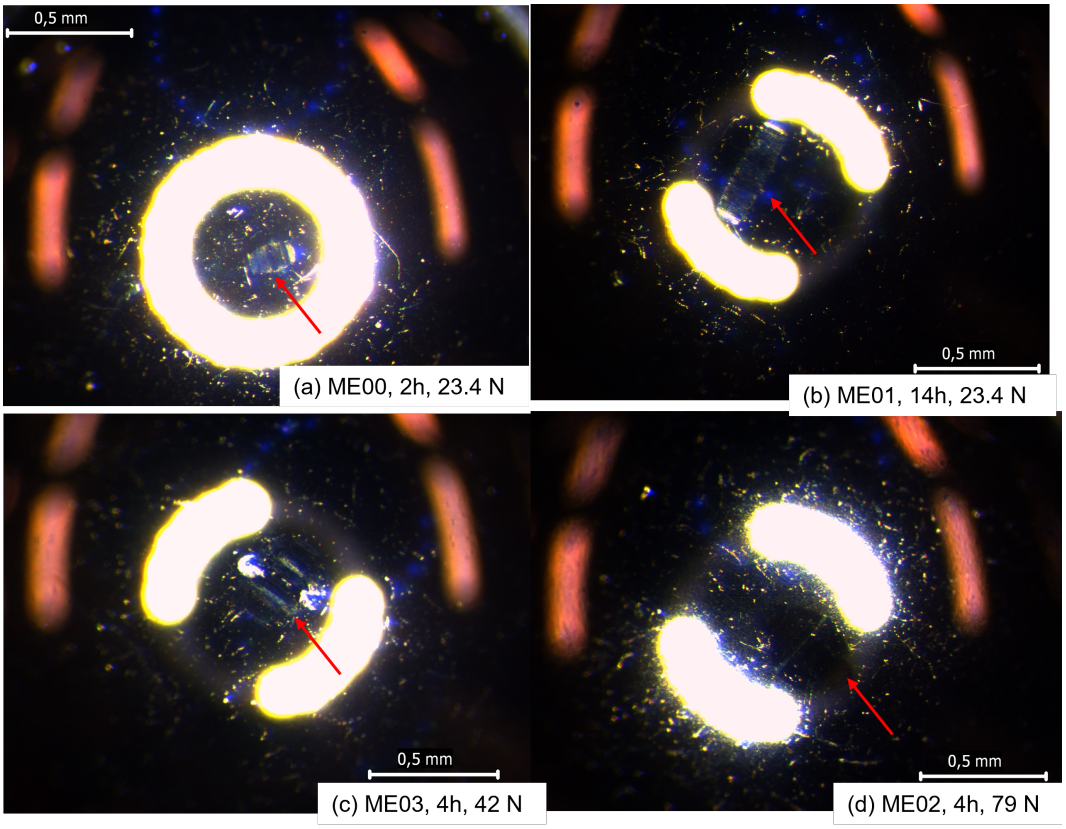


Figure 6.20 – The M2 balls after wear measurements.

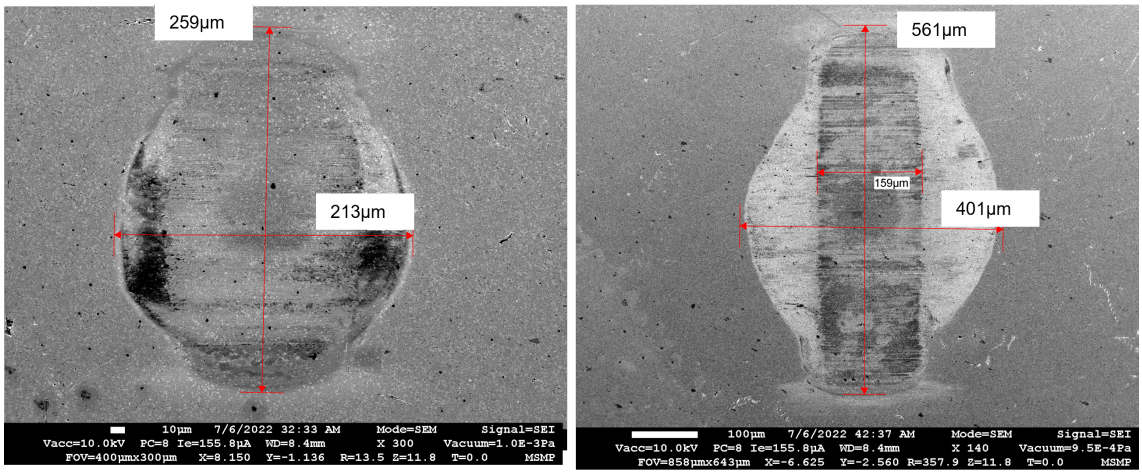
every two measurements is 100 µm. Figure 6.26 shows the wear profiles on ball ME01. The wear is observed in 7 profiles (1-7). The maximum wear depth is 0.37 µm, and the length of this wear track is estimated to be 600-800 µm. The profiles in the transversal direction are also measured, as shown in Figure 6.27. The length of the wear is measured as 709 µm. Nonetheless, it is complicated to determine where the wear locates regarding the curvature of the ball. Then, only the profiles in the sliding direction will be taken into account.

Figure 6.28 and Figure 6.29 show the wear profiles on the M2 ball ME03 (42 N, 4h) and ME02 (79 N, 4h). With a transfer film, it is difficult to measure the wear depth because it is impossible to split materials to perform the geometrical characterization. In profile 7 for the ball ME03 (42 N, 4h), the wear depth of 0.85 µm can be read. However, it should not be taken into account as the maximum wear depth due to the existence of the transfer film. On ball ME02 (79 N, 4h), the wear depth and the transfer film are more evident. The maximum wear depth could be 1.88 µm. The length of these two wear tracks is estimated in the same range as ball ME01.

6.2.2.7 3D analysis of the wear on the ball

The 3D characterization is performed with the help of the software MEX d'Alicona. The surface is tilted ± 5 degrees under SEM, three micrographs are input to generate the 3D analysis, as shown in Figure 6.30. The adhesive wear is observed, but the roughness can not be precisely given on this large scale due to the effect of the sphere and the function limit of the software.

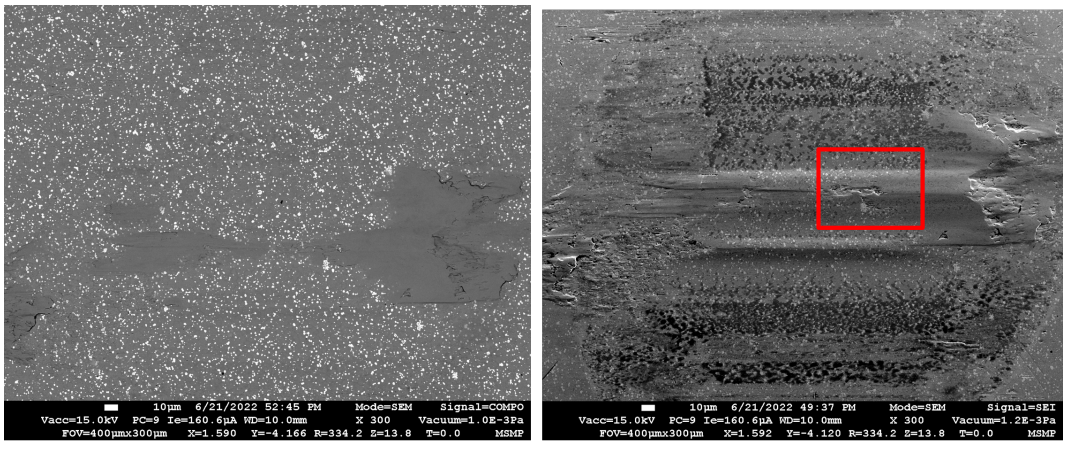
Figure 6.31 shows two profiles along two lines on the wear. Profile (a) is along the



(a) ME00, 2h, 23.4 N (b) ME01, 14h, 23.4 N

(c) ME03, 4h, 42 N (d) ME02, 4h, 79 N

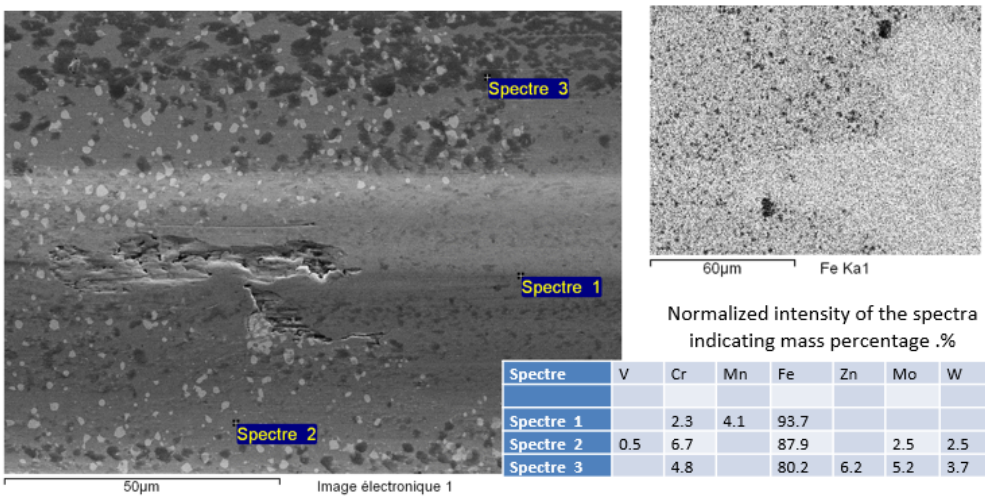
Figure 6.21 – The wear on the M2 balls under SEM.



(a) (b)

Figure 6.22 – The adhesion wear on M2 balls after wearing under 79 N on EPB disk for 4 hours.

sliding direction, corresponding to measurement at 400 µm in Figure 6.28. The profile passes a hole, and the depth is about 4 µm, which agrees to 4.37 µm from the 2D roughness measurement (Figure 6.28). Meanwhile, Figure 6.31 (especially profile (b)) shows the



Normalized intensity of the spectra indicating mass percentage .%

Spectre	V	Cr	Mn	Fe	Zn	Mo	W	Total
Spectre 1		2.3	4.1	93.7				100.0
Spectre 2	0.5	6.7		87.9		2.5	2.5	100.0
Spectre 3		4.8		80.2	6.2	5.2	3.7	100.0

Figure 6.23 – EDS analysis on the transferred film (the adhesion wear), corresponding to the zone in the red square in Figure 6.22.

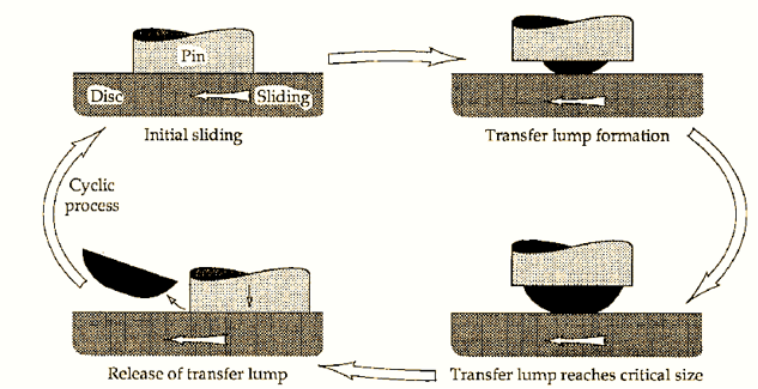


Figure 6.24 – Formation and removal of a transfer particle [175, 348].

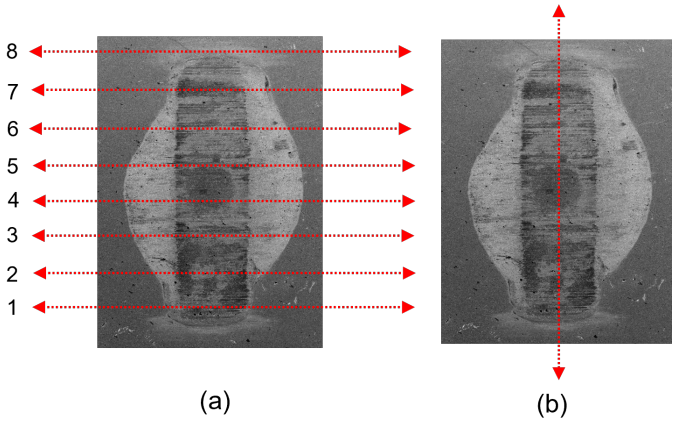


Figure 6.25 – The measurement on the wear track of M2 ball ME01 (23.4 N, 14h), (a) on the sliding direction, (b) transversal direction.

influence of the transfer film on the sphere perfection (in the red circle).

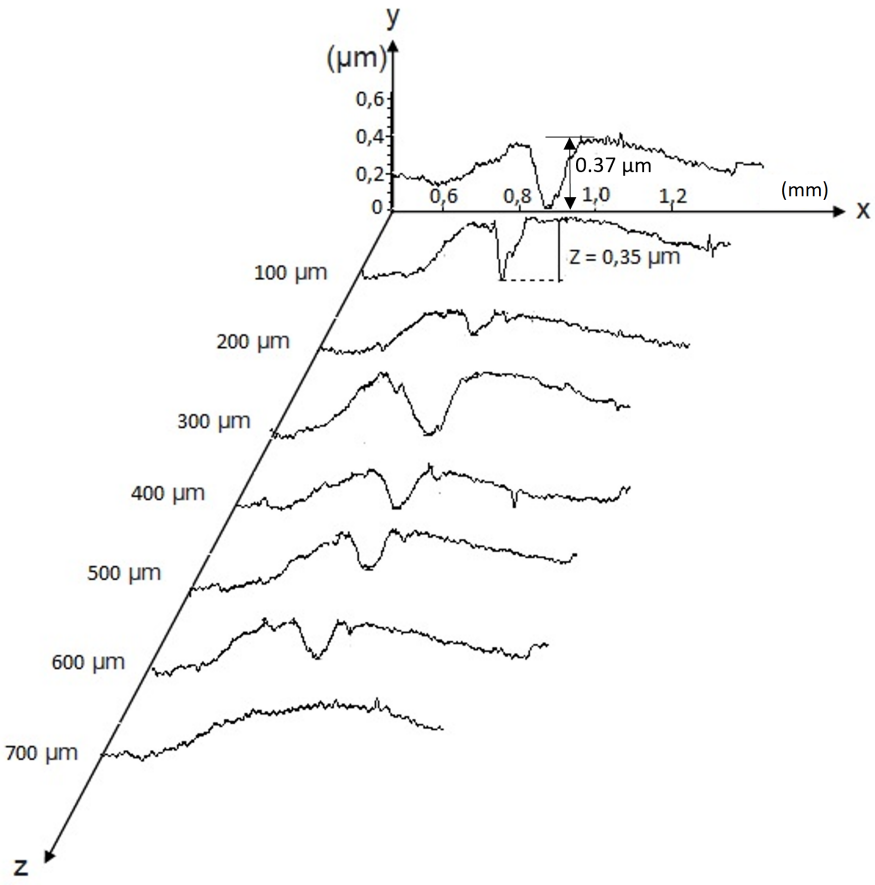


Figure 6.26 – The wear track profile on the sliding direction of M2 ball ME01 (23.4 N, 14h).

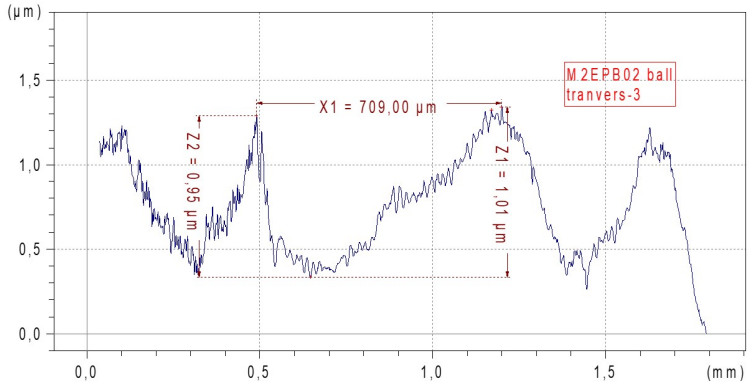


Figure 6.27 – The wear measurement of M2 ball ME01 (23.4 N, 14 h) on the direction perpendicular to the sliding.

6.2.3 Conclusions of the wear on non-nitrided M2 steel

The Sapphire ball/M2 disk wear measurements on the M2 steel disk show the effect of wear parameters on the friction coefficient and the wear. Increasing the load decrease the friction coefficient but increase the wear rate. The frequency is related to the sliding speed, but it doesn't influence the wear and the friction coefficient. The lubricant is, on

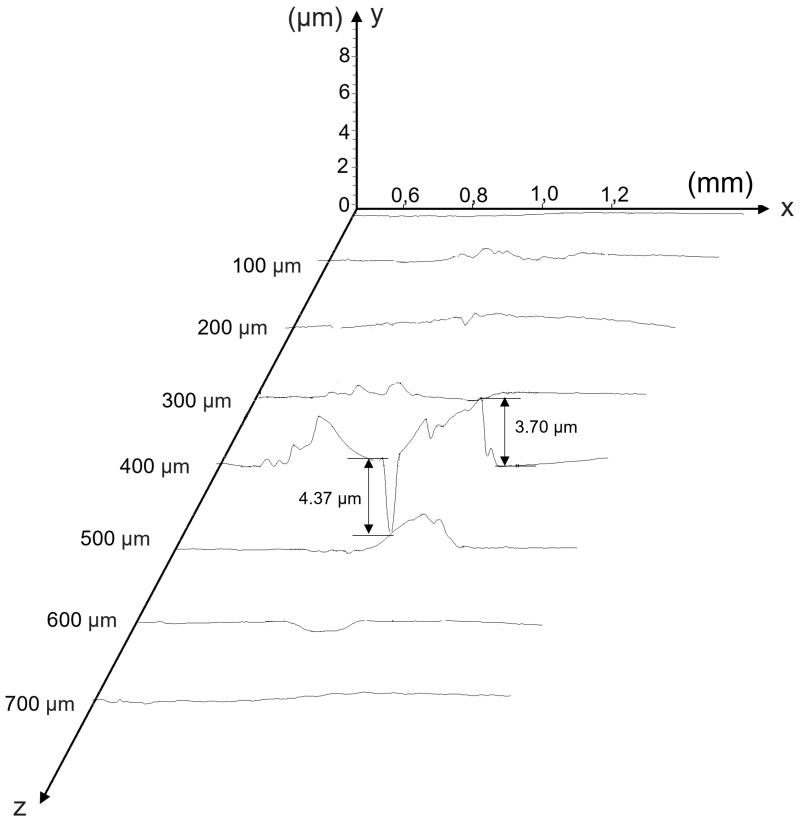


Figure 6.28 – The wear profile on the sliding direction of M2 ball ME03 (42 N, 4 h).

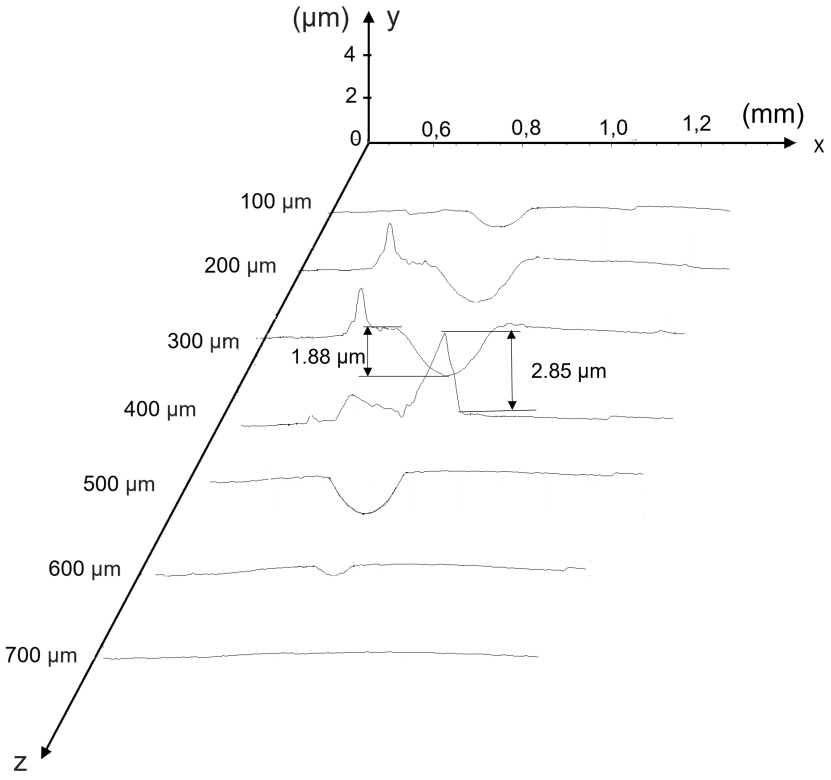


Figure 6.29 – The wear profile on the sliding direction of M2 ball ME02 (79 N, 4 h).

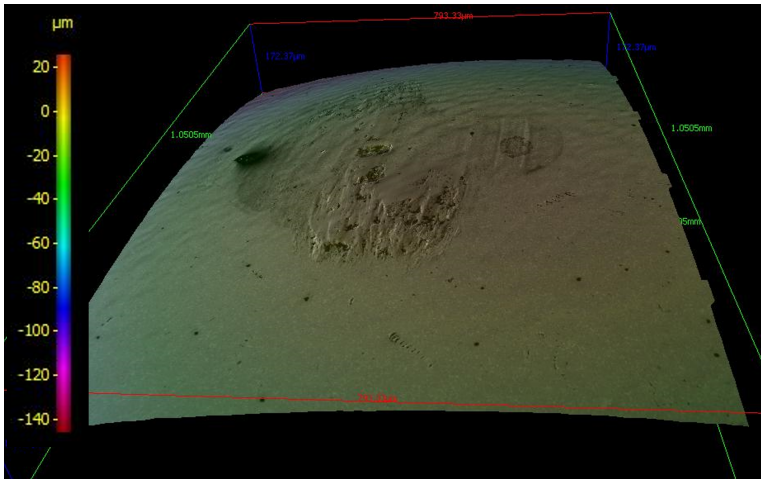


Figure 6.30 – 3D view of the wear on M2 ball ME03 (42 N, 4h).

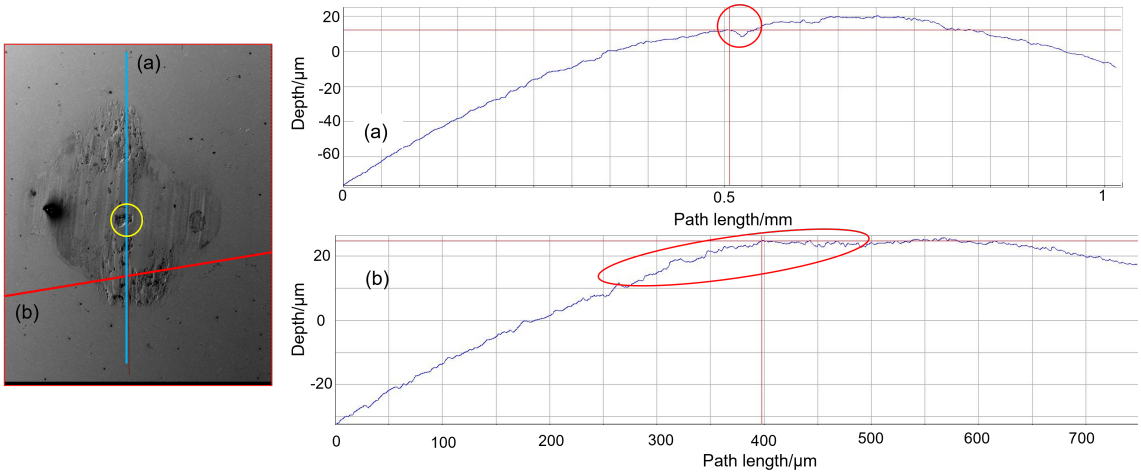


Figure 6.31 – Linear profiles on the wear on M2 ball ME03 (42 N, 4h).

the contrary, a very important factor impacting the wear. The M2 ball/EPB disk wear measurements demonstrate the evolution of the adhesion wear under different loading along with the effect of the wear parameters.

6.3 Effect of nitriding on the wear resistance of M2 steel

According to the studies on gas nitriding kinetics of M2 steel, nitriding with 4 groups of parameters is applied to the M2 disks and balls. The hardness and residual stress profiles in M2 samples are shown in Figure 6.32.

6.3.1 Wear of nitrided M2 disk

6.3.1.1 The wear measurements

If we consider a hypothetical average lifetime of 10^5 cycles for a rolling die, and because one alternative movement cycle allows two times loading contact on the disk, the final working cycle number of 5×10^4 is then considered for the measurements on the M2 disks. The higher load of 79 N leaves the non-nitrided M2 disk with similar microcracks (see 6.2.1) as on the crest of the rolling die thread. Hence, it is chosen to continue the wear

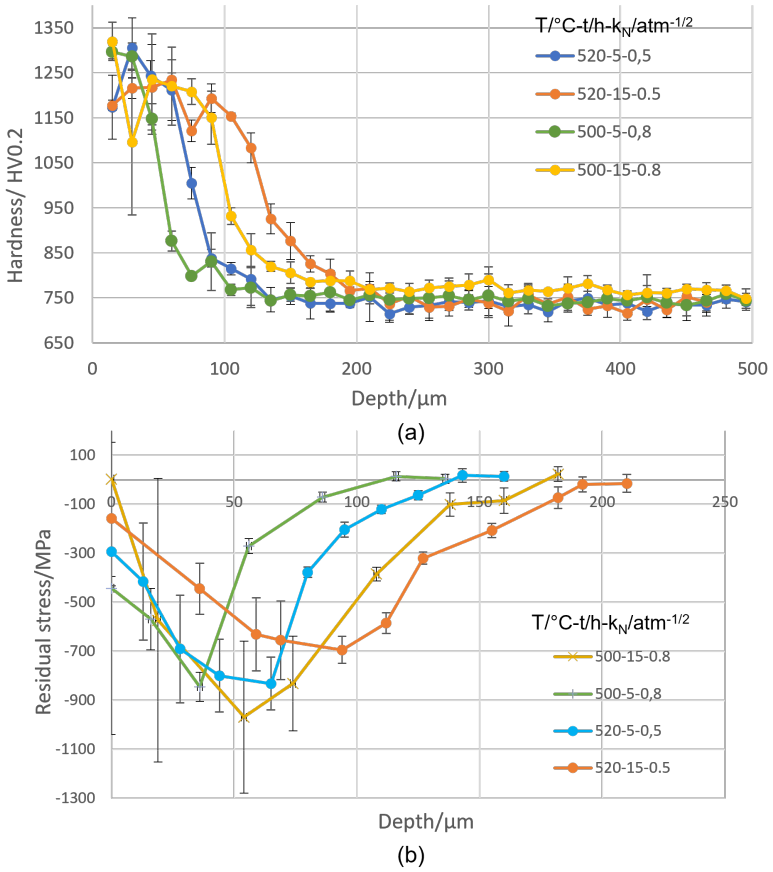


Figure 6.32 – The nitriding profiles of the M2 disk (the profiles are measured on other equivalent nitrided M2 steel samples) used for wear measurements (a) hardness, (b) residual stress.

measurement on the nitrided M2 steel.

6.3.1.2 Friction coefficient

The friction coefficient during the wear of sapphire ball on nitrided M2 disks is shown in Figure 6.33.

Compared to the non-nitrided M2 sample, after nitriding, the friction coefficient stays at the same level in the first 6000 contacts. However, except for the 500-5-0.8 nitrided sample, all the other three friction coefficient profiles show an increase at about 6000 contacts. This is probably brought by the sudden brittle cracks on the sapphire balls, as shown in Figure 6.34. The 500-5-0.8 nitrided M2 disk causes a smooth flat removal from the sapphire ball, while the sapphire balls working against the other nitrided disks show brittle cracks in the damaged part. This is assumed to concern the more profound nitriding depth of the M2 steel disks.

6.3.1.3 Wear track measurements on the nitrided M2 disk

As the round M2 disk is too big to be nitrided in the furnace, M2 samples are used to study the nitriding effect on wear, as shown in Figure 6.35.

Thanks to the high case hardness and compressive residual stresses in the nitrided M2 disk, the wear resistance is significantly improved (see in Figure 6.36). The reference M2 disk (non-nitrided) has a wear depth of about 0.7 µm, while no evident wear depth can

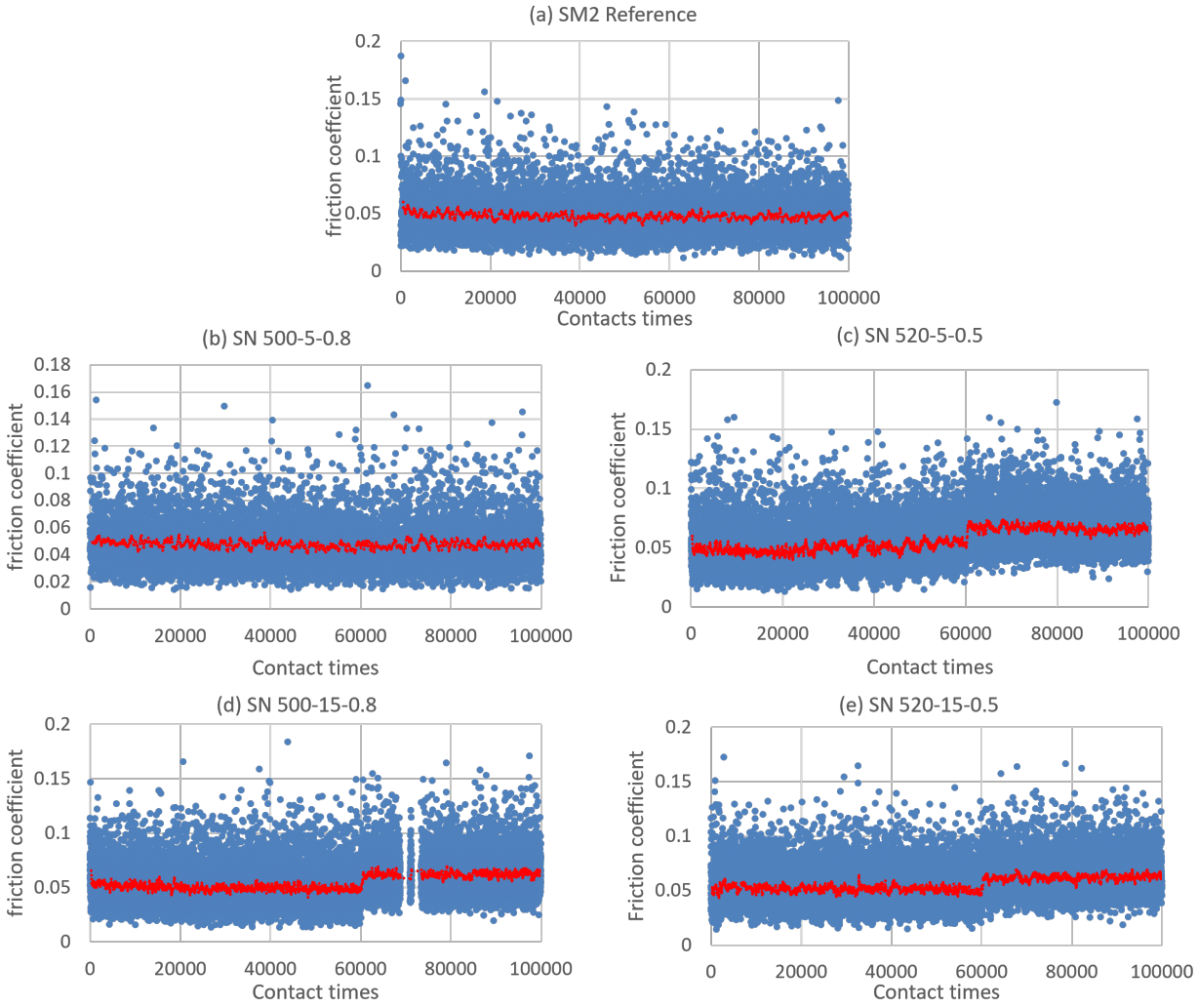


Figure 6.33 – The friction coefficient as a function of wear cycle on the nitrided M2 disk.

be measured on the nitrided disks. However, it is difficult to rank these four parameters because the worn zone can hardly detect even with a stylus with a radius of 2 μm. This is the product of the coupling of the high surface hardness and compressive residual stress under the surface. The surface hardness of these four nitrided M2 samples is nearly the same and higher than non-nitrided M2 steel. On the other hand, the maximum shear stress (the Tresca stress in Hertz contact) locates at 55 μm under the surface (assuming the Youngs modulus and Poisson ratio of M2 steel do not change after nitriding), and the residual stresses of the four applied nitriding profiles show high compressive levels at this depth. Table 6.4 summarizes the measurements and the wear depth.

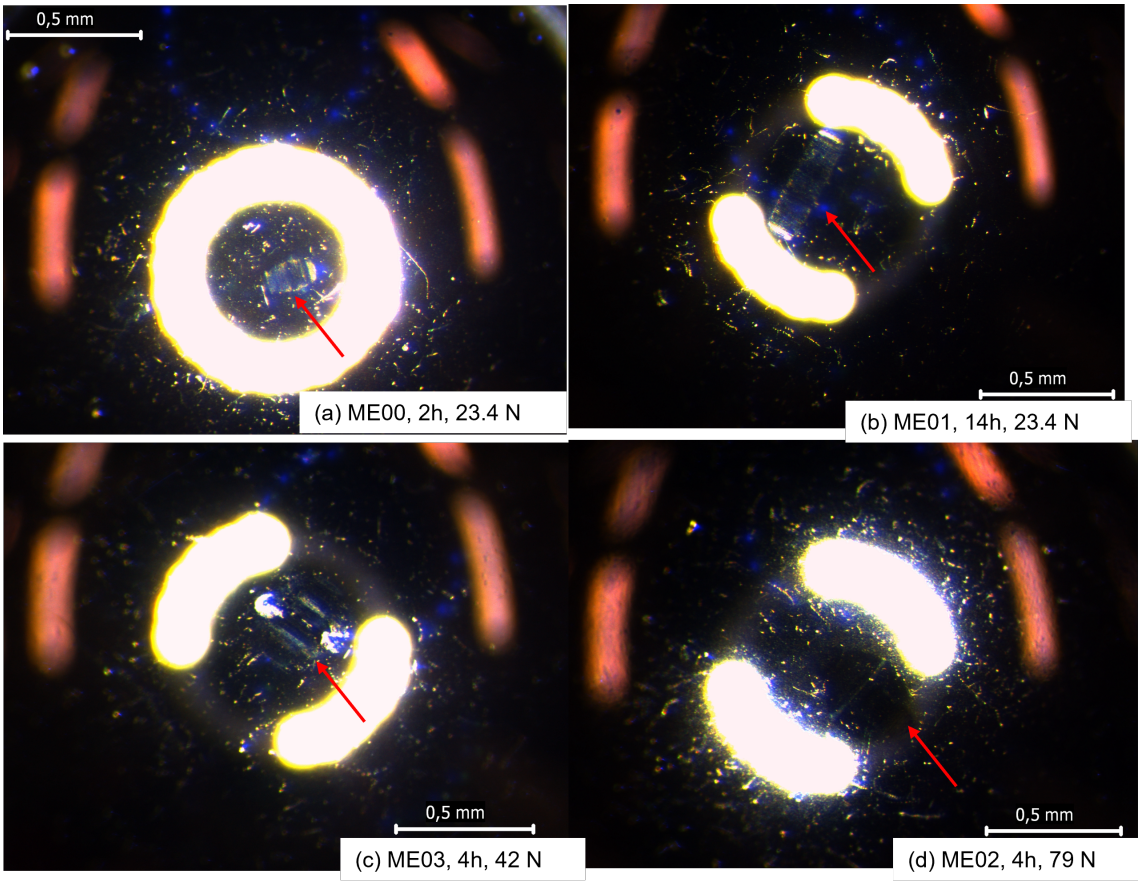


Figure 6.34 – The damage on the sapphire balls after wear measurements.



Figure 6.35 – The M2 sample disk used to study the nitriding effect.

Table 6.4 – Wear measurements on nitrided M2 steel disks.

Measurement	**Load /N**	**Cycles**	**Nitriding parameters T/°C-t/h-k_N/atm$^{-1/2}$**	**Wear depth/µm /µm**
SN520502	23.4	50000	520-5-0.5	<0.1
SM2 REF	79	50000	Not nitrided	0.7
SN520503	79	50000	520-5-0.5	<0.1
SN520151	79	50000	520-15-0.5	<0.1
SN500151	79	50000	500-15-0.8	<0.1
SN500501	79	50000	500-5-0.8	<0.1
SN500152	79	30000	500-15-0.8	<0.1

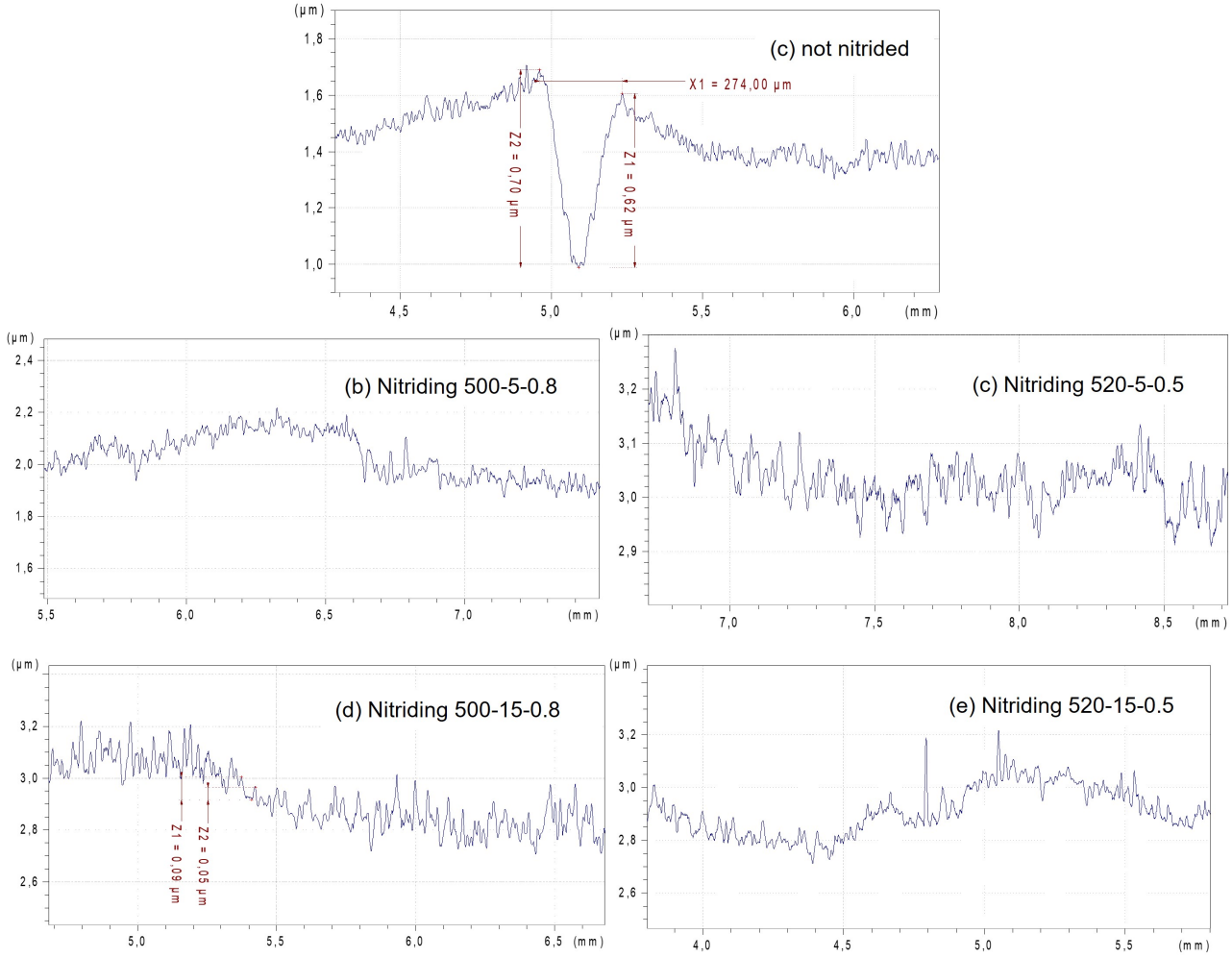
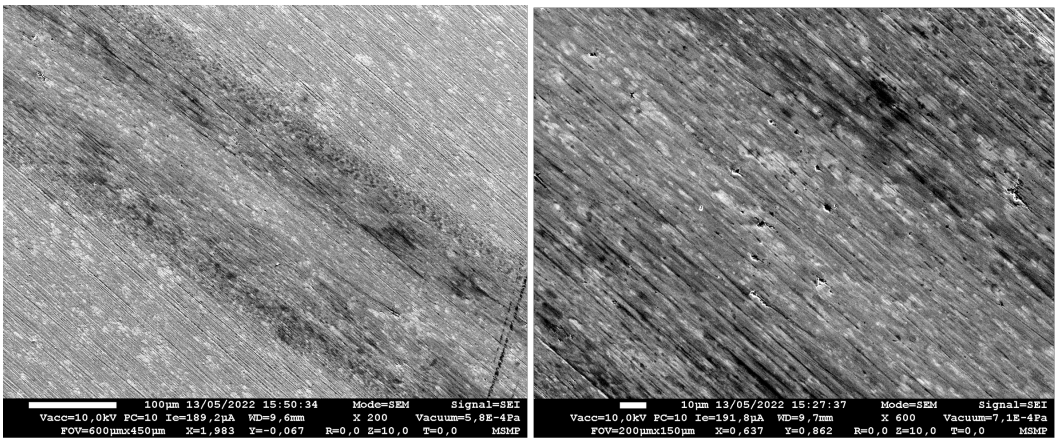


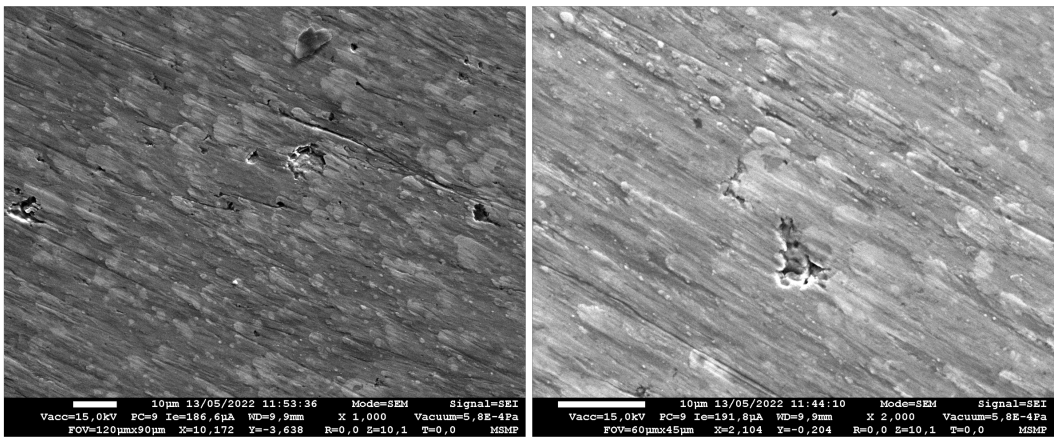
Figure 6.36 – The wear track profiles on the non-nitrided and nitrided M2 disks.

6.3.1.4 Observation of the wear on the nitrided M2 disk

The wear tracks are observed under SEM (Figure 6.37). Even though the wear depth on the nitrided M2 disk is regardless, some wear on the worn surface is observed to start to form, and this phenomenon is similar to the wear type on the thread flank of the rolling die observed in Figure 6.38 (or see 4.3). Sapphire particles are observed on the M2 disks, but it is not considered adhesive wear but debris from the damage of the sapphire ball, as shown in Figure 6.39.



(a) Nitrided disk 520-15-0.5



(b) Nitrided disk 520-5-0.5

Figure 6.37 – The microphotograph of the nitrided M2 disks after wear measurements.

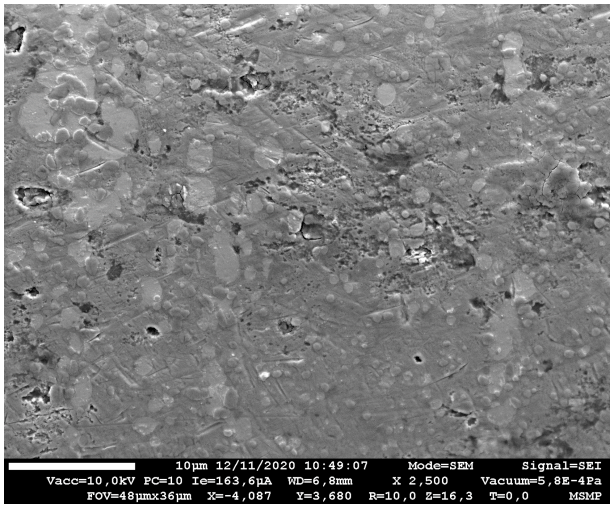


Figure 6.38 – The surface wear on the flank of the rolling die thread.

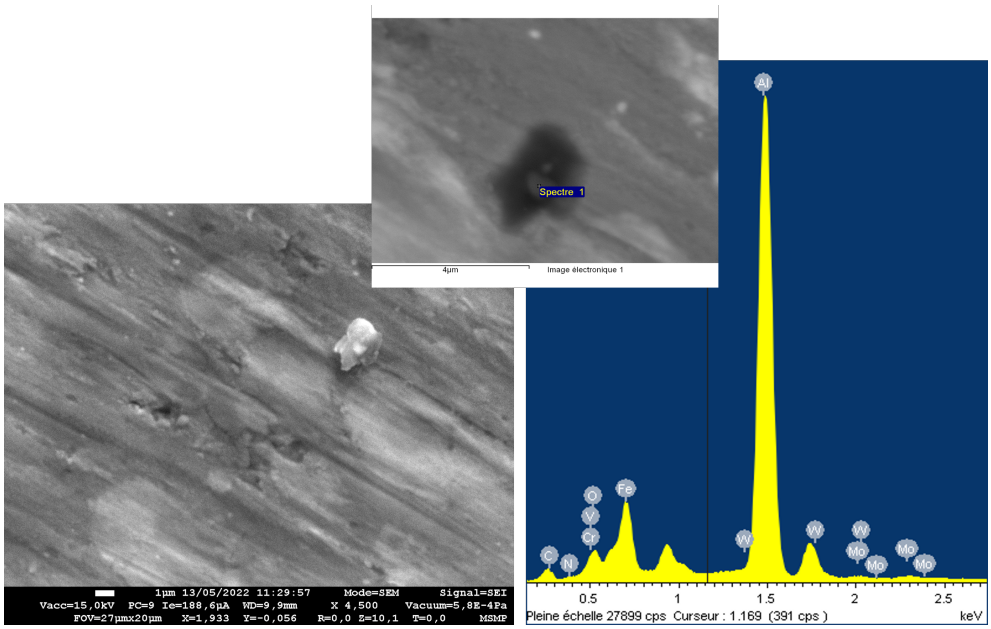


Figure 6.39 – The EDS spectrum of the particle found on the M2 disk after the wear measurement.

6.3.2 Wear on nitrided M2 ball

6.3.2.1 Nitriding layer of the M2 ball

The M2 balls are nitrided in the thermogravimeter in the MSMP laboratory with the selected parameters. The nitriding layer in the ball (Figure 6.40) has the same microstructure as in the M2 disk samples. In Figure 6.40 (b), the cementite can be observed at the grain boundary thanks to the contrast under back-scattered electron mode.

The hardness profile of M2 balls after nitriding is compared to that of M2 disk samples. In Figure 6.41, the hardness profile shows the same effective nitriding depth (effective nitriding depth Z_{eff} is the depth where HV = HV(core)+100 HV) and the tendency as that in the M2 disk despite the higher hardness. As the M2 balls have a higher core hardness, this shifted result for the nitrided layer was expected according to other similar studies on low alloy steels (in MSMP laboratory).

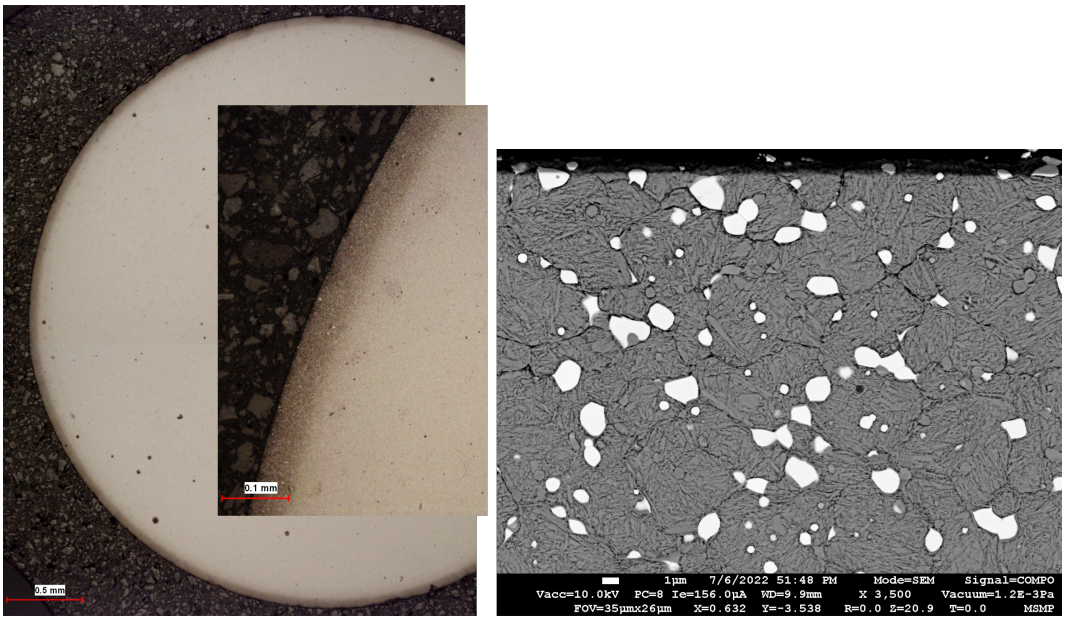


Figure 6.40 – The microstructure of nitriding layer of M2 ball (a) under an optical microscope, (b) under SEM. The nitriding parameter is 500 °C-5 h-0.8 $atm^{-1/2}$.

6.3.2.2 Wear measurements on nitrided M2 balls

The wear tracks on the EPB disks (Figure 6.42) show a similar depth (around 6 µm) and width (500-550 µm). The observation of the wear on the M2 balls under SEM is shown in Figure 6.43. The wear size measured under SEM is 500-600 µm for the length and 400-420 µm for the width for all these 4 balls. According to the observation under the back-scattered electron mode (Figure 6.43 (b)), no large amount of transfer film (adhesive wear) is observed on the nitrided ball wear.

The measurements are summarized in Table 6.5. The friction coefficient increases slightly after nitriding (Figure 6.44). Among them, the 500 °C-15 h-0.8 $atm^{-1/2}$ nitrided ball shows a mean friction coefficient closest to the non-nitrided ball, and the 520 °C-5 h-0.5 $atm^{-1/2}$ nitriding leads to the greatest increase in the friction coefficient. This slight difference might be due to the difference in the roughness of the sliding direction. The

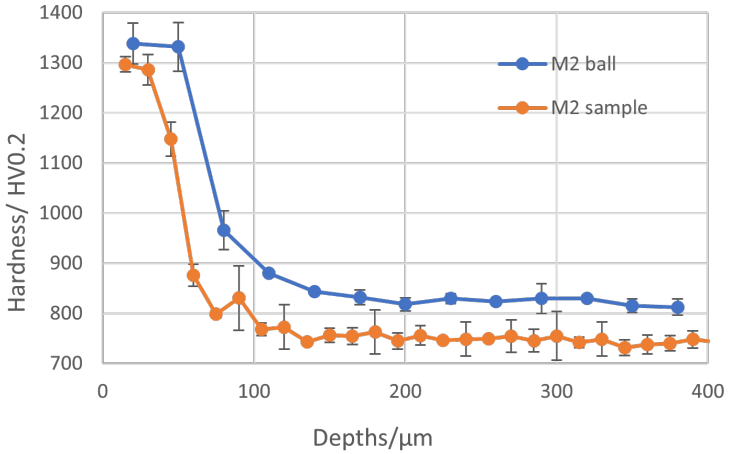


Figure 6.41 – The in-depth hardness profile of nitrided M2 balls and M2 sample.

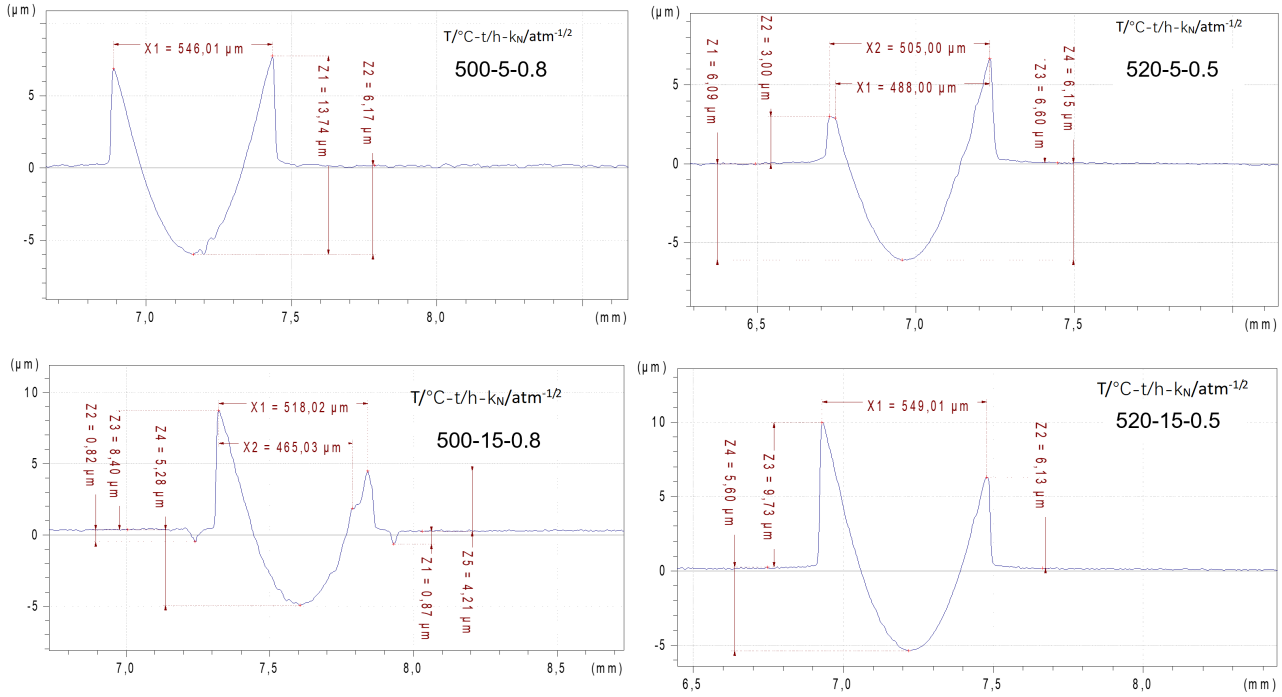


Figure 6.42 – The wear profiles on the EPB disks.

roughness after the 1200-grade polishing is lower in the polishing direction, which is also set as the sliding direction. However, a different angle can be brought during the manual measurement setup.

Table 6.5 – Wear measurements on nitrided M2 steel balls.

Measurement	**Load** /N	**Cycles**	**M2 ball nitriding** $T/°C\text{-}t/h\text{-}k_N/atm^{-1/2}$	**Friction coefficient**	**Wear depth** /µm
M2EPB02	79	14400	not nitrided	0.049±0.017	1.86
ME500501	79	14400	500-5-0.8	0.058±0.022	0.38
ME520501	79	14400	520-5-0.5	0.066±0.023	0.77
ME500151	79	14400	500-15-0.8	0.053±0.02	0.81
ME520151	79	14400	520-15-0.5	0.058±0.02	0.34

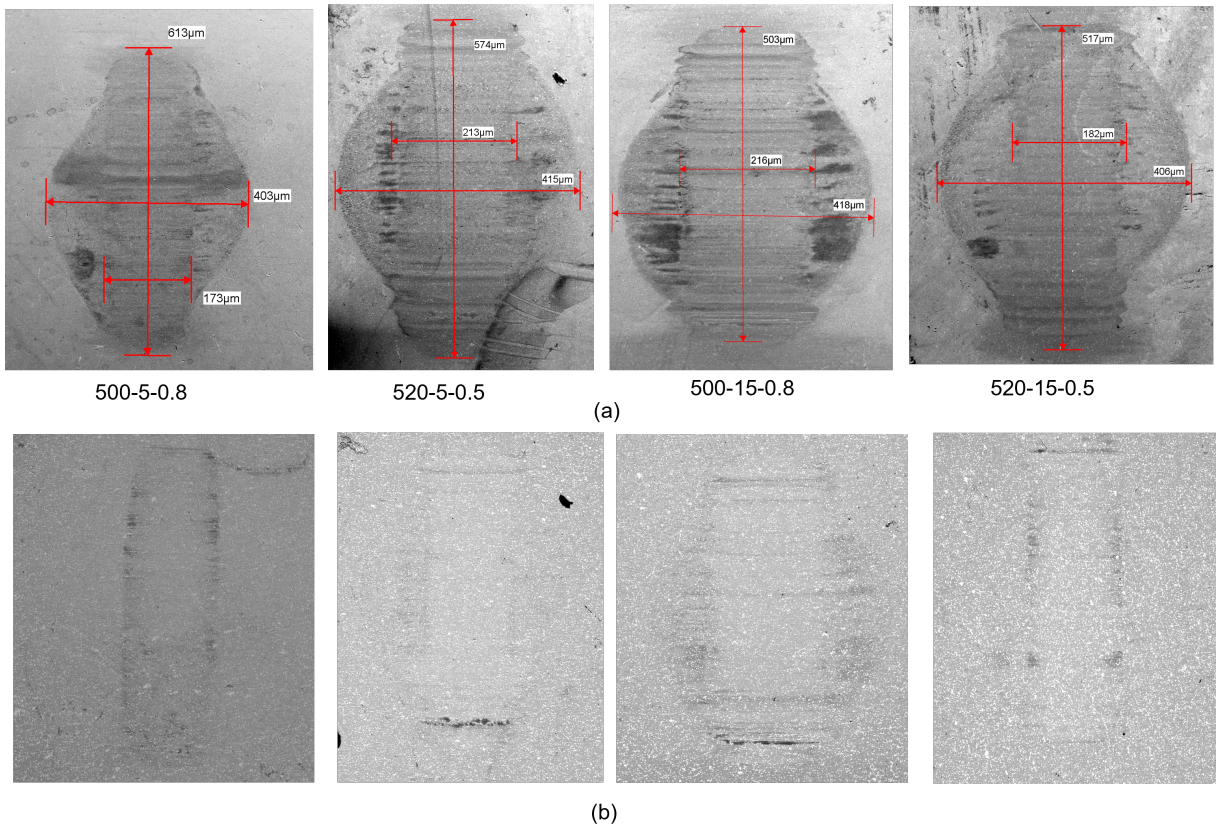


Figure 6.43 – The observation of the wear on the M2 balls under SEM (a) with secondary electron, (b) with back-scattered electron.

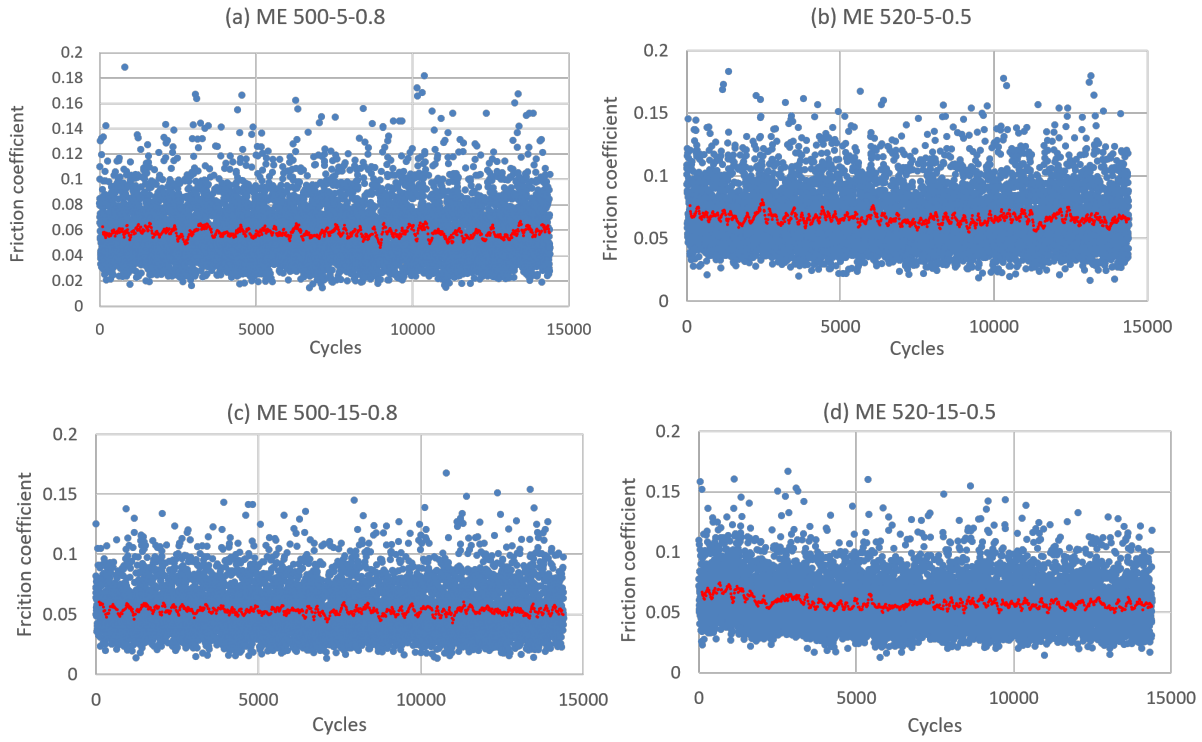


Figure 6.44 – The friction coefficient as a function of wear cycle (nitrided M2 balls on the EPB disk).

The wear depth is measured in the same way as in 6.2.2.6. Figure 6.45 shows the wear profile of the 500 °C-15 h-0.8 $atm^{-1/2}$ nitrided M2 ball. The most considerable wear depth is 0.81 μm among the wear profiles of all these 4 balls. Yet, the measurement is influenced by the positioning of the ball (the ball must be removed from the wear system, and the worn point placed manually on the stage for the topographical measurement), and the results should be taken with precautions. The wear profiles of other balls and the original profiles in 2D can be found in Appendix C (Figure C.1, C.3, C.4). The 3D analysis of the

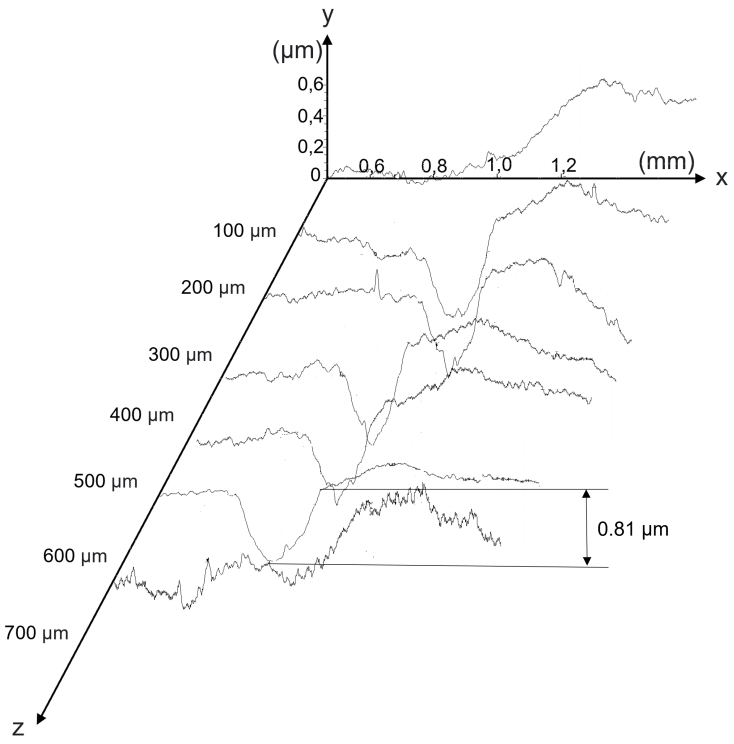


Figure 6.45 – The wear profiles on the M2 ball nitrided with 500 °C-15 h-0.8 $atm^{-1/2}$.

ball wear is performed. Figure 6.46 and Figure 6.47 show the 3D profile of the wear on M2 ball ME500501 and ME520501. The effec of the wear on the initial geometry of the sphere is negligible.

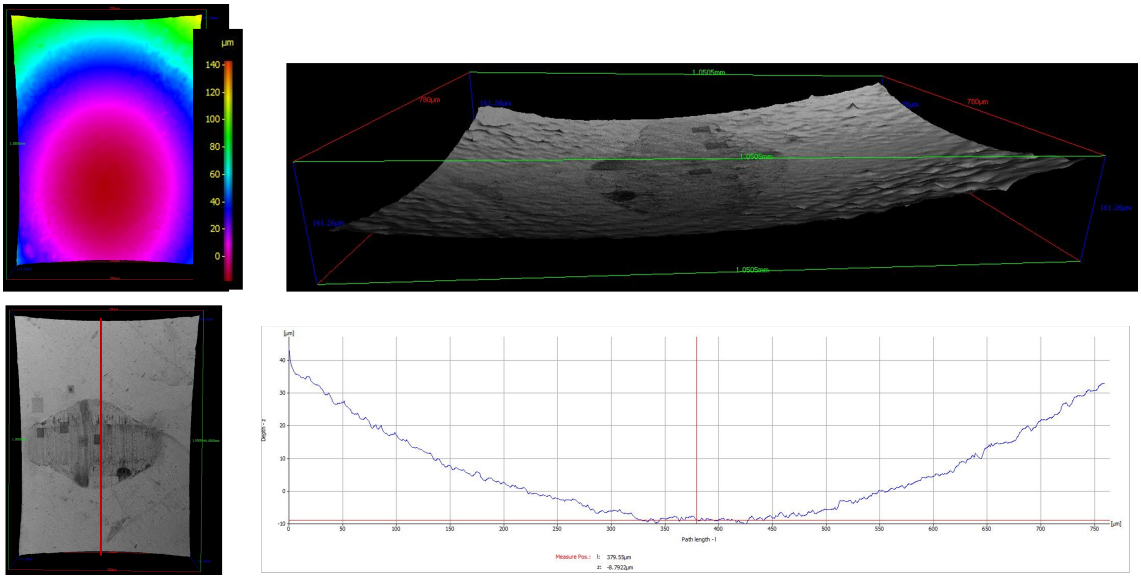


Figure 6.46 – The 3D view of the wear on the M2 ball nitrided with 500 °C-15 h-0.8 atm$^{-1/2}$.

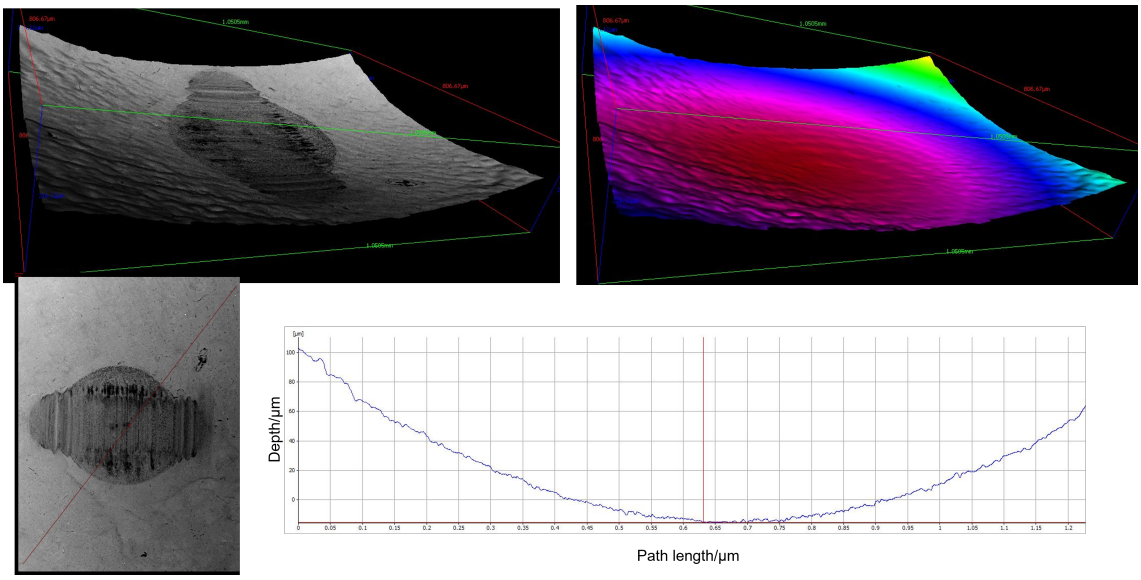


Figure 6.47 – The 3D view of the wear on the M2 ball nitrided with 520 °C-5 h-0.5 atm$^{-1/2}$.

6.4 Conclusions

To study the wear resistance of M2 steel and the effect of gas nitriding, 2 sections (four groups) of experiments were carried out. By using the sapphire ball/M2 disk system, cyclic loading can be obtained to study the fatigue behavior of the M2 steel.

The friction coefficient decreases when the load increases due to the change in the lubrication condition. The wear depth is strongly linked to the load and the lubrication but not the frequency. The surface stress asymmetry of the rolling contact (or the sliding effect) is low due to the low roughness of the sapphire ball and the M2 samples.

Gas nitriding with all selected parameters improves the wear resistance of the M2 disk effectively (from 0.7 µm to less than 0.1 µm, about 85%). But it is difficult to analyze the difference between these parameters because the wear tracks on nitrided M2 disks are hardly detected by the measuring device (Surfscan with a stylus with a radius of 2 µm and a resolution of 4 nm).

The high wear resistance is considered contributed by the high surface hardness, and an appropriate effective nitriding depth which allows a desired compressive residual stress profile. According to the Hertz theory, in the sapphire ball/M2 disk rolling contact, the maximum shear stress (Tresca) depth is 55 μm under the surface when the load of 79 N is applied. The residual stresses are high in compressive at that depth for all nitridings proposed.

M2 ball/EPB disk system realizes the actual contact of these two materials. The adhesive behavior is investigated, and a more significant wear rate is created on M2 steel for the convenience of detection. But as the ball's contact point continuously submitted a high pressure, no fatigue behavior could be studied. The results demonstrate that gas nitriding significantly improves the adhesive wear resistance of M2 steel, increases the friction coefficient effectively, and reduces the wear depth from 1.86 to 0.34 μm. The M2 balls have a higher core hardness and different microstructure due to the powder metallurgy fabrication method, which contributes to good wear resistance compared to the casted ones.

CHAPTER 7

CONCLUSIONS AND PERSPECTIVES

M2 high-speed steel is widely used to fabricate the rolling dies for cold forming the threads on the high-quality required screws, especially the safety-related component in automobiles (electronic parking brake screws are concerned in this work, also written as EPB). However, the work performance and the lifetime of the M2 dies need to be improved in the industry. Plasma nitriding is often applied on the rolling die for surface strengthening, which is geometry sensitive. This work focus on the rolling die analysis and gas nitriding on M2 steel, aiming to define nitriding parameters to improve the mechanical property of thread rolling die . Some results will be concluded.

7.1 Conclusions

The study on the current rolling dies

— Type E rolling dies are fabricated with M2 steel by casting. Strong carbide segregation is present in the microstructure. The core hardness of the die is about 900 HV. The surface plasma nitriding on the rolling dies is non-homogeneous. The nitriding depths show a large difference between each die. G rolling dies are made with powder metallurgy, but they are not made from M2 steel. Their microstructure is more homogeneous and the grains are finer. The salt bath nitriding offers the dies homogeneous case layers.

— Generally, the lifetime of the rolling dies increases as the maximum surface hardness and the effective nitriding depth increase (Figure 4.55).

— The cracks initiate from several micrometers below the surface. The initiation of microcracks often requires contact pressure, high shear stress and the inclusions (carbides) located at a critical position in the subsurface. Meanwhile, the morphology of the carbide inclusions is critical to abrasive wear resistance.

— Dang Van criterion shows that failures can initiate from the thread crest in the later period of the rolling process. Nitriding functions well in the steel close to the surface to prevent fatigue failure initiation by increasing the hardness and generating compressive residual stress.

Gas nitriding of M2 steel

— Surface mechanical conditions affect nitriding kinetics. Compared to the surfaces finished with grinding and polishing, the sandblasted surface gains the least nitrogen due to the high level of compressive residual stress before nitriding. The ground surface is the most difficult to be homogenously nitrided because of the contamination that is hard to remove from the particular surface roughness. The polished surfaces adsorb more nitrogen contrary to the sandblasted surfaces. The effect of roughness is considered but hard to be proved because different roughnesses induced by mechanical force are always coupled with different residual stress levels. The polished surfaces obtain easily homogeneous case layers because the contaminant is easy to be removed.

— A higher nitriding temperature and/or nitriding potential can promote nitriding kinetics, consequently, increase nitriding depth and evolve the compressive residual stress more profound. However, precipitates coarsening and decarburization kinetics are also increased at the same time.

— The pseudo-Lehrer diagram for M2 has been updated. The nitriding potentials reaching α/γ' limit are found for M2 steel nitriding at 500 and 520 °C to control the compound layer formation, which are 0.8 and 0.5 $atm^{-1/2}$, respectively.

— The hardness profile is consistent with the N concentration profile. The maximum hardness of the nitriding layer appears when the compound layer is formed, and will not keep increasing if nitriding continues, because the maximum nitrogen concentration at the interface of the diffusion zone and compound layer is limited by the chemical composition of iron nitrides.

— The residual stress profile involves carbide transformation and carbon redistribution along with nitrogen enrichment and nitride precipitation. When carbides start to decompose, carbon accumulates at a certain depth, more precipitates are formed. The extra volume expansion leads to the maximum compressive residual stress. The decrease in compressive residual stress can be the result of decarburization due to the reaction between carbon and the atmosphere, the precipitates coarsening depending on the N concentration nitriding time t, and the phase transformations that lead to negative volume expansion (needs to be proved with more experiments).

— Nitriding impacts also the core hardness. Increasing nitriding time or temperature decreases the core hardness.

The wear measurements of M2 steel before and after nitriding

Abrasive wear is the most rapid form of wear. A justified hardness and metallurgical phase can considerably enhance the abrasive wear resistance of steels. The high content of carbon and alloy elements provides M2 steel with high amounts of inclusions of hard carbides (chromium and molybdenum carbides) that provide additional abrasive wear resistance. Raising the surface hardness significantly increases the wear resistance of the steel. Adhesive wear is another serious form of wear that may cause high wear rates and unstable friction coefficients. Adhesion can be reduced by increasing the surface roughness or hardness of the contacting bodies.

Four sets of nitriding parameters are proposed from the study of nitriding kinetics. They are applied to the M2 steel balls and disks to study their wear behavior in two

different contact systems (M2 ball/EPB disk, Sapphire ball/M2 disk). The results are as concluded:

— The wear rate is strongly influenced by the load applied on the pin, but is less sensitive to the frequency and the number of cycles.

— Gas nitriding with all selected parameters improves the wear resistance of the M2 disk from 0.7 μm to less than 0.1 μm, about 85% (in the sapphire ball to M2 disk system).

— The wear depth on the nitrided M2 ball decreases to 0.34 μm from 1.86 μm on the non-nitrided M2 ball (in the M2 ball/EPB disk system).

— Nitriding significantly improves the adhesive wear between the M2 steel and 23MnB6 steel (the material for manufacturing the EPB screw studied in this work).

— The improvement of the wear resistance after nitriding results from the coupling of increased hardness and the high compressive residual stress level at the surface layer. The hardness reaches the maximum value at the surface while the compressive residual stress level at the maximum shear stress depth (55 μm in the case of contact between the Sapphire ball on M2 disk under the load of 79 N under the surface) is very high.

7.2 Perspectives

The scientific perspectives to be given to this work are the following:

— To characterize more rolling dies and find a more precise relation between the nitriding condition and the working performance.

— To further study the pseudo-Lehrer diagram for M2 steel by finding more nitriding potentials at different temperatures for α/γ' and γ'/ε limits.

— To study the phase transformations experimentally of M2 steel during nitriding with the help of X-ray diffraction and TEM (Transmission Electron Microscopy) and to study the effect of surface heterogeneities (carbides) on nitriding.

— To discover nitriding with designable programs. For example, higher temperature and nitriding potential could be applied at the beginning of nitriding to obtain a high nitrogen concentration at the steel surface (lower than that needed to form iron nitrides), then lower temperature and potential could be used to finish the nitriding layer growth. This could decrease the nitriding time while controlling the compound layer formation and decarburization.

— To improve the wear measurement with a more representative condition as the real rolling process.

— To decouple the effect of roughness and residual stress on nitriding kinetics.

Appendices

APPENDIX A

THERMO-CALC ANALYSIS: PHASE TRANSFORMATIONS IN M2 STEEL DURING NITRIDING

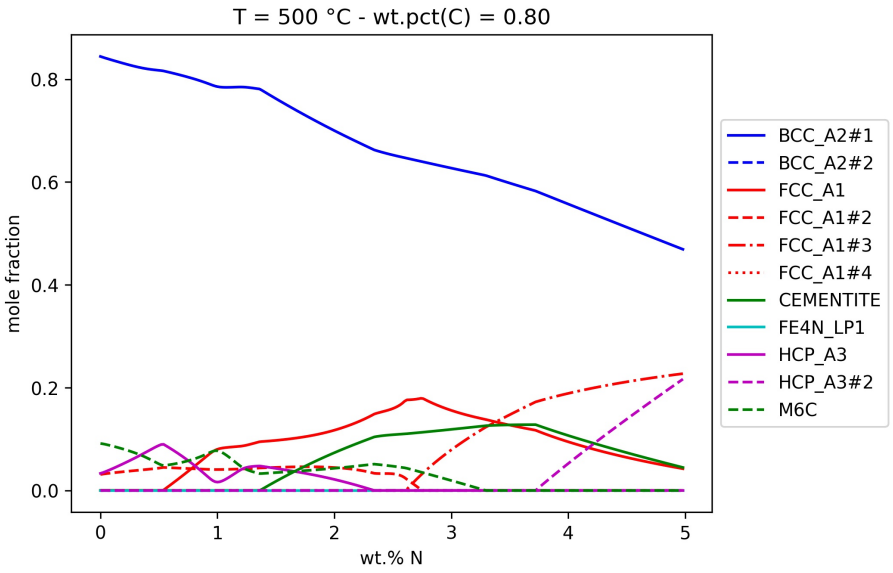


Figure A.1 – Phase transformation diagram of M2 steel (with carbon concentration 0.8%) as a function of N concentration at 500 °C

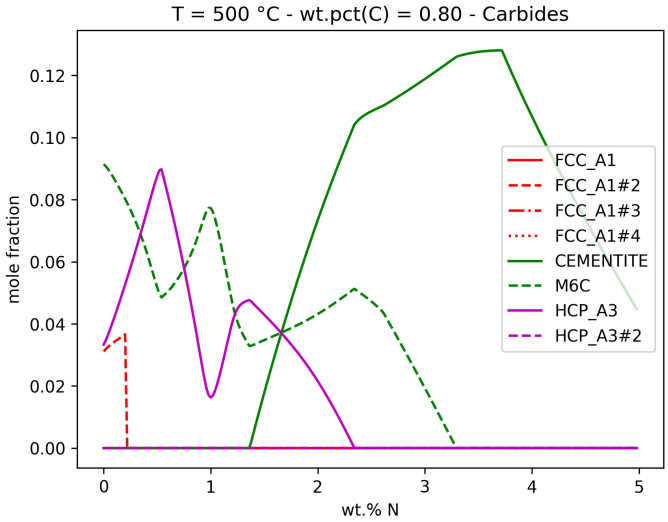


Figure A.2 – Carbides transformation diagram of M2 steel (with carbon concentration 0.8%) as a function of N concentration at 500 °C

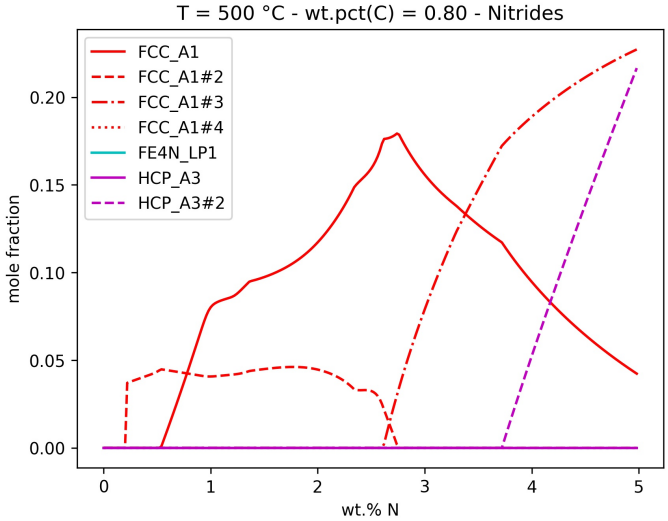


Figure A.3 – Nitrides transformation diagram of M2 steel (with carbon concentration 0.8%) as a function of N concentration at 500 °C

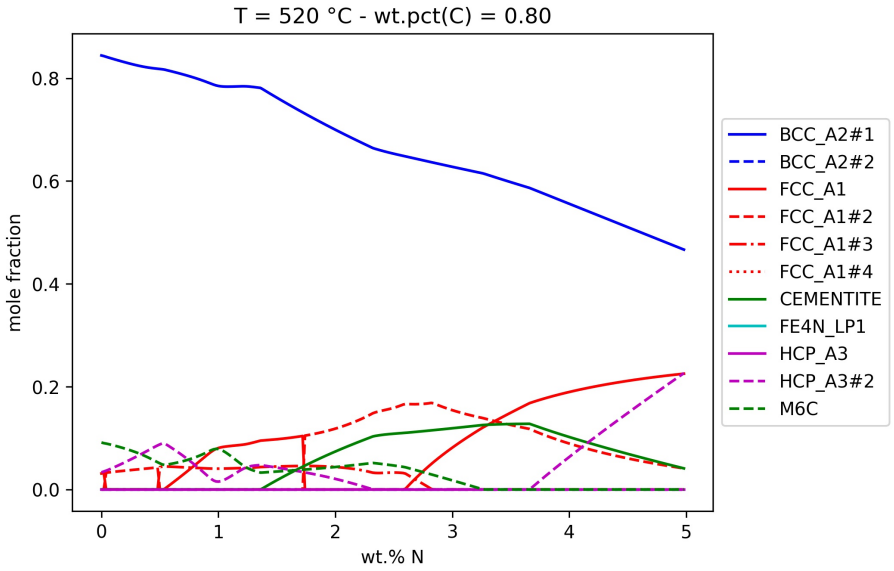


Figure A.4 – Phase transformation diagram of M2 steel (with carbon concentration 0.8%) as a function of N concentration at 520 °C

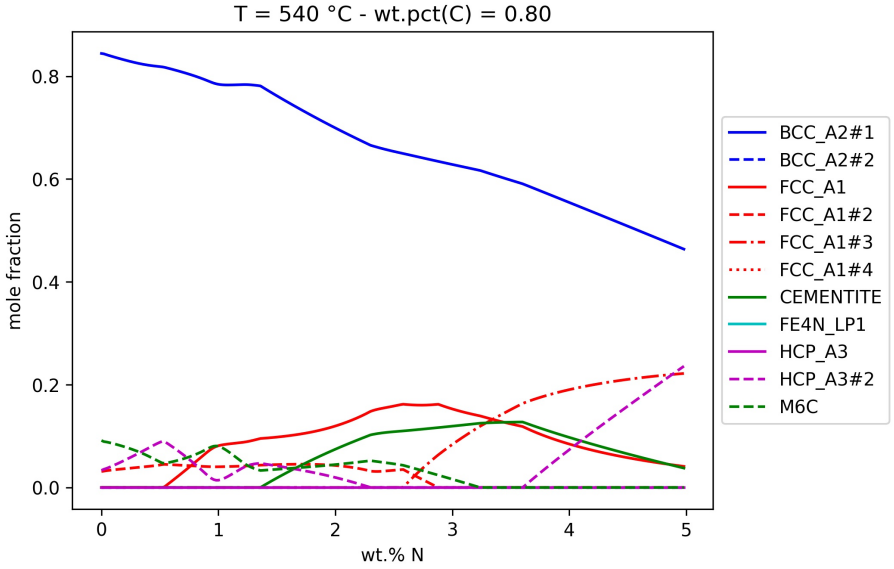


Figure A.5 – Phase transformation diagram of M2 steel (with carbon concentration 0.8%) as a function of N concentration at 540 °C

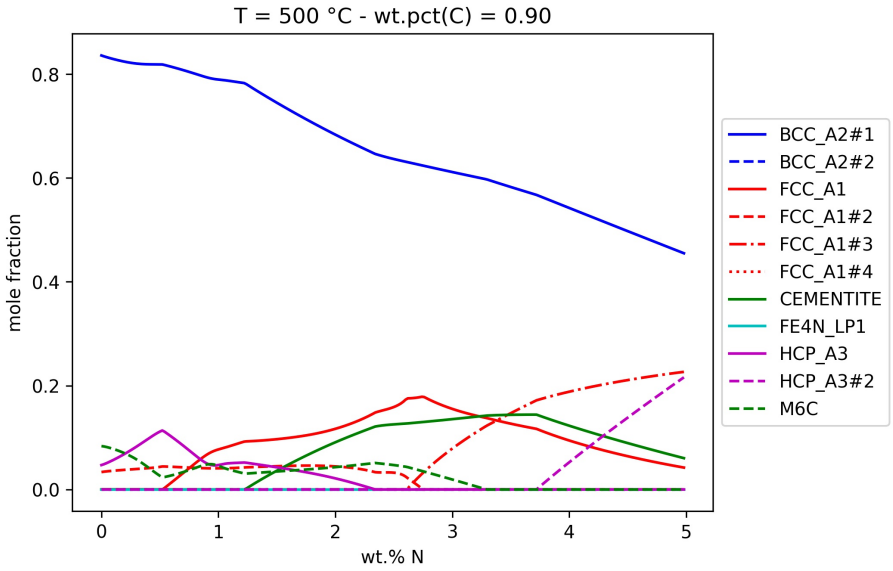


Figure A.6 – Phase transformation diagram of M2 steel (with carbon concentration 0.9%) as a function of N concentration at 500 °C

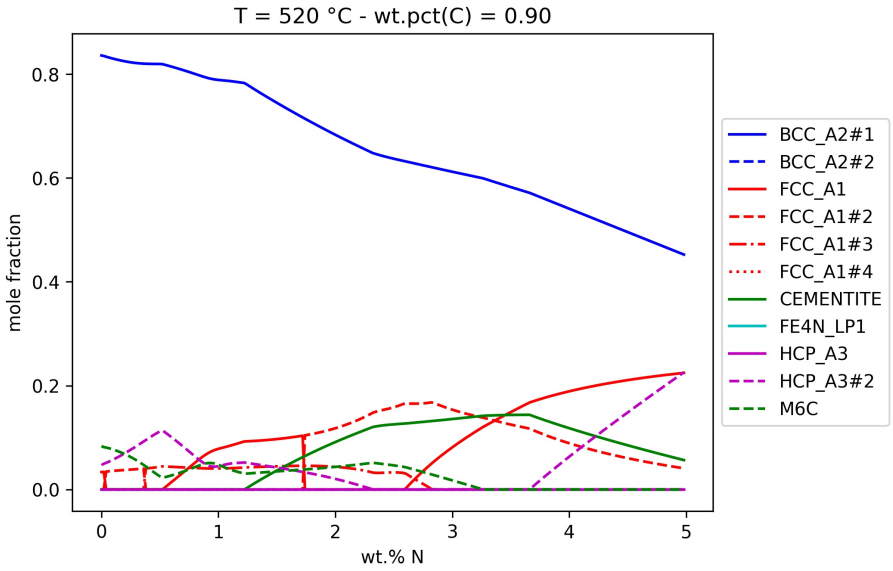


Figure A.7 – Phase transformation diagram of M2 steel (with carbon concentration 0.9%) as a function of N concentration at 520 °C

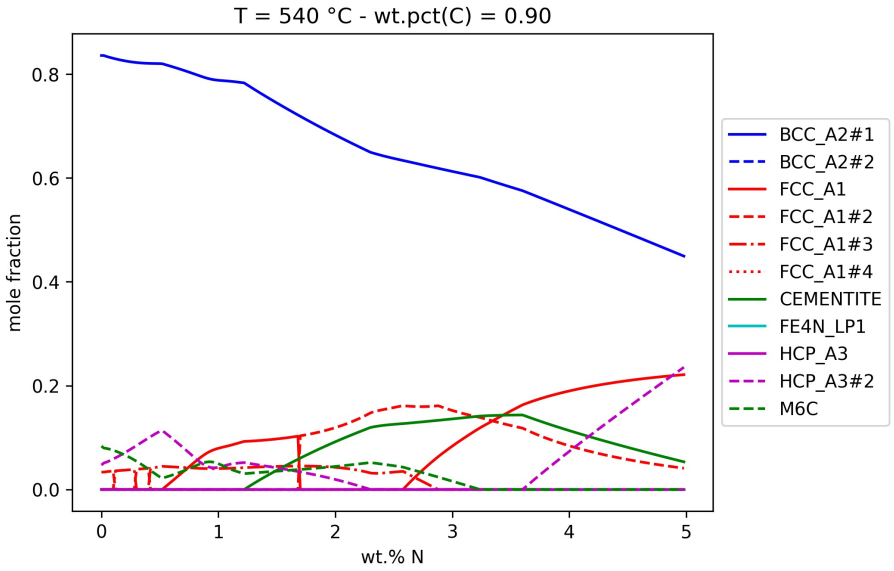


Figure A.8 – Phase transformation diagram of M2 steel (with carbon concentration 0.9%) as a function of N concentration at 540 °C

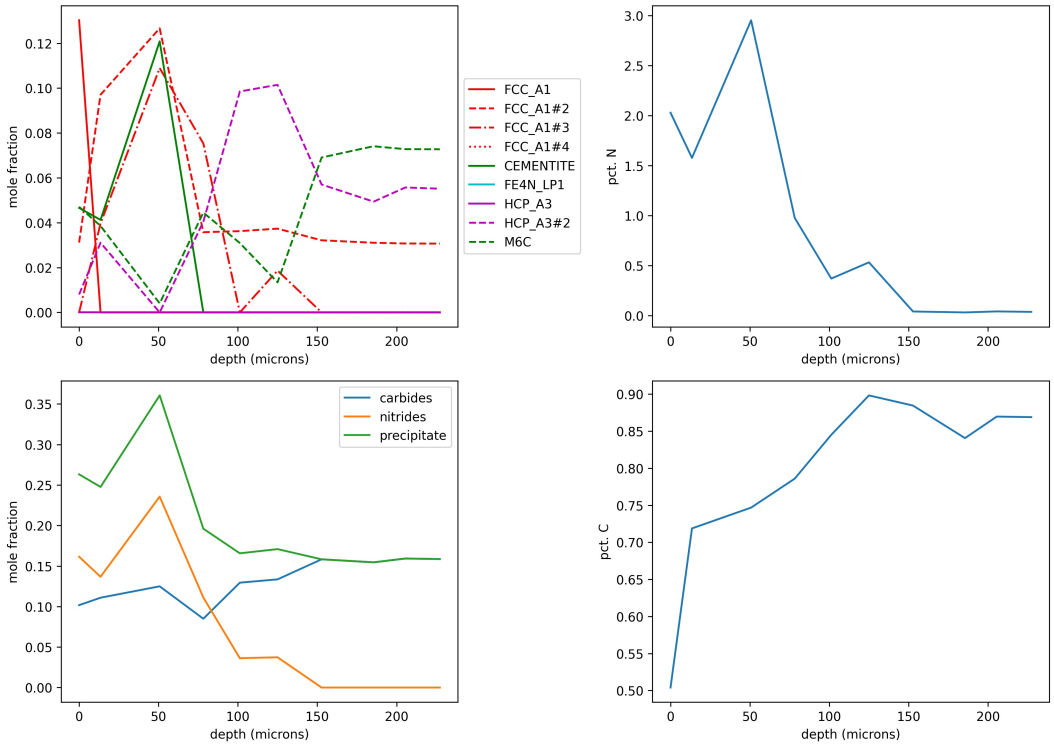


Figure A.9 – Phase composition in the nitriding layer of M2 steel as a function of depth (nitriding: 500 °C-10 h-1 $atm^{-1/2}$)

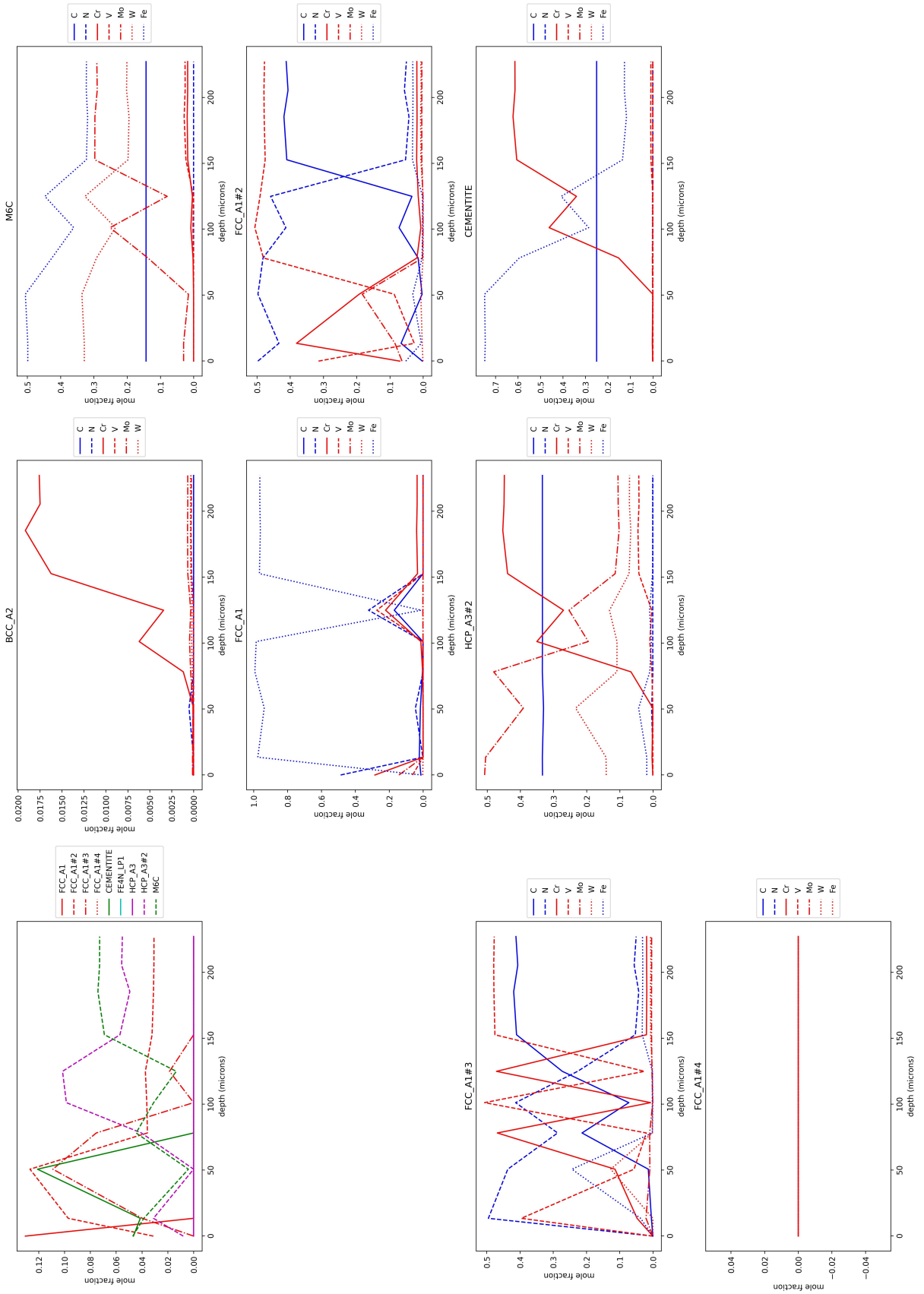


Figure A.10 – Chemical composition in each phase in the nitriding layer of M2 steel as a function of depth (nitriding: 500 °C-10 h-1 atm$^{-1/2}$)

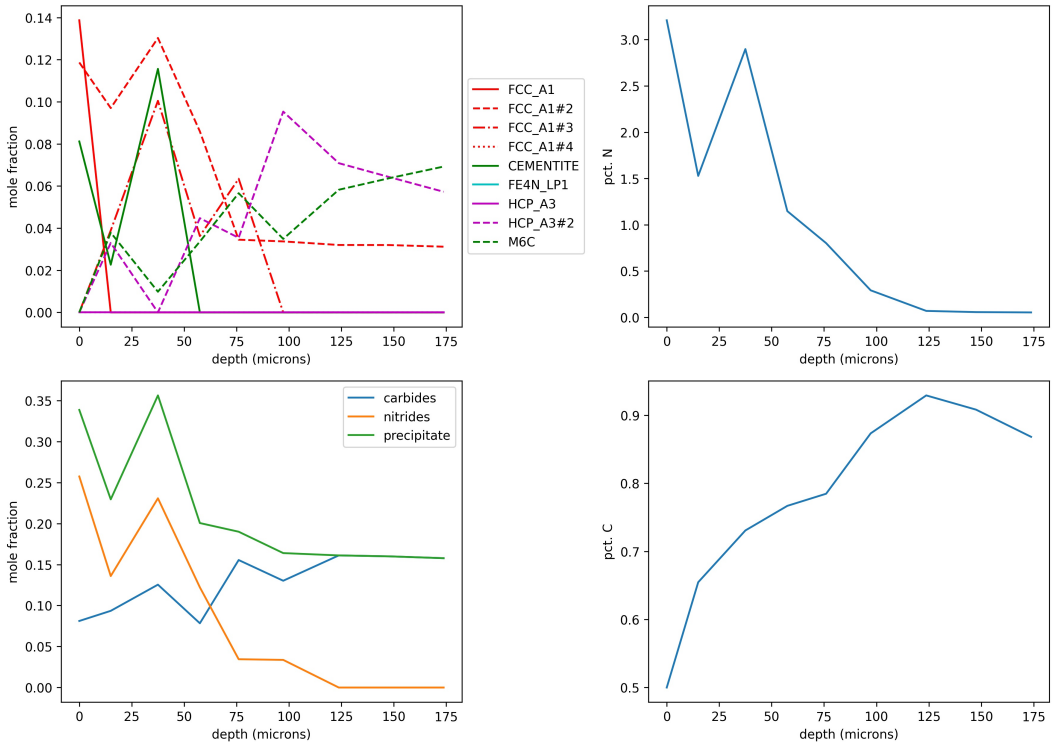


Figure A.11 – Phase composition in the nitriding layer of M2 steel as a function of depth (nitriding: 500 °C-15 h-0.5 $atm^{-1/2}$)

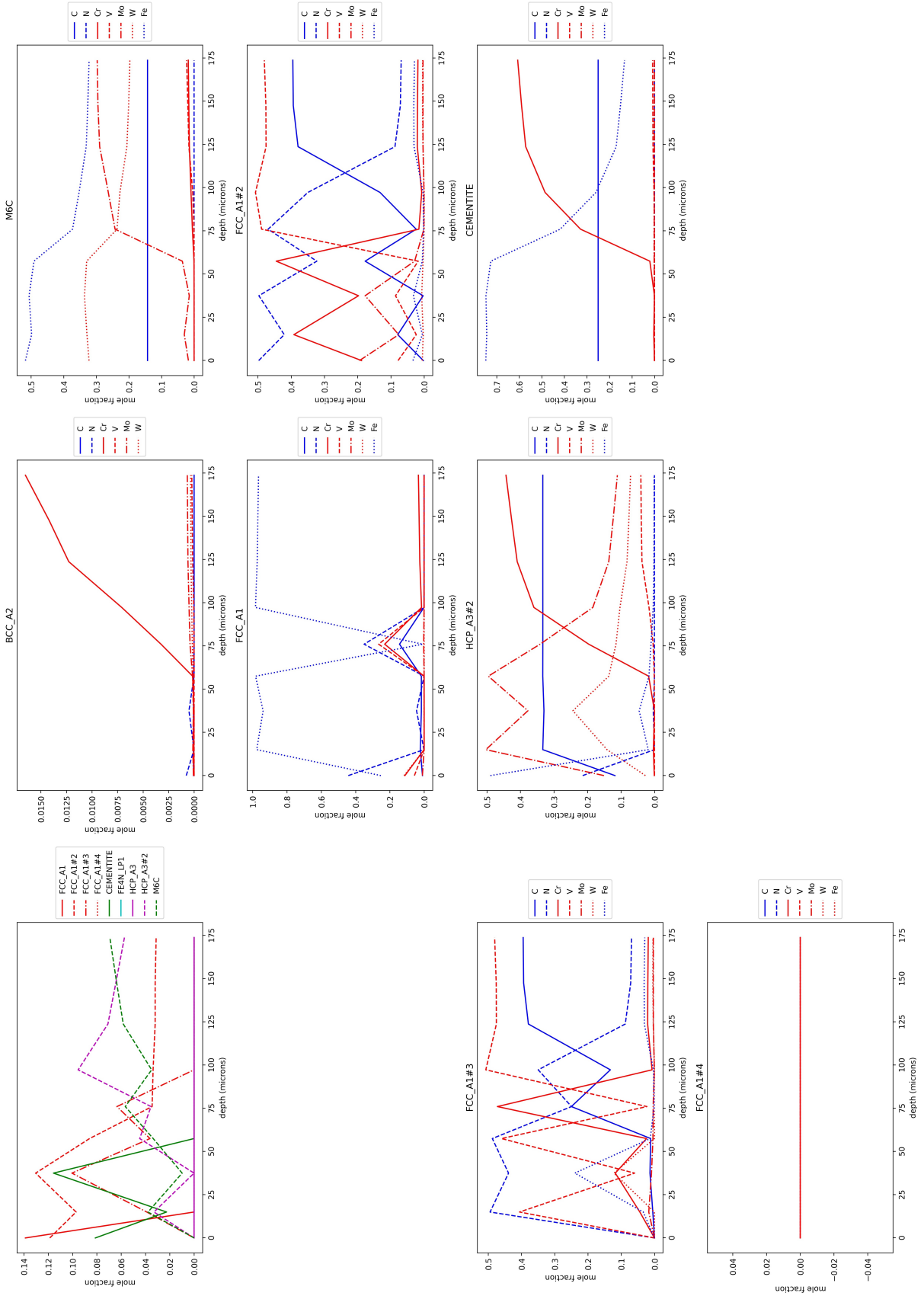


Figure A.12 – Chemical composition in each phase in the nitriding layer of M2 steel as a function of depth (nitriding: 500 °C-15 h-0.5 $atm^{-1/2}$)

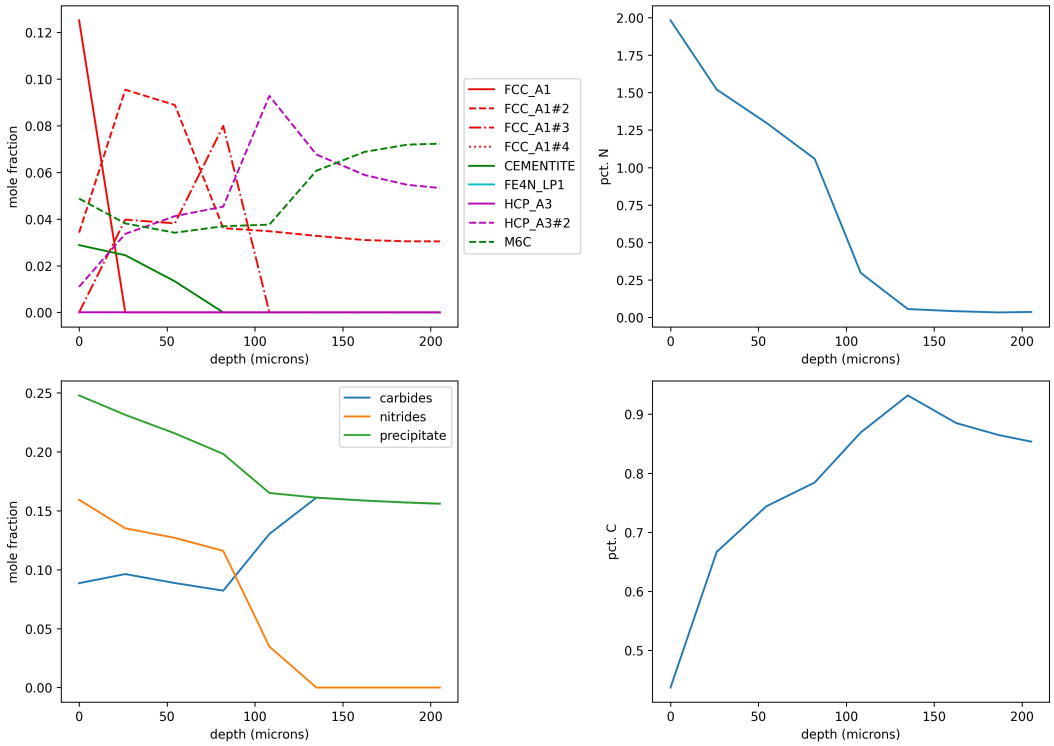


Figure A.13 – Phase composition in the nitriding layer of M2 steel as a function of depth (nitriding: 500 °C-15 h-0.8 $atm^{-1/2}$)

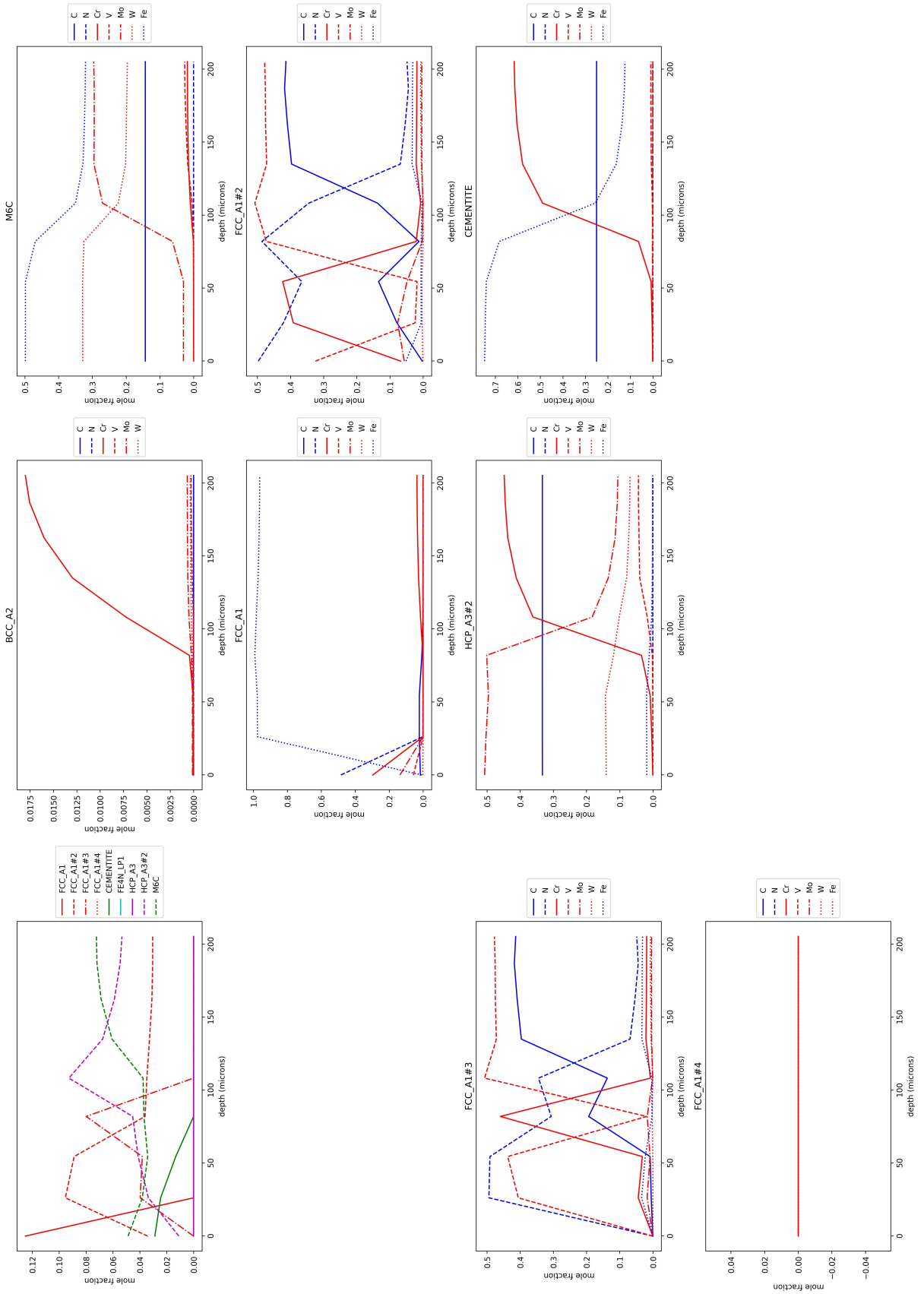


Figure A.14 – Chemical composition in each phase in the nitriding layer of M2 steel as a function of depth (nitriding: 500 °C-15 h-0.8 $atm^{-1/2}$)

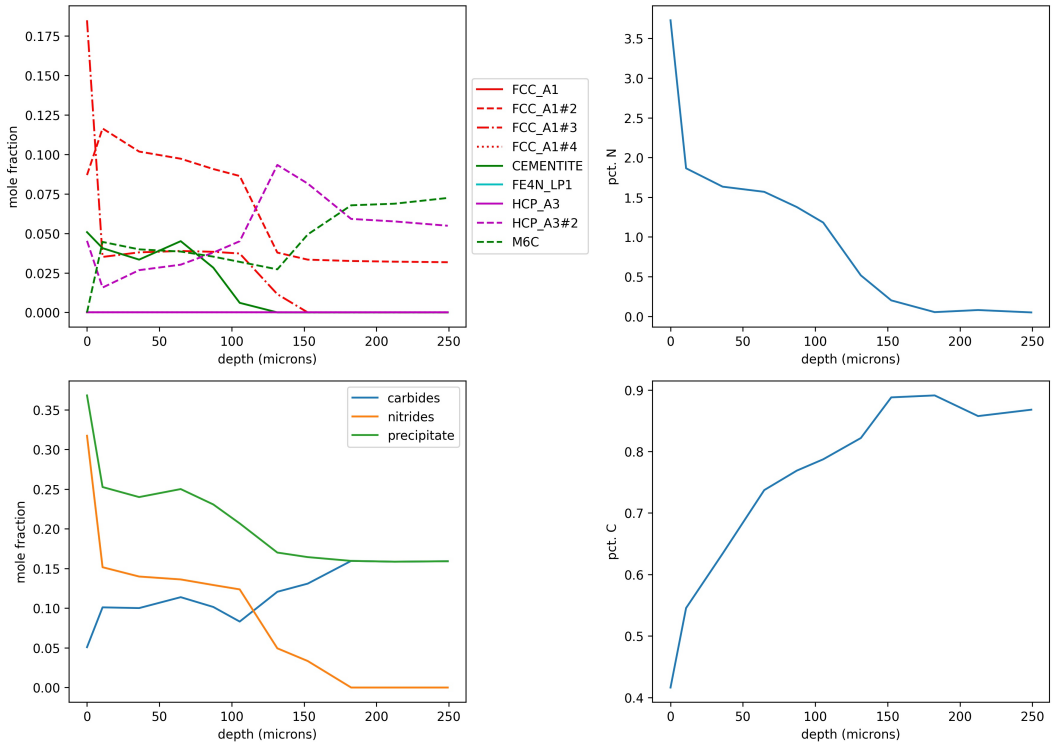


Figure A.15 – Phase composition in the nitriding layer of M2 steel as a function of depth (nitriding: 500 °C-15 h-1 $atm^{-1/2}$)

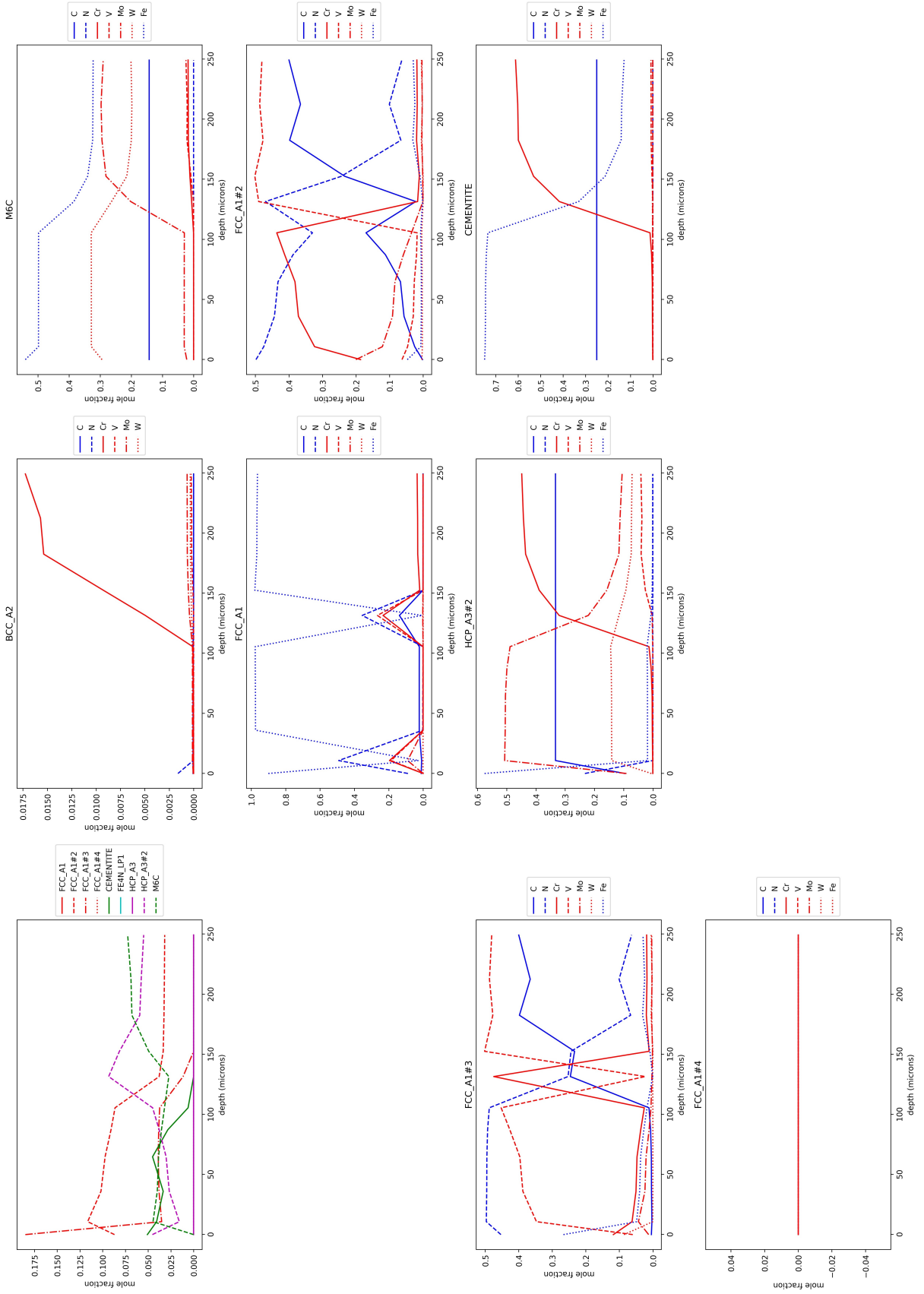


Figure A.16 – Chemical composition in each phase in the nitriding layer of M2 steel as a function of depth (nitriding: 500 °C-15 h-1 atm$^{-1/2}$)

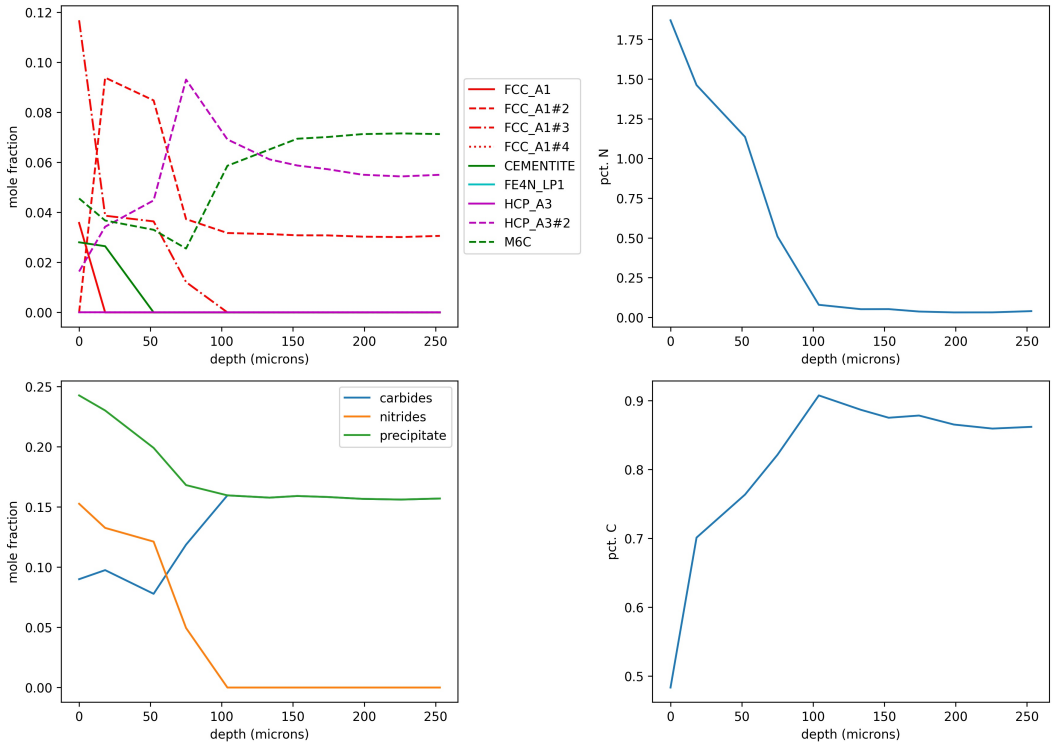


Figure A.17 – Phase composition in the nitriding layer of M2 steel as a function of depth (nitriding: 520 °C-5 h-0.8 $atm^{-1/2}$)

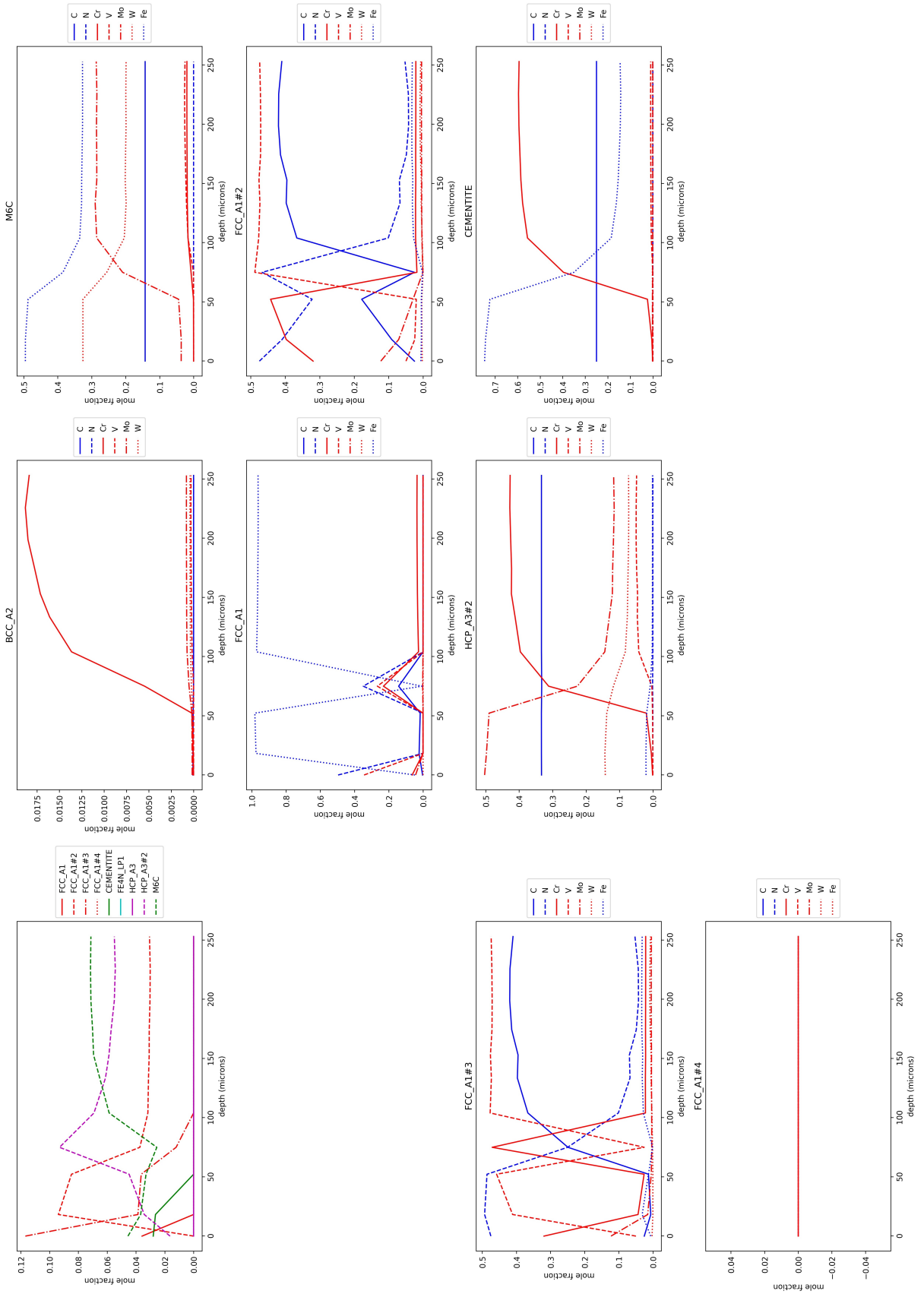


Figure A.18 – Chemical composition in each phase in the nitriding layer of M2 steel as a function of depth (nitriding: 520 °C-5 h-0.8 $atm^{-1/2}$)

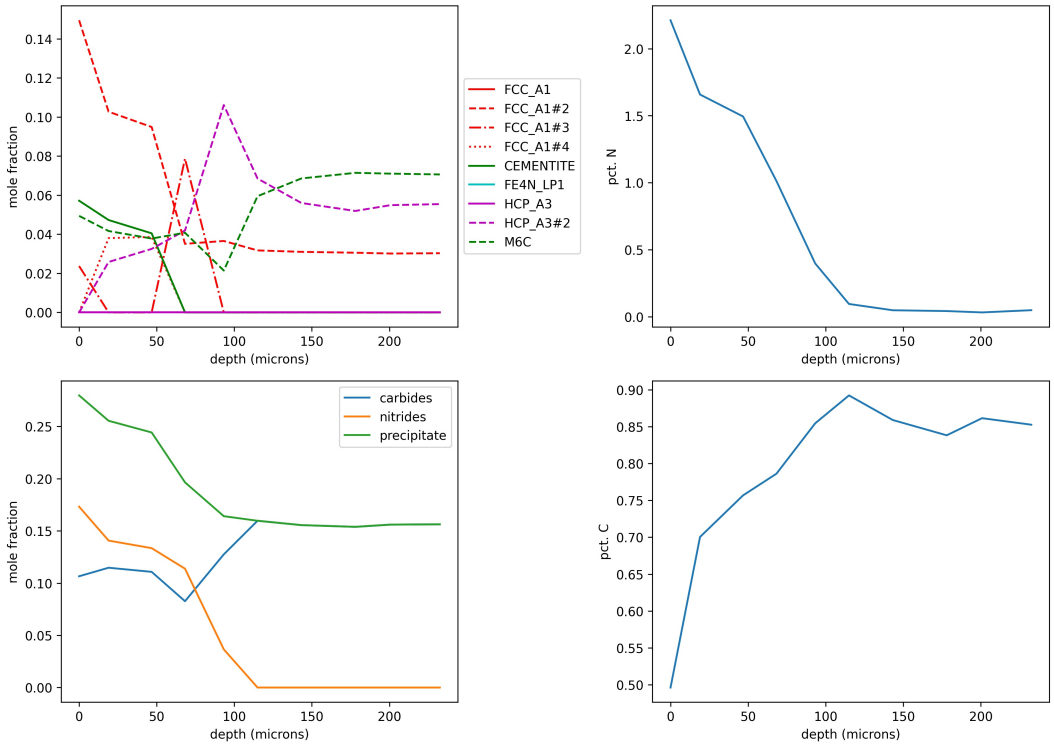


Figure A.19 – Phase composition in the nitriding layer of M2 steel as a function of depth (nitriding: 520 °C-5 h-1 $atm^{-1/2}$)

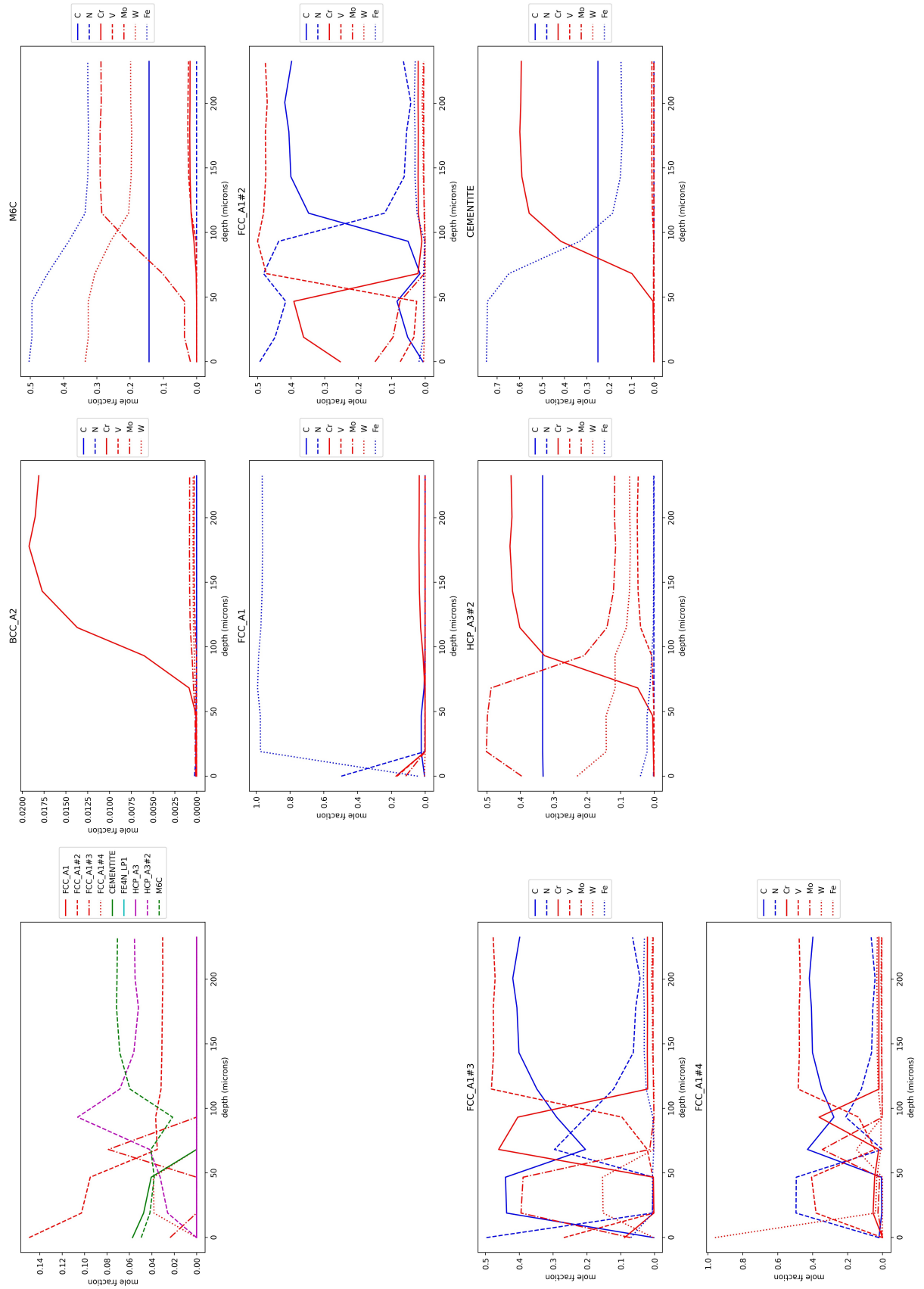


Figure A.20 – Chemical composition in each phase in the nitriding layer of M2 steel as a function of depth (nitriding: 520 °C-5 h-1 atm$^{-1/2}$)

APPENDIX B
THE CONTACT CONFIGURATIONS

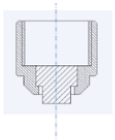
In the MSMP laboratory, 3 types of contact could be performed as shown in Figure B.1:

— superficial contact (two flat surface contact),

— linear contact (a cylinder on a flat surface),

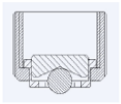
— punctual contact (a sphere on a flat surface).

Pin/disc contact



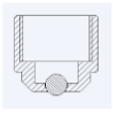
Contact geometry	surperficial
Contact between	Pin & disc
P (N), maximal normal load	250
Pm (MPa), constant pressure target	3000
Radius size (mm)	0,163

Cylinder/disc contact



Cas 1	Steel/Steel
a (mm), Lenght of contact line	1
P_L (N/L), linear load	250,0
b (mm), Half width of contact	0,053
R (mm) = Radius of roller	1,004
Po (MPa) = pressure required	3000,0

Ball/disc contact



Cas 1	
Optimization P/R^2	10,997581 41
target value	10,997581 41
R value constraint (mm)	1
Radius of the ball (mm)	2
P, value, R value constraint (N)	11
a (mm) = contact radius, calcul 2	0,042
delta (mm) = deep of the hertz point	0,002
Po (MPa) = maximal pressure target	2977
Pm (MPa) = mean pressure	1985

Figure B.1 – 3 types of contact for measuring wear rate.

However, it is impossible to reach a high-pressure value of 3000 MPa with superficial and linear contact with the current devices in the laboratory. The ball/disk system with a sphere surface on the pin will be used for the wear rate measurement. The dimensions of the pin and disk are shown in Figure B.2.

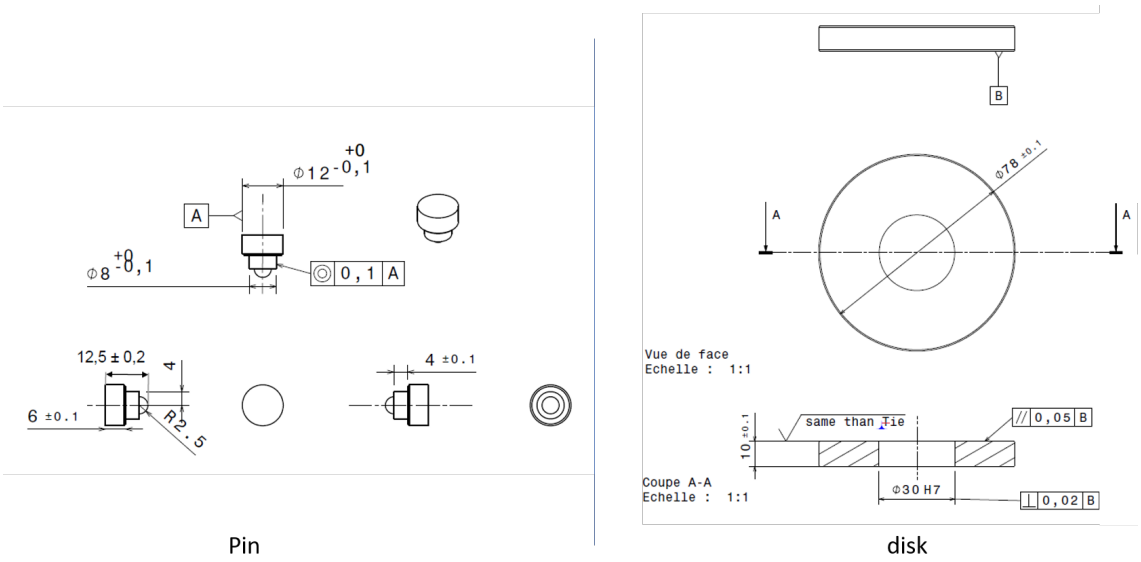


Figure B.2 – Dimensions of the pin and disk for wear rate measurement.

APPENDIX C

THE WEAR PROFILES ON M2 BALLS.

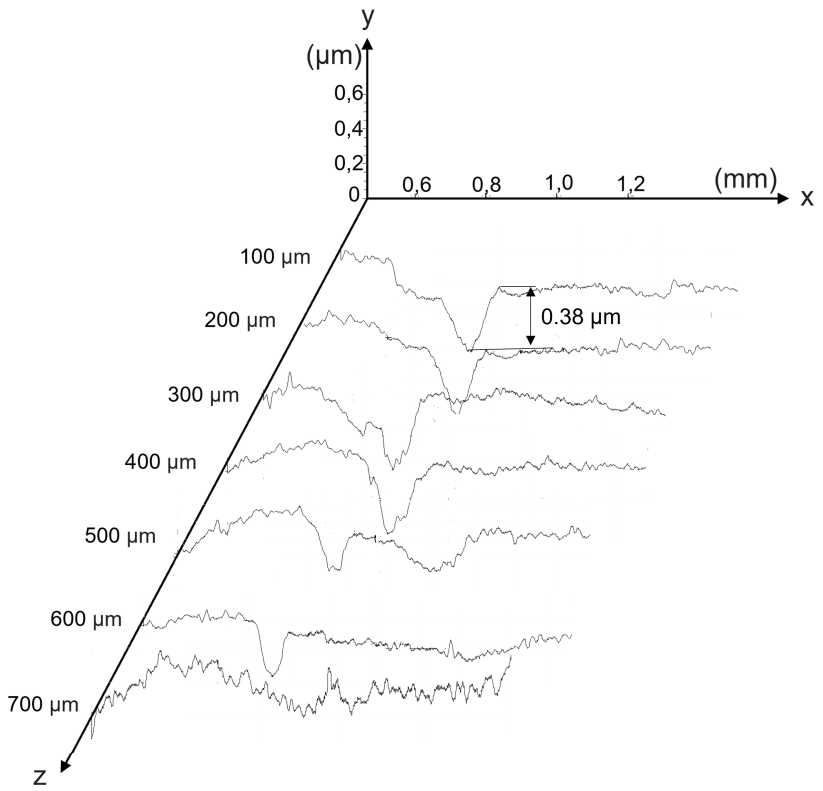


Figure C.1 – The wear profiles on the M2 ball nitrided with 500 °C-5 h-0.8 $atm^{-1/2}$ (3D plot).

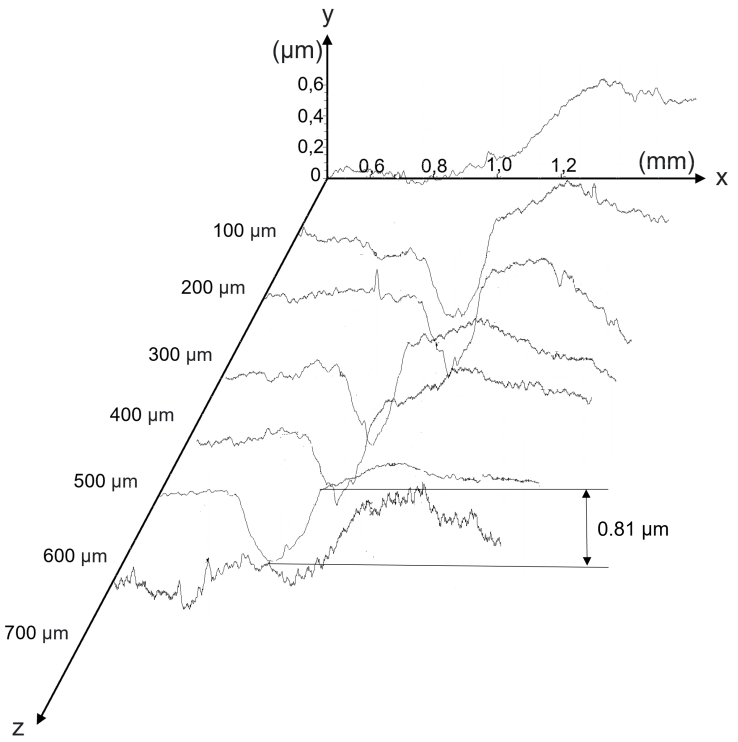


Figure C.2 – The wear profiles on the M2 ball nitrided with 500 °C-15 h-0.8 $atm^{-1/2}$ (3D plot).

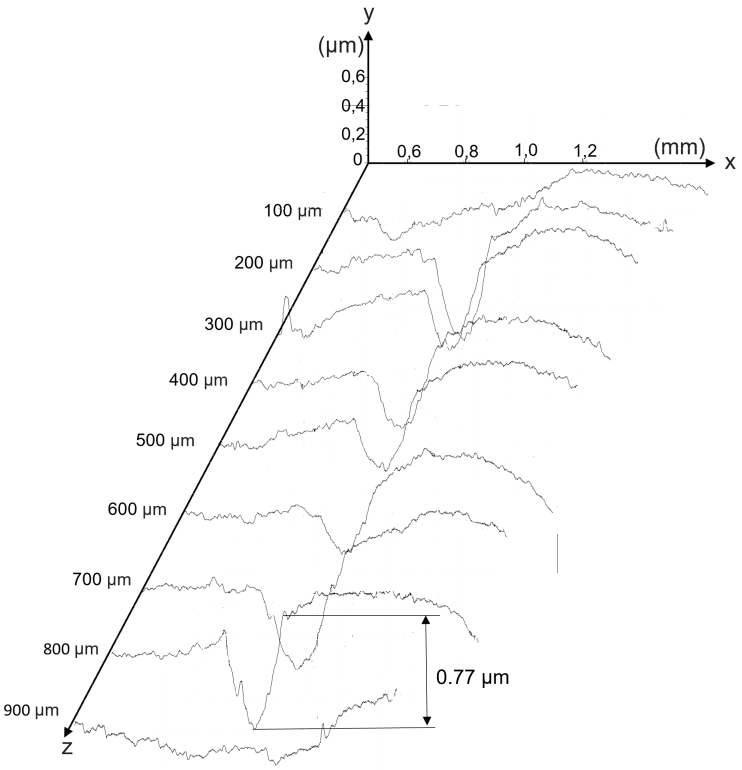


Figure C.3 – The wear profiles on the M2 ball nitrided with 520 °C-5 h-0.5 $atm^{-1/2}$ (3D plot).

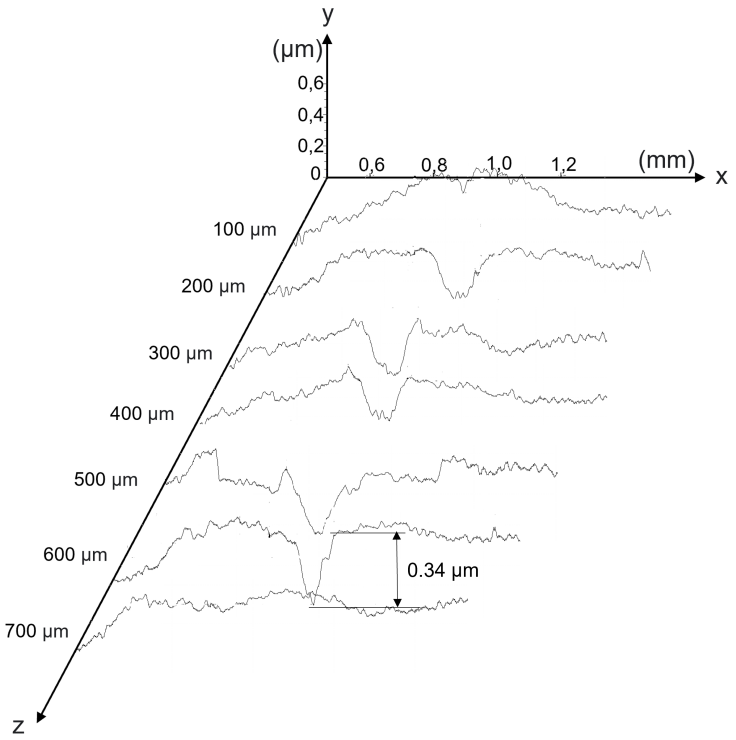


Figure C.4 – The wear profiles on the M2 ball nitrided with 520 °C-15 h-0.5 $atm^{-1/2}$ (3D plot).

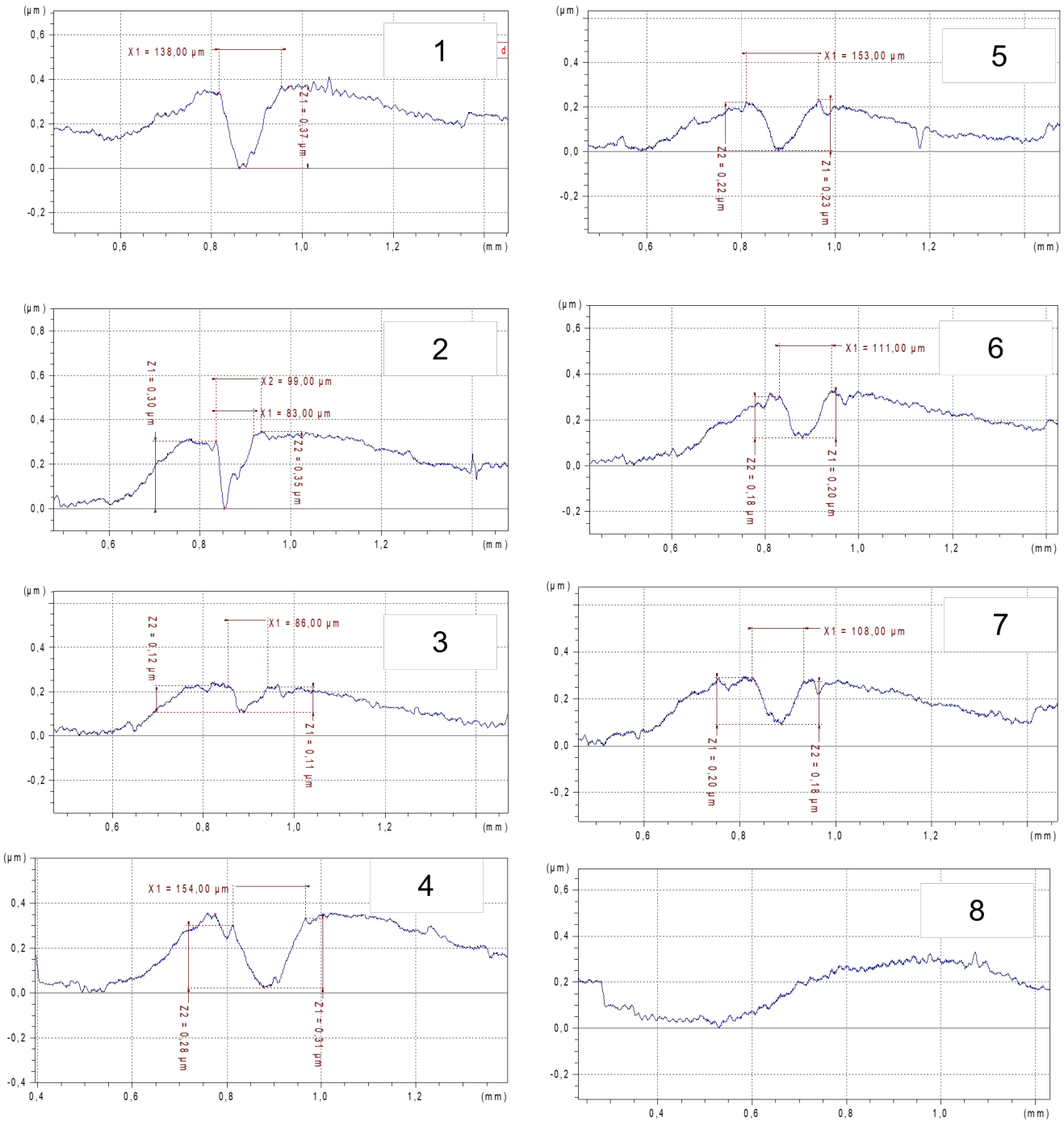


Figure C.5 – The wear profiles on the sliding direction of M2 ball ME01 (23.4 N, 14 h).

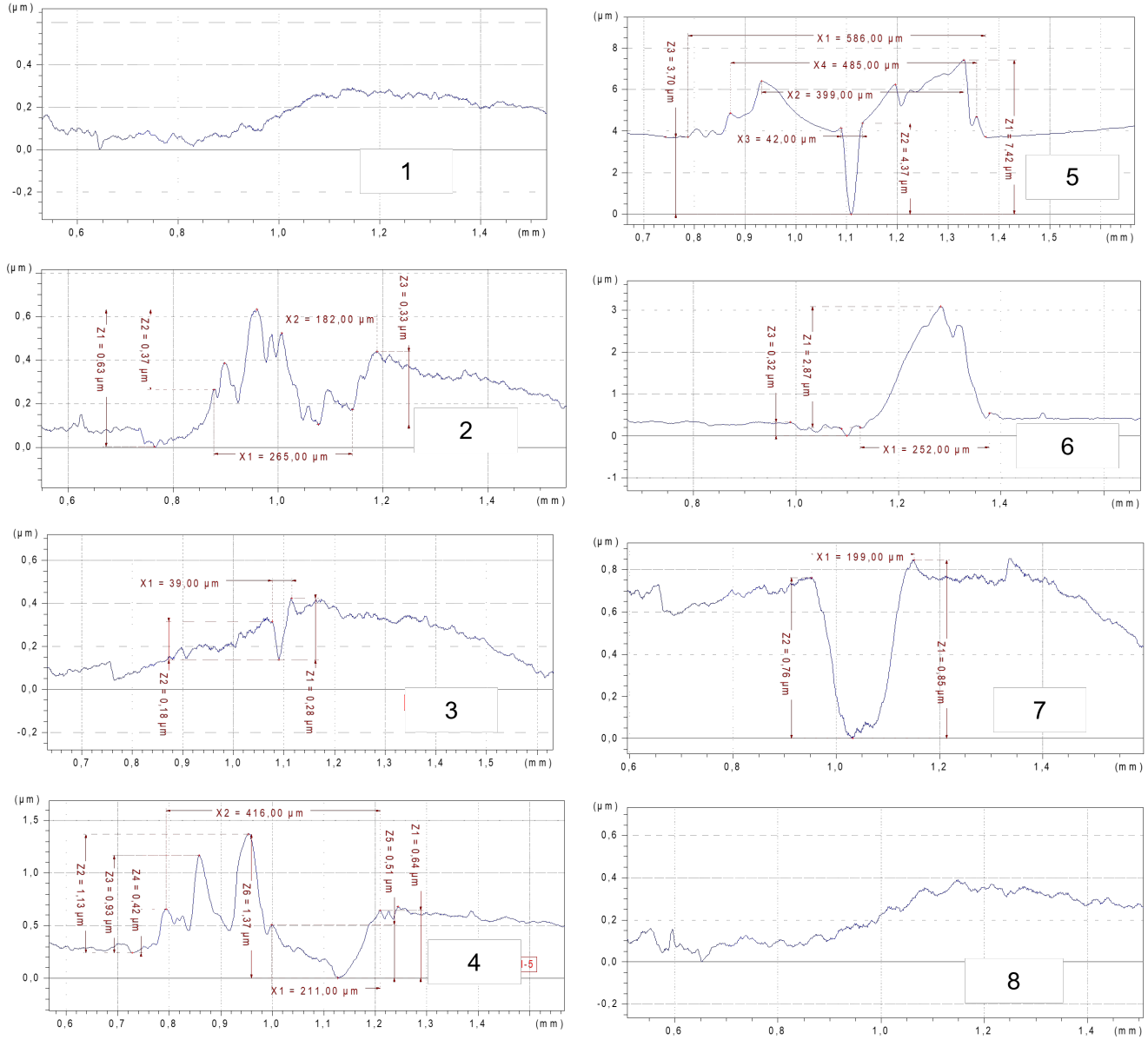


Figure C.6 – The wear profiles on the sliding direction of M2 ball ME03 (42 N, 4 h).

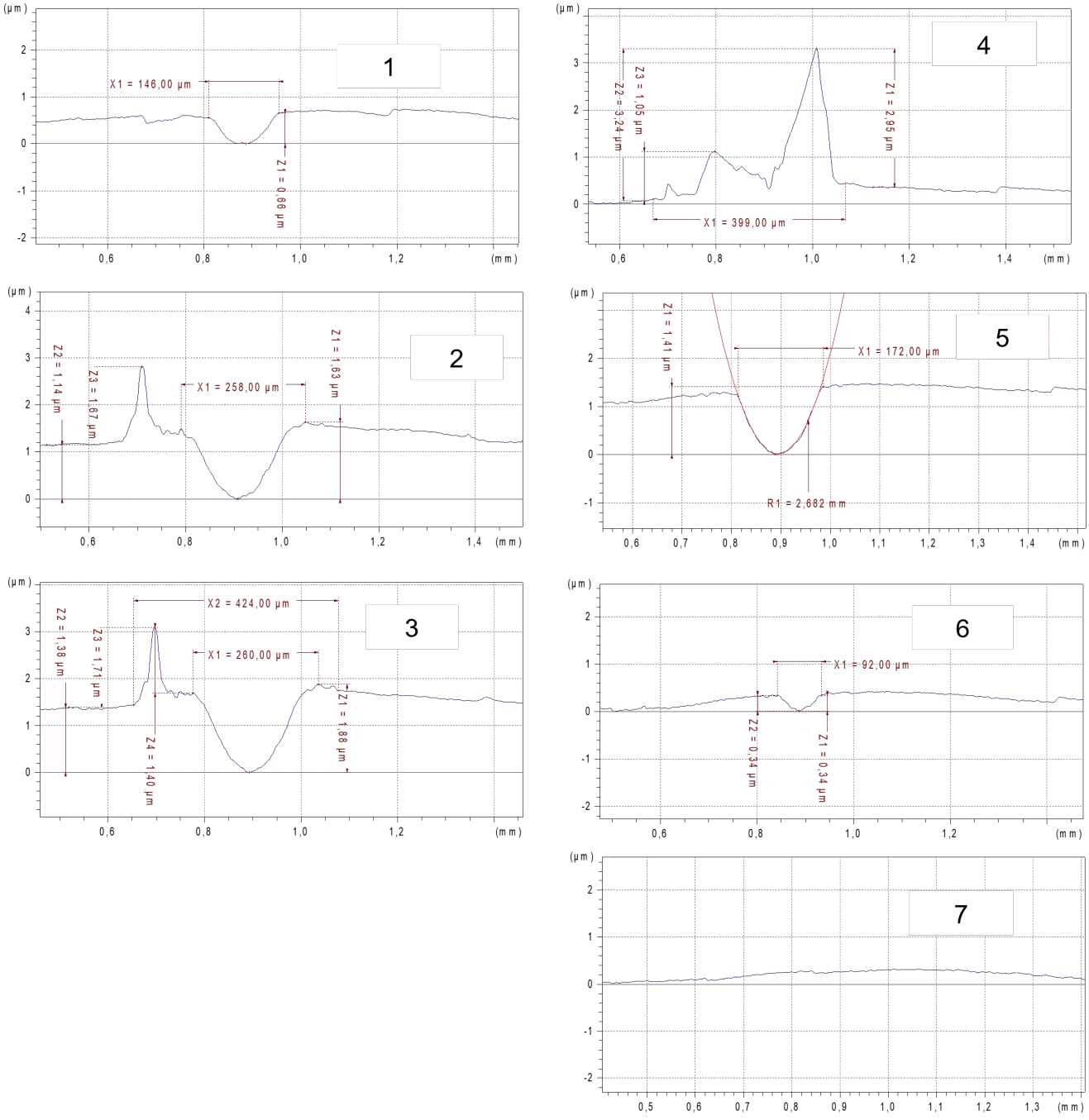


Figure C.7 – The wear profiles on the sliding direction of M2 ball ME02 (79 N, 4 h).

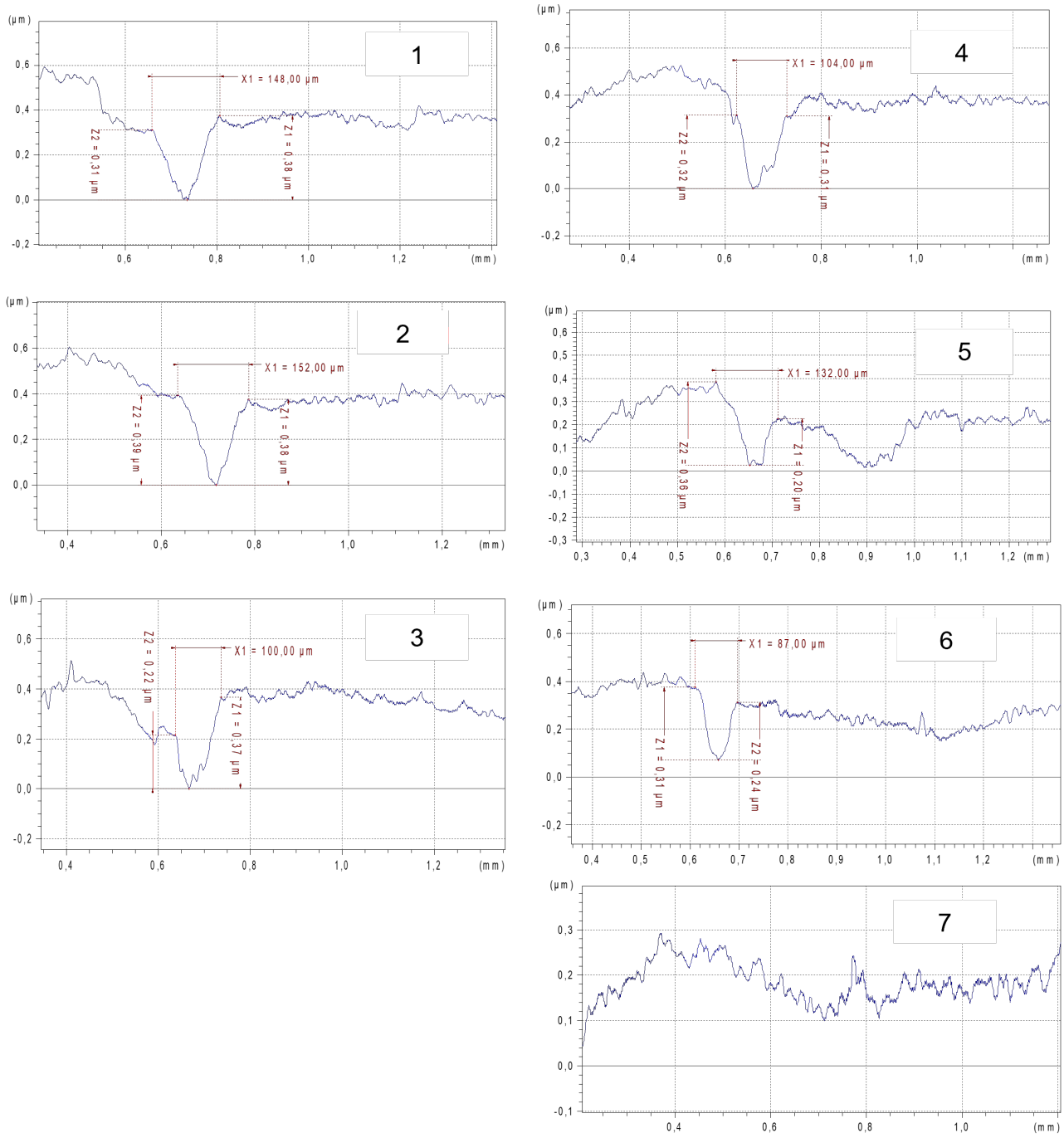


Figure C.8 – The wear profiles on the M2 ball nitrided with 500 °C-5 h-0.8 $atm^{-1/2}$.

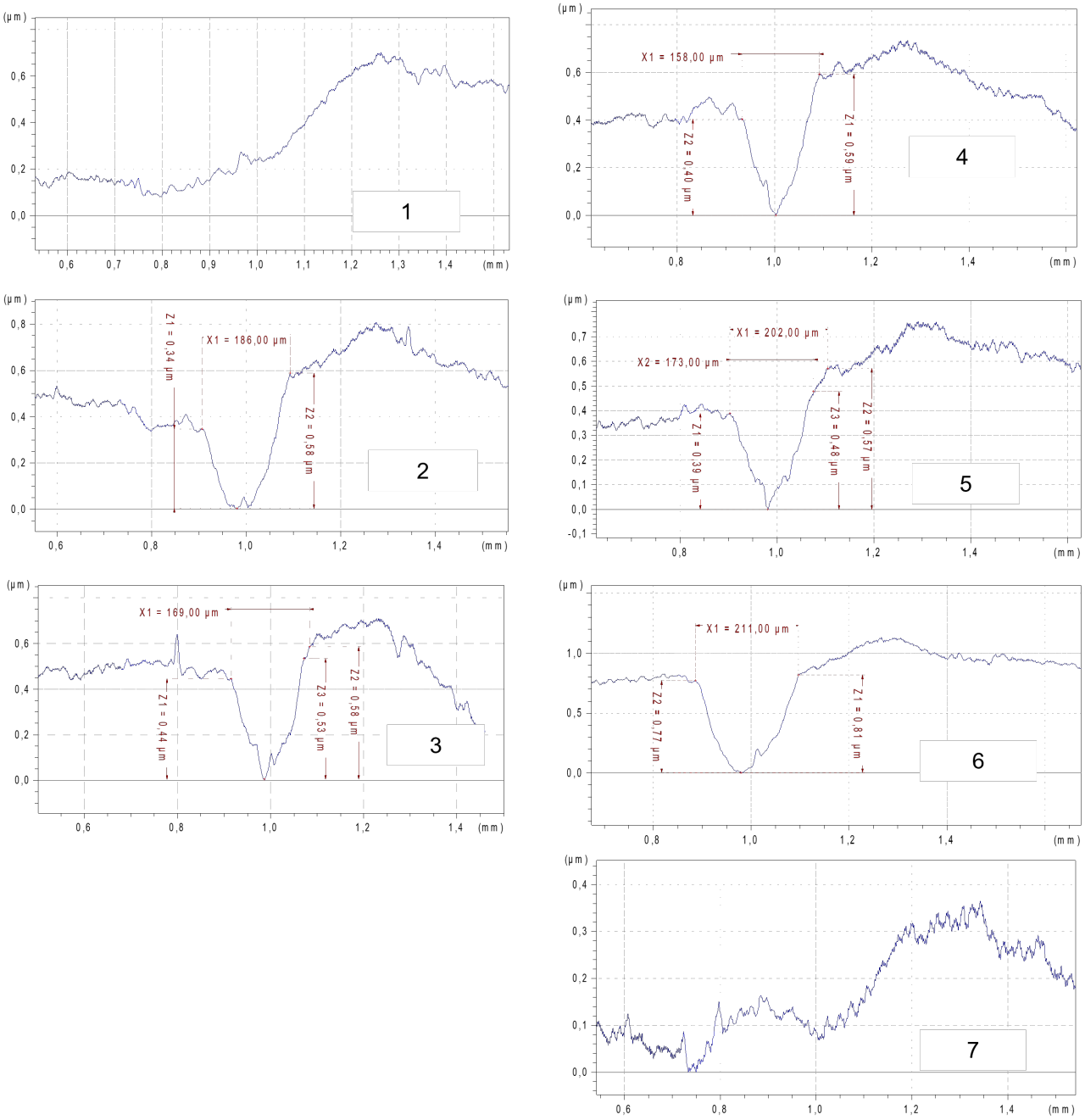


Figure C.9 – The wear profiles on the M2 ball nitrided with 500 °C-15 h-0.8 $atm^{-1/2}$.

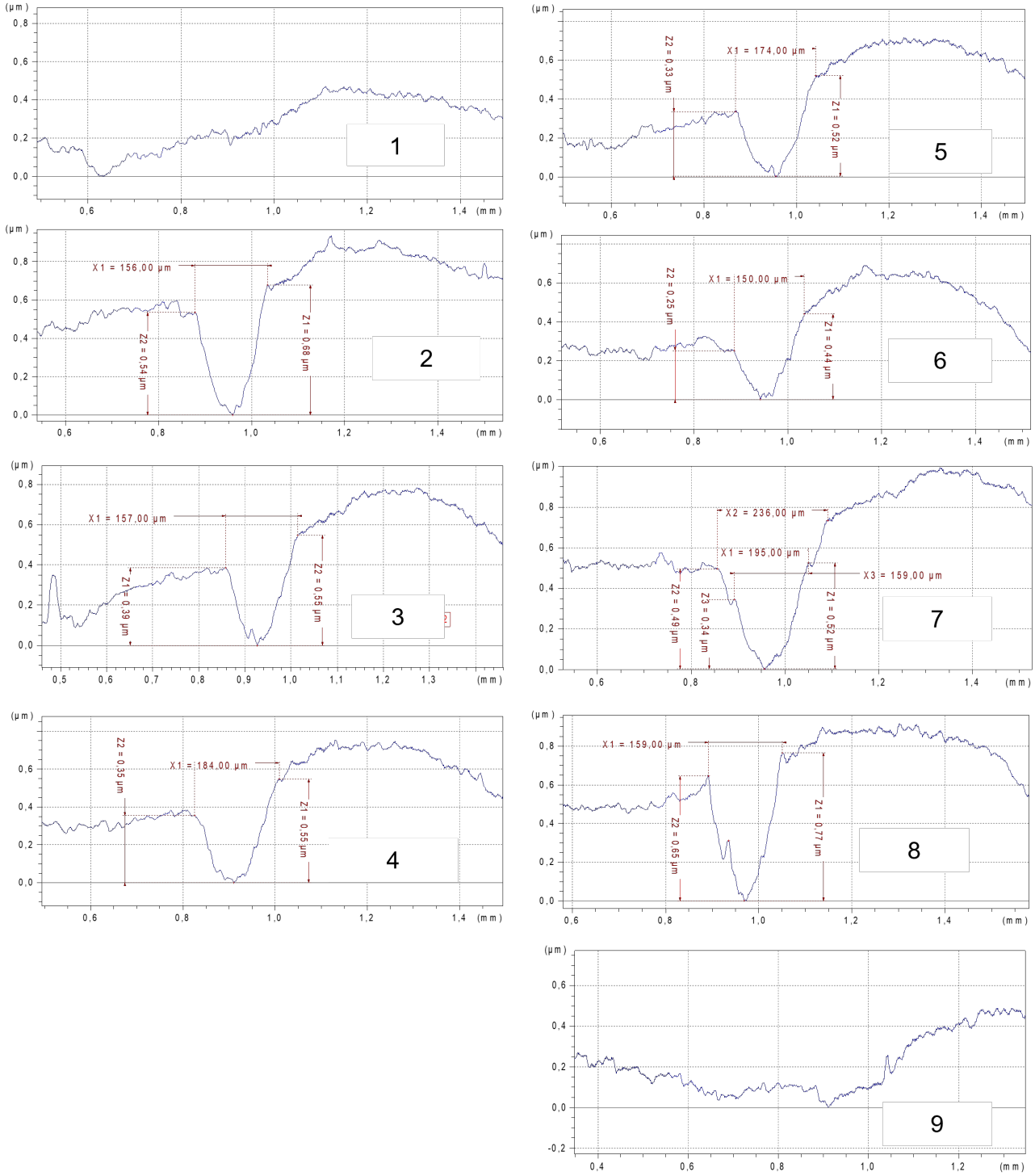


Figure C.10 – The wear profiles on the M2 ball nitrided with 520 °C-5 h-0.5 $atm^{-1/2}$.

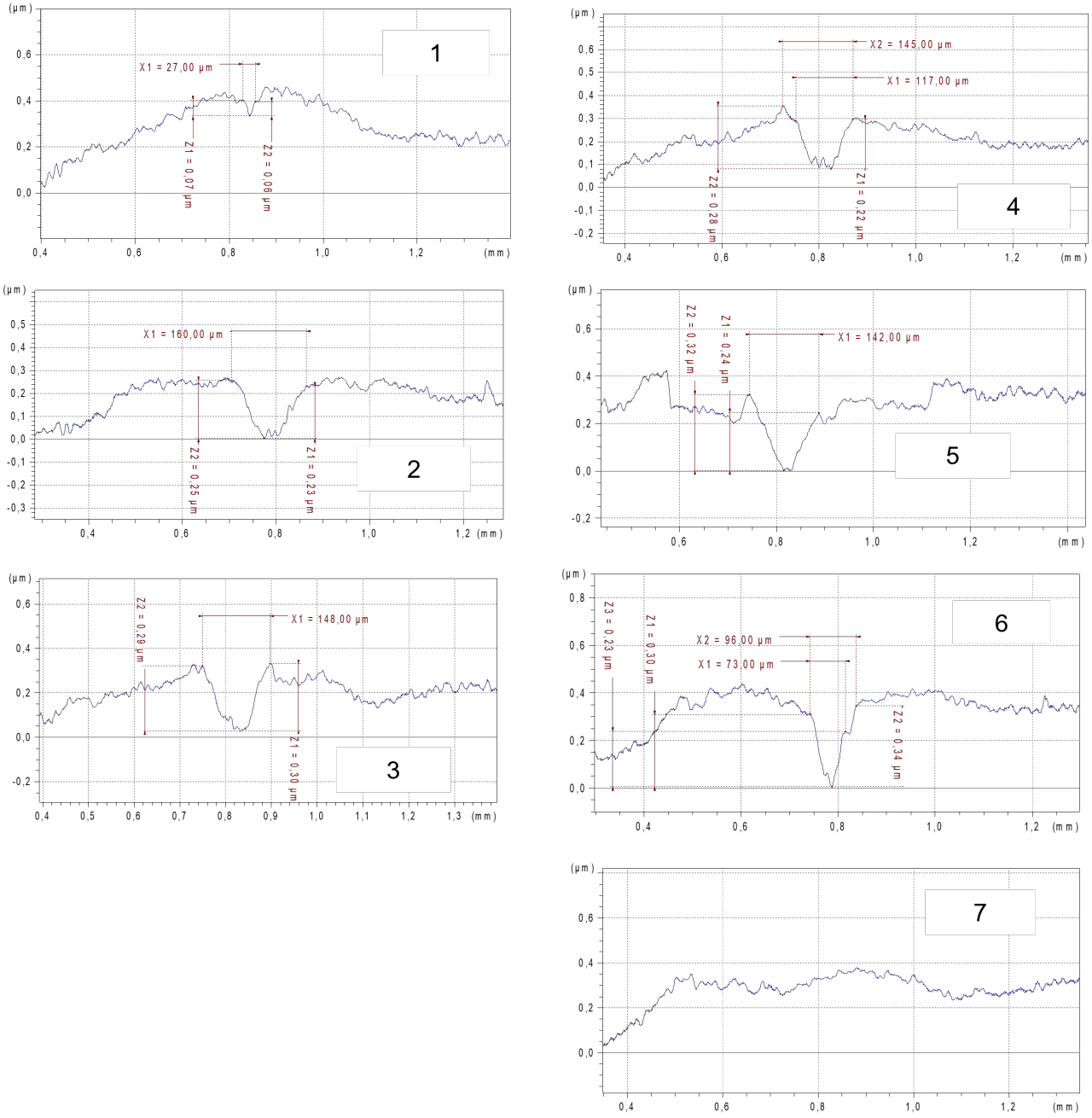


Figure C.11 – The wear profiles on the M2 ball nitrided with 520 °C-15 h-0.5 $atm^{-1/2}$.

BIBLIOGRAPHY

[1] Elizabeth A Bretz. By-wire cars turn the corner. *IEEE Spectrum*, 38(4):68–73, 2001. 1

[2] Ralf Schwarz, Rolf Isermann, Jürgen Böhm, Joachim Nell, and Peter Rieth. Clamping force estimation for a brake-by-wire actuator. Report 0148-7191, SAE Technical Paper, 1999. 1

[3] Young O Lee, Choong W Lee, Chung C Chung, Youngsup Son, Paljoo Yoon, and Inyong Hwang. Stability analysis of an electric parking brake (epb) system with a nonlinear proportional controller. *IFAC Proceedings Volumes*, 41(2):14247–14253, 2008. 1

[4] D Hyun, IS Kim, and H Seo. Study on a dynamic braking algorithm for an electronic parking brake. In *Proceedings of the KSAE autumn conference, Deoksan, Korea*, pages 950–5. 1

[5] Young Ok Lee, Minseok Jang, Wongoo Lee, Choong Woo Lee, Chung Choo Chung, and Young Seop Son. Novel clamping force control for electric parking brake systems. *Mechatronics*, 21(7):1156–1162, 2011. 1

[6] Chihoon Jo, Sungho Hwang, and Hyunsoo Kim. Clamping-force control for electromechanical brake. *IEEE Transactions on Vehicular Technology*, 59(7):3205–3212, 2010. 1

[7] Joo-Gon Kim, MyoungJune Kim, JaeHyung Chun, and Kunsoo Huh. Abs/esc/epb control of electronic wedge brake. Report 0148-7191, SAE Technical Paper, 2010. 1

[8] Bin Wang, Xuexun Guo, Chengcai Zhang, Zhe Xiong, and Jie Zhang. Modeling and control of an integrated electric parking brake system. *Journal of the Franklin Institute*, 352(2):626–644, 2015. V, 2

[9] Joseph P Domblesky and Feng Feng. A parametric study of process parameters in external thread rolling. *Journal of Materials Processing Technology*, 121(2-3):341–349, 2002. 2

[10] John Geise. *Tesker-Thread Rolling Process*. V, 2, 3

[11] J P Domblesky and F Feng. Two-dimensional and three-dimensional finite element models of external thread rolling. *Proceedings of the Institution of Mechanical Engineers, Part B: Journal of Engineering Manufacture*, 216(4):507–517, 2002. 2

[12] H Sağlam and R Kuş. Performance of internal thread rolling head and the mechanical properties of rolled thread. In *6th International Advanced Technologies Symposium*. 2

[13] Da-Wei Zhang, Sheng-Dun Zhao, and Hengan Ou. Analysis of motion between rolling die and workpiece in thread rolling process with round dies. *Mechanism and Machine Theory*, 105:471–494, 2016. V, IX, 3, 92

[14] MinCheol Lee, SooJin Jang, SeungSang Han, DukJae Yoon, and ManSoo Joun. New finite-element model of thread rolling. *Steel Res Int*, 9:214–217, 2010. 3

[15] CR Gagg. Premature failure of thread rolling dies: material selection, hardness criteria and case studies. *Engineering Failure Analysis*, 8(1):87–105, 2001. 3

[16] E Abakay, S Sen, and U Sen. Effect of aluminum addition to Nb-Al-C-N coatings on AISI M2 steel obtained by thermo-reactive deposition technique. *Acta Physica Polonica A*, 129(4):653–655, 2016. 4

[17] In-Sik Cho, Auezhan Amanov, and Jong-Deok Kim. The effects of alcrn coating, surface modification and their combination on the tribological properties of high speed steel under dry conditions. *Tribology International*, 81:61–72, 2015. 4

[18] Liang Hao, Zhengyi Jiang, Dongbin Wei, Yue Zhao, Jingwei Zhao, Ming Luo, Li Ma, Suzhen Luo, and Laizhu Jiang. Effect of extreme pressure agents on the anti-scratch behaviour of high-speed steel material. *Tribology International*, 81:19–28, 2015. 4

[19] Jerzy Narojczyk, Zbigniew Werner, Marek Barlak, and Dmitrij Morozow. The effect of ti preimplantation on the properties of TiN coatings on HS 6-5-2 high-speed steel. *Vacuum*, 83:S228–S230, 2009. 4

[20] FZ Bouanis, F Bentiss, M Traisnel, and C Jama. Enhanced corrosion resistance properties of radiofrequency cold plasma nitrided carbon steel: Gravimetric and electrochemical results. *Electrochimica acta*, 54(8):2371–2378, 2009. 4

[21] Saleem Hashmi. *Comprehensive materials processing*. Newnes, 2014. 4

[22] Ramandeep Singh Sidhu and Balwinder Singh Sidhu. Optimization of gas carburization process parameters for wear resistance of AISI 1020 low carbon steel. *INDUSTRIAL ENGINEERING JOURNAL*, 2018. 7

[23] L. H. P. Abreu, M. C. L. Pimentel, W. F. A. Borges, T. H. C. Costa, M. Naeem, J. Iqbal, and R. R. M. Sousa. Plasma nitriding of aisi m2 steel: performance evaluation in forming tools. *Surface Engineering*, pages 1–8, 2020. VII, 7, 51, 53, 54, 55

[24] Liam Blunt. *Introduction: the history and current state of 3D surface characterisation*, pages 1–13. Elsevier Inc., 2003. VII, 7, 57, 58, 102

[25] ED Doyle, AM Pagon, Paul Hubbard, SJ Dowey, Antony Pilkington, DG McCulloch, Kay Latham, and Johan DuPlessis. Nitriding of high speed steel. *International heat treatment and surface engineering*, 5(2):69–72, June 2011. 7, 51, 58

[26] Eric J Mittemeijer and Marcel AJ Somers. *Thermochemical surface engineering of steels*. Woodhead Publishing Cambridge, 2014. 7, 8

[27] Ian Hutchings and Philip Shipway. *Tribology: friction and wear of engineering materials*. Butterworth-Heinemann, 2017. V, 7, 8

[28] J Dutta Majumdar and I Manna. Laser surface engineering of titanium and its alloys for improved wear, corrosion and high-temperature oxidation resistance. In *Laser Surface Engineering*, pages 483–521. Elsevier, 2015. 7

[29] David Pye. *Practical nitriding and ferritic nitrocarburizing*. ASM international, 2003. 8, 11, 12, 14, 16, 21

[30] Shahid Hussain Abro, Muhammad Ali Siddiqui, Humair Ahmed Siddiqui, and Alidad Chandio. Impact of nano sized aluminum nitride second phase particles on gamma and alpha phase transformation in less carbon added manganese steel. *Pakistan Journal of Engineering and Applied Sciences*, 2020. 8

[31] Y Prawoto, MA Mat Yajid, and KJ Lee. Microstructural consideration on quantitative analysis of thermal treatment: Application to decarburization of steel. *Journal of King Saud University-Engineering Sciences*, 25(2):141–147, 2013. V, 9

[32] K. M. Winter, J. Kalucki, and D. Koshel. *3 - Process technologies for thermochemical surface engineering*, pages 141–206. Woodhead Publishing, Oxford, 2015. 9, 19, 21

[33] Frank Czerwinski. Thermochemical treatment of metals. *Heat Treatment–Conventional and Novel Applications*, 5:73–112, 2012. 9

[34] E. J. Mittemeijer and M. A. J. Somers. *2 - Kinetics of thermochemical surface treatments*, pages 113–140. Woodhead Publishing, Oxford, 2015. 9, 16, 17, 18

[35] E. J. Mittemeijer and M. A. J. Somers. Thermodynamics, kinetics, and process control of nitriding. *Surface Engineering*, 13(6):483–497, 1997. V, 9, 14, 15, 16, 22, 25

[36] EJ Mittemeijer. *Fundamentals of nitriding and nitrocarburizing*, pages 619–646. ASM International, 2013. V, VI, XV, 9, 11, 12, 14, 16, 21, 22, 23, 24, 25, 28, 29, 53, 126

[37] JT Slycke, Eric Jan Mittemeijer, and Marcel AJ Somers. *Thermodynamics and kinetics of gas and gas–solid reactions*, pages 3–111. Elsevier, 2015. 9

[38] KH Jack. The iron–nitrogen system: The crystal structures of ε-phase iron nitrides. *Acta Crystallographica*, 5(4):404–411, 1952. V, 10, 11

[39] Friedrich Karl Naumann and Gerhard Langenscheid. Beitrag zum system eisen–stickstoff–kohlenstoff. *Archiv für das Eisenhüttenwesen*, 36(9):677–682, 1965. 9

[40] Hong Du. A reevaluation of the Fe-n and Fe-cn systems. *Journal of phase equilibria*, 14(6):682–693, 1993. 10

[41] Joachim Kunze. *Nitrogen and carbon in iron and steel: thermodynamics; with 48 tables*. Akad.-Verlag, 1990. 10

[42] J Slycke, L Sproge, and J Agren. Nitrocarburizing and the ternary Fe–n–c phase diagram. *Scand. J. Metall.*, 17(3):122–126, 1988. 10

[43] Mei Yang and RD Sisson. Gaseous nitriding process control: application of customised lehrer diagrams. *International Heat Treatment and Surface Engineering*, 7(4):164–171, 2013. V, 10

[44] Marcel AJ Somers. *Development of Compound Layer and Diffusion Zone during Nitriding and Nitrocarburizing of Iron and Steels*, pages 413–437. Elsevier, 2014. V, VI, 11, 25

[45] Shuai Ye and Yujie Cao. Structure of iron nitrides under different nitridation temperatures. In *2016 4th International Conference on Advanced Materials and Information Technology Processing (AMITP 2016)*. Atlantis Press. V, 11, 12

[46] CM Fang, MA Van Huis, and HW Zandbergen. Stability and structures of the ε-phases of iron nitrides and iron carbides from first principles. *Scripta Materialia*, 64(3):296–299, 2011. 11

[47] Masataka Kano, Takashi Nakagawa, Takao A Yamamoto, and Masahiro Katsura. Magnetism, crystal structure and nitrogen content near the ε–ζ phase boundary of iron nitrides. *Journal of alloys and compounds*, 327(1-2):43–46, 2001. 11

[48] Kenneth Henderson Jack. Binary and ternary interstitial alloys i. the iron-nitrogen system: the structures of Fe_4N and Fe_2N. *Proceedings of the Royal Society of London. Series A. Mathematical and Physical Sciences*, 195(1040):34–40, 1948. 11

[49] Naim Syla, Fisnik Aliaj, and Nazmi Hasi. Study of the compound layer of gas nitrided 31CrMoV9 steel. In *The 4th Global Virtual Conference*. V, 13

[50] J Dossett and GE Totten. Fundamentals of nitriding and nitrocarburizing. *ASM Handbook: Steel Heat Treating Fundamentals and Processes; ASM International: Materials Park, OH, USA*, page 619, 2013. 12, 19

[51] H-J Spies and A Dalke. Case structure and properties of nitrided steels. 2014. V, VI, 12, 13, 28, 35, 36

[52] Hong Du, Marcel AJ Somers, and John Agren. Microstructural and compositional evolution of compound layers during gaseous nitrocarburizing. *Metallurgical and Materials Transactions A*, 31(1):195–211, 2000. 12, 51

[53] Hiroshi Yamagata. *8 - The crankshaft*, pages 165–206. Woodhead Publishing, 2005. 13, 19, 21, 51

[54] Yang Mei. Nitriding-fundamentals, modeling and process optimization. *A Dissertation for the Degree of Doctor of Philosophy in Material Science and Engineering*, page 134, 2012. 13, 15, 16

[55] Valter Luiz Jantara and Mayorkinos Papaelias. *Chapter 5 - Wind turbine gearboxes: Failures, surface treatments and condition monitoring*, pages 69–90. Butterworth-Heinemann, Boston, 2020. 13

[56] L Torchane, Ph Bilger, J Dulcy, and M Gantois. Control of iron nitride layers growth kinetics in the binary Fe-N system. *Metallurgical and Materials Transactions A*, 27(7):1823–1835, 1996. V, 13, 16, 17

[57] T. Bell and P.A. Dearnley. Environmental issues in surface engineering and related industrial sectors. *Surface Engineering*, 10(2):123–128, 1994. 14

[58] Kapil Gupta, Neelesh Kumar Jain, and Rudolph Laubscher. *Chapter 6 - Surface Property Enhancement of Gears*, pages 167–196. Academic Press, 2017. V, 14, 19, 20

[59] R. C. Shivamurthy, M. Kamaraj, R. Nagarajan, S. M. Shariff, and G. Padmanabham. *7 - Laser surface modification of steel for slurry erosion resistance in power plants*, pages 177–287. Woodhead Publishing, 2012. 14, 19

[60] Alfred Grill. *Cold plasma in materials fabrication*, volume 151. IEEE Press, New York, 1994. 14

[61] HA Wriedt, NA Gokcen, and RH Nafziger. The Fe-N (iron-nitrogen) system. *Bulletin of Alloy Phase Diagrams*, 8(4):355–377, 1987. 15

[62] B Guillot, Sébastien Jégou, and Laurent Barrallier. Degradation of gaseous nitriding of steel by lubricant contamination—effect of in-situ pre-treatments. *Surface and Coatings Technology*, 316:59–70, 2017. 16, 110

[63] Marcel AJ Somers and Eric J Mittemeijer. Layer-growth kinetics on gaseous nitriding of pure iron: Evaluation of diffusion coefficients for nitrogen in iron nitrides. *Metallurgical and Materials Transactions A*, 26(1):57–74, 1995. 16, 17, 18, 22

[64] JRG Da Silva and Rex B McLellan. Diffusion of carbon and nitrogen in bcc iron. *Materials Science and Engineering*, 26(1):83–87, 1976. 17, 29, 52, 129

[65] T Liapina, A Leineweber, and EJ Mittemeijer. Phase transformations in iron-nitride compound layers upon low-temperature annealing: Diffusion kinetics of nitrogen in ε-and γ-iron nitrides. *Metallurgical and Materials Transactions A*, 37(2):319–330, 2006. 17, 22

[66] Y Sun and T Bell. A numerical model of plasma nitriding of low alloy steels. *Materials Science and Engineering: A*, 224(1-2):33–47, 1997. 18

[67] A. Akbari, R. Mohammadzadeh, C. Templier, and J. P. Riviere. Effect of the initial microstructure on the plasma nitriding behavior of aisi m2 high speed steel. *Surface and Coatings Technology*, 204(24):4114–4120, 2010. VII, 18, 54, 55, 56, 57, 128

[68] Jeremie De Baerdemaeker, Julie Colaux, Guy Terwagne, and Charles Dauwe. Investigation of nitrided 304l stainless-steel coatings by positron annihilation spectroscopy. *Radiation Physics and Chemistry*, 68(3-4):605–608, 2003. 19

[69] A Fry. Stickstoff in eisen. *Stahl und Sonderstahl-ein neues Oberfl*ä*chenhärtungsverfahren Stahl und Eisen*, 40, 1923. 19

[70] S Epstein and J Wymore. Observations on the iron-nitrogen system. *Stahl und Eisen*, 43:1271, 1923. 19

[71] B Edenhofer. Physical and metallurgical aspects of ionitriding. pt. 1. *Heat Treatment Metals*, (1):23–28, 1974. 19

[72] Ramnarayan Chattopadhyay. *Advanced thermally assisted surface engineering processes*. Springer Science & Business Media, 2007. 19

[73] KH Prabhudev. *Handbook of heat treatment of steels*. Tata McGraw-Hill Education, 1988. 19

[74] SN Grigoriev, AS Metel, and SV Fedorov. Modification of the structure and properties of high-speed steel by combined vacuum-plasma treatment. *Metal Science and Heat Treatment*, 54(1):8–12, 2012. 20, 51, 53, 58

[75] Bong-Yong Jeong and Myung-Ho Kim. Effects of the process parameters on the layer formation behavior of plasma nitrided steels. *Surface and coatings Technology*, 141(2-3):182–186, 2001. 20

[76] Reinar Grün and Hans-Joachim Günther. Plasma nitriding in industry—problems, new solutions and limits. *Materials Science and Engineering: A*, 140:435–441, 1991. 20, 30

[77] Z Soltani Asadi and F Mahboubi. Effect of component's geometry on the plasma nitriding behavior of AISI 4340 steel. *Materials & Design*, 34:516–521, 2012. 20

[78] G Nayal, DB Lewis, M Lembke, W-D Münz, and JE Cockrem. Influence of sample geometry on the effect of pulse plasma nitriding of M2 steel. *Surface and Coatings Technology*, 111(2-3):148–157, 1999. 20, 52, 53

[79] Mazhyn Skakov, Bauyrzhan Rakhadilov, Michael Scheffler, Gaukhar Karipbayeva, and Merey Rakhadilov. Electrolyte plasma nitriding of high-speed steel. In *Applied Mechanics and Materials*, volume 379, pages 161–166. Trans Tech Publ, 2013. 20

[80] C Kwietniewski, W Fontana, C Moraes, A da S Rocha, T Hirsch, and A Reguly. Nitrided layer embrittlement due to edge effect on duplex treated AISI M2 high-speed steel. *Surface and Coatings Technology*, 179(1):27–32, 2004. 20, 51, 54, 55, 58, 59

[81] C. Alves, E.F. da Silva, and A.E. Martinelli. Effect of workpiece geometry on the uniformity of nitrided layers. *Surface and Coatings Technology*, 139(1):1–5, 2001. 20

[82] AGF Araujo, M Naeem, LNM Araujo, THC Costa, KH Khan, JC Díaz-Guillén, Javed Iqbal, MS Liborio, and RRM Sousa. Design, manufacturing and plasma nitriding of AISI-M2 steel forming tool and its performance analysis. *journal of materials research and technology*, 9(6):14517–14527, 2020. 20, 51, 53, 55

[83] Arash Yazdani, Mansour Soltanieh, Hossein Aghajani, and Saeed Rastegari. A new method for deposition of nano sized titanium nitride on steels. *Vacuum*, 86(2):131–139, 2011. 20

[84] Hossein Aghajani and Sahand Behrangi. *Plasma nitriding of steels*. Springer, 2017. 21, 55

[85] Thomas Bauer, Doerte Laing, and Rainer Tamme. Characterization of sodium nitrate as phase change material. *International Journal of Thermophysics*, 33(1):91–104, 2012. 21

[86] K Funatani. Low-temperature salt bath nitriding of steels. *Metal science and heat treatment*, 46(7-8):277–281, 2004. 21

[87] ASM International. Handbook Committee. *ASM handbook: Heat treating*, volume 4. Asm Intl, 1991. 21

[88] J Dossett and GE Totten. Introduction to surface hardening of steels. *ASM Handbook*, 4:389–398, 2013. 21

[89] PN Kalu, AT Taiwo, and OO Adewoye. Development of an environmentally friendly in-situ pack-cyaniding technique. *Journal of Minerals & Materials Characterization & Engineering*, 11(1):21–30, 2012. 21

[90] K Funatani. Nitro-carburizing and nitriding technology-the state and development of processing technology. In *Proc. 23rd Heat Treating Society Conference, Pennsylvania, USA*, 2005. 21

[91] Benjamin Guillot. *Etude de procédés de préparation de surface avant nitruration-fiabilité du procédé*. Thesis, 2016. V, 21, 109

[92] Marcel AJ Somers. Nitriding and nitrocarburizing; current status and future challenges. In *Heat Treat & Surface Engineering Conference & Expo 2013*, 2013. V, 22, 23, 25, 27, 51, 52, 53

[93] Tobias Steiner and Eric Jan Mittemeijer. Alloying element nitride development in ferritic Fe-based materials upon nitriding: A review. *Journal of Materials Engineering and Performance*, 25(6):2091–2102, 2016. V, 23, 24, 27, 34, 117

[94] CW Kang, Sai Ramudu Meka, RE Schacherl, and EJ Mittemeijer. Microstructure and kinetics of nitride precipitation in a quaternary iron-based model Fe-2.82 at. pct Cr-0.13 at. pct Mo-0.18 at. pct V alloy. *Metallurgical and Materials Transactions A*, 46(1):328–336, 2015. V, 23, 24, 117

[95] Sai Ramudu Meka and Eric Jan Mittemeijer. Abnormal nitride morphologies upon nitriding iron-based substrates. *JOM*, 65(6):769–775, 2013. VI, 24, 52, 117

[96] H Selg, E Bischoff, I Bernstein, T Woehrle, Sai Ramudu Meka, RE Schacherl, T Waldenmaier, and EJ Mittemeijer. Defect-dependent nitride surface layer development upon nitriding of fe–1 at.% mo alloy. *Philosophical Magazine*, 93(17):2133–2160, 2013. 24, 52, 117

[97] Sebastien Jegou, Laurent Barrallier, and Regis Kubler. Phase transformations and induced volume changes in a nitrided ternary fe–3 *Acta Materialia*, 58(7):2666–2676, 2010. VI, 25, 29, 30, 32, 34, 53, 55, 115, 126, 129

[98] Marcel AJ Somers. Nitriding and nitrocarburizing; current status and future challenges. In *Heat Treat and Surface Engineering Conference and Expo 2013*. 25

[99] R Braun and M Feller-Kniepmeier. Diffusion of chromium in α-iron. *physica status solidi (a)*, 90(2):553–561, 1985. 26

[100] Sai Ramudu Meka. Nitriding of iron-based binary and ternary alloys: microstructural development during nitride precipitation. 2011. 26

[101] Louis Toth. *Transition metal carbides and nitrides*. Elsevier, 2014. 26

[102] David A Porter and Kenneth E Easterling. *Phase transformations in metals and alloys (revised reprint)*. CRC press, 2009. VI, 26, 118

[103] G Sai Gautam and KC Hari Kumar. Elastic, thermochemical and thermophysical properties of rock salt-type transition metal carbides and nitrides: a first principles study. *Journal of alloys and compounds*, 587:380–386, 2014. 26

[104] Jean-Noël Locquet, Richard Soto, Laurent Barrallier, and Ahmed Charaï . Complete tem investigation of a nitrided layer for a Cr alloy steel. *Microscopy Microanalysis Microstructures*, 8(4-5):335–352, 1997. VI, 26, 27, 29, 38

[105] Sébastien Jegou. *Influence des éléments d'alliage sur la genèse des contraintes résiduelles d'aciers nitrurés*. Thesis, 2009. VI, 26, 34

[106] Sai Ramudu Meka, Ankur Chauhan, Tobias Steiner, Ewald Bischoff, PK Ghosh, and Eric Jan Mittemeijer. Generating duplex microstructures by nitriding; nitriding of iron based Fe-Mn alloy. *Materials Science and Technology*, 32(9):883–889, 2016. 27

[107] M Gouné, T Belmonte, A Redjaımia, P Weisbecker, JM Fiorani, and H Michel. Thermodynamic and structural studies on nitrided Fe–1.62% Mn and Fe–0.56% V alloys. *Materials Science and Engineering: A*, 351(1-2):23–30, 2003. 27

[108] JF Enrietto. Solubility and precipitation of nitrides in alpha-iron containing manganese. *Transactions of the Metallurgical Society of AIME*, 224(1):43, 1962. 27

[109] JD Baird. Precipitation of nitrides in iron-manganese-nitrogen alloys. *IRON STEEL INST J*, 204:1122–1130, 1966. 27

[110] Kazuhiro Nakata, Wataru Yamauchi, Katsuya Akamatsu, and Masao Ushio. Plasma nitriding behavior of low carbon binary alloy steels. *Surface and Coatings Technology*, 174:1206–1210, 2003. VI, 28, 36, 37, 52

[111] H. J. Spies and A. Dalke. *12.14 - Case Structure and Properties of Nitrided Steels*, pages 439–488. Elsevier, Oxford, 2014. VI, 28, 32, 37, 39, 40, 52

[112] Jean-Noel Locquet. *Caracterisations metallurgiques et mecaniques de couches nitrurees relation microstructure/comportement*. PhD thesis, Paris, ENSAM, 1998. 29, 38

[113] Laurent Barrallier. *Classical nitriding of heat treatable steel*, pages 393–412. Elsevier, 2015. VI, 29, 30, 31, 32, 34, 129

[114] Thomas K Hirsch, Alexandre Da S Rocha, Fabiano D Ramos, and Telmo R Strohaecker. Residual stress-affected diffusion during plasma nitriding of tool steels. *Metallurgical and Materials Transactions A*, 35(11):3523–3530, 2004. VII, 29, 52, 54, 58, 59, 118

[115] Sebastien Jegou, Regis Kubler, and Laurent Barrallier. On residual stresses development during nitriding of steel: Thermochemical and time dependence. In *Advanced Materials Research*, volume 89, pages 256–261. Trans Tech Publ. VI, 29, 30, 32, 33, 34

[116] Sebastien Jegou, Regis Kubler, Laurent Barrallier, and François Roch. Phase transormations involving residual stresses during gaseous nitriding of steel. 2009. 29, 30, 32

[117] Sebastien Jegou, Laurent Barrallier, Regis Kubler, and Marcel AJ Somers. Evolution of residual stress in the diffusion zone of a model Fe-Cr-C alloy during nitriding. *HTM Journal of Heat Treatment and Materials*, 66(3):135–142, 2011. 30, 32, 34, 55, 130

[118] Philip J Withers and HKDH Bhadeshia. Residual stress. part 2-nature and origins. *Materials science and technology*, 17(4):366–375, 2001. 30

[119] R. Mohammadzadeh, A. Akbari, and M. Drouet. Microstructure and wear properties of aisi m2 tool steel on rf plasma nitriding at different n 2 –h 2 gas compositions. *Surface and Coatings Technology*, 258:566–573, 2014. VII, 30, 40, 51, 53, 54, 55, 56

[120] T Gredić, Miodrag Zlatanović, N Popović, and Žarko Bogdanov. Properties of TiN coatings deposited onto hot work steel substrates plasma nitrided at low pressure. *Surface and Coatings Technology*, 54:502–507, 1992. 30

[121] VV Uglov, JA Fedotova, AK Kuleshov, AL Danilyuk, NT Kvasov, R Günzel, R Reuther, and E Richter. Evolution of microstructure of instrumental AISI M2 steel after plasma immersion nitrogen and carbon implantation. *Surface and Coatings Technology*, 136(1-3):226–230, 2001. 30, 53

[122] H.H. Huang, J.L. He, and M.H. Hon. Microstructure and mechanical properties of surface layer obtained by plasma nitriding and/or TiN coating on high speed steel. *Surface and Coatings Technology*, 64(1):41–46, 1994. 30

[123] Zbigniew Gawroński. Residual stresses in the surface layer of M2 steel after conventional and low pressure ('nitrovac 79') nitriding processes. *Surface and Coatings Technology*, 124(1):19–24, 2000. VII, 30, 51, 52, 55, 56

[124] T. Spalvins. Tribological and microstructural characteristics of ion-nitrided steels. *Thin Solid Films*, 108(2):157–163, 1983. 30

[125] V Goret. *Modélisation et simulation du traitement thermochimique de nitruration.* PhD thesis, PhD thesis, Arts et Métiers ParisTech, 2006. 30

[126] Philip J Withers and HKDH Bhadeshia. Residual stress. part 1–measurement techniques. *Materials science and Technology*, 17(4):355–365, 2001. 30

[127] Laurent Barrallier and Jean Barralis. On origin of residual stresses generated by nitriding treatment on alloy steels. In *Proc. 4th Int. Conf. Residual Stress, Baltimore*, volume 43, pages 629–642. 31

[128] George E Totten. *Handbook of residual stress and deformation of steel.* ASM international, 2002. 31

[129] Z Kolozsvary. Residual stresses in nitriding. *Handbook of Residual Stress and Deformation of Steel*, pages 209–219, 2002. 31

[130] H Oettel and B Ehrentraut. Makroskopische eigenspannungen in der verbindungsschicht gasnitrierter stähle. *HTM*, 40(4):183–187, 1985. 31

[131] G Fett. Importance of induction hardened case depth in torsional applications. *Heat Treating Progress*, 9(7):15–19, 2009. 32

[132] J. Grosch. *4 - Fatigue resistance of carburized and nitrided steels*, pages 209–240. Woodhead Publishing, Oxford, 2015. 32, 38, 39

[133] ICDD. Jcpds-international centre for diffraction data. *PCPDFWIN*, 2002. XV, 32, 33

[134] Laurent Barrallier. *Genèse des contraintes résiduelles de nitruration. Étude expérimentale et modélisation*. PhD thesis, Arts et Métiers ParisTech, 1992. XV, 33

[135] St Eriksson. Röntgenundersökningar över systemet järn-krom-kväve. *Jernkontorets Ann*, 118:530–542, 1934. 33

[136] Alexey Yu Ganin, Lorenz Kienle, and Grigori V Vajenine. Synthesis and characterisation of hexagonal molybdenum nitrides. *Journal of Solid State Chemistry*, 179(8):2339–2348, 2006. 33

[137] Tobias Steiner, Sai Ramudu Meka, Bastian Rheingans, Ewald Bischoff, Thomas Waldenmaier, Guma Yeli, Tomas L Martin, Paul AJ Bagot, Michael P Moody, and Eric J Mittemeijer. Continuous and discontinuous precipitation in Fe-1 at.%Cr-1 at.%Mo alloy upon nitriding; crystal structure and composition of ternary nitrides. *Philosophical Magazine*, 96(15):1509–1537, 2016. 33

[138] Harvey J Goldschmid. *Interstitial alloys*. Springer, 2013. 33

[139] W Daves and FD Fischer. Finite-element-simulation komplexer warmebehandlungsphanomene am beispiel des nitrierens. *BHM-Berg und Huttenmannische Monatshefte*, 141(5):204–207, 1996. 32

[140] H Oettel and G Schreiber. Eigenspannungsbildung in der diffusionszone. *Nitrieren und Nitrocarburieren*, 1989. 32

[141] H-J Spies, H Berns, A Ludwig, K Bambauer, and U Brusky. Warmhärte und eigenspannungen nitrierter stähle. *HTM. Härterei-technische Mitteilungen*, 53(6):359–366, 1998. 32

[142] PC Van Wiggen, HCF Rozendaal, and EJ Mittemeijer. The nitriding behaviour of iron-chromium-carbon alloys. *Journal of materials science*, 20(12):4561–4582, 1985. 34, 117

[143] P Buchhagen and T Bell. Simulation of the residual stress development in the diffusion layer of low alloy plasma nitrided steels. *Computational Materials Science*, 7(1-2):228–234, 1996. 34

[144] CW Kang, Sai Ramudu Meka, Tobias Steiner, Ralf Erich Schacherl, and Eric Jan Mittemeijer. Microstructural evolution of 31crmov9 steel upon controlled gaseous nitriding treatment. *HTM Journal of Heat Treatment and Materials*, 71(5):181–190, 2016. 34

[145] NE Vives Diaz, RE Schacherl, LF Zagonel, and EJ Mittemeijer. Influence of the microstructure on the residual stresses of nitrided iron–chromium alloys. *Acta Materialia*, 56(6):1196–1208, 2008. 34

[146] Alan J Ardell. Precipitation hardening. *Metallurgical Transactions A*, 16(12):2131–2165, 1985. 34

[147] L Petrova and O Chudina. Methodology of control of structure formation for development of hardening processes. *Metal Science & Heat Treatment*, 52, 2010. 34

[148] Michael F Ashby, Hugh Shercliff, and David Cebon. *Materials: engineering, science, processing and design*. Butterworth-Heinemann, 2018. VI, 34, 35

[149] Craig R Barrett, William D Nix, and Alan S Tetelman. *The principles of engineering materials*. Prentice hall, 1973. 34

[150] Vivek Pancholi. *Strenghening mechanism 3*. Department of Metallurgical and Materials Engineering, Indian Institute of Technology Roorkee, 1973. 34

[151] N Fo Mott and F Rs N Nabarro. An attempt to estimate the degree of precipitation hardening, with a simple model. *Proceedings of the Physical Society (1926-1948)*, 52(1):86, 1940. 34

[152] T Gladman. Precipitation hardening in metals. *Materials science and technology*, 15(1):30–36, 1999. VI, 34, 35, 36

[153] E Orowan. Symposium on internal stresses in metals and alloys. *Institute of Metals, London*, 451, 1948. 35

[154] H-J Spies and D Bergner. Innere nitrierung von eisenwerkstoffen. *HTM. Härtereitechnische Mitteilungen*, 47(6):346–356, 1992. 36, 52

[155] HJ Spies. Beitrag zum kontrollierten gasnitrieren von eisenwerkstoffen. *HTM. Härterei-technische Mitteilungen*, 39(1):1–6, 1984. 36

[156] LG Petrova and OV Chudina. Comparison of dispersion hardening by coherent and incoherent nitrides in nitriding of alloys based on iron, nickel, and cobalt. *Metal science and heat treatment*, 42(5):183–188, 2000. 37

[157] LG Petrova and OV Chudina. Prediction of hardening of binary iron alloys due to nitriding on the basis of calculation models. *Metal science and heat treatment*, 42(4):151, 2000. 37

[158] AV Gavrilova, SA Gerasimov, GF Kosolapov, and Yu D Tyapkin. The fine structure of nitrided steels. *Metal Science and Heat Treatment*, 16(3):210–216, 1974. 37

[159] Sébastien Jegou, Laurent Barrallier, and Guillaume Fallot. Gaseous nitriding behaviour of 33Crmov12-9 steel: Evolution of the grain boundaries precipitation and influence on residual stress development. *Surface and Coatings Technology*, 339:78–90, 2018. 38, 117, 118, 125, 126, 129

[160] GA Thomas, JG Speer, DK Matlock, G Krauss, and RE Hackenberg. Time-temperature equivalence in martensite tempering. In *International Conference on Martensitic Transformations (ICOMAT)*, pages 595–600. Wiley Online Library, 2010. 38

[161] DH Jack, PC Lidster, P Grieveson, and KH Jack. Kinetics of nitriding iron alloys. *Chemical Metallurgy of Iron and Steel, Iron and Steel Inst., London*, 1973. 38

[162] Gongyao Wang and Peter Liaw. Fatigue and fracture behavior. In *Bulk metallic glasses*, pages 169–203. Springer, 2008. 38

[163] David C Maxwell and Theodore Nicholas. A rapid method for generation of a haigh diagram for high cycle fatigue. In *Fatigue and Fracture Mechanics: 29th Volume*. ASTM International, 1999. 38

[164] OH Basquin. The exponential law of endurance tests. In *Proc Am Soc Test Mater*, volume 10, pages 625–630, 1910. 38

[165] Yukitaka Murakami, Toshio Takagi, Kentaro Wada, and Hisao Matsunaga. Essential structure of sn curve: Prediction of fatigue life and fatigue limit of defective materials and nature of scatter. *International Journal of Fatigue*, 146:106138, 2021. 38

[166] O Hengstenberg and R Mailänder. Biegeschwingfestigkeit von nitrieren stähler. *VDI-Z*, 77:1126–1128, 1930. 38

[167] NL Mochel. A note on fatigue tests of nitrided steel. In *Proceedings*, volume 30, page 406. American Society for Testing and Materials. 38

[168] Richard Mailänder. Eigenspannungen und biegewechselfestigkeit verstickter stahlproben. *Archiv für das Eisenhüttenwesen*, 10(6):257–261, 1936. 38

[169] Erich Theis. *Über die durch Nitrieren entsehenden Eigenspannungen und deren Auswirkungen auf die Wechselbiegefestigkeit*. Thesis, 1940. 38

[170] H Wiegand. Nitrieren im motorenbau htm härterei-techn. *Mitt*, 1:166–185, 1942. 38

[171] R. E. Peterson. The role of stress distribution in fatigue. *Experimental Mechanics*, 1(4):105–115, 1961. VI, 39

[172] Ramnarayan Chattopadhyay. *Surface wear: analysis, treatment, and prevention*. ASM international, 2001. 39

[173] Ingrid Kovaříková, Beáta Szewczyková, Pavel Blaškoviš, Erika Hodúlová, and Emil Lechovič. Study and characteristic of abrasive wear mechanisms. *Materials Science and Technology*, 1:1–8, 2009. 39

[174] John M Ziman. Electrons in metals: A short guide to the fermi surface. *Contemporary Physics*, 4(2):81–99, 1962. 40

[175] 12 adhesion and adhesive wear. In G.W. Stachowiak and A.W. Batchelor, editors, *Engineering TriBology*, volume 24 of *Tribology Series*, pages 613–635. Elsevier, 1993. XII, 40, 154, 157

[176] C Dawes, DF Tranter, and CG Smith. Reappraisal of nitrocarburizing and nitriding when applied to design and manufacture of non-alloy steel automobile components. *Metals Technology*, 6(1):345–353, 1979. 40

[177] K Stiller, S Karagöz, H-O Andrén, and H Fischmeister. Secondary hardening in high speed steels. *Le Journal de Physique Colloques*, 48(C6):C6–405–C6–410, 1987. VII, XV, 41, 45, 46, 49, 50

[178] Joseph R Davis et al. *ASM specialty handbook: tool materials*. ASM international, 1995. 41

[179] Alan M Bayer, B Becherer, and Teledyne Vasco. High-speed tool steels. *ASM Handbook.*, 16:51–59, 1989. 41

[180] George Adam Roberts, Richard Kennedy, and George Krauss. *Tool steels*. ASM international, 1998. 41, 42

[181] C García, Ana Romero, Gemma Herranz, Y Blanco, and F Martin. Effect of vanadium carbide on dry sliding wear behavior of powder metallurgy AISI M2 high speed steel processed by concentrated solar energy. *Materials Characterization*, 121:175–186, 2016. 41

[182] Ilyas Hacisalihoglu, Fatih Yildiz, and Akgun Alsaran. Wear performance of different nitride-based coatings on plasma nitrided AISI M2 tool steel in dry and lubricated conditions. *Wear*, 384-385:159–168, 2017. 41, 54, 55, 58

[183] Asok Joarder. *High speed steels*. National Metallurgical Laboratory, Jamshedpur, 1994. 41

[184] American Society for Testing and Materials. *ASTM A 600-92a: Standard Specification for Tool Steel High Speed*. ASTM International, 2004. VI, 41, 42

[185] D Bhattacharyya, A Hajra, A Basu, and S Jana. The effect of grain size on the wear characteristics of high speed steel tools. *Wear*, 42(1):63–69, 1977. 41

[186] TA Neumeyer and A Kasak. Grain size of high-speed tool steels. *Metallurgical Transactions*, 3(8):2281–2287, 1972. 41

[187] Edward G Herbert. Report on hot-hardness characteristics of some modern tool steels and alloys. *Proceedings of the Institution of Mechanical Engineers*, 118(1):681–692, 1930. 41

[188] Shaosong Xiang, Riming Wu, Wei Li, Tao Hu, and Shan Huang. Improved red hardness and toughness of hot work die steel through tungsten alloying. *Journal of Materials Engineering and Performance*, pages 1–14, 2021. 41

[189] Feng GAO, Yilong LIANG, Jie FENG, and Liangdeng LI. Effect of low-temperature tempering on red hardness of high speed steel. *Hot Working Technology*, 2009:24, 2009. 41

[190] Rejane A Nogueira, Leonardo FM Souza, João Franklin Liberati, Lucio Salgado, Francisco Ambrozio Filho, et al. Grain size of commercial high speed steel. In *Materials science forum*, volume 530, pages 16–21. Trans Tech Publ, 2006. 41

[191] EA Smol'nikov and LM Orestova. Red hardness of high-speed steels. *Metal Science and Heat Treatment*, 17(6):467–470, 1975. 41

[192] L Lu, LG Hou, JX Zhang, HB Wang, H Cui, JF Huang, YA Zhang, and JS Zhang. Improved the microstructures and properties of M3: 2 high-speed steel by spray forming and niobium alloying. *Materials Characterization*, 117:1–8, 2016. 41

[193] Baozhen Yang, Xiang Xiong, Rutie Liu, Jie Chen, Junhao Yang, and Huaizhuang Luan. Effect of yttrium hydride addition on microstructure and properties of powder metallurgy CM2 high speed steel. *Journal of Materials Research and Technology*, 14:1275–1283, 2021. 41

[194] Robert Wilson. *Metallurgy and heat treatment of tool steels*. McGraw-Hill Companies, 1975. 41

[195] AP Gulyaev and IK Kupalova. Effect of cobalt on the structure and properties of high-speed steels. *Metal Science and Heat Treatment*, 12(8):666–671, 1970. 41

[196] Jiang Hua and Rajiv Shivpuri. A cobalt diffusion based model for predicting crater wear of carbide tools in machining titanium alloys. *J. Eng. Mater. Technol.*, 127(1):136–144, 2005. 41

[197] Minyoung Lee. High temperature hardness of tungsten carbide. *Metallurgical Transactions A*, 14(8):1625–1629, 1983. 41

[198] Ranga Komanduri. Tool materials. *Kirk-Othmer Encyclopedia of Chemical Technology*, 2000. 41

[199] Kaiming Wang, Baohua Chang, Jiongshen Chen, Hanguang Fu, Yinghua Lin, and Yongping Lei. Effect of molybdenum on the microstructures and properties of stainless steel coatings by laser cladding. *Applied Sciences*, 7(10):1065, 2017. 41

[200] Shaikh Asad Ali Dilawary, Amir Motallebzadeh, Šárka Houdková, Rostislav Medlin, Stanislav Haviar, František Lukáč, Muhammad Afzal, and Huseyin Cimenoglu. Modification of M2 hardfacing: Effect of molybdenum alloying and laser surface melting on microstructure and wear performance. *Wear*, 404:111–121, 2018. 41

[201] Hardy Mohrbacher. Metallurgical effects of niobium and molybdenum on heat-affected zone toughness in low-carbon steel. *Applied Sciences*, 9(9):1847, 2019. 41

[202] Johnny Sjöström. *Chromium martensitic hot-work tool steels: damage, performance and microstructure*. PhD thesis, 2004. 41

[203] Wang Rong, H-O Andren, H Wisell, and GL Dunlop. The role of alloy composition in the precipitation behaviour of high speed steels. *Acta metallurgica et materialia*, 40(7):1727–1738, 1992. XV, 41, 46, 49, 50

[204] NF EN ISO 4957. *Tool steels*. Association Française de Normalisation, 2018. 41

[205] Peter Payson. *The metallurgy of tool steels*. Wiley, 1962. 41

[206] Eckhard Pippel, Jörg Woltersdorf, Gottfried Pöckl, and Gerhard Lichtenegger. Microstructure and nanochemistry of carbide precipitates in high-speed steel S 6-5-2-5. *Materials Characterization*, 43(1):41–55, 1999. VII, 41, 46, 50

[207] Xue Feng Zhou, Feng Fang, and Jian Qing Jiang. A study on the microstructure of AISI M2 high speed steel manufactured by continuous casting. In *Advanced Materials Research*, volume 146, pages 1211–1215. Trans Tech Publ, Trans Tech Publ, 2011. 41

[208] Jinwen Zhang, Zhigang Zhao, Wenxian Wang, and Yutian Wang. Comparison of the microstructure of M2 steel fabricated by continuous casting and with a sand mould. *Metals*, 9(5):560, 2019. VII, 41, 42, 43, 44

[209] S Sackl, H Leitner, H Clemens, and S Primig. On the evolution of secondary hardening carbides during continuous versus isothermal heat treatment of high speed steel HS 6-5-2. *Materials Characterization*, 120:323–330, 2016. VII, 41, 47, 48, 49

[210] S Sackl, G Kellezi, H Leitner, H Clemens, and S Primig. Martensitic transformation of a high-speed tool steel during continuous heat treatment. *Materials Today: Proceedings*, 2:S635–S638, 2015. 41, 47, 48

[211] Zhou Xuefeng, Fang Feng, and Jiang Jianjing. Solidification microstructure of M2 high speed steel by different casting technologies. *Research and Development*, 2011. VI, VII, 41, 43, 44

[212] M Boccalini and H Goldenstein. Solidification of high speed steels. *International Materials Reviews*, 46(2):92–115, 2001. 42

[213] Rafael Agnelli Mesquita and Celso Antonio Barbosa. Spray forming high speed steel-properties and processing. *Materials Science and Engineering: A*, 383(1):87–95, 2004. 42

[214] Hanlin Peng, Ling Hu, Tungwai Ngai, Liejun Li, Xianglin Zhang, Heng Xie, and Weiping Gong. Effects of austenitizing temperature on microstructure and mechanical property of a 4-GPa-grade PM high-speed steel. *Materials Science and Engineering: A*, 719:21–26, 2018. 42

[215] Rafael Agnelli Mesquita and Celso Antonio Barbosa. Evaluation of as-hipped PM high speed steel for production of large-diameter cutting tools. In *Materials science forum*, volume 416, pages 235–240. Transtec Publications; 1999, 2003. 42

[216] Hanlin Peng, Ling Hu, Liejun Li, Liyun Zhang, and Xianglin Zhang. Evolution of the microstructure and mechanical properties of powder metallurgical high-speed steel S390 after heat treatment. *Journal of alloys and Compounds*, 740:766–773, 2018. 42

[217] Yan Jianxin and Li Zaiyuan. Development of MP high speed steel. *Kentanium*, 27(5):i316–320, 2010. 42

[218] Haixia Sun, Fang Yang, Zhimeng Guo, Xinyue Zhang, and Qian Qin. Complex-shaped high speed steel with high mechanical performance fabricated by gelcasting sintering. *International Journal of Materials Research*, 110(11):1074–1082, 2019. 42

[219] M Manuela Oliveira. High speed steel based materials for cutting tools. *Metal Powder Report*, 49(11):32–35, 1994. 42

[220] K-D Bouzakis, W König, and K Vossen. Use of powder metallurgical high speed steel in gear hobbing and gear shaping. *CIRP Annals*, 31(1):25–29, 1982. 42

[221] HF Fischmeister, R Riedl, and S Karagöz. Solidification of high-speed tool steels. *Metallurgical Transactions A*, 20(10):2133–2148, 1989. 42

[222] Rafael Agnelli Mesquita and Celso Antonio Barbosa. High-speed steels produced by conventional casting, spray forming and powder metallurgy. In *Materials science forum*, volume 498, pages 244–250. Trans Tech Publ, 2005. 42

[223] M Rosso, D Ugues, and M Actis Grande. The challenge of MP tool steels for the innovation. *Journal of Achievements in Materials and Manufacturing Engineering*, 18(1-2):175, 2006. 42

[224] Santiago Benito, Nils Wulbieter, Fabian Pöhl, and Werner Theisen. Microstructural analysis of powder metallurgy tool steels in the context of abrasive wear behavior: a new computerized approach to stereology. *Journal of Materials Engineering and Performance*, 28(5):2919–2936, 2019. 42

[225] J Badger. Grindability of conventionally produced and powder-metallurgy high-speed steel. *CIRP annals*, 56(1):353–356, 2007. 42

[226] A Kasak and EJ Dulis. Powder-metallurgy tool steels. *Powder Metallurgy*, 21(2):114–123, 1978. 42

[227] Christian Sohar, Agnieszka Betzwar-Kotas, Christian Gierl, Herbert Danninger, and Brigitte Weiss. Gigacycle fatigue response of tool steels produced by powder metallurgy compared to ingot metallurgy tool steels. *International journal of materials research*, 101(9):1140–1150, 2010. 42

[228] MR Ghomashchi. Quantitative microstructural analysis of M2 grade high speed steel during high temperature treatment. *Acta materialia*, 46(14):5207–5220, 1998. VI, 43

[229] RM Lima, Edilson Rosa Barbarosa Jesus, and Jesualdo Luiz Rossi. Effect of heat treatment on the microstructure of spray formed AISI M2 high-speed steel. 2003. 43

[230] Xuefeng Zhou, Feng Fang, Gang Li, and Jianqing Jiang. Morphology and properties of M_2C eutectic carbides in AISI M2 steel. *ISIJ international*, 50(8):1151–1157, 2010. 43, 44, 45

[231] XF Zhou, F Fang, F Li, and JQ Jiang. Morphology and microstructure of M_2C carbide formed at different cooling rates in AISI M2 high speed steel. *Journal of materials science*, 46(5):1196–1202, 2011. 43

[232] MR Ghomashchi and CM Sellars. Microstructural changes in as—cast M2 grade high speed steel during hot forging. *Metallurgical Transactions A*, 24(10):2171–2180, 1993. VII, 44, 45, 46

[233] Fu-sheng Pan, Wei-qing Wang, Ai-tao Tang, Li-zhi Wu, Ting-ting Liu, and Ren-ju Cheng. Phase transformation refinement of coarse primary carbides in M2 high speed steel. *Progress in Natural Science: Materials International*, 21(2):180–186, 2011. 44, 45

[234] Ke Xiaotao and Chen Liang. Effect of nitrogen on carbonitride in high speed steel. *Juniper Online Journal Material Science*, 5(4):1–5, 2019. 45

[235] A Dziedzic. The influence of tempering on the microstructure and microhardeness of HS 6-5-2 steel in the area of overlapping remelting obtained with the use of the gtaw method. *Archives of foundry engineering*, 10(1), 2010. 46

[236] P Bała and J Pacyna. The influence of kinetics of phase transformations during tempering on high-speed steels mechanical properties. *Journal of Achievements in Materials and Manufacturing Engineering*, 43(1):64–71, 2010. VII, 46, 47, 48

[237] MNC Ijomah. The structure and properties of engineering materials, 1992. 47

[238] P Bała, J Pacyna, and J Krawczyk. The kinetics of phase transformations during the tempering of HS6-5-2 steel. *Archives of Materials Science and Engineering*, 35(2):69–76, 2009. 47

[239] Stephanie Sackl, Harald Leitner, Michael Zuber, Helmut Clemens, and Sophie Primig. Induction hardening vs conventional hardening of a heat treatable steel. *Metallurgical and Materials Transactions A*, 45(12):5657–5666, 2014. 47, 48

[240] P Bała. *The kinetics of phase transformations during tempering and its influence on the mechanical properties*. PhD thesis, PhD thesis, AGH University of Science and Technology, Cracow, 2007 (in Polish), 2007. 47

[241] NN Cherenda, VV Uglov, VM Anishchik, AK Stalmashonak, and VM Astashinski. Structure-phase transformations in high-speed steel treated by compression plasma flow. *Vacuum*, 78(2-4):483–487, 2005. 51

[242] FAP Fernandes, SC Heck, CA Picone, and LC Casteletti. On the wear and corrosion of plasma nitrided AISI H13. *Surface and Coatings Technology*, 381:125216, 2020. 51

[243] MAJ Somers and EJ Mittemeijer. Formation and growth of compound layer on nitrocarburizing iron: kinetics and microstructural evolution. *Surface engineering*, 3(2):123–137, 1987. 51

[244] T Bell. Ferritic nitrocarburizing. *Heat-Treat. Met.*, 2(2):39–49, 1975. 51

[245] Eun-Kab Jeon, Ik Min Park, and Insup Lee. Plasma post-oxidation of nitrocarburized sum 24l steel. *Materials Science and Engineering: A*, 449-451:868–871, 2007. 51

[246] Yucel Birol. Effect of post-oxidation treatment on thermal fatigue behaviour of plasma nitrided hot work tool steel at elevated temperatures. *Surface and Coatings Technology*, 205(8-9):2763–2769, 2011. 51

[247] Bin Liu, Bo Wang, Xudong Yang, Xingfeng Zhao, Ming Qin, and Jianfeng Gu. Thermal fatigue evaluation of AISI H13 steels surface modified by gas nitriding with pre-and post-shot peening. *Applied Surface Science*, 483:45–51, 2019. 51, 55

[248] A da Silva Rocha, T Strohaecker, V Tomala, and T Hirsch. Microstructure and residual stresses of a plasma-nitrided m2 tool steel. *Surface and coatings technology*, 115(1):24–31, 1999. 51, 52, 53, 55

[249] M Wolfart, AS Rocha, TR Strohaecher, and TK Hirsch. Nitretação ionica de aço ferramenta para trabalho a frio abnt d6. In *Technical Conf. Wire Technology*, page 303. ABM São Paulo, 1996. 51

[250] G Jaeger, I Endler, K Bartsch, M Heilmaier, and A Leonhardt. Fatigue behavior of duplex treated TiC_xN_{1-x}- and $Ti_{1-x}Al_xN$-hard coating steel compounds. *Surface and Coatings Technology*, 150(2):282–289, 2002. 51, 52, 58

[251] Shengli Ma, Yanhuai Li, and Kewei Xu. The composite of nitrided steel of H13 and TiN coatings by plasma duplex treatment and the effect of pre-nitriding. *Surface and Coatings Technology*, 137(2):116–121, 2001. 51, 55, 58

[252] Y. Sun and T. Bell. Combined plasma nitriding and PVD treatments. *Transactions of the Institute of Metal Finishing*, 70(pt 1):38–44, 1992. 51, 58

[253] M Tier, A Bloyce, T Bell, and T Strohaecker. Wear of plasma nitrided high speed steel. *Surface engineering*, 14(3):223–228, 1998. 51, 55

[254] Larisa Petrova, Victor Vdovin, Peter Demin, and Alexandra Sergeeva. Nitriding of high speed steel for improvement of tools resistance. *Modern Trends in Manufacturing Technologies and Equipment: ICMTMTE 2021*, 21:204, 2022. 51, 52

[255] OI Butenko. Ionic nitriding. *Metal Science and Heat Treatment*, 7(10):687–690, 1965. 52

[256] Levon Capan, Omer Cimen, Hasan Cep, and Zerrin Oktem. Nitruration par échange d'ions de l'acier rapide pour outils AISI M2. *Matériaux & Techniques*, 84:13–16, 1996. 52

[257] MA Tier, F Kieckow, TR Strohaecker, AS Rocha, and T Bell. A study of carbon redistribution during plasma nitriding of steel. *Proceedings of the 15th IFHTSE-International Federation for Heat Treatment and Surface Engineering*, pages 193–199, 2006. 52

[258] M Tier, AV Dos Santos, and C Kuhnen. A study of grain boundary precipitation during plasma nitriding of steel. In *Fifteenth International Conference on Surface Modification Technologies*, pages 225–231, 2001. 52, 53

[259] DH Jack and KH Jack. Invited review: carbides and nitrides in steel. *Materials Science and Engineering*, 11(1):1–27, 1973. 52

[260] Y. Sun and T. Bell. Plasma surface engineering of low alloy steel. *Materials Science and Engineering: A*, 140:419–434, 1991. Second International Conference on Plasma Surface Engineering. 52

[261] Rezső Nemények. *Controlled Atmospheres for Heat Treatment: The Pergamon Materials Engineering Practice Series*. Elsevier, 2013. 52

[262] P Egert, AM Maliska, HRT Silva, and CV Speller. Decarburization during plasma nitriding. *Surface and Coatings Technology*, 122(1):33–38, 1999. 52

[263] André Francis Rousseau. Metallurgical characterization and performance of high speed steel tool materials used in metal cutting applications. *Melbourne: Swinburne University of Technology*, 2016. 52

[264] H Klümper-Westkamp, F Hoffmann, and P Mayr. Nitrierschichtbildung und kohlenstoffdiffusion in abhängigkeit von der nitrierkennzahl. *HTM Journal of Heat Treatment and Materials*, 44(6):346–355, 1989. 53

[265] O.T. Inal and C.V. Robino. Structural characterization of some ion-nitrided steels. *Thin Solid Films*, 95(2):195–207, 1982. 53

[266] D Scott and J Blackwell. Étude de matériaux pour pièces de roulement à chaud et sans lubrification. *Revue de Métallurgie*, 63(3):257–264, 1966. 53

[267] GS Fox-Rabinovich. Structure of complex coatings. *Wear*, 160(1):67–76, 1993. 54

[268] P Jurci, J Suchánek, and P Stolar. Effect of various plasma nitriding procedures on surface characteristics of P/M high speed steel. In *5 th ASM Heat Treatment and Surface Engineering Conference in Europe and the 3 rd International Conference on Heat Treatment with Atmospheres*, pages 197–208, 2000. 54

[269] MIKROSTRUKTURA IN LASTNOSTI. Plasma nitriding of P/M M2 tool steel-structure and properties. *Materiali in Tehnologije*, 37:3–4, 2003. 54

[270] Philipp Kramer and Peter Groche. Defect detection in thread rolling processes–experimental study and numerical investigation of driving parameters. *International Journal of Machine Tools and Manufacture*, 129:27–36, 2018. 54, 60, 141, 152

[271] Yun tao Xi, Dao xin Liu, and Dong Han. Improvement of corrosion and wear resistances of AISI 420 martensitic stainless steel using plasma nitriding at low temperature. *Surface and Coatings Technology*, 202(12):2577–2583, 2008. 54

[272] Bojan Podgornik and Jože Vižintin. Wear resistance of pulse plasma nitrided AISI 4140 and A355 steels. *Materials Science and Engineering: A*, 315(1-2):28–34, 2001. 54

[273] Y Sun, T Bell, and G Wood. Wear behaviour of plasma-nitrided martensitic stainless steel. *Wear*, 178(1-2):131–138, 1994. 54

[274] MS Libório, GB Praxedes, LLF Lima, IG Nascimento, RRM Sousa, M Naeem, TH Costa, SM Alves, and Javed Iqbal. Surface modification of M2 steel by combination of cathodic cage plasma deposition and magnetron sputtered MoS_2-TiN multilayer coatings. *Surface and Coatings Technology*, 384:125327, 2020. 54

[275] A daS Rocha, T Strohaecker, and T Hirsch. Effect of different surface states before plasma nitriding on properties and machining behavior of m2 high-speed steel. *Surface and coatings technology*, 165(2):176–185, 2003. VII, 55, 58, 59, 112, 118

[276] K Höck, G Leonhardt, B Bücken, H-J Spies, and B Larisch. Process technological aspects of the production and properties of in situ combined plasma-nitrided and PVD hard-coated high alloy tool steels. *Surface and Coatings Technology*, 74:339–344, 1995. 55, 58

[277] Mazhyn Skakov, Bauyrzhan Rakhadilov, Michael Scheffler, and Erlan Batyrbekov. Microstructure and tribological properties of electrolytic plasma nitrided high-speed steel. *Materials testing*, 57(4):360–364, 2015. 55

[278] Sule Yildiz Sirin, Kahraman Sirin, and Erdinc Kaluc. Effect of the ion nitriding surface hardening process on fatigue behavior of AISI 4340 steel. *Materials Characterization*, 59(4):351–358, 2008. 55, 93

[279] T Bell and NL Loh. The fatigue characteristics of plasma nitrided three pct Cr-Mo steel. *Journal of Heat Treating*, 2(3):232–237, 1982. 55

[280] Tarang Shinde, Rohit Chavan, Piyush Savadekar, Indrajit Patil, Omkar Walke, and Gauri Wagh. Analysis of nitrided H13 steel in rotating bending fatigue. *Materials Today: Proceedings*, 44:2507–2510, 2021. 55

[281] Mario Guagliano and L Vergani. Effect of nitriding on low-cycle fatigue properties. *International journal of fatigue*, 19(1):67–73, 1997. 55

[282] JM Cowling and JW Martin. Fatigue of nitrided en41b steel: effect of internal-stress distribution. *Metals Technology*, 8(1):289–296, 1981. 55

[283] Hadrien Weil. *Modélisation du besoin fonctionnel pour la nitruration gazeuse*. PhD thesis, Paris, ENSAM, 2017. 55

[284] Hadrien Weil, Laurent Barrallier, Sébastien Jégou, Nancy Caldeira-Meulnotte, and Guillaume Beck. Optimization of gaseous nitriding of carbon iron-based alloy based on fatigue resistance modelling. *International Journal of Fatigue*, 110:238–245, 2018. 55, 63

[285] K DANG VAN and B Griveau. On a new multiaxial fatigue limit criterion- theory and application. *Biaxial and multiaxial fatigue(A 90-16739 05-39). London, Mechanical Engineering Publications, Ltd., 1989,*, pages 479–496, 1989. VIII, 55, 61, 62, 63

[286] Hernan Desimone, Andrea Bernasconi, and Stefano Beretta. On the application of dang van criterion to rolling contact fatigue. *Wear*, 260(4-5):567–572, 2006. VIII, 55, 61, 62, 63

[287] K Dang Van and MH Maitournam. Rolling contact in railways: modelling, simulation and damage prediction. *Fatigue & Fracture of Engineering Materials & Structures*, 26(10):939–948, 2003. 55, 62

[288] AMG Langueh, J-F Brunel, Eric Charkaluk, Philippe Dufrenoy, J-B Tritsch, and F Demilly. Effects of sliding on rolling contact fatigue of railway wheels. *Fatigue and Fracture of engineering materials and Structures*, 36(6):515–525, 2013. 55, 60, 62

[289] ARS Ponter, AD Hearle, and KL Johnson. Application of the kinematical shakedown theorem to rolling and sliding point contacts. *Journal of the Mechanics and Physics of Solids*, 33(4):339–362, 1985. VIII, 55, 61, 62

[290] T Bruce, Hu Long, and RS Dwyer-Joyce. Threshold maps for inclusion-initiated micro-cracks and white etching areas in bearing steel: the role of impact loading and surface sliding. *Tribology letters*, 66(3):1–18, 2018. 55, 59, 60, 97

[291] VA Alves, CMA Brett, and A Cavaleiro. Influence of heat treatment on the corrosion of high speed steel. *Journal of applied electrochemistry*, 31(1):65–72, 2001. 56

[292] Valéria A Alves and Christopher MA Brett. Influence of alloying on the passive behaviour of steels in bicarbonate medium. *Corrosion science*, 44(9):1949–1965, 2002. 56

[293] Pavel Novák, Dalibor Vojtěch, and Jan Šerák. Wear and corrosion resistance of a plasma-nitrided MP tool steel alloyed with niobium. *Surface and Coatings Technology*, 200(18-19):5229–5236, 2006. 56

[294] CX Li and Thomas Bell. Corrosion properties of active screen plasma nitrided 316 austenitic stainless steel. *Corrosion Science*, 46(6):1527–1547, 2004. 56

[295] AR Mashreghi, SMY Soleimani, and S Saberifar. The investigation of wear and corrosion behavior of plasma nitrided DIN 1.2210 cold work tool steel. *Materials & Design*, 46:532–538, 2013. 56

[296] J Mankowski and J Flis. The pitting corrosion of plasma nitrided chromium steels in sulphate solution. *Corrosion science*, 35(1-4):111–116, 1993. 56

[297] Samad Vakili, Alireza Akbari, and Roghayeh Mohammadzadeh. Corrosion resistance of plasma nitrided AISI M2 high speed steel. *Protection of Metals and Physical Chemistry of Surfaces*, 51(4):630–636, 2015. 56

[298] Yu M Lakhtin and AA Lyubkin. Effect of original structure on the depth and hardness of the nitrided case. *Metal Science and Heat Treatment*, 12(3):234–237, 1970. 56

[299] S.A. Gerasimov, A.V. Zhikharev, V.A. Golikov, M.A. Gress, and G.I. Zubarev. *Met. Sci. Heat Treat*, 42:226–227, 2000. 56, 57

[300] VV Simochkin. Effect of prior heat treatment on the properties of nitrided structural and tool steels. *Metal Science and Heat Treatment*, 28(3):211–214, 1986. 56

[301] Ming Chen, Huabing Liu, Liaobo Wang, Zhou Xu, Vincent Ji, and Chuanhai Jiang. Residual stress and microstructure evolutions of SAF 2507 duplex stainless steel after shot peening. *Applied Surface Science*, 459:155–163, 2018. 58

[302] M Multigner, E Frutos, José Luis González-Carrasco, José Antonio Jiménez, P Marín, and Joaquín Ibáñez. Influence of the sandblasting on the subsurface microstructure of 316LVM stainless steel: Implications on the magnetic and mechanical properties. *Materials Science and Engineering: C*, 29(4):1357–1360, 2009. 58

[303] JM Guilemany, N Llorca-Isern, and PJ Szabo. Residual stress characterisation of grit blasted steel surfaces. *Surface engineering*, 12(1):77–79, 1996. 58

[304] Robert E Reed-Hill and Reza Abbaschian. Physical metallurgy principles, pws, 1992. 58

[305] Raymond Edward Smallman. *Modern physical metallurgy*. Elsevier, 2016. 58

[306] W Heinke, A Leyland, A Matthews, G Berg, C Friedrich, and E Broszeit. Evaluation of PVD nitride coatings, using impact, scratch and rockwell-c adhesion tests. *Thin solid films*, 270(1-2):431–438, 1995. 58

[307] A. Matthews and A. Leyland. Hybrid techniques in surface engineering. *Surface and Coatings Technology*, 71(2):88–92, 1995. 58

[308] A Matthews, A Leyland, B Dorn, PR Stevenson, M Bin-Sudin, Claus Rebholz, Andrey Voevodin, and J Schneider. Plasma-based surface engineering processes for wear and corrosion protection. *Journal of Vacuum Science & Technology A: Vacuum, Surfaces, and Films*, 13(3):1202–1207, 1995. 58

[309] J. Nickel, A.N. Shuaib, B.S. Yilbas, and S.M. Nizam. Evaluation of the wear of plasma-nitrided and TiN-coated HSS drills using conventional and micro-pixe techniques. *Wear*, 239(2):155–167, 2000. 58

[310] Marion Le, Fabrice Ville, Xavier Kleber, Jérôme Cavoret, Marie C Sainte-Catherine, and Laurence Briancon. Influence of grain boundary cementite induced by gas nitriding on the rolling contact fatigue of alloyed steels for gears. *Proceedings of the Institution of Mechanical Engineers, Part J: Journal of Engineering Tribology*, 229(8):917–928, 2015. 59

[311] L Barrallier, V Traskine, and S Botchenkov. Morphology of intergranular cementite arrays in nitrided chromium-alloyed steels. *Materials Science and Engineering: A*, 393(1-2):247–253, 2005. 59

[312] AR Chintha. Metallurgical aspects of steels designed to resist abrasion, and impact-abrasion wear. *Materials Science and Technology*, 35(10):1133–1148, 2019. VII, 59, 60

[313] Farshid Sadeghi, Behrooz Jalalahmadi, Trevor S Slack, Nihar Raje, and Nagaraj K Arakere. A review of rolling contact fatigue. 2009. 59, 89

[314] NSK Ltd. *NSK Premium Technology For Wind*. Nippon Seikō Kabushiki-gaisha, 2001. VII, 60

[315] Heinrich Hertz. On the contact of elastic solids. *Z. Reine Angew. Mathematik*, 92:156–171, 1881. 60

[316] H Hertz. On the contact of rigid elastic solids and on hardness, chapter 6: Assorted papers by h. hertz, 1882. 60

[317] Geneviève Inglebert, Tony Da Silva Botelho, and Isabelle Lemaire Caron. Théorie du contact de hertz-contacts ponctuels ou linéiques. *Techniques de l'ingénieur*, 33, 2011. VII, 61, 142, 147

[318] Jonas W Ringsberg. Life prediction of rolling contact fatigue crack initiation. *International Journal of fatigue*, 23(7):575–586, 2001. VIII, 61, 62

[319] K Ls Johnson. Plastic flow and residual stresses in rolling and sliding contact. In *Proc. Symp. on Fatigue in Rolling Contact, Inst. Mech. Eng., London, 1963*, volume 177, pages 54–65, 1963. 61

[320] Kenneth Langstreth Johnson. *A shakedown limit in rolling contact*. Division of Engineering, Brown University, 1962. 61

[321] Anders Ekberg. Rolling contact fatigue of railway wheels—a parametric study. *Wear*, 211(2):280–288, 1997. 61

[322] Anders Ekberg. Rolling contact fatigue of railway wheels–computer modeling and in-field data. In *Proceedings of 2nd mini conf. Contact mechanics and wear of railway systems*, pages 154–163, 1996. 61

[323] Anders Ekberg and Peter Sotkovszki. Anisotropy and rolling contact fatigue of railway wheels. *International journal of fatigue*, 23(1):29–43, 2001. 61

[324] Michel Chaussumier. *Un modèle statistique de calcul en fatigue multiaxiale pour les pièces mécaniques en acier nitruré*. Thesis, Paris, ENSAM, 1999. 63

[325] Andr 'e Raymond Christian Deperrois. *On the calculation of endurance limits of steels*. PhD thesis, Palaiseau, Polytechnic School, 1991. 63

[326] Ekkehart Kröner. Berechnung der elastischen konstanten des vielkristalls aus den konstanten des einkristalls. *Zeitschrift für Physik*, 151(4):504–518, 1958. 67

[327] PH Contet and J-F Ville. Surfascan 3d-an industrial 3d surface texture characterisation instrument. *International Journal of Machine Tools and Manufacture*, 35(2):151–156, 1995. 67

[328] M Arvinth Davinci, NL Parthasarathi, Utpal Borah, and Shaju K Albert. Effect of the tracing speed and span on roughness parameters determined by stylus type equipment. *Measurement*, 48:368–377, 2014. VIII, 67

[329] ERASTEEL. Em2. *Erasteel*, 1993. X, 72, 108

[330] American Society for Testing and Materials. *ASTM E112: Standard Test Methods for Determining Average Grain Size*. ASTM International, 2013. 78

[331] Ch R Sohar, A Betzwar-Kotas, Ch Gierl, B Weiss, and H Danninger. Fatigue behavior of m2 and m42 high speed steel up to the gigacycle regime. *Kovove Materialy-Metallic Materials*, 47:147–158, 2009. 92

[332] J Rogan. *Fatigue Strength of Tool Steels T1, M2 and M42 Subjected to High Compressive-Low Tensile Stress Cycling*, pages 1615–1620. Springer, 1979. 93

[333] Kazuaki Shiozawa and Lian Tao Lu. Internal fatigue failure mechanism of high strength steels in gigacycle regime. In *Key Engineering Materials*, volume 378, pages 65–80. Trans Tech Publ, 2008. 93

[334] Hideto Suzuki, Shingo Sugawara, Takeshi Kasuya, and Manabu Yasuoka. Fatiguereliability of the high-speed tool steel skh-51 by surface modification. In *The Japan Society of Mechanical Engineers 2002*, pages 253–254. The Japan Society of Mechanical Engineers, 2002. 93

[335] Przemysław Strzelecki and Tomasz Tomaszewski. Analysis of axial load and bending load effects on the fatigue life. In *AIP Conference Proceedings*, volume 2028, page 020019. AIP Publishing LLC, 2018. 93

[336] Yung-Li Lee, Jwo Pan, Richard Hathaway, and Mark Barkey. *Fatigue testing and analysis: theory and practice*, volume 13. Butterworth-Heinemann, 2005. 93

[337] Hans Achim von Philipp. *Über den Einfluß von Querschnittsgröße und Querschnittsform auf die Dauerfestigkeit bei ungleichmäßig verteilten Spannungen.* PhD thesis, 1941. 93

[338] T Lagoda, Anna Kulesa, Andrzej Kurek, and Justyna Koziarska. Correlation of uniaxial cyclic torsion and tension-compression for low-cycle fatigue. *Materials Science*, 53(4):522–531, 2018. 93

[339] BM Korevaar, S Coorens, Y Fu, J Sietsma, and S Van Der Zwaag. Effects of nitriding on fatigue strength of quenched and tempered steel: role of interstitial nitrogen. *Materials science and technology*, 17(1):54–62, 2001. 93

[340] PH Dawson. Effect of metallic contact on the pitting of lubricated rolling surfaces. *Journal of Mechanical Engineering Science*, 4(1):16–21, 1962. 97

[341] Gustaf Lundberg and Arvid Palmgren. Dynamic capacity of rolling bearings. 1949. 97

[342] Norimune Soda and Takashi Yamamoto. Effect of tangential traction and roughness on crack initiation/propagation during rolling contact. *ASLE TRANSACTIONS*, 25(2):198–206, 1982. 97

[343] Le Flour. Contact fatigue of automotive gears: evolution and effects of residual stresses introduced by surface treatments. *Fatigue & Fracture of Engineering Materials & Structures*, 23(3):217–228, 2000. 97

[344] Jean-Noël Locquet, Richard Soto, Laurent Barrallier, and Ahmed Charaï. Complete tem investigation of a nitrided layer for a cr alloy steel. *Microscopy Microanalysis Microstructures*, 8(4-5):335–352, 1997. 117

[345] Jae Hoon Jang, Chang-Hoon Lee, Yoon-Uk Heo, and Dong-Woo Suh. Stability of (ti, m) c (m= nb, v, mo and w) carbide in steels using first-principles calculations. *Acta Materialia*, 60(1):208–217, 2012. 118

[346] Federico Bottoli, Grethe Winther, Thomas L Christiansen, and Marcel AJ Somers. Influence of plastic deformation on low-temperature surface hardening of austenitic stainless steel by gaseous nitriding. *Metallurgical and Materials Transactions A*, 46(6):2579–2590, 2015. 118

[347] LD Jaffe and B Swartz. Time-temperature relations in tempering steel. Technical report, WATERTOWN ARSENAL LABS MA, 1944. 136

[348] Tadashi Sasada, Susumu Norose, and Hiroshi Mishina. The behavior of adhered fragments interposed between sliding surfaces and the formation process of wear particles. 1981. XII, 154, 157

Titre de la thèse : Nitruration gazeuse de l'acier à outil M2 pour amélioration des propriétés mécaniques de surface des molettes de roulage

Superviseurs : Pr. Laurent Barrallier, Dr. Sébastien Jégou, Dr. David Mercs

Résumé : Les molettes de roulage en acier rapide M2 pour la fabrication de vis de freins de stationnement électriques sont souvent confrontées à une défaillance prématurée en service. Les dommages et l'initiation des fissures se produisent à plusieurs micromètres sous la surface de la denture de la molette en raison de la charge élevée de contact, avec effet de glissement, et par la présence de gros carbures ségrégés. Une analyse de cas industriel utilisant le critère de fatigue de Dang Van montre que la nitruration augmente la résistance à la fatigue en proche surface du matériau.

Les cinétiques de nitruration gazeuse de l'acier M2 sont étudiées avec plusieurs jeux de paramètres. L'augmentation du potentiel de nitruration et de la température de traitement accélèrent le processus de nitruration en raison de la modification des conditions aux limites et de la cinétique de la réaction thermochimique, respectivement. Le traitement de nitruration gazeuse est sensible à la propreté et à la méthode de finition mécanique de la surface traitée.

Le gradient de dureté dans la couche de nitruration est généralement cohérent avec le gradient de concentration en azote, dont le maximum se situe à la surface. L'évolution des contraintes résiduelles dépend fortement du changement de volume induit par les transformations de phase provoquées par la nitruration. Elles atteignent leur maximum après l'accumulation du carbone (à une profondeur plus faible, avant que l'azote ne diminue de façon importante) et diminue près de la surface.

Le potentiel limite de nitruration pour la formation de la couche de combinaison est identifié pour atteindre la dureté la plus élevée à la surface sans formation de couche de combinaison. Sa grande fragilité et sa morphologie spécifique (comme la porosité) sont des problèmes pour l'application du matériau.

Les paramètres de nitruration sont finalement définis en considérant une contrainte résiduelle de compression élevée à la surface et un faible effet sur la dureté au cœur du matériau. Des essais de résistance à l'usure sont ensuite définies et réalisées.

L'usure, en particulier l'adhérence, est significative sur l'échantillon M2 non nitruré. Les paramètres de nitruration sélectionnés améliorent efficacement la résistance à l'usure de l'acier M2.

Mots-clés : Nitruration gazeuse, Acier M2, Contraintes résiduelles, Dureté, Résistance à l'usure, Fatigue superficiel.

Table des matières

1. Introduction iii
   1.1. Contexte iii
   1.2. Objectifs iii
2. Étude des molettes de roulage iv
   2.1. Caractérisations microstructurales iv
   2.2. Observation de la défaillance sur les filets des molettes v
   2.3. L'effet de la nitruration sur la durée de vie des molettes filetages vi
3. Nitruration vii
   3.1. Microstructure de la couche nitrurée vii
   3.2. Étude du diagramme de Lehrer viii
   3.3. Cinétique de nitruration ix
      3.3.1. Profil azote et carbone ix
      3.3.2. Profil de dureté x
      3.3.3. Profil de contraintes résiduelles xi
   3.4. Absence de couche de combinaison xii
   3.5. Effet de la température xiii
   3.6. Potentiel de nitruration xv
   3.7. Analyse Thermo-Calc xvi
4. Résistance à l'usure des surfaces nitrurées xvii
   4.1. Mesures de l'usure sur les disques en acier M2 xvii
   4.2. Mesures de l'usure des billes M2 sur disque en acier des pièces EPB xx
5. Conclusions xxii
   5.1. L'étude sur les molettes filetages actuelles xxii
   5.2. L'étude de la cinétique de nitruration gazeuse de l'acier M2 xxii
   5.3. L'effet de la nitruration sur le comportement d'usure de l'acier M2 xxiii

1. Introduction

1.1. Contexte

Ce travail de recherche, en collaboration avec LISI Automotive, est consacré à l'étude des performances de fonctionnement de la molette de roulage utilisée pour former les vis de frein de stationnement électrique (EPB : electric parking brake). LISI Automotive fournit des solutions de fixation et d'assemblage innovantes en métal et en plastique pour les secteurs automobiles et industriels du monde entier.

Dans l'industrie automobile, les fixations et les boulons exigent de plus en plus de durabilité et de fiabilité. La vis du système EPB doit tout particulièrement être garantie en tant que pièce de sécurité au niveau du système de freinage. Les molettes de roulage EPB sont fabriquées en acier rapide M2, mais les fabricants sont toujours confrontés au problème de la courte durée de vie et des défaillances prématurées de leurs molettes de roulage (Figure 1).

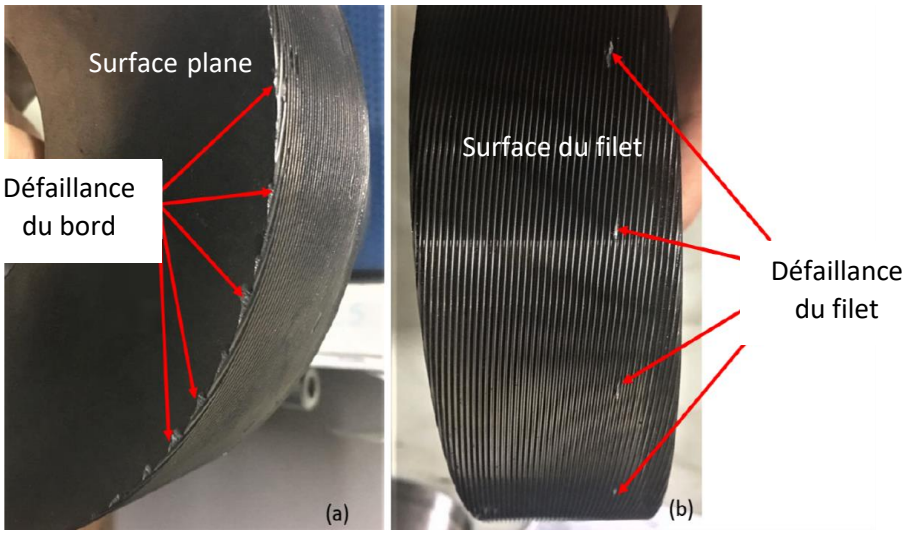


Figure 1 : Défaillances typiques sur la molette de roulage de l'EPB (les photos proviennent de LISI Automotive).

L'ingénierie de surface vise à modifier la microstructure et la composition de la surface ou des régions proches de la surface afin d'en améliorer la résistance et la durée de vie en offrant des propriétés différentes de celles du matériau de base. La nitruration est un traitement de surface thermochimique permettant de générer un gradient de microstructure et de contraintes résiduelles par diffusion d'azote dans l'acier.

1.2. Objectifs

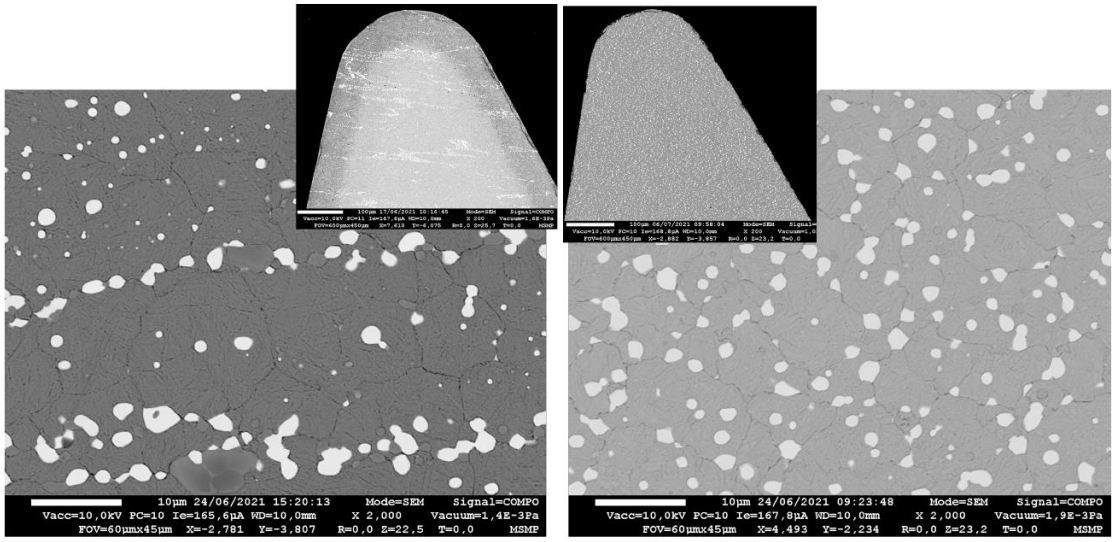
L'un des objectifs de ce travail est de comprendre l'évolution des défaillances mécaniques sur la molette de roulage en analysant la simulation numérique par éléments finis du processus de roulage et en observant les défaillances sur les molettes réelles. Ce travail vise également à comprendre la cinétique de la nitruration gazeuse sur l'acier à outils M2 en relation avec le renforcement de la surface et l'optimisation des paramètres de nitruration.

2. Étude des molettes de roulage

2.1. Caractérisations microstructurales

Les aciers rapides sont des aciers contenant une quantité significative d'éléments d'alliage tels que le chrome, le vanadium, le molybdène, le tungstène, etc., qui peuvent augmenter la trempabilité et la dureté de la matrice en développant de la martensite et des carbures alliés lors du traitement thermique de trempe et de revenu. L'évolution des carbures dépend de chaque étape du traitement thermique. La microstructure finale de l'acier M2 comprend des carbures primaires (M_6C, MC) et secondaires (MC, M_2C).

Des molettes de types E et G sont utilisés pour produire des profils des fillets différents et, elles ont été observées. L'analyse chimique montre que les matrices du type E sont fabriquées en acier M2, alors que celles du type G se caractérise par une composition chimique qui s'écarte de la norme de cette nuance. De plus, les molettes de type G sont fabriquées par métallurgie des poudres, et aucune ségrégation significative de carbure n'est observée (Figure 2).



(a) (b)

Figure 2: Microstructure des molettes sous un microscope optique (a) type E, (b) type G.

La proche surface se caractérise par un gradient de microstructure inférieure à 10 µm. Le traitement est relativement homogène d'après les micrographies du flanc et fond de denture. En raison de la fabrication par coulée, les bandes de carbures sont très claires dans les matrices du type E. La nitruration plasma conduit à une couche de nitruration non homogène (Figure 3). Les profondeurs de nitruration entre chaque type de molette varient et certaines présentent des couches de combinaison, d'autres non.

Les molettes de type E et de G présentent une dureté à cœur élevée, et supérieure à 900 et 1000 HV, respectivement. Compte tenu des dimensions des filets, la composition chimique et les contraintes résiduelles mesurées en surface ont été analysées du côté plan non utilisé des molettes (voir la Figure 1). Cependant, la nitruration n'étant pas effectuée de manière équivalente entre la surface plane

et la surface du filet (ré-usinage possible des filets en cours de production), aucune corrélation ne peut être faites entre filet et surface plane.

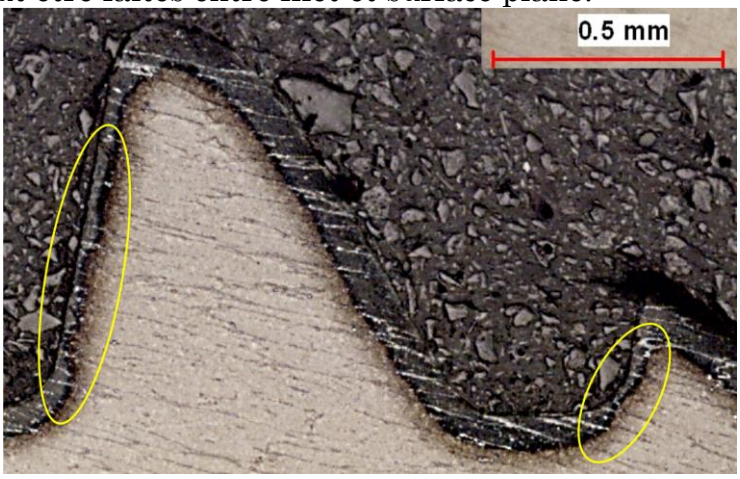


Figure 3 : Non-homogénéité locale du traitement de nitruration sur E3.

2.2. Observation de la défaillance sur les filets des molettes

L'initiation de fissures se trouve plusieurs micromètres sous la surface. La fissure semble s'initier à partir des carbures (le carbure de tungstène blanc et le carbure de vanadium foncé). Pour créer une défaillance finale, les fissures se terminent en s'ouvrant sur la surface avec un angle d'environ 20° comme le montre la Figure 4. L'usure de la surface est également observée, comme le montre la Figure 5. Quelques fissures existent dans les bandes de carbures.

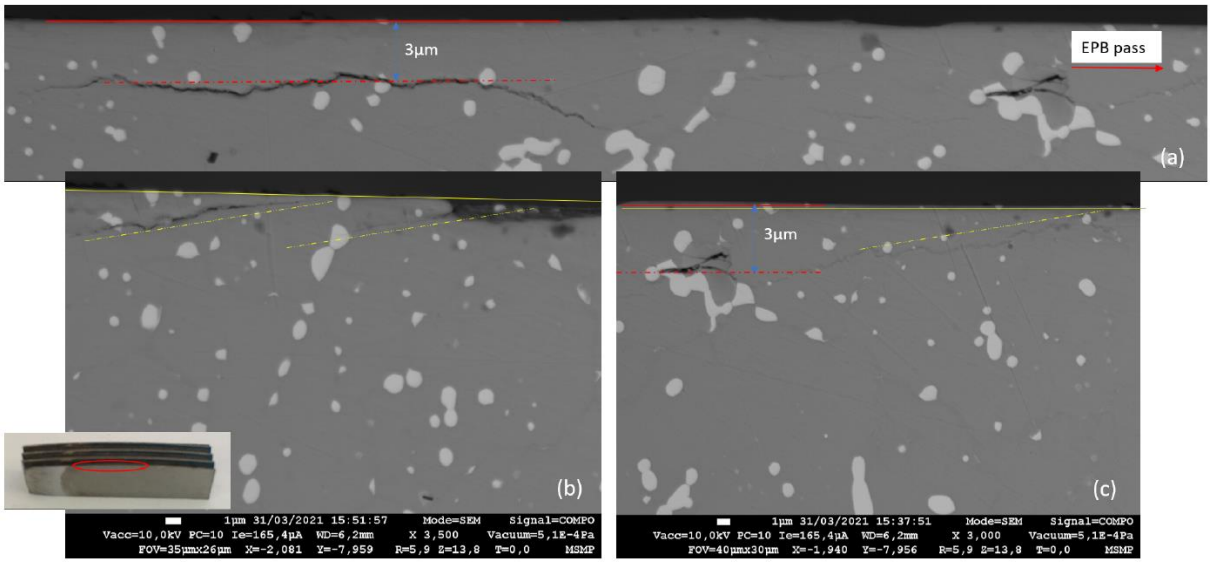


Figure 4 : Initiation de fissures observées sur la section transversale.

L'initiation des microfissures nécessite trois éléments : des niveaux élevés de pression de contact, des contraintes de traction en proche surface (friction) et des inclusions (carbures) situées à une position critique en sous couche. Le mécanisme de défaillance est proche de ce que l'on peut trouver dans la fatigue de contact par roulement et glissement. La fissure doit s'amorcer à l'endroit où se trouvent les contraintes de cisaillement maximales. Dans le mécanisme de rupture par fatigue

de contact de roulement, les fissures s'amorcent généralement sous la surface du chemin de roulement à des profondeurs proches de l'emplacement de la contrainte de cisaillement maximale avant de se propager vers la surface.

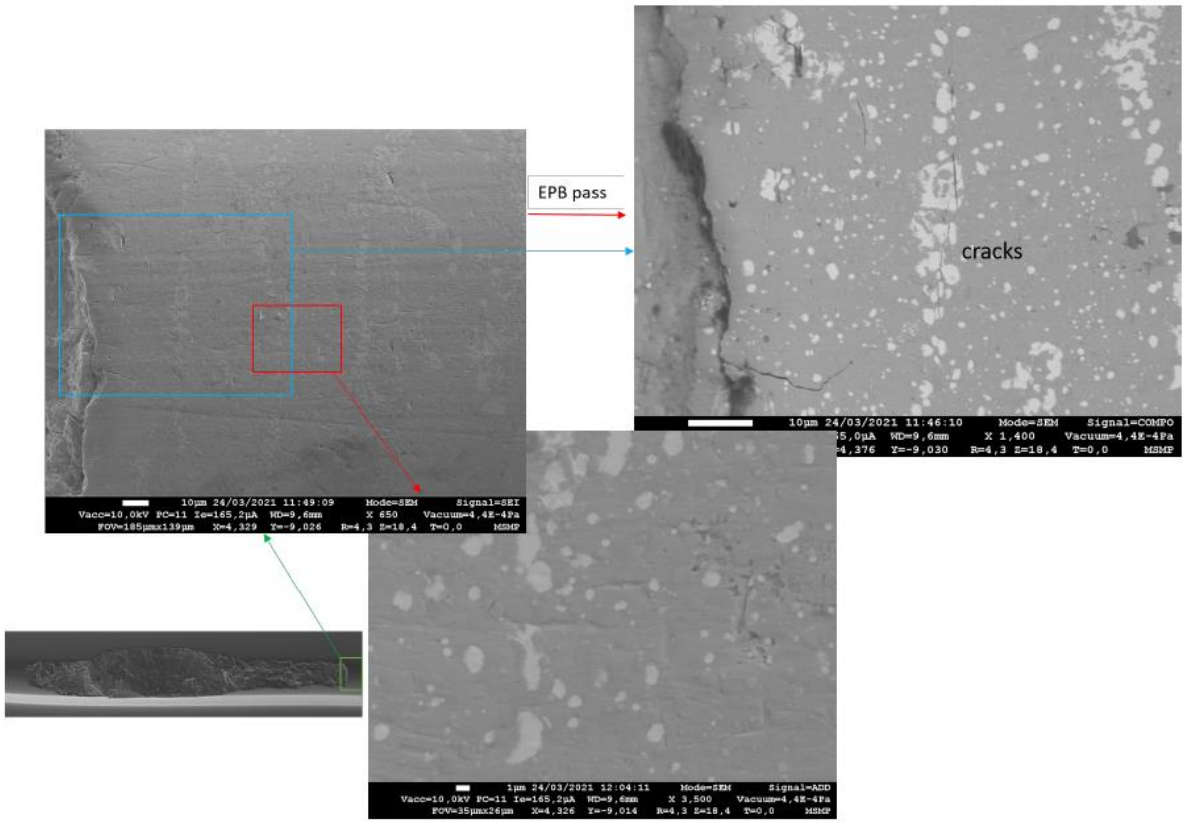


Figure 5 : Endommagement sur la surface de la crête à côté du bord droit de la rupture.

2.3. L'effet de la nitruration sur la durée de vie des molettes filetages

Des simulations numériques par éléments finis du processus de roulage des molettes a été fournis par Transvalor à LISI Automotive. Le critère de Dang Van a été appliqué pour analyser les résultats.

Le critère de Dang Van est basé sur l'application des principes de secousses élastiques à l'échelle mésoscopique, et il est mieux adapté à l'analyse de la fatigue de subsurface sous chargement multiaxial. La caractérisation habituelle du cycle de fatigue est remplacée par le chemin de chargement local à chaque cycle.

L'analyse le long des chemins de chargement (Figure 6) montre que la nitruration fonctionne près de la surface pour retarder l'initiation de la rupture par fatigue. Cependant, la fatigue de contact de roulement est très complexe, et la simulation a simplifié de nombreuses conditions, comme les conditions de lubrification, et le coefficient de frottement.

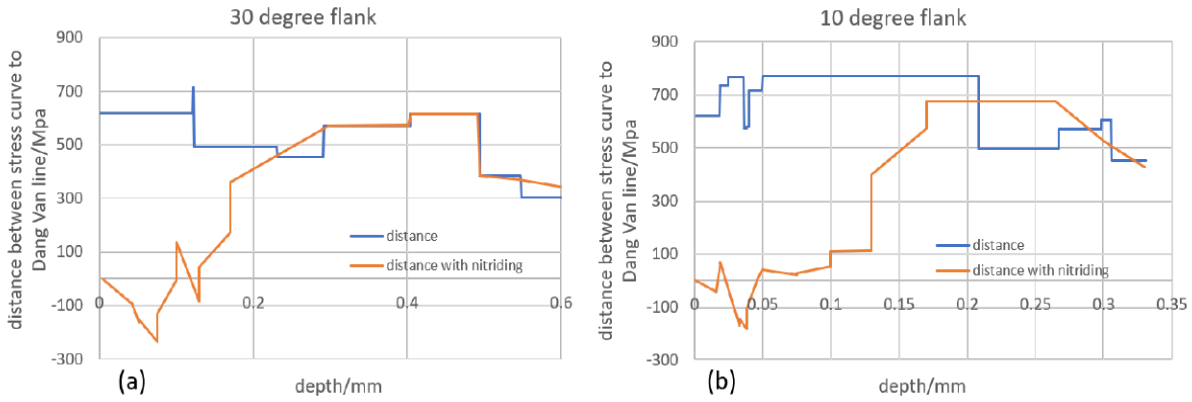


Figure 6 : Distance entre la courbe de contrainte et la ligne Dang Van en fonction de la profondeur le long du chemin (a) vertical au flanc de 30 degrés, (b) vertical au flanc de 10 degrés.

3. Nitruration

La nitruration gazeuse est généralement effectuée à une température comprise entre 480 et 570 °C dans une atmosphère contenant de l'ammoniac NH_3. Comparé à l'azote gazeux, N_2, dont le potentiel chimique est extrêmement faible, le potentiel d'azote est relativement plus élevé en présence d'ammoniac et cela dès les basses températures. L'ammoniac se décompose catalytiquement à la surface de l'acier en azotes élémentaires, qui après adsorption, se diffuse en surface du matériau traité. Afin de contrôler le potentiel de nitruration, le mélange gazeux est généralement composé d'ammoniac NH_3, de dihydrogène H_2 et de diazote N_2.

3.1. Microstructure de la couche nitrurée

La Figure 7 montre la microstructure de la couche nitrurée d'un échantillon d'acier M2 nitruré à 500 °C sous un potentiel de nitruration K_N de 1 $atm^{-1/2}$ durant 10 heures. Une couche de combinaison d'environ 1,5 µm est formée, des précipités de types nitrures d'éléments d'alliage et de la cémentite aux joints de grains sont observés.

Lors de la nitruration, les carbures initiaux se transforment en nitrures au niveau du front de diffusion de l'azote, et le carbone libéré réagit avec les éléments d'alliage dans la solution solide ferritique. Les carbures formés se transformeront plus tard en cémentite aux joints de grains. Lorsque la concentration en azote atteint une valeur plus élevée, la cémentite aux joints de grains se transforme en nitrures de fer. La Figure 7 montre un exemple de gradient de microstructures avec les nitrures de fer, la cémentite ou un mélange de ces deux phases aux joints de grains.

D'autres échantillons ont été observés au MEB en mode électrons rétrodiffusés avec la même méthode. Les profondeurs moyennes de nitrures (GB nitrures), cémentite (GB cémentite) ou d'un mélange des deux, présent aux joints de grains sont données sur la Figure 8. Comme supposé dans le cas d'un traitement dont le phénomène de diffusion est limitant, l'évolution des profondeurs des couches est linéaire en fonction de la racine carrée du temps de nitruration.

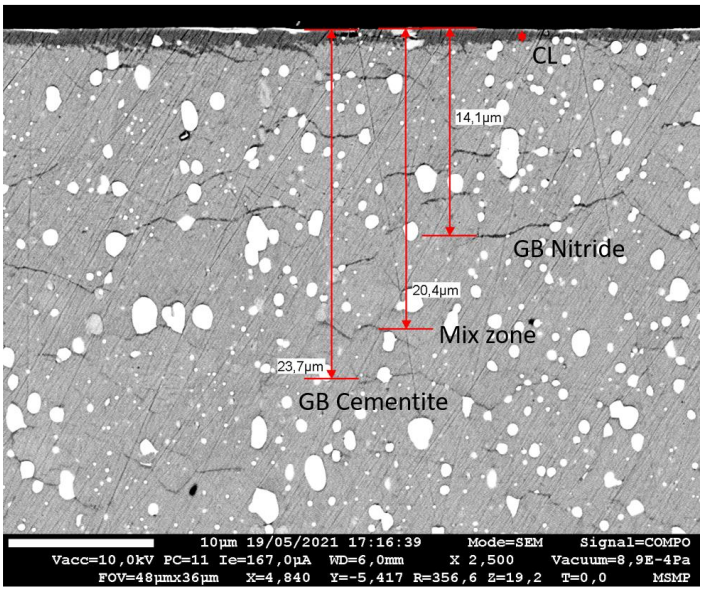


Figure 7 : Microstructure de la couche nitrurée dans un échantillon d'acier M2 (500 °C, 10 h, 1 $atm^{-1/2}$).

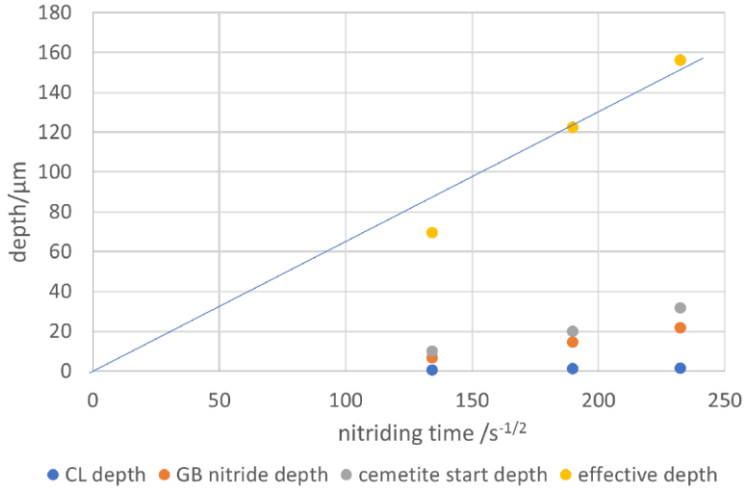


Figure 8 : Profondeur de la couche en fonction de la racine carrée du temps de nitruration (température de nitruration T=500 °C, k_N = 1 $atm^{-1/2}$).

La couche de combinaison présente l'évolution la plus faible. Cela s'explique par le fait que, pour une même croissance, la couche de combinaison nécessite la plus grande quantité d'azote. La cémentite commence normalement à se former au niveau du front de diffusion de l'azote. Lorsque la concentration d'azote dépasse la limite de solubilité dans la ferrite, tous les éléments d'alliage présents en solution solide précipitent sous forme de nitrures. Les précipités de cémentite se transforment en nitrures GB si la fraction d'azote augmente en proche surface.

3.2. Étude du diagramme de Lehrer

La couche nitrurée de l'acier M2 se compose principalement d'une couche de combinaison et d'une zone de diffusion. La couche de combinaison peut être évitée en contrôlant les paramètres de nitruration. Le potentiel de nitruration définit l'équilibre thermodynamique à l'interface entre l'atmosphère gazeuse et le

matériau. Le diagramme de Lehrer décrit la stabilité du système Fe-N en fonction du potentiel de nitruration $K_N = \frac{p_{NH3}}{p_{H2}^{3/2}}$.

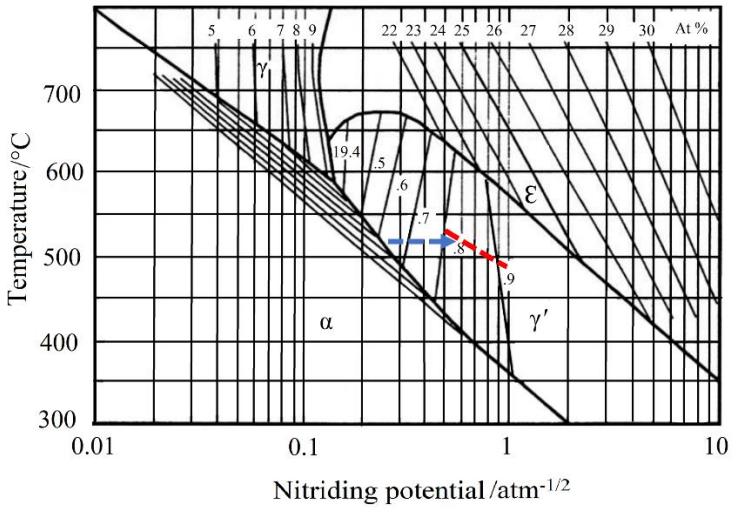


Figure 9 : Comparaison de la limite α/γ' dans le diagramme de Lehrer pour le fer pur et l'acier M2 (en rouge).

Au cours de la nitruration, la phase γ′-Fe_4N ne peut se former que lorsque la concentration en azote à la surface dépasse la valeur compatible avec l'équilibre α/γ'. Avant cela, c'est le temps d'incubation pour la formation des nitrures de fer. La Figure 9 rappelle le diagramme de Lehrer pour le fer pur. La couche de combinaison est normalement constituée de phases γ' et ε. En fonction de la teneur en éléments d'alliage précipitant sous forme de nitrures MN (M = Cr, V …), le pseudo diagramme de Lehrer pour l'acier M2 peut avoir une tendance de courbe similaire, et le but est de définir au moins deux points de la limite α/γ'. Le potentiel de nitruration pour la formation de la couche de combinaison dans l'acier M2 pendant la nitruration a été déterminé expérimentalement entre 0,8 et 0,9 $atm^{-1/2}$ à 500 °C, et entre 0,5 et 0,6 $atm^{-1/2}$ à 520 °C. Par rapport à la limite α/γ′ dans le diagramme de Lehrer pour le fer pur, comme le montre la ligne rouge sur Figure 9, la limite se déplace vers des concentrations en azote plus élevée en raison de l'existence d'éléments d'alliage.

3.3. Cinétique de nitruration

3.3.1. Profil azote et carbone

La Figure 10 montre le profil de concentration de l'azote et du carbone des trois échantillons nitrurés pendant 5, 10 et 15 heures respectivement à 500 °C pour K_N = 1 $atm^{-1/2}$. L'azote diffuse plus profondément lorsque le temps de nitruration augmente. Cependant, la concentration maximale d'azote près de la surface est à peu près la même. De manière plus intéressante, le carbone s'accumule au niveau du front de diffusion de l'azote, comme le montre le plateau de la courbe de concentration du carbone. Cette accumulation s'accompagne par la formation de carbures d'éléments d'alliage, qui se transforment en nitrures d'éléments d'alliage, puis en cémentite GB. L'étendue du plateau est d'environ 100 µm pour les conditions de nitruration considérées. La profondeur des nitrures GB et le début de la cémentite GB sont tous deux situés à des concentrations en azote

relativement élevées. Plus la nitruration est longue, plus la concentration en carbone à la surface est faible. La courbe de carbone grise de l'échantillon nitruré pendant 15 heures présente une concentration de carbone plus faible à la surface que les autres échantillons nitrurés pendant une durée plus courte.

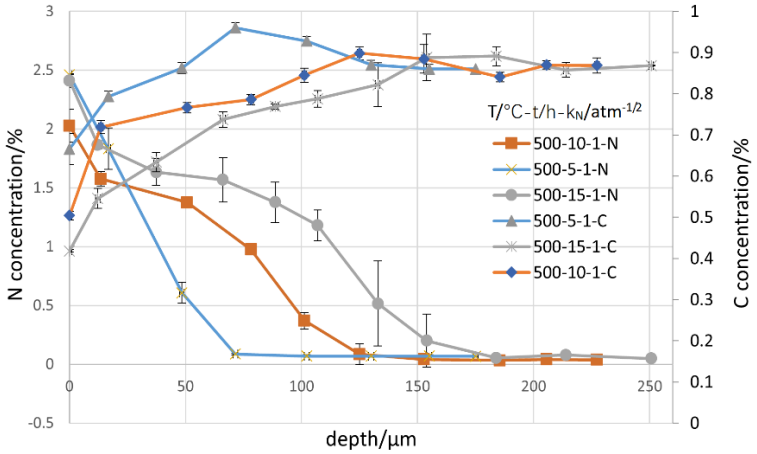


Figure 10 : Profils de concentration de N, C en fonction de la profondeur de nitruration (T=500 °C, KN = 1 atm-1/2).

3.3.2. Profil de dureté

La Figure 11 montre le profil de dureté des trois échantillons nitrurés pendant 5, 10 et 15 heures respectivement à 500 °C pour K_N = 1 $atm^{-1/2}$. La profondeur effective de nitruration augmente avec le temps de nitruration, mais la dureté maximale en surface varie peu. L'augmentation de la dureté est due à la précipitation de nitrures d'éléments d'alliage dans la couche de nitruration, en particulier dans la zone de diffusion. Ainsi, plus la diffusion est profonde dans l'acier au cours d'une période de nitruration plus longue, plus la profondeur de nitruration effective est importante. Cependant, la concentration d'azote atteint la même limite en raison de la limite de concentration des éléments d'alliage dans le matériau et de la précipitation maximale de nitrures d'éléments d'alliage. Ainsi, la dureté maximale atteint des valeurs similaires malgré les différents paramètres de nitruration. Si l'on trace la profondeur de nitruration effective en fonction de la racine carrée du temps de nitruration, la fonction est quasi linéaire (Figure 8).

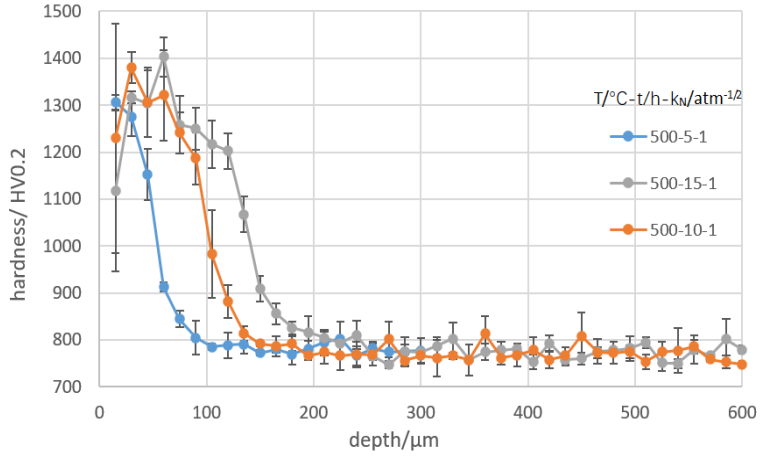


Figure 11 : Profil de dureté en fonction de la profondeur de nitruration pour 3 durées de nitruration (T=500 °C, kN = 1 atm-1/2).

3.3.3. Profil de contraintes résiduelles

La Figure 12 montre les profils de contraintes résiduelles en profondeur obtenus à partir des analyses en diffraction des rayons X (DRX). Les profils de contraintes résiduelles se caractérisent par des contraintes de compression liées aux déformations volumiques positives accompagnant la précipitation de nitrures d'éléments d'alliage au sein de la matrice ferritique. Les nitrures MN (M = Cr, V...) sont en effet caractérisés par un volume spécifique plus élevé que la matrice ferritique. L'expansion volumétrique varie en fonction de la fraction d'azote qui réagit avec les éléments d'alliage initialement présents dans la solution solide ferritique et les carbures primaires et secondaires. Pendant la nitruration, la genèse des contraintes résiduelles de compression est dominée par les transformations de phases. Les échantillons sont chauffés et refroidis à une vitesse de 10 °C/min, l'effet de la dilatation thermique est supposé négligeable.

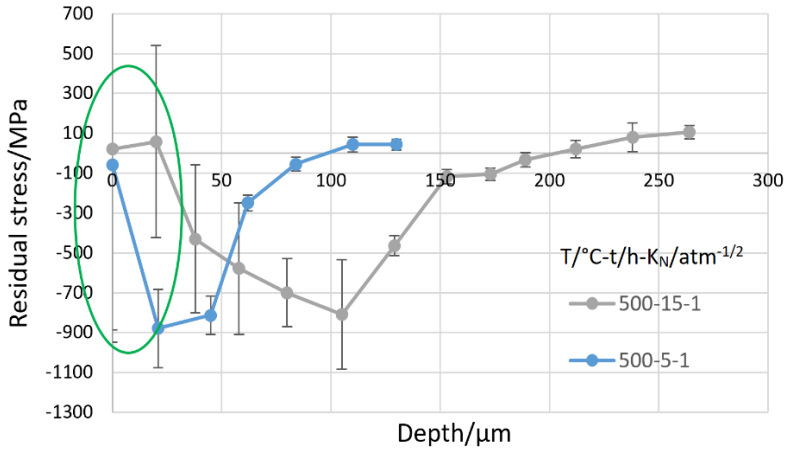


Figure 12 : Profil de contraintes résiduelles de l'échantillon M2 nitruré (T=500 °C, KN = 1 atm-1/2, pendant 5 et 15 heures).

Sur la Figure 12, la contrainte résiduelle de compression maximale se déplace vers une profondeur plus importante après une nitruration plus longue de 15 heures, mais la valeur maximale varie peu. Les contraintes résiduelles de compression près de la surface diminuent et peuvent même devenir positive. Au début de la nitruration, les nitrures précipitent à partir de la solution solide, ce qui provoque une expansion du volume, et la déformation élastique entraîne une contrainte résiduelle de compression. Lorsque la nitruration se poursuit, certaines transformations de phase entraînent une expansion volumique négative. Une variation de volume négative, même minime, peut conduire à une déformation élastique importante. Ainsi, accompagnée par la décarburation et le grossissement des précipités, une contrainte résiduelle positive serait générée après que les contraintes résiduelles élastiques soient complètement équilibrées. Par rapport à la Figure 10, les contraintes résiduelles maximales se situent juste avant le plateau de carbone.

Du point de vue des transformations de phases, à la profondeur où les contraintes résiduelles atteignent la valeur maximale (si ce n'est pas à la surface), tous les éléments d'alliage sont sous forme de nitrures. La transformation des carbures initiaux en nitrures diminue la cinétique de la nitruration et est contrecarrée par la précipitation de cémentite. Cela diminue la variation de volume

et donc des contraintes résiduelles pendant la nitruration. Durant la nitruration, l'évolution des nitrures et des carbures peut être résumée en 4 étapes :

- Précipitation des nitrures : au début du traitement, de fins nitrures semi-cohérents précipitent à partir de la solution solide grâce à la grande affinité des éléments d'alliage pour l'azote.

- Transformation des carbures initiaux en nitrures incohérents, ce qui entraîne un changement de volume moins important en raison d'une différence de volume spécifique plus faible.

- Diffusion du carbone au front de diffusion : les éléments d'alliage forment d'abord des carbures puis se transforment en nitrures incohérents, ce qui diminue la quantité de nitrures semi-cohérents et entraîne une moindre expansion du volume au cours de la nitruration.

- Transformation, en proche surface, de la cémentite en nitrure de fer provoque la décarburation, ce qui diminue le chargement élastique causé par la transformation de phase antérieure pendant la nitruration.

Pendant la nitruration, ces quatre étapes peuvent se produire simultanément. Ces étapes conduisent à des changements de volume et à une évolution des contraintes résiduelles différente. Dans les profondeurs plus importantes, les deuxièmes et troisièmes types de transformations de phase se produisent de manière plus significative. Il en résulte que moins d'éléments d'alliage se joignent au premier type de transformations de phase, ce qui provoque l'expansion de volume minimal parmi ces trois. Ainsi, la valeur maximale des contraintes résiduelles de compression tend à diminuer au cours du temps de nitruration. Une fois les contraintes résiduelles maximales atteinte, tout comme l'effet du temps de vieillissement sur la taille des précipités, la poursuite de la nitruration entraîne le remplacement des nitrures cohérents et semi-cohérents par des nitrures incohérents et relativement plus grands. C'est ce qu'on appelle le grossissement des précipités et cela conduit à la redistribution des contraintes résiduelles. La décarburation de la surface implique une diminution de la fraction volumique de cémentite pendant la nitruration, ce qui entraîne un déchargement de la surface et donc une redistribution des contraintes résiduelles. Les contraintes résiduelles de compression diminuent davantage près de la surface de l'échantillon nitruré pendant 15 heures, ce qui concorde avec la plus faible concentration de carbone près de la surface (Figure 10).

3.4. Absence de couche de combinaison

Les potentiels de nitruration permettant de limiter la formation de la couche de combinaison ont été déterminés à 500 et 520 °C. Une étude de nitruration de plus longue durée à ces deux températures avec un potentiel de nitruration de 0.8 et 0.5 $atm^{-1/2}$ a été réalisée. Jusqu'à 50 heures de nitruration, aucune couche de combinaison n'est formée. Les profils de nitruration pour 520 °C à 0.5 $atm^{-1/2}$ sont présentés dans la Figure 13. La relation entre les trois profils répond aux mêmes règles que la nitruration avec couche de combinaison et ceci est encore plus évident lorsque le temps de nitruration est plus long. Comme indiqué par les étoiles rouges sur la Figure 13, les contraintes résiduelles atteignent la valeur maximale à la profondeur où la concentration d'azote et le profil de dureté évoluent vers la fin du plateau. C'est également là que se termine l'accumulation de carbone.

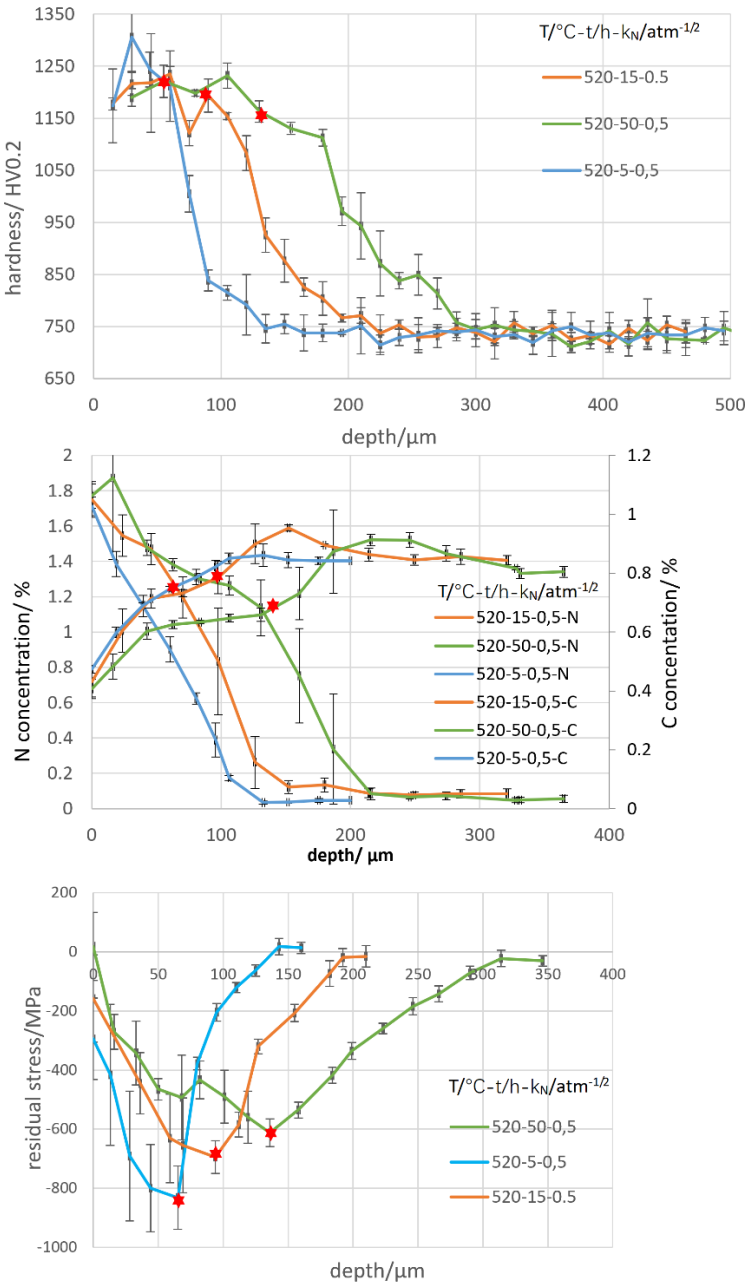


Figure 13 : Profils de nitruration de l'acier M2 (520 °C, 0.5 atm$^{-1/2}$, 5-50 h).

Les contraintes résiduelles maximales diminuent lorsque la profondeur augmente, le maximum est d'environ -830 MPa à 520 °C après 5 heures de nitruration, et de -970 MPa à 500 °C après 15 heures de nitruration. Les deux contraintes résiduelles maximales sont à environ 60 µm de profondeur. Cela montre qu'une variation de température de 20 °C est critique pour modifier la cinétique de nitruration et que les contraintes résiduelles peuvent atteindre des valeurs plus élevées à des températures inférieures. Les températures plus élevées affectent davantage le matériau de base.

3.5. Effet de la température

La Figure 14 montre les profils de gradients chimiques et mécaniques des échantillons M2 après nitruration avec K_N = 0,5 atm$^{-1/2}$ à des températures de 500

et 540 °C. Pour les profils d'azote et de dureté, la valeur atteint le maximum à la surface et diminue progressivement jusqu'au niveau du cœur. Le durcissement est lié à la précipitation des éléments d'alliage en nitrures MN (M=Cr, V, Mo...), qui sont finement dispersés dans la matrice ferritique, et donc à la teneur et à la diffusion de l'azote à travers la surface traitée. La nitruration à basse température (500 °C) conduit à des profondeurs de nitruration plus faibles, comme le montre la Figure 14 (c). Cela correspond à un enrichissement moindre en azote, comme le montre la Figure 14 (a). Sur la Figure 14 (a), la concentration en carbone de l'échantillon nitruré à 540 °C est plus faible. On peut remarquer que la dureté du matériau de base de l'échantillon nitruré à 540 °C est plus faible. La nitruration est équivalente à un effet de revenu pour le matériau à cœur, car 540 °C est proche de la température de revenu de 560 °C.

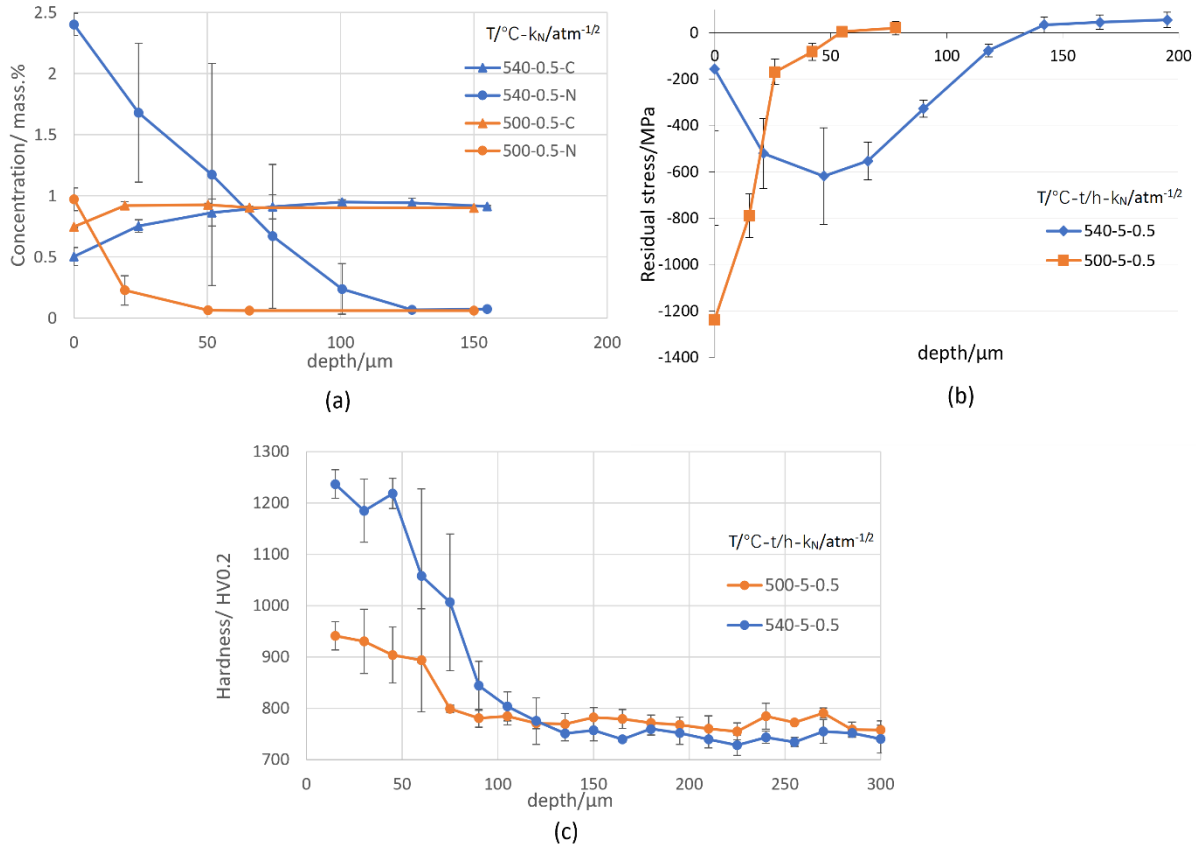


Figure 14 : Profil de la surface en profondeur de l'acier M2 après nitruration gazeuse avec kN = 0,5 atm-1/2 à différentes températures (a) profil N, C, (b) contrainte résiduelle, (c) profil de dureté.

La couche de nitruration croît plus rapidement avec l'augmentation de la température de nitruration, et la contrainte résiduelle maximale se produit à une profondeur plus importante sous la surface. Dans la Figure 14 (b), les contraintes résiduelles ont des valeurs plus élevées à la surface de l'échantillon nitruré à 500 °C, alors que ce maximum se retrouve à environ 50 µm de profondeur pour l'échantillon nitruré à 540 °C. Les contraintes résiduelles à la surface diminuent avec l'augmentation de la température. Cette redistribution des contraintes est

due à la diminution de volume induite par certaines transformations de phase, la cinétique de diffusion du carbone et le probable grossissement des précipités.

3.6. Potentiel de nitruration

Le potentiel de nitruration affecte directement la concentration d'azote dans l'atmosphère à la surface, donc les conditions aux limites de diffusion. Un potentiel de nitruration plus élevé signifie une pression partielle d'ammoniac plus élevée, augmentant la fraction d'azote à la surface et le gradient en fonction de la profondeur. Les faibles contraintes résiduelles et la faible concentration de carbone se trouvent près de la surface en raison de la décarburation.

La concentration d'azote et la dureté ont toujours la valeur maximale à la surface puis diminuent progressivement jusqu'à la même valeur que dans le cœur. La Figure 15 montre le profil N, C, de dureté et de contraintes résiduelles. La profondeur de nitruration effective est plus importante lorsque le potentiel de nitruration est de 3,7 $atm^{-1/2}$, tout comme la profondeur des contraintes résiduelles maximales. Elles sont le résultat de la précipitation des nitrures car la concentration en azote est plus élevée dans l'échantillon nitruré avec K_N =3.7 $atm^{-1/2}$.

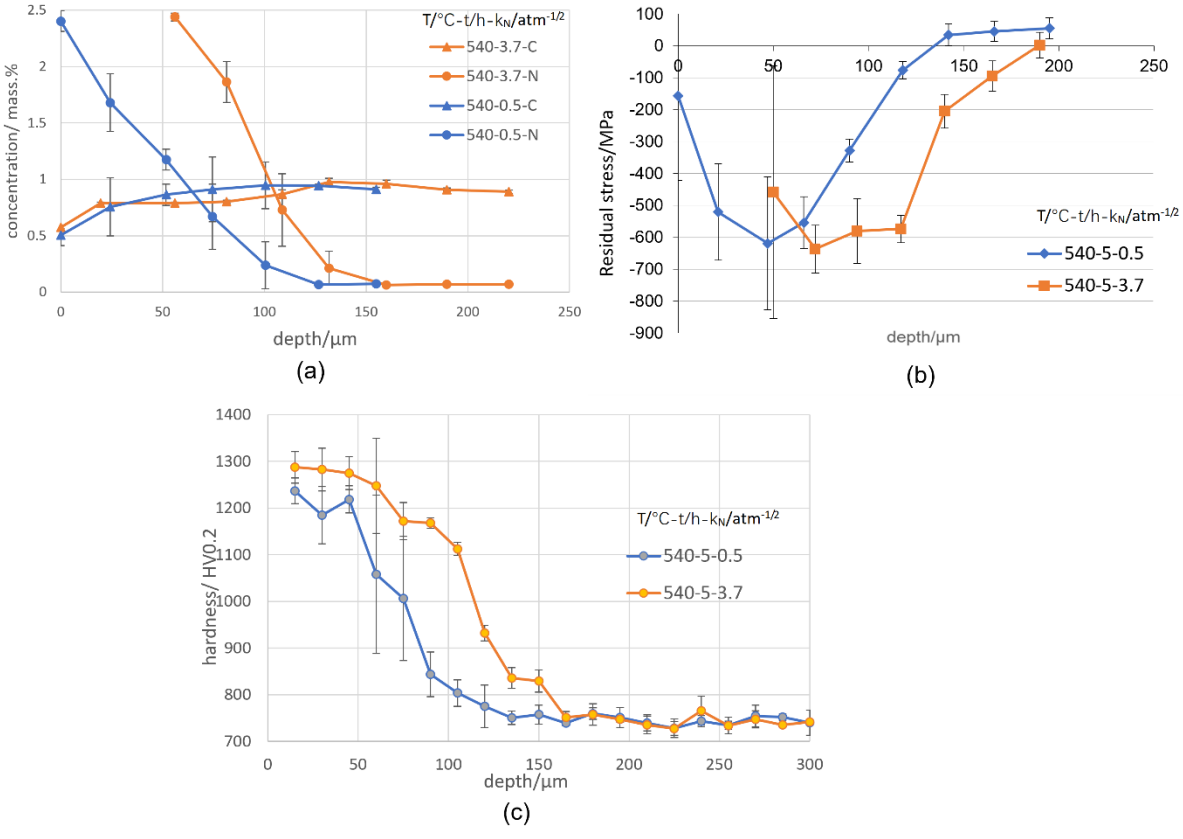


Figure 15 : Le profil en profondeur de l'acier M2 après nitruration gazeuse à 540 °C avec différents potentiels de nitruration (a) profil N, C, (b) contrainte résiduelle, (c) profil de dureté.

3.7. Analyse Thermo-Calc

Le logiciel de calcul thermodynamique Thermo-Calc est utilisé pour effectuer l'analyse des transformations de phase pendant la nitruration. La Figure 16 présente le diagramme de transformations de phase de l'acier M2 (avec une concentration en carbone de 0,8%) en fonction de la concentration en azote à 500 °C. Lorsque la concentration en N augmente, les nitrures de type MN commencent à précipiter, comme le montre la ligne rouge pleine. Les carbures (types M_2C, MC et M_6C) diminuent et le carbone libéré diffuse vers l'intérieur sous la force motrice de diffusion de l'azote.

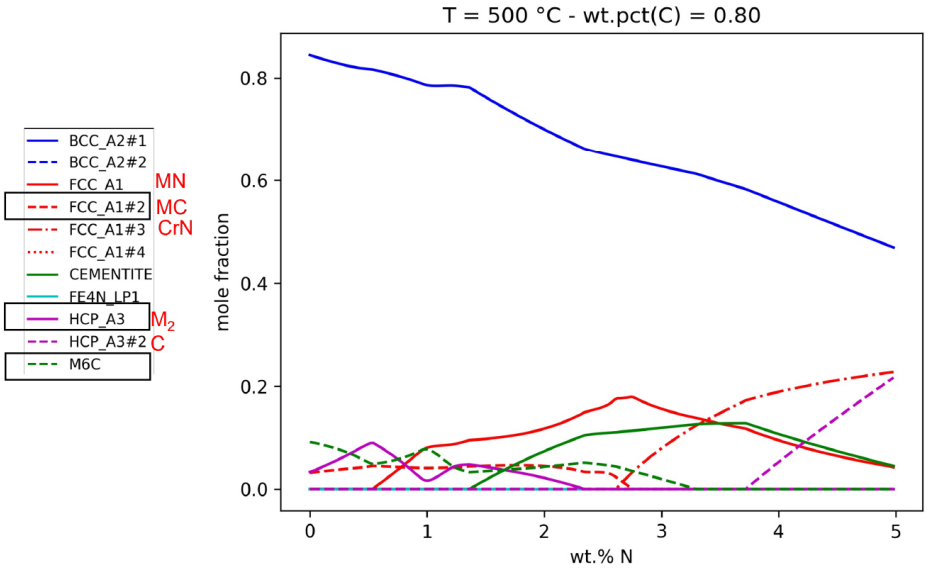


Figure 16 : Diagramme de transformation de phase de l'acier M2 (avec une concentration en carbone de 0,8%) en fonction de la concentration en N à 500 °C

L'analyse est également réalisée à partir de la composition chimique en fonction de la profondeur mesurée par spectroscopie d'émission optique. La Figure 17 montre l'analyse du profil de nitruration de l'échantillon M2 nitruré à 500 °C avec $K_N = 0,8\ atm^{-1/2}$ pendant 15 heures en fonction de la profondeur. Le profil peut être divisé en 4 zones. La zone 1 représente le cœur du matériau où l'azote commence à augmenter. La zone 2 est le front de diffusion de l'azote. Ici, les carbures de type M_6C se décomposent, le carbone libéré s'accumule, puis les carbures de type M_2C augmentent, ce qui provoque l'augmentation des contraintes résiduelles de compression. Dans la zone 3, l'azote continue d'augmenter et la concentration en nitrures augmente, ce qui conduit la contrainte résiduelle à sa valeur maximale. Avec la décomposition des carbures de type M_2C, la phase cémentite commence à se former. Dans la zone 4, les carbures M_2C continuent de diminuer, le carbure M_6C et la cémentite augmentent, et l'azote atteint la valeur maximale. Ces transformations de phase, accompagnées d'une décarburation, diminuent les contraintes résiduelles de compression.

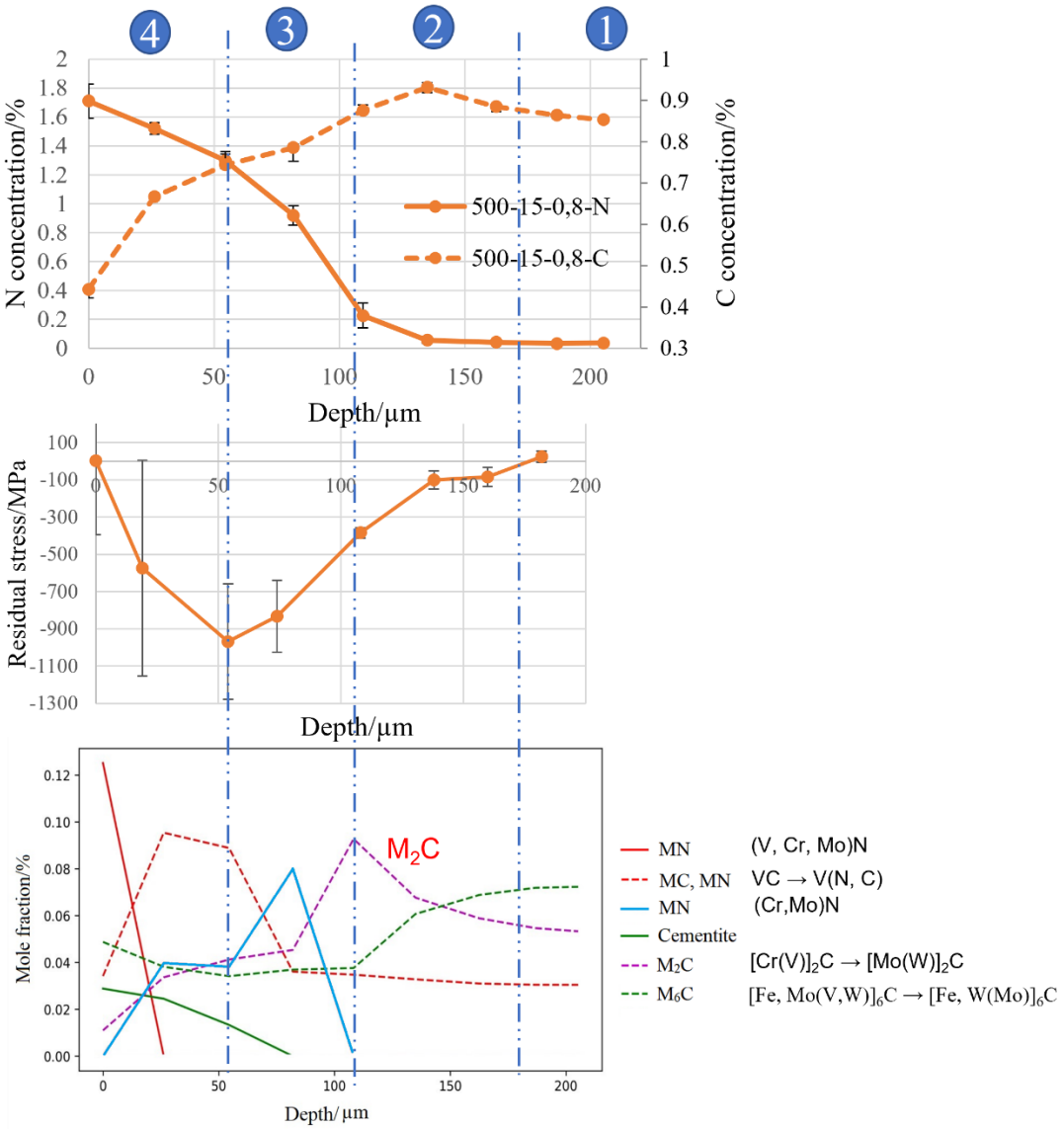


Figure 17 : Composition des phases en fonction de la profondeur de l'échantillon M2 après nitruration à 500 °C avec k_N = 0,8 atm-1/2 pendant 15 heures.

4. Résistance à l'usure des surfaces nitrurées

Un montage bille/disque est utilisé pour la mesure du taux d'usure. La mesure de l'usure est réalisée à l'aide d'un tribomètre, comme le montre la

Figure 18. Le lubrifiant est l'huile utilisée pour le processus de roulage industriel chez LISI Automotive. Les mesures sont effectuées sur un disque en acier M2 avec des billes en saphir pour connaître le comportement à l'usure et de fatigue sous chargement cyclique. Des essais avec des billes M2 sur un disque en acier des pièces EPB sont également appliquées pour étudier le comportement à l'usure par adhésion et pour augmenter la contrainte sur l'acier M2 en localisant la charge.

4.1. Mesures de l'usure sur les disques en acier M2

Les mesures d'usure sont d'abord effectuées sur le disque en acier M2 avec la bille en saphir correspondante (Tableau 1). Les chargements utilisés ont été définis

à partir de l'étude de pièces usées et les résultats de la simulation du processus de roulage. La fréquence de chargement ne change pas le coefficient de friction ou la profondeur des traces d'usure. Cependant, en augmentant la charge, le coefficient de friction diminue de manière significative, et la largeur de la trace d'usure augmente.

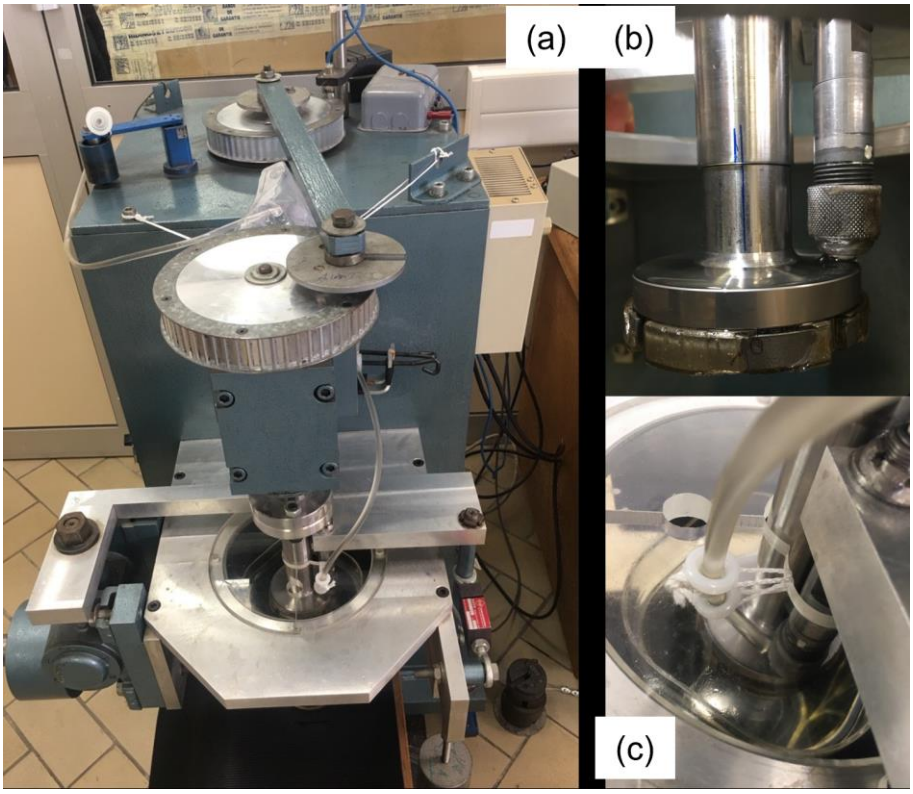


Figure 18 : (a) le montage pour la mesure de l'usure, (b) le contact goupille/disque, (c) le système de lubrification.

Tableau 1 : Mesures d'usure de la bille en saphir/du disque en acier M2.

Mesure	**Charge /N**	P_0 **/MPa**	**Fréquence /Hz**	**Cycles**	**Durée /h**	**Lubrifiant**	**Coefficient de frottement**
SM01	23.4	3000	0,5	7200	4	oil	0.17±0.05
SM02	23.4	3000	1	7200	2	oil	0.172±0.055
SM03	79	4500	1	7200	2	oil	0.067±0.019
SM04	23.4	3000	1	36000	10	oil	0.169±0.058
SM05	79	4500	1	36000	10	oil	0.064±0.017
SM06	23.4	3000	1	7200	2	nothing	0.327±0.071

La largeur d'usure du disque SM05 est plus importante que celle du disque SM04 en raison du niveau de charge plus élevé. Davantage de fissures peuvent être observées. Sur la Figure 19 (b), des microfissures sont initiées au voisinage des carbures. Ce mécanisme est proche de ce qui a été observé sur la crête du filet de la molette. La charge de 79 N est choisie pour continuer la mesure de l'usure sur l'acier M2 nitruré.

Une bonne nitruration pour le filet de la molette doit prendre en compte la dureté, la contrainte résiduelle, la couche de combinaison et la profondeur de la couche durcie. Le profil de dureté entre l'échantillon nitruré et la molette réelle qui a produit le plus de pièces vissées est comparé, le profil de nitruration le plus proche est de 500 °C-0.8 $atm^{-1/2}$-15 h.

Un temps de nitruration court est également souhaité pour des raisons économiques et énergétiques si les profils de nitruration sont également appropriés. Les nitrurations de 5 heures à la même température et au même potentiel de nitruration ont une dureté de surface proche, mais une profondeur de nitruration plus faible. Elles satisfont également les conditions de contraintes résiduelles de compression élevée et d'absence de couche de combinaison. En particulier, les nitrurations de courte durée ont moins d'impact sur la dureté à cœur et la redistribution des contraintes résiduelles. Il est alors possible que 5 heures de nitruration puissent remplacer 15 heures. Il s'agit des couples de paramètres 500 °C-0.8 $atm^{-1/2}$-15 h, 500 °C-0.8 $atm^{-1/2}$-5 h, 520 °C-0.5 $atm^{-1/2}$-15 h, 520 °C-0.5 $atm^{-1/2}$-5 h.

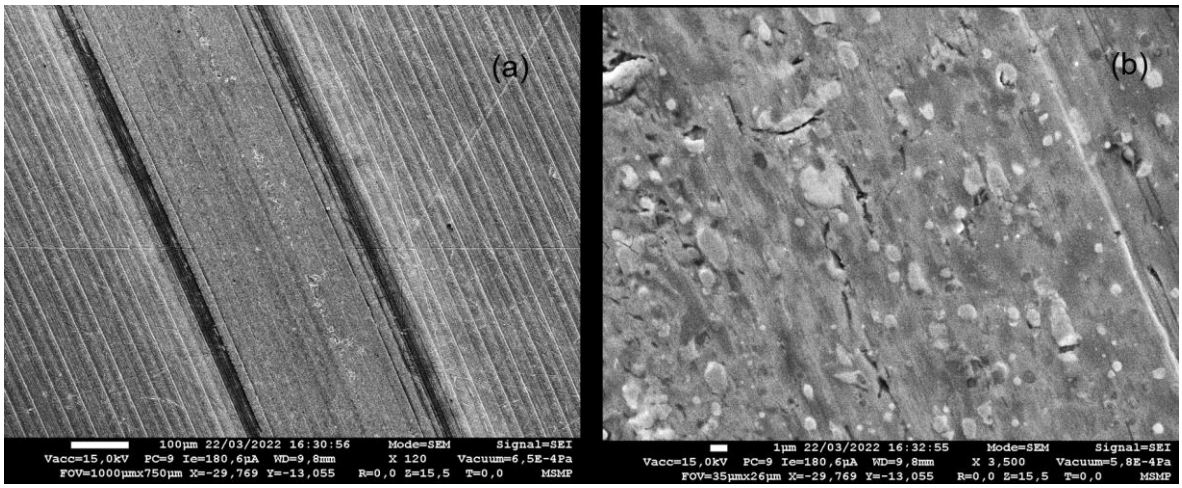


Figure 19 : L'usure du disque M2 après la mesure FM05 (79 N, 1 Hz, 10h).

En raison de la dureté de nitruration élevée et des contraintes résiduelles de compression dus à la nitruration, le taux d'usure est considérablement amélioré, comme le montre la

Figure 20. Le disque M2 de référence (non nitruré) présente une profondeur d'usure d'environ 0,7 µm, alors qu'aucune usure évidente n'a été observée sur les disques nitrurés. Cependant, il est difficile de classer ces quatre paramètres car l'usure est difficilement détectable même avec un stylet du rayon de 2 µm. Ceci est attribué à la dureté de surface de ces quatre échantillons M2 nitrurés qui est à peu près la même, et bien plus élevée que celle de l'acier M2 non nitruré.

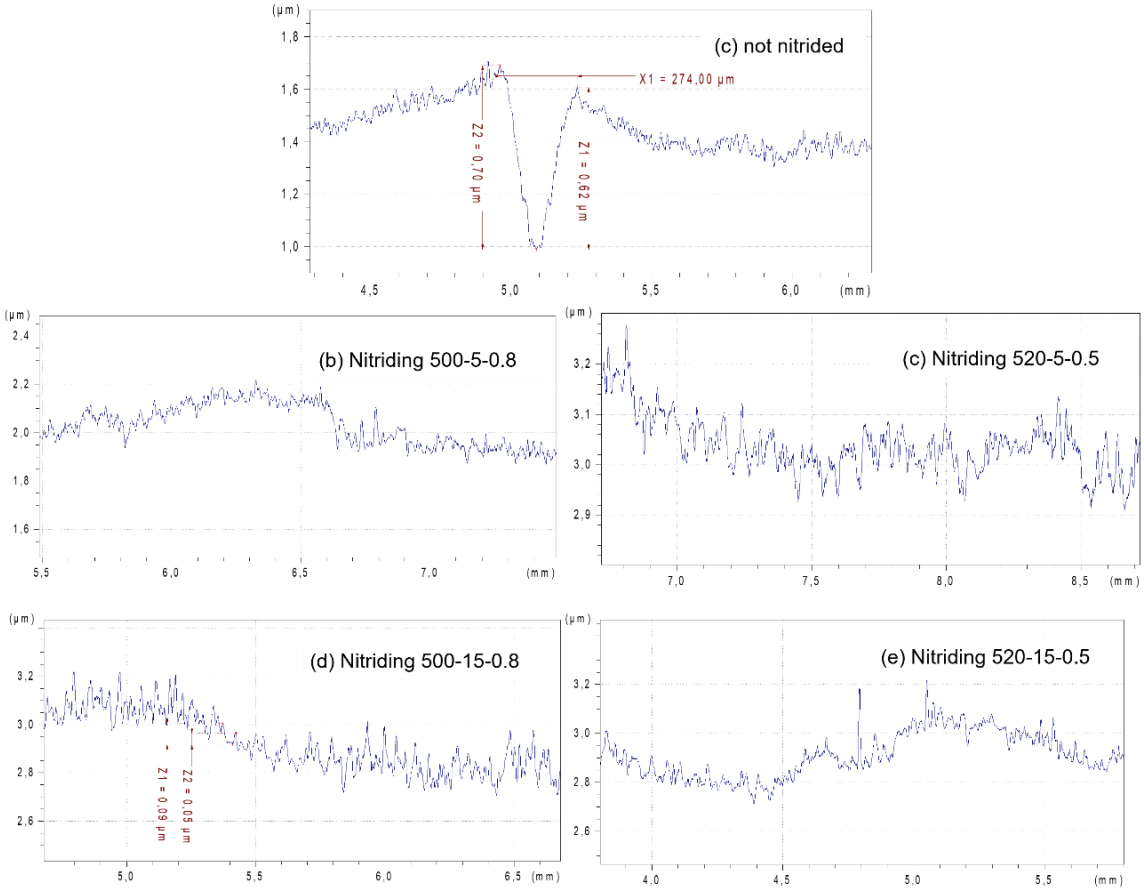


Figure 20 : Les profils d'usure sur les disques M2 (non-nitrurés et nitrurés avec différents paramètres).

4.2. Mesures de l'usure des billes M2 sur disque en acier des pièces EPB

La Figure 21 montre l'usure des billes M2 après les quatre essais réalisés. La zone d'usure est plus grande après un cycle d'usure plus long. Aucune usure significative n'est observée sur la bille usée sous un chargement de 79 N, mais sur celles usées sous une charge plus élevée. Sur la Figure 21, la taille du film de transfert sur la bille usée sous un chargement de 42 N est plus grande que celle sous un chargement de 79 N. La formation d'un film de transfert est une caractéristique de l'usure par adhérence. Le matériau est transféré d'une surface à l'autre avant d'être libéré sous forme de particules d'usure. La bille M2 frotte contre le disque EPB, et l'acier 23MnB6 forme un film de transfert qui finit par recouvrir la piste d'usure (comme le montre la Figure 21), puis la particule de transfert sera éliminée. Il convient de noter que le film de transfert peut être fortement écroui et capable d'user le disque lui-même. La formation d'un film de transfert ou de particules de transfert peut avoir un effet spectaculaire sur le taux d'usure et distingue l'usure par adhérence de la plupart des autres mécanismes d'usure.

L'usure par abrasion est la forme d'usure la plus rapide. La morphologie des inclusions de carbures est déterminante pour la résistance à l'usure par abrasion. Les grandes inclusions lamellaires contribuent davantage à la résistance à

l'abrasion lorsque les grains sont gros, tandis que les petites inclusions sphériques empêchent l'abrasion lorsque les grains sont comparables. La teneur élevée en carbone et en éléments d'alliage confère à l'acier M2 de grandes quantités d'inclusions de carbures durs (carbures de chrome et de molybdène) qui apportent une résistance supplémentaire à l'usure par abrasion. La méthode de base de contrôle de l'usure abrasive consiste à augmenter la dureté de la surface usée.

L'usure par adhérence est une forme d'usure grave qui peut entraîner des taux d'usures élevés et des coefficients de frottement instables. La formation d'un film de transfert est une caractéristique de l'usure par adhésion et la distingue des autres mécanismes d'usure. L'adhérence peut être réduite en augmentant la rugosité ou la dureté de la surface des corps en contact. Sur les billes M2 nitrurées, l'usure par adhérence est à peine observée.

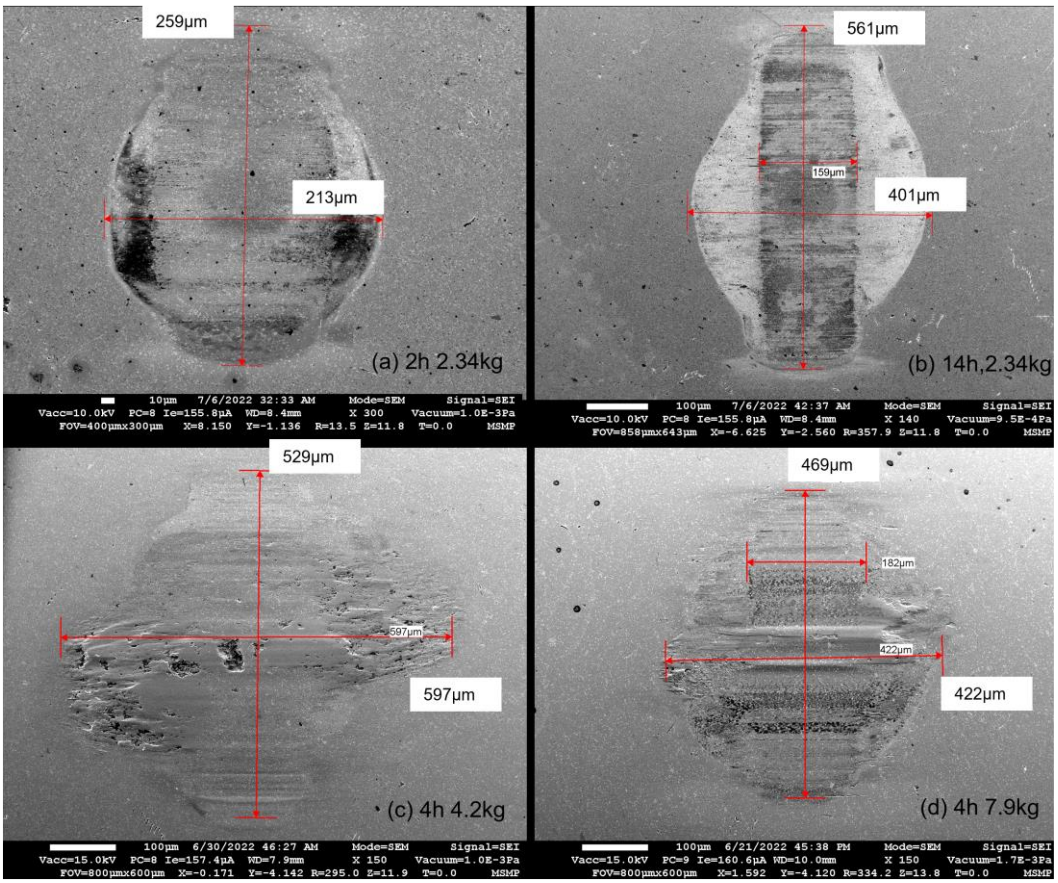


Figure 21 : L'usure sur les billes M2 sous SEM.

Le système bille M2/disque EPB simule le contact réel de ces deux matériaux. Il contribue à observer le comportement d'adhésion et à créer un taux d'usure plus important de l'acier M2. Mais comme le point de contact de la bille est soumis en permanence à une pression élevée, aucun comportement de fatigue n'a pu être étudié. Les résultats montrent que la nitruration gazeuse améliore significativement la résistance adhésive pendant l'usure, augmente le coefficient de friction et réduit la profondeur d'usure de 1,86 à 0,34 µm (Tableau 2).

Tableau 2 : Mesures d'usure sur les billes en acier M2 nitruré.

Mesure	Charge /N	Cycles	Nitruration à billes M2 T(°C)-t(h)-$k_N(atm^{-1/2})$	Coefficient de frottement	Profondeur d'usure/µm
M2EPB02	79	14400		0.049±0.017	1.86
ME500501	79	14400	500-5-0.8	0.058±0.022	0.38
ME520501	79	14400	520-5-0.5	0.066±0.023	0.77
ME500151	79	14400	500-15-0.8	0.053±0.02	0.81
ME520151	79	14400	520-15-0.5	0.058±0.02	0.34

5. Conclusions

5.1. L'étude sur les molettes filetages actuelles

Les molettes de roulage de type E sont fabriquées en acier M2 par coulée. Une forte ségrégation de carbure est présente dans la microstructure. La dureté à cœur des matrices est d'environ 900 HV. La nitruration au plasma de la surface des molettes est non homogène. Les profondeurs de nitruration présentent une grande différence entre chaque matrice. Les molettes de type G sont fabriquées par métallurgie des poudres mais, avec une composition chimique qui s'écarte de l'acier M2. La microstructure est plus homogène et les grains sont plus fins. La nitruration en bain de sel offre aux molettes des couches de nitruration homogènes.

En général, la durée de vie des molettes de roulage augmente avec la dureté maximale de la surface et la profondeur effective de nitruration.

Les fissures commencent à partir de plusieurs micromètres sous la surface. L'initiation des microfissures nécessite souvent une pression de contact, une contrainte de cisaillement élevée et des inclusions (carbures) situées à une position critique en sous couche. Parallèlement, la morphologie des inclusions de carbures est déterminante pour la résistance à l'usure par abrasion.

Le critère Dang Van montre que les défaillances peuvent s'amorcer à partir de la crête du filet dans la dernière période du processus de roulage. La nitruration fonctionne bien près de la surface pour empêcher l'initiation de la rupture par fatigue en raison du niveau de dureté élevé et de la contrainte résiduelle de compression.

5.2. L'étude de la cinétique de nitruration gazeuse de l'acier M2

Les conditions de préparation mécaniques de la surface affectent la cinétique de la nitruration. Par rapport à la rectification et au polissage, la surface sablée gagne le moins d'azote en raison du niveau élevé de contrainte résiduelle de compression avant la nitruration. La surface rectifiée est la plus difficile à nitrurer de manière homogène en raison de la contamination difficile à éliminer due la rugosité particulière de la surface. Les surfaces polies adsorbent plus d'azote que les surfaces sablées. L'effet de la rugosité est considéré mais difficile à prouver car les différentes rugosités sont toujours couplées à différents niveaux de contraintes résiduelles. Les surfaces polies obtiennent facilement des couches de nitruration homogènes car le contaminant est facile à éliminer.

Une température et/ou un potentiel de nitruration plus élevés, peuvent favoriser la cinétique de nitruration, et par conséquent, augmenter la profondeur de nitruration et faire évoluer la contrainte résiduelle de compression plus profondément. Mais les cinétiques de grossissement des précipités et de décarburation sont également accrues.

Le pseudo-diagramme de Lehrer pour l'acier M2 a été mis à jour. La limite de formation de couches de combinaison est trouvée pour la nitruration de l'acier M2 à 500 et 520 °C pour limiter la couche de combinaison qui est de 0,8 et 0,5 atm-1/2, respectivement.

Le profil de dureté est cohérent avec le profil N. La dureté maximale de la couche de nitruration apparaît lorsque la couche de combinaison est formée, et ne continuera pas à augmenter si la nitruration se poursuit, car la concentration maximale en azote est limitée par la composition chimique des nitrures de fer et d'éléments d'alliage.

Le profil des contraintes résiduelles implique la transformation des carbures et la redistribution du carbone, ainsi que l'enrichissement en azote et la précipitation des nitrures. Lorsque les carbures commencent à se décomposer, le carbone s'accumule à une certaine profondeur et, davantage de précipités se forment. L'expansion du volume supplémentaire conduit à la contrainte résiduelle de compression maximale. La diminution de la contrainte résiduelle de compression peut résulter de la décarburation due à la réaction entre le carbone et l'atmosphère, de l'augmentation de la taille des précipités en fonction de la concentration en azote et du temps de nitruration t, ainsi que des transformations de phase qui entraînent une expansion volumique négative (transformations des carbures).

L'augmentation du temps ou de la température de nitruration diminue la dureté du matériau de base.

5.3. L'effet de la nitruration sur le comportement d'usure de l'acier M2

Quatre paramètres de nitruration sont proposés pour l'acier M2 après étude de la cinétique de nitruration. L'étude de leur comportement à l'usure permet de conclure à certains résultats :

Le taux d'usure est fortement influencé par la charge appliquée sur l'axe, mais est moins sensible à la fréquence et au nombre de cycles.

La nitruration gazeuse avec tous les paramètres sélectionnés améliore la résistance à l'usure du disque M2 de 0,7 μm à moins de 0,1 μm, soit environ 85% (dans le système bille saphir/disque M2).

La profondeur d'usure sur la bille M2 nitrurée diminue à 0,34 μm contre 1,86 μm sur la bille M2 non nitrurée (dans le système bille M2/disque 23MnB6).

La nitruration améliore significativement l'usure par adhérence entre l'acier M2 et l'acier 23MnB6 (le matériau de la vis du frein de stationnement électrique étudié dans ce travail).

L'amélioration de la résistance à l'usure après nitruration résulte de l'augmentation de la dureté de surface (le gradient de dureté où le maximum est à la surface) et du niveau élevé de contrainte résiduelle de compression.

La dureté superficielle élevée et le niveau de contrainte résiduelle de compression à la profondeur maximale de la contrainte de cisaillement (55 μm dans le cas du contact entre la bille en saphir et le disque M2 sous une charge de 79 N) sous la surface améliorent la résistance à l'usure de l'acier M2 de manière couplée.

Yanxue ZHANG

Gas nitriding of M2 high-speed steel to improve the surface mechanical properties of rolling die

Abstract

Thread rolling dies made of M2 high-speed steel for manufacturing electronic parking brake screws often face premature in-service failure. Damage and crack initiation occur several micrometers under the die thread surface. It is linked to the high surface rolling contact load, sliding effect and the presence of big carbides. An industrial case analysis using the Dang Van fatigue criterion shows that nitriding improves fatigue strength at the surface layer.

The kinetics of gas nitriding of M2 steel is studied by controlling the parameters. Increasing nitriding potential and temperature accelerate the nitriding process due to the modification of the boundary condition and the thermochemical reaction kinetics, respectively. Gas nitriding is sensitive to the surface condition (cleanness and mechanical finishing).

The hardness gradient in the nitriding layer is generally consistent with the nitrogen concentration gradient, of which the maximum value is at the surface. The residual stress evolution highly depends on the volume change induced by phase transformations during nitriding. It reaches the maximum after the carbon and decreases near the surface.

The limit nitriding potential for the compound layer formation is found to reach the highest surface hardness and avoid the compound layer due to its high brittleness and special microstructure (e.g. porosity).

Nitriding parameters are finally proposed for M2 rolling dies. Wear resistance measurements are designed and carried out. The wear, especially adhesion, is significant on the non-nitrided M2 sample. The selected nitriding parameters effectively improved the wear resistance of M2 steel.

Keywords: Gas nitriding, M2 steel, Residual stresses, Hardness, Wear resistance, Rolling contact failure

Résumé

Les molettes de roulage en acier rapide M2 pour la fabrication de vis de freins de stationnement électriques sont souvent confrontées à une défaillance prématurée en service. Les dommages et l'initiation des fissures se produisent à plusieurs micromètres sous la surface de la denture de la molette en raison de la charge élevée de contact, avec effet de glissement, et par la présence de gros carbures ségrégés. Une analyse de cas industriel utilisant le critère de fatigue de Dang Van montre que la nitruration augmente la résistance à la fatigue en proche surface du matériau.

Les cinétiques de nitruration gazeuse de l'acier M2 sont étudiées avec plusieurs jeux de paramètres. L'augmentation du potentiel de nitruration et de la température de traitement accélèrent le processus de nitruration en raison de la modification des conditions aux limites et de la cinétique de la réaction thermochimique. Le traitement de nitruration gazeuse est sensible à la propreté et à la méthode de finition mécanique de la surface traitée.

Le gradient de dureté dans la couche de nitruration est généralement cohérent avec le gradient de concentration en azote, dont le maximum se situe à la surface. L'évolution des contraintes résiduelles dépend fortement du changement de volume induit par les transformations de phase provoquées par la nitruration. Elles atteignent leur maximum après l'accumulation du carbone et diminue près de la surface.

Le potentiel limite de nitruration pour la formation de la couche de combinaison est identifié pour atteindre la dureté la plus élevée à la surface sans formation de couche de combinaison. Sa grande fragilité et sa morphologie spécifique (comme la porosité) sont des problèmes pour l'application du matériau.

Les paramètres de nitruration sont finalement définis pour les molettes en acier M2. Des essais de résistance à l'usure sont ensuite définies et réalisées.

L'usure, en particulier l'adhérence, est significative sur l'échantillon M2 non nitruré. Les paramètres de nitruration sélectionnés améliorent efficacement la résistance à l'usure de l'acier M2.

Mots-clés : Nitruration gazeuse, Acier M2, Contraintes résiduelles, Dureté, Résistance à l'usure, Fatigue superficiel